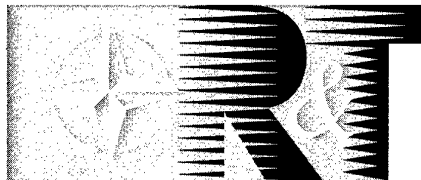


NORTH ATLANTIC TREATY ORGANIZATION



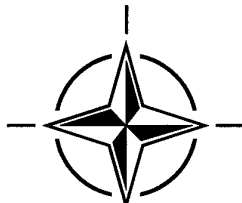
RESEARCH AND TECHNOLOGY ORGANIZATION

BP 25, 7 RUE ANCELLE, F-92201 NEUILLY-SUR-SEINE CEDEX, FRANCE

RTO MEETING PROCEEDINGS 15

**Fluid Dynamics Problems of Vehicles
Operating Near or in the Air-Sea Interface**
(Problèmes de dynamique des fluides des véhicules évoluant
dans ou près de l'interface air-mer)

*Papers presented and discussions recorded at the RTO Applied Vehicle Technology Panel (AVT)
Symposium (organised by the former AGARD Fluid Dynamics Panel), held in Amsterdam, The
Netherlands, 5-8 October 1998.*



19990315 026

DISTRIBUTION STATEMENT A:
Approved for Public Release -
Distribution Unlimited

Published February 1999

Distribution and Availability on Back Cover

The Research and Technology Organization (RTO) of NATO

RTO is the single focus in NATO for Defence Research and Technology activities. Its mission is to conduct and promote cooperative research and information exchange. The objective is to support the development and effective use of national defence research and technology and to meet the military needs of the Alliance, to maintain a technological lead, and to provide advice to NATO and national decision makers. The RTO performs its mission with the support of an extensive network of national experts. It also ensures effective coordination with other NATO bodies involved in R&T activities.

RTO reports both to the Military Committee of NATO and to the Conference of National Armament Directors. It comprises a Research and Technology Board (RTB) as the highest level of national representation and the Research and Technology Agency (RTA), a dedicated staff with its headquarters in Neuilly, near Paris, France. In order to facilitate contacts with the military users and other NATO activities, a small part of the RTA staff is located in NATO Headquarters in Brussels. The Brussels staff also coordinates RTO's cooperation with nations in Middle and Eastern Europe, to which RTO attaches particular importance especially as working together in the field of research is one of the more promising areas of initial cooperation.

The total spectrum of R&T activities is covered by 6 Panels, dealing with:

- SAS Studies, Analysis and Simulation
- SCI Systems Concepts and Integration
- SET Sensors and Electronics Technology
- IST Information Systems Technology
- AVT Applied Vehicle Technology
- HFM Human Factors and Medicine

These Panels are made up of national representatives as well as generally recognised 'world class' scientists. The Panels also provide a communication link to military users and other NATO bodies. RTO's scientific and technological work is carried out by Technical Teams, created for specific activities and with a specific duration. Such Technical Teams can organise workshops, symposia, field trials, lecture series and training courses. An important function of these Technical Teams is to ensure the continuity of the expert networks.

RTO builds upon earlier cooperation in defence research and technology as set-up under the Advisory Group for Aerospace Research and Development (AGARD) and the Defence Research Group (DRG). AGARD and the DRG share common roots in that they were both established at the initiative of Dr Theodore von Kármán, a leading aerospace scientist, who early on recognised the importance of scientific support for the Allied Armed Forces. RTO is capitalising on these common roots in order to provide the Alliance and the NATO nations with a strong scientific and technological basis that will guarantee a solid base for the future.

The content of this publication has been reproduced
directly from material supplied by RTO or the authors.



Printed on recycled paper

Published February 1999

Copyright © RTO/NATO 1999
All Rights Reserved

ISBN 92-837-0004-X



*Printed by Canada Communication Group Inc.
(A St. Joseph Corporation Company)
45 Sacré-Cœur Blvd., Hull (Québec), Canada K1A 0S7*

Fluid Dynamics Problems of Vehicles Operating Near or in the Air-Sea Interface

(RTO MP-15)

Executive Summary

This Symposium concentrated on issues associated with vehicles operating near the sea surface, issues common to aeronautics and hydrodynamics, issues involving air-sea interactions; and on providing the opportunity of bringing together scientists and engineers from Western Europe, North America, Australia, Russia, and Ukraine.

One-third of the papers were authored by scientists from Russia and Ukraine. The two major topics covered during the Symposium included: Aerodynamics around Ships, and Non-Classical Aircraft flying near the air-sea interface i.e. Ekranoplanes. In addition, there were papers on Surface Effect Ships, Ship Stabilization, Hydrofoil Boats, Underwater Missile Launch, and Ship Bow Waves and Water Entry.

Aerodynamics around ships is militarily important because ship superstructures create highly unsteady 3-D flows with massive regions of flow separation behind them, and this situation can create severe problems for the landing of helicopters on the deck. It was very apparent from the presented papers that current means of calculating these flows are developing, but they are currently very limited. Many research opportunities exist involving unstable and separated flows and their simulation.

Several papers covered ground effect aerodynamics, specifically Russian technology in this area, as evidenced by the development of Ekranoplanes. By utilizing ground effect, the gap between slow and inexpensive ships and fast but expensive aircraft can possibly be filled. However, economic studies, which include sea state operability, need to be performed. An innovative means of reducing drag during take-off and thus enabling a reduction in engine power requirements was presented. There were proposals to use Ekranoplanes in a grand air/sea rescue system, and also a proposal for a future Symposium on "Marine Vehicles for Rapid Disaster Response".

For vehicles operating in the air-sea interface, load control and vertical control are very difficult and extraordinarily important. It is necessary to keep vertical accelerations very small, under 1/10th of a G and, therefore, expectations of 1/4 of a G for some Surface Effect Ships and Hydrofoils present a very serious problem. A new implementation of an automated moving weight scheme together with sophisticated fins, which reduced ship motions on an Air Craft Carrier, while ensuring navigational capability, was presented.

The material assembled in this report was prepared under the combined sponsorship of the NATO Partnership for Peace Program, the RTO Applied Vehicles and Technology Panel, the United States Office of Naval Research International Field Office - Europe, and the United States Air Force European Office of Aerospace Research and Development.

Problèmes de dynamique des fluides des véhicules évoluant dans ou près de l'interface air-mer

(RTO MP-15)

Synthèse

Ce symposium a porté essentiellement sur l'exploitation de véhicules évoluant à proximité de la surface de la mer. Il s'agit de questions relevant à la fois de l'aéronautique et de l'hydrodynamique, avec des interactions air-mer. Des scientifiques et des ingénieurs de l'Europe occidentale, de l'Amérique du nord, de l'Australie, de la Russie et de l'Ukraine ont pu être réunis à cette occasion.

Un tiers des communications a été présenté par des scientifiques russes et ukrainiens. Les deux principaux sujets couverts par le symposium comprenaient : l'aérodynamique à proximité des navires et les aéronefs non-conventionnels évoluant à proximité de la surface de la mer, c'est à dire les ekranoplanes. En outre, des communications ont été présentées sur les navires à effet de surface, sur la stabilisation des navires, sur les navires hydroptères, le lancement de missiles à partir de sous-marins, les vagues d'étrave et la pénétration dans l'eau.

Les conditions aérodynamiques à proximité des navires sont d'un grand intérêt militaire, car les superstructures créent, en aval, des écoulements tridimensionnels fortement instationnaires avec des zones de décollement très importantes, ce qui pose parfois de sérieux problèmes pour l'appontage des hélicoptères. Des communications présentées, il est apparu très clairement que des méthodes de calcul de ces écoulements sont en cours de développement mais restent très limitées. De nombreuses possibilités de recherche existent, centrées autour des écoulements instationnaires et décollés et autour de leur simulation.

L'aérodynamique des effets de sol a fait l'objet de nombreuses communications. La technologie russe a bien été mise en évidence avec le développement des ekranoplanes. Par le biais des effets de sol, il se pourrait que l'écart qui existe entre les navires lents mais peu coûteux, et les avions rapides mais chers, puisse être éliminé. Cependant, cela impliquerait la réalisation d'études économiques, entre autres sur la tenue à la mer. Un moyen novateur de réduire la traînée au décollage, permettant ainsi de réduire les besoins en propulsion, a été présenté. Des projets ont également été proposés visant l'utilisation d'ekranoplanes dans un vaste système de sauvetage en mer, ainsi qu'une proposition de symposium sur « les véhicules maritimes pour une réaction rapide en situation de catastrophe ».

Pour les véhicules à proximité de la surface de la mer, le contrôle de la charge et le contrôle vertical sont extrêmement difficiles et importants. Il faut réduire les accélérations verticales au minimum (moins d'un dixième de g) et, par conséquent, les prévisions d'un quart de g, pour certains navires et hydroptères à effets de surface, posent un problème sérieux. Une nouvelle configuration a été présentée, comprenant un système automatisé de poids amovible, comportant des dérives sophistiquées, qui permet de réduire les mouvements d'un porte-avions, tout en conservant l'aptitude à la navigation.

Ce rapport a été élaboré sous l'égide conjointe du Programme OTAN de Partenariat pour la paix, de la Commission RTO de technologies appliquées aux véhicules, du bureau extérieur international - Europe, du Directeurat des États-Unis de la recherche navale, et du Bureau européen de recherche et développement aérospatial de l'armée de l'air américaine.

Contents

	Page
Executive Summary	iii
Synthèse	iv
Recent Publications of the Former Fluid Dynamics Panel	vii
Applied Vehicle Technology Panel Programme Committee	ix
Reference	
Technical Evaluation Report by M.P. Tulin	T
Recent Developments in the Analytical Investigation of Shipboard Rotorcraft Engage and Disengage Operations by E.C. Smith, J.A. Keller and H. Kang	1
CFD Predictions of the Influence of External Airflow on Helicopter Operations when Operating from Ship Flight Decks by N.H. Wakefield, S.J. Newman and P.A. Wilson	2
Higher Order Accurate Solutions of Ship Airwake Flow Fields Using Parallel Computers by L.N. Long, J. Liu and A.V. Modi	3
Simulation and Analysis of LHD Ship Airwake by Navier-Stokes Method by T.C. Tai	4
Prediction of Ship Air Wakes Over Flight Decks using CFD by P. Tattersall, C.M. Albone, M.M. Soliman and C.B. Allen	5
Aerodynamic Perturbations Encountered by a Helicopter Landing on a Ship - Effects on the Helicopter Flight Dynamics by A. Taghizad, Ch. Verbeke and A. Desopper	6
Analysis of Patrol Frigate Air Wakes by S.J. Zan, G.F. Syms and B.T. Cheney	7
Modelling and Simulation of Ship Air Wakes for Helicopter Operations - A Collaborative Venture by C.H. Wilkinson, S.J. Zan, N.E. Gilbert and J.D. Funk	8
The Experience of Aerodynamic Disturbances Research behind an Aircraft-Carrier Ship with Elements for Safe Operation of Ship-Based Aircraft by L.A. Maslov, N.O. Valuev and A.V. Zharinov	9
Simulation Tools in the Calculation of Aircraft-Ship Interface Operational Limits (Application des outils de simulation pour le calcul des limites opérationnelles de l'interface dynamique aéronef-navire) by B. de Ferrier and B. Langlois	10
Piloting of a VTOL-UAV to Shipboard Recovery by C. Reboulet, P. Mouyon, B. de Ferrier and B. Langlois	11
Motions and Added Resistance Due to Waves of Surface Effect Ships by J.C. Moulijn	12

Cobblestone Effect on SES by T. Ulstein and O.M. Faltinsen	13
Heel Compensation for the Charles de Gaulle Aircraft Carrier: Principles and Control Structure by S. Kummer, G. Hardier and C. Lambert	14
New Advances in Sailing Hydrofoils by F. Lefaudeux	15
Unsteady Flow Around a Hydrofoil Beneath Waves by U.P. Bulgarelli, M. Greco, M. Landrini and C. Lugni	16
Hydrodynamic Characteristics of Rudders Operating in Air-Sea Interface by V.T. Savchenko	17
Hydrodynamical Characteristics of an Ekranoplane Wing Flying Near the Wavy Sea Surface by V.G. Byelinskyy and P.I. Zinchuk	18
Theoretical Analysis of Dynamics of a Wig Vehicle and Extreme Ground Effect by K.V. Rozhdestvensky	19
Longitudinal Stability of Ekranoplans and Hydrofoils Ships by V.I. Korolyov	20
Aerodynamic Scheme of Ekranoplane Optimization with Reference to New Areas of Application by A.V. Nebylov and E.Th. Zhigalko	21
Conceptual Bases of WIG Craft Building: Ideas, Reality and Outlooks by E.A. Aframeev	22
Progress Report on Aerodynamic Analysis of a Surface Piercing Hydrofoil-Controlled Wing-In-Ground Effect SEABUS Configuration by C.M. van Beek, B. Oskam and G. Fantacci	23
The First Commercial Ekranoplan "Amphistar" and Prospects for the Development of Passenger Ekranoplans by D.N. Sinitsyn and A.I. Maskalik	24
A View of the Present State of Research in Aero- and Hydrodynamics of Ekranoplans by A.I. Maskalik, K.V. Rozhdestvensky and D.N. Sinitsyn	25
On the Prediction of Nonlinear Free-Surface Flows Past Slender Hulls Using 2D+<i>t</i> Theory: The Evolution of an Idea by E. Fontaine and M.P. Tulin	26
The Complex Boundary Integral Equation Method for a Problem of Entry of a 2D Solid Body in an Incompressible Liquid by D.I. Cherniy	27
Evolution de la bulle de culot et jets rentrants derrière un projectile lancé en immersion by J.B. Paquet, J.P. Flodrops and A. Dymant	28
Undisturbed Motion of Vehicles in the Fluid by Yu.N. Savchenko	29
The Hoverwing Technology-Bridge between WIG and ACV by H. Fischer and K. Matjasic	30
General Discussion	GD

Recent Publications of the Former AGARD Fluid Dynamics Panel

AGARDOGRAPHS (AG)

Turbulent Boundary Layers in Subsonic and Supersonic Flow
AGARD AG-335, July 1996

Computational Aerodynamics Based on the Euler Equations
AGARD AG-325, September 1994

Scale Effects on Aircraft and Weapon Aerodynamics
AGARD AG-323 (E), July 1994

Design and Testing of High-Performance Parachutes
AGARD AG-319, November 1991

Experimental Techniques in the Field of Low Density Aerodynamics
AGARD AG-318 (E), April 1991

Techniques Expérimentales Liées à l'Aérodynamique à Basse Densité
AGARD AG-318 (FR), April 1990

A Survey of Measurements and Measuring Techniques in Rapidly Distorted Compressible Turbulent Boundary Layers
AGARD AG-315, May 1989

REPORTS (R)

Fluid Dynamic Research on Supersonic Aircraft
RTO Report EN-4, November 1998

High Speed Body Motion in Water
AGARD R-827, February 1998

Turbulence in Compressible Flows
AGARD R-819, Special Course Notes, June 1997

Advances in Cryogenic Wind Tunnel Technology
AGARD R-812, Special Course Notes, January 1997

Aerothermodynamics and Propulsion Integration for Hypersonic Vehicles
AGARD R-813, Special Course Notes, October 1996

Parallel Computing in CFD
AGARD R-807, Special Course Notes, October 1995

Optimum Design Methods for Aerodynamics
AGARD R-803, Special Course Notes, November 1994

Missile Aerodynamics
AGARD R-804, Special Course Notes, May 1994

Progress in Transition Modelling
AGARD R-793, Special Course Notes, April 1994

Shock-Wave/Boundary-Layer Interactions in Supersonic and Hypersonic Flows
AGARD R-792, Special Course Notes, August 1993

Unstructured Grid Methods for Advection Dominated Flows
AGARD R-787, Special Course Notes, May 1992

Skin Friction Drag Reduction
AGARD R-786, Special Course Notes, March 1992

Engineering Methods in Aerodynamic Analysis and Design of Aircraft
AGARD R-783, Special Course Notes, January 1992

ADVISORY REPORTS (AR)

A Selection of Test Cases for the Validation of Large-Eddy Simulations of Turbulent Flows
AGARD AR-345, April 1998

Ice Accretion Simulation
AGARD AR-344, Report of WG-20, December 1997

Sonic Nozzles for Mass Flow Measurement and Reference Nozzles for Thrust Verification
AGARD AR-321, Report of WG-19, June 1997

Cooperative Programme on Dynamic Wind Tunnel Experiments for Manoeuvring Aircraft
AGARD AR-305, Report of WG-16, October 1996

Hypersonic Experimental and Computational Capability, Improvement and Validation
AGARD AR-319, Vol. I, Report of WG-18, May 1996

Aerodynamics of 3-D Aircraft Afterbodies
AGARD AR-318, Report of WG-17, September 1995

A Selection of Experimental Test Cases for the Validation of CFD Codes
AGARD AR-303, Vols. I and II, Report of WG-14, August 1994

Quality Assessment for Wind Tunnel Testing
AGARD AR-304, Report of WG-15, July 1994

Air Intakes of High Speed Vehicles
AGARD AR-270, Report of WG-13, September 1991

Appraisal of the Suitability of Turbulence Models in Flow Calculations
AGARD AR-291, Technical Status Review, July 1991

Rotary-Balance Testing for Aircraft Dynamics
AGARD AR-265, Report of WG11, December 1990

Calculation of 3D Separated Turbulent Flows in Boundary Layer Limit
AGARD AR-255, Report of WG10, May 1990

CONFERENCE PROCEEDINGS (CP)

Missile Aerodynamics
RTO Report MP-5, November 1998

Advanced Aerodynamic Measurement Technology
AGARD CP-601, May 1998

Aerodynamics of Wind Tunnel Circuits and Their Components
AGARD CP-585, June 1997

The Characterization & Modification of Wakes from Lifting Vehicles in Fluids
AGARD CP-584, November 1996

Progress and Challenges in CFD Methods and Algorithms
AGARD CP-578, April 1996

Aerodynamics of Store Integration and Separation
AGARD CP-570, February 1996

Aerodynamics and Aeroacoustics of Rotorcraft
AGARD CP-552, August 1995

Application of Direct and Large Eddy Simulation to Transition and Turbulence
AGARD CP-551, December 1994

Wall Interference, Support Interference, and Flow Field Measurements
AGARD CP-535, July 1994

Computational and Experimental Assessment of Jets in Cross Flow
AGARD CP-534, November 1993

High-Lift System Aerodynamics
AGARD CP-515, September 1993

Theoretical and Experimental Methods in Hypersonic Flows
AGARD CP-514, April 1993

Aerodynamic Engine/Airframe Integration for High Performance Aircraft and Missiles
AGARD CP-498, September 1992

Effects of Adverse Weather on Aerodynamics
AGARD CP-496, December 1991

Manoeuvring Aerodynamics
AGARD CP-497, November 1991

Vortex Flow Aerodynamics
AGARD CP-494, July 1991

Missile Aerodynamics
AGARD CP-493, October 1990

Aerodynamics of Combat Aircraft Controls and of Ground Effects
AGARD CP-465, April 1990

Computational Methods for Aerodynamic Design (Inverse) and Optimization
AGARD CP-463, March 1990

Applications of Mesh Generation to Complex 3-D Configurations
AGARD CP-464, March 1990

Fluid Dynamics of Three-Dimensional Turbulent Shear Flows and Transition
AGARD CP-438, April 1989

Applied Vehicle Technology Panel

CHAIRMAN:

Prof. Dr. Horst KÖRNER
Direktor Institut für Entwurfsaerodynamik des DLR e. V.
P.O. Box 3267
D-38022 BRAUNSCHWEIG - GERMANY

PROGRAMME COMMITTEE

Prof. Dr. R. DECUYPERE
Ecole Royale Militaire
30, Avenue de la Renaissance
B-1000 Brussels-Belgium

Prof. Richard J. KIND
Department of Mechanical and
Aerospace Engineering
Carleton University
Ottawa, Ontario K1S 5B6 - Canada

IGA B. MASURE (**Chairman**)
Université d'Orléans
6, rue Eudoxe Marcell
45000 Orléans - France

Dr. Ing. Horst KÖRNER
Direktor Institut fur
Entwurfsaerodynamik der DLR e. V.
Lilienthalplatz 7
D-38108 Braunschweig - Germany

Assoc. Prof. S. TSANGARIS
Dept. of Mechanical Engineering
National Technical University of Athens
P.O. Box 64070
15710 Zografou-Athens - Greece

Prof. C. GOLIA
CIRA
Via Maiorise
81043 CAPUA (CE) - Italy

Prof. Dr. Ir. Jan L. van INGEN
Dept. of Aerospace Engineering
Delft University of Technology
Kluiverweg 1
2629 HS Delft - Netherlands

Prof. Dr. Tor YTREHUS
Division of Applied Mechanics
The Norwegian University of
Science and Technology
N-7034 Trondheim - NTNU - Norway

Prof. A.F. de O. FALCAO
Depart. Engenharia Mecanica
Instituto Superior Tecnico
1096 Lisboa Codex - Portugal

Prof. Javier JIMENEZ
Escuela Technica Superior de
Ingenieros Aeronauticos
Departamento de Mecanica de Fluidos
Plaza del Cardenal Cisneros 3
28040 Madrid - Spain

Prof. Dr. Cahit ÇIRAY
Aeronautical Eng. Department
Middle East Technical University
Inono Bulvari PK: 06531
Ankara - Turkey

Mr. David A. LOVELL
Research Manager Applied Aerodyn.
Aero/Structures Dept
X80 Building
Defence Research Agency
Farnborough Hants GU14 6TD - United Kingdom

Dr. L. Patrick. PURTELL (**Deputy Chairman**)
Program Officer - Mechanics and
Energy Conversion Division
Code 333 - Office of Naval Research
800 North Quincy Street
Arlington, VA 22217-5660 - United States

PANEL EXECUTIVE

Mr. J.K. MOLLOY

Mail from Europe:

R.T.A.
BP 25, 7, Rue Ancelle
F-92201 Neuilly-sur-Seine Cedex
France

Mail from USA and Canada:

R.T.A./NATO
Unit PSC 116
APO AE 09777

Tel: 33 (1) 55 61 22 75
Fax: 33 (1) 55 61 22 98

Technical Evaluation Report
Applied Vehicle Technology Panel Symposium on
Fluid Dynamics Problems of Vehicles
Operating Near or in the Air-Sea Interface

Professor Marshall P. Tulin
 Director, Ocean Engineering Laboratory
 University of California
 Santa Barbara, CA93106-1080 USA
 email: mpt@vortex.ucsb.edu

1 Introduction

This Symposium, organized by an international program committee under the Chairmanship of IGA Bernard Masure (Orleans, France), "concentrated on fluid dynamic issues associated with vehicles operating near the sea surface." There was an emphasis on technologies which spanned the interface itself, combining aerodynamic and hydrodynamic phenomena, and which are therefore, "not traditionally covered by conferences on either aeronautics or naval hydrodynamics." Specific well-covered examples of the latter technologies, permitting a good evaluation, were:

- (A) Aerodynamics around ships (10 papers)
- (B) Non-classical aircraft flying near the air-sea interface; i.e. Ekranoplanes(11 papers)

There were, in addition, papers on a variety of other technologies lightly covered (C):

- Surface effect ships (2 papers)
- Ship stabilization (2 papers)
- Hydrofoil boats (2 papers)
- Underwater missile launch (1)
- Ship bow waves, and water entry (2)
- Miscellaneous (2)

The meeting brought together about 125 engineers and scientists from 16 countries, 14 in Europe plus the US and Canada. There was a very good representation from ship research as well as from aeronautical research almost equally divided between the two fields. In this respect the meeting was most unusual, and the Chairman, B. Masure, and his other organizers and the Dutch hosts are to be congratulated for bringing about this difficult fusion as they have in such a pleasant and effective venue.

An important and significant feature of this Symposium was the very active participation of Russian engineers and scientists from Moscow (TsAGI), Nizhny-Novgorod (Technologies Transport JSC), and St. Petersburg, and Ukrainians from Kiev. In particular, the Russian participation allowed a very good view of their important and even remarkable development of Ekranoplane (ground effect) vehicles.

The general theme of this symposium, in addition to the statements made in the first paragraph above, can be summed up as, Aerodynamics meets Hydrodynamics at the Sea Interface. In view of the military and commercial importance of operation at the interface, the organizers are to be thanked for addressing this theme.

It is to be understood that the two major topics covered A & B above, were chosen: (A)

because of the military importance of the mating of helicopters and small naval combatants like frigates, and because of the complexity of the aerodynamics behind the ships structure approaching the deck, and (B) because of the military and commercial interest in the potential of wind in ground effect vehicles, so-called Ekranoplanes. The Scope of technical coverage of these two subjects was certainly sufficiently broad and the presenters sufficiently expert to permit in the case of (A) an assessment of the overall problem and an understanding of the complex fluid dynamics involved and the state of present research, and in the case of (B) an overview of actual vehicle development, especially in Russia, a good view of the evolution of thinking and techniques, and a fair view of detailed aerodynamic problems, especially related to stability and control.

It seemed entirely appropriate to include together with the mainly aerodynamic considerations mentioned above, a section on hydrodynamic aspects with a close connection to aeronautics. These were included in (C) and listed earlier. Many of these have a clear and immediate connection with aeronautics and its techniques, as in the paper on underwater missile launch or on hydrofoil boats. It is apparent that the lightness of the coverage of the items under (C) do not permit a reasonable evaluation of those subjects.

2 Aerodynamics Around Ships

This main sector of the meeting has focussed on the modelling and simulation of ship air wakes for helicopter operations. Research in this field is largely carried out as part of an international cooperative program (TTCP) involving four nations: the UK, Canada, Australia and the USA. A very good reportage from participants in the TTCP was presented, including a Summary of the history, role, and present status of the subject (Paper #9). This paper is extremely important for anyone interested in this subject at this time.

The flow around ships is induced both by their forward motion, their seaway induced motions, and by winds near the sea surface. The shape of the ship itself, and particularly its superstructure leads to highly unsteady flows character-

ized by massive regions of flow separation and large unsteady vortical patterns. It is clear that these flows create problems for helicopter operations, especially from small ships like frigates, and they do in fact limit helicopter operations in stormy weather. Problems must also arise in heavy wind operations from commercial ocean structures like drilling platforms, although these were not discussed at this Symposium.

The training of military helicopter pilots through the use of flight simulators requires an accurate simulation of the atmospheric environment and this requires effective modeling of the ship's wake and especially near the landing deck, which is usually located behind the superstructure, a particularly noisy place to operate. As stated in Paper # 9, "An air wake model of appropriate fidelity is...an essential element of a training simulation." From a longer range point of view, it is clear that effective simulation of these complex flows could also lead to improvement in the wake characteristics through careful alterations in the design of superstructures. In this connection, Russian (TsAGI) work on the full scale installation of vortex control devices at the forward end of aircraft carrier decks is very noteworthy; it is discussed later here.

An air wake model for simulator use could be derived in principal from either full scale or wind tunnel observations and measurements, or from computer simulations (CFD). Each poses its own difficulties. Full scale measurements are difficult and costly to obtain and the conditions cannot be repeated or called up at will; it was recounted in Paper # 9 that Australian attempts at full scale measurements in 1989 on a frigate failed because of "benign" wind conditions during much of the test; it is remarkable how often this kind of difficulty arises during field work at sea. Extensive wind tunnel experiments have been conducted in the UK and in Canada and limited model-scale tests "are also conducted on each new ship entering service." Further tests have been conducted in the US. So a wind tunnel data base is growing.

A variety of serious efforts have been made at numerical simulations of these flows, which involve unstable shear regions leading to large unsteady vortical structures of distinctly three dimensional character. These originate from all of the bluff body features above the deck. Finally, behind the last large deck structure before the tanking area a large separated flow region forms

of finite length, no doubt partially stabilized by the presence of the horizontal landing deck surface. The simulation is complicated by uncertainties in the wind field over the ocean, which is unsteady and effected by atmospheric stratification. A further complication arises from uncertainties due to the motion of the ship in a seaway.

Finally, the action of the helicopter rotor itself can have a large influence on the deck flow and vice versa, as the rotor induces substantial velocities directed downwards over an area often not very much larger than the helicopter. Most of the simulations were made in the absence of the rotor flow and these are first discussed below.

How effective is the state of the art in CFD simulation for these turbulent flows? Five papers reflect on this question (#2, 3, 5, 6, 8 and 9). A major limitation at this time is that current RANS codes (Reynolds averaged Navier Stokes) are constituted to handle steady, i.e. mean flows only. How well do these RANS code simulate mean flows? How well do they compare with each other? The latter question cannot be answered at all since comparisons were not made, although similar separated region topology can be seen among several papers. The former question can be answered only roughly. In #3, oil flow streaklines on deck are compared with flow vector simulations in a qualitatively favorable way. In #8 favorable comparisons of the topology of the aft deck separation region are made. However, it was noted that the measured shear regions were much heavier than in the simulations. **It is recommended that priority be given to careful comparisons between the numerical results of different research groups and with the results of a benchmark experiment.** This has proved effective in other applications, as for instance in the calculation of ship stern flows. Finally, it is possible, as mentioned by one of the authors, that the RANS codes are insufficient for these separated flows and that large eddy simulation or other more sophisticated approaches are necessary.

The possibility of extending the RANS mean flow calculation to the simulation of unsteady components was discussed in #3. This involved the solution of the so-called non linear disturbance equations, (NLDE), for the unsteady flow as driven by a known mean flow (RANS). The unsteady flow depends upon initial disturbances

which must be imposed. Calculated velocity perturbations around a deck structure were shown, but no comparisons with experiments were made; in these calculations, the viscous driving terms were neglected. This approach to unsteady simulation seems worthwhile, although the influence of the initial disturbances is very worrisome. In these calculations, wind turbulence was used to drive the unsteady deck flow. However, it seems highly unlikely that the deck flow unsteadiness is, in essence, controlled by wind turbulence. As in the Karman vortex strut, it seems likely that an inherent instability of the shear flows produced by separation from the deck structure reaches some equilibrium quasi-oscillatory state through the balance of non-linear processes, with little effect from small ambient disturbances.

One of the most interesting approaches to unsteady separated flow calculation, paper #6, involved the use of the incompressible Euler equations, allowing for the distortion and propagation of vorticity fields, once created, in the absence of viscosity. In this connection we can think of the simulation of vortex sheet roll-up by inviscid theory, or of von Karman's prediction of vortex street geometry by an inviscid analysis of stability. In the present case, the question arises as to the origin of the vorticity which appears behind the deck structures. In the absence of viscous boundary layers here, the vorticity which presumably appears here in the form of shear layers at separation points must be an artifice of the numerical calculation, and must presumably depend upon the roundness of the corners where separation occurs, the grid size, and the numerical scheme. It is nevertheless a most interesting phenomena and one to be taken advantage of, as was done here. Once created, the distortion and propagation of the inviscid vorticity field will occur according to the Euler equations. It is not surprising that highly unsteady flows appear once vorticity is introduced at separation points, since vortex sheets tend to be inherently unstable. The interesting question occurs as to the connection between these unstable, inviscid, vortical fields and the real flow fields with viscosity. In simple separated wakes at high Reynolds number it is known that the length of the separated flow behind the body depends on Reynolds stresses acting on the boundary of the separation cavity, and the success of an inviscid simulation would

therefore depend on the inviscid simulation of these stresses. These questions concerning inviscid simulations deserve careful study in view of the potential value which lies in this approach.

Two papers (#2, 6) showed techniques for including the effect of rotor action on the flow fields and vice versa. One of these (#6) showed the strong effect of the rotor and helicopter fuselage in modifying the separation regions behind the deckhouse. These studies both create the incentive for including the helicopter action in future simulations and show the way to do this.

The bottom line regarding computer simulations is that qualitative pictures and effects are reproduced, but the degree of accuracy has not yet been established. It seems very likely, considering the fluid dynamic complexities here, that highly accurate numerical simulations lie some distance in the future. This stresses the importance of detailed wind tunnel measurements, which certainly seem feasible and capable of providing the information needed by the training simulators.

It is to be noted that none of the helicopter-related papers on ship wake flows were concerned with modification of the deck structures to control the flow and thereby improve the engage-disengage environment. Here one can think in terms of the modification of sharp corners on the aft of the deck structure or of reshaping it at the rear; here automotive know-how would be very instructive.

In the above connection, a very interesting Russian paper from TsAGI is to be noted (#11); it concerned "provision of aerodynamic capability of ship-based aircraft and carrier," whose "aim was design and realization of measures of reduction of (wind flow deck) disturbances and ... gradients up to level required for take off landing operation safety." In the first step, the origin and trajectory of large rolled up vortices were determined; these largely originated from the lateral edge of the main deck, the sponson, and the island structure. Recommendations resulted: for decrease of the island aspect ratio and its relative width, and to move it forward; for the inclusion of flat and curved path deflectors and suitable fairings on the deck and sponson edges. These innovative approaches deserve detailed attention.

3 What Price Speed? Ekranoplanes

The real transport efficiency of ships decreases with increasing speed beyond some optimum speed which is determined by the balance between fuel and fixed cost including amortization of both ship and cargo. At this time, the optimum speed is in the range of 20-35 kts, and the transport efficiencies are much higher than those of modern aircraft. Of course, there is a premium to be paid for speed in the case of very valuable cargos or those whose value decreases with time. Therefore people and mail are carried long distances by aircraft, while oil and automobiles, etc. are carried by large ships at less than 1/10 the speed, but at considerably reduced cost.

For speed in water over about 50 kts severe new problems arise. These have led to alternative vehicles beyond the simple monohull displacement ships: planing hulls, catamarans, hydrofoil boats, and surface effect ships (SES). The boldest projections of feasible speeds that could be achieved in regular practice by any of these marine vehicles does not exceed 100 kts., and the feasible hydrodynamic efficiencies do not exceed those of a large modern aircraft; structural weights in the water also tend to be high.

It has for at least 70 years been known, that the induced resistance of a wing decreases continuously as it approaches the ground; the so called ground effect. As a result, when a wing is optimized in ground effect, its aspect ratio (span/chord) decreases, and its lift coefficient increase relative to flight at altitude. This held forth the theoretical possibility of ground effect wings of smaller area and span, and higher efficiencies than conventional optimized aircraft at the same speed.

The gifted Russian hydrofoil boat designer, Rostislav Alexeev from Gorki, began in the 1960's the development of large vehicles of 120-550t based in the ground effect, which he called Ekranoplanes. These were, however, not developed with commercial use foremost in mind, but at the order of the Russian Navy for presumed amphibious use. The earliest open technical publication on the subject may be a paper by P.E.Kumar on "Some Stability Problems of Ground Effect Vehicles in Forward Motion," Aeronautical Quarterly, vol. XVII, Feb. 1972.

At the present time, given the reality of a va-

riety of Russian vehicles as well as some others abroad, coupled with a high current interest in increasing the speed of marine vehicles, there seems a high interest in Ekranoplanes, and their future. For example, the list of References in paper #30 refers to a variety of relevant conferences in the last ten years.

The papers presented here, notably but not only the Russian contributions offer a good opportunity for an evaluation, and particularly #32 (a review of the present state of research), and #29 (an objective and critical look at technical performance and possibilities by E.A. Aframeev from St. Petersburg).

Did the Ekranoplanes in actual practice realize an improvement in the aerodynamic efficiency (L/D) of modern aircraft? The answer is **no improvement**, only **similar performance**, depending on the degrading effect of increasing sea states, Fig. 1 of #29. In some other performance aspects however the Ekranoplane is **quite inferior**: payload efficiency, thrust/weight requirements, and structural weight of both hull and wing, see figures 4, 5, 8 of #29. The main reason for this inferiority lies in requirements arising from marine operation, for instance the necessity to augment take-off and to provide for water loads.

Can present performance shortcomings be overcome? The Russians had augmented lift for take-off by diverting the engine jet to stagnate underneath to wind. In paper #30, progress on a hybrid hydrofoil-Ekranoplane was described. The prognosis does not sound good as it was stated that "the resulting operational efficiencies puts this vehicle in the helicopter class." This is not surprising as structurally and seaway effective hydrofoils at speeds over 100 kts will have efficiencies for below those of wings in air. A more promising approach to improve take-off is being taken by Fisher-Flugmechanic, paper #37, who propose to use the propellers to pump air underneath the wind and seal it partially underneath with a hovercraft type bag-seal which can be retracted after take-off. They call this vehicle a Hoverwing. A hybrid hovercraft-Ekranoplane results. In terms of performance, paper #37 shows higher thrust weight ratios for WIGS (Ekranoplanes), at between 4 and 5, then Aframeev in #29, between 3 and 4, and Fisher projects a value of about 7 for his Hoverwing-80, of which a model is already flying. This value would be substantially in excess

of the best aircraft figure, 5, shown by Aframeev, Fig. 8 of #29. Of course, actual values must take into account the necessity of operation in reasonable seaways.

Do special missions exist fitting the technical strength of the Ekranoplane, which is to operate near the sea at speeds up to 400 km/h and in weights up to, perhaps, 1000 t? The use of Ekranoplanes to provide a launching and landing base for reuseable aerospace planes or Space Shuttles was discussed in paper #27. The requirement of high launch payload (600 t) and high speed (220 m/sec) could, they suggested be carried out by a large Ekranoplane.

A clearcut vision for the future development of Ekranoplanes was provided by E.A. Aframeev from the Kylov Shipbuilding Research Institute, paper #29. He discounted competition with aircraft which seem, if anything, technically superior to the Ekranoplane. He stressed the ability of the latter to operate in **two-modes** both as a ship **and** as an airplane. He therefore proposed a new direction of development in which large Ekranoplanes would be designed for full and sustained marine operation at cruising speeds up to, say, 15 kts, and flight speeds of, say 250 kts in seas up to 3.5 m significant wave height. Loaded weight of 750 t and payload of 250-300 t with a range of 3-4000 km were projected. For this two-mode vehicle he imagines use for commercial passenger and cargo transportation, including car-passenger ferries, rescue, and tourism (perhaps, cruise ships). He stressed a special application to create a global international sea rescue system. **This idea and this paper deserve careful study.** At minimum, Aframeev has provided what seems to be a critical evaluation of Russian Ekranoplane technical performance, as already touched upon in preceding paragraphs.

The systematic technical development of Ekranoplane aerodynamics was carried out following their introduction in the 70's. Considering the high degree of stability required, it is not surprising that stability in ground effect has been intensively studied. This is briefly reviewed in #32, and a more detailed asymptotic analysis is presented by Kiril Rozhdestvesky of St. Petersburg in paper #22. Fortunately, a high degree of longitudinal and lateral stability seems obtainable through the application of known results; indeed, this makes the Ekranoplane feasible. It is particularly fascinating that a par-

ticular airfoil shape (S shaped camber) allows stability without a tail surface; this was mentioned by both Rozhdestvensky and Fisher but is not documented in the written papers. Finally, the relative role of the upper and lower surfaces in providing lift and stability are most important and interesting. In paper #30, the wing investigated at the NLR in the Netherlands shows a thick foil (thickness/chord about 20%) with maximum thickness far forward and with a flat bottom and trailing edge flap, Fig. 7; this foil develops substantial negative pressures on its upper surface over the "bump" there, and it seems remarkable that the upper surface pressure distribution is almost unchanged in and out of ground effect. On the other hand, "when a wing flies very close to an underlying surface, the prevailing contribution to its aerodynamics comes from the *channel flow* underneath." This, of course, simplifies design and analysis.

Waves inevitably play a large role in determining the design and inevitably degrading the performance of marine interface vehicles; for example, main shortcomings of the Ekranoplane (paper #29, section 3.2) include "the complexity of take off, particularly at rough sea, the necessity for qualified pilot team and their constant training." Other authors also mentioned the high mean vertical accelerations during flight over waves. It was therefore welcome to see data on wing performance as effected by flight over waves, paper #21 from Kiev, including extensive data on smooth sea performance, too. The most important aspect of these data are the fluctuations in vertical force due to flight over waves, from which the seaway induced vertical accelerations may be deduced. Since human tolerance to sustained mean accelerations is limited to about 0.10 g, limitations on performance in a seaway are implied. This has always been a serious problem for hydrofoil craft and led to the adoption in the US of fully submersible controllable foils. A monograph (in Russian) exists on the dynamic control of Ekranoplanes, including a brief history which was published in St. Petersburg in 1994; the author is A.V. Nebylov.

Finally, a very upbeat presentation was made by H. Fisher, paper #37, describing the development of Ekranoplane vehicles, utilizing hovercraft ideas for take-off, as mentioned earlier. High performance was promised for a 100 kt vehicle for the transport of 80 passengers. Should this development succeed, the prospect for pas-

senger and car transport in ground effect will be very much brightened.

4 Other Interface Vehicles and Problems

A variety of isolated papers on SES vehicles, hydrofoils, ship control, missile water exit, and special problems in interface hydrodynamics were presented. These contributed to the breadth, balance, and interest of the Symposium, without allowing for evaluations of the subjects involved. A paper, #15, on SES accelerations (the cobblestone effect) due to dynamic compression of the air cushion by waves illustrated again the problems of comfort associated with operation in a seaway. A number of the papers presented interesting hydrodynamic phenomena and ideas, #35 and #36, and #33 presented a review of an important emerging technique for the simulation of certain high speed non-linear features at the interface.

5 Concluding Remarks

The Symposium was highly successful in that it gathered together experts from both aerodynamics and hydrodynamics, in almost equal number, to discuss interface operations.

Helicopter-ship mating poses severe problems requiring accurate simulation. Further research on the aerodynamics around and behind ship superstructures is necessary, both theoretical, numerical, and experimental, as are validation of numerical results. Systematic wind tunnel data bases are desirable. Further fundamental research on unsteady three dimensional separated flows and its application would be helpful.

The participation of a substantial Russian delegation made possible a good review of the status of the Ekranoplane. Technical performance exceeding that of aircraft has **not** so far been achieved. Emphasis was put on equal development of both hull borne and wing borne operation (joint mode) for special applications as global marine disaster response.

Other subjects such as SES, hydrofoils, missile water exit were briefly treated; further attention to interface vehicles and their technical problems by this Panel would certainly seem warrented.

RECENT DEVELOPMENTS IN THE ANALYTICAL INVESTIGATION OF SHIPBOARD ROTORCRAFT ENGAGE AND DISENGAGE OPERATIONS

Edward C. Smith*, Jonathan A. Keller†, and Hao Kang‡

*Department of Aerospace Engineering
The Pennsylvania State University
University Park, PA 16802-1401*

This paper presents an overview of recent developments in an effort to predict transient aeroelastic rotor response during shipboard engage and disengage sequences. The blade is modeled as an elastic beam undergoing deflections in flap, lag, extension and torsion. The blade equations of motion are formulated using Hamilton's principle and they are spatially discretized using the finite element method. The discretized blade equations of motion are integrated for a specified rotor speed run-up or run-down profile. Blade element theory is used to calculate quasi-steady or unsteady aerodynamic loads in linear and nonlinear regimes. The analysis is capable of simulating both articulated, hingeless, and gimbaled rotor systems. Validation of the rotor code is discussed, including correlation with droop stop impact tests and wind tunnel experiments. Predictions of safe engagement and disengagement envelopes, limited by excessive blade tip deflections or hub moments, are presented. Future directions of study are also discussed.

Introduction

THIS paper presents an overview of the research that has been conducted at Penn State University since 1995 to predict the transient aeroelastic response of rotors during shipboard engage and disengage operations. Unique and often hazardous conditions are encountered when rotorcraft are operated from ship based platforms. One troublesome rotorcraft/ship interface problem can occur during the engagement and disengagement of the rotor system while the aircraft is on the flight deck. In this low rotor speed region, the centrifugal stiffening is low but aerodynamic forces may be large, particularly in high wind and sea states. Excessive aeroelastic flapping due can be the result. This problem often limits the safe operating envelope for the rotorcraft and can severely restrict flight operations at sea.

For articulated rotor systems, the rotor blade can deflect several feet and contact the fuselage of the helicopter, resulting in a "tunnel strike" in tandem rotor configurations; or the tailboom, resulting in a "tailboom strike" in single rotor configurations. The H-46 Sea Knight, a tandem rotor helicopter used by the U.S. Navy and Marines, has encountered over 100 tunnel strikes since 1964 and still occasionally experiences

them. Most tunnel strikes cause minor damage such as denting or tearing the synchronization shaft cover or cracking the synchronization shaft mounts. Major damage involves severing the synchronization shaft, blade failure, or droop stop failure.

For gimbaled rotor systems, such as the V-22 Osprey tiltrotor, the entire hub can tilt and can contact the gimbal restraint, resulting in high loads on the gimbal spring and hub component. Potentially, these loads could be much larger than the peak design loads.

Shipboard engage and disengage behavior has been the subject of much research at the University of Southampton¹⁻⁶. The transient blade response was investigated using a flapwise elastic rotor code for a hingeless rotor system using analytic run-up and run-down rotor speed time histories and quasi-steady aerodynamics, including a trailing edge separation model. The ship airwake environment included ship roll motion effects on wind and simple deterministic gusts which were developed from model scale wind tunnel surveys correlated with full scale ship airwake data. The aerodynamic model was later improved by including flap-torsion coupling and the deterministic gust model was correlated with additional wind tunnel experiments. The

*Associate Professor, Member AIAA, AHS.

†Rotorcraft Fellow, Student Member AIAA, AHS.

‡Visiting Scholar, Nanjing University of Aeronautics and Astronautics

elastic flap code was modified to model articulated rotor systems in which blade motion is constrained from excessive upward and downward flapping motion by mechanical flap and droop stops. Recent studies were conducted to validate the rotor analysis in which a model rotor system with rigid, teetering blades was placed aboard a scaled ship deck and tested in a wind tunnel. The influence of the ship's airwake was proven to be very important to the blade's behavior.

Overview of Previous Research

RESEARCHERS at Penn State University, in conjunction with the US Navy, have also been developing simulation tools to predict transient aeroelastic rotor response during shipboard engage/disengage operations⁷⁻¹⁰. This research differs from the efforts in Refs. 1-6 in several ways. The rotor model included both flap and torsion elastic blade motions with Bernoulli-Euler beam bending theory. Using the finite element method, radial variations in elastic, inertial, and aerodynamic properties are easily accommodated; and different hub types are modeled with greater ease. Either a quasi-steady or a time domain unsteady aerodynamic model based on indicial response is used to calculate airloads in the attached flow, nonlinear separation and dynamic stall regimes. Experimentally measured rotor run-up and rundown rotor speed time histories were employed in the prediction of the transient blade response. As an example, the measured rotor speed run-up profile for the H-46 Sea Knight can be seen in Figure 1.

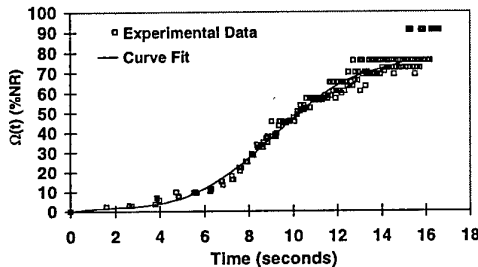


Figure 1: Measured H-46 Rotor Speed Run-up Profile

Given a ship airwake environment, the blade equations of motion were integrated in either physical or modal space using a fourth order Runge-Kutta integrator to solve for the transient aeroelastic response.

The assumptions in the original analysis in Refs. 7-10 included that: the total rotor thrust is close to zero which precludes the need for inflow and ground effect models; gravity forces are necessary since the blade operates at low rotor speeds; ship motion effects on blade inertial loads are negligible due to low ship motion frequencies relative to the rotor frequency; and lead-lag degrees of freedom are neglected because the portion of the engage/disengage sequence in which the majority of tunnel strikes occur is where $\Omega(t)$ is less than 20% of Ω_0 . In this region Coriolis forces are small. However, axial and lag degrees of freedom have since been added to the analysis and are detailed in Ref. 17.

Quasi-steady airloads, including noncirculatory effects and either linear or nonlinear separation using a Kirchoff model can be predicted. In addition, unsteady aerodynamic loads, including attached flow, unsteady trailing edge separation, and dynamic stall effects can be included.

The following sections will give a brief introduction to the analytical development of the helicopter structural and aerodynamic model, examples of validation of the model with experimental data, and examples of the parametric studies conducted to date. For example, the effects of collective and cyclic control settings, droop stop angle, and ship motion on blade response were investigated⁷⁻¹⁰. A preliminary study of the effectiveness of a flap damper in reducing tip deflections was also conducted^{9,10}. The importance of torsion and unsteady aerodynamics to the simulation of the blade response was also determined^{9,10}.

Engagement and Disengagement Analysis

I. Structural Model Formulation

The partial differential equations governing blade motion are derived using the generalized Hamilton's Principle

$$\delta\Pi = \int_{t_i}^{t_f} (\delta T - \delta U + \delta W) dt = 0 \quad (1)$$

where δT is the variation of kinetic energy, δU is the variation of strain energy, and δW is the virtual work due to external forces. Detailed formulations of all terms are presented in Ref. 7. The variation of strain energy and virtual work are composed of aerodynamic forces, gravity forces, pitch link stiffness, and droop stop stiffness and are expressed below

$$\delta U = \delta U_B + \delta U_{DS} + \delta U_{PL} + \delta U_{FS} \quad (2)$$

$$\delta W = \delta W_G + \delta W_{AF} + \delta W_{FD} \quad (3)$$

where the subscript *B* is for the blade, *DS* is for the droop stop, *PL* is for the pitch link, *FS* is for the flap stop, *G* is for gravity, *AF* is for the aerodynamic forces, and *FD* is for the flap damper. Brief formulations of the variation of droop and flap stop strain energy and flap damping are presented below.

The rotor system features most important to the engage/disengage process for an articulated rotor system are the droop and flap stops. The droop stop, shown in Figure 2, restrains the downward rotation of the flap hinge during low rotor speeds and at rest. The flap stop restrains upward flap hinge motion using the same type of mechanism.

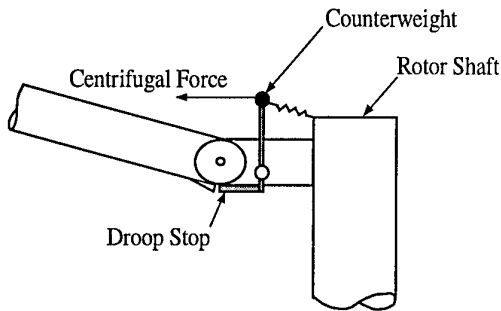


Figure 2: Droop Stop Schematic

The droop and flap stop interactions with the blade are modeled using a conditional rotational spring located at the flap hinge. While the droop stop is extended, the rotational spring stiffness is zero for hinge angles greater than the droop stop angle and large enough to restrict the flap hinge rotation to less than 0.1° for hinge angles equal to or below the droop stop angle. The variation in the strain energy for the droop stop is expressed as

$$\delta U_{DS} = K_\beta (\Delta w' - w'_{DS}) \delta \Delta w' \quad (4)$$

where K_β is the droop stop spring stiffness, $\Delta w'$ is the flap hinge angle, and w'_{DS} is the droop stop angle.

Results of Refs. 7-8 indicate that under certain wind conditions the blade violently strikes the droop stop, causing a transfer of system energy from kinetic to strain. Preliminary rotor engage simulations are performed investigating the possibility of reducing the blade deflection by adding a rotational damper acting at the flap hinge. Flap dampers have been used on early

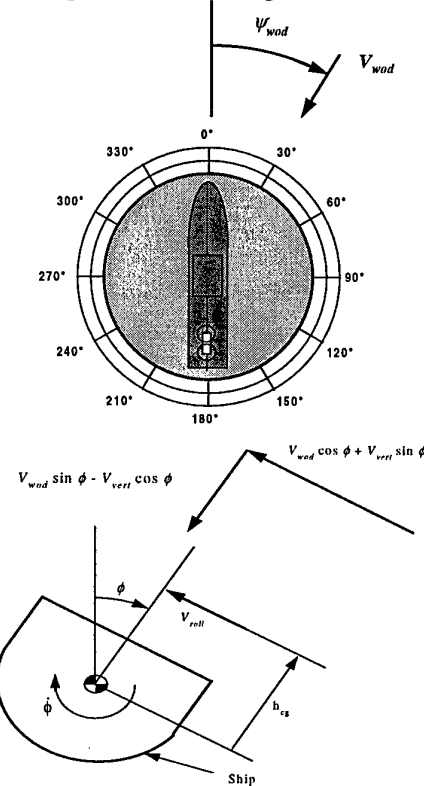
shipborne helicopters such as the HUP-1 through HUP-4 series to reduce excessive blade flapping during low rotor speed operation, but are not in use on the H-46. The flap damper is assumed to act through the entire angular range between the droop and flap stops. The virtual work performed on the blade due to the flap damper is

$$\delta W_{FD} = -C_\beta \Delta w' \delta \Delta w' \quad (5)$$

where C_β is the flap damper strength, and $\Delta w'$ is the flap hinge velocity

II. Aerodynamic Model Formulation

The shipboard aerodynamic environment consists of ship roll motion effects on ambient winds and deterministic gust distributions over the rotor disk. Except for roll motion, the ship is assumed to be stationary with respect to the inertial coordinate system,. The atmospheric winds relative to the ship are uniform and are termed the relative Wind-Over-Deck (WOD) conditions defined by V_{wod} the wind velocity, ψ_{wod} the wind direction, and V_{vert} , the vertical wind component as seen in Figures 3a-b.



Figures 3a-b: Wind Over Deck Convention

Recall that ship motion effects on blade inertia forces were assumed negligible; however, ship motion effects on blade airloads are included. The ship roll motion aerodynamic model consists of the transformed relative WOD conditions due to the ship roll angle and a wind component at the hub height due to the angular roll velocity. Ship roll motion is governed by sinusoidal variation of ϕ_s , the ship roll angle, and can be expressed as

$$\phi_s = \phi_{max} \sin\left(\frac{2\pi\bar{\psi}}{P}\right) \quad (6)$$

where ϕ_{max} is the maximum roll angle, $\bar{\psi} = \Omega_0 t$ is the nondimensional time, and P is the nondimensional roll period. The roll angular velocity causes a lateral wind velocity at the hub height given by

$$V_{roll} = \phi_{max} h_{cg} \left(\frac{2\pi}{P} \right) \cos\left(\frac{2\pi\bar{\psi}}{P}\right) \quad (7)$$

where h_{cg} is the height of the rotor above the cg of the ship.

Two gust models that simulate the airflow over a ship's flight deck subjected to a crosswind are explored in this analysis. The first model, the linear gust developed in Ref. 2, is adopted to explore the effects of local wind variations over the rotor disk on the blade response. This gust consists of an upward wind component on the windward half of the rotor disk transitioning linearly to a downward wind component on the leeward half of the disk. The second model, the uniform gust detailed in Ref. 7, is used to determine the effects of uniform vertical winds on the blade response. This gust consists of a uniform downward velocity across the rotor disk. In addition, each model features a lateral wind component in the direction of the relative WOD velocity. The wind velocity due to the either gust model can be expressed as

$$\mathbf{V}^{gust} = V_x^{gust} \hat{I}_H + V_y^{gust} \hat{J}_H + V_z^{gust} \hat{K}_H \quad (8)$$

where the subscript H denotes the hub fixed coordinates system. In the linear gust distribution the individual components are defined as

$$V_x^{gust} = V_{wod} \kappa_{lat} \cos(\psi_{wod}) \quad (9a)$$

$$V_y^{gust} = -V_{wod} \kappa_{lat} \sin(\psi_{wod}) \quad (9b)$$

$$V_z^{gust} = V_{wod} \kappa_{vert} x \cos(\psi - \pi + \psi_{wod}) \quad (9c)$$

where κ_{lat} is the vertical wind component and x is the nondimensional distance along the blade.

In the uniform gust distribution the individual components are defined as

$$V_x^{gust} = V_{wod} \cos(\alpha_w) \cos(\psi_{wod}) \quad (10a)$$

$$V_y^{gust} = -V_{wod} \cos(\alpha_w) \sin(\psi_{wod}) \quad (10b)$$

$$V_z^{gust} = -V_{wod} \sin(\alpha_w) \quad (10c)$$

where α_w is the angle of the wind relative to the horizontal.

The quasi-steady aerodynamics development follows an unsteady thin airfoil theory development by Johnson¹¹. This development includes the airloads due to virtual mass (noncirculatory) effects and allows for either linear or nonlinear predictions using Kirchhoff's nonlinear separation model. The unsteady aerodynamic was developed by Leishman and Beddoes¹²⁻¹⁴. This time domain approach includes attached flow, unsteady trailing edge separation, and dynamic stall effects. The attached flow, unsteady model predicts both circulatory and noncirculatory airloads. The unsteady trailing edge separation model accounts for trailing edge separation, leading edge pressure lags, and unsteady boundary layer effects. The dynamic stall model calculates the additional lift and large downward pitching moment created by the shedding vortex.

III. Discretized Blade Equations of Motion

The generalized Hamilton's principle, Eqn. 1, is used to formulate the blade equations of motion and the finite element method is used to discretize them. Each flexible element has seven degrees of freedom and is cubic in flap bending and quadratic in torsion. The energy expressions are spatially discretized by substituting shape functions into the elemental virtual energy expressions and integrated in space using a six point Gaussian quadrature method. The elemental mass, damping, and stiffness matrices and load vector are then assembled to form the global mass matrix \mathbf{M} , the damping matrix \mathbf{C} , and the stiffness matrix \mathbf{K} ⁷. The global degrees of freedom are \mathbf{q} . The global discretized equation of motion becomes

$$\mathbf{M}\ddot{\mathbf{q}} + \mathbf{C}\dot{\mathbf{q}} + \mathbf{K}\mathbf{q} = \mathbf{F} \quad (11)$$

IV. Analysis

The blade transient response is calculated by integrating the discretized blade equations of

motion. Recall that the rotor speed and blade azimuth are functions of time and are used in the calculations of \mathbf{M} , \mathbf{C} , \mathbf{K} , and \mathbf{F} which must be recalculated at every time step. The time integration is performed by a 4th order Runge-Kutta scheme. The blade static deflection is used as the initial conditions for rotor run-up solutions. The steady state response at the operational rotor speed is used as initial conditions for run-down solutions. Blade response can be computed in either the full finite element space or modal space, but modal space is recommended for computational efficiency

Model Validation

I. Blade Fan Diagram

The H-46 Sea Knight is a three-bladed tandem rotor helicopter, but the present research only models a single rotor blade of the aft rotor system. Proper stiffness and mass distributions are verified by comparing the predicted static tip deflection to experimental data. The predicted static tip deflection of 15.3 inches is within 2.6 percent of the Boeing test data average. A fan diagram is also developed to determine how well the finite element approach models the H-46 flap and torsion rotating natural frequencies. Figure 4 illustrates the first four coupled flap-torsion frequencies overlaid with test data for the second through the fourth flap modes from Ref. 7. The flap-torsion elastic analysis is in satisfactory agreement with the blade data.

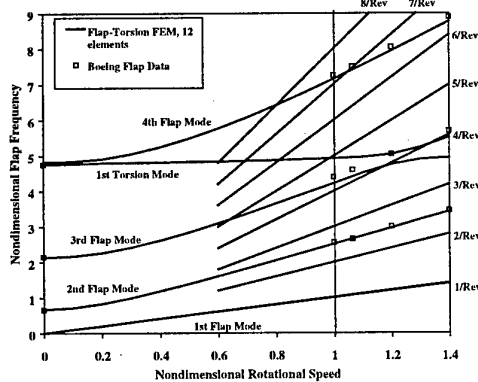


Figure 4: H-46 Flap-Torsion Fan Diagram

II. Droop Stop Impacts

An important feature of articulated rotor blades is the droop stop mechanism. During the engagement and disengagement of the rotor system, excessive flapping can cause the rotor blade to repeatedly impact the droop stop. An investigation to the behavior of a model blade

was undertaken in Ref. 15-16. The boundary conditions of the blade change dramatically during such an event. When the blade is not in contact with the droop stop, the flap hinge is free to rotate and the blade acts as a hinged beam. When the blade is in contact with the droop stop, the flap hinge is restrained from further downward rotation and the blade acts as a cantilevered beam. Recall that a very stiff rotational spring is added to \mathbf{K} to freeze the hinge angle during blade contact with either the droop or flap stop.

For computational efficiency, it is common to transform the global equations of motion into a modal coordinate system

$$\mathbf{q} \equiv \Phi(\mathbf{x})\alpha(t) \quad (12)$$

where Φ is the mode shape and α is the modal amplitude. Substitution of Eqn. 12 into Eqn. 11 and multiplication by Φ^T yields

$$\bar{\mathbf{M}}\ddot{\mathbf{a}} + \bar{\mathbf{C}}\dot{\mathbf{a}} + \bar{\mathbf{K}}\mathbf{a} = \bar{\mathbf{F}} \quad (13)$$

Two different stiffness matrices are used in this transient analysis - one corresponding to the cantilevered condition of the beam and one corresponding to the hinged condition of the beam. Therefore, two independent sets of natural frequencies and mode shapes are generated

$$\begin{aligned} \omega &= \omega_h \quad \text{and} \quad \Phi = \Phi_h \quad \text{if} \quad \beta > \beta_{ds} \\ \omega &= \omega_c \quad \text{and} \quad \Phi = \Phi_c \quad \text{if} \quad \beta \leq \beta_{ds} \end{aligned} \quad (15)$$

where ω is the natural frequency, β is the flap hinge angle, and β_{ds} is the droop stop angle. The equations of motion can be solved using three different techniques. The first and simplest technique is a direct solution of Eqn. 11 in full finite element space, called a "*Physical Space*" integration. The second technique is a solution of Eqn. 13 using only the hinged modes of the beam regardless of blade-droop stop contact, called a "*Modal Swapping Off*" integration. The third and most complicated technique is a solution of Eqn. 13 using either the hinged or cantilevered modes depending on droop stop contact, called a "*Modal Swapping On*" integration. In this method, the modal amplitudes must be adjusted to maintain the physical shape of the beam when the mode shapes are changed or discontinuities can arise in the solution. The deflection of the beam can be approximated by either set of modal matrices and modal amplitudes

$$\mathbf{q} \equiv \Phi_h \mathbf{a}_h \equiv \Phi_c \mathbf{a}_c \quad (16)$$

During a transient analysis, a switch from hinged mode shapes to cantilevered mode shapes is necessary when the beam contacts the droop stop. When this situation occurs, the modal amplitudes must also be adjusted to maintain the physical shape of the beam. Premultiplying Eqn. 16 by $\Phi_c^T \mathbf{M}$ yields

$$\Phi_c^T \mathbf{M} \Phi_c \mathbf{a}_c = \Phi_c^T \mathbf{M} \Phi_h \mathbf{a}_h \quad (17)$$

If the mode shapes have previously been mass normalized, $\Phi_c^T \mathbf{M} \Phi_c = \mathbf{I}$, and

$$\mathbf{a}_c = \Phi_c^T \mathbf{M} \Phi_h \mathbf{a}_h \quad (18)$$

A similar procedure is used when a switch from the cantilevered mode shapes to the hinged mode shapes is performed when the beam leaves contact with the droop stop.

A Froude scaled structural model of an H-46 rotor blade was constructed from 6061-T6 aluminum and is shown in Figure 5. In order to focus on the impact between the rotor blade and the droop stop, a series of drop tests were conducted. Each drop test was performed at zero rotational since most H-46 tunnel strikes occur at less than 20% of the full rotor speed. In each drop test the root end of the blade was clamped between vice grips. Then the section of the blade outboard of the flap hinge was rotated upward and given an initial flap hinge angle ranging from 2° to 10°. Once the desired flap hinge angle was reached, the blade was held in place by an electromagnet located just beyond the flap hinge.

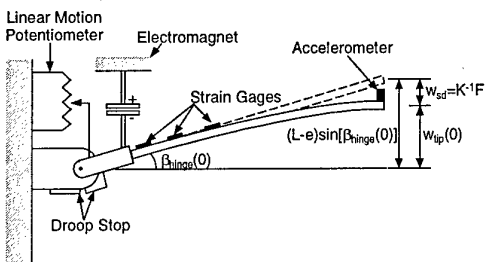


Figure 5: Model Blade Schematic

Each drop test commenced when the electromagnet was shut off. Without anything to support it, the blade section outboard of the flap hinge rotated downward about the flap hinge until it contacted the droop stop, set at an angle of 0°. Once the blade contacted the droop stop, it could not rotate downward any further; however,

the inertia of the blade caused it to continue bending elastically. Once the blade tip reached its point of maximum downward deflection, the excess strain energy is then converted back into kinetic energy in the upward rebounding of the blade tip. The motion of the blade was measured for one full cycle of downward bending and upward rebounding. This process was repeated four times for each initial flap hinge angle to determine the repeatability of the data.

At the beginning of each drop test, the initial shape of the beam is a combination of the static droop under its own weight and a known rotation of about the flap hinge. The initial condition for the tip deflection is given by

$$q_{ip}(t=0) = (L - e) \sin(\beta_{hinge}(t=0)) + q_{sd} \quad (19)$$

where L is the blade length, e is the hinge offset and the subscript SD is the static deflection. The initial velocity was set equal to zero since the blade was released from rest. Once the initial position and velocity of the blade tip were specified, the measured tip accelerations can be used to calculate the measured tip displacement and tip velocity

$$\begin{aligned} \dot{q}(t) &= \frac{\Delta t}{2} [\ddot{q}_{ip}(t) + \ddot{q}_{ip}(t - \Delta t)] \\ q(t) &= \frac{\Delta t}{2} [\dot{q}_{ip}(t) + \dot{q}_{ip}(t - \Delta t)] \end{aligned} \quad (20)$$

The results for an example drop test from 9.7° are shown in Figures 6a-c. The transient response of the flap hinge angle is shown in Figure 6a. The cause of the sudden upward rotation of the flap hinge angle at $t = 0.10$ seconds is because the blade flexes while it falls. The experimental data tracks well with the analytical prediction before the impact and while in contact with the droop stop.

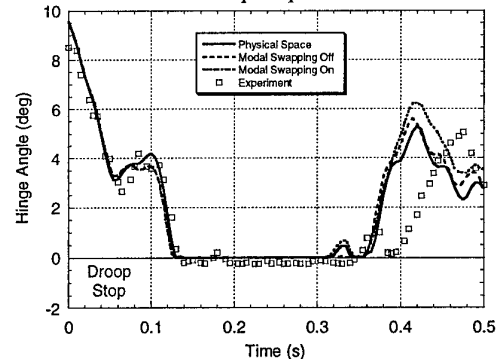


Figure 6a: Flap Hinge Angle Time History

The transient response of the tip deflection is shown in Figure 6b. Much like the upward movement of the flap hinge angle, the cause of the upward motion of the blade tip at $t = 0.04$ seconds is due to the flexing of the blade while falling. Both the experimental data and analytical predictions capture this phenomenon. The maximum tip deflection, w_{tip}/L , of -0.17 at $t = 0.25$ seconds for the analytic methods is in excellent agreement with the experimental data.

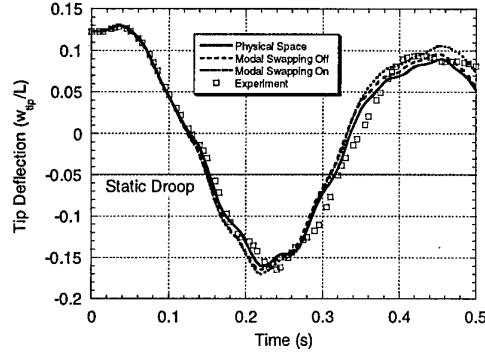


Figure 6b: Tip Deflection Time History

The transient response of the strain gage at $x/L = 0.20$ is shown in Figure 6c. There is excellent agreement in the peaks and valleys of the measured and predicted strain. Note that the strain becomes negative at $t = 0.05$ seconds, indicating the beam is actually curved upwards, and is indicative of the blade flexing as it falls. The maximum strain of 1400 $\mu\epsilon$ is captured well captured by the experimental data and analytic predictions.

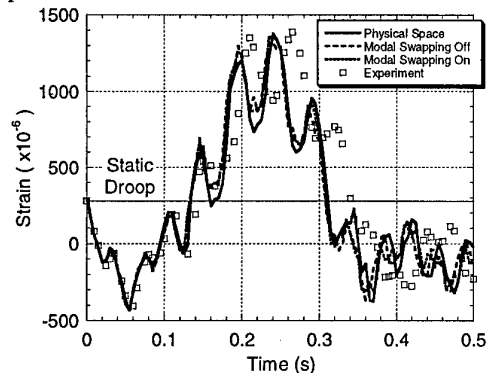


Figure 6c: Strain Gage Time History

As seen in the previous sections, each of the analytic techniques presented - the *Physical Space* Integration, the *Modal Swapping Off* integration, and the *Modal Swapping On* integration provide almost identical solutions for

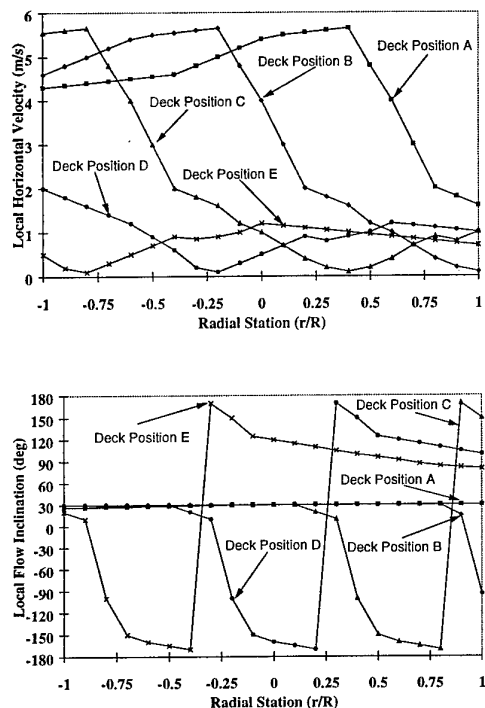
each drop test. However, both the accuracy and the computational efficiency of each solution method are of importance. Each drop test simulates 0.5 seconds of real time. The *Physical Space* solution method requires the most CPU time, a total of 70 seconds, because 41 degrees of freedom are used. The *Modal Swapping Off* solution is the next most efficient model, requiring 24 seconds of CPU time. Instead of integrating 41 coupled equations of motion, only 6 normal modes are required. The *Modal Swapping On* solution is the most efficient of the three analytic methods, requiring only 13 seconds of CPU time because only four normal modes were required for the solution.

The differences in CPU time to generate even the longest drop test solution are not very substantial; however, the rotor blade and droop stop impact event is a very small part of a larger picture – the complete rotor engagement and disengagement simulation. Many computationally intensive features such as blade element unsteady aerodynamics which result in motion dependent terms and large numbers of degrees of freedom including flap and torsion in the aeroelastic rotor analysis make computational efficiency essential. A dramatic difference in CPU time can result using the three integration techniques in the aeroelastic analysis in Refs. 6-9. The *Physical Space* engagement solution is again the longest, requiring 160 hours of CPU time on an RS-6000 workstation. If the engagement simulation is performed using the *Modal Swapping Off* integration, the size of the problem is reduced to 6 normal modes. This reduces the length of the simulation to 10 hours, which is still fairly substantial. Finally, if the *Modal Swapping On* integration is used, 30 minutes is required for the engagement simulation. Clearly, when the issue of computational efficiency is considered along with accuracy, the *Modal Swapping On* integration is the superior method for use in the rotor engagement/disengagement simulation.

III. Wind Tunnel Validation Studies

Experimental data was gathered at the University of Southampton on the engagement and disengagement of a model helicopter on board a scale ship deck^{5,6}. First, airwake measurements at five different positions were taken without the helicopter model. For each rotor hub location, winds were measured along

the direction of wind flow. The variation over the rotor disk is shown for each of the five hub locations (A-E) in Figure 8a. The results tend to indicate a very distinct division between laminar and turbulent flow regions. Figure 8b illustrates the variation of flow inclination to the horizontal over the rotor disk for the five hub locations. Note the large change in flow inclination for the three leeward hub locations which is indicative of reverse flow.



Figures 7a-b: Model Ship Airwake Measurements from Refs. 5-6

Then, a radio control helicopter model was mounted on the scale model flight deck. This ship/helicopter combination was subjected to beam winds in the wind tunnel and a series of engage and disengage operations were performed. The rotor hub was tested in the 5 locations on the flight deck as shown in Figure 8.

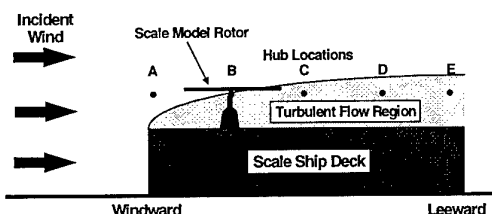
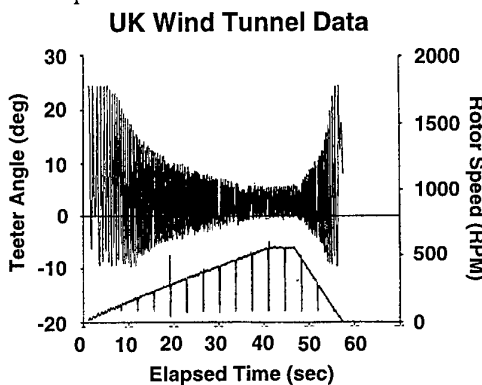


Figure 8: Model Ship and Rotor Wind Tunnel Experiment Schematic from Refs. 5-6

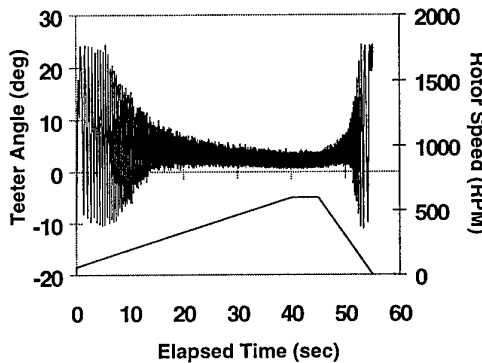
The experimental data gathered in Refs. 5-6 was then used to validate the transient dynamic response predicted by the Penn State aeroelastic analysis. Correlation of the Penn State analysis results with the single-bladed scale model rotor results was reported in Ref. 9.

The comparisons between the experimentally measured rotor response and the predictions are for deck positions A and E are shown in Figures 9a-b and 10a-b, respectively. For each figure, the experimental response measured in Refs. 5-6 is shown on top and the theoretical predictions from the Penn State analysis are shown on bottom.

Figures 9a-b show the comparison for deck position A. Note that the experimental data shows very little random behavior as might be expected in a laminar airwake. In this case, the theoretical predictions show good agreement with experimental results.



PSU/NAWCAD Analysis

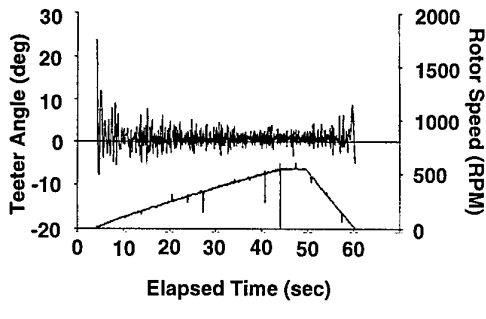


Figures 9a-b: Deck Position A

Figures 10a-b shows the comparison for deck position E. Note the difference in behavior when the rotor is fully immersed in the turbulent airwake, as seen in the random blade response.

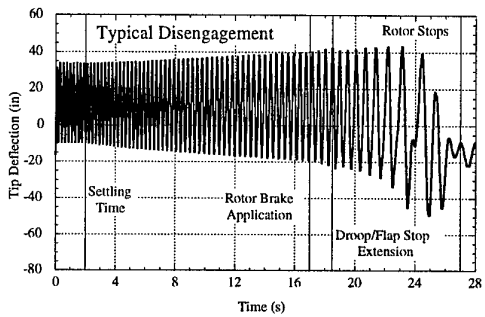
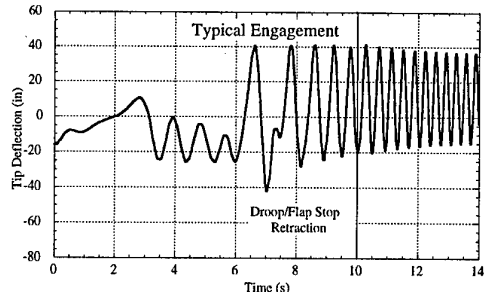
The conclusion, in agreement with Refs. 5-6, was that different large scale airwake characteristics (i.e. different deck positions) are very important to the blade sailing phenomenon.

UK Wind Tunnel Data



Figures 10a-b: Deck Position E

maximum downward tip deflection occurs at approximately 7 seconds into the engagement. During rotor disengagement, the blade deflections steadily grow. Note that when the rotor brake is applied, the tip deflections grow more rapidly and the maximum deflection occurs within the last two seconds.



Figures 11a-b: Rotor Engagement and Disengagement

Parametric Studies

I. Typical Rotor Engagement and Disengagement

After the validation was performed, a series of parametric studies for the H-46 helicopter was conducted. First, a typical rotor engagement and disengagement were examined. During all rotor engage/disengage sequences, the collective is 3°, the longitudinal cyclic is 2.5°, and the lateral cyclic is 0.07°. These control inputs are termed the standard control inputs and are derived from the "auto" cyclic trim settings used in actual H-46 operations. The standard control inputs are used for all parametric studies unless otherwise noted. The experimentally measured rotor run-up profile in Figure 1 and the run-down profile with rotor brake application at 55% of full rotor speed are used. A linear gust model, with $V_{wod} = 40$ knots, $\kappa_{ven} = 25\%$, and $\psi_{wod} = 90^\circ$ was used. The unsteady aerodynamic model and dynamic stall effects were used. Representative blade responses using are shown in Figures 11a-b. Note for rotor engagement, the tip deflections decrease as the rotor speed increases, and the

II. Engage Envelope Study

The engage envelope analysis determines the blade-to-fuselage clearance for multiple wind-over-deck conditions using the maximum downward tip deflection calculated from the blade transient response. The safe engage region is composed of all wind-over-deck conditions with blade-to-fuselage clearances greater than 8 inches.

An H-46 baseline engagement envelope developed using standard control inputs and a uniformly distributed gust with $\alpha_w = 15^\circ$ is shown in Figure 12. Note that the H-46 is limited to wind speeds of 30 knots for port WOD conditions and is limited to 35 knots for most starboard WOD conditions. The predicted envelope shows safe engagements for winds speeds up to 40 knots for WOD directions of 45° to 75°. Results of sensitivity studies performed in Ref. 7 showed that control inputs have a moderate effect on maximum downward tip deflections. The two following studies show the

effect of 2° variations in collective and cyclic pitch controls from the standard control inputs.

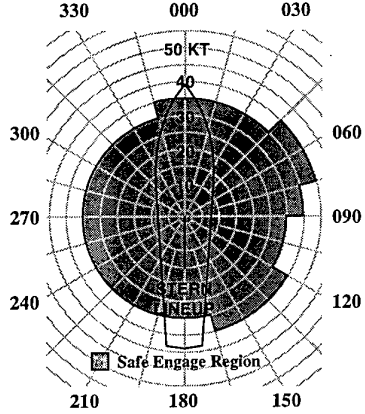


Figure 12: Baseline Safe Engage Envelope

The predicted H-46 engage envelope for a collective pitch *decrease* of 2° from standard control inputs is shown in Figure 13. A comparison with the baseline engagement envelope shows a 5 knot reduction in the safe engagement region for WOD directions of 45° to 75° and 120° to 285° .

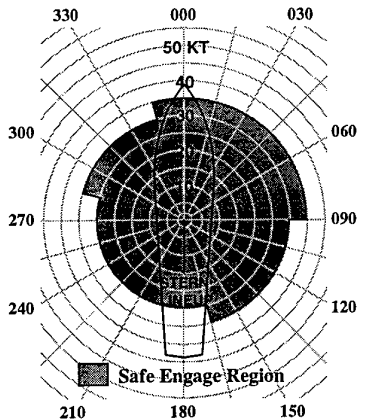


Figure 13: Safe Engage Envelope for 2° Collective Decrease

The predicted H-46 engage envelope for a lateral cyclic pitch *increase* of 2° from standard control inputs is shown in Figure 14. Unlike the small decrease in wind speed over large portions of the envelope for the collective pitch change, note the substantial reduction in engagement capability for port winds. WOD speeds are reduced by 10 to 15 knots for WOD directions from 120° to 150° and from 225° to 330° . These results illustrate that during engagements in uniformly distributed winds, small changes in

collective and cyclic inputs can moderately effect the safe engage region.

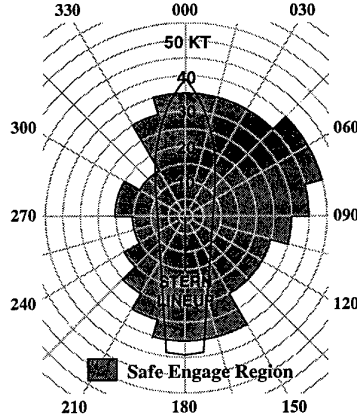


Figure 14: Safe Engage Envelope for 2° Lateral Cyclic Increase

III. Flap Damping Study

In an effort to reduce the frequency of tunnel strike occurrences, a preliminary investigation was conducted into the effectiveness of adding a rotational damper at the flap hinge of the H-46 to dissipate energy in the flapping degree of freedom. Preliminary results for the current H-46 flap and droop stop settings, of -54° and 1.5° respectively, indicated that the flap damper, regardless of its strength, was not effective in reducing the blade deflection because the angular range of motion was too small. At very large damper strengths, the flap damper simply freezes the flap hinge angle because the energy necessary to rotate the highly damped hinge is much higher than the energy necessary to deform the blade. However, raising the flap stop angle permits the damper to act through a larger angular range of motion and dissipate more energy. Combinations of flap stop settings from 1.5° to 10° and flap damper strengths ranging from zero to five times the H-46's lead/lag damper strength, or 17500 ft-lb/(rad/s), were investigated as means of reducing the blade deflection.

Tip deflection time histories for rotor engagement are presented in Figure 15. Two flap stop settings and flap damper combinations are examined. The flapping behavior of the rotor blade becomes excessive at both 2 and 6 seconds into the engagement because it is both rotating into the WOD and experiencing a strong upflow from the specified gust distribution. The maximum negative tip deflection occurred 7 seconds after engagement in both configurations.

For a flap damper four times the strength of the lead/lag damper and a flap stop setting of 10°, enough energy is dissipated to prevent a tunnel strike.

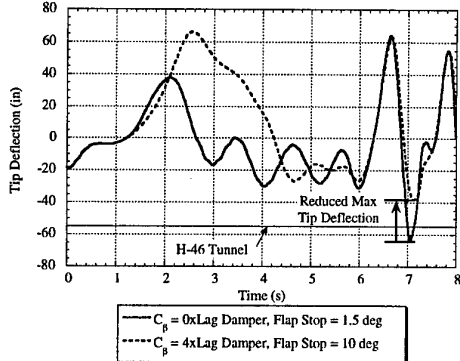


Figure 15: Flap Damping Study

Current Research

MUCH of the current research at Penn State has focused upon the engagement and disengagement operations for tiltrotors¹⁷. Present tiltrotor configurations, such as the V-22 Osprey, feature the use of a gimballed rotor system. Unique rotor characteristics include a gimbal spring and a gimbal restraint as shown in Figure 16. In addition, gimballed rotor blades are typically short and highly twisted.

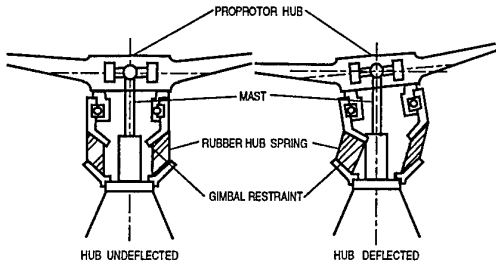


Figure 16: Gimballed tiltrotor

A gimballed rotor has three or more blades attached to the hub without flap and lag hinges. The hub is attached to the rotor shaft by a universal joint, or gimbal. Compared to articulated or hingeless rotor systems, the gimballed rotor has some unique structural and aerodynamic characteristics related to shipboard engagement and disengagement operations. The inflow distribution, associated with the ship airwake, on all blades contributes to gimbal flapping moments so the motion of all blades is coupled together through the rotor hub. In addition, the highly twisted blades introduce significant structural flap-lag coupling and can

also result in high angles of attack at very low rotor speeds.

An analytical model for steady-state aeroelastic response and stability of gimballed tiltrotors was developed in Ref. 18. The rotor model included coupled flap-lag bending modes and torsion degrees of freedom. The gimbal tilt was described by using the gimbal degrees of freedom, β_{GC} and β_{GS} , which are the pitch and roll of the rotor disk in nonrotating frame. They are determined by the trim equations in steady-state analysis. For this type of analysis, the steady periodic response of the rotor can be obtained by considering the response of an equivalent single blade. For transient engage and disengage analyses, the motion of blades is non-periodic. In addition, gimbal restraint impacts make the individual blades respond differently and the inflow distribution on all blades contributes to gimbal motion. The entire multi-bladed gimballed rotor has to be modeled to analyze the transient response during engage and disengage operations. The overall goal of this research was to systematically investigate the transient response of gimballed tiltrotors during shipboard engage/disengage operations.

Engagement and Disengagement Analysis

I. Structural Model Formulation

A fixed rotor support was considered in the present research (i.e. rigid wing/pylon). The multi-bladed gimballed rotor is modeled as several slender elastic beams attached to a hub and undergoing flap bending, lag bending, elastic twist, and axial deflection. The blades are discretized into a number of beam elements using the finite element method. Each beam element consists of fifteen degrees of freedom¹⁸. The motion of gimbal is expressed by using two degrees of freedom in the rotating system. Hamilton's Principle, Eqn 1, is again used to develop the equations of motion. However, the contributions to these energy expressions must be summed over each blade

$$\delta U = \left(\sum_{m=1}^{N_b} \delta U_B^m \right) + \delta U_{GS} + \delta U_{GR} + \delta U_{PL} \quad (21a)$$

$$\delta T = \left(\sum_{m=1}^{N_b} \delta T_B^m \right) \quad (21b)$$

$$\delta W = \left(\sum_{m=1}^{N_b} \delta W_B^m \right) \quad (21c)$$

where N_b is the number of blades, B refers to the blade, GS to the gimbal spring, GR to the gimbal restraint, and PL to the pitch link.

The variation of gimbal restraint strain energy is given by

$$\delta U_{GS} = K_{\beta_{GS}} \beta_{GS} \delta \beta_{GS} + K_{\beta_{GC}} \beta_{GC} \delta \beta_{GC} \quad (22)$$

The degrees of freedom in the rotating system are used to express the motion of gimbal. The transformation matrix is given by

$$\begin{Bmatrix} \beta_{GC} \\ \beta_{GS} \end{Bmatrix} = \begin{bmatrix} \cos \psi & -\sin \psi \\ \sin \psi & \cos \psi \end{bmatrix} \begin{Bmatrix} \beta \\ \phi \end{Bmatrix} \quad (23)$$

where ψ is the azimuth angle of rotating frame, and β and ϕ are the gimbal tilt degrees of freedom in the rotating system. The gimbal degree of freedom in nonrotating and rotating coordinate systems are shown in Fig. 17.

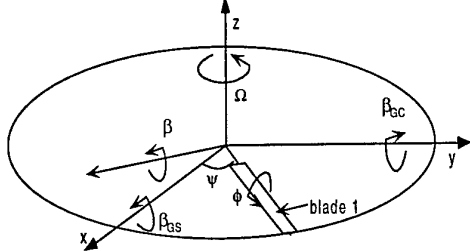


Figure 17: Gimbal Degrees of Freedom

This analysis models the gimbal restraint interaction with the rotor using a conditional rotational spring in nonrotating frame, much like the earlier droop stop modeling. The variation of strain energy due to the gimbal restraint is expressed as

$$\delta U_{GR} = K_\beta (\beta_{max} - \beta_{restr int}) \delta \beta_{max} \quad (24)$$

The maximum tilt angle, β_{max} , is given in rotating system by

$$\beta_{max} = (\beta \cos \psi - \phi \sin \psi) \cos \psi_{max} + (\beta \sin \psi + \phi \cos \psi) \sin \psi_{max} \quad (25)$$

where ψ_{max} is the azimuth where the maximum tilt angle located and given by

$$\psi_{max} = \tan^{-1} \left(\frac{\beta \sin \psi + \phi \cos \psi}{\beta \cos \psi - \phi \sin \psi} \right) \quad (26)$$

II. Aerodynamic Model Formulation

A quasi-steady aerodynamic model is used in this analysis. Detailed descriptions of the quasi-steady aerodynamic modeling and the

shipboard aerodynamic environment are given in Ref 7.

III. Discretized Blade Equations of Motion

An illustration of the blade finite element discretization is shown in Figure 18. Each of the flexible elements consists of fifteen degrees of freedom. These degrees of freedom are distributed over five element nodes, two external and three internal, which describe the elemental flap deflection (w, w'), lag deflection (v, v'), twist (ϕ), and axial deflection (u).

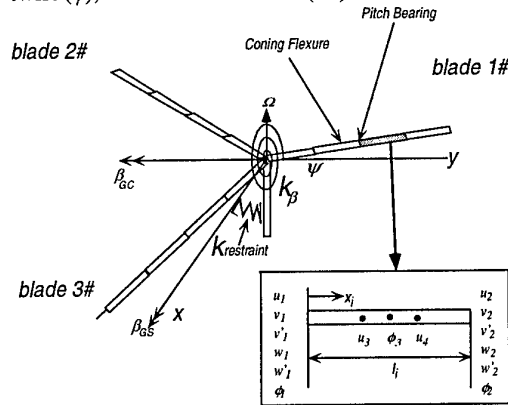


Figure 18: Finite Element Model of Gimbaled Rotor

Figure 19 shows the global degrees of freedom for the gimbaled rotor. The first two degrees of freedom describe the gimbal tilt. The last degree of freedom at the left-hand node of the second element of each blade describes the rotation of the pitch bearing. The second element in each blade represents the blade flexure. For ten elements in each blade, there are 275 global DOF.

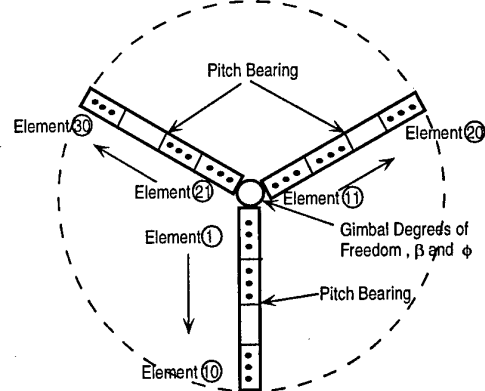


Figure 19: Global Degrees of Freedom

The energy expressions are spatially discretized by substituting the shape functions into the elemental virtual energy expressions. The virtual energy expression for multi-bladed tiltrotor in terms of the elemental matrices and load vector becomes

$$\begin{aligned}\delta\Pi = & \int_{V_1}^{\Psi} \left(\sum_{m=1}^{N_b} \sum_{i=1}^N \delta q_i^m \right) (M_i^m \ddot{q}_i^m \\ & + C_i^m \dot{q}_i^m + K_i^m q_i^m - F_i^m) d\Psi \\ & + \int_{V_1}^{\Psi} [\delta\beta, \delta\phi] [k_G] \begin{Bmatrix} \beta \\ \phi \end{Bmatrix} \\ & + k_{restraint} (\beta_{max} - \beta_{restraint}) \delta\beta_{max} d\Psi\end{aligned}\quad (27)$$

where $[k_G]$ is the stiffness of matrix due to gimbal restraint and is expressed as

$$[k_G] = \begin{bmatrix} k_{\beta_{ac}} \cos^2\psi + k_{\beta_{as}} \sin^2\psi, & -k_{\beta_{ac}} \cos\psi \sin\psi \\ -k_{\beta_{ac}} \cos\psi \sin\psi, & +k_{\beta_{ac}} \cos^2\psi + k_{\beta_{as}} \sin^2\psi \end{bmatrix} \quad (28)$$

where N is the number of finite elements for each blade. For a gimballed tiltrotor, the blade is fixed to the hub at the blade root. The hub is attached to the rotor shaft by a gimbal. The motion of the hub is expressed using two degrees of freedom in this analysis, β and ϕ , which rotate with the rotor. The root slope, w_1^m and twist, ϕ_1^m , of each blade are not restrained and can be expressed as a function of two gimbal degrees of freedom in the rotating frame, β and ϕ .

$$w_1^m = \beta \cos \psi_m + \phi \sin \psi_m \quad (29)$$

$$\phi_1^m = -\beta \sin \psi_m + \phi \cos \psi_m \quad (30)$$

where the subscript 1 indicates the left-hand node of the first element blade and ψ_m is the azimuth of m th blade in rotating frame and can be expressed as

$$\psi_m = \frac{2\pi}{N_b} (m-1) \quad (31)$$

Eqns. (29) and (30) are then substituted into Eqn. (28). The stiffness matrix, mass matrix, damping matrix and force vector are assembled to form their global counterparts. The discretized equation of rotor motion is obtained as

$$\mathbf{M}\ddot{\mathbf{q}} + \mathbf{C}\dot{\mathbf{q}} + \mathbf{K}\mathbf{q} - \mathbf{F} = \mathbf{0} \quad (32)$$

where \mathbf{M} , \mathbf{C} , \mathbf{K} , and \mathbf{F} are for the *entire rotor*. They include the linear structural, inertial and aerodynamic contributions. The force vector includes the constant structural, inertial and aerodynamic contributions as well as the nonlinear structural and aerodynamic contributions.

IV. Hub Moments

During gimbal restraint impacts, it is important to calculate blade and hub loads for design limits. The flap bending moment, lag bending moment, and twisting moment in the deformed coordinate system are defined by¹⁹

$$M_x^* = EI_z (v^* \sin(\theta + \phi) - w^* \cos(\theta + \phi)) - EC_z \phi' \quad (33a)$$

$$M_y^* = -EAe_z (u' + \frac{v'^2}{2} + \frac{w'^2}{2}) - EB_z \phi' \theta' + EI_z (v^* \cos(\theta + \phi) - w^* \sin(\theta + \phi)) \quad (33b)$$

$$\begin{aligned}M_z^* = & GJ\phi' + EAK_z(\theta + \phi)' \left(u + \frac{v'^2}{2} + \frac{w'^2}{2} \right) \\ & + EB_z \theta' \phi' - EB_z \theta' (v^* \cos \theta + w^* \sin \theta) \\ & - [EC_z \phi' + EC_z (v^* \cos \theta - w^* \sin \theta)]\end{aligned} \quad (33c)$$

where θ is the pitch angle and defined as

$$\theta = \theta_0 + \theta_{lc} \cos \psi_m + \theta_{ls} \cos \psi_m + \theta_{fw} (r - 0.75) - K_p w_1^m \quad (34)$$

Rotor hub moments are obtained by transforming the blade root moments to the non-rotating hub-fixed coordinate system and summing over each blade. The roll moment, pitch moment and torque are expressed as

$$M_x^m = \sum_{i=1}^N (M_x^* \cos \psi - M_y^* \sin \psi - M_z^* \beta_r \cos \psi) \quad (35a)$$

$$M_y^m = \sum_{i=1}^N (M_x^* \sin \psi + M_y^* \cos \psi - M_z^* \beta_r \sin \psi) \quad (35b)$$

$$M_z^m = \sum_{i=1}^N (M_z^* \beta_r + M_z^*) \quad (35c)$$

where M_x^m , M_y^m and M_z^m are the flap bending moment, lag bending moment and twist moment at the root of m th blade in the undeformed coordinate system, and are given by

$$M_x^* = M_x^* \cos \phi - M_y^* \sin \phi \quad (36a)$$

$$M_y^* = M_x^* w' + (1 - \frac{w'^2}{2}) (M_x^* \sin \phi + M_y^* \cos \phi) \quad (36b)$$

$$M_z^* = M_z^* (1 - \frac{w'^2}{2}) - M_x^* w' \sin \phi - M_y^* w' \cos \phi \quad (36c)$$

Model Validation

I. WRATS Bending Moments in Hover

Experimental data for blade bending moments and twisting moment in hover condition of a 1/5th scale model of V-22 WRATS gimballed rotor was used to validate the analysis. The test was conducted for hover condition with varying collective pitch (zero cyclic pitch) at a rotor speed of 875 RPM. Eighteen rotor modes are used in the transient analysis, including three flap, two lag and one torsion. The flap bending moment, lag bending moment, and twisting moment at six blade sections was measured. A comparison of these experimental results with the predictions of the present analysis is shown in Figures 20a-b and 21a-b. The flap and lag moments predicted by this analysis show good correlation with the experimental test data at moderate collective pitch, $\theta_{75} = 5^\circ$, and fair correlation at high collective pitch, $\theta_{75} = 7.5^\circ$. Note that the element between section 0.11R and 0.15R represents the coning-flexure of the blade.

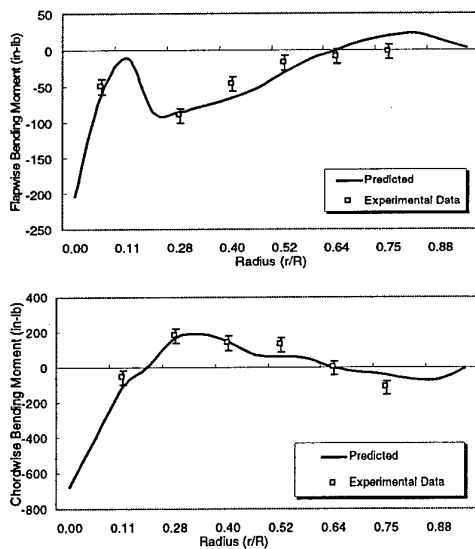


Figure 20a-b: Flap and Lag Bending Moment Comparisons ($\theta_{75} = 5^\circ$)

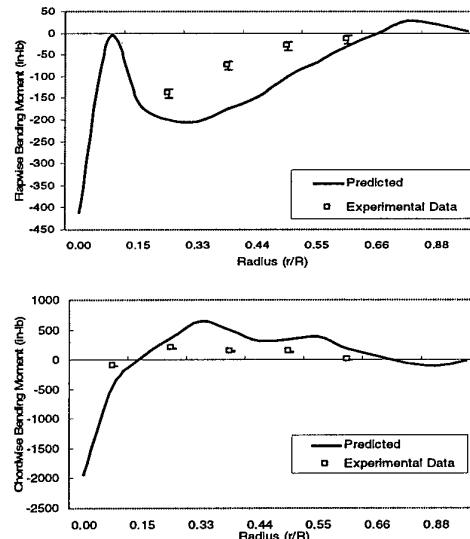


Figure 21a-b: Flap and Lag Bending Moment Comparisons ($\theta_{75} = 7.5^\circ$)

Parametric Studies

I. Transient Response Analysis

Using the analysis described in previous section, parametric studies are carried out to investigate the effects of wind speed and blade flexure stiffness on the rotor response and loads. The rotor properties are similar to the Bell-NASA 1/5th scale aeroelastic model of the V-22. The normal rotor speed of the model is 888 RPM (helicopter mode). The blade transient response is calculated by integrating the discretized rotor equations of motion for a specified rotor speed run-up profile.

In an effort to clearly understand engage/disengage behavior, an investigation was focused on the motions of the tiltrotor gimbal and bending moments of the blades. The tiltrotor operation was simulated for a starboard WOD of $\mu = 0.075$. A 25% upflow through the windward half of the rotor disk and a 25% downflow through the leeward half were simulated. The corresponding full-scale wind speed is equivalent to the 35 knots. The rotor collective pitch is set $\theta_{75} = 0^\circ$ with zero cyclic control input.

Figure 22 shows the time-history of transient response of gimbal tilt, β and ψ , and the maximum tilt, β_{max} , of tiltrotor. The maximum tilt indicates when the impacts between rotor and gimbal restraint occur.

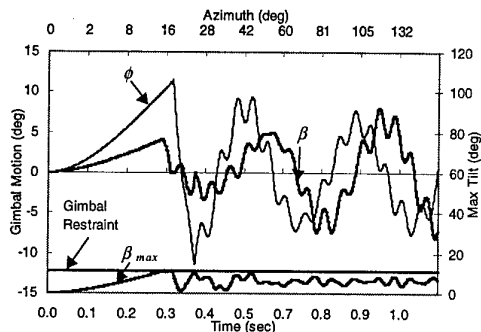


Figure 22: Transient Response for Gimballed Tiltrotor

The first impact event is illustrated in Fig. 23. The t_0 , t_1 , and t_2 refer to the time of beginning rotating, first connection between rotor and gimbal restraint, and disconnection, respectively. The rotor first impacts gimbal restraint when blade 1 rotates 16°. The azimuth where the gimbal impacts the hub is located at 101°. The rotor keeps connection with gimbal restraint while the blade 1 rotates to 20°, while the azimuth of connection moves counter clockwise from 101° to 118° during this period.

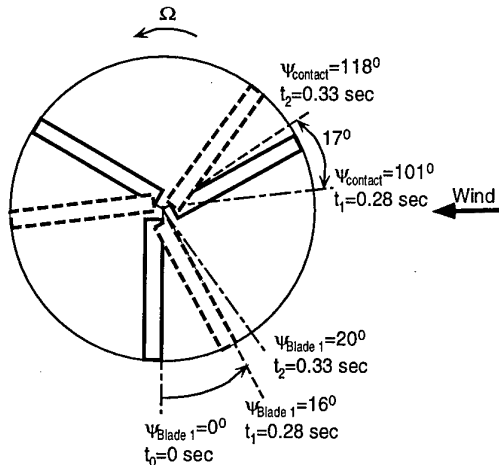


Figure 23: The First Impact Event

II. Hub Moments

The flap and lag bending moment time histories at the inboard section of the coning flexure are shown in Fig 24. It can be seen that impacts between rotor and gimbal restraint cause substantial increases in blade bending moments.

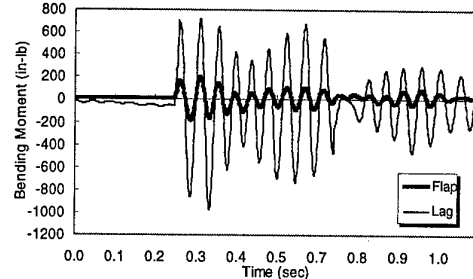


Figure 24: Bending Moment Response on Blade 1 at the Coning Flexure

Figure 25 shows the peak roll moment, peak pitch moment, and peak vector sum of roll and pitch moment during an engage operation at a higher WOD speed of $\mu = 0.086$. The hub moment vector sum is 18 times static hub load for 4° gimbal tilt angle operations and 6 times static hub loads for 11° gimbal tilt operations, which is the maximum amount of gimbal tilt.

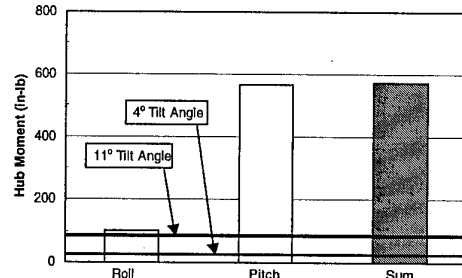


Figure 25: Hub Loads During Run-up Operation

Ongoing Work

Several areas of investigation are currently underway. For articulated rotors, control of the tunnel strike phenomenon is being investigated. One manner of reducing the tip deflections is to increase the flapwise stiffness of the blade by increasing the collective pitch setting. The total flapwise stiffness is equal to

$$EI_{flap} = EI_{yy} \cos^2 \theta + EI_{zz} \sin^2 \theta \quad (37)$$

This would only be performed in the very low rotor speed region of a rotor engagement or disengagement where $\Omega < 20\%NR$. Figure 26 shows the increase in flapwise stiffness achieved for various collective pitch settings. Two radial locations are shown. The first location ($r/R = 0.10$) is just outboard of the pitch bearing and the second location ($r/R = 0.25$) is the beginning of the blade airfoil section. Note that the flapwise

stiffness can be increased over three times its value at the standard collective pitch setting at $r/R = 0.25$. However, increasing the collective pitch may also increase blade deflections due to the increased angle of attack. In addition, large chordwise blade bending moments may be a concern.

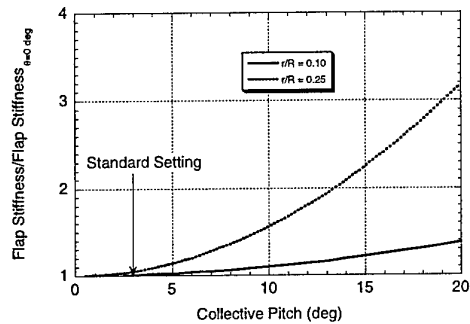


Figure 26: Variation of Flapwise Stiffness with Collective Pitch Setting

The other way to increase flapwise stiffness of the rotor is through active stiffening of the rotor blade by means of piezoelectric actuators. For gimballed rotors, pylon degrees of freedom are being added to the simulation to model the finite stiffness of the wing and pylon. Incorporation of the airwake results from CFD analyses of simple ship configurations, such as in Ref. 20, is also underway.

Acknowledgments

This research was carried out with support from the Naval Air Warfare Center Aircraft Division at Patuxent River, Maryland (technical monitors: LCDR Mark Whittle, Mr. Kurt Long, Mr. Larry Trick, and Mr. Bill Geyer); the Naval Aviation Depot at Cherry Point, North Carolina (technical monitor: MAJ Robert Hellar); the NASA/Army National Rotorcraft Technology Center; and the Office of Naval Research (technical monitor Dr. Pat Purtell). The authors also want to thank Mr. Ben Settle of Bell Helicopters and Dr. Mark Nixon from US Army at NASA LaRC, for valuable technical support and rotor data for tiltrotor configurations.

References

- Hurst, D.W. and Newman, S.J., "Wind Tunnel Measurements of Ship Induced Turbulence and the Prediction of Helicopter Rotor Blade Response," *Vertica*, Vol. 12, No. 3, 1988, pp. 267-278.

2. Newman, S.J., "A Theoretical Model for the Predicting the Blade Sailing Behaviour of a Semi-Rigid Rotor Helicopter," *Vertica*, Vol. 14, No. 4, 1990, pp. 531-544.

3. Newman, S.J., "The Application of a Theoretical Blade Sailing Model to Predict the Behaviour of Articulated Rotor Helicopters," *Aeronautical Journal of the Royal Aeronautical Society*, Vol. 96, No. 956, pp. 233-239.

4. Newman, S.J., "The Problems of Rotor Engagement and Disengagement of a Shipborne Helicopter," *Journal of Naval Sciences*, Vol. 20, No. 1, 1994, pp. 56-64.

5. Newman, S.J., "The Verification of a Theoretical Helicopter Rotor Blade Sailing Method by Means of Windtunnel Testing," *Aeronautical Journal of the Royal Aeronautical Society*, Vol. 99, No. 982, 1995, pp. 41-51.

6. Newman, S.J., "An Investigation into the Phenomenon of Helicopter Blade Sailing," Ph.D. Dissertation, Dept. of Aeronautics and Astronautics, University of Southampton, Southampton, United Kingdom, Mar. 1995.

7. Geyer, W.P., "Aeroelastic Analysis of Transient Blade Dynamics During Shipboard Engage/Disengage Operations," M.S. Thesis, Dept. of Aerospace Engineering, Pennsylvania State University, University Park, PA, Aug. 1995.

8. Geyer, W.P. and Smith, E.C., "Aeroelastic Analysis of Transient Blade Dynamics During Shipboard Engage/Disengage Operations," *Proceedings of the 2nd International AHS Aeromechanics Specialists' Meeting* (Fairfield County, CT), Alexandria, VA, 1995, pp. 8-91-8-114.

9. Geyer, W.P., Smith E.C., and Keller, J., "Validation and Application of a Transient Aeroelastic Analysis for Shipboard Engage/Disengage Operations," *Proceedings of the 52nd Forum of the American Helicopter Society* (Washington, D.C.), American Helicopter Society, Alexandria, VA, pp. 152-167.

10. Geyer Jr., W.P., Smith, E.C., and Keller, J.A., "Aeroelastic Analysis of Transient Blade Dynamics During Shipboard Engage/Disengage

- Operations," *AIAA Journal of Aircraft*, Vol. 35, No. 3, pp. 445-453.
11. Johnson, W., *Helicopter Theory*, Dover, New York, 1994.
12. Leishman, J.G., and Beddoes, T.S., "A Generalised Model for Airfoil Unsteady Aerodynamic Behaviour and Dynamic Stall Using the Indicial Method," *Proceedings of the 42nd Forum of the American Helicopter Society*, Washington, D.C., June 1986.
13. Beddoes, T.S., and Leishman, J.G., "A Semi-Empirical Model for Dynamic Stall," *Journal of the American Helicopter Society*, Vol. 34, No. 3, 1989, pp. 3-17.
14. Bir, G., and Chopra, I., *University of Maryland Advanced Rotorcraft Code (UMARC) Theory Manual*, University of Maryland, UM-AERO94-18, College Park, MD, July 1994.
15. Keller, J.A., Smith, E.C., and Knarr, C., "Experimental/Theoretical Correlation of Analysis for Helicopter Rotor Blade/Droop Stop Contacts," *Proceedings of the 38th AIAA/ASME/ASCE/AHS/ASC Structures, Structural Dynamics, and Materials Conference* (Kissimmee, FL), American Institute of Aeronautics and Astronautics, Inc., Reston, VA, pp. 345-357.
16. Keller, J.A., "An Experimental and Theoretical Correlation of an Analysis for Helicopter Rotor Blade and Droop Stop Impacts," M.S. Thesis, Department of Aerospace Engineering, The Pennsylvania State University, University Park, PA, December 1997.
17. Hao, K., and Smith, E.C., "Transient Response Analysis of Gimbaled Tiltrotors During Engage and Disengage Operations," *Proceedings of the 39th AIAA/ASME/ASCE/AHS/ASC Structures, Structural Dynamics and Materials Conference* (Long Beach, CA), American Institute of Aeronautics and Astronautics, Inc., Reston, VA.
18. Johnson, W. "Analytical Mode for Tilting Proprotor Aircraft Dynamics, Including Blade Torsion and Coupled Bending Modes, and Conversion Mode Operation," NASA TM X-62,369, Aug. 1974.
19. Hodges D.H., and Dowell E.H., "Nonlinear Equations of Motion for the Elastic Bending and Torsion of Twisted Nonuniform Rotor Blades," NASA TN D-7818, 1994.
20. Long, L.N., and Liu, J., "High Order Accurate Ship Airwake Predictions for the Helicopter/Ship Interface Problem," *Proceedings of the 54th Forum of the American Helicopter Society* (Washington, DC), American Helicopter Society, Alexandria, VA.

CFD PREDICTIONS OF THE INFLUENCE OF EXTERNAL AIRFLOW ON HELICOPTER OPERATIONS WHEN OPERATING FROM SHIP FLIGHT DECKS.

N.H. Wakefield, Department of Ship Science,
 S.J. Newman, Department of Aeronautics and Astronautics,
 P.A. Wilson, Department of Ship Science.
 University of Southampton, Southampton, SO17 1BJ, UK.

1. Abstract.

A CFD model of a hovering helicopter main rotor is developed to examine airflow in the presence of ship structures and side winds. The rotor is modelled by modifying the governing Navier-Stokes equations in the region of the disc. The extra terms added to the governing equations apply a downforce to the fluid; these forces are independent of the flow around the rotor and equal to the helicopter weight. The boundaries of the computational domain are also modified in order to generate a physically correct solution. Flow solutions in both two and three dimensions are achieved using the commercial flow solver CFX 4.1. The flow solutions exhibit very good correlation with established momentum and power principles.

In order to model helicopter operations from a ship's flight deck, typically a frigate, the rotor is modelled at several positions above a ship profile. Cross winds are applied to the computational domain. The thrust of the rotor is held constant and the resulting flow solutions are calculated. The power exerted at the rotor is obtained and compared to the ideal hover condition and computational flow solution.

The flow solutions show that the airflow accelerates over the flight deck and a helicopter operating in this region encounters large cross winds and velocity gradients. The results also show that the helicopter control margins are more likely to limit the safe operating limit than the power margin.

Using the modified boundary conditions, this method demonstrates the viability of CFD for predicting the ship airwake and the reduced power margins a helicopter experiences whilst operating in the vicinity of the ship. This study has been exploratory and limited by computing resources, but future models will include helicopter fuselage, tail rotor, time dependant boundary conditions and dynamic flight.

2. Introduction

The demand for use of helicopters in marine environments such as ships and oil rigs has risen steadily in recent years. The helicopter provides a fast method of transport whilst requiring less storage space and take-off

facilities than fixed wing aircraft. The helicopter has also developed specialised military uses such as submarine detection and air to surface targeting.

The flexibility of helicopters is reflected in the increased demand to operate in ever worsening environmental conditions. At present, the established method for determining safe helicopter operating limits is a very costly series of full scale trials. This usually involves waiting at sea for appropriate environmental conditions to occur when a test pilot performs the takeoff and landing manoeuvres. The landing is rated according to the work load the pilot experiences and varies from low to dangerous. The whole procedure has to be repeated for every ship/helicopter combination.

An experimental SHOL (Safe Helicopter Operating Limit) such as this has the advantage of being realistic but it also requires the provision of vast resources both in finance and time. These studies also provide no systematic information about the areas in which the pilot experienced difficulties. Obtaining such a SHOL, by definition, contains a degree of danger.

A CFD analysis has many advantages. The most evident is the cost and speed at which one can be obtained. Results from such an analysis are repeatable and not subject to either measurement error or personal subjection. The solution is complete and, therefore, once obtained, pressure and velocity components are known at every location throughout the model. The flow data obtained can be used in simulators so that pilots can practice landing on ships safely. A CFD study can also be performed on ship designs whilst in the conceptual stage. Thus the effectiveness of helideck and hangar designs can be tested to reduce turbulence over the flight deck. Naturally the fidelity of the predictions must be of the highest quality.

3. Modelling the Rotor.

A simple theoretical model of the helicopter main rotor was constructed within the computational domain. The method solves the governing Navier-Stokes equations as shown in Equation 3.1. The main rotor was designed to reflect the loading and geometry of a Westland Lynx, that is the rotor radius is 6.5m and the mass is 5.2 tonnes. The thrust exerted by the rotor was evenly distributed across the disc. The force was exerted within

the computational domain of Figure 3.1. The figure indicates that the rotor thrust is exerted within the hatched areas. In these regions the Navier-Stokes equations are modified by the addition of the vector \bar{B} as shown in Equation 3.1. The force applied to the fluid acts vertically downwards.

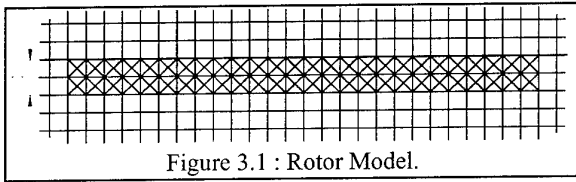


Figure 3.1 : Rotor Model.

$$\rho \frac{d\bar{U}}{dt} + \rho \nabla \cdot (\bar{U} \otimes \bar{U}) = \bar{B} + \nabla \cdot (\sigma - \rho \bar{u} \otimes \bar{u}) \quad \text{Equation 3.1}$$

The vector term \bar{B} has units of force per unit volume, therefore to exert the required thrust to the fluid, \bar{B} was defined as in Equation 3.2. The thrust is distributed evenly across the span of the rotor model.

$$\bar{B} = \begin{bmatrix} 0 \\ 0 \\ \text{Thrust / Area / H} \end{bmatrix} \quad \text{Equation 3.2.}$$

Only thrust is applied to the fluid to evince the rotor, which has two implications. Firstly, the flow is in no way predetermined at the location of the rotor; the velocity and pressure are solved in exactly the same way as they are throughout the rest of the domain. Secondly, the resultant vertical velocity component determines the induced power exerted across the rotor whilst the thrust always remains constant and acting through the centre of the rotor.

In all the flow solutions described within this paper the grid cell dimensions are $0.50\text{m} \times 0.50\text{m}$. The rotor is therefore 26 cells wide. Ideally the rotor would be one cell deep, but the flow solver can not resolve the sharp pressure gradients, this problem is alleviated by making the rotor two cells deep.

4. Modified Boundary Conditions

The default boundary conditions available within CFX 4.1 and other commercial CFD software packages are applicable to external flows which comprise a free stream velocity and some body causing a perturbation such as a wing or a building.

The air flow around a hovering helicopter is fundamentally different because there is no free stream velocity and all fluid flow is induced by the helicopter rotor itself. For this reason, applying any of the available boundary conditions such as an imposed velocity or pressure is unjustifiable and gives physically incorrect flow solutions. An example is the flow solution in Figure 4.1, generated by allowing the velocity to vary around the boundary whilst the pressure remains

constant. There are many features of this flow that conflict with established understanding of both rotors and actuator discs. Figure 4.1 shows that the fluid flows upwards throughout most of the domain, including the outer region of the rotor. Quantitative study yields that momentum in the downwash does not equate to the thrust applied at the rotor.

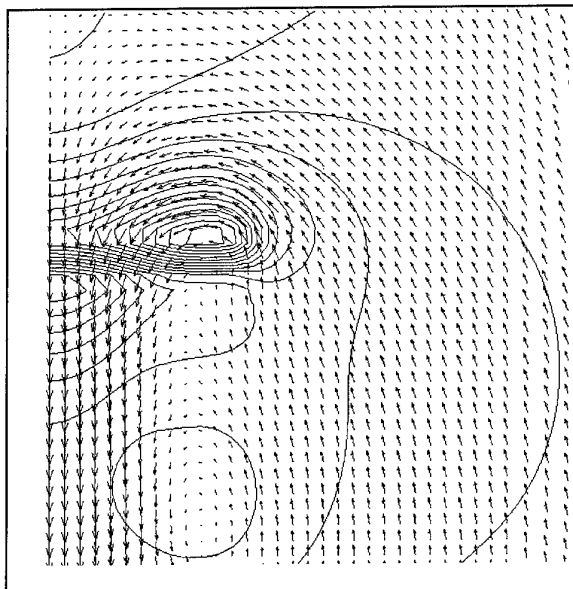


Figure 4.1: Hover Flow Solution, Existing Boundary Conditions

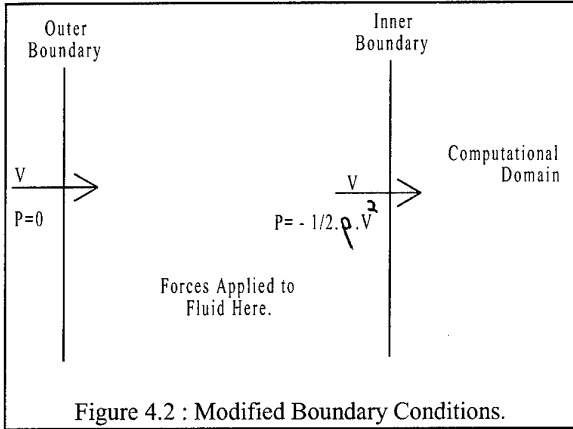
To restore a realistic flow pattern, the boundary conditions have been modified. At the modified boundaries neither a pressure nor a velocity is applied but instead a relationship between the two is used based upon Bernoulli's equation. It is assumed that at an infinite distance from the rotor the velocity is zero. The pressure is atmospheric pressure, and is defined as the datum or zero. Therefore any fluid entering the domain must have the pressure/velocity relationship defined in Equation 4.1.

For this assumption to be strictly accurate, the viscous effects that act on the fluid between infinity and the domain boundary must be neglected. In reality the domain size makes negligible difference to the flow solution, thus validating this assumption.

$$p + \frac{1}{2} \cdot \rho \cdot V^2 = 0 \quad \text{Equation 4.1}$$

In order to instigate the given relationship the computational domain must be constructed with two boundaries, an inner and an outer. At the outer boundary, the extremity of the domain, the pressure is defined as zero. This is achieved using a 'pressure boundary', a boundary condition readily accessible within most CFD solvers.

The inner boundary was placed a small distance from the outer boundary within the computational domain, as shown in Figure 4.2. In the region between the outer and inner boundaries additional terms were added to the Navier-Stokes equations enabling forces to be applied to the fluid to alter the fluid pressure.



Other than at the walls, the entire fluid domain is surrounded by the boundary outlined above.

5. Rotor In Hover

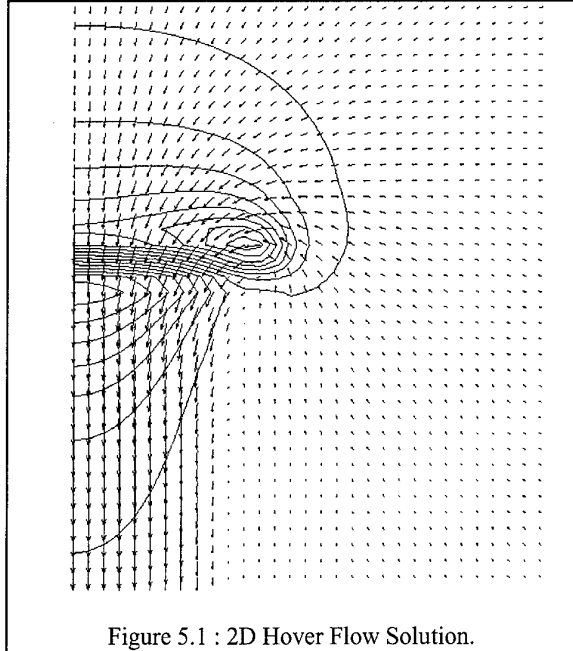
To verify that both the boundaries employed and the rotor model work as intended, a test case was run to model the rotor in hover with no cross wind. Both two and three dimensional cases were obtained. In each case the fluid used was air with a density 1.2kg/m^3 and viscosity $1.8 \times 10^{-5}\text{Ns/m}^2$. The fluid was considered isothermal, incompressible and turbulent.

The two dimensional case modelled a disc of diameter 13m and unit thickness. The thrust per unit area used is described in Equation 5.1, these values were chosen to reflect the Westland Lynx. The total thrust exerted was 4996.2N. Half of the flow solution is shown in Figure 5.1. The contours represent pressure variations of 25Pa.

$$\text{Thrust / Area} = 5200 * 9.81 / (\pi 6.5^2) = 384.3\text{Pa} \quad \text{Equation 5.1}$$

In order to gauge the validity of the flow solution, momentum and energy principles from existing actuator disc theory were compared to the computational disc.

The momentum in the downwash was obtained, as described in Equation 5.2. This integral was evaluated 20m below the plane of the disc, across the downwash.



$$\frac{dM}{dt} = \rho \int w^2 dA = 4980\text{N} \quad \text{Equation 5.2}$$

The discrepancy between the momentum in the downwash and the thrust exerted at the rotor is 0.3%. This indicates that momentum has been effectively conserved within the system and Newton's equation is satisfied.

The power exerted by the rotor was evaluated as described in Equation 5.3. This integral is performed across the plane of the rotor itself. The power derived is per unit depth, and thus is not comparable to the power exerted over the whole rotor plane.

$$P_H = \int w \cdot \Delta p \cdot dA = 67.4\text{kW} \quad \text{Equation 5.3}$$

The ideal power as found from standard actuator disc theory is shown in Equation 5.4. The difference between the predicted ideal power and the measured power is 7%.

$$P_{ID} = T \cdot \sqrt{T / (2 \cdot \rho \cdot A)} = 63.2\text{kW} \quad \text{Equation 5.4}$$

The 7% discrepancy between the two values can be attributed to variations in the induced velocity across the rotor that are not predicted within actuator disc theory. Such a difference is realistic since 10-15% is a typical range used in the helicopter industry. The calculated power 67.4kW is carried forward to studies of the flow around the ship helideck.

A further study of a three dimensional rotor was performed, with the thrust per unit area kept constant. The flow solutions is shown in Figures 5.2. The solution is axisymmetric, Figure 5.2 corresponds to an azimuth

angle of 0° . The vectors represent speed and the contours pressure variations of 25Pa.

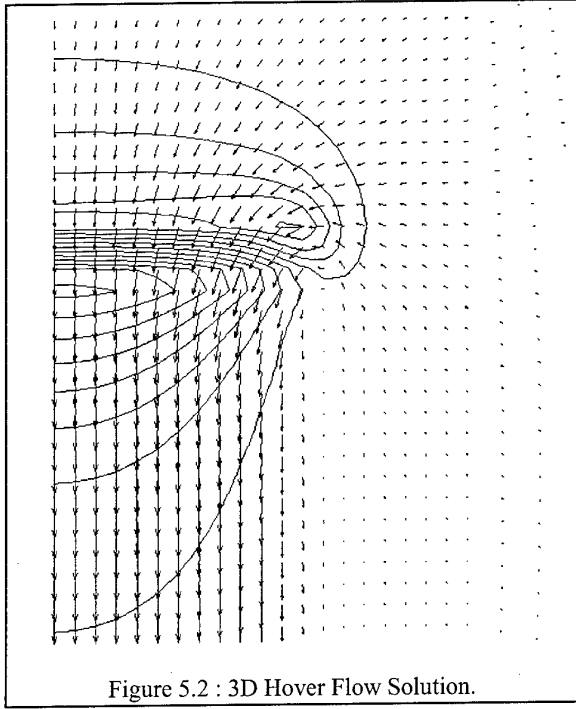


Figure 5.2 : 3D Hover Flow Solution.

Comparison of momentum in the downwash and thrust applied yielded a 0.2% discrepancy. The power exerted at the plane of the disc was 3% greater than the ideal value predicted by actuator disc.

6. Ship Airwake

Apart from operational and performance calculations, the airflow around the ship in the absence of the helicopter thrust is of interest for other reasons, such as helicopter blade strike predictions during rotor engagement and disengagement.

A flow solution was obtained for a 2D model of a helideck. The geometry of the ship is shown in Figure 6.1. The domain extended 75m upwind, downwind and above the centre of the ship. A horizontal free stream velocity of 30 knots was imposed. The dimensions of the helideck are those used by the TTCP Nations for their research into the Helicopter Ship Dynamic Interface¹.

Both the sea and ship were modelled as walls; zero flow imposed at these surfaces. The k- ϵ turbulence model was used and the flow was assumed to be turbulent,

incompressible and isothermal. Reference [1] was used to determine the turbulent kinetic energy imposed at the windward edge of the domain. Reference [2] was used to determine a realistic mixing length for the initial turbulence dissipation constant, epsilon.

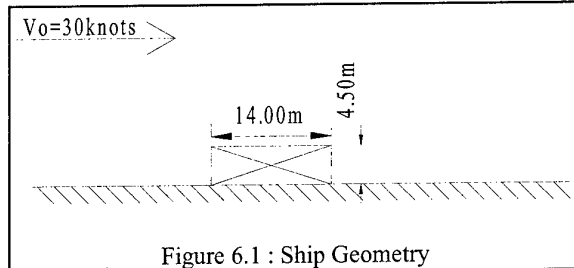


Figure 6.1 : Ship Geometry

The flow solution is shown in Figure 6.2. The arrows represent the velocity vectors, the contours are pressure contours at 25Pa intervals. The figure shows the flow separating at the windward edge of the helideck and a large region of recirculation both above and downwind of the ship. This flow pattern agrees with experimentally measured data such as reference [3].

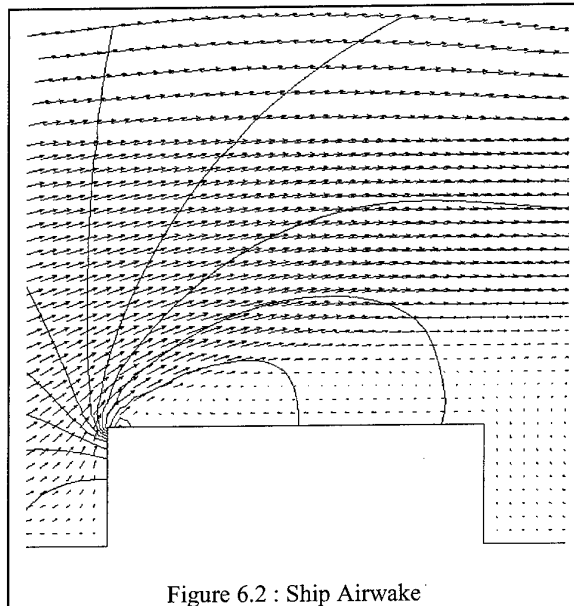
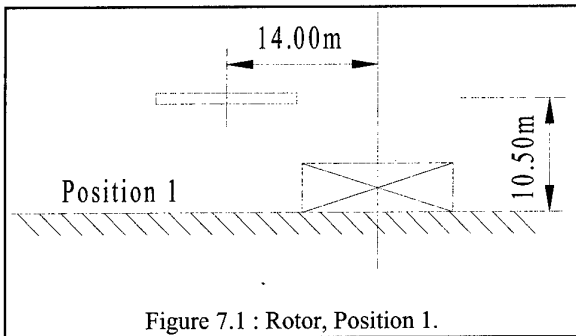


Figure 6.2 : Ship Airwake

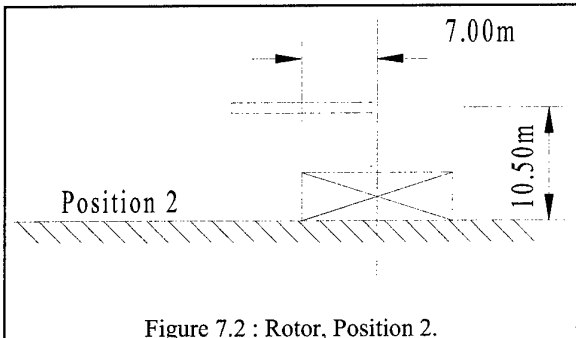
7. Ship/Helicopter Interaction

The geometry of the ship used is the same as that described in Section 6. Three positions for the main rotor were chosen. The first position is shown in Figure 7.1, the rotor is at a height of 10.5m above sea level and 14m to port of the centreline of the helideck. The second position is 7m to port of the centreline as shown in Figure 7.2, and the rotor is placed over the centreline of the ship in Position 4 shown in Figure 7.3.

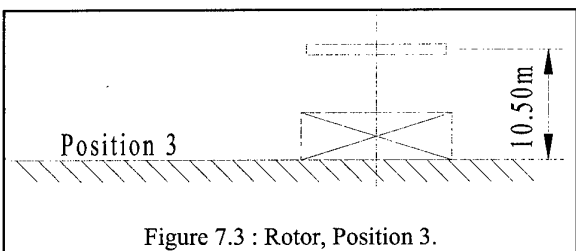
¹ Tripartite Technical Co-operation Program, national defence research organisations from, UK, USA, Canada and Australia.



Four wind velocities were chosen relative to the ship, zero, 30 knots port to starboard, 30 knots starboard to port and 60 knots port to starboard. Flow solutions were obtained for all of these wind velocities, with the rotor at each of these positions.



The flow solution was solved as incompressible, isothermal and turbulent. The $k-\epsilon$ turbulence model was used, the turbulent kinetic energy and energy dissipation parameters were determined as described in Section 6.



The solver could not achieve a steady state solution for any of the problems due to the turbulent unsteady nature of the flows, the solutions were obtained using a time-stepping approach. The results presented in the following sections are therefore instantaneous and represent a snapshot of the flow solution, after the rotor has been stationary in the given location for at least 30 seconds.

There are two factors that limit helicopter operations in adverse weather conditions, namely power and control. The pilot must have adequate quantities of both in order to perform manoeuvres. As outlined in Section 5, the power required to hover out of ground effect in still air is

67.4kW. The power to hover in a stationary position with the given cross winds was calculated using Equation 7.1. For each of the flow solutions generated the corresponding power was calculated accordingly.

$$P = \int w \cdot \Delta p \cdot dA \quad \text{Equation 7.1}$$

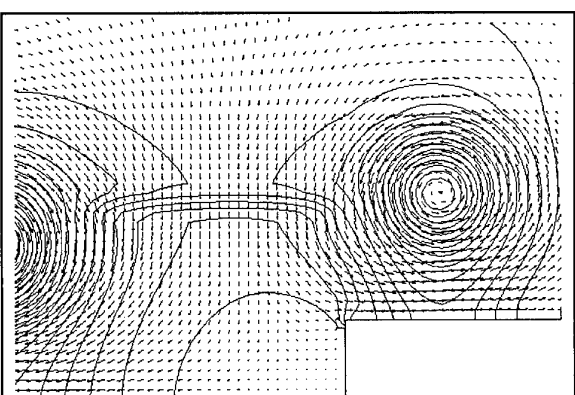
The lateral wind that the rotor experiences was also quantified. V_{AV} is the average lateral velocity component across the entire span of the rotor.

Whilst the power required to maintain a certain hover position is important, control requirements are as significant. For this reason the vertical flow velocities have been recorded near the extremities of the rotor. W_p and W_s correspond to the vertical flow 5m to port and 5m to starboard of the rotor centre respectively. (5m is approximately 75% of the rotor radius.) These values not only indicate the velocity gradients across the rotor but provide a measure of control demanded. ΔW is difference between the vertical components W_p and W_s .

For future development, a three dimensional analysis could be extended to include blade element theory and inverse simulation. Vertical velocity components would provide an estimate of cyclic and collective pitch variations that achieve the required thrust magnitude and distribution. This has not been attempted to date because these flow solutions are two dimensional and provide a qualitative understanding of the flow regimes. The techniques are under development and 2D cases are much less demanding of time during the validation phases of the model.

7.1. Zero Wind

The flow solutions for hover in each of the three positions are shown in Figures 7.1.1-3. The arrows represent velocity vectors and the contours are spaced at 100Pa in the first two flow solutions and 40Pa in the final flow figure. The computed power requirements are shown in Table 7.1.1.



In Position 1, shown in Figure 7.1.1, there are vortices present on both sides of the rotor. These cause significant recirculation, which in turn increases the power requirements to a value greater than the simple hover case, since the rotor is effectively in climb. The flow through the rotor itself is approximately vertical.

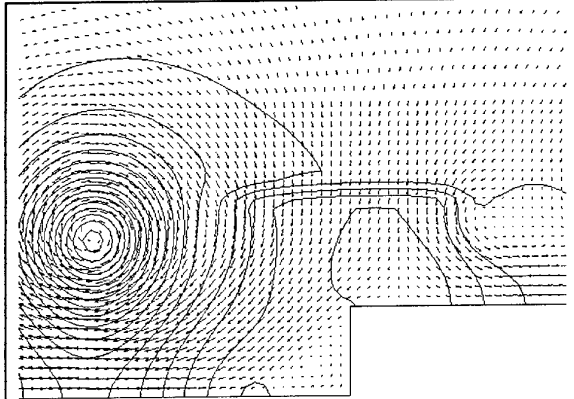


Figure 7.1.2 : Rotor in Position 2.

The rotor in Position 2 has a vortex present at the outboard edge of the rotor but there is no vortex over the ship. The combination of the vortex and the beneficial ground effect give a power requirement comparable to the hover case.

Figure 7.1.3 displays the flow solution for the rotor over the ship's centreline. The rotor has no recirculation at the tips. There is a high pressure region directly beneath the rotor and on the deck. The favourable ground effect the ship generates, gives a power requirement significantly less than the hover.

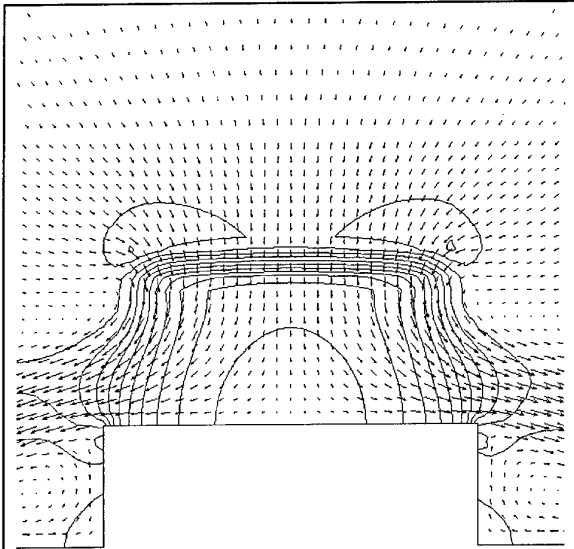


Figure 7.1.3: Rotor in Position 3.

</div

ship. This is reflected in the power exerted, as shown in Table 7.2.1. There is however a large vertical velocity gradient across the rotor. The fluid is passing upwards through the rotor on the port side and downwards at the starboard side. This represents increased control requirements.

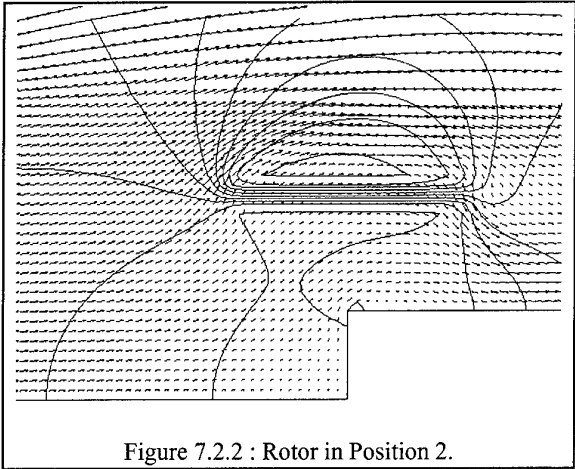


Figure 7.2.2 : Rotor in Position 2.

Figure 7.2.2 shows the flow solution with the rotor over the side of the ship. At this position the helicopter is resting in the upflow generated by the blockage of the ship. The power requirements are negative as shown in Table 7.2.1. This indicates an autorotative state. The lateral velocity the rotor experiences is 4.6m/s or 9 knots. This is in fact less than the undisturbed free stream velocity of 15 knots. This flow also exhibits a large vertical velocity variation across the span, 10.9m/s with correspondingly high resulting control demands.

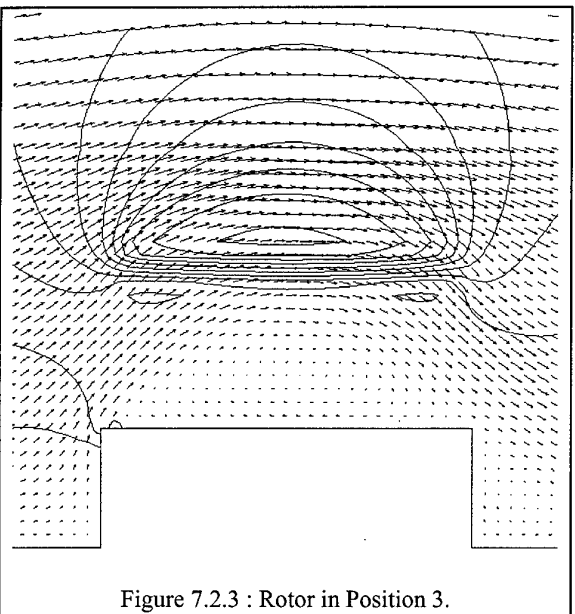


Figure 7.2.3 : Rotor in Position 3.

The rotor over the ship's centreline is shown Figure 7.2.3. Similar to the other positions the induced power is small due to the upflow across the rotor. The most

noticeable feature of the flow solution is the lateral velocity the rotor experiences, 10.9m/s or 21knots. This is more than double the other two positions caused by only a small change in position of the rotor. As with the other two positions the fluid is flowing upwards through the rotor on the port side and downwards on the starboard side.

Position	1	2	3
P (kW)	-0.2	-1.0	0.0
%P _H	0	-1	0
V _{AV} (ms ⁻¹)	3.5	4.6	10.9
W _P	3.9	4.2	6.1
W _S	-7.0	-6.6	-7.6
ΔW	10.9	10.8	13.7

Table 7.2.1 : Power and Control Requirements, 30 Knots
Port to Starboard.

Table 7.2.1 shows that in these cases there is little power exerted at the rotor and the rotor is operating in significantly less lateral wind than the free stream of 15.4m/s. However the rotor is experiencing widely varying flow vertical flow across its span. In reality this would necessitate large cyclic pitch variations to trim the helicopter.

7.3. Wind 60 Knots, Port to Starboard

These three flow solutions were generated using a free stream velocity of 60 knots acting from port to starboard. The pressure contours are spaced at 75Pa.

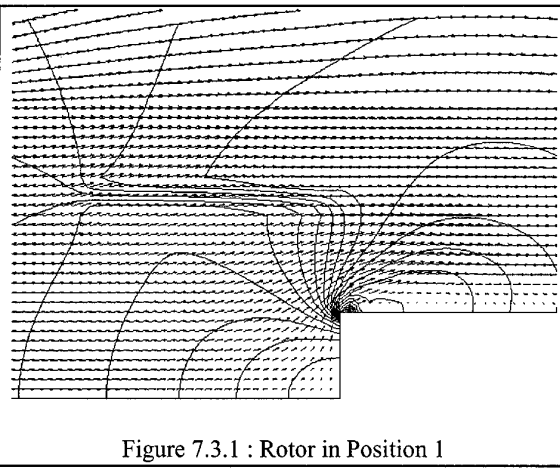


Figure 7.3.1 : Rotor in Position 1

Figure 7.3.1 shows that the flow around the rotor in Position 1 is largely influenced by the free stream and the presence of the ship's helideck. The greatest

pressure gradients occur at the windward edge of the deck, not at the rotor. The rotor is operating in a strong upflow resulting in a negative power requirement, as shown in Table 7.3.1. The lateral wind speed across the rotor is 23.8m/s which is less than the undisturbed free stream velocity.

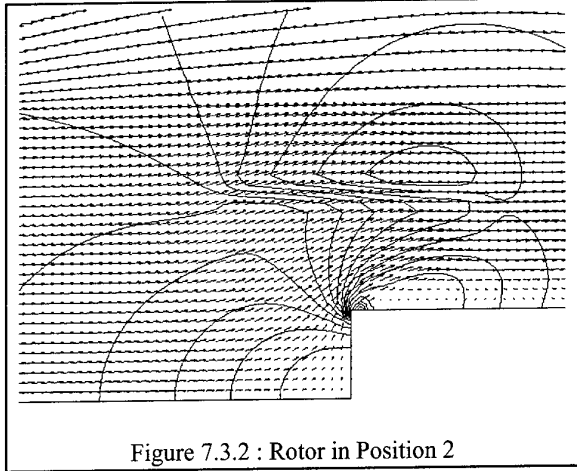


Figure 7.3.2 : Rotor in Position 2

The flow solution for the rotor above the side of the ship is shown in Figure 7.3.2. In many respects this is similar to the rotor in the outboard position. The rotor is operating within an upflow greater than the outboard position, shown in Figure 7.3.1, resulting in a larger negative power at the rotor. The rotor is operating in 28.2m/s cross wind flow, this is similar to the free stream velocity of 60 knots.

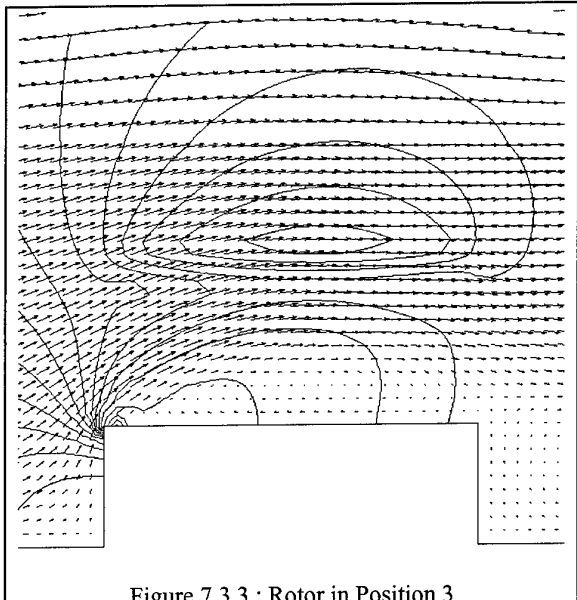


Figure 7.3.3 : Rotor in Position 3

The flow solution for the rotor over the centreline of the ship is shown in Figure 7.3.3. The airflow and pressure variations are clearly dominated by the ship. The rotor is operating in an upflow generated from the ship, causing a large negative power requirement. The lateral

wind speed across the rotor is 65 knots, this is greater than the free stream velocity. The vertical flow of fluid through the rotor varies by 13.3m/s between the port and starboard reference points.

Position	1	2	3
P (kW)	-21.8	-26.1	-20.1
%P _H	-32	-39	-30
V _{AV} (ms ⁻¹)	23.8	28.2	33.3
W _P	5.8	7.9	10.5
W _S	3.4	0.9	-2.8
ΔW	2.4	7.0	13.3

Table 7.3.1 : Power and Control Requirements, Wind 60 Knots, Port to Starboard.

These flow solutions indicate that although power requirements are small or negative the helicopter has to contend with accelerated side winds and large velocity gradients across the span of the rotor.

7.4. Wind 30 Knots, Starboard to Port

The flow solutions within this section were obtained with a free stream velocity of 30 knots, which appears right to left in the figures.

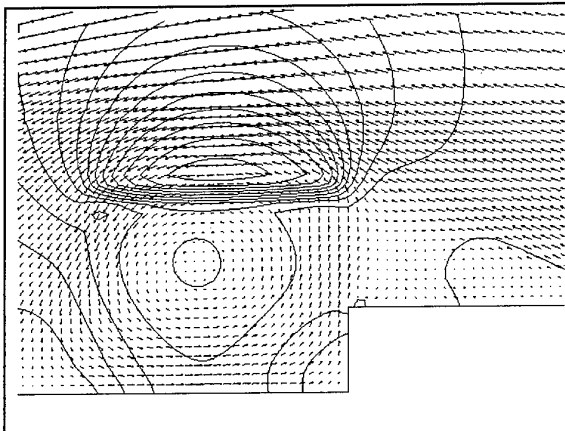


Figure 7.4.1 : Rotor Position 1.

The rotor operating in the outboard position is shown in Figure 7.4.1. The solution shows that the flow separates at the windward edge of the helideck and the deck is covered in an area of recirculation. There is another recirculation region downstream of the ship, where the downwash of the rotor travels down to the sea surface and upwind to the ship, and finally up towards the rotor. This vortex appears to be small and does not contribute adversely to the power requirements as given in Table

7.4.1. The power exerted at the rotor is only a fraction of the power exerted in the simple hover case. The flow across the rotor is a 8m/s, this is less than the free stream velocity. The variation between the vertical velocity component at the port and starboard end of the rotors is large, 16.8m/s.

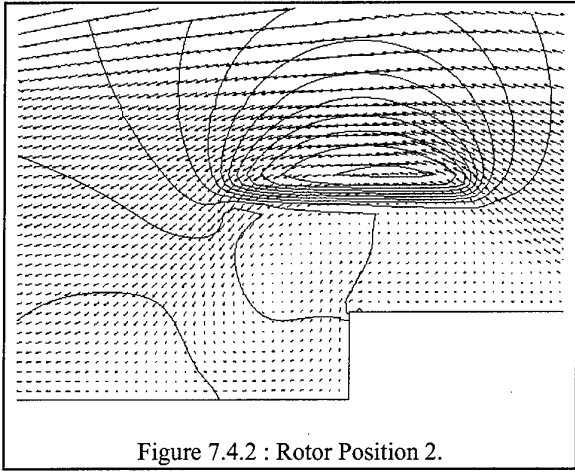


Figure 7.4.2 : Rotor Position 2.

The flow pattern corresponding to the rotor in Position 2 is shown in Figure 7.4.2 above. The rotor has a large region of low pressure above the rotor whereas there is little pressure increase below the rotor. The angle of the separation at the windward edge of the deck is greater than that found in the previous flow solution, indicating the rotor downwash being ‘fed’ into the separation region above the deck. The power exerted by the rotor within the solution is only 8.8kW, which is only 14% of the power required in hover.

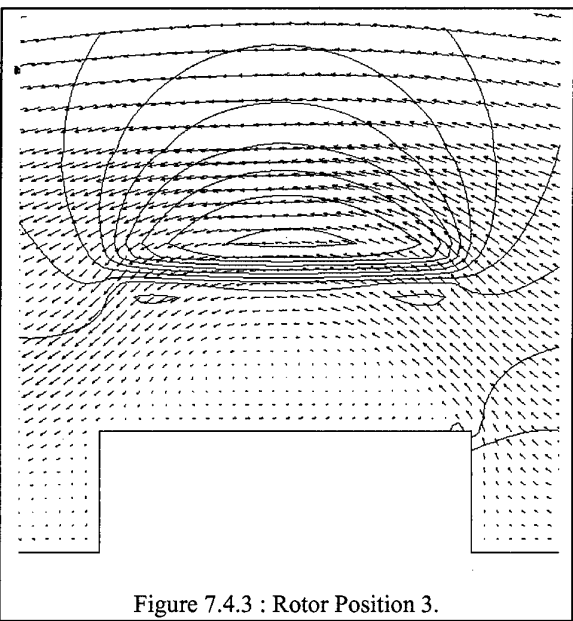


Figure 7.4.3 : Rotor Position 3.

Figure 7.4.3 shows the flow solution for the rotor over the ship centreline, which is an exact reflection of Figure 7.2.3. The upflow of the air over the ship causes the air

to flow upwards through the rotor at the windward end. At the leeward end of the rotor the air is flowing downwards. The net effect of the up and down flow is a zero power requirement. The lateral wind speed across the rotor, shown in Table 7.4.1, is 10.9m/s, this is less than the free stream velocity.

Position	1	2	3
P (kW)	8.7	6.8	0.0
%P _H	13	10	0
V _{AV} (ms ⁻¹)	-8.0	-6.0	-10.9
W _P	-11.5	-9.0	-7.6
W _S	5.4	3.3	6.1
ΔW	-16.8	-12.3	-13.7

Table 7.4.1: Power and Control Requirements, Wind 30 Knots, Starboard to Port.

These three flow solutions exhibit limited power requirements and lateral flow speeds but large velocity gradients across the rotor span.

8. Conclusions

These results combine the ship airwake and the helicopter induced flow and from the results clear indications of power and control requirements are evident. With no side winds the helicopter rotor experiences slight power increases, but there are negligible lateral flows to contend with. The vertical flow is approximately constant across the span of the disc so the control requirements are limited.

The three cases that considered the 30 knot wind from the port side all exhibited power requirements of around zero. However the large velocity gradients across the rotor indicate high demands on pilot and rotor control.

The 60 knot wind cases indicated that the ship airwake was predominant and the helicopter thrust caused small disturbances by comparison. In these cases the power requirements were negative. The helicopter over the ship’s centreline experienced local wind speeds greater than the free stream velocity. In these cases the variation of vertical velocity flow across the span was actually less than those in the 30 knot cases.

Regarding wind from the starboard side of the ship shown in Section 7.4, once again the power requirements were minimal compared to that of the hover. However the rotor experiences the most dramatic vertical velocity gradients across the rotor in these cases.

This study indicates that the control requirements of the helicopter are more likely to limit safe operations than the power limitations. The vertical velocity variations evident in the flow solutions are not found in any other normal operations, such as hover or forward flight.

The geometries considered have only dealt with a lateral wind relative to the ship and therefore do not include any downflows due to the influence of the ship's superstructure.

These results provide a qualitative measure of the flow variations around the ship and helicopter because of the two dimensional nature. In reality the flow is far from two dimensional and some of the features exhibited in these solutions will be less prominent. For example, the upflow through the rotor when the rotor is upwind of the ship. In a three dimensional solution, the air can travel longitudinally around the rotor, rather than remaining in the same plane and being forced through the rotor. This will, in turn, affect the power predictions which are predicted from induced velocities at the rotor plane.

The boundary conditions and rotor model employed for a three dimensional case are identical to those used for the two dimensional study. The computational resources for a three dimensional study far exceed those of the two dimensional study undertaken presently. However this study demonstrates the viability of CFD in order to predict accurate flow solutions and resultant power and control requirements.

9. Nomenclature

All Units S.I. unless otherwise stated.

A = area of rotor.

Δp = thrust/area at rotor.

p = pressure.

P = power exerted at rotor.

P_H = power required to hover in still air.

% P_H = power exerted at rotor as percent of hover, P_H

P_{ID} = ideal power of actuator disc in hover.

T = total thrust of rotor.

u,v,w = longitudinal, lateral, and vertical velocity components.

V = velocity scalar.

V_{AV} = average lateral velocity component at rotor.

W_P = vertical velocity component at 5m port of rotor centreline.

W_S = vertical velocity component at 5m starboard of rotor centreline.

$$\Delta W = W_P - W_S.$$

10. References

- [1] Plate E.J.(ed.), 'Engineering Meteorology', Elsevier, Amsterdam, The Netherlands, 1982, Ch.13.
- [2] Versteeg H.K., Malalasekera W., 'An Introduction to Computational Fluid Dynamics, The Finite Volume Method', Longman, 1995.
- [3] Newman S.J., 'A Theoretical and Experimental Investigation Into The Rotor Blade Aeroelastic Behaviour of a Shipborne Helicopter During Rotor Engagement and Braking', AGARD Conference Proceedings No. 552., 75th Fluid Dynamics Symposium, Berlin, Oct. 1994.

Higher Order Accurate Solutions of Ship Airwake Flow Fields Using Parallel Computers

Lyle N. Long *; Jingmei Liu †
and Anirudh V. Modi ‡

Department of Aerospace Engineering
The Pennsylvania State University
University Park, PA 16802
lnl@psu.edu

Summary

This paper presents a new method for simulating ship airwake flow fields. These flows are inherently unsteady, and very difficult to predict. The method presented (NLDE) is fourth-order accurate in space and time. In this method we first solve for the steady state flow field, then we solve for the unsteady fluctuations. Steady and unsteady results are presented for a generic frigate shape. Considering the complex geometry of real ship, the unstructured grid approach is most useful. The mean flow results are compared with oil flow visualization photographs. Parallel computational methods are a necessity for ship air wake problems and MPI is used in the NLDE solver. The parallel performance on various computers is presented also.

Introduction

Sharp-edged box-like ship super-structures create numerous aerodynamic and fluid dynamic problems. Unsteady separated flow from sharp edges (and excessive ship motions) make landing helicopters on ships a very hazardous operation. In addition, the strong unsteady flows can cause severe rotor blade deformations. There have been numerous incidences where the helicopter blades have actually impacted the helicopter fuselage, which is called a "tunnel strike".^{9,10} In order to avoid this and other engage/disengage problems, determining safe operating envelopes is very costly and time consuming. On the other hand, many numerical simulation attempts have not been successful due to the inherently unsteady nature of flow and the low-speed character of the flow (which may cause numerical stiffness).

Research on ship airwakes has been conducted using several different approaches.⁵ One of the sources of relevant research is building aerodynamics which shows the

general features of flow about blunt bodies of different aspect ratios. The simplest model of a ship, admittedly rather crude, is a sharp edged blunt body. The super-structure of most modern ships is very complicated, including towers, antennae, radar dishes, exhaust stacks, etc. The flow around these obstacles is very difficult to predict.

Geometrically precise studies are needed and have been done in wind tunnels.^{7,8,18} There have also been full scale tests performed by the US Navy,¹¹ which gives some important information on real ship airwakes. Of course it is difficult to perform very controlled experiments on real ships. It is also difficult to measure the flow field accurately in the harsh ocean environment and in the presence of the strong electromagnetic fields on most ships.

Most wind tunnel tests include measurements made in the wake of a model ship exposed to a uniform velocity profile and almost zero turbulence level. One more realistic test was conducted at NASA Ames in the "Shipboard Simulator" with a neutrally buoyant atmospheric boundary layer.⁷

Another reference for simulations is that by NRC-CNRC.²³ A wind tunnel investigation of the characteristics of the airwake behind a model of a generic frigate was conducted. The wind tunnel simulation incorporated a correctly-scaled atmospheric boundary layer. Measurements of streamwise and vertical components of airwake velocity were made. Time average, standard deviations, spectral densities and time correlations are presented for both velocity components for various position in the airwake. All these experimental tests are crucial for validating numerical models.

Figs. 1 and 2 show a frigate and an LHA, respectively. These are very different ships, and their airwakes are very different also. The frigates typically carry one or two SH-2G Seasprites or SH-60B Seahawks. On the frigate we are mainly interested in studying the hangar deck area (aft portion of the ship), and the separated

*Professor

†Research Associate

‡Graduate Research Assistant

flow that effects this region. On the LHA, helicopters can land on many different locations on the deck, and each of these can experience quite different flow fields. The LHA's can carry 9 CH-53D Sea Stallion or 12 CH-46D Sea Knight helicopters, and 6 AV-8B Harriers. The forward portion of the deck is primarily influenced by the separated flow off the deck edge. Very strong vortex sheets emanate from these edges. One of the authors (Long) spent three days on an LHA (U.S.S. Saipan) and helped Kurt Long measure ship airwakes. We found in some cases the flow velocity ranged from 40 knots 12 feet off the deck to zero velocity 3 feet off the deck. In the mid-section of the ship the very large island has a strong effect on the flow and tunnels the flow tangential to the island.

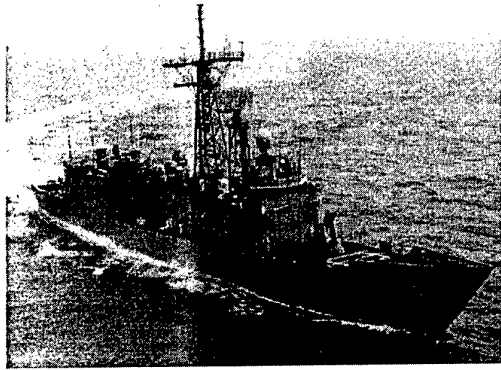


Figure 1: Oliver Hazard Perry Class Guided Missile Frigate (length=445 feet, beam=45 feet.)

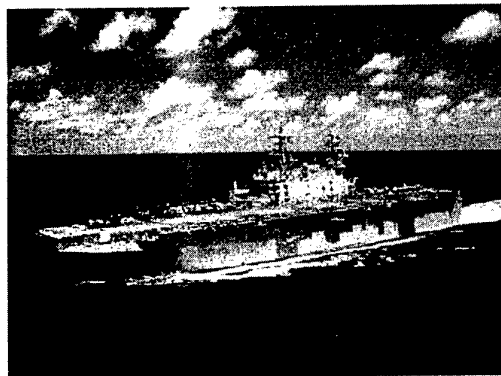


Figure 2: Tarawa Class LHA (length = 820 feet, beam = 132 feet).

The need for numerical simulations comes from the high cost of determining the safe operating envelopes for helicopters in a ship environment (and the huge testing backlog). It would be very useful to have numerical methods that could accurately simulate ship airwakes. There have been other attempts at numerically simulating ship airwakes. The airwake about a DD-963 ship configuration was simulated using a steady-state flow solver based on the 3D multi-zone, thin-layer Navier-Stokes method.²⁰ A US navy destroyer, DDG51 was chosen to validate an unsteady inviscid solver with an unstructured grid and low-order method.^{12,13} No method to-date has been entirely satisfactory for predicting these flow fields.

Flow Nature of Ship Airwake Simulation

From previous studies, it has been shown that the key features of ship airwakes are (1) a low Mach number (about 0.05), (2) inherently unsteady flow, and (3) large regions of separated flow. The large separated regions from superstructure sharp edges are quite difficult to capture accurately. In addition, the wind conditions over rough seas have to be considered, such as, the atmospheric turbulent boundary layer and the effect of the wind/ship speed ratio on the turbulence intensity. When this ratio is increased, the turbulence intensity will decrease and its spectrum will shift to a high value in the streamwise direction. The wind direction can vary a great deal, since the air flow can impact the ship at any yaw angle (even 180 degrees). The complex ship geometry makes unstructured grid solvers and parallel computers very attractive. In this paper, preliminary attempts at high order accurate ship airwake predictions have been made by solving a steady flow field with a well-developed CFD method (CFL3D¹⁹) and a perturbation field with a high-order method. The result is high-order-accurate 3D simulations. We also have some preliminary results for steady flow predictions from an unstructured solver (PUMA).

Nonlinear Disturbance Equations (NLDE)

The methodology used here is based on the nonlinear disturbance equations, which is a newly developed numerical method.¹⁵ The general Navier-Stokes equations in a Cartesian coordinate system are:

$$\frac{\partial q}{\partial t} + \frac{\partial F}{\partial x} + \frac{\partial G}{\partial y} + \frac{\partial H}{\partial z} = \frac{\partial R}{\partial x} + \frac{\partial S}{\partial y} + \frac{\partial E}{\partial z} \quad (1)$$

where F , G , and H are the inviscid terms and R , S , E are the viscous terms. The results presented here will

all be inviscid. The flow field is then split into a mean and a fluctuating part:

$$q = q_o + q' \quad (2)$$

where

$$q = \begin{Bmatrix} \rho \\ \rho u \\ \rho v \\ \rho w \\ e \end{Bmatrix} \quad (3)$$

and

$$q_o = \lim_{T \rightarrow \infty} \frac{1}{T} \int_{t_0}^{t_0+T} q(t) dt \quad (4)$$

Substitution of equation (2) into (1) and rearranging results in the nonlinear disturbance equations (NLDE):

$$\frac{\partial q'}{\partial t} + \frac{\partial F'}{\partial x} + \frac{\partial G'}{\partial y} + \frac{\partial H'}{\partial z} = Q \quad (5)$$

Where

$$q' = \begin{Bmatrix} \rho' \\ \rho_o u' + \rho' u_o + \rho' u' \\ \rho_o v' + \rho' v_o + \rho' v' \\ \rho_o w' + \rho' w_o + \rho' w' \\ e' \end{Bmatrix} \quad (6)$$

On the left hand side of the NLDE are terms related to the perturbation properties and the cross terms (linear and nonlinear), whereas the right hand side contains strictly mean flow terms.

The convective fluxes involving the perturbation quantities F' , G' and H' are given as

$$F' = \begin{Bmatrix} \rho_o u' + \rho' u_o + \rho' u' \\ \rho' u_o^2 + 2\rho_o u_o u' + \rho' u' u' \\ + 2\rho' u' u_o + (\rho_o + \rho') u' u' \\ \rho_o u_o v' + \rho_o v_o u' + \rho' u_o v_o \\ + \rho' v' u_o + \rho' u' v_o + (\rho_o + \rho') u' v' \\ \rho_o u_o w' + \rho_o w_o u' + \rho' u_o w_o \\ + \rho' w' u_o + \rho' u' w_o + (\rho_o + \rho') u' w' \\ u'(e_o + p_o) + (u_o + u')(e' + p') \end{Bmatrix} \quad (7)$$

$$G' = \begin{Bmatrix} \rho_o v' + \rho' v_o + \rho' v' \\ \rho_o v_o u' + \rho_o u_o v' + \rho' u_o v_o \\ + \rho' v' u_o + \rho' u' v_o + (\rho_o + \rho') u' v' \\ \rho' v_o^2 + 2\rho_o v_o v' + \rho' v' v' \\ + 2\rho' v' v_o + (\rho_o + \rho') v' v' \\ \rho_o v_o w' + \rho_o w_o v' + \rho' v_o w_o \\ + \rho' w' v_o + \rho' v' w_o + (\rho_o + \rho') v' w' \\ v'(e_o + p_o) + (v_o + v')(e' + p') \end{Bmatrix} \quad (8)$$

$$H' = \begin{Bmatrix} \rho_o w' + \rho' w_o + \rho' w' \\ \rho_o w_o u' + \rho_o u_o w' + \rho' u_o w_o \\ + \rho' w' u_o + \rho' u' w_o + (\rho_o + \rho') u' w' \\ \rho_o w_o v' + \rho_o v_o w' + \rho' w_o v_o \\ + \rho' w' v_o + \rho' v' w_o + (\rho_o + \rho') v' w' \\ \rho' w_o^2 + 2\rho_o w_o w' + \rho' w' w' \\ + 2\rho' w' w_o + (\rho_o + \rho') w' w' \\ w'(e_o + p_o) + (w_o + w')(e' + p') \end{Bmatrix} \quad (9)$$

The mean flow source term Q is time independent:

$$Q = - \left(\frac{\partial F_o}{\partial x} + \frac{\partial G_o}{\partial y} + \frac{\partial H_o}{\partial z} \right) + \frac{\partial R_o}{\partial x} + \frac{\partial S_o}{\partial y} + \frac{\partial E_o}{\partial z} \quad (10)$$

If the NLDE is time averaged, it becomes the Reynolds-averaged Navier-Stokes equation, where the Reynolds stresses are on the left hand side. Thus, for a laminar flow $Q = 0$.

We seek a solution of the perturbation variables q' with a known mean flow field which can be obtained from existing well-developed CFD codes (e.g. CFL3D,¹⁹ INS3D, OVERFLOW, PUMA,¹ ...) for steady flow. This methodology allows us to use the most effective algorithms for the steady and unsteady portions of field, respectively. It also minimizes round-off error since we are only computing perturbations. We can even use different grids for the steady and unsteady solution. More discussion on this new method is in the reference.¹⁵

Characteristic Boundary Conditions for NLDE

The boundary conditions for the NLDE are developed by applying Thompson's characteristic method²² to the nonlinear disturbance equations.¹⁴

This type of boundary condition treatment allows one to easily introduce a disturbance at the incoming boundary by deriving an expression for one of the incoming

characteristics with a source term. Atmospheric boundary layer conditions can be incorporated in this manner at incoming boundaries. At the outflow boundaries, the boundary conditions are essentially non-reflecting. The ship superstructure and ocean surface are both treated as hard wall boundary conditions.

Numerical Method and Parallel Methodology

The NLDE are cast in a generalized coordinate system and solved numerically using a finite difference based scheme. The discretized equations are solved in a time accurate manner by taking advantage of computational aeroacoustics (CAA) methods. The spatial flux derivatives are calculated using seven point stencils of the fourth order optimized Dispersion Relation Preserving (DRP) scheme of Tam and Webb.²¹ The time integration is a fourth order accurate Runge-Kutta method.

Efficient computing performance is achieved by using a three dimensional domain decomposition strategy. The code is written in Fortran 77 plus Message Passing Interface (MPI)¹⁶ and is scalable in three dimensions. As mentioned early, the ship geometry is very complicated, even for a generic frigate test model. This makes multi-block grid simulations and domain decomposition very difficult. In order to make the code scalable and flexible, a three dimensional single-block grid is used. The whole computational domain is divided into many three dimensional zones. The grid points are evenly distributed across each processor.

The NLDE solver is implemented portably on parallel computers, such as, the IBM SP2 (e.g. Penn State, Npaci, MHPCC), SGI Power Challenge and Pentium II Cluster. A comparison of code performance for the ship airwake run on various machines is shown in Fig. 3. While a 24-processor IBM SP2 is 8.4 times faster than eight 266 MHz Pentium II's networked together, the SP2 costs roughly 28 times more than the PC cluster. Fig. 4 gives the wall clock time for a ship air wake case with 1.86 million grid points using various number of processors. A 64-processor SP2 is roughly 2.6 time faster than a 16-processor SP2 (when problem size is kept fixed).

Results and Discussions

In the helicopter/ship interface problem, the most important data for coupling the airwake solution to the dynamics analysis of the main rotor blades of helicopter are the mean flow field, the intensity of flow perturbations, and its dominant frequencies. Such an approach is presented in this paper. So far we have been concentrating on two types of ships: (1) frigates with helicopter landing pads on the deck behind the hangar and (2) aircraft carriers and LHA's with several helicopter landing

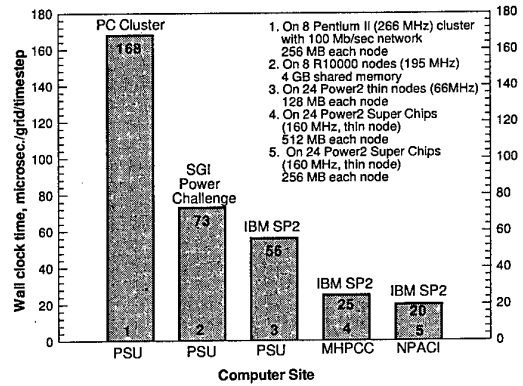


Figure 3: Timings for a ship air wake case on several parallel computers.

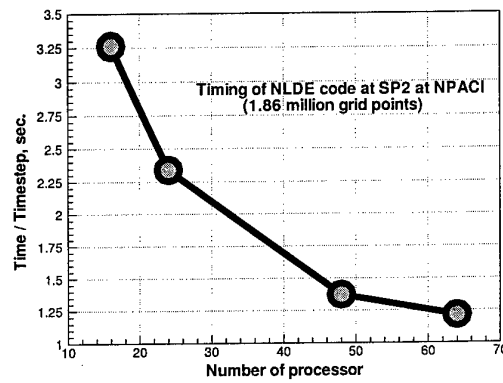


Figure 4: Timings for a ship air wake case on SP2.

spots on the deck around the control tower. The airwake influences on the helicopter are quite different in these two cases. For frigates the flow separation area behind the hangar cube has a strong effect on a landing helicopter, while on aircraft carriers and LHA's the deck leading edge vortex and separation are the key flow phenomena.

In this paper some preliminary simulations have been done for a generic ship shape (TTCP ship). In fact, this is a generic frigate model and it is shown in Fig. 5 in a computational mesh. It is 240 feet long, 45 feet wide and 55 feet high. It was chosen because there are some experimental investigations using the same configuration. It is acknowledged that the ship superstructure does not resemble a typical frigate superstructure in detail. However, from an aerodynamic point of view the airwake should still be representative of that for an ac-

tual frigate since this study is concerned with the macroscopic flow properties and large scale phenomena in the hangar wake.

Special attention is given to the helicopter landing area which is the square, aft section of the ship. There is a 20 feet drop down to the landing deck from the hangar structure, which will lead to vortex shedding over the deck causing landing approach hazards.

The computational grid for this problem is $201 \times 109 \times 85$ which results in a grid resolution of two feet or less in each direction around the ship, grid stretching was used to enlarge the domain. So far both mean flow based on the structured grids and NLDE simulations were based on the same grid in order to avoid three dimensional interpolation. In fact, the NLDE needs much fewer grid points than CFL3D.

Mean flow simulation based on structured grids

NASA Langley and Ames research centers have devoted significant resources in the past decades to developing modern CFD technology. The CFL3D 5.0 package from NASA Langley is used here to simulate the mean flow which will be given as a background flow to the unsteady flow computation of NLDE. The code is a Reynolds-Averaged thin-layer Navier-Stokes flow solver for structured grids. A finite volume algorithm with a spatial-factored diagonalised, implicit scheme is used in discretization of the partial differential equations. The upwind-biased-differencing using the flux-difference-splitting technique is employed.

From the experimental results, it is known that the flow is mostly separated, with free vortices originating from the sharp corners. There are two types of separation: one due to viscosity and the other due to sharp corners of the blocked structures. The former is heavily influenced by the Reynolds number. The latter is purely an inviscid phenomenon, independent of Reynolds number. The air wake is greatly influenced by both of them. In this mean flow simulation, we are concerned primarily with the inviscid phenomenon and used the Euler solver of CFL3D. The TTCP ship computational domain is divided into 10 blocks.

The Mach number chosen for the simulation is a high wind case. The incoming flow speed is 41 knots. The water surface is assumed to be a hard wall boundary. Fig. 6 and fig. 7 show the contour plots of velocity magnitude on the surface of the TTCP ship for the zero and 40 degree yaw angle wind cases from CFL3D results. The symmetry property of zero yaw angle flow is captured very well. The flow is accelerated around the sharp corners and there are several reverse flow regions near the walls close to each corner. After the blocked structures there is massive flow separation; the separation line is clearly shown after each block.

Of importance to the landing operation is the flow condition over the flight deck. Fig. 8 depicts the contour of velocity magnitude at the ship's center plane. It is shown that the large region of recirculating flow extends over the flight deck and rises higher than the hangar. This flow region is in the landing path.

Fig. 9 shows velocity vectors in two horizontal planes 4.75 feet and 8.75 feet above the flight deck. Our numerical results are compared with a flow pattern obtained from an experimental study¹⁸ in fig. 10. It shows the flow pattern from experiments, where four distinct flow regions are behind the hangar. This three dimensional vortex and reverse flow has very low speed but generally is very unsteady and yaw-dependent. Comparing to the experiment, the physical flow features are well captured by the simulation. In the numerical plots, the vortex pair in the higher plane is much close to the center line and the hangar. This indicates that there is a horse shoe vortex as shown by the topological drawing in fig. 10.

In fig. 11 the velocity vector on the flight deck floor is compared with flow visualization results for the TTCP ship.²⁴ The figure (a) is the results from CFL3D using structured grids and the figure (c) is from another solver (PUMA) using unstructured grids, which will be discussed in the next section. The photograph in the middle is from oil flow visualization.²⁴ There are differences in the attachment line and the position of the vortex center. This is probably due to our inviscid approach.

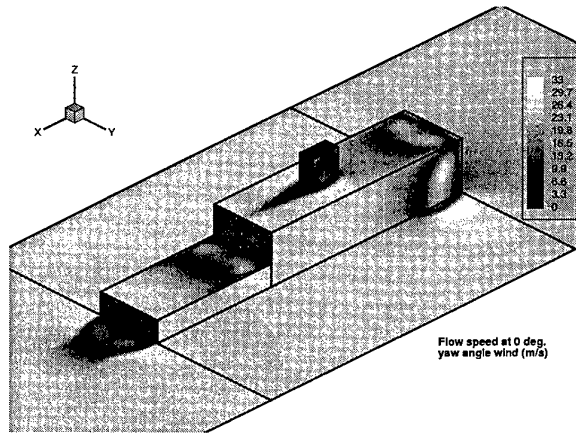


Figure 6: Flow speed contours on the surface of TTCP ship with 0 degree yaw angle wind (CFL3D).

A case with 40 degree yaw angle wind was also simulated. The numerical results on the front and middle bridge-deck, and flight-deck are compared with oil visualization photographs in fig. 12, fig. 13 and fig. 14. The three dimensional separation lines are clearly shown. Comparing fig. 12 (a) and (b) the flow patterns on the

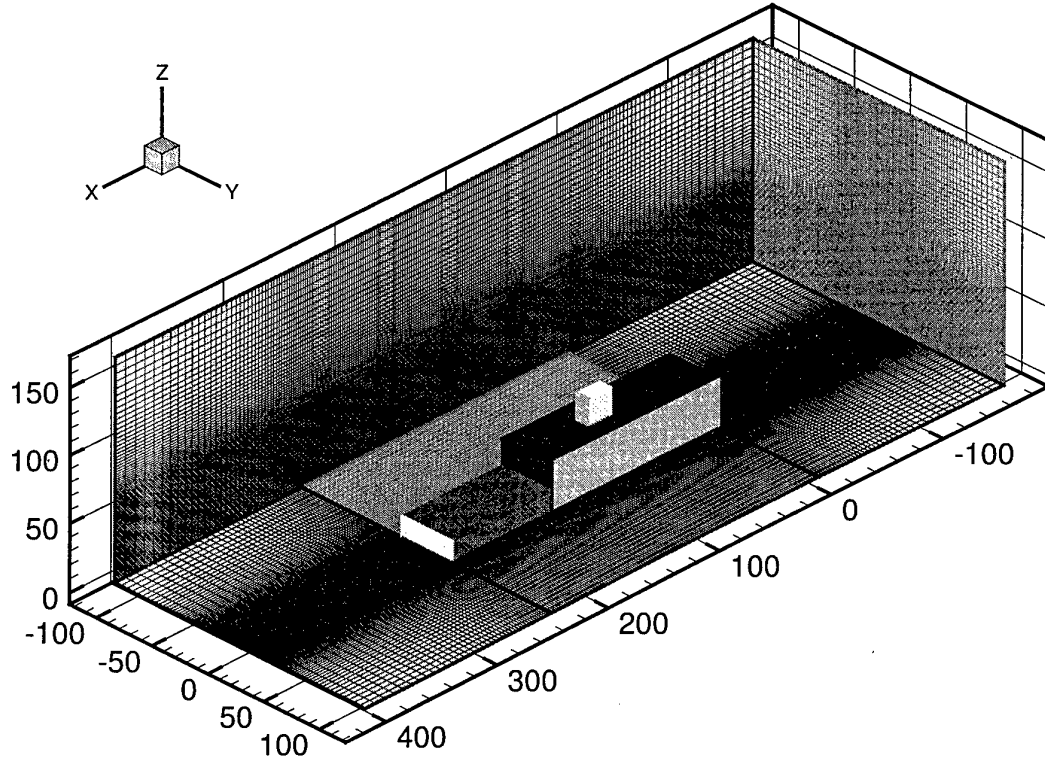


Figure 5: Configuration of TTCP ship and computational mesh (1.86 million grid points).

front part of bridge deck are very similar and close to each other since this part of the flow is less influenced by the viscosity and our nonviscous simulation is more capable of accurately capturing the flow. Comparing fig. 13 (a) and (b) and fig. 14 (a) and (b), the flow nature is partially captured since the viscous effects become stronger downstream. In the next section, the same comparisons are made for a 30 degree yaw angle case using the unstructured grid solver PUMA.

Finally in fig. 15 the performance of CFL3D (a serial code) is shown. We use 1.86 million grid points and for a typical run it needs about 10,000 time iterations. For this TTCP ship configuration it takes days to get the steady state results using an SGI Power Challenge (Single Processor).

Mean flow simulation based on the unstructured grids

While we have simulated relatively simple geometries here, more complex geometries (such as the 'island' or control tower on the LHA) are important. Preliminary results using unstructured grids are discussed in this section.

For the unstructured grid flow field predictions we are using the PUMA code¹ from Dr. Chris Bruner (NAWC). PUMA (Parallel Unstructured Maritime Aerodynamics) is a computer program for the analysis of internal and external non-reacting compressible flows over arbitrary geometries. PUMA is written entirely in ANSI C and uses MPI (Message Passing Interface) to ensure high portability and good performance.

PUMA is based on FVM (Finite Volume Method) and supports mixed-topology unstructured grids composed of tetrahedra, wedges, pyramids and hexahedra. The code may be run so as to preserve time accuracy for unsteady problems, or may be run using a pseudo-unsteady formulation to enhance convergence to steady-state. Either explicit or implicit time integration may be used. Primitive flow quantities (density, velocity, and pressure) are computed at the cell centers and saved on exit.

Because PUMA uses DMA (Dynamic Memory Allocation), problem size is limited only by the amount of memory available on the machine. Since PUMA is targeted for distributed-memory parallel computers, which usually have an abundance of memory, little effort has been

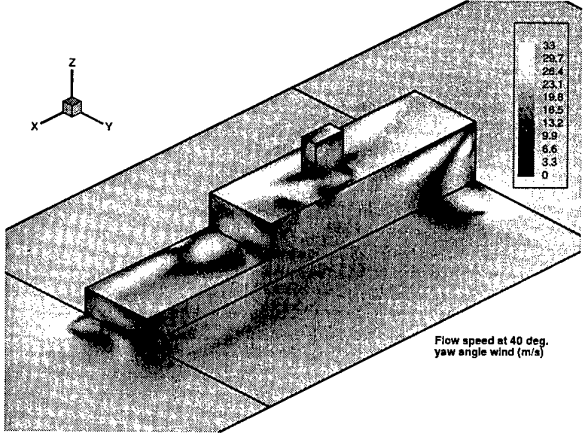


Figure 7: Flow speed contours on the surface of TTCP ship with 40 degree yaw angle wind (CFL3D).

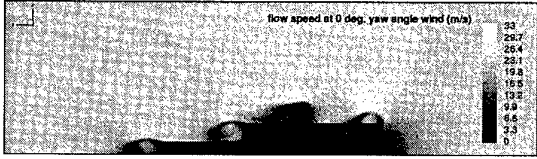


Figure 8: Flow speed contours on center plane of the TTCP ship (CFL3D).

placed on reducing PUMA's memory requirements. Currently, with double precision floating point variables used throughout the code, PUMA needs 582 bytes/cell and 624 bytes/face, not including message passing overhead. For tetrahedral grids, this amounts to 2002 bytes/cell (or 250 words/cell). This requirement can be reduced significantly by compiling the code using single precision floating point variables for which an option is provided.

We ran the TTCP ship in PUMA by converting the structured grids (used in CFL3D and NLDE code) to unstructured tetrahedral grids for PUMA. There are 1,718,080 cells and 1,769,837 nodes used in PUMA.

A case with 30 degree yaw angle wind is simulated using PUMA. The numerical results on the front and middle part bridge-deck, and flight-deck are compared with oil flow visualization photographs in fig. 16, 17 and 18. The flow pattern at all three locations are similar to the experimental results, such as the vortex location after the island in fig. 17 and the three dimensional separation line is very similar in fig. 18.

Based on the discussion above, in fact, the flow pattern shown represents a very rough mean of the flow. They are intended only to give approximate envelopes for the different regions and provide the background flow for NLDE simulations. There are large fluctuations about

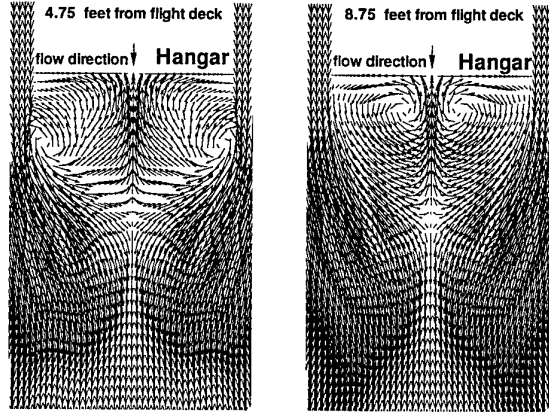


Figure 9: Flow velocity vectors at two horizontal planes over flight deck (CFL3D).

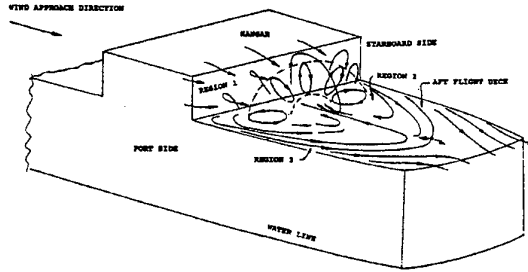


Figure 10: Topological drawings from experimental study.¹⁸

this mean flow. The flow field is generally very unsteady. In the following section, the results from NLDE simulations are discussed based on this mean flow.

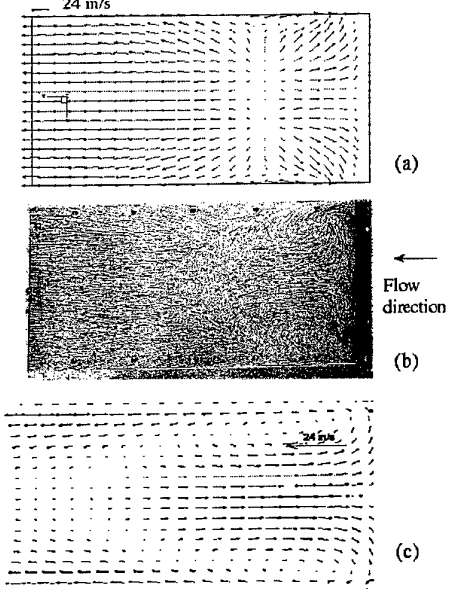
Perturbation simulation

As mentioned before, NLDE has been developed for solving more complex geometries, such as the TTCP ship, which allow multi-solid-boxes inside the computational domain. This makes the boundary condition implementation difficult, especially combined with a domain decomposition parallel technique. To overcome this difficulty, a single block domain was chosen for the NLDE code. The TTCP ship is divided into 88 solid boxes. Characteristic boundary conditions are used at the surfaces, edges and corners of these boxes. At each time step, after the single block computation is finished, the solid box wall boundary conditions are applied to update the value at wall grid points.

The high wind speeds relevant to the ship/helicopter interface problem arise from storm centers far from the actual ship and are called neutrally stratified. This wind condition is considered at our inflow boundary. The

Computer	Architecture	Nodes	Compile option	Iter	Sec	MFLOPs
grimm	P-II 266 cluster	8	mpicc -O4	500	983	105.21
SP2	IBM Power II	8	mpicc -O3 (pwr2)	500	736	140.52
power	SGI Power Chall.	8	cc -O3 (64 bit)	500	577	179.24

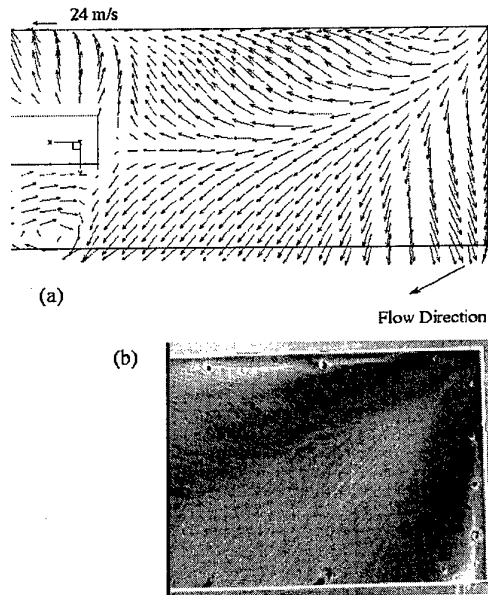
Table 1: Some Performance Comparison of PUMA on Different Computers

Figure 11: Predicted surface flow velocities compared to surface oil flow images on the flight deck.²⁴ (a) CFL3D, (b) oil flow visualization, (c) PUMA

principal parameters of the free stream airflow are (1) the mean wind speed, time-averaged over an appropriate scale; (2) the turbulence intensity; (3) the longitudinal (or integral) length scale of the turbulent velocity fluctuations. Empirical relationships are available (ESDU data items 74030,74031) for the above four parameters as a function of the mean wind speed, elevation and roughness length scale.³

Incoming characteristics with source terms are introduced from the inflow boundary. The magnitude of the incoming disturbance is determined by the turbulence intensity. Its spectrum is obtained from the wind spectrum by using a random walk (random phase) technique.

Fig. 19 and 20 give contour plots of longitudinal velocity perturbations u' in the center plane at two different

Figure 12: Predicted surface flow velocities on the front part of bridge-deck compared to surface oil flow images with 40 degree yaw angle wind.²⁴ (a) CFL3D, (b) oil flow visualization

time steps. Fig. 21 gives contour plots of the longitudinal velocity intensity $\sqrt{u'^2}$. From these unsteady results, it is shown that large perturbations occur around the TTCP ship structure, especially in the area after the hangar and after the leading edge. In the field far from the ship the flow is quite steady. Vortex shedding from the hangar can be clearly observed.

In fig. 22 and 23, contour plots of vertical and transverse perturbation velocity v' , w' are shown. In fig. 24 the vertical perturbation intensity $\sqrt{w'^2}$ is given in the center plane. High instantaneous vertical perturbations are found in the region just after the hangar trailing edge. Since this is a zero yaw angle case, the transverse pertur-

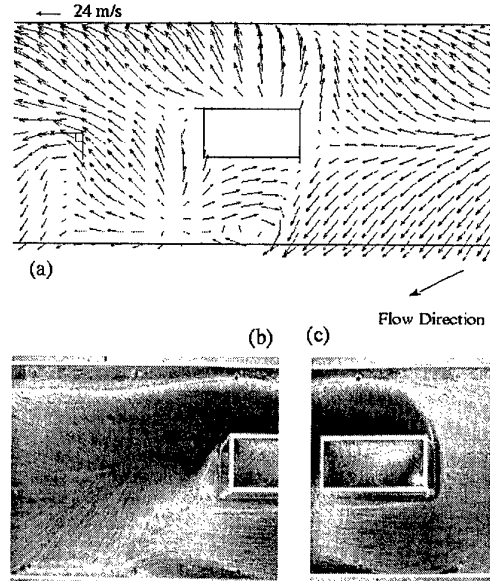


Figure 13: Predicted surface flow velocities on the middle part of bridge-deck compared to surface oil flow images with 40 degree yaw angle wind.²⁴ (a) CFL3D, (b) oil flow visualization

bation is quite weak over the flight deck. By comparing the instantaneous perturbations in fig. 19 and 23, the perturbation length scale of longitudinal perturbations is different from that of vertical perturbations.

The unsteady three-dimensional flow is of interest throughout the domain but in particular the flow unsteadiness is important around the helicopter landing deck. Fig. 25 presents a contour plot of perturbation intensity in a horizontal plane 17 feet above the deck, where the helicopter rotor would be.

From those preliminary results, the unsteady features of a TTCP ship air wake are captured qualitatively. However, detailed experimental data is not yet available. In the meantime, the NLDE code is being improved and prepared for quantitative evaluation and analysis.

Concluding Remarks

This paper presents steady and unsteady flow field predictions for frigate class ships. A nonlinear disturbance equation solver has been developed using parallel computers. The parallel performance of the code has been compared on various computers. By comparing to experimental results, our present results are qualita-

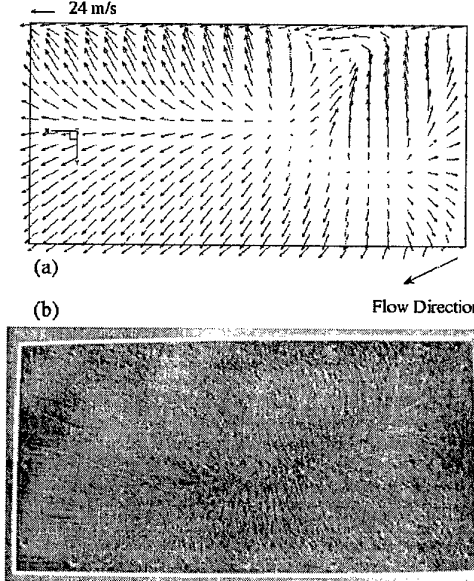


Figure 14: Predicted surface flow velocities on the flight-deck compared to surface oil flow images with 40 degree yaw angle wind.²⁴ (a) CFL3D, (b) oil flow visualization

tively correct, and show that the key flow phenomena can be captured using a steady-state code followed by the NLDE code.

The unstructured grid approach can be used for more complex geometry and practical simulations, such as a real ship shape.

Future work will concentrate on more detailed comparisons to experiment, the inclusion of more geometrical features of the ships, and the inclusion of viscous effects.

Acknowledgments

We gratefully acknowledge ONR Grant No. N00014-97-1-0530. We would also like to thank Steve Zan (NRC Canada) and Kurt Long (USN Pax River).

References

- [1] Bruner, C.W.S. and R.W. Walters, "Parallelization of the Euler Equations on Unstructured Grids", AIAA 97-1894.
- [2] Carico, D., Reddy, B., and Dimarzio, C., "Ship Airwake Measurements and Modeling Options for

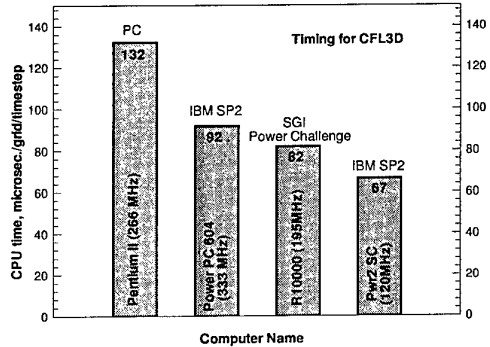


Figure 15: Timing for CFL3D on several computers.

Rotorcraft Applications," In: Aircraft Ship Operations, AGARD CP-509, November 1991.

- [3] ESDU Data Items 74030, 74031, Engineering Sciences Data Unit International, McLean, VA.
- [4] Funk, J.D. and T. A. Egolf, "A Comparison of Helicopter Rotor Inflow Predictions in Turbulence using Blade Element and Vortex Lattice Models," Proceedings of the 50th American Helicopter Society Forum, Washington, D.C., May, 1994.
- [5] Healey, J. Val., "The Prospects for Simulating the Helicopter/Ship Interface," Naval Engineers Journal, March 1987, pp. 45-63.
- [6] Johns, M.K. and J. Val Healey, "The Airwake of a DD-963 Class Destroyer," Naval Engineers Journal, May, 1989.
- [7] Healey, J. Val., "Establishing a Database for Flight in the Wake of Structures," Journal of Aircraft, Vol. 29, No.4, July-Aug. 1992, pp. 559-564.
- [8] Hurst, D. W., and Newman, S.J., "Wind Tunnel Measurements of Ship Induced Turbulence and the Prediction of Helicopter Rotor Blade Response," Vertica, Vol. 12, No.3, 1988, pp. 267-278.
- [9] Geyer, W.G., J. Keller, and E.C. Smith, "Validation and Application of a Transient Response Analysis for Shipboard Engage/Disengage Operations," Proceedings of the 52nd American Helicopter Society Forum, Washington, D.C., June, 1996.
- [10] Keller, J. and E.C. Smith, "Experimental / Theoretical Correlation of Analysis for Helicopter Blade-Droop Stop Impacts," submitted for publication in the Proceedings of 38th

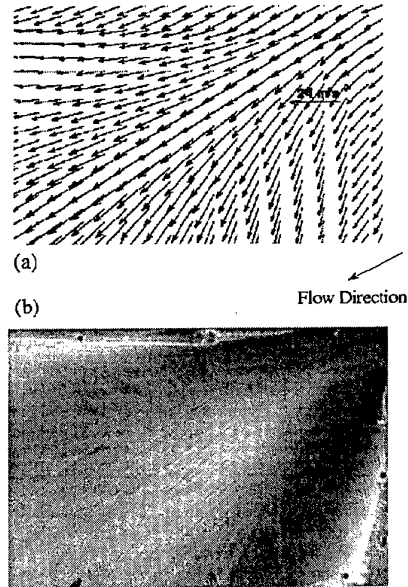


Figure 16: Predicted surface flow velocities on the front part of bridge-deck compared to surface oil flow images with 30 degree yaw angle wind.²⁴ (a) PUMA, (b) oil flow visualization

AIAA/ASME/ASCE/AHS/ASC Structure, Structural Dynamics, and Materials Conference, Orlando, April, 1997.

- [11] Williams, S. and Long, K.R., "Dynamic Interface Testing and the Pilots Rating Scale," The 53rd AHS Forum, April, 1997.
- [12] Landsberg, A.M., Young, T.R., Jr. and Boris, J.P., "An Efficient, Parallel Method for Solving Flows in Complex Three-Dimensional Geometries", 32nd Aerospace Sciences Meeting & Exhibit, January 10-13, 1994, Reno, NV.
- [13] Landsberg, A.M., W.C. Sandberg, T.R. Young, and J.P. Boris, "DDG-51 Flt-IIA Airwake Study, Part 2: Hangar Interior Flow," NRL/MR/6410-96-7898, Nov., 1996
- [14] Liu, J., and Long, L.N., "Higher Order Accurate Ship Airwake Predictions for the Helicopter/Ship Interface Problem", American Helicopter Society 54th Annual Forum, Washington, DC, May, 1998.
- [15] Morris P.J., Long L.N., Bangalore A. and Wang Q., "A Parallel Three-Dimensional Computational Ae-

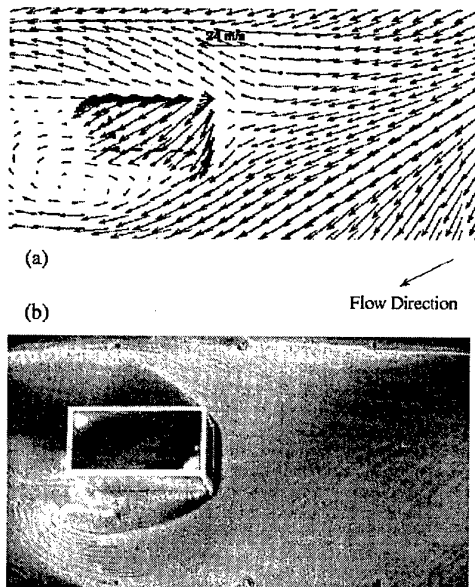


Figure 17: Predicted surface flow velocities on the middle part of bridge-deck compared to surface oil flow images with 30 degree yaw angle wind.²⁴ (a) PUMA, (b) oil flow visualization

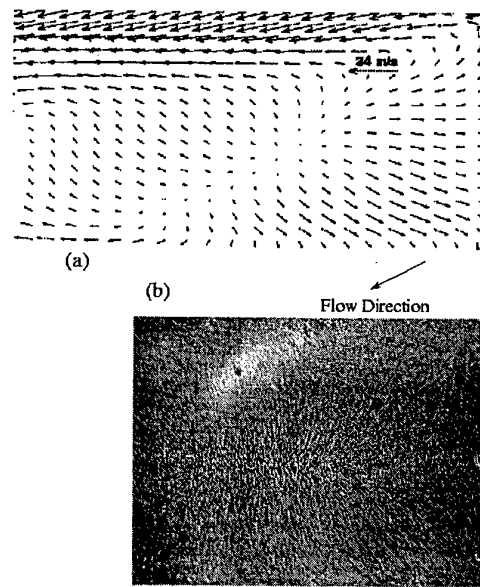


Figure 18: Predicted surface flow velocities on the flight-deck compared to surface oil flow images with 30 degree yaw angle wind.²⁴ (a) PUMA, (b) oil flow visualization

- rocoustics Method Using Non-Linear Disturbance Equations”, J. Computational Physics, Vol. 133, 1997 and AIAA 97-1598.
- [16] Pacheco, P.S., “Parallel Programming with MPI,” Morgan Kaufmann, San Fransisco, 1997
 - [17] Prasad, J.V.R., Mavris, D.N., and Schrage, D. P., “Ship Airwake Modeling and Simulation, Phase I: Methodology Development,” Research Report submitted to Naval Air Warfare Center, School of Aerospace Engineering, Georgia Institute of Technology, Atlanta, August 1992.
 - [18] Rhoades, M. M., and Healey, J. Val., “Flight Deck Aerodynamics of a Nonaviation Ship,” Journal of Aircraft, Vol. 29, No.4, July-August 1992, pp. 619-626.
 - [19] Krist, S.L., R.T. Biedron, and C.L. Rumsey, “CFL3D User’s Manual (Version 5.0),” NASA Langley, Nov., 1996.
 - [20] Tai, T.C. and Carico, D., “Simulation of DD-963 Ship Airwake by Navier-Stokes Method,” AIAA 93-3002.
 - [21] Tam C.K.W., and Webb, J.C., “Dispersion-Relation-Preserving Finite Difference Schemes for Computational Aeroacoustics,” J. of Computational Physics, Vol.1, 1993.
 - [22] Thompson K.W., “Time-Dependent Boundary Conditions for Hyperbolic System”, J. of Computational Physics 89, 1990.
 - [23] Zan, S.J. and E.A. Garry, “Wind Tunnel Measurements of the Airwake Behind a Model of a Generic Frigate,” NRC-CNRC Report LTR-AA-13, June, 1994.
 - [24] Zan, S.J., Unpublished data from the Aerodynamics Laboratory, Institute for Aerospace Research, National Research Council of Canada, 1998.

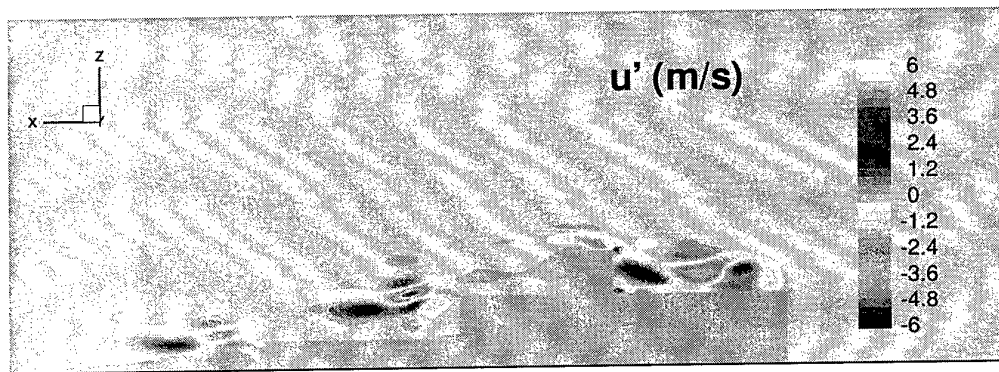


Figure 19: Contour of instantaneous longitudinal velocity perturbations at $t = t_1$ (NLDE).

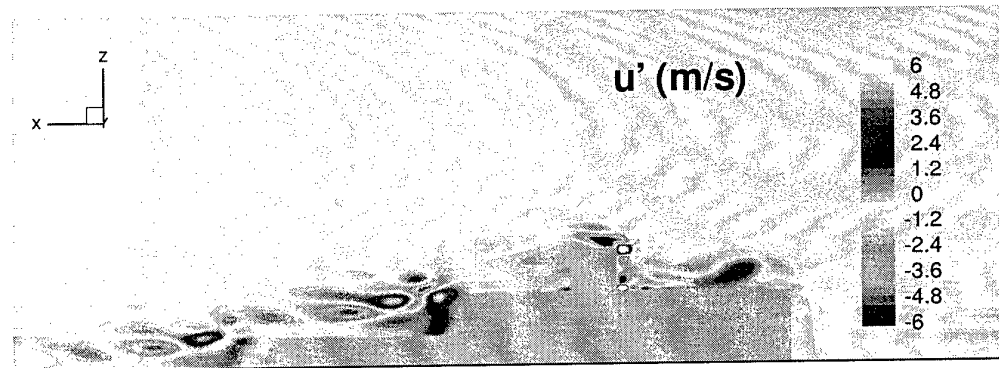


Figure 20: Contour of instantaneous longitudinal velocity perturbations at $t = t_2$ (NLDE).

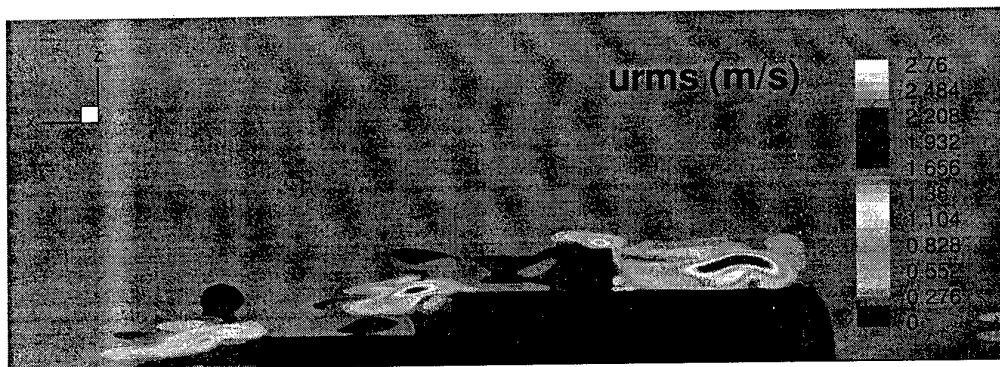


Figure 21: Contour of longitudinal velocity intensity.

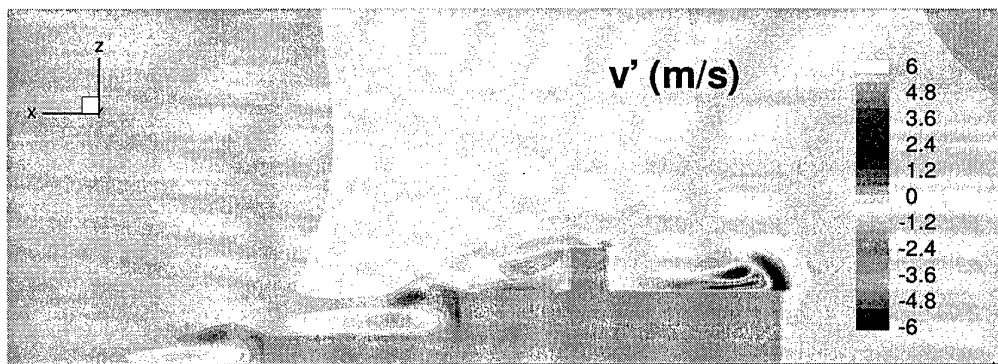


Figure 22: Contour of instantaneous transverse velocity perturbations (NLDE).

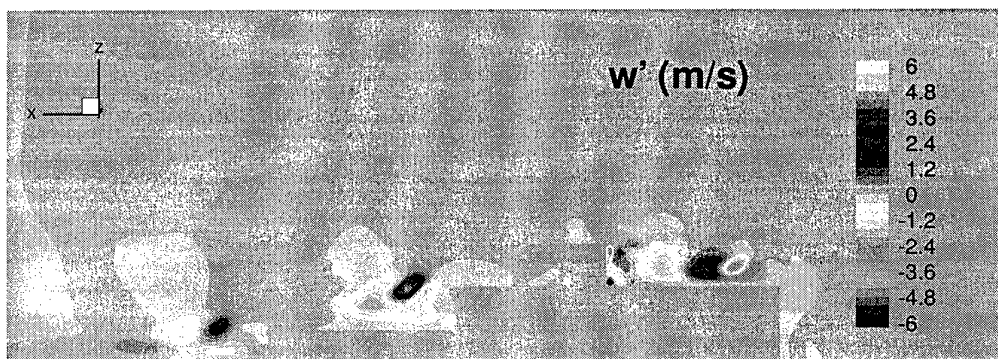


Figure 23: Contour of instantaneous vertical velocity perturbations (NLDE).



Figure 24: Contour of vertical velocity intensity (NLDE).

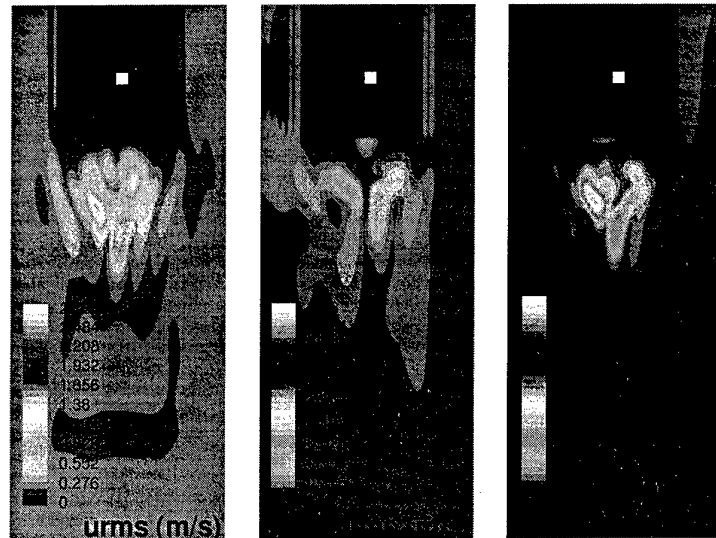


Figure 25: Contour plots of perturbation velocity intensity in the rotor plane of helicopter (NLDE).

Simulation and Analysis of LHD Ship Airwake by Navier-Stokes Method

Tsze C. Tai*

Naval Surface Warfare Center, Carderock Division
Code 5300, Bldg 4E Carderock Div.
9500 McArthur Boulevard
West Bethesda, MD 20817-5700, USA

1. SUMMARY

A multi-zone, thin-layer Navier-Stokes method is utilized to investigate the airwake about an LHD ship configuration. The ship's superstructure is modelled with blocked structures that closely represent the actual geometry. The freestream has a wind speed of 12.87 m/s (25 knots) at a direction of zero, 10 and 20 degrees. The flow is fully turbulent with a Reynolds number of 221 million based on ship length. In general, the flow is largely separated behind the superstructure. Major flow features including viscous-vortex interactions observed experimentally are captured in the simulation. Typical results in the form of particle traces and the velocity field over and aft of the ship are presented.

2. INTRODUCTION

It is well known that the interface between aircraft and ship poses problems in operations and survivability of naval aircraft. Current aircraft/helicopter operations aboard ship are characterized by restrictions due to weather and the need to often alter the ship's course into the wind to establish necessary wind-over-the-deck conditions for a successful landing. The interface environment becomes more complicated by the presence of massive, turbulent airwake from the ship's superstructure [1, 2].

The technical issues involve aspects concerning both the air vehicle and the ship. For aircraft, the lift characteristics become very sensitive to the surrounding environment due to relatively low freestream velocity and the use of high lift devices. In case of unmanned air vehicles (UAV), controllability in the final approach and landing is greatly influenced by the ship airwake.

The ship airwake is defined as an arbitrary volume of air, namely an air burble, surrounding the ship. The effect of airwake on the aircraft/ship interface operation is determined by the airflow disturbances caused by the ship that are perceptible to the pilot, and the final approach and landing patterns required for shipboard operations [3]. Physically, the airwake consists of mainly the steady flow with some unsteady components. Free vortices from the ship top-side geometry generated by the viscous-inviscid interactions, and vortices due to sharp corners or edges are generally referred to as unsteady flow. These unsteady components are usually of high frequency and diminish fairly quickly, their mean values can be captured reasonably well by the steady-state solution of a vortical flow. The critical unsteady flow in a ship airwake is, in fact, attributed to atmospheric turbulence, including gusts and fluctuations due to the ship motion (pitch, roll, and heave). These sources of unsteadiness are real causes of an unsteady airwake, but are unfortunately often ignored in both theoretical and experimental treatments, including recent unsteady computational schemes that also neglect these unsteady sources..

Nevertheless, the complexity of the problem requires the use of modern computational fluid dynamics to provide some analysis of the problem. At present, options are open to model the airwake flow either by the unsteady Euler type inviscid solution or by the steady-state solution to the Navier-Stokes equations. Either option ignores the unsteadiness due to atmospheric turbulence and ship motion. Previously, the steady-state Navier-Stokes solution has offered useful data in ship airwake simulation. Tai and Carico [4] applied three-dimensional, implicit finite-volume type Reynolds-averaged Navier-Stokes (RANS) scheme to consider the airwake problem about a simplified DD-963 ship configuration. Computed viscous flow results have demonstrated good correlation with measurements [5]. Later, Tai [6] simulated the airwake flowfield about an LPD ship with rather complex surface

* Senior Research Scientist, Marine and Aviation Department. Associate Fellow AIAA.

Presented at the NATO RTO Symposium on Fluid Dynamics Problems of Vehicles Operating near or in the Air-Sea Interface, Amsterdam, The Netherlands, October 1998.

geometry representation and obtained reasonably useful steady-state flow results.

The present effort is an extension of previous work on the DD-963 and LPD ships. The same multi-zone, RANS scheme used in Refs. 4 and 6 is employed with an enhanced grid in the simulation.

3. SIMULATION METHOD

The simulation method, or the computational method employed has been described previously. For completeness, the method is briefly described here. It contains two main elements: 1) the grid generation and 2) the flow solving.

3.1 Grid Generation and Grid Topology

A structured, curvilinear, body-conforming grid is generated. The numerical model for the surface grid is derived by using the Tai simplification scheme called the area-volume rule for representing the surface components of a ship [8]. Figures 1 and 2 show the actual ship and resulting numerical models. In the latter, the cargo door and elevators are closed and the antennas are neglected.

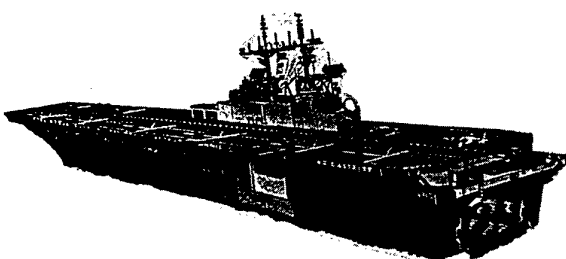


Fig. 1 - LHD ship configuration.

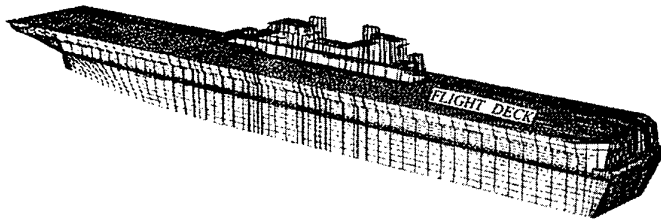


Fig. 2 - The numerical LHD ship model

The NASA Ames 3DGRAPE code [8] is used for basic grid generations. A cylindrical grid topology is adopted for its capability to treat a body with a sharp nose. The topology is basically an H-O mixed type, with H-type in the longitudinal plane, and O-type in the crossflow plane. The outer cylindrical surface is set at 2.5 ship lengths from the ship centerline. The most forward plane is set at 1.0 ship length from the bow of the ship, and 3.0 ship lengths for the wake.

An overall coarse grid is generated first by 3DGRAPE using a multi-block procedure. The radial distances are then clustered near the surface and stretched in the outer region for shear layer development. The complete grid has a total of 187 x 123 x 57 points with 57 points in the radial direction. This number is larger than those used for analysis of aircraft because of the very low speed freestream involved in the present work. Previous work [9] indicates that when using a compressible flow code at low Mach numbers, an increased mesh density is needed. The details of the grid generation and advantage of the grid topology adapted are presented in Ref. 7. The grid resolution was enhanced by increasing the number of points in all three directions.

3.2 Flow Solver

The NASA Langley thin-layer Navier-Stokes code, the CFL3D code [10] with multi-zone capability, is used as the basic flow solver. Appropriate modifications to the code for applying specific boundary conditions are implemented. The code is based on a finite volume algorithm with a spatially factored diagonalized, implicit scheme for discretizing the three-dimensional, Reynolds-averaged Navier-Stokes equations. The upwind-biased differencing technique is used for the inviscid terms and central differencing for all viscous terms. The method is globally second-order accurate and well suited for patched grids in a multizone domain. Details are given by Thomas et al [10].

The code is upgraded with a variety of turbulence models, including the basic Baldwin and Lomax algebraic model, the one-equation models, along with the standard two-equation models, among others. In the present work, the Baldwin and Lomax model [11] with the Degani-Schiff modification [12], along with the extension by Tai [13] is used. The former determines proper length scales for separated flows while the latter uses curvilinear arc length in place of normal distance. Although simple, the

model has been regarded as the best turbulence model for flowfield dominated by vortical flow.

3.3 Boundary Conditions

The boundary conditions for the Navier-Stokes flow solver are: 1) atmospheric boundary layer flow upstream, 2) atmospheric pressure recovery downstream, 3) characteristic form of inflow-outflow at the cylindrical outer boundary, and 4) viscous nonslip flow at the surface of the ship. The atmospheric boundary layer is approximated by a power-law profile:

$$U/V_\infty = (z/h)^n \quad (1)$$

where h is reference height and n varies from 0.10 to 0.14 [14]. The h is set to be the height of flight deck above the water surface, $h = 0.104$ ship length, and n is set to its mean value of 0.12.

At the downstream boundary condition, instead of imposing the usual freestream recovery, the static atmospheric pressure condition is satisfied along with velocity components being extrapolated from the interior. The use of characteristic form of inflow-outflow boundary condition at the cylindrical outer boundary is known to improve convergence of solution at low speed.

The water surface is assumed to be flat and waveless, and the flow properties in the airwake remain unmixed with the water. This assumption corresponds the water surface as neither viscous nor inviscid. Thus, a reflective boundary is applied and the vertical velocity component must vanish at the water surface. This approach was reached after some other attempts at treating the water boundary failed. It turns out to be a good approximation.

4. RESULTS AND DISCUSSIONS

Numerical results of the flow over a LHD ship configuration subject to an atmospheric wind speed of 12.87 m/s (25 knots) and a wind direction of 0, 10, and 20 degrees are obtained. The flow condition yields a Reynolds number of 221 million based on the ship length for the full scale ship. If the ship's beam is used for the Reynolds number basis, the above Reynolds number would have to be reduced approximately by a factor of 8. Whichever way the Reynolds number is calculated, the flow falls into the turbulent flow range.

All the computations were performed on the Cray facilities at the DoD High Performance Computing facility at the Naval Oceanographic Center. Converged solutions were obtained in about 8,000 to 9,000 iterations (time steps) requiring approximately 8 to 9 hours of Cray C-90 CPU time. The large number of iterations is due to the very low freestream Mach number used in the compressible flow solver. The required CPU time is reasonable and affordable in today's environment of computer capability and resources.

4.1 Particle Trace

Various views of the particle trace of the streamlines emanating from various stations on the ship surface are shown in the following three pages for three wind directions, namely wind at zero, 10, and 20 degrees with a speed of 12.87 m/s (25 knots). Figure 3 shows the perspective view of the airwake particle trace, while Figs. 4 and 5 give the profile and astern views of the same airwake over the ship at even keel. Even at zero wind angle, the figures all indicate that the flow is mostly separated, with free vortices originating from virtually all sections.

There are two types of separation: one due to viscosity and the other due to sharp corners of the volume blocks representing the superstructure. The former is closely influenced by the types of flow involved which is Reynolds number dependent. The latter is purely an inviscid phenomenon, independent of the Reynolds number. Both types of separation create free vortices as evidenced by the streamlines rolling up forward and aft of the superstructure, on the rear flight deck, and aft of the stern. The mechanism of the vortical flow involving free vortices is well demonstrated by the present steady-state solution. The use of the Navier-Stokes method ensures the basic physical features of the airwake, namely the three-dimensional flow separation which occurs over all the geometric surfaces, are captured.

The profile view helps indicate the actual height of the air burble (airwake) which might be misleading in the perspective view. Of course the height, as well as the overall size, of the air burble grows as the flow proceeds downstream. The height can be twice as much as shown here in about three ship lengths away. The airwake experiences a dip right aft of the stern. This is confirmed by the astern view shown in Fig. 5. The astern view also depicts how the airwake grows in size and shape. Further,

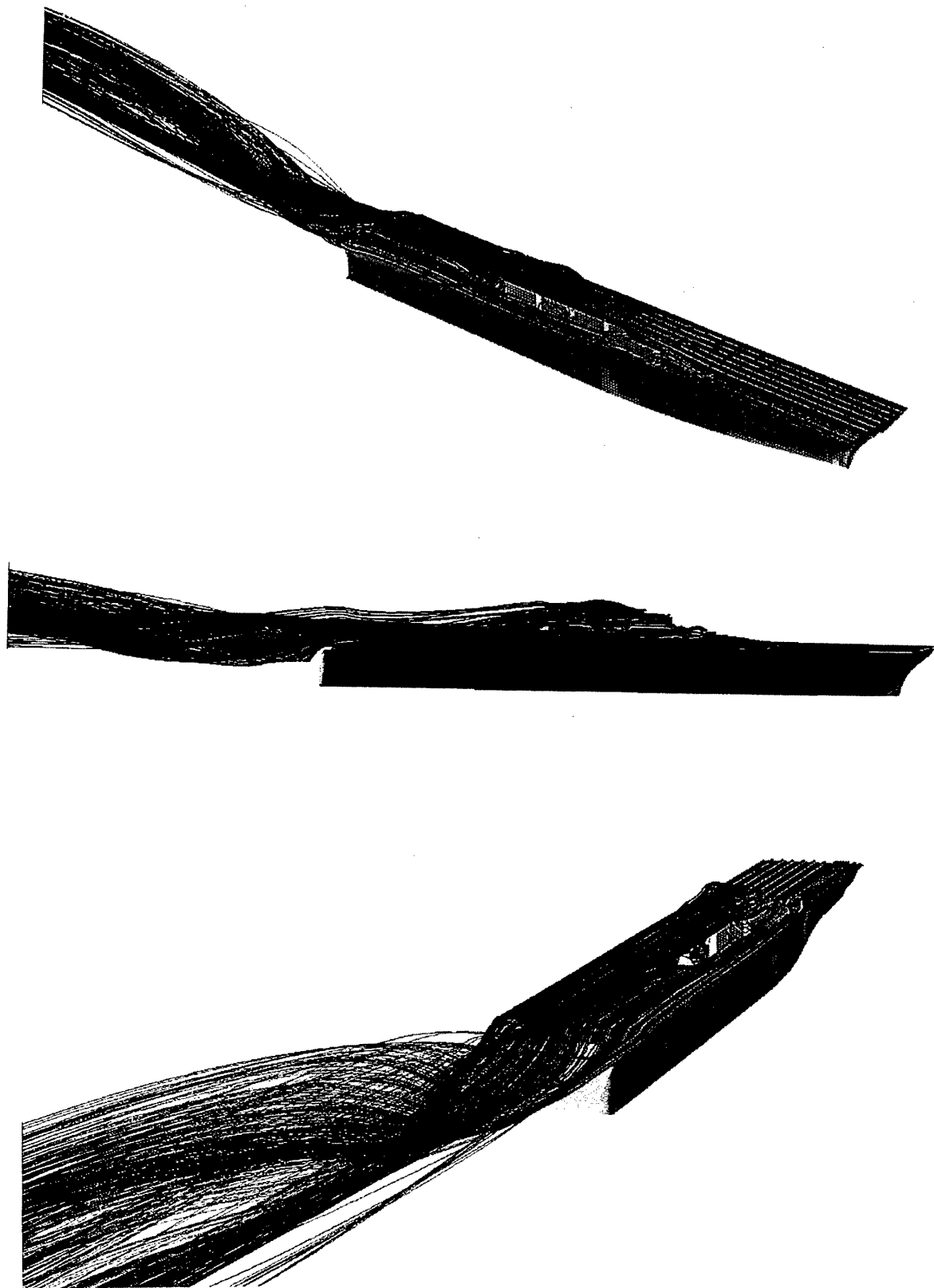


Fig. 5 - Particle trace over LHD ship at even keel at 12.87m/s (25 knots)
and zero wind angle. Astern view.

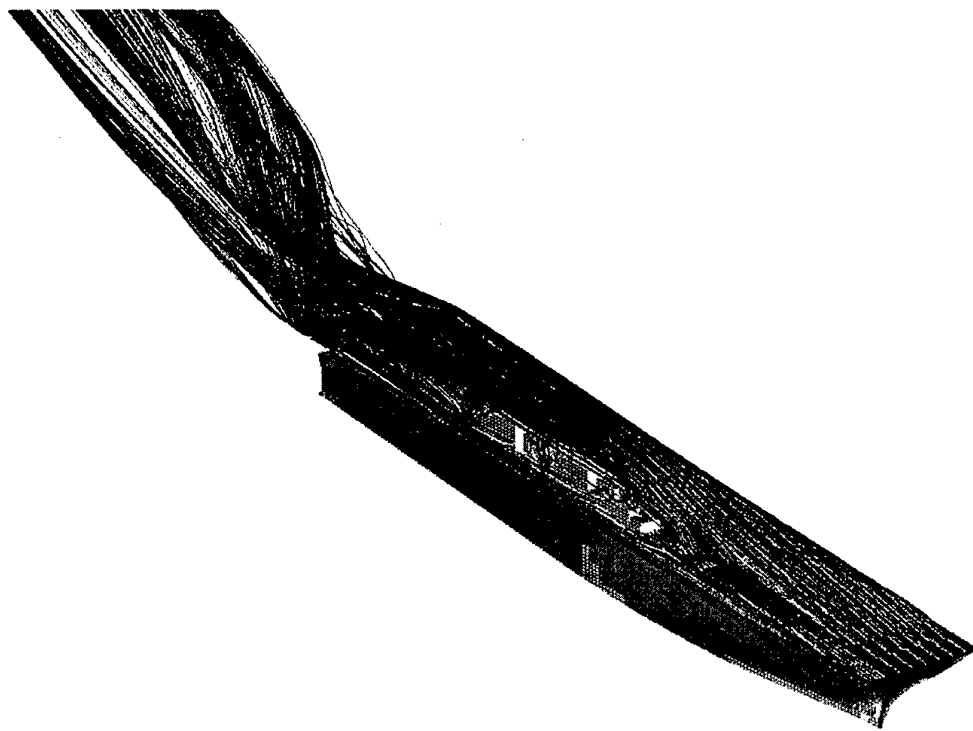


Fig. 6 - Particle trace over LHD ship at even keel at 12.87 m/s (25 knots) and wind angle of 10 degrees. Perspective view.

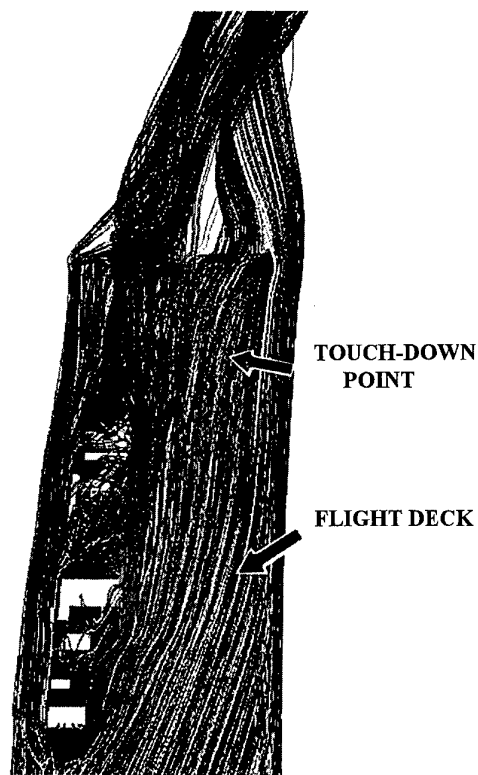


Fig. 7 - Particle trace over LHD ship at even keel at 12.87 m/s (25 knots) and wind angle of 10 degrees. Front view.

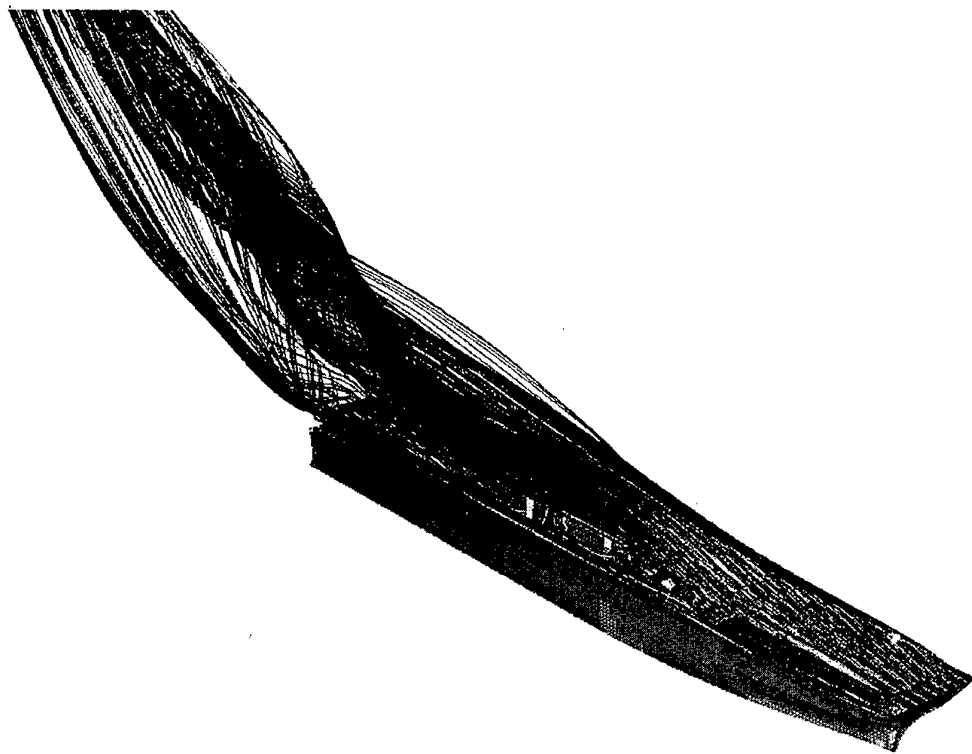


Fig. 8 - Particle trace over LHD ship at even keel at 12.87 m/s (25 knots)
and wind angle of 20 degrees. Perspective view.



Fig. 9 - Particle trace over LHD ship at even keel at 15.44 m/s (25 knots)
and wind angle of 20 degrees. Astern view.

the airwake is highly asymmetric even at zero wind angle because of one-sided location of the superstructure.

The asymmetry of the airwake becomes more evident at a wind angle of 10 degrees, see Fig. 6. More vortex rolling up takes place aft of the stern as a result of more severe flow separation generated by viscous-inviscid interactions. The region of separated flow is generally restricted to the starboard side of the ship where the superstructure is located. On the flight deck (in the rear of port side), on the other hand, the flow seems to be unseparated as shown in Fig. 7.

This is in contrast to one's intuition that the touch-down area is in the shadow of the superstructure (due to wind angle) and therefore should be in the separated flow region. The reason for this lies on the fact that the flow actually experiences mild acceleration due to the narrowed flow path between the superstructure and the streamlines along the edge of the deck. Note that streamlines near the edge of the deck do not peel off from the deck at this 10-degree wind angle. Previous work, both experimentally on DD-963 [5] and FFG-7 [15], and computationally on DD-963 [4] and LPD [6], indicated the leeside streamlines would even swerve slightly inward in the flight deck area. The reason for swerving inward is because of a low pressure region created behind the large superstructure on these ships.

Although the flight deck of the LHD ship is not located right behind the superstructure, there is still a low pressure region behind the superstructure which can influence the rear portion of the flight deck, including the touch-down area, see Fig. 7. However, this phenomena occurs up to certain wind angles. As the wind angle increases to 20 degrees, the separation becomes extremely massive, and the leeside streamlines may in fact depart from the edge of the deck. Figures 8 and 9 show the perspective and astern views of the particle trace over the LHD ship at a wind angle of 20 degrees. Rolling up of the vortex flow intensifies as depicted in Fig. 8 and the leeside streamlines fall off the cliff, see Fig. 9. As a consequence, the flow on the rear portion of the flight deck including the touch-down area becomes separated, see Fig. 10. It indicates that the characteristics of the airwake flowfield of the LHD configuration is very much wind-angle dependent.

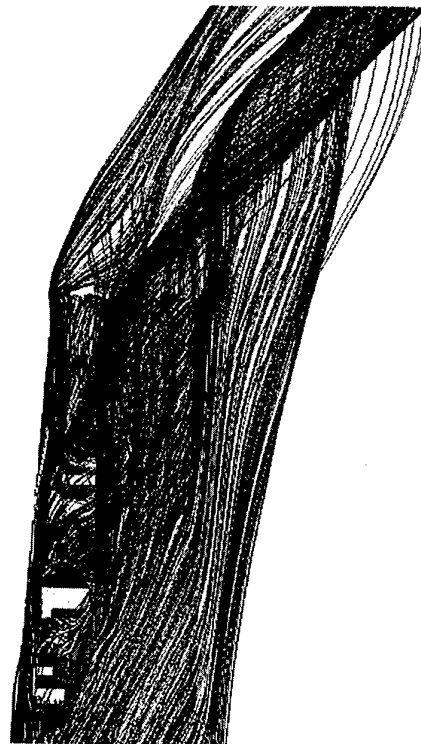


Fig. 10 - Particle trace over LHD ship at even keel at 12.87 m/s (25 knots) and wind angle of 20 degrees.
Front view.

4.2 Velocity Distribution

The particle traces offer is an indication of whether the simulated airwake contains the right physics it should have. The usefulness of the resulting airwake, however, depends on the ability to provide the correct velocity distributions needed to define the flight envelope for aircraft shipboard operation. For flight envelope analysis, the velocities U , V , W are examined at two vertical lines, one directly at the touch-down location and the other about one-ship length aft of the touch-down location, as defined in Fig. 11. These lines lie in a port-side plane 30 feet from the ship's centerplane.

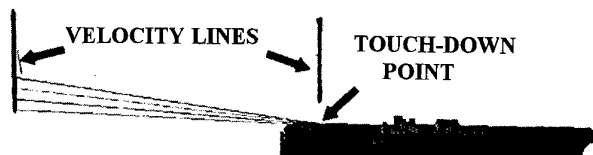


Fig. 11 - Geometry of velocity lines

The longitudinal, transverse, and vertical velocities (U , V , W) on the vertical plane directly at the touch-down point are plotted in Figs. 12, 13, and 14 respectively, for the case of 12.87 m/s wind with a zero wind angle. The coordinate gives the velocity magnitude in feet per second, while the abscissa measures the vertical distance from the touch-down point. These velocity components are taken from interpolated rectangular meshes that actually are too coarse to cover the clustered spacing inside the boundary layer. At the touch-down point, (strictly speaking, at the edge of the boundary layer) the U velocity has a magnitude of 41 ft/sec (12.5 m/s) which is very close to the freestream velocity of 42 ft/sec (12.87 m/s). The flow at this point is apparently unseparated as discussed in the previous section on particle traces. Under the influence of nearby wake behind the superstructure, the U velocity gradually decreases to 34 ft/sec (10.36 m/s) at a height 100 feet above the touch-down; then it monotonically approaches the freestream value, see Fig. 12..

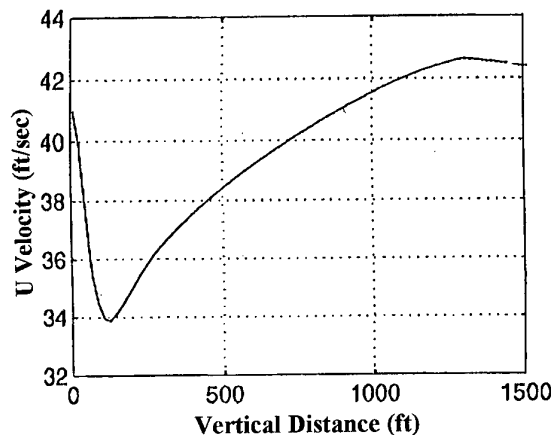


Fig. 12 - Longitudinal velocity distribution above touch-down; $V_\infty = 12.87 \text{ m/s (25 knots), } \beta = 0.$

The velocity in the transverse direction, V , has slightly negative values (from starboard to port) at low altitude, but gradually becomes positive above 100 feet from touch-down. It then diminishes to zero as the altitude increases, see Fig. 13. Again, these values are outside the boundary layer. The variation is rather small because of the zero wind angle. The vertical velocity, W , starts at a slightly positive value (upward) and then becomes negative (downward) in the entire altitude range before it vanishes, see Fig. 14.

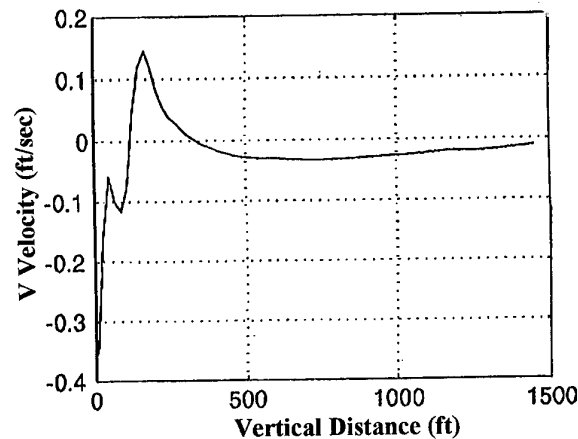


Fig. 13 - Transverse velocity distribution above touch-down; $V_\infty = 12.87 \text{ m/s (25 knots), } \beta = 0.$

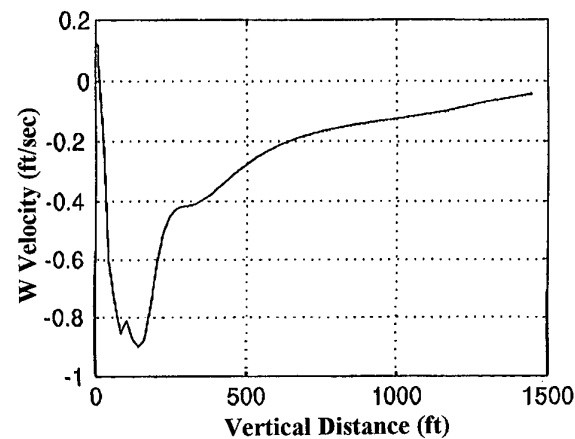


Fig. 14 - Vertical velocity distribution above touch-down; $V_\infty = 12.87 \text{ m/s (25 knots), } \beta = 0.$

Larger variations in velocity components are observed along the line about one-ship length aft of the touch-down point. Completely out of the narrowed flow path and almost totally in the wake, the longitudinal velocity U exhibits large deficiencies at low altitude. It recovers with a steep ascent between 50 to 150 feet, and then gradually approaches the freestream value as altitude increases, see Fig. 15. The reason for changes in the velocity slope above 150 feet level is believed to be due to the height of the superstructure involved.

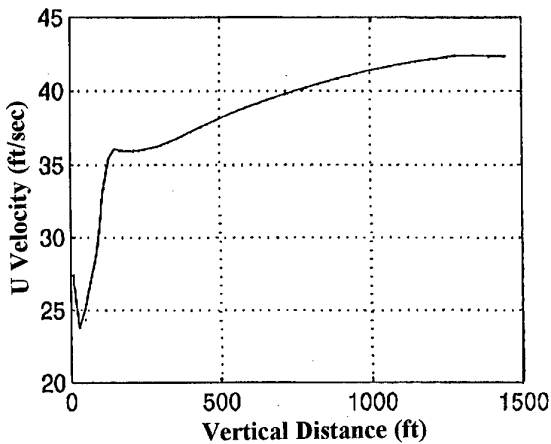


Fig. 15 - Longitudinal velocity distribution in the plane one-ship length aft touch-down; $V_\infty = 12.87 \text{ m/s}$ (25 knots), $\beta = 0$.

Figures 16 and 17 show the transverse and vertical velocity components, V and W, respectively. Here the V values are mostly negative (starboard to port) with increased magnitude due to influence from the wake. The location where the change of velocity slope takes place is consistent with the longitudinal velocity, i.e., at about 150-feet level. For the vertical velocity shown in Fig. 17, the upward magnitude is considerably higher than those in the touch-down plane. This upward velocity is the primary source for the growth of the air bubble. As observed experimentally, the air bubble will double its size about two-ship lengths aft of the ship stern. Similar to U and V, there is a change of W velocity slope at about 150-feet height.

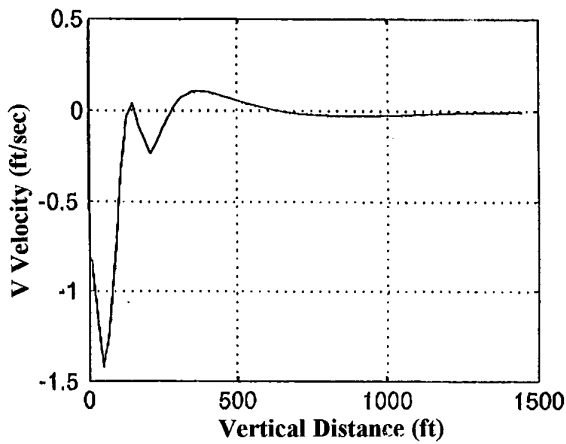


Fig. 16 - Transverse velocity distribution in the plane one-ship length aft touch-down; $V_\infty = 12.87 \text{ m/s}$ (25 knots), $\beta = 0$.

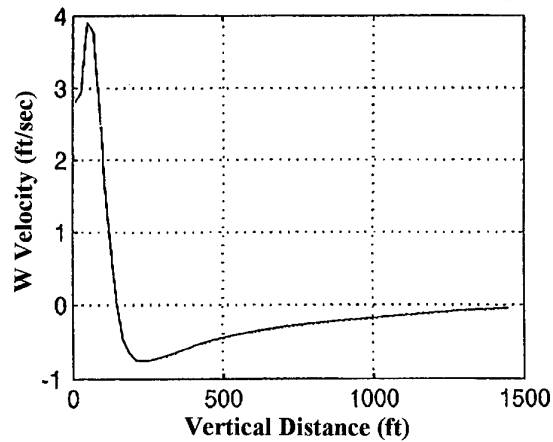


Fig. 17 - Vertical velocity distribution in the plane one-ship length aft touch-down; $V_\infty = 12.87 \text{ m/s}$ (25 knots), $\beta = 0$.

Mach Contours

The Mach contours four longitudinal stations for the case of $V_\infty = 12.87 \text{ m/s}$ (25 knots) at a wind angle of 10 degrees are given in Fig. 18. In general, the flow in the windward side has high speed that in certain area exceeds the freestream wind speed imposed. At some distance behind the ship, however, the Mach contours exhibit the wake characteristics, i.e., the flow has low velocities in the central region and high velocities in the surrounding, see Fig. 18. The area with velocity deficiency grows as the flow proceeds downstream. This confirms the growth of the airwake discussed in the aforementioned sections.

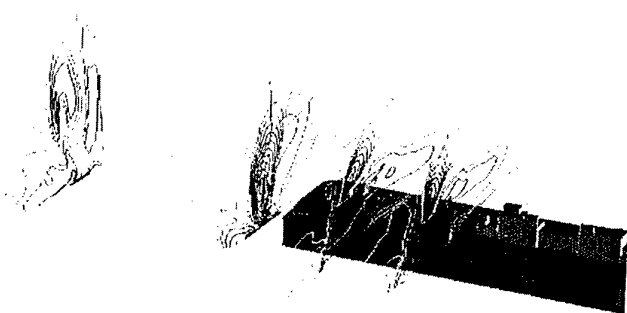


Fig. 18 - Mach contours at four longitudinal stations $V_\infty = 12.87 \text{ m/s}$ (25 knots), $\beta = 10 \text{ deg}$.

Lastly, the Mach contour is presented at a plane that runs over the ship's superstructure for the case of $V_\infty = 12.87 \text{ m/s}$ (25 knots), $\beta = 10$ degrees, see Fig. 19. On the fore deck, the flow closely resembles that of a flat plate until it reaches the superstructure represented by blocks. Over the superstructure, the flow undergoes deceleration with very thick shear layers. The local Mach number exhibits large deficiencies between the two large structured blocks, behind the end structure, and immediately behind the stern that are usually observed in the backward facing steps. Thus, the flow in these regions can be characterized by that of a backward-facing step: having massive flow separation involving reversed flow accompanied by circulation.

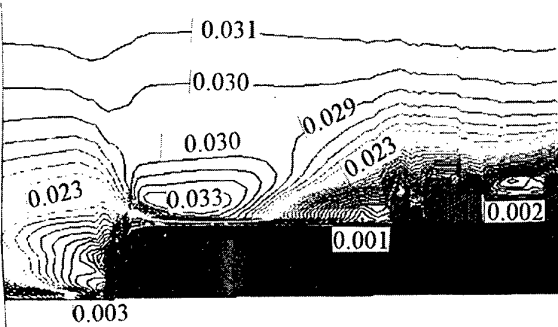


Fig. 19 - Mach contour in a longitudinal plane
 $V_\infty = 12.87 \text{ m/s}$ (25 knots), $\beta = 10$ degrees,

5. CONCLUDING REMARKS

The airwake of an LHD ship configuration subject to atmospheric wind of 12.87 m/s (25 knots) at wind angles of zero, 10, and 20 degrees is simulated by using a multi-zone, thin-layer Navier-Stokes method. The resulting flow contains regions of massive flow separation along with free vortices. Major flow features including viscous-vortex interactions are captured. Some concluding remarks may be drawn from the results of this study:

- (1) The LHD airwake is asymmetric and wind-angle dependent; the flow over the rear flight deck is influenced by the wake of the superstructure.
- (2) The flow over and behind the superstructure has characteristics of a backward facing step with massive flow separation involving reversed flow accompanied by circulation.
- (3) The flow over the fore deck resembles that of a flat plate and is unaffected by the superstructure.

6. ACKNOWLEDGMENT

The present work was supported by the Naval Air Warfare Center, Aircraft Div. (Richard Huff, technical monitor) and the Research Venture Program at NSWC, Carderock Div. The DoD High Performance Computing facility at NAVO provided the Cray CPU time.

7. REFERENCES

- [1] Garnett, T.S. Jr., "Investigation to Study the Aerodynamic Ship Wake Turbulence Generated by a DD963 Destroyer," Report No. NADC-77214-30, Boeing Vertol Company, Philadelphia, Oct 1979.
- [2] Healey, J.V., "The Prospects for Simulating the Helicopter/Ship Interface," *Naval Engineers Journal*, Vol. 99, No. 2, 1987. pp.45-63.
- [3] Carico, D., Reddy, W., DiMarzio, C., "Ship Airwake Measurement and Modeling Options for Rotorcraft Applications," AGARD Symposium on Aircraft Ship Operations, Seville, Spain, May 1991.
- [4] Tai, T.C. and Carico, D., "Simulation of DD-963 Ship Airwake by Navier-Stokes Method," AIAA Paper 93-3002, Jul 1993. Also *Journal of Aircraft*, Vol. 32, No. 6, 1995. pp. 1399-1401.
- [5] Healey, J.V., "The Airwake of a DD-963 Class Destroyer," *Naval Engineers Journal*, Vol. 101, No. 2, 1989. pp. 36-42.
- [6] Tai, T.C., "Simulation of LPD Ship Airwake by Navier-Stokes Method," *Proceedings of the Sixth Asian Congress of Fluid Mechanics*, May 1995, Singapore
- [7] Tai, T.C., "A Single Structured Grid for Complex Ship Geometry," in *Numerical Grid Generation in Computational Fluid Dynamics and Related Fields*, Edited by N.P. Weatherill, Pineridge Press Limited, Swansea, U.K. Apr 1994.
- [8] Sorenson, R.L., "The 3DGRAPE Book: Theory, Users' Manual, Examples," NASA Technical Memorandum 102224, Jul 1989.
- [9] Volpe, G., "On the Use and Accuracy of Compressible Flow Codes at Low Mach Numbers," AIAA Paper 91-1662, Jun 1991.
- [10] Thomas, J.L., Krist, S.T., and Anderson, W.K., "Navier-Stokes Computations of Vortical Flows over Low-Aspect-Ratio Wings," *AIAA Journal*, Vol. 28, No. 2, 1990. pp. 205-212.
- [11] Baldwin, B.S., and Lomax, H., "Thin-Layer Approximation and Algebraic Model for Separated Turbulent Flows," AIAA Paper 78-0257, Jan 1978.
- [12] Degani, D., and Schiff, L.B., "Computation of Supersonic Viscous Flows Around Pointed Bodies at Large Incidence," AIAA Paper 83-0034, 1983.
- [13] Tai, T.C., "Extension of Baldwin-Lomax Turbulence Model to Three-Dimensional Flow," AIAA Paper 97-0209, Jan 1997.
- [14] Plate, E.J., *Engineering Meteorology*, Elsevier Scientific Publishing Co., Amsterdam, 1982, pp. 527-569.
- [15] Gilbert, N.E., "Helicopter/Ship Simulation Model for Seahawk/FFG-7," Paper presented at TTCP HTP-6 Dynamic Interface Workshop, Lakehurst, NJ, Apr 1995.

PREDICTION OF SHIP AIR WAKES OVER FLIGHT DECKS USING CFD

P.Tattersall

C.M.Albone

M.M.Soliman

Aero/Structures Department, DERA,
Farnborough, GU14 0LX, UK

C.B.Allen

Department of Aerospace Engineering,
University of Bristol,
Bristol, BS8 1TR, UK

SUMMARY

A Computational Fluid Dynamics (CFD) method is presented for calculating the airflow over a ship superstructure, with emphasis on the flow over aft-located helicopter decks on conventional naval ships. The non-aligned grid generation and flow solution methods are described, including discussion of the modelling of time-accuracy and rotor downwash effects. Work on the coupling of the CFD results with a rotor performance code (CRFM) is also described. Example solutions are shown to illustrate the current capabilities of the method.

1. INTRODUCTION

Helicopters returning to their parent ship frequently encounter a hostile aerodynamic environment, characterised by complex, unsteady interaction of vortices, in the vicinity of an aft-located flight deck. This environment, which arises from the airflow over the ship superstructure, can cause severe handling problems during the transition over the flight deck and the landing itself, making helicopter recovery a difficult and potentially hazardous task. In addition, with certain ships, downdraughts occur, or are induced by the helicopter, at landing spots close to the ship's hangar which significantly reduce thrust margins during takeoff and landing.

In order to reduce the hazard, it is necessary to be able to predict the main flow features that constitute the hostile environment and to minimise them, either through improved superstructure design or special measures, such as alternative direction of helicopter approach or post design geometric fixes. One of the major approaches available for prediction of airflow around ships is the use of Computational Fluid Dynamics (CFD), which has a proven track record, in the field of aircraft aerodynamics, for providing tools of great value for practical design purposes. Whilst commercial software which could be applied to the prediction of ship air wakes is available, the option chosen at DERA Farnborough has been to develop an in-house modelling capability. This offers the advantages of a tool adapted specifically for the problem and the greater understanding of the critical

modelling issues involved which can only come from method development.

There is no doubt that, to achieve a completely faithful representation of the kind of flow field associated with airflow over a conventional naval ship, a time-accurate, viscous flow calculation would be required. Given the current state of turbulence modelling for bluff body flows [1], it seems likely that nothing less than a Large-Eddy Simulation (LES) would be sufficient. Such a level of modelling is not practical at the present time. However, CFD tools relying on lower fidelity than LES have been used in aircraft design for many years [2]. This is because the ability to correctly predict the trends in the flow, as a design is modified, is often sufficient to help limit the envelope of possible designs. Therefore, at the outset of the project, a number of important questions were asked. What are the important geometric and flow features to be modelled and the underlying fluid mechanisms? What degree of and types of information are likely to be required? What is likely to be achievable from a CFD code intended for routine use within the next few years? The answers to these questions have a great bearing on the computational approach to be adopted and none of the answers are obvious.

In the first place, it was assumed that representation of the geometry would need to be as accurate as possible, though not necessarily precise in every detail. This would mean that CFD methods relying on structured, surface-aligned grids would become steadily more difficult to apply as the geometry was made more complex. Unstructured grids are a viable alternative but they carry associated efficiency penalties and there are particular concerns over their accuracy for viscous flows. Thus, it was decided to adopt a non-aligned grid approach. This renders grid generation relatively simple for even the most complicated geometry. The route taken to a practical method is described in section 2.

In terms of flow modelling, the assumption was made that, for conventional naval ships, the principal flow features in the vicinity of a flight deck arise from vortical separations originating at sharp edges. The generation and early development of these can be

predicted with good accuracy using the (inviscid) Euler equations. Accurate modelling of the downstream development of the vortices, however, requires the inclusion of viscous effects. There are a number of arguments in favour of neglecting viscous effects, as was chosen to do here, at least as a first step. The most important is that, since the area of biggest concern for flow prediction is in the immediate vicinity of the flight deck and separation from sharp edges can be captured by an inviscid method, it is reasonable to investigate how accurately the resulting flow field can be modelled without viscous effects included. In this context, the information required from a flow prediction is important. If the complete, accurate interaction and downstream decay of vortices is needed, then an inviscid model is unlikely to be adequate. If, on the other hand, a general indication of flow severity, such as maximum downwash in the plane of the helicopter rotor, is sufficient, an inviscid model may well prove effective.

It was expected that the influence of the helicopter rotor on the air wake would be significant and the capability to model this by the actuator disc approach was included. Methods for improving the rotor downwash representation have been investigated recently and are described later. It was intended that a CFD tool should be produced which could be used for routine design purposes within the next few years. This means that a time-accurate, viscous method is unlikely to be a viable candidate. Of the two aspects, it was expected that it would be more important to model the variation with time. The evidence to date suggests that this is a valid assumption and this enhancement is currently being developed. Initial results are presented later in this paper.

2. MESH GENERATION

In light of the considerations described in the introduction, it was decided that a “non-aligned grid” approach should be adopted. This makes the generation of a computational grid very easy, but necessitates some special procedure within the flow solution code in order to apply the solid surface boundary condition accurately. It should be emphasised, at this point, that the approach taken was not to develop a state-of-the-art, non-aligned grid capability [3]. This would have entailed starting “from scratch,” requiring more development time than was available. Instead, an existing CFD method [4], known as FAME (Feature Associated Mesh Embedding) was used as the starting point.

FAME was developed, originally, for civil and military aircraft applications. It solves the problem of generating surface-aligned grids for highly complex geometry by using a series of overlapping and embedded, Cartesian and curvilinear meshes. The whole region of interest (away from solid surfaces) is covered by a set of regular, Cartesian blocks, which do not, in general, align with the geometry. They are

successively embedded, such that smaller grid cells occur near a solid surface. In order to apply solid surface boundary conditions, a particular type of curvilinear mesh is associated with each “feature” of the geometry. For example, an O-type mesh is associated with an aircraft wing section, whereas a cylindrical polar mesh is associated with the intersection line between a wing and a fuselage. These curvilinear meshes overlap each other and the Cartesian blocks. They also control the embedding of the blocks. Communication between the various meshes is governed by a set of hierarchical rules.

For application to ship air wake prediction, the whole curvilinear mesh philosophy was removed from FAME, partly because generation of these grids, for bodies as complex as ships, is very time-consuming. Control of the embedding of the Cartesian blocks, originally carried out by the curvilinear meshes, now takes place with a very small set of user-specified parameters. The finest grid which can be used to obtain a flow solution, on an SG Indigo 2 workstation with 32 MW of RAM, takes less than ten minutes to generate. This includes all the flagging of the various types of grid point (internal to body, normal field, actuator disc, interpolation required, etc.), for any geometry.

A computationally convenient device is currently used to describe the ship geometry. The ship is defined by a collection of hexahedral elements, because each hexahedron can be divided into six tetrahedra and there exists a very simple test to find whether a point lies within a tetrahedron. This is useful because, during the grid generation process, special points, which lie inside the body but have neighbours outside, must be identified, since these are required for the implementation of solid-surface boundary conditions. More general numerically defined geometry can be handled by routines existing within the FAME suite. However, this has not yet proved to be necessary. A section through a typical grid, for an AOR (Auxiliary Oiler Refueller), plus a simplified helicopter body, is shown in fig.1, highlighting the embedding of the blocks near the ship and the non-aligned nature of the grid.

3. FLOW SOLUTION

Two alternative numerical techniques have been used to obtain the flow solutions presented here. In both cases, a compressible flow solution code already existing within the FAME system was modified to solve the incompressible Euler equations, using the technique of artificial compressibility [5].

3.1 Governing equations

The approximation of incompressible flow is a valid one for the prediction of ship air wakes. The equations can be solved by conventional CFD methods by adding a fictitious time derivative of pressure term to the continuity equation. This term vanishes in the steady

state, but its presence alters the mathematical nature of the equation set, allowing time-marching techniques to be used. The equations to be solved are:

$$\underline{U}_t + \underline{E}_x + \underline{F}_y + \underline{G}_z = \underline{0}, \quad (1)$$

where

$$\begin{aligned}\underline{U} &= (p, u, v, w)^T, \\ \underline{E} &= (\beta u, u^2 + p, uv, uw)^T, \\ \underline{F} &= (\beta v, vu, v^2 + p, vw)^T, \\ \underline{G} &= (\beta w, wu, wv, w^2 + p)^T.\end{aligned}$$

Here, x , y and z are the Cartesian co-ordinates, u , v and w are the associated velocity components and p is the pressure. These are the 3D incompressible Euler equations, augmented by the pressure derivative in the mass continuity equation. The term β is the artificial compressibility parameter. Formally, it has the dimensions of a velocity and its optimum value is dependent on the non-dimensionalisation used, but, in practice, it is generally set to one.

3.2 Finite-difference method

An incompressible version of a finite-difference method [6] was developed first, since it was most mature at the start of this work on ship air wake prediction. It cannot, however, be easily extended to time-varying or viscous flows. The solution progresses towards the steady state by simple Euler time-stepping, augmented by multigrid convergence acceleration. Although the FAME mesh environment is less than ideal for multigrid, the technique still improves convergence by a factor of two or three. The underlying spatial discretisation is based on first-order upwinding. For the incompressible Euler equations with artificial compressibility, the decomposition used is:

$$\begin{aligned}\underline{\overline{U}}_t + & \left(\begin{array}{cc} \frac{\beta}{2a_x} & \frac{\beta(u+a_x)}{2a_x} \\ \frac{(u+a_x)}{2a_x} & \frac{(u+a_x)^2}{2a_x} \\ \frac{v}{a_x^2} \left[\frac{u+a_x}{2} - u^+ \right] & \frac{v}{a_x^2} \left[\frac{(u+a_x)^2}{2} - uu^+ \right] \\ \frac{w}{a_x^2} \left[\frac{u+a_x}{2} - u^+ \right] & \frac{w}{a_x^2} \left[\frac{(u+a_x)^2}{2} - uu^+ \right] \end{array} \right) \underline{\overline{U}}_x \\ & + \left(\begin{array}{cc} \frac{-\beta}{2a_x} & \frac{\beta(-u+a_x)}{2a_x} \\ \frac{(-u+a_x)}{2a_x} & \frac{(-u-a_x)^2}{2a_x} \\ \frac{v}{a_x^2} \left[\frac{u-a_x}{2} - u^- \right] & \frac{v}{a_x^2} \left[\frac{(u-a_x)^2}{2} - uu^- \right] \\ \frac{w}{a_x^2} \left[\frac{u-a_x}{2} - u^- \right] & \frac{w}{a_x^2} \left[\frac{(u-a_x)^2}{2} - uu^- \right] \end{array} \right) \underline{\overline{U}}_x\end{aligned}$$

+ (similar) v and w terms = $\underline{0}$.

Here, \underline{U} is as in equation 1, $a_x = \sqrt{u^2 + 1}$, the arrows indicate forward or backward differencing and

$$\begin{aligned}& \text{if } u > 0, u^+ = u, u^- = 0, \\ & \text{if } u < 0, u^+ = 0, u^- = u.\end{aligned}$$

Second-order spatial accuracy is achieved by the use of defect-correction. In short, this entails periodically taking central differences of the solution and adding the result, as a source term, to the equations which are then operated on by first-order upwinding again. Although this method is relatively rarely used, the algorithm was attractive during the early development of the FAME system because it requires only a seven point stencil in 3D, reducing the memory requirements significantly in comparison with more conventional CFD techniques. This algorithm is used for the steady-state solutions shown later, including those with actuator disc representations of the helicopter rotor effects.

3.3 Finite-volume method

Recently, a finite-volume method has been developed, within the FAME system, originally for inviscid flow [7]. It is currently less efficient for steady flows than the finite-difference method, since it does not include multigrid convergence acceleration. An incompressible version has been developed, for ship air wake predictions, which solves equations (1), using the normal, explicit finite-volume approach. The equations are written in the conservative form:

$$\frac{d}{dt} \int \underline{U} dV + \int_{\partial V} \underline{F}^{FV} \cdot \underline{n} dS = \underline{0},$$

where, again, \underline{U} is as in equation (1) and \underline{F}^{FV} is the total flux vector. V represents a computational cell volume, ∂V is the boundary of V , dS is an element of ∂V and \underline{n} is the outward normal to dS . The spatial discretisation uses the TVD approach. Although this complex method is not necessary for ship air wake flows, it has been retained to avoid diverging too much from the original method [7]. Temporal discretisation uses an explicit, multi-stage Runge-Kutta scheme and local time-stepping is adopted as an acceleration technique.

3.4 Time-accurate method

More recently the finite-volume method has been extended to time-varying flows [8]. If a fully explicit time-stepping scheme is used for time-varying flows, the whole domain must be integrated forward by the same time-step, which must be equal to the smallest time-step over the whole domain for stability reasons. This results in excessive run times. A particularly efficient alternative is to make the code implicit, using the dual-time approach [9], which has been shown to be effective for upwind schemes [10,11]. The implicit form of the differential equation for each computational cell is considered,

$$\frac{\partial(V^{n+1}\underline{U}^{n+1})}{\partial t} + R(\underline{U}^{n+1}) = 0,$$

where V is the time-dependent cell volume and R is the upwind flux integral. The superscript refers to the time level, $n+1$. To date, in this application, only stationary geometries have been attempted, so that the cell volumes need not be recomputed at each time step. The implicit temporal derivative is then approximated by a second-order backward difference, giving

$$\begin{aligned} \frac{3}{2\Delta t} \left[V^{n+1} \underline{U}^{n+1} \right] - \frac{2}{\Delta t} \left[V^n \underline{U}^n \right] + \\ \frac{1}{2\Delta t} \left[V^{n-1} \underline{U}^{n-1} \right] + R(\underline{U}^{n+1}) = 0. \end{aligned}$$

\underline{U}^{n+1} must now be iterated on to satisfy the equation. To achieve this, a new residual $R^*(\underline{U})$ is defined as

$$\begin{aligned} R^*(\underline{U}) = \frac{3}{2\Delta t} \left[V^{n+1} \underline{U} \right] - \frac{2}{\Delta t} \left[V^n \underline{U} \right] + \\ \frac{1}{2\Delta t} \left[V^{n-1} \underline{U}^{n-1} \right] + R(\underline{U}) \end{aligned}$$

and then a new differential equation can be written in terms of a fictitious time τ , (called pseudo-time)

$$V^{n+1} \frac{d\underline{U}}{d\tau} + R^*(\underline{U}) = 0.$$

This is simply time-marched to convergence in the fictitious time τ , for each real time step. As $R^* \rightarrow 0$, $\underline{U} \rightarrow \underline{U}^{n+1}$. Hence, although \underline{U}^{n+1} is an unsteady solution, it satisfies a steady equation. Steady acceleration techniques can thus be implemented in pseudo-time. As in the steady case, only local time-stepping is used at present. There is now no limit to the size of the real time step that can be taken, leading to a large reduction in CPU times. The time step is now limited by accuracy, rather than stability, considerations.

4. ROTOR INFLUENCE

The airflow over a flight deck during helicopter operations is undoubtedly influenced by the downwash induced by the helicopter rotor and vice versa. It seems obvious that some representation of the rotor effects should be included in any CFD calculation of such a flow field. Various levels of approximation can be employed in order to model rotor effects. The ideal is to perform a fully integrated calculation in which the geometry and rotating motion of the individual blades is included, in a time-accurate sense, within a time-varying ship air wake. However, even with state-of-the-art computing facilities, such a calculation will be unfeasible for a number of years. On the other hand, there are a number of approximations that can be made in order to include rotor effects within CFD. Perhaps the simplest is to represent the disc as a discontinuity,

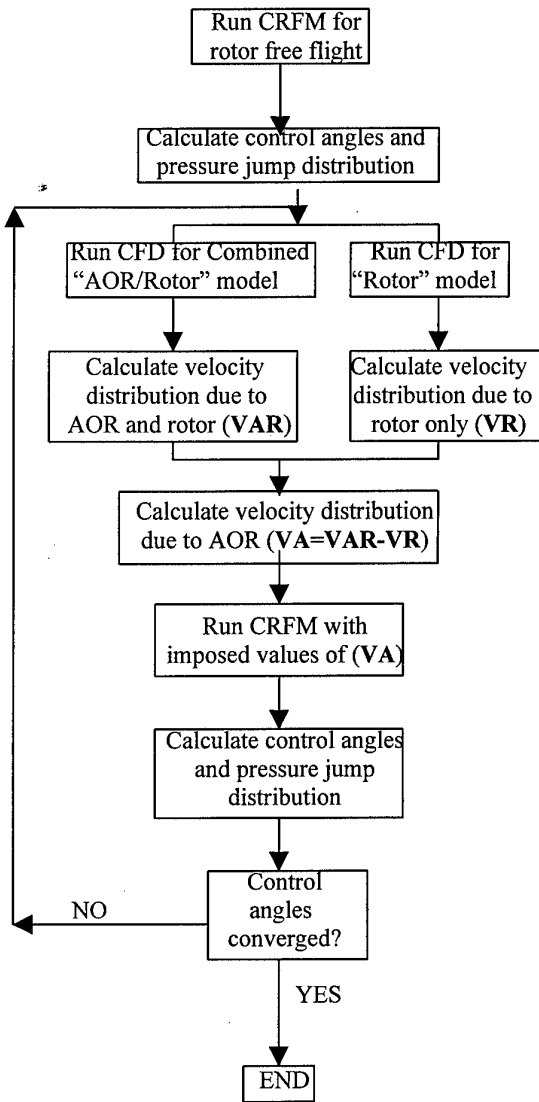
across which a “jump” in one or more flow variables is prescribed. In accordance with simple momentum theory (see e.g. [12]), the rotor is modelled by a constant pressure jump across the rotor disc. For convenience, the position of the disc is assumed to be equivalent to the nearest grid line (this usually entails an error of a few centimetres on the ship scale) and the pressure jump is simply added in to the flux evaluation at that point, in a computationally convenient way.

Whilst this simple actuator disc technique gives the gross effect of the rotor downwash on the overall flow field, it can clearly be improved upon quite easily by, for example, imposing a more representative pressure jump across the disc. A real rotor generates lift, which varies in both radial and azimuthal directions. Hence, a similarly varied pressure jump should represent the influence of the rotor more accurately. Such a pressure jump distribution can be calculated and supplied to the CFD calculations if the full interaction between the ship and the rotor are well represented. The interaction is influenced by the ship geometry, the operational conditions and the rotor performance.

The rotor analysis code CRFM (Combined Rotor-Fuselage Model) is used in this study to perform the rotor side of the calculations. The code was developed jointly by DERA Farnborough and GKN-Westland Helicopters to predict the aeroelastic behaviour of helicopters [13]. The code is used here, initially, to supply the distribution of pressure jumps as an input to the CFD code. However, it is essential that the flow field, surrounding the rotor, which is supplied to the CRFM code is accurately represented before the pressure jumps are calculated. Since this flow information is supplied by the CFD code, it follows that accurate modelling in both codes can only be achieved through a process of iteration between the two.

The process of iteration starts from the CRFM code, which assumes that the helicopter is in free flight away from the influence of the ship. The code calculates spatial and azimuthal values of the pressure jumps from the blade load calculations, then feeds this as an input to the CFD code. An initial run of the CFD code, with these pressure jumps, produces a flow field at the rotor disc that reflects the influence of ship structure as seen by the rotor. The CRFM code is then run again but with the flow field from the CFD code imposed on its own flow calculations. A new set of pressure jumps is then fed to the CFD code, which returns a new set of flow velocities to CRFM ... and the iteration continues. This process is outlined in the flow diagram below.

The iterative process eventually converges when the rotor control angles, as calculated by CRFM, do not change considerably between the last two iterations. The control angles are used as a criterion for convergence detection because these are sensitive to changes in the flow field. The first test case with this



approach is described in the next section. It was found that three or four iterations between the two codes were enough to achieve stable convergence.

5. RESULTS

An example of a ship air wake, calculated using the steady, finite-difference, Euler code, is shown in fig.2. The flow around the AOR plus simple helicopter is shown, in fig.2a, by the use of velocity vectors in the vertical plane through the helicopter centre line. The rotor itself is assumed to be stationary in this case. The flow appears quite mild since a scaling of the vectors has been chosen to facilitate comparison with later cases. However, the air over the deck is significantly disturbed by the presence of the superstructure. This is more obvious in fig.2b, where the generation of vortices is shown more clearly by the use of "stream ribbons," which are linked pairs of streamlines.

This ship/helicopter combination is used for most of the results given here to illustrate the calculation of a realistic situation, although no experimental data are available for comparison in this case. A significant amount of validation against both wind tunnel and full-scale experimental data has taken place at DERA. A particularly useful exercise, undertaken under the auspices of TTCP AER-TP-6 KTA-2, involved the comparison of results with those from other CFD codes and data from a wind tunnel experiment on a simple shape exhibiting the main features of a typical frigate. This exercise is described elsewhere in this Symposium [14]. The result of this and other exercises was that the Euler code does correctly predict the main flow features arising from sharp edges.

The effect on the overall flow field of including rotor influence is shown in fig.3. In this case, an actuator disc is used with a constant jump in pressure across the disc equivalent to that needed to keep a large helicopter in a steady hover. As expected, the impact on the flow field is dramatic, as can be seen by comparison with fig.2a. The importance of including some representation of the helicopter body (albeit a relatively crude one in this case) is shown by the fact that a small fountain effect is seen below the body, which does not arise if the actuator disc is included in the calculation without a body. Another interesting feature is the way in which the downwash from the front part of the rotor strikes the deck and is then deflected upwards by the hangar face before being drawn back into the rotor. This feedback interaction has been suggested as a cause of problems observed during some trials, in which the proximity of the helicopter to a vertical surface gives rise to handling difficulties entirely independent of the natural airflow over the ship superstructure.

In fig.4, a result is shown for a similar calculation. Here, a spatially varying pressure jump is imposed across the actuator disc. The distribution used here is that which is calculated by CRFM for the helicopter in free flight, where the helicopter is assumed to be a Merlin.

As an illustration of the interaction of the CFD code with the rotor performance code CRFM, two CFD solutions are shown in fig.5a. These are the first and fourth calculations in a sequence as outlined in section 4. In the first, the imposed pressure distribution is that which is predicted by CRFM for a Merlin in free air with a 20 knot wind coming from 20 degrees to port. (This is a closer view of fig.4). In the fourth and final calculation, the distribution imposed is that resulting from successive applications of CRFM with the velocity components from the CFD solution. Again, velocity vectors are shown in a plane through the helicopter centreline. Under close examination, some differences can be seen between the two, although they are not dramatic. In the absence of experimental data, there is no reason to suppose that this is a particularly severe case. Also, a relatively coarse CFD grid was

used to reduce turnaround times, since the main point of this exercise was to check that the CFD/CRFM interaction process was feasible. Since much of the detailed change in disc loading is concentrated in relatively small areas, particularly near the outer edge, it may be that a finer CFD grid is necessary to capture the resulting changes in the flow field satisfactorily. Fig.5b shows how the sequence of CFD/CRFM calculations produces a predicted change in collective pitch and cyclic control settings and that the iterative sequence achieves convergence. It is hoped that the veracity of the predicted changes, for this or a similar case, can be checked against experimental data in the near future.

The air wake over a real ship superstructure is highly unsteady. Indeed, it is not obvious that a steady CFD solution would be of any use whatsoever in predicting this situation. The general conclusion from the testing carried out to date is that steady solutions can be of use, although more evidence is still needed to back this up. However, it is undoubtedly the case that the effects of variation of the flow field with time must be investigated. The route chosen towards time-accurate CFD solutions was described earlier. An initial result has been obtained for the geometry tested as part of the TTCP collaboration described in ref.14. A relatively coarse spatial grid was used to facilitate a more rapid turnaround of the solution. This particular test case involves a port/starboard symmetric geometry and a yaw angle of zero degrees (wind from dead ahead). It is to be expected that the real flow will vary with time, but that a long time-averaged view of the flow pattern will look symmetrical. Fig.6 shows two views of the computed flow field, one corresponding to a particular instant in time and one to an average of the solution over a large number of real time steps. It is clear that the instantaneous solution is highly asymmetric, whereas the averaged view is almost perfectly symmetrical. This average solution agrees reasonably well with that observed in the experiment [14], although it was found, in the context of steady flow solutions, that a finer grid is necessary to really obtain a good representation of this situation. Thus, for a very preliminary investigation, this result can be regarded as highly encouraging.

6. CONCLUSIONS

A method has been presented for modelling the air wake over a conventional naval ship, with particular attention paid to the region of an aft-located helicopter landing deck. Grid generation is reduced to a very simple problem, by use of the "non-aligned mesh" technique, in which no attempt is made to align any grid lines with solid geometrical surfaces. Accuracy is enhanced in the region of solid surfaces by the use of grid embedding.

The airflow is modelled by solution of the Euler equations. This relies on the assumption that the dominant flow features over an aft-located helicopter

deck will be separations from sharp edges, which can be predicted by numerical solution of the inviscid equations. It is essential to include some representation of helicopter rotor effects on the airflow. This can be done, as a first step, by a constant actuator disc approach. Improved modelling can be achieved by use of a variable actuator disc. One way to decide on the variation required across the disc is to use initial CFD results as boundary conditions within a helicopter performance code. Such a code can produce a new variation across the disc, which is then fed into an updated CFD calculation, before returning to the performance code, etc. This iterative process has two potentially important effects. The first is to produce a more accurate CFD solution than that obtained with a constant actuator disc model. The second is to provide predictions of the effect of the air wake on the helicopter, hence aiding the understanding of the handling problems suffered by the pilot during shipborne operations.

The highly unsteady nature of a real ship air wake will undoubtedly be an important consideration. Modification of the existing code to include time-varying effects has taken place, using an efficient implicit scheme. Initial results are encouraging, although much more testing and potential development is necessary.

Even with steady, inviscid flow solutions, much progress has been made on the prediction of realistic ship air wakes. Indications are that a useful predictive tool has been developed during this project.

REFERENCES

1. Breuer M, Lakehal D and Rodi W. *Flow around a surface-mounted cuboidal obstacle: comparison of LES and RANS – results*. In Notes on Numerical Fluid Mechanics, vol.53, Vieweg.
2. Albone C M, Catherall D C, Hall, M G, Joyce Gaynor. *An improved numerical method for solving the transonic small-perturbation equation for the flow past a lifting aerofoil*. RAE TR74056.
3. Powell K G. *Solution of the Euler and magnetohydrodynamic equations on solution-adaptive Cartesian grids*. VKI Lecture series 1996-06.
4. Albone C M. *An approach to geometric and flow complexity using feature-associated mesh embedding (FAME): strategy and first results*. In Numerical methods for fluid dynamics III, Oxford University Press, 1988.
5. Chorin A J. *A numerical method of solving incompressible viscous flow problems*. Jnl. Comp. Phys., Vol.2, pp.12-26, 1967.
6. Albone C M. *A second-order accurate scheme for the Euler equations by deferred correction of a first-order upwind algorithm*. RAE TR88061.

7. Onslow S H and Peshkin D A. *A TVD flow algorithm for FAME*. Proceedings 5th ICFD Conference, Oxford, 1995.
8. Allen C B, Onslow S H and Tattersall P. *Parallel implementation of an unsteady Euler solver using overlapping and embedded meshes*. 4th ECCOMAS CFD Conference, Athens, 1998.
9. Jameson A. *Time dependent calculations using multigrid, with applications to unsteady flows past airfoils and wings*. AIAA paper 91-1596.
10. Allen C B. *The reduction of numerical entropy generated by unsteady shock waves*. Aero. Jnl., Vol.101, No.1001, 1997, pp7-16.
11. Allen C B. *Grid adaptation for unsteady flow computations*. IMechE Journal of Aero Eng., Vol 211, 1997, pp.237-250.
12. Payne P R. *Helicopter dynamics and aerodynamics*. Pub. Pitman, London, 1959.
13. Hansford R E. *The development of the Coupled Rotor-Fuselage Model*. 48th AHS Forum, 1992.
14. Wilkinson C H, Zan S J, Gilbert N E, Funk J D. *Modelling and simulation of ship air wakes for helicopter operations. A collaborative venture*. Paper No. 9, AGARD Symposium, Amsterdam, 1998.

ACKNOWLEDGEMENTS

This research is funded by the UK MOD under ARP package 15f, assignment 2, research objective 1.

© British Crown Copyright 1998/DERA

Published with the permission of the Controller of Her Britannic Majesty's Stationery Office.

ILLUSTRATIONS

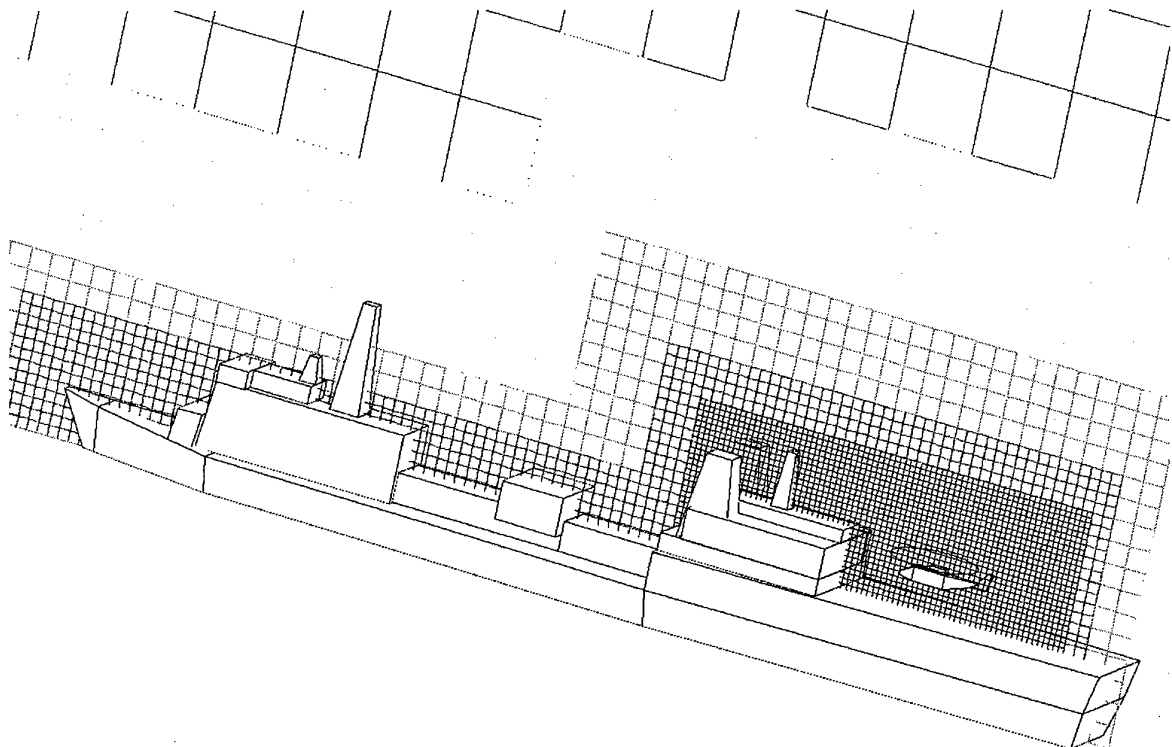


Figure 1. Section through computational grid for AOR + helicopter

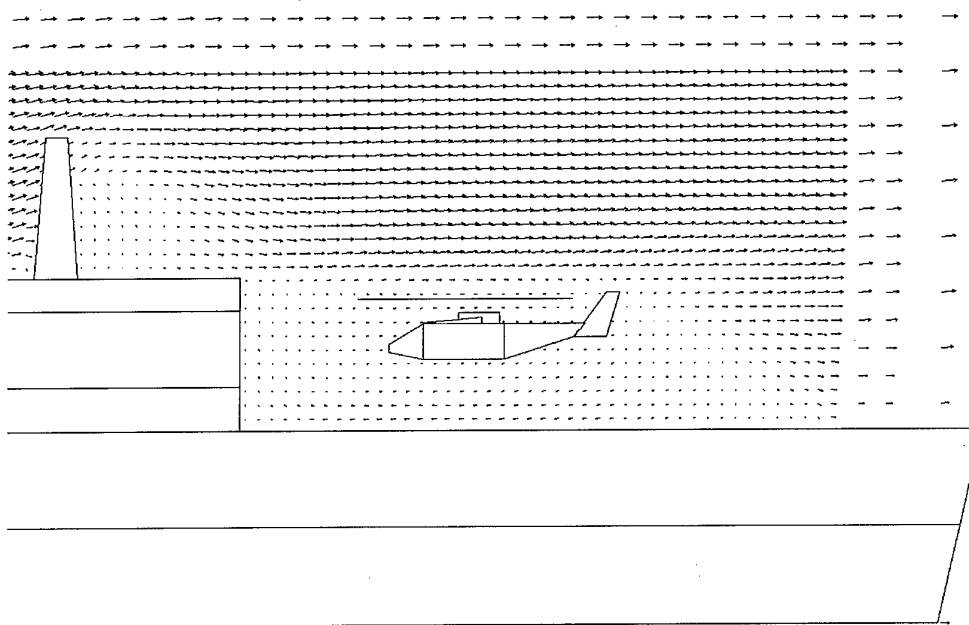


Figure 2a. Air wake over AOR + helicopter with no rotor effects-velocity vectors

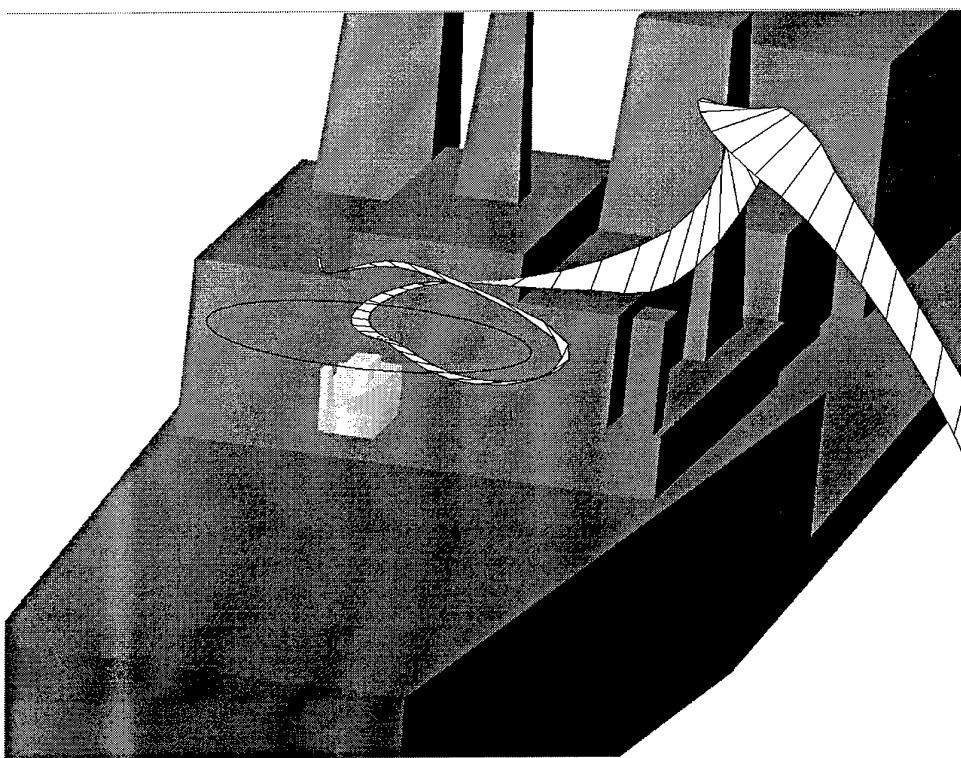


Figure 2b. Air wake over AOR + helicopter with no rotor effects-stream ribbons

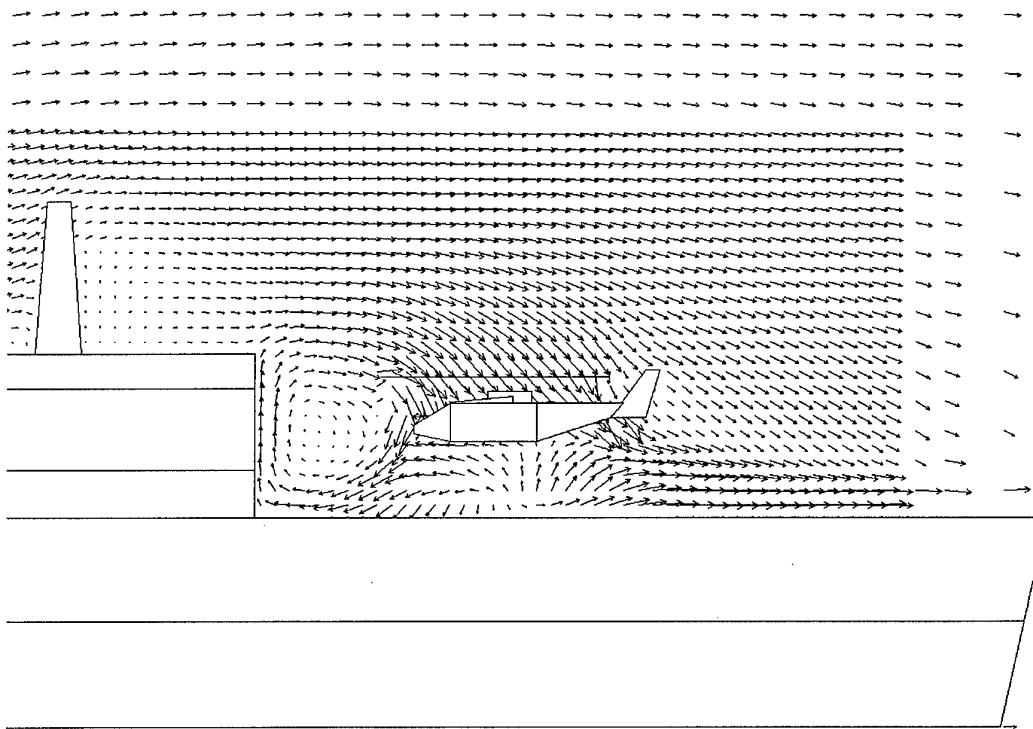


Figure 3. Air wake over AOR + helicopter with constant actuator disc

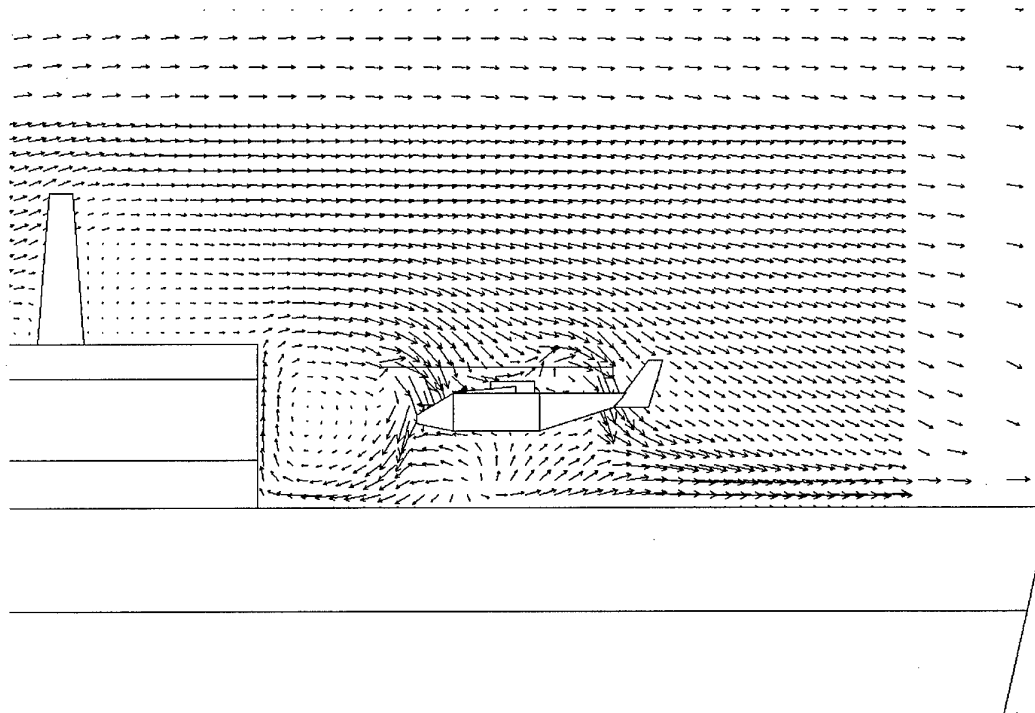
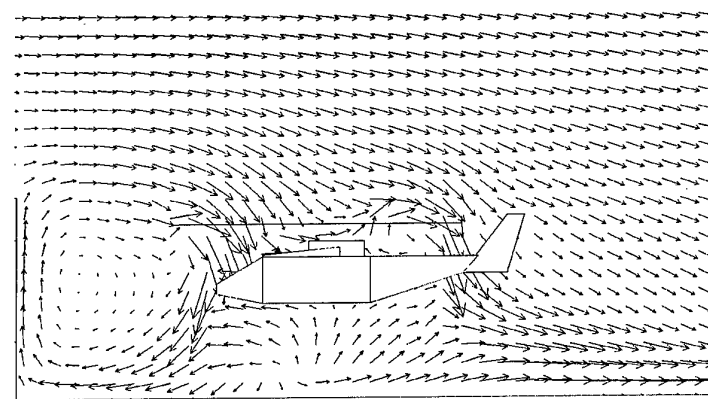
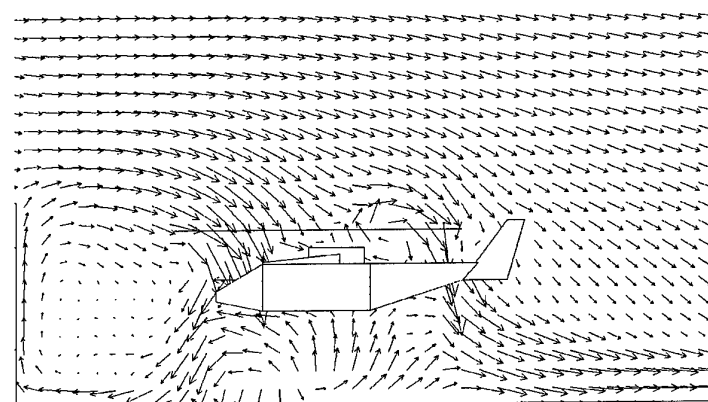


Figure 4. Air wake over AOR + helicopter with variable actuator disc



First CFD calculation



Fourth CFD calculation

Figure 5a. Results from sequence of iterations between CFD and helicopter performance code

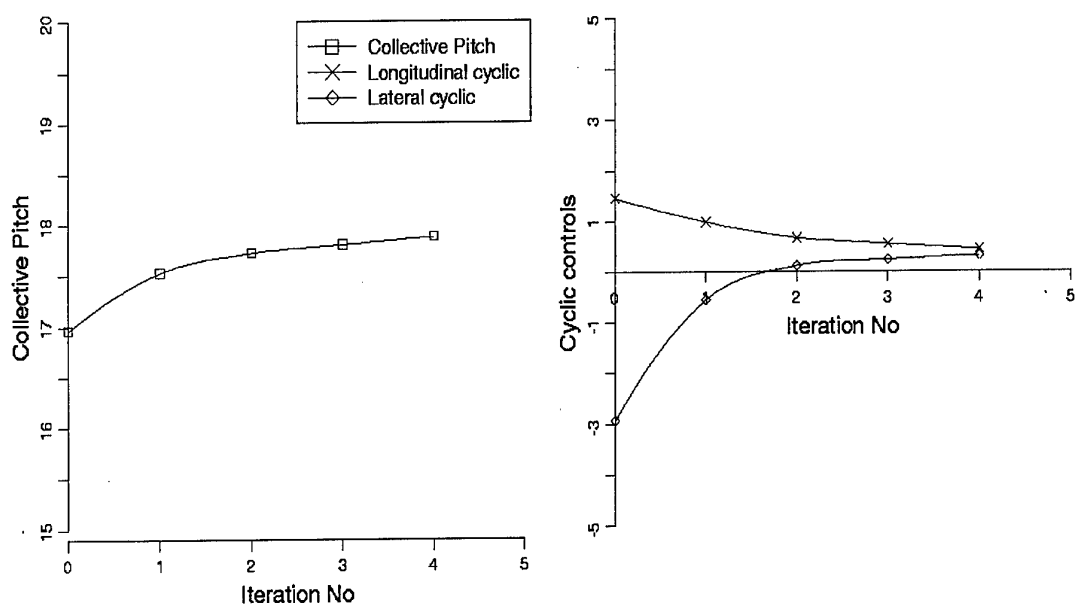


Figure 5b. Results from sequence of iterations between CFD and helicopter performance code

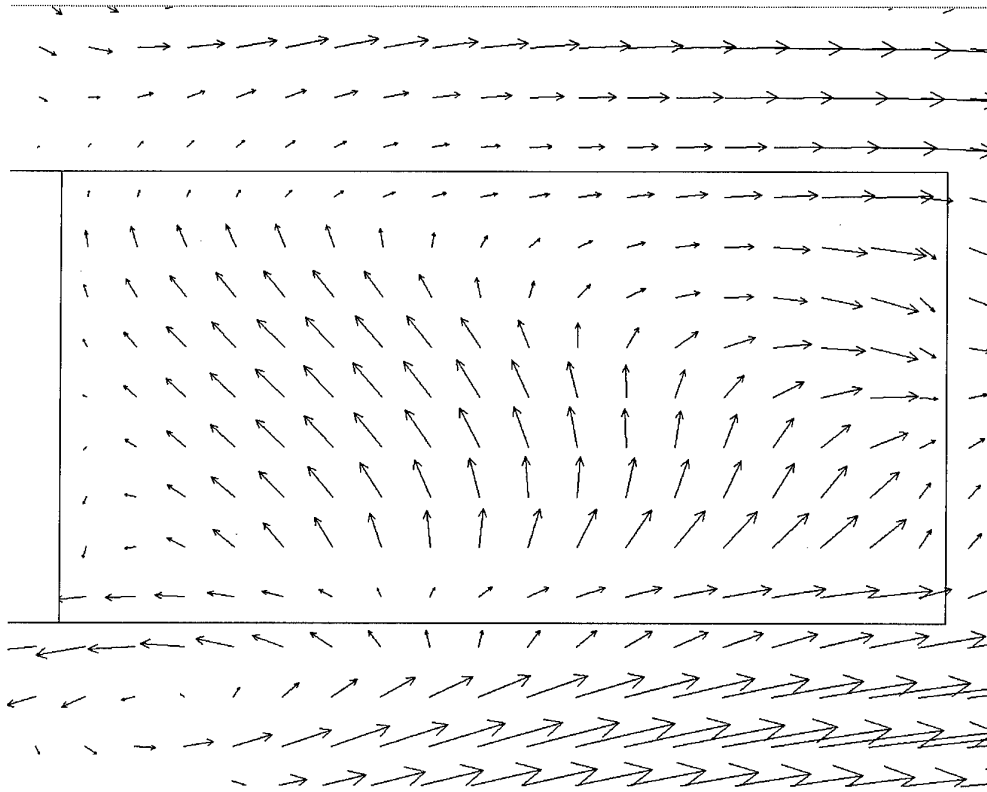


Figure 6a. Unsteady calculation – instantaneous solution

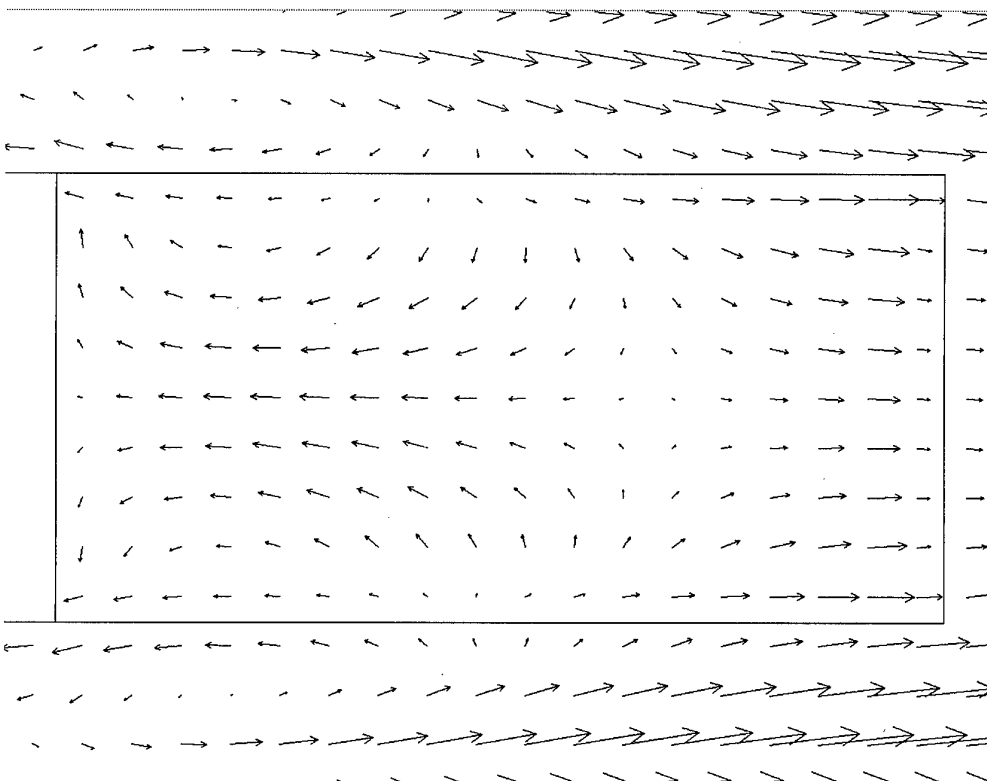


Figure 6b. Unsteady calculation – time-averaged solution

Aerodynamic Perturbations Encountered by a Helicopter Landing on a Ship - Effects on the Helicopter Flight Dynamics

A. Taghizad* , Ch. Verbeke** , A. Desopper*

* ONERA - Département Commande des Systèmes et Dynamique du Vol
BA 701 - Ecole de l'Air
13661 Salon - Air
France

** ONERA-IMFL - Département Aérodynamique Appliquée
5- Boulevard Paul Painlevé
59045- Lille cedex
France

1. ABSTRACT

This paper describes a French activity on helicopter ship landing operations simulation improvement. ONERA, under SPAé funding (Service des Programmes Aéronautiques), has developed an aerodynamic disturbance model around the landing deck of a frigate La Fayette, and has tested its effects on helicopter flight dynamics.

Wind tunnel tests were carried out in ONERA-IMFL with a 1/50th scaled model of the La Fayette. Three dimensional measurements of the mean wind speed and velocity fluctuations were performed around the landing deck area.

The La Fayette aerodynamic wake model includes a mean wake model [1] to which a turbulence model adds velocity fluctuations. The turbulence model is realised using power spectral densities of velocity fluctuations measurements.

The model was connected to the Eurocopter Helicopter Overall Simulation Tool (HOST). Simulations of flights above the deck with this model demonstrated important effects of the ship air-wake on the helicopter flight dynamics.

This paper describes the test results obtained and the work performed in modelling the La Fayette wake and its influence on the helicopter flight dynamics

2. INTRODUCTION

Flying a helicopter above or around a frigate deck, landing on it or taking off from, are considered by pilots as highly risked operations. Indeed, not only the frigate moves, but also in the neighbourhood of the deck, the helicopter has to face with the changing aerodynamic wake of the ship superstructure. This unsteady flow provides high mean speed gradients to which aerodynamic turbulence (fluctuations) is added. These conditions have important effects on helicopter global performance, and behaviour.

Under SPAé funding, ONERA has realised wind tunnel tests on a 1/50th scaled La Fayette frigate model, and has developed an aerodynamic wake model of the ship landing area. This model was then used in order to study the effects on flight mechanics.

The main following topics are presented in this paper :

- 1- Wind tunnel tests,
- 2- Analysis of the test results obtained,
- 3- Definition and development of a mean air-wake model,
- 4- Definition and development of a turbulence model,
- 5- Implementation in HOST (Helicopter Overall Simulation Tool),
- 6- Demonstration of the frigate wake effects (mean velocities + fluctuations) on helicopter loads and flight dynamics.

3. WIND TUNNEL TESTS

3.1 Test equipment description

Wind tunnel measurements were carried out in the ONERA-IMFL low speed wind tunnel (SH). This wind tunnel has a closed circuit and a test section of 2.4 m in diameter. The first 50 meters of the marine atmospheric boundary layer was also simulated.

Measurements were performed on a 1/50th La Fayette frigate model, configured with its Crotale Missiles (figure 1). Because of the model and the test section sizes, the relative wind side-slip angles were limited to ±15° around the frigate longitudinal axis.

3D unsteady velocities were measured using crossed hot film anemometer. Two velocity components were simultaneously measured (u , v), and then (u , w) after a 90° rotation of the sensor. Thus, 2 redundant longitudinal velocity measurements (U_v , U_w) were provided. Speed measurements error is estimated as 2.6% of the infinite upstream wind.

3.2 Test configurations

The 3 unsteady ship air-wake velocity components were measured in a volume surrounding the landing deck. Figures 2 and 3 show the test volume and the selected test points positions inside ; 8 horizontal planes above the deck were considered.

Detailed data measurements were realised with a 50 kt wind and three side-slip conditions (0°, 15° and 180°). Some tests at 25 kts and 0° of side-slip were also performed. Figure 4 gives a summary of these test configurations.

4. DATA ANALYSIS

4.1 Velocity decomposition

The three velocity components are decomposed into two parts ; the mean value and the fluctuations around this mean value. For example, the longitudinal velocity is decomposed into:

$$U(x, y, z, t) = U_{mean}(x, y, z) + u(x, y, z, t)$$

U_{mean} : the longitudinal velocity mean value,

u : fluctuations around U_{mean}

x, y, z : space co-ordinates of the local point

t : time variable

The fluctuations (u , v and w) can be considered as turbulent terms.

In addition, measured velocities are normalised by the free stream velocity.

$$Um(x, y, z) = \frac{U_{mean}(x, y, z)}{V_{free stream}}$$

$$Du = \frac{u(x, y, z, t)}{V_{free stream}} = \frac{U(x, y, z, t)}{V_{free stream}} - Um(x, y, z)$$

The normalised velocity fluctuations are characterised by their Power Spectral Densities (PSD):

$$Du \Rightarrow pu : longitudinal turbulence PSD$$

$$Dv \Rightarrow pv : lateral turbulence PSD$$

$$Dw \Rightarrow pw : vertical turbulence PSD$$

This approach is similar to the one used in [2] and [3].

For the frequency, the results will be presented function of scale 1 frigate (wind tunnel frequency / 50).

4.2 Ship air-wake mean velocity measurements distribution

This topic has already been discussed in a previous paper [1]. Therefore, we will confine our discussion to a brief presentation of some results and the synthesis of mean velocities measurements.

Figure 5 gives the evolution of the mean velocity components (Um , Vm , Wm) along the vertical axis, on the deck centre (point A), for a 50 kt wind speed without side-slip ($\beta = 0^\circ$). Figures 6 and 7 show the same parameters evolution respectively along the longitudinal symmetry axis (height 4.4 m above the deck) and the lateral axis which crosses the deck at point A (height 4.4 m).

These 3 figures show a clear downward deviation of the flow ($Wm < 0$), due to the hangar wall cliff-effect ($h=6.60m$). The mean vertical velocity is all the time negative, denoting a general down wash on the deck and behind it. The longitudinal component of the mean air-wake decreases with the height above the deck and when moving to the rear. This last effect is due to the second flow deviation on the back side of the deck. The maximum vertical velocity is reached on the centre line, while the longitudinal velocity decreases to a minimum in the same area. At last, the air-wake is deviated from both sides toward the centre.

The different effects described above can be seen again in the 3D flow visualisation of figure 8. Arrows represent the mean velocity projections on visualisation planes, whereas coloured areas show turbulence levels. Light colours corresponds to the highest turbulence level. The downward flow deviation can easily be seen and a high turbulence level is noticeable on the deck, especially below the hangar height. Due to the aerial elements (missiles, funnel, radar, ...), a clear asymmetry of the turbulence distribution is obtained.

Figures 9 and 10 are 3D flow visualisations of measurements at 50 kts with respectively 15° and 180° (rearward) side-slip conditions. The effect of the lateral hangar wall can be seen for a side-slip angle of 15° .

Comparisons of mean velocities evolution for 2 wind speed conditions (50 kts and 25 kts) without side-slip ($\beta = 0^\circ$) and 3 side-slip conditions at 50 kts ($\beta = 0^\circ$, 15° , 180°) [1] provide the following conclusions on the mean air-wake model usage domain :

- A detailed database is available at 50 kts of frontal wind ($\beta=0^\circ$) ;
- A detailed database is also available at 50 kts with 15° of side-slip. The mean flow changes considerably compared to the case of 0° side-slip. However, it has been decided that interpolation between 15° and 0° of side-slip at 50 kts will be “tolerated”, in order to extend the database to intermediate side-slips;
- A partial database has been generated at 25 kts, without side-slip. This investigation shows that except above the deck, the mean wind normalised components have similar evolution. Above the deck, these components will have to be interpolated or extrapolated using the results at 25 and 50 kts ;
- A 50 kt rear wind database is also available.

4.3 Aerodynamic wake fluctuations

a- Wind velocity = 50 kts, Side-slip $\beta = 0^\circ$

Figure 11 gives an example of normalised velocity fluctuations on the deck centre (point A), at 2.4 m above it, for a 50 kt wind speed and 0° side-slip.

Figure 12 shows a 3D presentation of the vertical velocity (w) Power Spectral Density (PSD) evolution along the vertical axis on point A. We can notice high turbulence rates concentrated below the hangar wall height.

Figure 13 presents the 3 velocity components spectral densities on different test planes above the deck centre. For planes below the hangar height (first 3 rows from the bottom), spectral densities show an energy concentration approximately around 0.5 Hz. This maximum of energy decreases with the height. For the planes above the hangar height, PSDs start getting flat.

Figures 14 and 15 illustrate the vertical velocity (w) PSD evolution respectively along the median axis (on the deck and one deck length behind) at a height of 2.4 m (fig. 14) and along the lateral axis crossing the centre point A (from one deck width left side to one deck width right side) at the same height (fig. 15). These figures show again that turbulence is much higher above the deck than beside it. A small asymmetry

around the median axis (longitudinal), is to be noticed. This asymmetry is due to higher deck's aerial elements.

b- Wind velocity = 50 kts, Side-slip $\beta = 15^\circ$

In order to study the side-slip effect on air-wake velocity fluctuations, measurements have been done at 50 knots with a 15 degree side-slip.

Two points have been selected, in order to illustrate a comparison between the 2 tested side-slip configurations (figure 16) :

- 1- point A, which remains in the frigate superstructure main wake for both cases,
- 2- point B, which is out of this main wake at 15° side-slip.

Figures 17 and 18 are comparisons, respectively on A and B, of the 3 velocity components PSDs along the vertical axis. Large differences can be seen between the 2 cases.

As it was already concluded for the side-slip effect on mean velocities [1], these results show that the side-slip angle is a quite important factor acting on turbulence PSDs and it is not possible to extrapolate these results for side-slip configurations higher than 15° . Even an interpolation between 0 and 15° is critical. However, it was decided to extend, by interpolation, the La Fayette aerodynamic turbulence model to intermediate side-slips (0 to 15°) at 50 knots of wind speed.

c- Wind velocity = 25 kts, Side-slip $\beta = 0^\circ$

Limited measurements were performed in 25 kt frontal wind conditions ($\beta=0^\circ$).

Three points, A, C and D, were selected in order to compare the results for the 2 wind conditions (25 and 50 kts). These points are respectively located on the deck centre, at the rear and behind the deck (figure 19).

Figures 20 to 22 illustrate the power spectral densities of the velocity components fluctuations (D_{uv} , D_{uw} , D_v , D_w) on different test planes above these points. The first row of plots from the bottom corresponds to the lowest test plane and the last one to the highest test plane.

A clear wind speed effect on PSD amplitudes is visible on point A. Indeed, normalised power spectral densities amplitudes on this point are higher at 25 kts than at 50 kts. On point C and D this effect seems to get reduced.

Additional investigations have shown that the wind speed effect on PSD amplitudes is much reduced when the point considered is far from the deck.

Concerning the frequency of PSDs maximum (f_{max}), a relationship between f_{max} and the wind speed (Strouhal number similarity) can be expected:

$$St_{25kts} = \frac{C \cdot \Omega_{25kts}}{V_{25kts}}$$

$$St_{50kts} = \frac{C \cdot \Omega_{50kts}}{V_{50kts}}$$

C being a characteristic length

$$\text{if } St_{25kts} = St_{50kts} \Rightarrow \Omega_{25kts} = \frac{V_{25kts}}{V_{50kts}} \cdot \Omega_{50kts}$$

Thereby, further investigations were carried out to consider this question. Comparisons of PSDs at 50 kts and 25 kts were done on several test points. In our investigation, the ratio of fmax at 50 kts on fmax at 25 kts was found between 1.4 and 2.3.

Due to the fact that the determination of the frequency of the maximum amplitude is not always very easy, the assumption of Strouhal number similarity will be considered for the turbulence model realisation.

d- Wind velocity = 50 kts, Side-slip $\beta = 180^\circ$

Measurements were also performed for a rear wind condition at 50 kts. Obviously, non comparison can be done with forward wind configurations. Figure 10 is a 3D visualisation of the test measurements.

e- Synthesis on velocity fluctuations measurements

The following conclusions come out from the measurements:

- A detailed database is available at 50 kts of frontal wind ($\beta=0^\circ$);
- A detailed database is also available at 50 kts with 15° of side-slip. Fluctuations PSDs change considerably compared to the case of 0° side-slip. It has been decided that, in order to extend the database, interpolation between 15° and 0° of side-slip at 50 kts will be “tolerated”;
- A partial database has been generated at 25 kts, without side-slip. This investigation shows that except above the deck, the normalised velocity components fluctuations have similar evolutions with however, the respect of Strouhal number similarity. Above the deck, PSDs will have to be interpolated or extrapolated using the results at 25 and 50 kts;
- A 50 kt rear wind database is also available.

5. LA FAYETTE FRIGATE AERODYNAMIC WAKE MODEL

5.1 Model structure

Measurements synthesis done above, makes it possible to describe the model structure and to define its limits of validity:

- In every frontal wind velocity condition ($\beta=0^\circ$) the model can provide air-wake components (UF, VF, WF), including mean velocity and turbulence.
- At 50 kts of wind, for any side-slip between 0° and 15° , the model will give an air-wake by interpolation.
- For rear wind, air-wake components can also be calculated at 50 kts.

5.2 Model realisation

The La Fayette air-wake model includes a mean wake model and a model of velocity fluctuations (turbulence).

a- Mean air-wake model

The test area above and around the ship deck is actually a grid according to the test points definition. At any point (H) of this area the 3 mean air-wake components are interpolated, using the mean air-wake measurements of neighbouring points.

The approach consists in locating the helicopter centre of gravity in the test area elementary parallelepiped (figure 23). The mean air-wake on this point is defined via its components in the frigate axes, using a linear combination of measured mean velocities on the elementary parallelepiped tops, in respect with their distance to the considered point.

In order to avoid any velocity discontinuity when going in/out of the test area, a transition region has been defined, where velocities are interpolated between the test area and the free stream. Figure 24 illustrates this method.

b- Velocity fluctuations model (turbulence)

Velocity fluctuations are generated using the 3 velocity components PSDs.

The approach consists in locating the helicopter centre of gravity in the test area elementary parallelepiped. Fluctuations PSDs on this point are defined using a linear combination of measured PSDs on the elementary parallelepiped tops, in respect with their distance to the considered point.

Fluctuations are then processed using a signal generation method ensuring the similarity between PSDs of measurements and of the generated signal.

The method consists in:

- a- Calculation of measured velocity fluctuations PSD.
- b- Identification of a mathematical model (S) fitting the experimental PSD.

- c- Velocity fluctuations computation from the identified PSD, using the following method [4]:

Example of u generation:

$$u(x, y, z, t) = 2 \sum_{i=1}^N \sqrt{S(x, y, z, f_i)} \cdot \Delta f \cdot \cos[2\pi f_i t + \varphi_i(x, y, z)]$$

N : Number of samples in S

f_i : Temporal frequency for i^{th} sample

φ_i : Random phase between 0 and 2π with a uniform probability density

Figure 25 is an example of vertical turbulence generation on the deck centre (height = 2.4m) at 50 knots of wind speed.

6. EFFECTS ON HELICOPTER LOADS AND FLIGHT DYNAMICS

The frigate air-wake model has been connected to the Eurocopter simulation code HOST (Helicopter Overall Simulation Tool) [5]. The connection was done assuming the helicopter as a mass point.

The air-wake model uses some general data coming from HOST (wind velocity and direction), and specific ship state data (velocity and heading). The ship trajectory is then calculated in the air-wake model, assuming a constant speed. Figure 26 illustrates this implementation.

The air-wake model fulfils the following tasks:

- generating the ship trajectory.
- locating the helicopter in the test area grid.
- calculating the 3 velocity components at the helicopter CG.

In order to demonstrate the frigate aerodynamic wake effects on helicopter flight dynamics, off time open loop simulations of flights above the deck were carried out with HOST.

Typical results are presented on figures 27 to 29 for a descending flight on the deck at a speed of 10 kts and a slope angle of -1° . The frigate is still and faces with a 50 kt forward wind ($\beta=0^\circ$). The helicopter, a 3.5 t Dauphin, is trimmed with the local mean air-wake conditions at the starting point located on the longitudinal symmetry axis ($y=0$), 9 m above the deck and 23 m behind its rear extremity ($X=25$ m in the frigate axes).

The simulation being realised in open loop, the helicopter controls keep their trim values (figure 27). Figure 28 illustrates the local wind components (UF-FGW, VF-FGW, WF-FGW), the helicopter flight

parameters (helicopter attitudes, ground speed components, ...) and trajectory coordinates. Figure 29 shows the aerodynamic loads on different helicopter elements (main rotor, fuselage and horizontal stabiliser). Blades flapping and the local turbulence terms (DUF-FGW, DVF-FGW, DWF-FGW) are also presented on this figure.

These plots show a short deceleration at the beginning of the simulation and a quick fall in altitude with a large lateral deviation (20 m to the left).

It is interesting to compare these results obtained with turbulence and mean aerodynamic velocities, with those coming from the same simulation but in mean velocities effect only.

Figures 30 and 31 illustrate this case. Figure 30 shows that the longitudinal component of the air-wake (UMF-FGW) decreases during the approach because the helicopter comes closer to the deck. The vertical air-wake (WMF-FGW) is all the time negative (down wash) and changes not only with height but also with helicopter X and Y positions above the deck.

The combined effects of these two air speed components result in a general decrease of the main rotor lift (FZG-RP), and consequently a loss of altitude. The helicopter pitches down and accelerates because of the pitch moment decrease (MYG-RP). Simulation stops after 8 seconds when helicopter altitude is zero and attitudes have changed by -7° in pitch, -11° in roll and -25° in heading.

The comparison of these 2 trajectories shows that for the first simulation (mean air-wake + turbulence), the altitude loss has been delayed because of an initial lift raise, this last being caused by 'favourable' initial turbulence conditions. Other simulations have demonstrated the opposite effect, with a higher altitude loss compared to the simulation with the only mean air-wake. In these cases, 'non favourable' initial turbulence generates a lift loss and a quicker altitude fall.

It comes out from these open loop simulations that turbulence can have a positive or a negative influence. However, these turbulence effects occur around a general tendency given by the mean velocities and will certainly have an effect on piloted simulations.

7. CONCLUSION

This paper presents an ONERA activity on helicopter ship landing operations simulation improvement.

The first phase of this activity started with wind tunnel tests in ONERA-IMFL, on a 1/50th model of the French frigate La Fayette. A detailed database was provided at 50 kts for 3 wind side-slip configurations (0° , 15° , 180°). A partial database was also generated at 25 kts of wind with 0° side-slip. The data analysis showed

important aerodynamic effects due to the hangar cliff-effect and ship lateral wall effects.

These data were used in order to define and to develop a ship air-wake model of the La Fayette deck area. It includes a mean air-wake model and a model of velocity fluctuations (turbulence).

This model, connected to the Eurocopter HOST code (Helicopter Overall Simulation Tool) demonstrated important effects of the ship mean and turbulence aerodynamic wake on helicopter loads, moments and generally on its flight dynamics.

Follow-on activities will consist in :

- completion of the data base with new wind tunnel tests for a 15° side-slip and a 10° roll angle of the ship ;
- transferring the model to Eurocopter for implementation on Eurocopter real time simulator. Modifications of the model will certainly be needed for real time applications.

[5] P. Eglin
(Eurocopter)
Aerodynamic Design of the NH90 Helicopter Stabilizer.
23rd European Rotorcraft Forum,
Dresden, Germany, September 1997.

REFERENCES

- [1] A. Taghizad, Ch. Verbeke, A. Desoppe (ONERA)
Modelling the fregate La Fayette aerodynamic wake for helicopter landing operations
To be published in Aerospace Science and Technology (AST).
- [2] H. Zhang, J.V.R. Prasad, D.N. Marvis (School of Aerospace Engineering-Georgia Institute of Technology)
Ship air wake effects on helicopter rotor aerodynamic loads.
AIAA, 1994.
- [3] D.N. Marvis, J.V.R. Prasad, D.P. Schrage (School of Aerospace Engineering-Georgia Institute of Technology)
A Simulation Methodology for Modelling Ship-Air wake Turbulence.
25th Annual International Symposium of the Society of Flight Test Engineers, Washington Aug. 1-5, 1994.
- [4] M. Shinozuka (Columbia University, New York), C.-M. Jan (Gibbs and Hill Inc. New York)
Digital simulation of random processes and its applications.
Journal of Sound and Vibration (1972) 25 (1), 111-128.

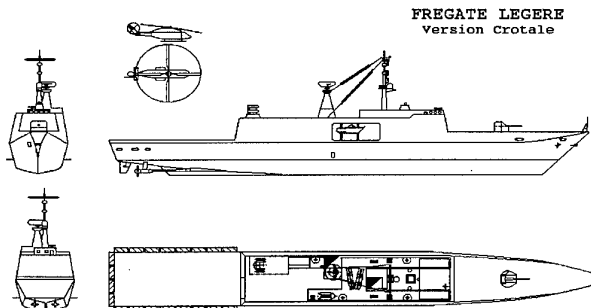
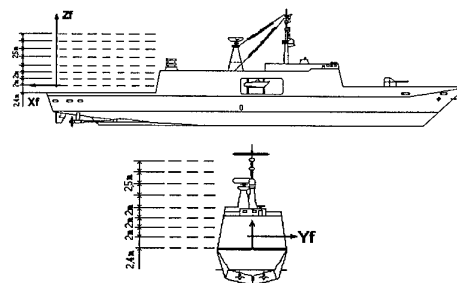
Figure 1: Frigate La Fayette 1/50th model

Figure 2 : Test planes position

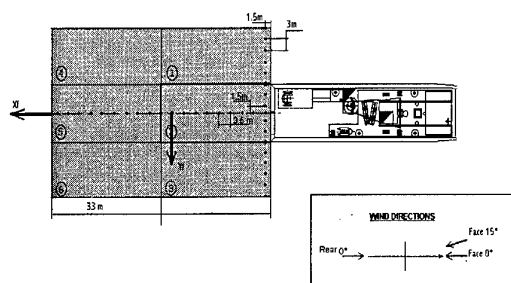


Figure 3 : Test points position

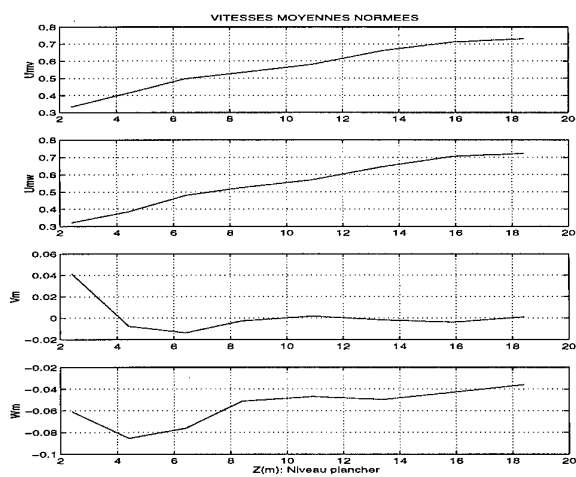
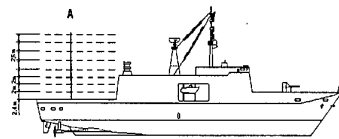
Test Configurations

- Fwd Wind 0° (50 and 25 kts) : Areas 1 to 6 22584 points
- Fwd Wind 15° (50 kts) : Areas 2, 3, 5 et 6 1824 points
- Rear Wind 0° (50 kts) : Area 1 et 1/2 Area 2 720 points

Planes height to the deck

2,4 m / 4,4 m / 6,4 m / 8,4 m / 10,9 m / 13,4 m / 15,9 m / 18,4 m

Figure 4 : Summary of test configurations

Figure 5 : Mean velocities evolution along the vertical axis on the deck centre (pt A) - Wind = 50 kts, $\beta = 0^\circ$ 

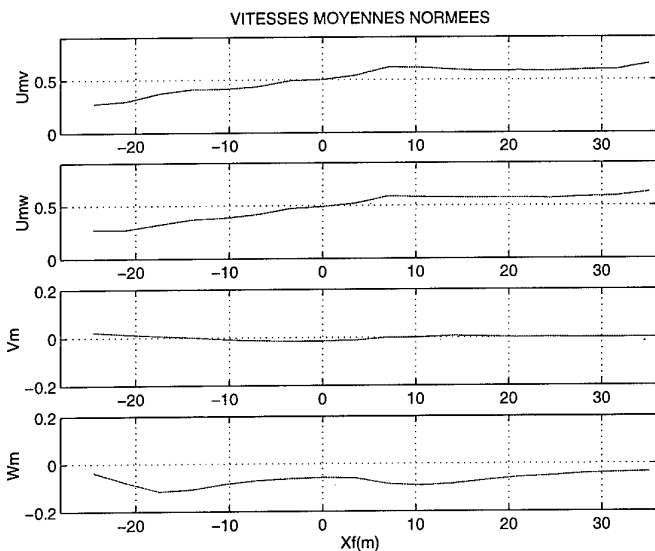


Figure 6 : Mean velocities evolution along the longitudinal axis on the deck centre line (height=4.4m)
Wind = 50 kts, $\beta = 0^\circ$

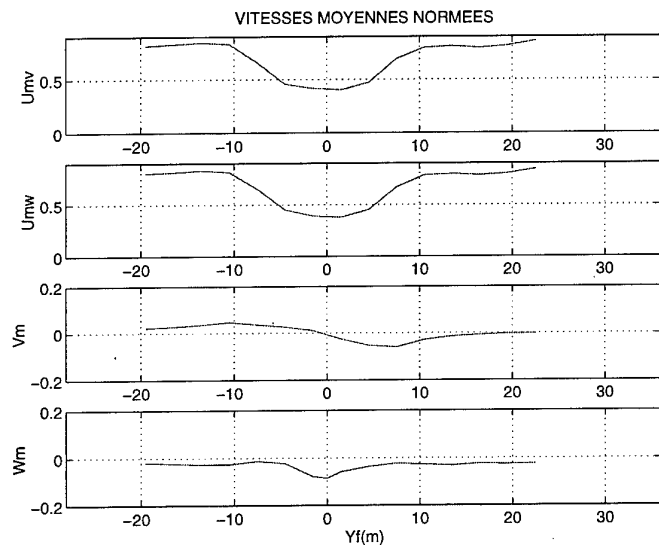
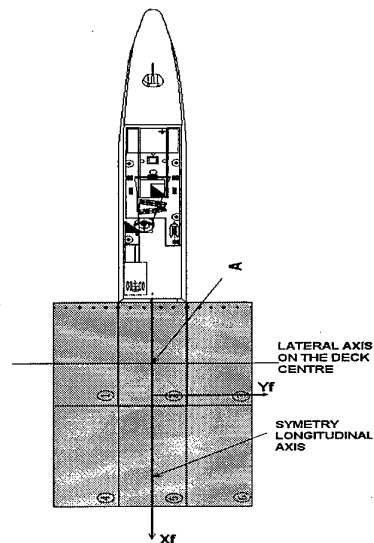


Figure 7 : Mean velocities evolution along the lateral axis on the deck centre
(pt A, height=4.4m)
Wind = 50 kts, $\beta = 0^\circ$

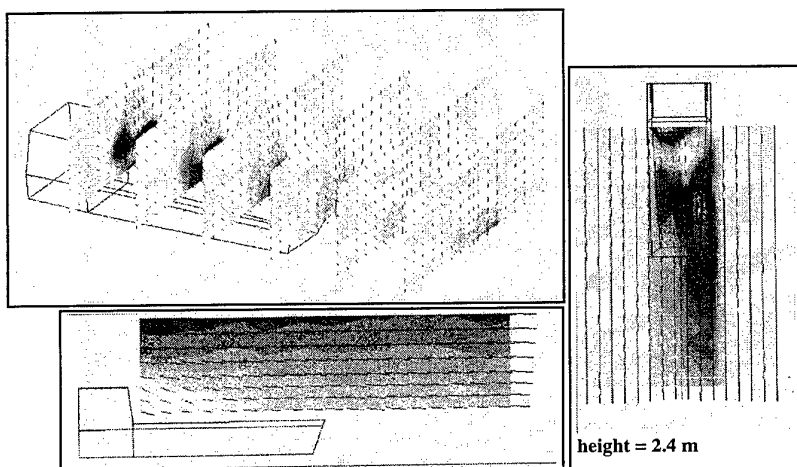


Figure 8 : 3D visualisation of tests at 50 kts ; $\beta = 0^\circ$

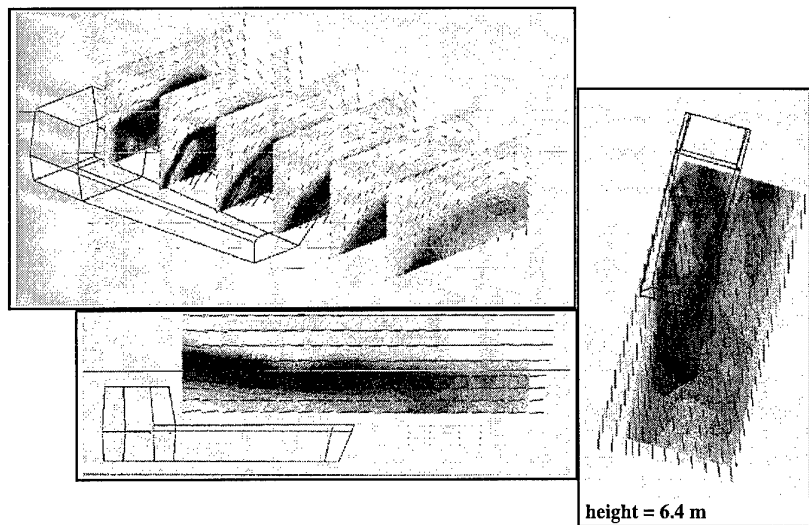


Figure 9 : 3D visualisation of tests at 50 kts ; $\beta = 15^\circ$

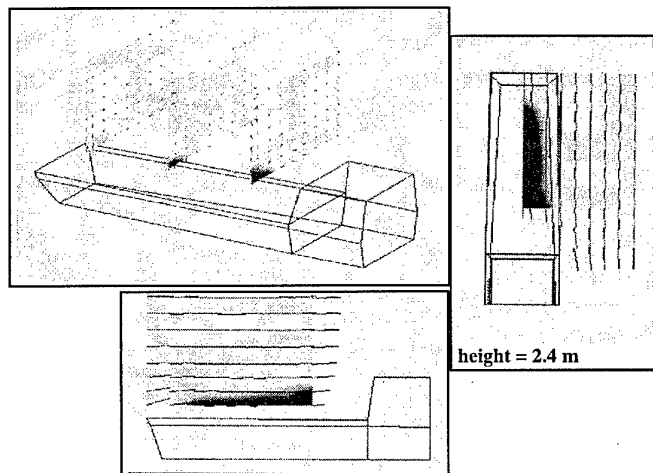


Figure 10 : 3D visualisation of tests at 50 kts ; $\beta = 180^\circ$

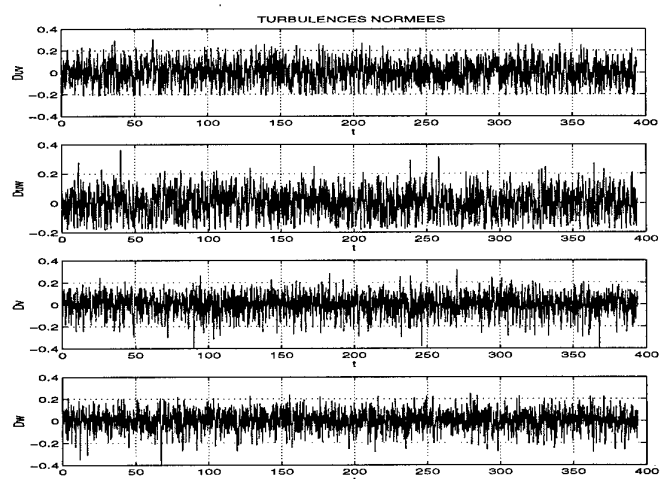


Figure 11 : Example of normalised velocity fluctuations, on the deck centre
Wind = 50 kts ; $\beta = 0^\circ$

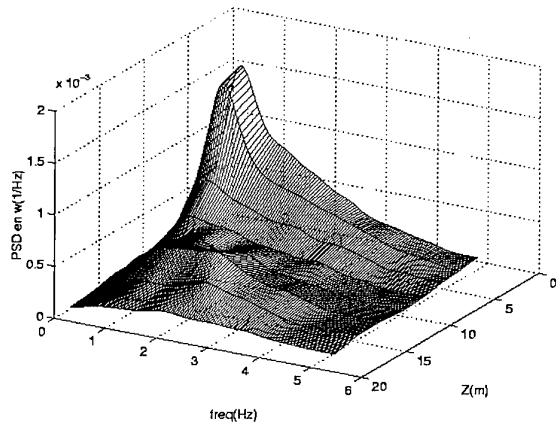


Figure 12 : Vertical velocity PSD evolution with altitude above the deck centre
Wind = 50 kts ; $\beta = 0^\circ$

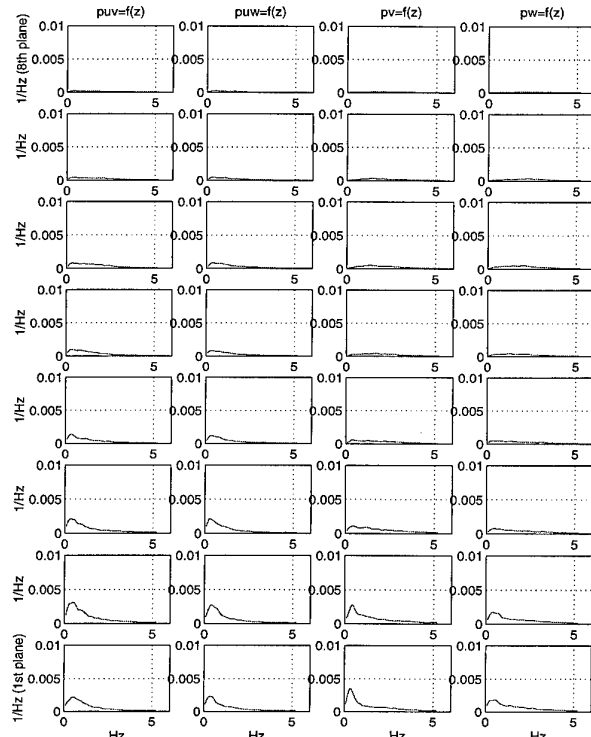


Figure 13 : u, v, w PSDs evolution above the deck centre
Wind = 50 kts ; $\beta = 0^\circ$

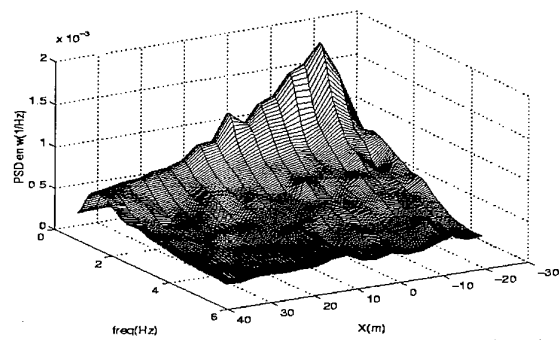


Figure 14 : Vertical velocity PSD evolution along the deck median axis
(height 2.4m) - Wind = 50 kts ; $\beta = 0^\circ$

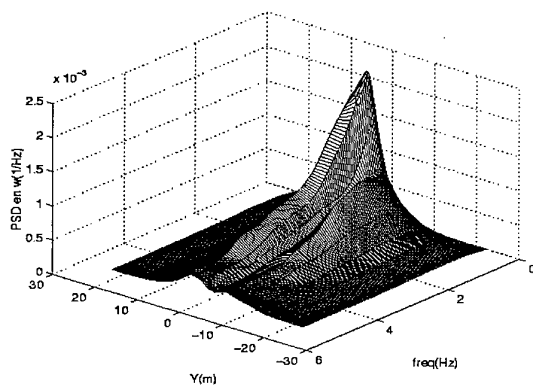
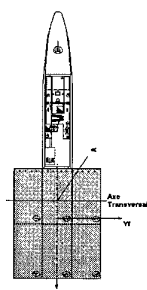


Figure 15 : Vertical velocity PSD evolution along the lateral axis on the
deck centre (height 2.4m) - Wind = 50 kts ; $\beta = 0^\circ$



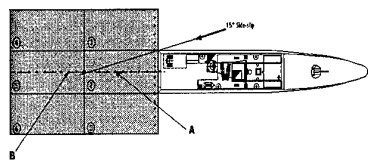


Figure 16 : Selected points for comparison of tests at
50 kt wind, $\beta = 0^\circ$ / 50 kt wind $\beta = 15^\circ$

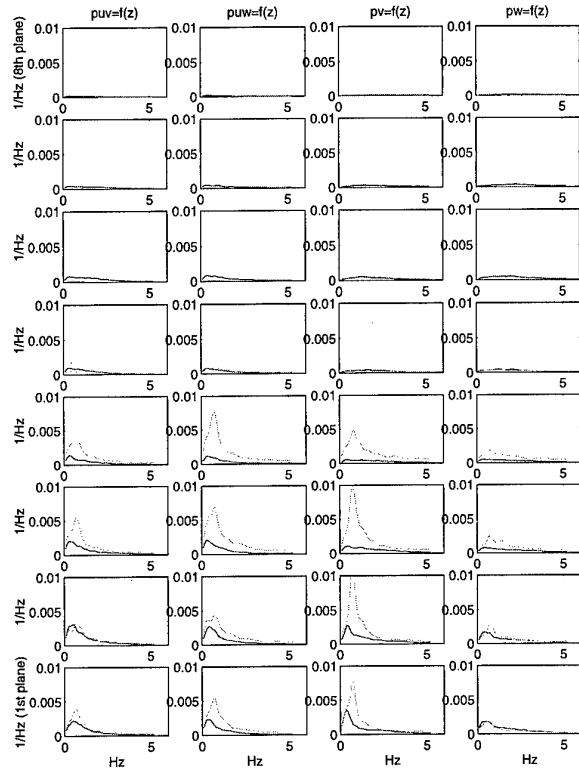


Figure 17 : Comparison of u, v, w PSDs evolution in altitude on the deck centre
(pt A), wind = 50 kts ; side-slip 0°/15°

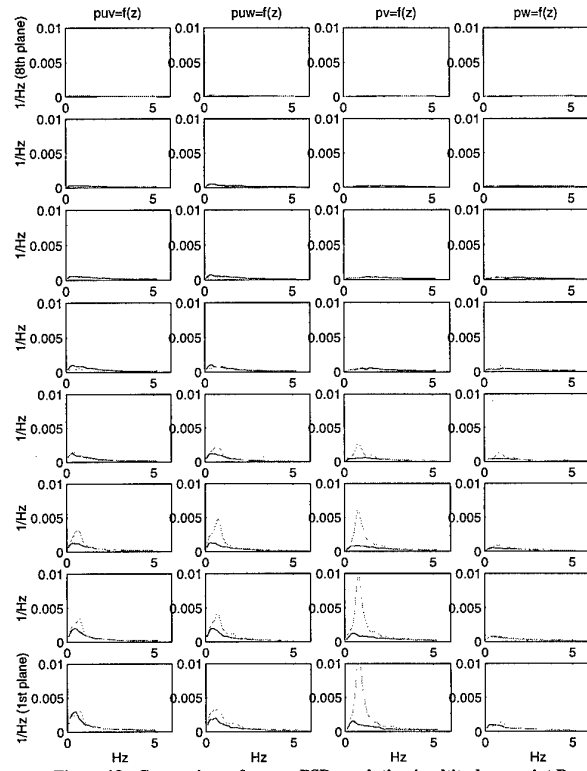


Figure 18 : Comparison of u, v, w PSDs evolution in altitude on point B
wind = 50 kts ; side-slip 0°/15°

— $\beta=0^\circ$
— $\beta=15^\circ$

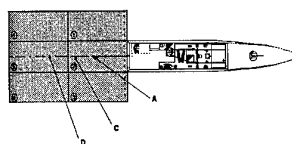


figure 19 : selected points for comparison of tests at 50 kts and
25 kts ($\beta=0^\circ$)

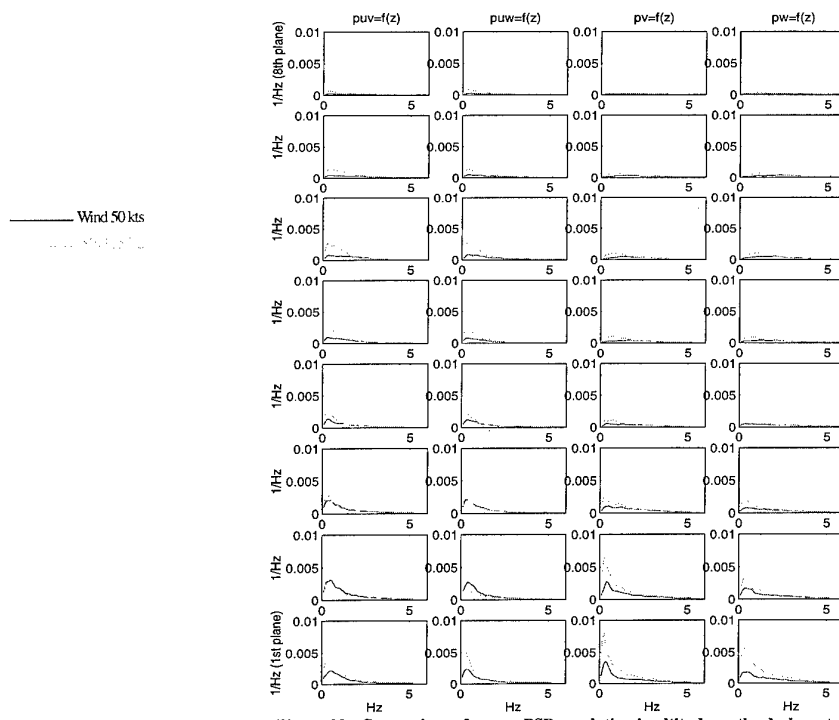


Figure 20 : Comparison of u, v, w PSDs evolution in altitude on the deck centre
(pt A)
wind = 50 kts and 25 kts ; side-slip 0°

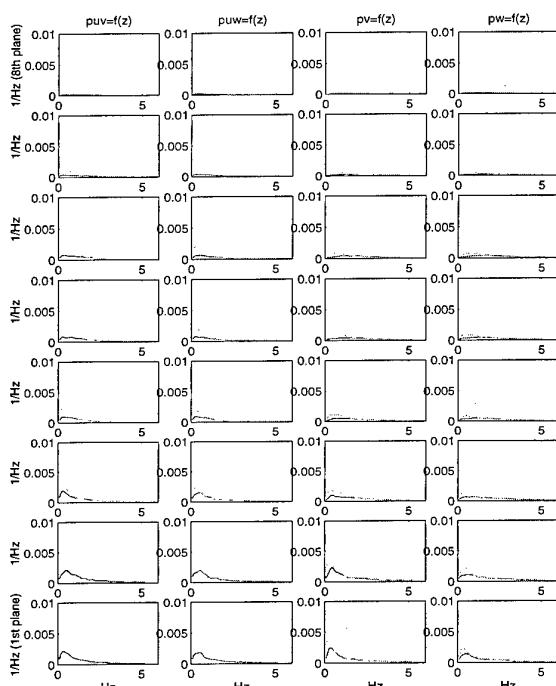


Figure 21 : Comparison of u, v, w PSDs evolution in altitude on point C
wind = 50 kts and 25 kts ; side-slip 0°

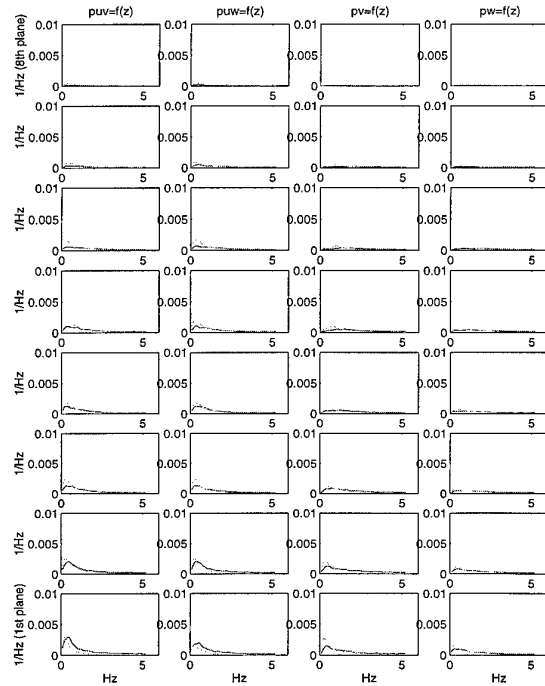


Figure 22 : Comparison of u, v, w PSDs evolution in altitude on point D
wind = 50 kts and 25 kts ; side-slip 0°

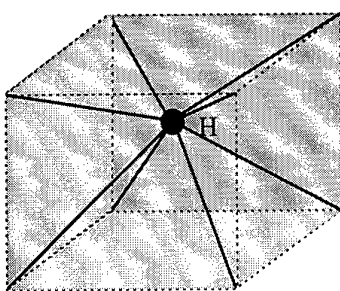


Figure 23 : Test area elementary parallelepiped

Objective :
Avoiding velocity discontinuity when entering the test area

Method :

- 1- Creation of a transition area.
- 2- Interpolation of air-wake mean velocity between the test area and infinite free stream.

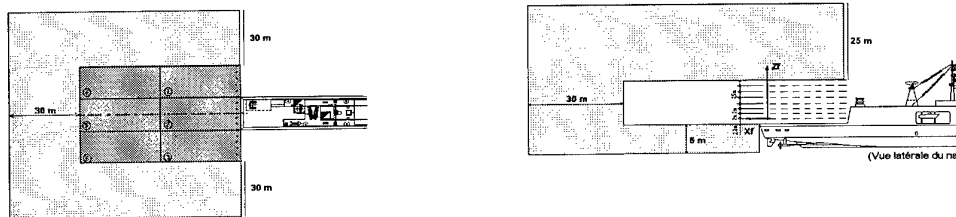


Figure 24 : Model limit conditions

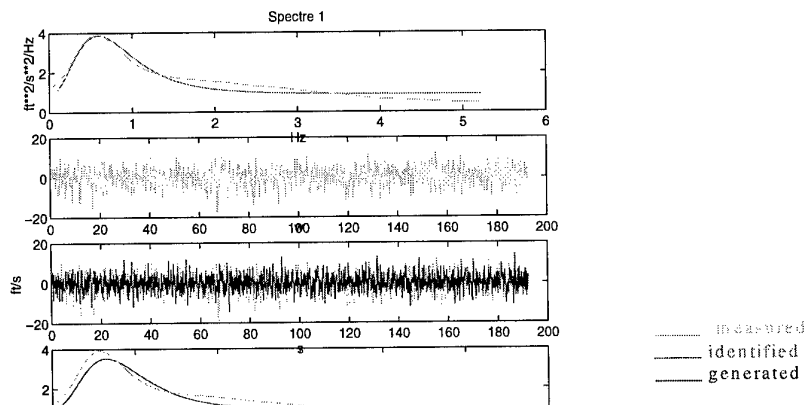


Figure 25 : Example of vertical velocity turbulence generation on the deck centre

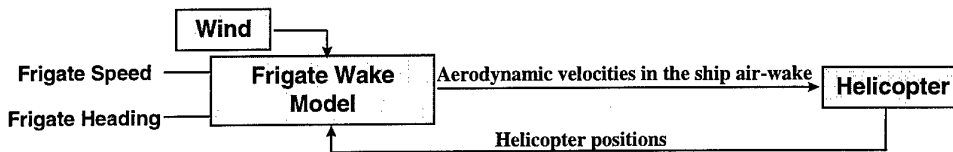


Figure 26 : Ship mean air-wake model implementation in HOST

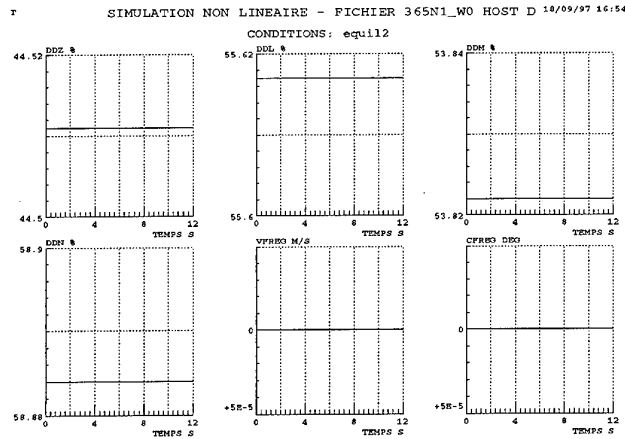


Figure 27 : HOST simulation - Helicopter commands
flight above the deck at 10 kts; slope angle = -1°
relative wind 50 kts ; $\beta = 0^\circ$; frigate still
(mean velocities and turbulence effect)

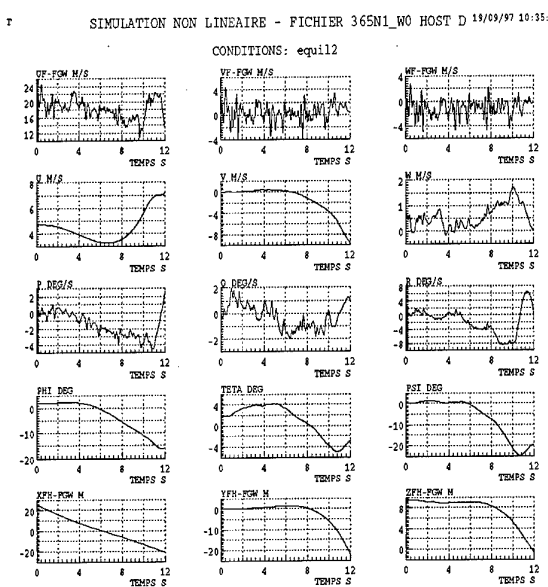


Figure 28 : HOST simulation - Helicopter parameters
flight above the deck at 10 kts; slope angle = -1°
relative wind 50 kts ; $\beta = 0^\circ$; frigate still
(mean velocities and turbulence effect)

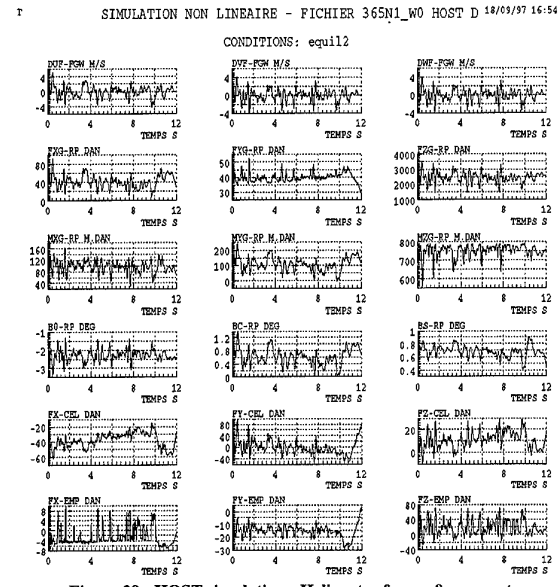


Figure 29 : HOST simulation - Helicopter forces & moments
flight above the deck at 10 kts; slope angle = -1°
relative wind 50 kts ; $\beta = 0^\circ$; frigate still
(mean velocities and turbulence effect)

SIMULATION NON LINÉAIRE - FICHIER 365N1_W0 HOST D 19/09/97 10:00:

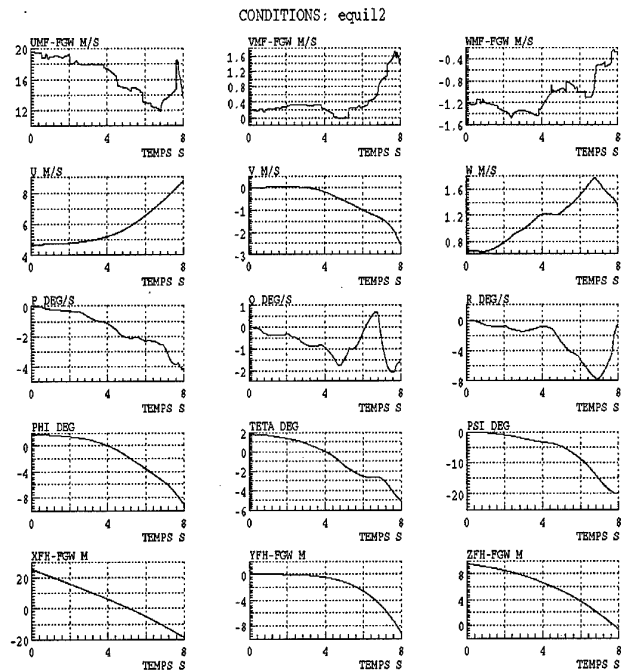


Figure 30 : HOST simulation - Helicopter parameters

flight above the deck at 10 kts; slope angle = -1°

relative wind 50 kts ; $\beta = 0^\circ$; frigate still
(mean velocities isolated effect)

SIMULATION NON LINÉAIRE - FICHIER 365N1_W0 HOST D 19/09/97 10:28:

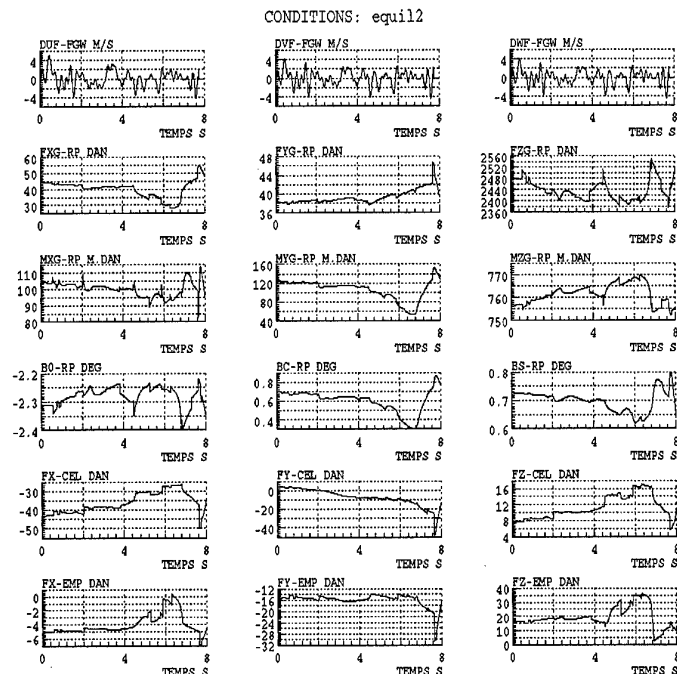


Figure 31 : HOST simulation - Helicopter forces & moments

flight above the deck at 10 kts; slope angle = -1°

relative wind 50 kts ; $\beta = 0^\circ$; frigate still
(mean velocities isolated effect)

ANALYSIS OF PATROL FRIGATE AIR WAKES

S.J. Zan, G.F. Syms, B.T. Cheney
 Aerodynamics Laboratory
 Institute for Aerospace Research
 National Research Council Canada
 Ottawa, Canada
 K1A 0R6

1. SUMMARY

The operation of helicopters from a ship-based platform is a challenging procedure from a pilot's perspective. In addition to manoeuvring near a moving platform, the pilot must respond to the complex, unsteady flow field which exists over the flight deck. The flow over the ship superstructure generates an air wake which contains significant spatial gradients in the mean wind velocities as well as increased turbulence levels; both may significantly alter the performance of an immersed helicopter rotor. To address this issue completely, one must deal with a fully-coupled problem including both the helicopter rotor and the ship air wake. However, as a first step, the ship air wake can be mapped out to estimate what inflow the rotor might experience.

A program is under way in the National Research Council of Canada Aerodynamics Laboratory (NRC/AL) to analyze the air wake formed behind the Halifax-Class Patrol Frigate (CPF). It contains an experimental component and a computational one. Using hot-film anemometers and the AL 5m Vertical Wind Tunnel, the experimental element maps out the flow field (14x13x16 matrix) in the vicinity of the flight deck of a 1:50 scale CPF model at 0° yaw and 12° yaw. The region measured included the boundaries of the recirculation zone that exists behind the hangar. An atmospheric boundary layer profile was created by placing a set of horizontal rods upstream of the model, which generated a properly scaled variation of mean velocity with height.

To complement this work, the flow field around a modified CPF was computed using a Navier-Stokes flow solver. This modification exists for these experiments only. No such modifications exist on the real ships. In order to facilitate grid generation, simplifications were made to the bridge and several of the smaller structures around the flight deck were removed. A structured, multi-block, pressure-based Navier-Stokes flow solver was used to compute the steady-state flow field. The atmospheric boundary layer was included in the numerical simulation. This modified ship geometry was also placed in the wind tunnel for validation of the numerical solutions.

The results of the wind tunnel experiments show the recirculation zone behind the hangar as well as the asymmetries in the flow field caused by the 20mm Phalanx CIWS found on the starboard roof of the hangar. The numerical results agree favourably with the modified CPF experimental results and give further details of the air wake.

2. INTRODUCTION

The launching of helicopters from and recovery of helicopters onto small, so-called "non-aviation" ships presents considerable challenges to a pilot. The operational envelope for such manoeuvres (known as ship-helicopter operating limits or SHOLs) is almost always reduced when compared to the normal operating envelope for the helicopter. Reductions to the operational envelope arise for a number of reasons, some of which are: inadequate yaw control, engine-torque limitations, a reduction in usable cue environment thus requiring changes in helicopter attitude, increased turbulence

and decreased mean wind velocities in the lee of the ship superstructure, and large-amplitude ship motion. Many of these limitations are due, in whole or in part, to the air wake, the region of complex flow around the ship superstructure. Air wakes, such as that in the lee of a ship superstructure are characterized as complex, unsteady flow fields containing recirculation regions, "flapping" shear layers, strong vortical flows and turbulence with length scales of the order of helicopter rotor diameter.

Inadequate yaw control will occur when the flow through the tail rotor is reduced because of the air wake. Torque limitations can become important when the pilot is attempting to track large vertical deck motions in high sea-states and as the rotor translates toward the flight deck on the final descent. In the latter case the rotor is immersed in the reduced-momentum flow of the air wake thereby causing a decrease in thrust and requiring the pilot to initiate a corresponding increase in rotor collective. A reduction in the usable cue environment can occur because sea spray is obscuring the pilot's vision, or because the existing windshields on the helicopter do not permit adequate viewing of the flight deck during the final stages of landing. In the latter case, the pilot may choose to pitch, bank or yaw the helicopter in order to improve the visual cueing. Such changes in helicopter attitude can result in changes to the stability and control characteristics of the helicopter when compared to the same attitude away from a ship because of the non-uniformity of the air wake. Increased turbulence arising from separated and/or vortical flow in the lee of the superstructure will effect time-varying changes in rotor output and be sensed by the pilot's inertial cueing system. These motion cues are likely to occur over a frequency bandwidth wherein the pilot will attempt corrective action (McRuer, 1994). The air wake turbulence, characterized by intensities and length scales, will correlate with the pilot's "aerodynamic workload." That is, as turbulence increases, the effort required to maintain trim at a fixed location over the flight deck will be increased. Large-amplitude ship motion, which gives rise to increased difficulty in tracking the flight deck prior to landing, is caused by the response of the ship to excitation from the wave spectrum. It is evident that of the above-discussed factors leading to reduced SHOLs, many are due to the influence of the ship air wake. In the case of smaller non-aviation ships wherein the helicopter must land in close proximity to the ship superstructure, the air wake will assume a greater importance.

In the Canadian context, all at-sea helicopter landings are made on small ships. Over the past five years the Aerodynamics Laboratory of the Institute for Aerospace Research (IAR) has developed a collaborative program with the Air Vehicle Research Section of the Canadian Department of National Defence (DND) to investigate the air wake and rotor loads in and around the Canadian Patrol Frigate (CPF). This paper deals with the analysis and characterization of the air wakes and comments briefly on the effects on rotor loads.

Determination of air wake characteristics is not a trivial task. The current Canadian efforts are focussed on obtaining wind tunnel and computational fluid dynamics (CFD) data. There

exists some full-scale airwake data acquired from a CPF wind over deck survey (Kowal, 1991) and in this paper the current wind tunnel data is compared to those measurements where possible. This comparison is intended to "validate" the wind tunnel as a tool for airwake measurements. When acquiring air wake data, wind tunnels have the advantages of reduced cost and time, and a controlled environment when compared to at-sea trials. CFD offers an attractive option for producing air wake data, especially when simulation is the end-product of the air wake data. CFD results must also be validated. In the present context, CFD calculations were made on a "Modified" CPF configuration, since it is possible to include only limited structural details in a numerical model. To overcome a possible limitation with respect to validation of the CFD data, a second experimental configuration was wind tunnel tested, which had the identical geometry to the model used in the CFD calculations. As a by-product of this test plan, the air wake differences between the wind tunnel results for the two configurations can be examined to determine the sensitivity of the air wake to superstructure configuration changes.

3. EXPERIMENT DETAILS

A 1:50 scale model of the above-water form of the CPF was constructed from applicable drawings (see Figure 1b). Several of the smaller structures on the ship and ahead of the helicopter hangar such as missile launch installations, wire antennas, handrails, a small lattice radar-mast and 57mm cannon were not included in the model. From an aerodynamic point of view however, the air wake should still be highly representative of a fully-detailed CPF since individual wake signatures of small structures will blend into the flow field as one moves aft. Exhaust flows from the ship's funnel and mechanical units were also not included in the model.

In the second part of the experiment, modifications were made to the CPF wind tunnel model in order to match precisely the "Modified" CPF model (MCPF) used in the CFD analysis of the same problem. The structures modified/removed from the CPF model were: the 20mm Vulcan Phalanx CIWS from the starboard rear of the hangar roof; the aft fire control radar from the front of the hangar roof; the landing officer's shelter from the flight deck; and the large lattice radar-mast from atop the bridge. A minor modification was also effected to the bridge.

The CPF model was installed in the NRC-IAR Vertical Wind Tunnel. The 15' circular test section of the tunnel was modified with a test section insert to obtain a rectangular 10' x 7' open jet section with one solid wall representing the sea surface. The solid wall provided a flat, vertical surface on which to mount the ship model. A turbulent, graded sea boundary layer profile was generated by a grid structure inserted at the test section entrance. The boundary layer profile represented wind flow over rough water encountering the ship steaming into the wind. This boundary layer profile is representative only as, in reality, the wind profiles would vary according to the varying sea states and ship speeds.

For an experiment such as this one that is insensitive to Reynolds number effects and conducted in incompressible flow, the experimenter is free to choose any two of length, time and velocity scalings. With the length scaling chosen to be 1:50 as previously mentioned, and the time scaling chosen to be 10:1, the velocity scaling defaults to 1:5.

The wind tunnel velocity was held constant with a freestream velocity of 5 m/s. The wind tunnel freestream velocity

represented wind velocity relative to the ship at a height of 40.15m above sea level (ASL). This represents a wind speed of 20.6m/s(40 kts) relative to the ship at a height of 10 meters ASL. This height is consistent with the standard meteorological practice for a reference wind speed. However, for the purpose of this paper, the wind speed as measured at the ship's anemometer height of 24.5 meters ASL will be used as the reference wind speed. In practice, a ship at sea has only an anemometer with which to measure the relative wind speed. Thus, this experiment simulated a 46-knot wind, measured at 24.5 meters ASL, encountering the ship steaming at 10 knots into wind. The moving ship in this case would show 56 knots on the anemometer reading.

The Reynolds number for the full scale CPF is approximately 30×10^6 , based on the ship beam of 16.4 meters. The Reynolds number for the experiment was 107×10^3 , based on the ship beam of 0.328 meters. Although these are not equal, the model had sharp edges that reduced the sensitivity to Reynolds number effects. In addition, the Reynolds number is well in excess of the minimum 11×10^3 recommended for the wind tunnel modelling of ships (Healey, 1992).

Wind tunnel measurements were made of the longitudinal, lateral and vertical winds over the CPF helicopter flight deck. Approach wind directions of 0° (head wind) and 12° from starboard were investigated. The measurements were made with a TSI cross hot-film anemometer. A cross hot-film anemometer is capable of measuring flow in the nominal streamwise direction and in an orthogonal direction that is in the plane of the films. By rolling the probe axis 90° , the films are then sensitive to the second orthogonal direction. In addition, the data set that provides the second orthogonal direction also provides a redundant set of data for the streamwise flow component. For the film calibrations, the relationship between cooling velocity and output voltage was described by means of a least-squares fit to a quartic function. While the hot-film probe has good resolution and fast response, it cannot differentiate between forward and reversing flows. Thus, under conditions of reversing flow, such as in the near wake of the hangar, the longitudinal flow directions determined from the mean velocity components will be in error. In highly turbulent flows, the results yielded by the probe will show a lower than actual turbulence intensity and a higher than actual velocity component (Tutu and Chevray, 1975). Specifically, the errors associated with turbulence intensity values are small, being about 2% for turbulence intensity less than about 50% and reaching 12% at a turbulence intensity of 70% (Keffer, 1986).

Each measurement consisted of 2048 data samples acquired at a rate of 100 Hertz for each of the two hot-film sensors. The measured wind speeds were normalized by the reference wind speed, V_{anem} , as determined from the wind tunnel freestream. The turbulence intensity components are expressed as the root mean square values of the wind gusts divided by the local streamwise wind component. More explicitly, the data were reduced to the following non-dimensional quantities:

$\frac{U(x,y,z)}{V_{\text{anem}}}$	$\frac{V(x,y,z)}{V_{\text{anem}}}$	$\frac{W(x,y,z)}{V_{\text{anem}}}$
$\frac{u'(x,y,z)}{U(x,y,z)}$	$\frac{v'(x,y,z)}{U(x,y,z)}$	$\frac{w'(x,y,z)}{U(x,y,z)}$

where $U(x,y,z)$ is the local mean streamwise velocity
 $u'(x,y,z)$ is the local rms streamwise velocity
 $V(x,y,z)$ is the local mean lateral velocity
 $v'(x,y,z)$ is the local rms lateral velocity

$W(x,y,z)$ is the local mean vertical velocity
 $w'(x,y,z)$ is the local rms vertical velocity
and V_{anem} is the velocity of the relative wind at the anemometer height, 24.5 meters ASL.

The hot-film anemometer was installed on a traversing mechanism that was free to move in the vertical direction relative to the ship. In order to survey the air wake in three dimensions, the CPF model was moved laterally or longitudinally in the wind tunnel. The 14X x 13Y x 16Z matrix of surveyed points defines a full-scale rectangular volume measuring 41.3m x 41.9m x 14.5m, extending from 3.9m aft of the hangar and from 2.0m above the surface of the helideck.

4. CFD DETAILS

A CFD simulation will provide a more detailed picture of the flow around the frigate. However, to get such an answer using a reasonable amount of computing resources, the flow must be simplified by either simplifying the equations that are solved or the geometry being analysed. The choice made here was to simplify the CPF shape. As mentioned previously, a "Modified" CPF was designed in which smaller pieces were removed and the bridge shape was modified to introduce more 90° angles. The details of the geometry are found in Figure 1c.

The full-scale MCPF was studied using the commercially available software package CFD-ACE (CFDRC, 1998). The code is a finite volume, structured, multi-block Navier-Stokes flow solver using body-fitted coordinates. It is a pressure-based solver employing a SIMPLEC pressure-correction algorithm. The convective terms in the governing equations were discretised using a second-order accurate upwind scheme with a blending of first-order upwinding to maintain solver stability.

CFD-ACE offers a range of turbulence models. For this work, the k-ε model based on Launder and Spalding (Launder and Spalding, 1974) was used with wall functions. Previous work (Syms 1997) has shown that the k-ε model with wall functions will produce answers similar to those of the k-ω model integrated to the wall on simplified frigate shapes. Thus with a fair degree of confidence, the advantages of using wall functions can be realised. Grid spacing near solid boundaries was kept so that y^+ values ranged between 50 and 150.

The multi-block grid created for this geometry was "H"-topology based (Figure 2). Thirty-five blocks containing approximately 903,000 grid points were sufficient to model the MCPF. This could be considered a medium-size grid considering the complexity of the MCPF model. Further work is being carried out into refinement of this grid to address grid sensitivity issues.

The ship was considered to be stationary in a steady atmospheric boundary layer giving rise to a steady-state solution. Profiles in streamwise velocity and length scale (Figure 3) were based on a logarithmic profile (Simiu and Scanlan, 1986). The surface condition was taken to be an ocean with a wind velocity of 20m/s at 10 meters off the surface. These conditions generate a surface skin friction coefficient of 2.53×10^{-3} and a roughness length of 3.51×10^{-3} meters. The turbulent kinetic energy was set slightly higher ($6.51 \text{ m}^2/\text{s}^2$) than that in the referred to analysis ($3.26 \text{ m}^2/\text{s}^2$) to compensate for the lack of turbulence sustaining mechanisms in the CFD model which exist in the real atmosphere. These

profiles were applied to the upstream, side and top boundaries while the downstream boundary was treated as an "outlet" or constant pressure boundary. The upstream boundary was placed 3.9 ship lengths (L) ahead of the bow and the domain was 14.3 L long, 7.5 L wide and 3.7 L high.

5. RESULTS AND DISCUSSION

5.1 0° Yaw Wind Tunnel Data

The variation in streamwise velocity component in the vicinity of the flight deck as a function of location is presented in Figure 4. The origin of the coordinate system is the bull's eye on the flight deck as shown in Figure 1b. The figure depicts a classical bluff-body wake in that the momentum deficit is lessened as one moves downstream and the wake widens as it progresses downstream. For the slices closest to the hangar ($x < 0$), a cut-out is indicated reflecting a region of recirculating flow. Stationary hot-film data cannot be considered reliable here, and as demonstrated in Syms and Zan (1995), valid data can be obtained with a flying probe. The flying probe was not used here. Streamwise turbulence intensities of thirty-five percent or more are used to define the boundary between valid and suspect data. The asymmetry in the air wake due to the presence of the Phalanx gun located on the aft starboard corner of the hangar is evident. This asymmetry is lessened as x becomes more positive. In this and subsequent similar plots, the x -direction has been stretched to aid in visualization of the data.

The projection of the flow vectors onto planes normal to the free stream (Figure 4) depict the air wake directed inward over most of the flight deck, again reflecting the streamline deformation toward the region of low pressure behind the hangar. Once more, asymmetry about the ship centreline is evident. The starboard side exhibits far greater lateral velocities than does the port side. In fact, it is as though the downward vertical component of the port side is largely replaced by an inward lateral component on the starboard side. This said, the lateral component of velocity reportedly has the least effect on helicopter operations for the 0° wind direction.

A similar plot, but for the vertical velocity is presented in Figure 5. It is clear that the air wake is directed downward over most of the flight deck, reflecting the fact that the streamlines are bending toward the region of low pressure behind the hangar face. Again the asymmetry due to the Phalanx gun is evident. The fact that the air wake is angled downward suggests that as the rotor enters the air wake, a nose-down pitching moment will be generated and this is corroborated by pilot testimony. The results suggest flow angles of up to six degrees in the absence of rotor downwash.

Significant gradients exist in the time-averaged value of the streamwise and vertical air wake velocity components. As these gradients are manifested over distances of the order of a rotor diameter, it could be expected that the non-uniform inflow will have an effect on the helicopter trim.

The turbulence intensities for the streamwise and vertical velocities are shown in Figures 6 and 7 respectively. The levels of turbulence increase monotonically as one approaches the flight deck. Flow recirculation exists when turbulence intensities exceed about 35%. Even in the region outside the recirculation zone, the intensities are still a factor of two to three greater than that found in the atmosphere. Since the length scales are of the order of a rotor radius, the increased turbulence will no doubt contribute to pilot workload. Vertical turbulence intensities of up to 20% suggest local flow

angles approaching 30°. For a blade tip speed of 250 m/s in a 20 m/s wind, this suggests local blade angle of attack fluctuations of about 2.3°, enough to invoke significant changes in rotor thrust, pitching moment and rolling moment.

5.2 Wind Tunnel and Sea-Trial Data Comparison

For validation purposes, these wind tunnel data are compared to full-scale at-sea data taken on a CPF (Kowal, 1991) acquired using a standard three-component vane-type anemometer. The sea-trial data is more limited in that measurements were acquired at fewer locations. The sea-trial data were acquired for a period of 30 seconds, which is a practical limit in the situation, but probably an insufficient length of time to ensure the results are statistically significant for a stationary process. By way of contrast the wind tunnel data were averaged for a full-scale equivalent of 204.8 seconds (3 min 25 sec).

In order to facilitate comparison of wind tunnel data with the sea-trial data, the wind tunnel data were interpolated using a bi-linear interpolation algorithm to arrive at values for locations identical to those for the sea-trial data. The latter data were acquired at two heights above the flight deck, 5.5 and 9 meters, for the following (x,y) locations:

Table 1: Locations of Measurements for Sea-Trial Data		
Location (arbitrary number)	X (full-scale in meters)	Y (full scale in meters)
8	-6.5/-6.0	0.0/0.0
12	-1.2/-0.6	-5.5/-5.5
13	-1.2/-0.6	0.0/0.0
14	-1.2/-0.6	5.2/5.2
18	5.2/5.8	0.0/0.0

In the above table, the numbers preceding the slashes refer to the (x,y) location of the measurement at 5.5 meters above deck and the numbers following the slashes refer to the location of the measurement at 9 meters above deck. The offsets (.61m) are due to specific anemometer positions on the towers on which the anemometers were mounted.

The sea-trial results present data at two wind velocities, 20 knots and 30 knots, although no Reynolds number effects would be expected for this flow. The fact that different values were obtained for each of the velocities is probably indicative of the statistical uncertainty in the measurement and not of different air wake characteristics.

In addition to the difficulties associated with obtaining at-sea measurements, it is also accepted that the wind tunnel cannot duplicate faithfully all details of the actual CPF. In particular, effects of stack gas efflux are not modelled in the wind tunnel test, though this is not a difficult aspect to incorporate in an experiment.

Despite these limitations to the comparison of data sets, there is generally good agreement between the wind tunnel and sea-trial data. Eighty percent of the data points match at the 5.5 meter height while seventy percent match at the 9 meter height. Where the data is not an exact match, the wind tunnel data features consistent trends with the sea-trial data. For example, local U/V_{anem} velocities increase with height. There are also consistent trends in location; for example, the velocities at Location 12 are higher than at the other locations for both heights.

Figure 8 compares the normalized streamwise velocity components of the wind tunnel and at-sea data. There is some scatter in the sea-trial data, likely due to the short measuring times. The wind tunnel data falls within this scatter range for every location at the 5.5 meter height. The wind tunnel underestimated the streamwise components at three of the five 9 meter heights, but only by about 0.1 U/V_{anem} .

The lateral and vertical velocities, Figures 9 and 10, are considerably smaller and more difficult to measure in both cases than the streamwise component. Again, the wind tunnel data are in reasonable agreement. For these comparisons, the sea-trial data will be compromised by small changes in approach wind angle, while in the wind tunnel no such concerns arise. The consistent positive values for the normalized sea-trial lateral velocity data at 20 knots is almost certainly due to a "red" wind. This likelihood is further increased when one considers that the sea trial data was taken under conditions of a prevailing 20-knot wind. Therefore, one surmises, the 20-knot sea-trial data was achieved with a stationary ship facing into wind. Without forward water speed, the ship would be unable to maintain a heading for extended periods, being pushed off heading by both the wind and the waves. The 30-knot data would thus be achieved by steaming the ship at 10 knots into the prevailing wind, and allowing much greater control of alignment with the prevailing wind. Therefore, it is believed that the sea-trial 30-knot data would be more accurate than the 20-knot data.

For the vertical velocity component, there is again considerable scatter in the sea-trial data, reflecting the short averaging times. The wind tunnel data are consistent with the trends in the sea-trial data.

The turbulence intensities, Figure 11, are plotted as the horizontal resultant (i.e. UV) wind intensity normalized by the ship anemometer velocity. The data are presented in this way, as opposed to separating out the streamwise and lateral components, since the latter are unavailable for the sea-trial data. Every wind tunnel data point matches, or falls within 1% turbulence intensity, of one of the sea-trial data points.

On a point of clarification, the wind tunnel data for the 5.5 meter height at Location 8 was omitted in the air wake plots, Figures 4 and 5, due to high turbulence levels recorded in the hot-film measurement. However, the value is nevertheless presented here for comparison purposes. In non-reversing low turbulence flow, u'/U would be some value (<30%) and the statistical skew of the data measured by the cross-film anemometer would be near zero. The actual measured u'/U value at Location 8 is 47% and the statistical skew of the U/V_{anem} time history is 0.8. These values suggest a region that experiences intermittent flow reversal (Zan and Garry, 1994). Thus data at location 8 are marginal in terms of acceptance based on previously defined criteria. As previously explained, the result of such a flow condition on the interpreted data is to increase the mean velocity and decrease, by small amount, the turbulence intensity. Accepting the presence of error, the wind tunnel value should be used with caution. It can be noted, however, that by reducing the U/V_{anem} value at this location in compensation for the error, an even more favourable agreement might be obtained with the sea-trial data.

5.3 MCPF and CPF Air Wakes at 0° Yaw Comparison

The CPF and MCPF configurations were both tested in the wind tunnel. The MCPF, a symmetric model, generates a classic bluff-body air wake over the helideck. Streamlines follow downward and inward trajectories as described below.

The CPF air wake, however, is somewhat different. While the flow on the port side of the CPF centreline is akin to a classic bluff-body air wake, the flow on the starboard side of centreline is decidedly not. The CIWS generates a streamwise flow deficit, and associated turbulence, that extends 15m aft of the hangar until smoothing into the larger air wake structure. The flow on the starboard side possesses a greater lateral inward component than the port side. Further, the vertical flow above the port side of the helideck is almost completely deleted on the starboard side due to the presence of the CIWS. The presence of the CIWS is thus seen to cause a substantially different air wake structure over the helideck than might otherwise be expected. Another significant difference between the two air wakes is generated by the CPF large lattice radar mast. This mast contributes to a streamwise flow deficit, and associated turbulence, at the height of the mast and extends well beyond the stern of the ship. Other differences between the ship models were not seen to have appreciable impact on the airwake.

5.4 0° Yaw CFD Results

The results of a numerical simulation provide details of the flow around the complete MCPF geometry. Since changes were made to the bridge and all smaller add-ons were removed, analysing the flow ahead of the hangar would provide only a small amount of information pertinent to the study of the air wake. (It must be remembered that the changes to the bridge were assumed to have minimal impact on the flow over the flight deck). So, the present discussion focuses on the area behind the hangar.

Figure 12 shows the general character of the flow over the flight deck. The transparent surface marks the region of the recirculation zone (i.e. zero streamwise velocity). This surface shows that the flow re-attaches just aft of the centre of the flight deck. The black particle trace shows the outline and foot of the vertical horseshoe vortex standing in the recirculation zone behind the hangar. The remaining traces show the rather benign flow around and over the hangar onto the flight deck. The topology of this air wake is similar to wakes seen behind three-dimensional bluff bodies (Larousse, Montinuzzi and Tropea, 1991).

5.5 Wind Tunnel and CFD Data Comparison

The MCPF geometry was also examined in the wind tunnel for purposes of CFD validation. To facilitate comparison of the CFD to experimental data, the CFD results were interpolated onto the experimental grid. Figure 13 shows a comparison of the two sets of data. Displayed are a set of crossflow planes which are coloured according to the nondimensional streamwise velocity with the vectors representing the in-plane velocity components.

The first point to observe is that both flow fields show the same flow topology. There is a wake behind the funnel and recirculation zones behind the hangar and the stern of the ship. The major difference between the measured and computed velocities exists in the flow gradients; the CFD showing much higher gradients. In general, the experimental results show a much more diffusive flow. This results in the computed solution exhibiting higher values in each of the three velocity components. In particular, the streamwise component shows a larger value at the higher elevations. This is a consequence of the flow being energized by the front edge of the funnel and not being dissipated by the time it reaches the flight deck.

Although a reasonable agreement is obtained between the computed and measured data, a more comprehensive

experiment obtaining more detailed information (in particular about the size and shape of the recirculation zone) is required to further validate the CFD results.

5.6 12° Yaw Wind Tunnel Data

In order to assess the effects of a non-zero incident wind on the air wake, the CPF model was yawed 12° to port in the wind tunnel to effect a “green 12” wind. (Because of installation restrictions, the actual angle was 11.8°). The variation in the time-averaged non-dimensional U-component velocity is shown in the upper half of Figure 14. The U-component is defined with respect to the ship axes system and not the wind axes. The V-component, or lateral velocities (not shown) can be characterized in much the same way as for the U-component velocities, although the U-component velocity magnitudes are appreciably greater. Thus, the horizontal velocity contours are approximated by the U-component data presented. Again data are “blanked” where reversing flow is suspected.

While the predominant wake deficit is aligned with the free stream at higher elevations, the separation zone immediately aft of the hangar and closer in elevation to the flight deck is more closely aligned to the ship axis. This suggests the horizontal component of the air wake contains a gradient in direction as a function of vertical distance from the deck. For high wind speeds as the landing is effected, this type of flow could be expected to affect the thrust generated by the tail rotor and the yawing moment acting on the fuselage. The change in tail rotor output and fuselage moment will induce a yaw rotation of the helicopter, thereby requiring corrective action by the pilot. It would be expected that larger wind angles would result in larger gradients and vortical flows which would require a larger corrective input from the pilot. At some point a control limit would be reached, thereby defining one part of the SHOL. This is borne out in practice. The connection between air wake directional gradients and the SHOL limit is plausible, but remains a conjecture in the absence of experimental and/or numerical analysis.

The magnitudes of vertical velocity for the 12° yawed wind are depicted in the lower half of Figure 14. It is evident that the windward side of the deck experiences an upwash caused by the onset flow rising over the flight deck and probably rolling up into a tight vortex with a relatively shallow helix angle. Conversely, data for the leeward side of the flight deck indicates a downwash on this side as the streamlines curve toward the low pressure region aft of and beside the ship above the sea surface. These changes in direction of vertical flow with lateral position could lead to rapid changes in rotor-generated rolling moments as the pilot traverses from the lee side of the ship over the flight deck. However, SHOLs defined by cyclic-input limitations are uncommon, suggesting the rotor downwash dominates in this particular case.

6. CONCLUSIONS

This paper has examined the air wake of a CPF using several sources of information: wind tunnel measurements, full-scale sea-trial data and computational fluid dynamic simulation. From this investigation, the following conclusions can be drawn:

- Good correlation between wind tunnel data and full-scale sea-trial data has been demonstrated. Either could be used for CFD validation.

- The air wake is substantially affected by the addition of the Phalanx CIWS atop the starboard aft corner of the hangar.
- Based on examination of velocity and directional gradients in the air wake, inferences can be drawn about the qualitative effects on helicopter operations. Further study is required to quantitatively correlate air wake characteristics and helicopter operations.
- The current CFD solution produces a flow field with the correct topology but with higher velocity gradients indicating an under-diffusive flow in the numerical simulations.

7. REFERENCES

CFDRC (1998) "CFD-ACE Theory Manual" CFD Research Corporation, Huntsville, Alabama, 1998.

Healey, J.V. (1992) "Establishing a Database for Flight in the Wakes of Structures", *J. Aircraft*, v29n4, pp. 559-564, Jul-Aug 1992.

Keffer, James R. (1986) "Introduction to Hot-Wire Anemometry", Lecture 3: A Short Course on Hot-Wire and Laser-Doppler Anemometry, Department of Mechanical Engineering, University of Waterloo, Waterloo, Ontario May 1986.

Kowal, H.J. (1991) "Wind Over Deck Survey & CH-124A/CPF Flight Deck Qualification Trials", Flight Dynamics Technical Memorandum FD TM 91/05, Aerospace Engineering Test Establishment, Department of National Defence, Canada, December 1991.

Larousse, A., Montinuzzi, R. and Tropea C., (1991) "Flow Around Surface-Mounted, Three-Dimensional Obstacles," Proceedings 8th Symposium on Turbulent Shear Flows, Munich, FRG, 1991.

Lauder, B.E., and Spalding, D.B. (1974) "Computational Methods: Applied Mechanical Engineering", Volume 3, p269, 1974.

McRuer, D.T. (1994) "Interdisciplinary Interactions and Dynamic Systems Integration", *Int. J. Control*, v59, n1, pp3-12, 1994.

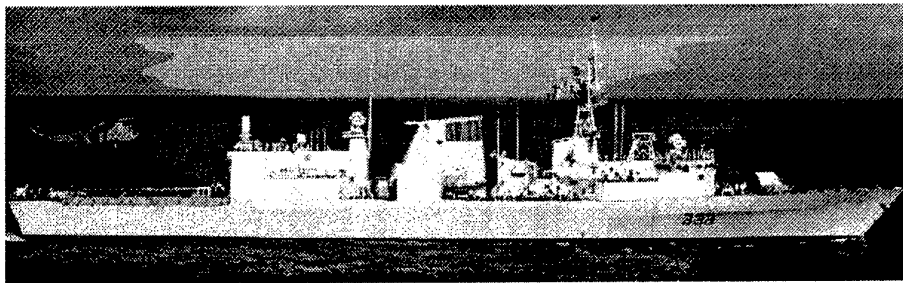
Simiu, E. and Scanlan, R.H. (1986) "Wind Effects on Structures", John Wiley & Sons, 1986.

Syms (1997) Unpublished work.

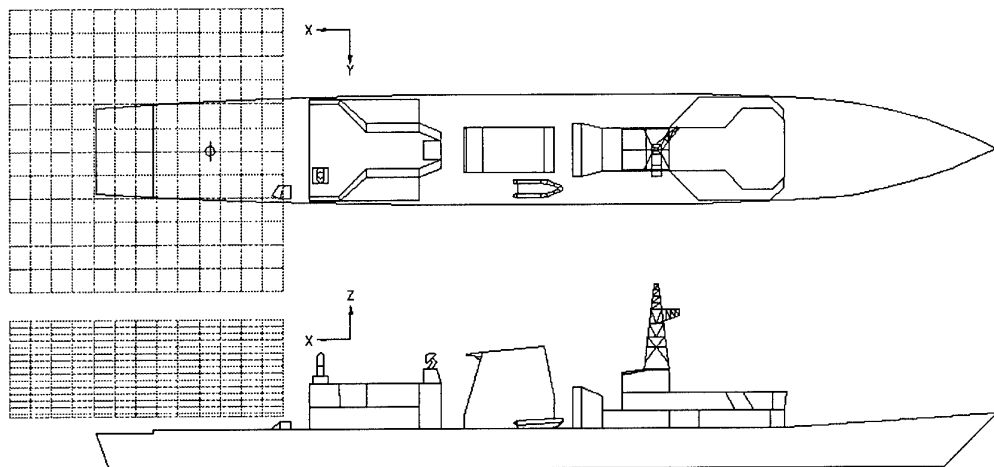
Syms, G.F. and Zan, S.J. (1995) "Analysis of Rotor Forces in a Ship Air Wake", AGARD-CP-552, Aerodynamics and Aeroacoustics of Rotorcraft, Paper 31, August 1995.

Tutu, N.K. and Chevray, R. (1975) "Cross-Wire Anemometry in High Turbulence Intensity", *J. Fluid Mech.*, v. 71 pp. 785-800, 1975.

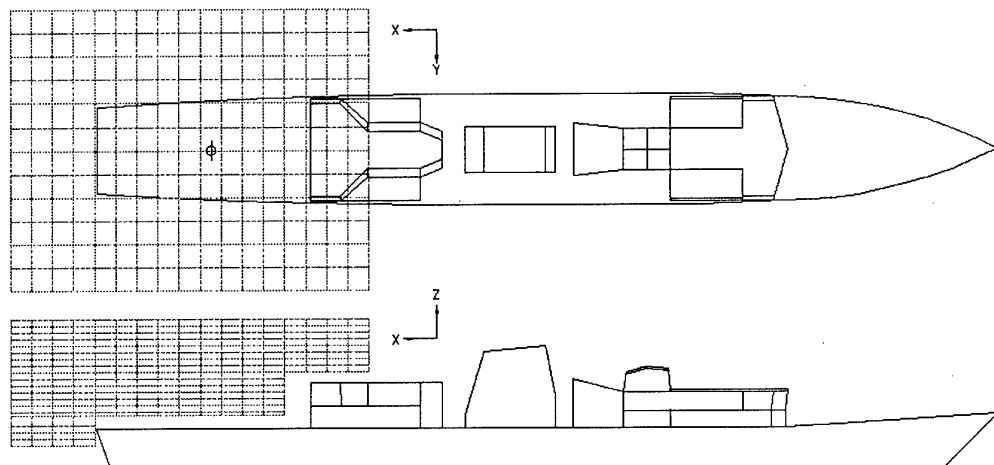
Zan, S.J. and Garry, E.A. (1994) "Wind Tunnel Measurements of the Air Wake Behind a Model of a Generic Frigate", National Research Council of Canada, Applied Aerodynamics Laboratory, Ottawa, Ontario, Canada NRC-LTR-AA-13, June 1994.



a) Canadian Patrol Frigate: HMCS Toronto (FFH 333)
Displacement: 5235 Tons Full Load
Dimensions: 135.5 x 16.4 x 6.15 meters



b) Canadian Patrol Frigate (CPF) Wind Tunnel Geometry



c) Modified Canadian Patrol Frigate (MCPF) Wind Tunnel and CFD Geometry

Figure 1: Wind Tunnel Models and Measured Air Wake Matrix

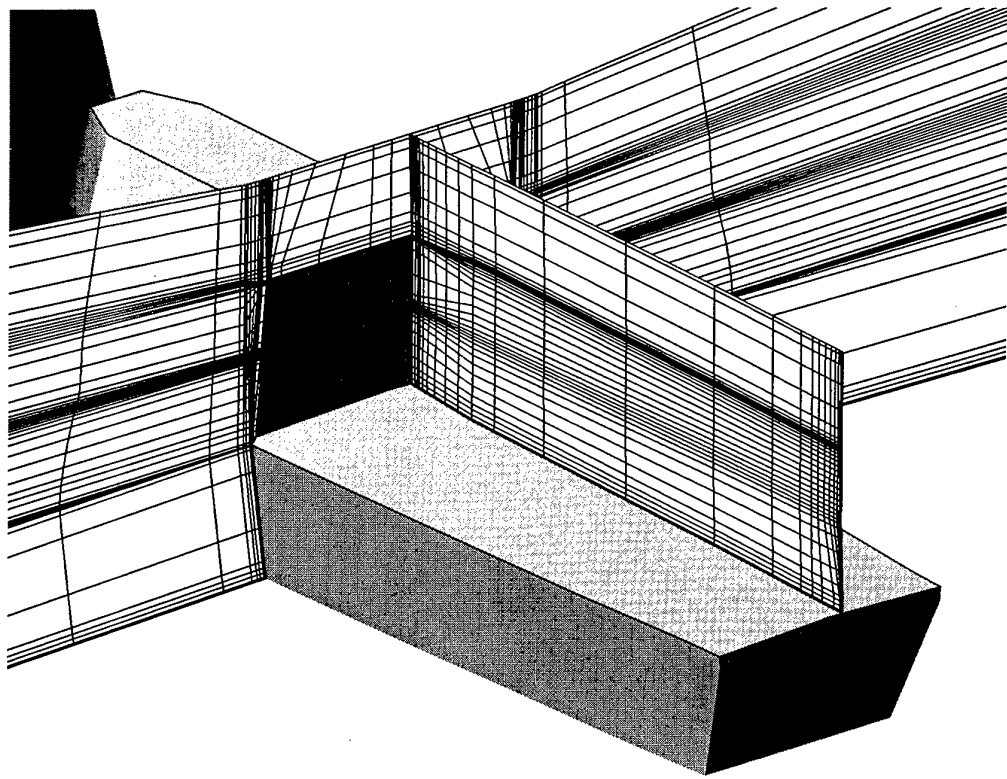


Figure 2: Sample portions of computational grid

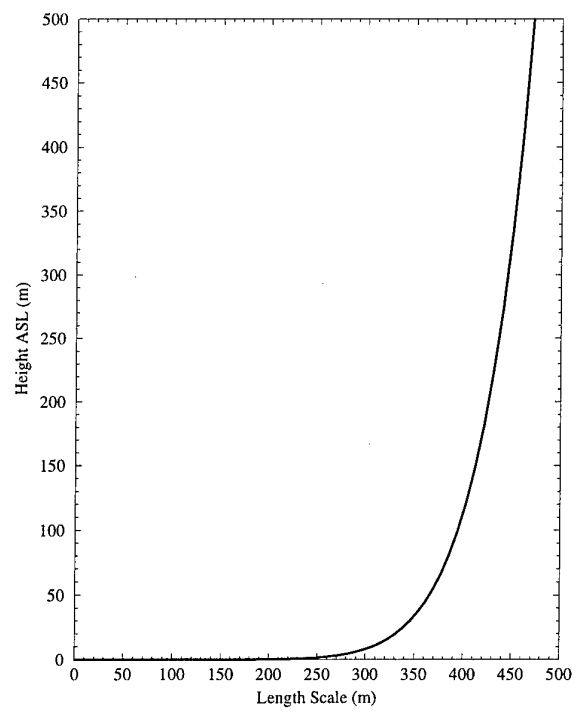
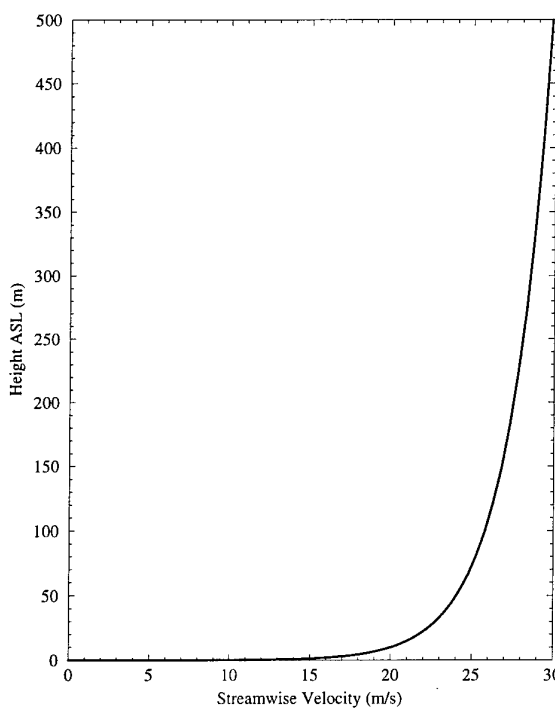


Figure 3: Numerical Boundary layer profile

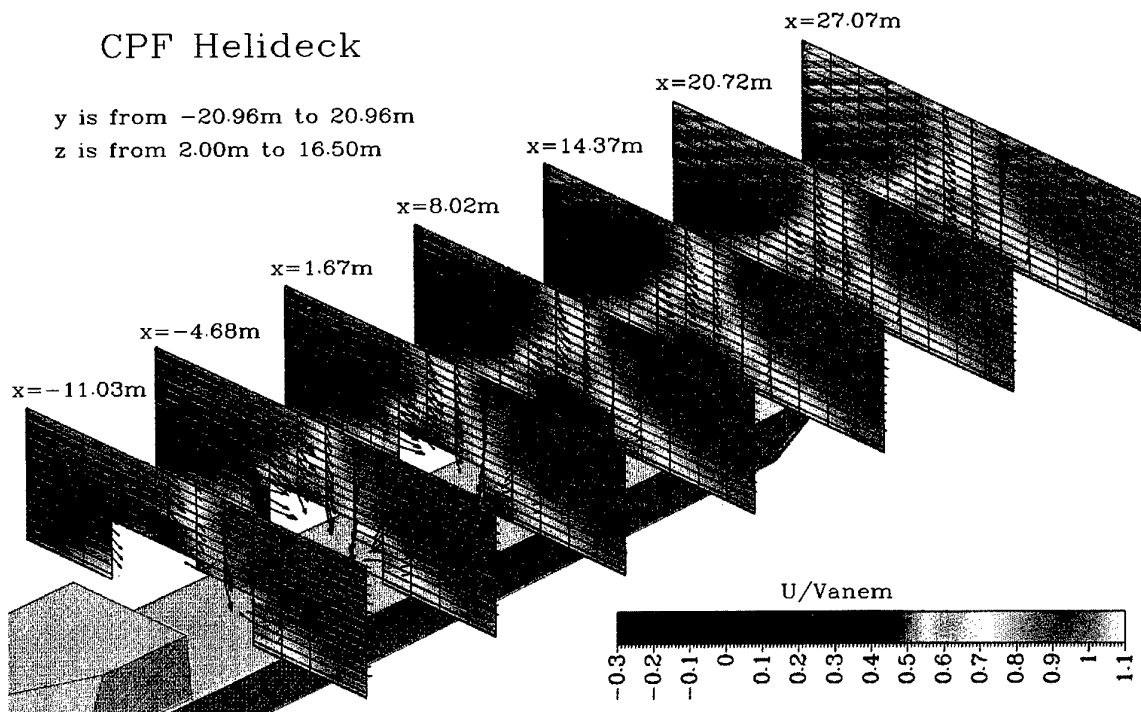


Figure 4: Variation of U/Vanem in YZ Planes
(Note: X dimension has been visually scaled by 2.5 for clarity)

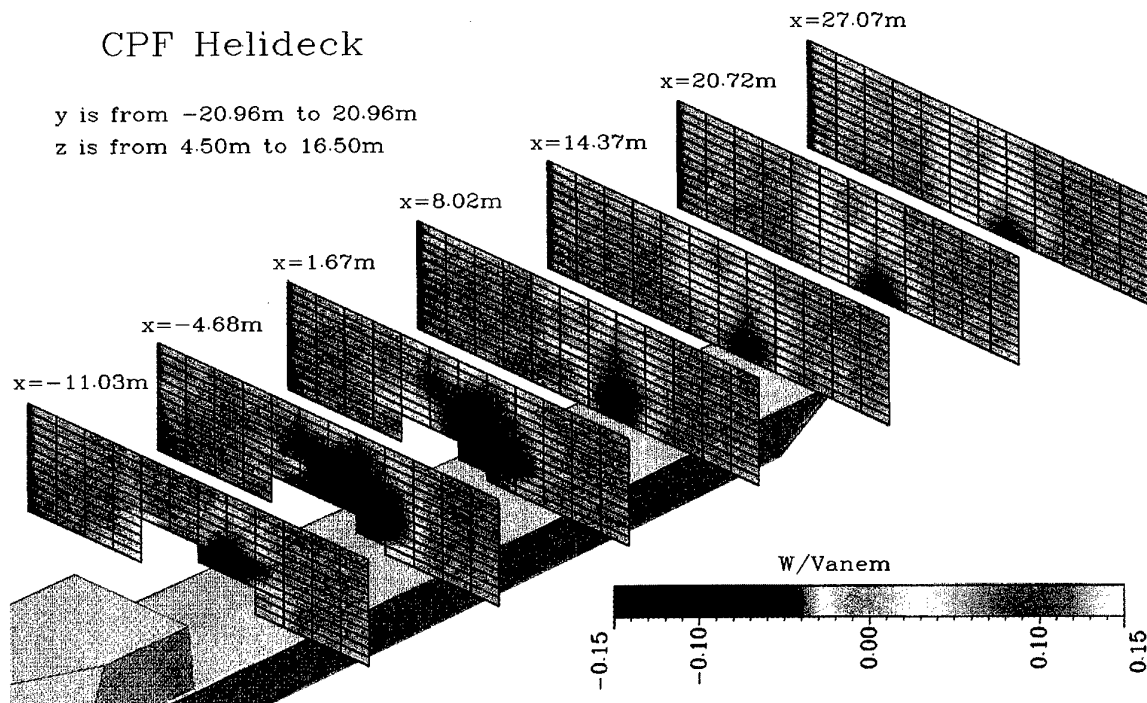


Figure 5: Variation of W/Vanem in YZ Planes
(Note: X dimension has been usually scaled by 2.5 for clarity)

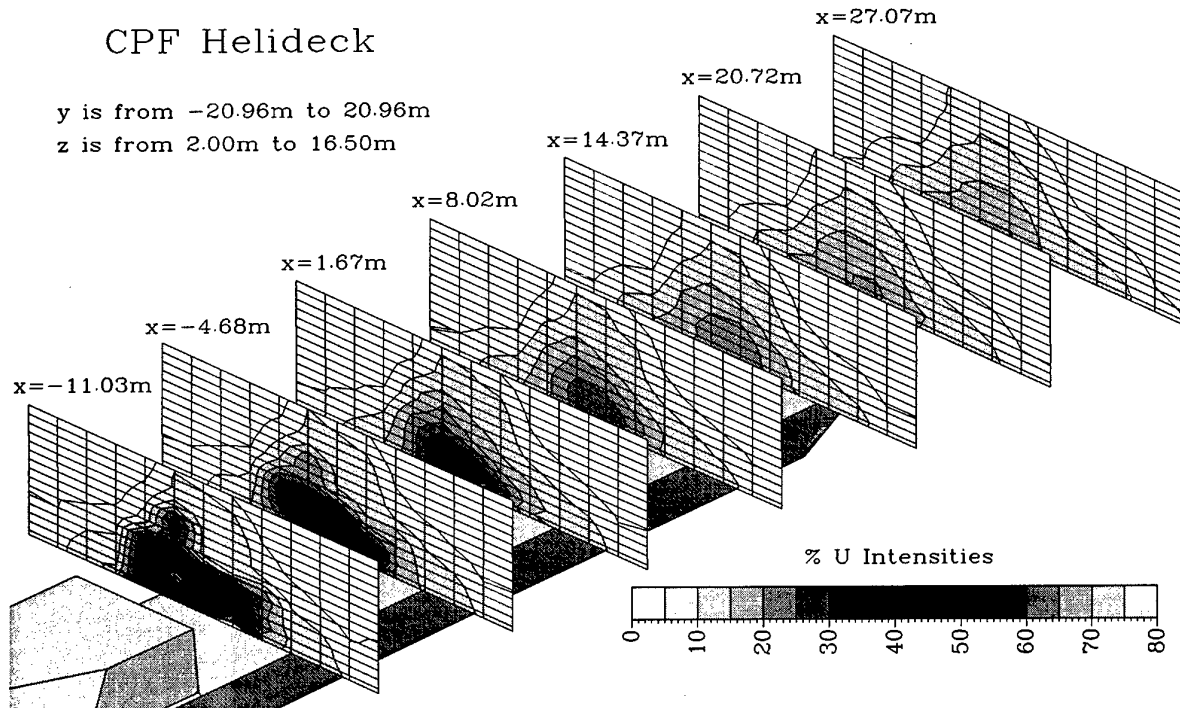


Figure 6: Variation of % U Intensities in YZ Planes
(Note: X dimension has been visually scaled by 2.5 for clarity)

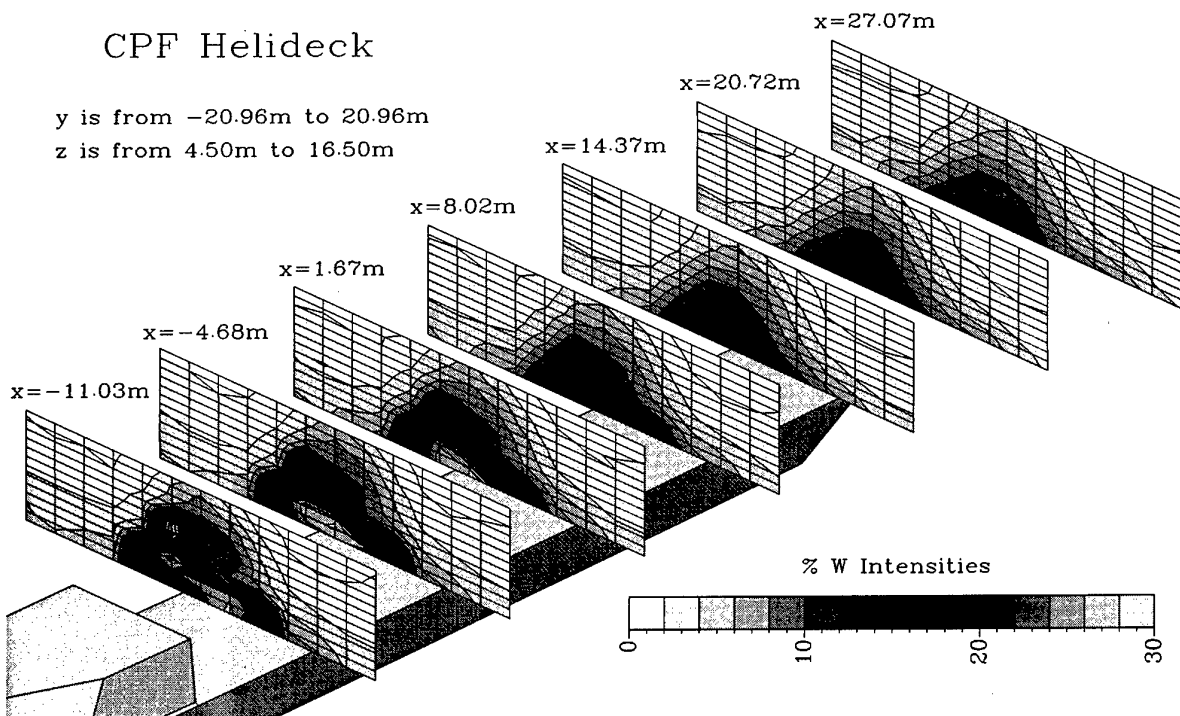
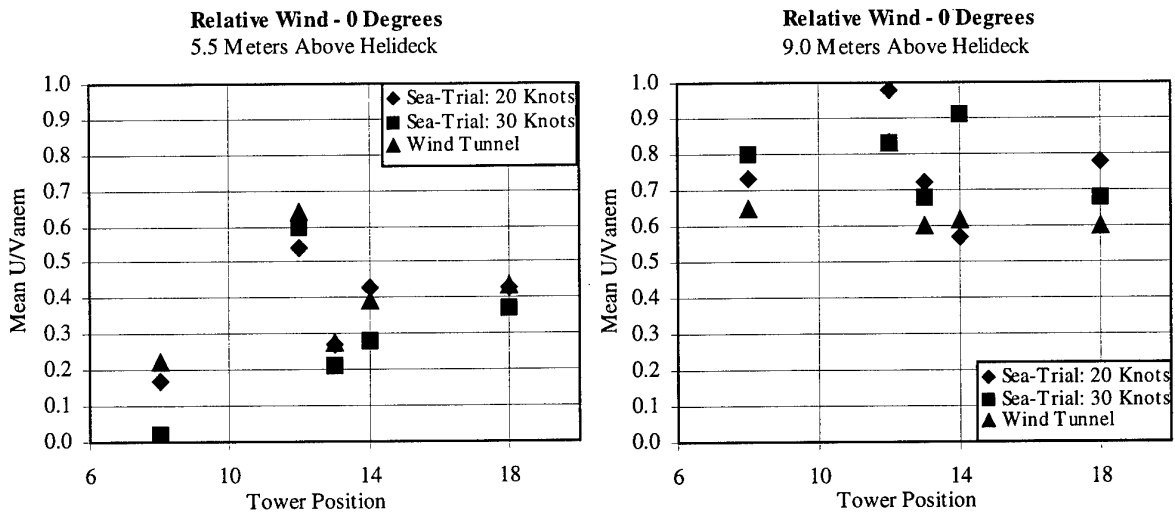
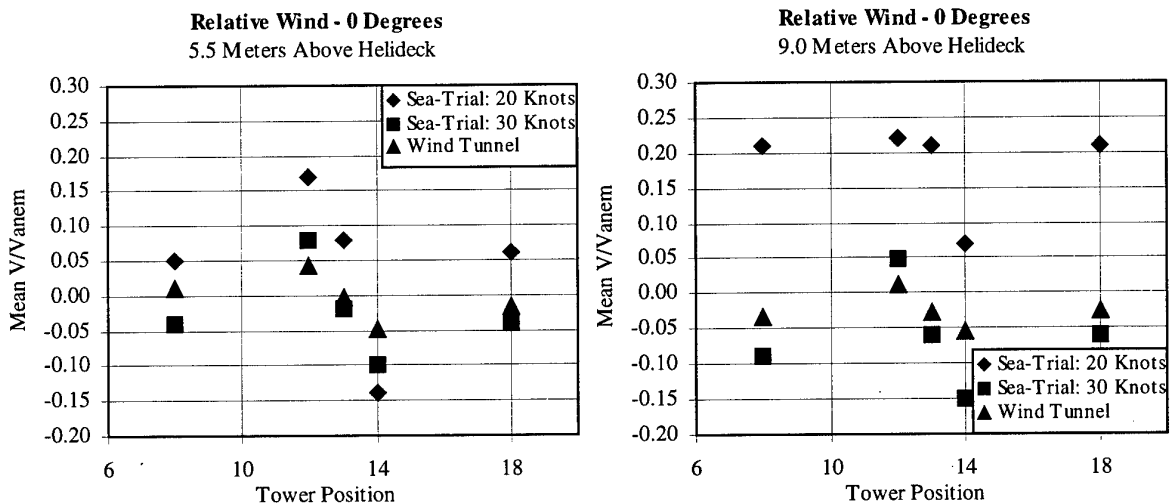
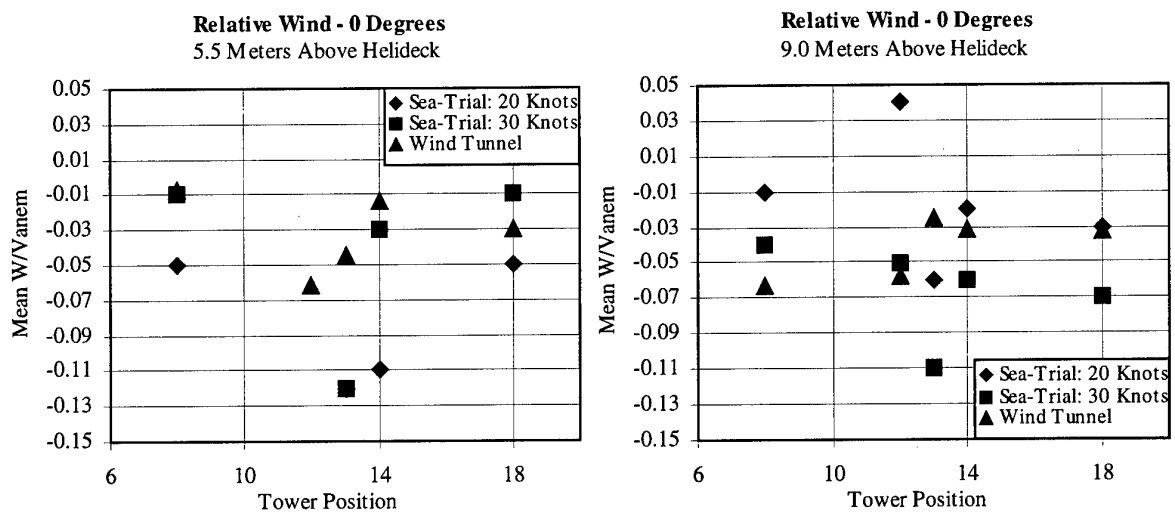


Figure 7: Variations in % W Intensities in YZ Planes
(Note: X dimension has been visually scaled by 2.5 for clarity)

Figure 8: Comparison of Wind Tunnel and Full-Scale U/V_{anem} VelocitiesFigure 9: Comparison of Wind Tunnel and Full-Scale V/V_{anem} VelocitiesFigure 10: Comparison of Wind Tunnel and Full-Scale W/V_{anem} Velocities

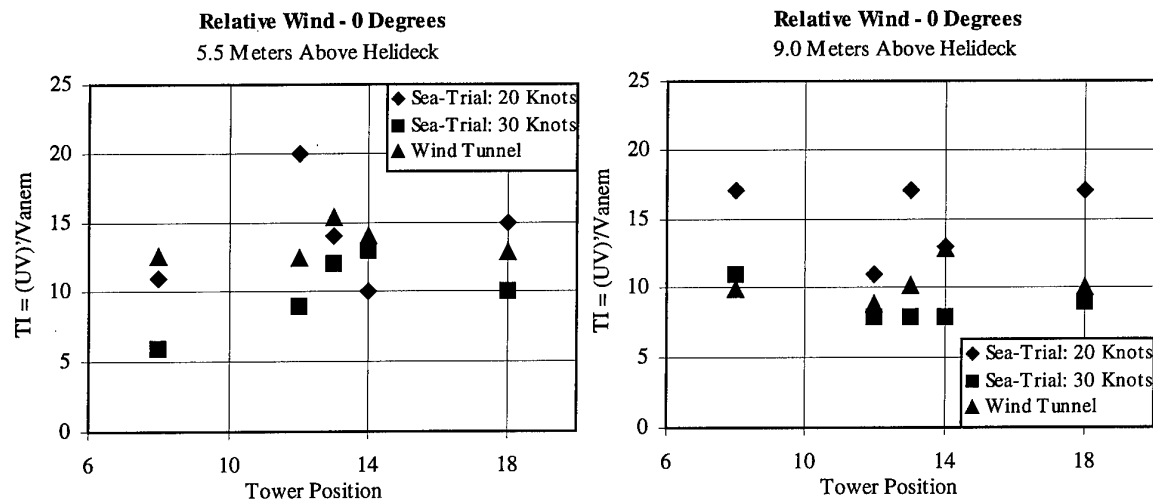


Figure 11: Comparison of Wind Tunnel and Full-Scale Turbulence Intensities

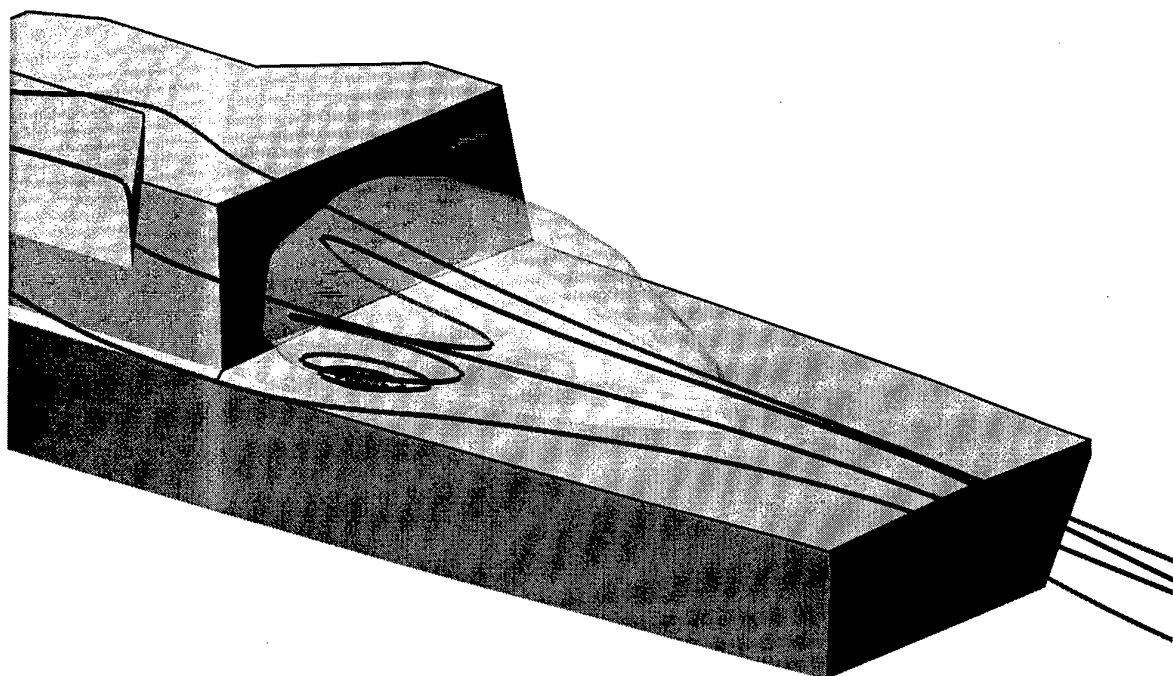


Figure 12: Boundary and Topology of Flight Deck Recirculation Zone

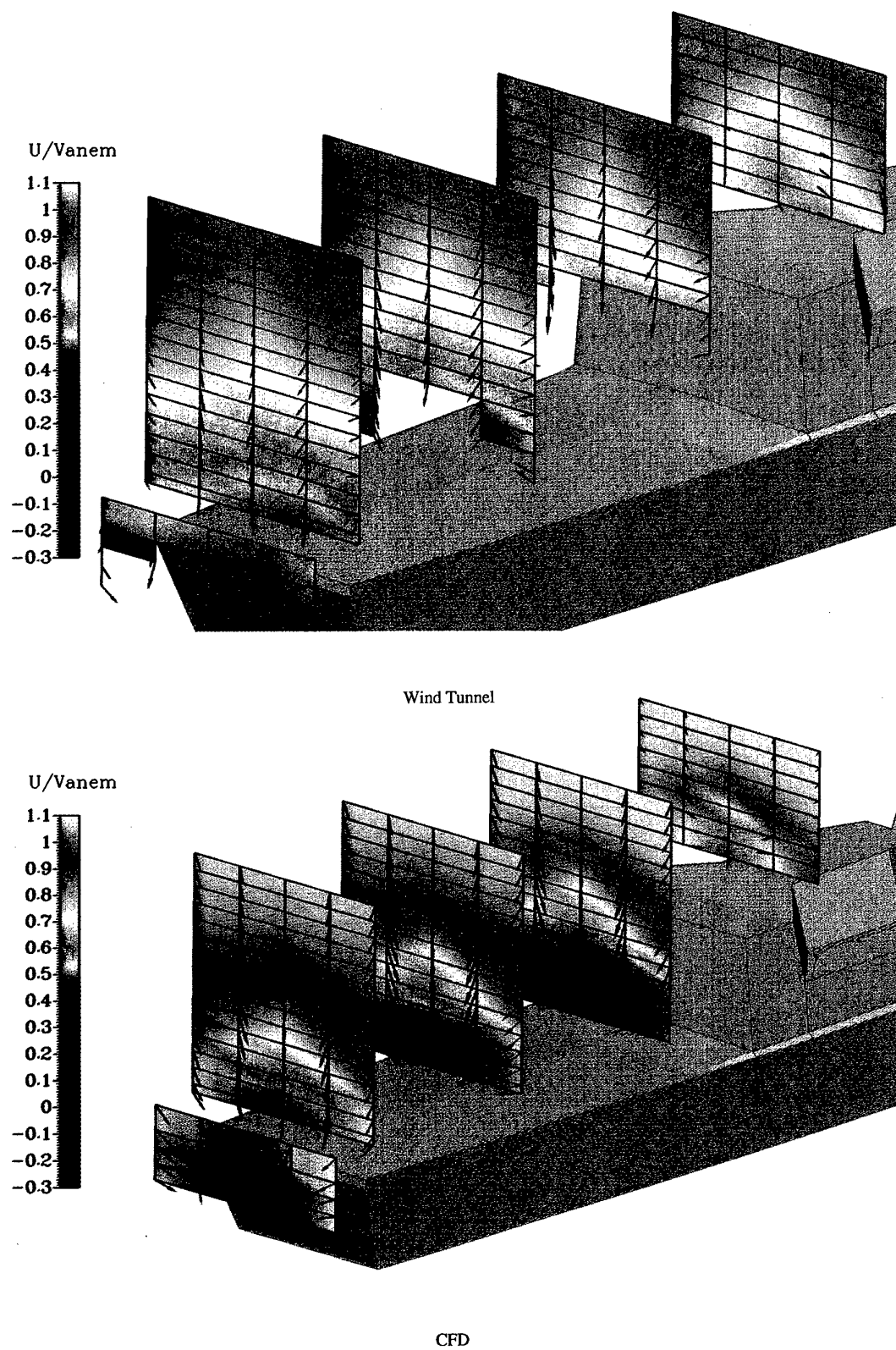


Figure 13: "Modified" CPF Wind Tunnel Results VS. CFD Solution

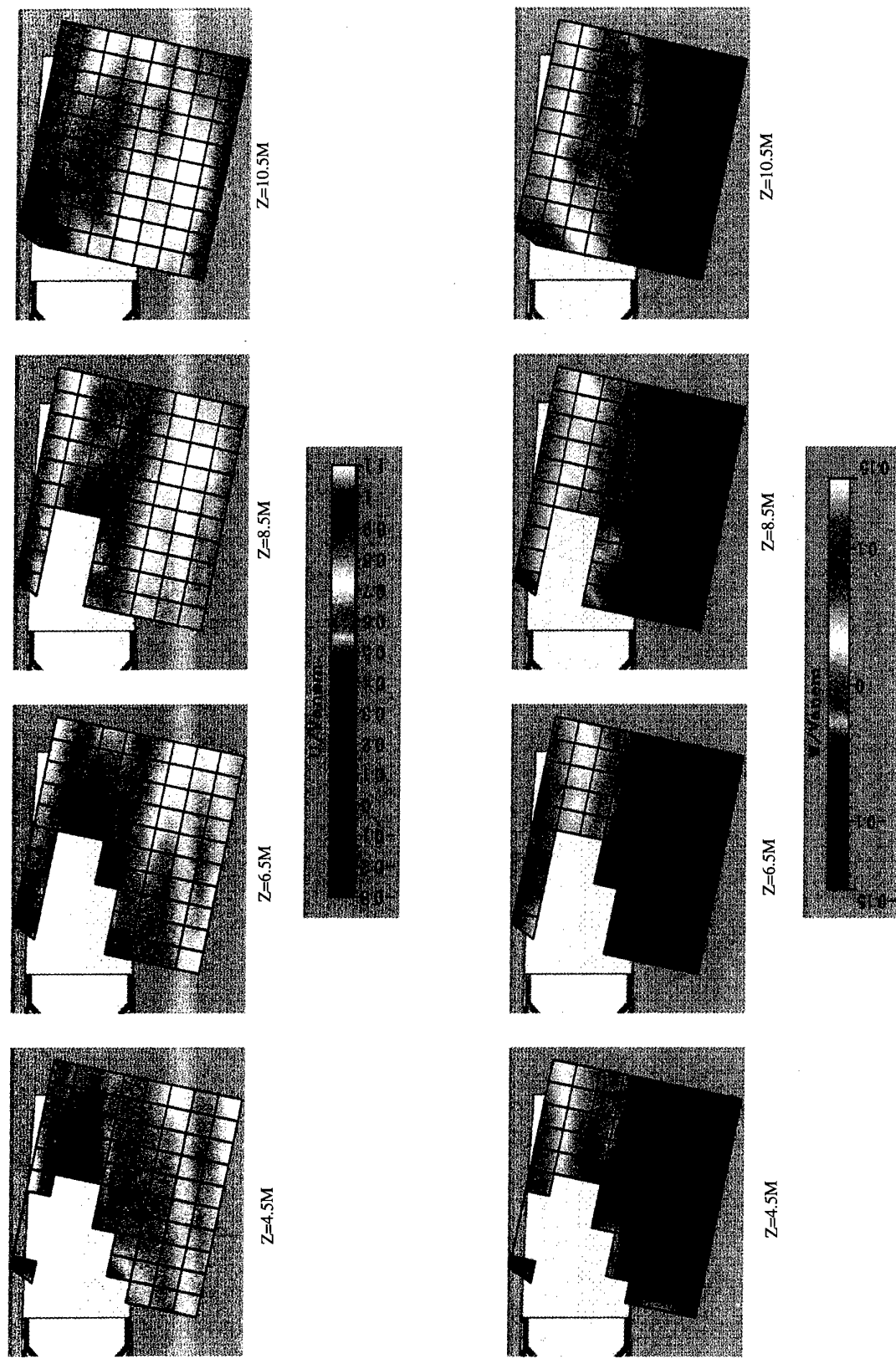


Figure 14: Effect of Streamwise and Lateral Position on U and W Velocities in $Z = \text{Planes} - \text{Ship Yawed } 12 \text{ Degrees to Port of Incident Wind}$

MODELLING AND SIMULATION OF SHIP AIR WAKES FOR HELICOPTER OPERATIONS – A COLLABORATIVE VENTURE

C H Wilkinson	S J Zan	N E Gilbert	J D Funk
Flight Management and Control Department, Defence Evaluation and Research Agency, Bedford, MK41 6AE, United Kingdom	Institute for Aerospace Research, National Research Council, Building M2, Ottawa, Ontario, K1A 0R6, Canada	Aeronautical and Maritime Research Laboratory, Defence Science and Technology Organisation, 506 Lorimer Street, Fishermens Bend, VIC 3207, Australia	Naval Air Warfare Center Aircraft Division, Flight Dynamics, Building 2187 MS #3, Patuxent River, Maryland, MD 20670, USA

1 SUMMARY

The development of simulation for application to the helicopter-ship dynamic interface has been an activity under an international collaborative panel of The Technical Co-operation Programme since 1990. Modelling the ship air wake and its effect on helicopter behaviour is regarded by the panel as one of the most significant technical challenges. Increasing the fidelity in this area can enhance the effectiveness of simulation in research, qualification and training, and open up opportunities to predict and correct for ‘troublespots’ in the design of new ships. A number of approaches are being pursued concurrently aimed at applying Computational Fluid Dynamics and other, more empirical, analyses to achieve a modelling capability. All participants in the collaboration are also actively involved with conducting full- and model-scale testing to gain an improved understanding of the key features of the air wake topology and to develop a validation database.

This paper details the collaborative efforts being pursued by the member nations, under the co-ordination of the authors. It summarises the work being conducted and draws together the various research aspects and validation tests. The aim is to present a comprehensive and co-ordinated approach to modelling and simulation of the air wake problem at the dynamic interface, putting into an operational context the more technical aspects to be discussed elsewhere in the Symposium. The paper demonstrates the applications of air wake prediction in ship and aircraft design, and the value of air wake simulation in research and training.

2 INTRODUCTION

2.1 Ship air wakes – the problem

Landing a helicopter on the flight deck of a moving ship is one of the most demanding of all piloting tasks. The difficulties are frequently compounded by low visibility obscuring the horizon and high sea states resulting in severe ship motion. At night the visual cues available to the pilot are degraded or lost altogether and lighting is often limited due to tactical

considerations. The pilot, however, is still expected to land on the deck within a tightly defined area without overstressing the undercarriage. The unsteady air wake generated by the ship as the wind flows over the superstructure exacerbates the problem still further and can impact severely on the operational availability of the helicopter. As the helicopter enters the ship air wake, the pilot is forced to compensate for disturbances, initially to the aircraft flight path, and finally to the position over the landing spot. Unexpected gusts may force the aircraft dangerously close to the flight deck and superstructure, or may move the helicopter away from the ship into a position where the pilot loses vital visual references. While the pilot is fighting to maintain accurate position, he has less spare capacity to consider his next move and the situation becomes unpredictable. In extreme wind conditions, the pilot may reach the limits of control authority with the result that there is insufficient manoeuvre power to compensate for the air wake disturbance.

2.2 Role of modelling and simulation

Clearly, the operators of maritime helicopters would aim for maximum aircraft availability and the ability to operate in the most severe environmental conditions. This is particularly true for the military, but an all-weather capability is also of prime importance to civilian operators, for example those serving off-shore oil installations. Modelling and simulation offers substantial opportunities to increase the operational availability of maritime helicopters through improved training, as well as the development of procedures, new technologies and qualification techniques. With simulation, control of the environment, including the air wake, sea state, light level and visibility, can be maintained with none of the flight safety issues associated with live flying. Piloted flight simulation enables aircrew training to be conducted safely and significantly reduces the requirement to dedicate costly ships or aircraft to this non-operational role, while off-line simulation can be used to test new ship designs for aircraft compatibility before the ship is built.

Modelling the ship air wake, and its effect on helicopter behaviour, is regarded as one of the most significant technical challenges for the dynamic interface (DI) simulation community. The irregular nature of a typical ship superstructure, the effect of ship motion and the influence of the helicopter rotor combine to produce a highly complex and dynamic flow field dominated by separations, vortical flows and recirculation. Validation of an air wake prediction is complicated by the difficulties associated with gathering quantitative measurements of the flow field around a ship, at full-scale or in a wind tunnel.

2.3 TTCP collaboration and involvement

The development of simulation for application to the helicopter-ship DI has been a collaborative activity under the auspices of The Technical Co-operation Programme (TTCP) since 1990. The working-level participants consist of representatives from the UK's Defence Evaluation and Research Agency (DERA), the National Research Council of Canada - Institute for Aerospace Research (NRC - IAR), the Naval Air Warfare Center (NAWC) in the USA and Australia's Defence Science and Technology Organisation (DSTO). The goals of the work are to progress the application of simulation to maritime helicopters in requirements capture, design, and test and evaluation with increased pace and effectiveness through collaboration. Within the group, the behaviour of helicopters operating in the vicinity of a ship is addressed under the topic, 'Ship air wake effects on rotor behaviour'. Through this topic, all participants have been actively involved with improving their air wake models, conducting full- and model-scale testing to gain an improved understanding of the key features of an air wake topology and to develop a validation database. A number of approaches are being pursued concurrently aimed at applying Computational Fluid Dynamics (CFD) and other, more empirical, analyses to achieve a predictive capability and to enhance piloted simulation. The high potential pay-off from shared learning has proved to be a strong motivation for the different nations to align activities where possible and to present and discuss the different facets of their work openly with other TTCP members.

2.3 Aims of the paper

This paper is intended to provide an overview of the air wake modelling activities within the TTCP collaboration. The paper details the collaborative efforts being pursued by the member nations, under the co-ordination of the authors. It summarises the work being conducted by each of the nations and draws together the various research aspects and validation tests. The aim is to present a comprehensive and co-ordinated approach to modelling and simulation of the air wake problem at the DI, putting into an operational context the more

technical aspects to be discussed elsewhere in the symposium. The paper demonstrates the applications of air wake prediction in ship-aircraft qualification, and the value of air wake simulation in research and training. The paper discusses the piloting problems associated with ship air wakes and the necessity for air wake modelling. Methods of air wake prediction are discussed and model validation issues are addressed.

3 OPERATIONAL PROBLEMS OF AIR WAKES

3.1 Effect on pilot workload and performance

When departing or returning to the ship, helicopter pilots need to consider the conditions that enable them to safely land on a moving deck. Although the size of the deck area varies considerably for different classes of ship, for ships such as destroyers and frigates the area is frequently not much larger than the helicopter. Pilots must often position the helicopter with sufficient accuracy to engage an aircraft-mounted probe in a ship-mounted capture mechanism, which may be as small as 2 metres². Significant factors affecting such operations include visibility (day, night, or degraded through poor weather conditions or spray), ship motion, and aerodynamic interactions of the helicopter with the turbulent air flow near the ship. These all contribute to pilot workload, which may not allow the pilot to safely take-off or land. Other factors limiting launch and recovery include exceeding torque and control limits; in certain wind conditions, the pilot may have insufficient control authority, in particular tail rotor authority in a crosswind, to maintain position relative to the ship.

3.2 Ship helicopter operating limits (SHOLs)

In order to assist pilots, maritime helicopter operators develop SHOLs to define safe operating parameters. These are usually represented in diagrammatic form, an example of which is at Figure 1. The wind speed and direction must be within the safe operating envelope shown on the diagram for the helicopter to land or take-off safely; if they are not, the ship may be forced to change course and speed to achieve a safe wind condition. SHOLs may also include structural limits of both ship and aircraft, as well as on deck limits to prevent toppling and sliding, with and without securing devices such as lashings or a ship-mounted capture system. However, these limits are not considered in this paper.

The proliferation of ship and helicopter type variations means that each individual country generally operates its own unique combination of ship and helicopter. There are no agreed international standards for SHOLs and each country usually determines their own. The development of these SHOLs is an expensive and exacting task currently determined through intensive and costly First of Class Flying Trials (FOCFTs), which limit

the final operational envelopes to environmental conditions similar to those encountered during the trials. The use of modelling and simulation to support SHOL development offers substantial benefits in terms of reduced costs, improved safety and potentially larger operating envelopes. Perhaps the most important component of such a simulation is a high fidelity air wake model that generates representative levels of workload in piloted simulation and allows aircraft control limits to be accurately predicted.

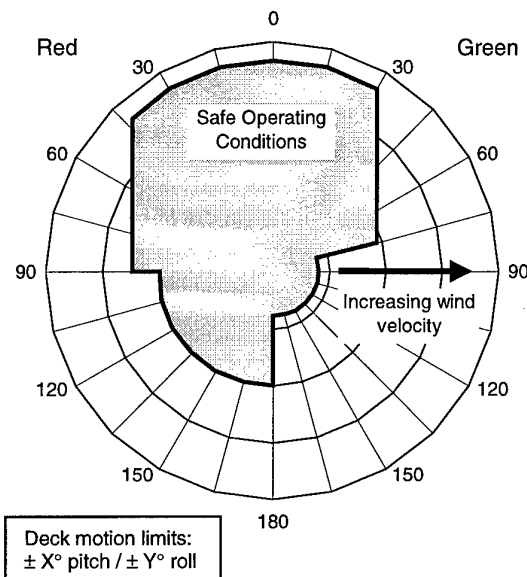


Figure 1; A typical SHOL

3.3 Simulation in support of deck landing training
Until recently, deck landing training has not been possible in a simulator due to insufficient fidelity, both visual and environmental, in the vicinity of the flight deck. The trainee pilot's first introduction to the hostile environment of the dynamic interface is when he first flies to the ship and, while his initial deck landings will be conducted under the watchful gaze of an instructor, he is unlikely to experience the most severe conditions until he is flying operationally. Recent advances in simulation technologies, coupled with an improved understanding of the dynamic characteristics of helicopters in this environment, have reached a stage where comprehensive aircrew training in helicopter-ship operations is now believed to be possible. This opens opportunities for the student to be exposed to the full range of operating conditions which he is likely to encounter before he ever joins a ship, with obvious advantages in terms of safety and cost.

In training, it is important that the student replicates the same control strategy in the simulator as in flight; failure to do so will negate the advantages of

simulator training and may, in extreme circumstances, prove dangerous. The air wake has an important part to play in deck landing training as it has a considerable impact on both workload and performance, which, in turn, will influence the control strategy adopted by the pilot. If the simulated air wake is more benign than in reality, a student may gain a false sense of security in the simulator, while, if the air wake is too severe, there is a danger that the pilot will lose confidence before he has even started. An air wake model of appropriate fidelity is, therefore, an essential element of a training simulation.

4 AIR WAKE MODELLING AND VALIDATION

4.1 Background

For the purposes of this paper, modelling refers to the use of numerical techniques to extract quantitative air wake characteristics and to provide numerical data for input to a simulator. Validation data refer to acquired air wake data, from either at-sea trials or in wind tunnel tests, which are used to provide benchmarks for the modelling.

The modelling of air wakes for high-fidelity simulation continues to present a substantial challenge. The nature of the air wake is such that there are sharp gradients in all three components of the mean flow velocity, as well as substantial levels of turbulence caused by separated shear layers and vortical flows. The flow field is further complicated by changes in the speed and direction of the approaching natural wind. In a simulation, appropriate values for the air wake must be generated at all required locations in real-time. Interpolation schemes are required to generate values for wind at locations not measured or calculated, and to account for changes in onset wind direction. The air wake is also affected by a moving ship, a fact which will assume greater importance in higher sea states. It is thought that movement of the air wake could be treated as a quasi-steady phenomenon, with a specific time-lag relative to ship motion but this has not been verified. Incorporation of correct temporal and spatial correlations into real-time simulation remains a substantive challenge.

Before an air wake can be modelled with acceptable fidelity in a simulator, test data must be acquired from which the model can be derived. This is not a trivial task. There are several approaches to acquiring air wake data, each of which has its advantages and limitations. Full-scale data can be collected, suitably normalised and characterised so that it can be replicated in a simulator. It is difficult to collect such data for regions other than directly above the flight deck, yet there are often flow structures such as vortices and oscillating shear layers emanating from the hangar corners and sides. Standard engineering practice relies on obtaining

stationary data from which to generate valid representations of an air wake. Unfortunately, the nature of full-scale atmospheric characteristics is such that data can rarely be collected for long enough times to satisfy the stationary criterion. One notable exception was an Australian at-sea trial where wind conditions were benign for some time and the air wake was thus generated by the relative ship motion.

The other source for validation data is the wind tunnel. This involves sub-scale tests which are generally insensitive to Reynolds number; however problems can arise from an inability to scale accurately the smaller geometric details which exist on most ships. Few studies have been undertaken to assess the level of detail required for such wind tunnel tests. The advantages of wind tunnel tests for air wake measurements are common to most wind tunnel investigations, for example control of parameters such as wind direction and the ability to average results over a suitable time to ensure a high level of confidence in the data. Such wind tunnel tests should be carried out in a simulated atmospheric boundary layer to enhance the replication of full-scale conditions.

4.2 CFD methods for modelling

A technique which can be used to generate an air wake for use in a simulator is to use CFD methods. CFD is, at first glance, a promising technique, since the velocities can be determined at any point in the vicinity of the ship. This is not currently possible in real-time for incorporation into a simulator. Even for relatively simple ship-like shapes, at least 600,000 grid points are required; thus several million could be required for a more realistic ship model. It must also be recognised that CFD developments in the aviation community over the past several decades have been primarily focused on developing solvers for conventional streamlined shapes, often in the transonic regime. However, there are codes which have been developed for incompressible industrial flows which are possibly better suited to the problem of modelling a ship air wake.

Part of the TTCP collaboration has been aimed at validating CFD codes for a Simple Frigate Shape (SFS). The geometry of this model is shown in Figure 2. Although the model bears little resemblance to an actual ship, there will exist separations and reattachments similar to those found on typical frigates. The geometry was chosen for ease of defining a grid and to avoid curved surfaces. Several organisations in the four countries are actively computing the flow around the SFS for wind angles of 0°, 15°, 45°, and 90°. In Canada, the IAR is conducting wind tunnel tests in support of qualitative and quantitative data for CFD validation. Surface-oil flow visualisation has been completed and a wind tunnel test to determine time-averaged pressure

coefficients at approximately 200 locations on the SFS is scheduled for September of 1998. The surface oil flow revealed a surprisingly complex flow topology for yawed winds and served to reinforce the difficulties of obtaining a CFD solution for a realistic ship configuration.

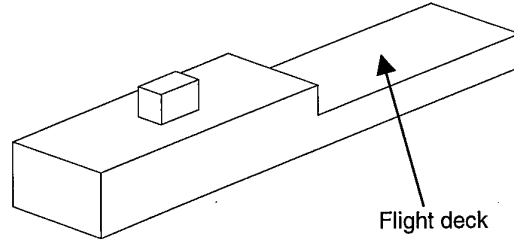


Figure 2; Simple Frigate Shape

Several codes have been used to calculate the air wake over the SFS. Both Australia and Canada employ Navier-Stokes solvers, while the UK and US use both Euler and Navier-Stokes solvers. The efforts to date indicate that CFD produces a realistic result for a 0° wind, but as the yaw angle increases to 45°, and finally 90°, the agreement between the CFD and wind tunnel results is reduced. One advantage of the four country collaboration is the ability to evaluate the strengths and weaknesses of different CFD strategies as applied to the air wake problem. For completeness, a brief overview of each nation's approach is included here. These efforts are often focused on real ship geometries in addition to the SFS.

The Australian CFD effort has involved the use of a commercially-available Navier-Stokes code [1]. Investigations have been made of grid independence, although there were limitations due to a structured grid. Turbulence modelling to date has focused on the $k-\varepsilon$ approach. Future efforts will be focused on unstructured grids and the Renormalisation-Group $k-\varepsilon$ turbulence model.

Canadian efforts have also been expended on a commercial Navier-Stokes package (not the one used in Australia). These efforts are discussed in detail elsewhere [2]. The approach in Canada has been to use the $k-\varepsilon$ turbulence model with wall functions, having examined both it and the $k-\varepsilon$ approach (without wall functions). The plans for the upcoming year include incorporation of a helicopter rotor in solving for the air wake around the Canadian Patrol Frigate.

In the UK, the work to date [3] has primarily used Euler solvers with the justification that the separation points are well defined and the flows are often dominated by strong vortices. The Euler codes will be less effective in predicting re-attachments, which

do occur on the flight deck. The UK is developing a time-accurate inviscid code and is working towards inclusion of viscous effects. Future developments include incorporation of moving geometries and inclusion of stack gas effects, as well as incorporation of the helicopter rotor. Much of this work is directed towards solving for the air wake around Royal Navy ships to aid in ship design.

In the United States, CFD efforts applied to the SFS have used two approaches. In one case a NASA-developed time-accurate Navier-Stokes code was used which produced encouraging results, although time-averaged data were not available. In another effort [4], a fourth-order time- and space-accurate code was used. In the latter case, the steady flow field solution was developed using an Euler solver from NASA, and the unsteady flow field followed using a viscous solver. Significant CFD efforts towards air wake modelling on United States Navy ships have been reported by Tai [5] and Landsberg *et al* [6].

4.3 Empirical methods

4.3.1 UK Advanced Flight Simulator simulation

The UK has implemented an air wake model in the Advanced Flight Simulator (AFS) at DERA Bedford under a contract aimed at establishing the potential of a simulator to support deck landing training. The model, described by Woodfield [7], can produce estimates of the air wake around a ship of any shape for which the model has been configured. Configurations currently exist for the Type 23 frigate and the Landing Platform Helicopter (LPH).

The model is built on the underlying assumption that the main features of the flow field in the lee of a ship can be predicted by adding together the effects of basic flow elements located at various parts of the ship geometry. Before being added together the relative magnitudes of the flows caused by each basic flow element are calculated according to the dimensions of the geometric feature to which they are attached. The relationships between the magnitude of a flow and a geometry of a particular type have been derived from empirical data and have undergone several stages of refinement since the creation of the first version of the model.

Air wakes behind bluff bodies can be described by a combination of steady wind components that vary spatially but are independent of time and unsteady or turbulent components that vary in space and time. The UK model was originally intended to provide an estimate of the steady flow field pattern only, as a function of the position in space. A more recent version has been upgraded to also include a prediction of turbulence intensity (the magnitude of the time varying wind component) as a function of the position in space, which can be multiplied by an

appropriate random time history that represents the profile of the turbulent winds.

Time-dependent turbulence is generated in the strong shear layers that exist between the flow past the superstructure and the low velocity regions immediately downstream of the superstructure. Initially the turbulence is in small eddies and these rapidly amalgamate to form larger eddies of the order of that of the superstructure. As the shear regions dissipate further downstream, fewer new turbulent eddies are formed and the larger eddies decay into smaller ones. The turbulence intensities are calculated from two new modules that relate to the flow behind bluff bodies (Profile Drag Turbulence) and the flow behind the edge of a bluff body (Edge Turbulence). The geometric properties of the ship that contribute to these effects are already held in the steady air wake modules for the basic flow elements. Turbulence intensities are calculated independently for the vertical, longitudinal and lateral axes as the values are typically uncorrelated. Also modelled is the attenuation of the vertical component of turbulence near to a horizontal surface (such as the deck of the ship) owing to the boundary condition which will not let any flow penetrate the deck and hence at this point the intensity must be zero.

In order to make use of the model results in a real-time simulation, a look-up table is generated of sufficient size to capture all the features of the model output without requiring a prohibitive amount of computer memory for storage. This requires a non-uniform calculation grid which packs a higher number of calculation points where the flow pattern is expected to vary rapidly with distance, and less closely-spaced points where the flow is expected to be approximately constant. It is assumed that both the pattern of steady winds and the turbulence intensities will be independent of wind over deck (WOD) velocity and therefore a new table is required for each wind azimuth case where all the results are normalised by the WOD velocity. This assumption is expected to hold well for moderate and strong winds but may become increasingly less appropriate for cases where the wind is weak and the flow pattern may have significantly changed.

A large amount of data and pilot comment has been collected from using the UK air wake model throughout a range of research programmes. The model datasets have also been supplied to government representatives in Australia and the USA in support of their own studies into the simulation of the DI under the auspices of TTCP. The combination of these programmes has built a level of confidence in the model allowing it to be used to investigate some of the operational problems associated with the deck landing task.

4.3.2 Inverse simulation

Another approach, suggested by the US, to determine the air wake is to use inverse simulation. In this approach, data from actual deck landings and take-offs are used as input control strategies for a high-fidelity simulator which does not incorporate an air wake model. Differences in force summation, and/or helicopter position, between actual and simulated manoeuvres, would be assumed to be caused by the unknown air wake. This approach has not yet been closely looked at and may prove difficult because of solution sensitivities. The UK is currently investigating the application of inverse simulation to the prediction of SHOLs, a method which is discussed further in Section 5.4.

4.4 Experimental methods for validation

The difficulties associated with quantitative air wake measurements for both full-scale and model-scale measurements have been discussed. All of the collaborating TTCP nations have made such measurements, however, and there are encouraging collapses of the air wake data when velocities are normalised by ship anemometer airspeed, and positions are normalised by ship hangar height. However, in one case full-scale air wake measurements made by two nations on a virtually identical ship operated by those two nations produced a factor-of-three difference in the turbulence levels.

4.4.1 Full-scale measurements

The UK has conducted a number of full-scale trials aimed at collecting sufficient data to aid in the validation of air wake models. A mast-mounted anemometer, borrowed from NAWC Patuxent River, was used in 1994 to record air flow measurements over the flight deck of a Type 23 frigate. A single mast with ultrasonic anemometers in 3 orthogonal directions at 3 heights was located at a series of up to 14 locations on the flight deck. Simultaneous measurements were made of ship angular motion, linear accelerations, speed, heading and standard wind-over-deck direction and speed.

A later trial on an Auxiliary Oiler Replenishment (AOR) vessel used a single, trolley-mounted laser anemometer scanning conically at 5 heights above the deck to gather data. Since a laser anemometer is only able to determine the wind component along the direction of the laser beam, it is necessary to scan the beam in order to resolve the various components of the flow field. Various scan patterns may be utilised but the simplest is the conical scan about a vertical axis. Plotting the results of the scan in polar form (Figure 3) generates two approximately circular lobes where the orientation of the lobes gives the wind direction and analysis of the size of the lobes gives the wind speed. Variations from the circle indicate unsteady fluctuations in the air flow.

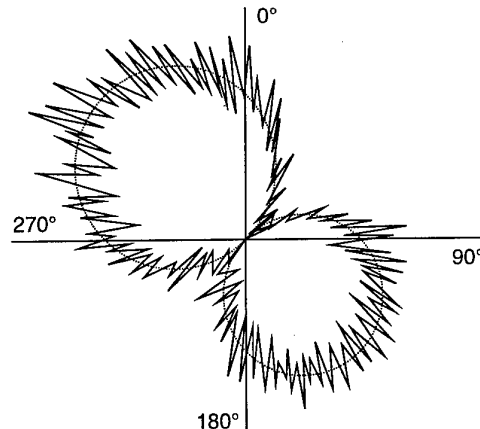


Figure 3; Typical results from a conical scan

A significant limitation of current full-scale measurement methods is the inability to measure air flow vectors over a wide range of points in a short space of time. Furthermore, most data can only be recorded directly over the ship flight deck. To overcome these limitations, the Shipboard Aircraft LIDAR (Light Detection and Ranging) Turbulence Sensor (SALTS) is being developed by NAWC Lakehurst, with UK Ministry of Defence (MOD) funding support. By using three co-ordinated lasers mounted on or near the flight deck (Figure 4) a picture of the flow field can be generated by scanning the lasers over the flight deck and along the aircraft flight path. Analysis of SALTS data will increase understanding of the air wake characteristics occurring through the launch/recovery area, and hence can be used to improve future ship and aircraft designs, to validate CFD codes and to model air wake systems for simulators.

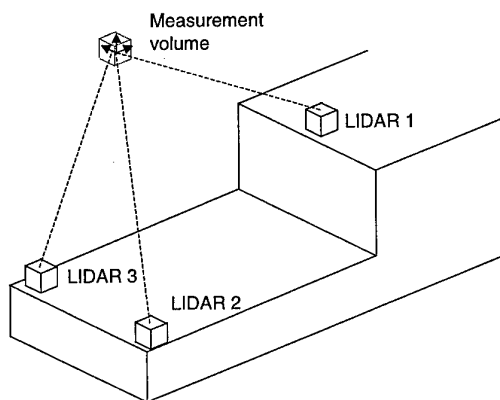


Figure 4; Principle of the SALTS system

In September 1989, an Australian trial was undertaken aboard HMAS Darwin, an FFG-7 frigate [8]. The objective of the trial was to measure the ship motion and air wake over the flight deck for a variety of relative wind speeds. An unexpected

development of the trials was that wind conditions were benign for much of the tests. While this permitted easy generation of 0° wind data, it was a greater challenge to generate data for yawed winds. Even though an air wake was often generated by relative ship motion in the calm conditions, operational constraints during the trial meant that the duration of recording at each mast position was often inadequate (typically 90 seconds rather than a more appropriate duration of 5 minutes). Also, the number of grid measurement locations (13 positions at three heights) was inadequate (Figure 5).

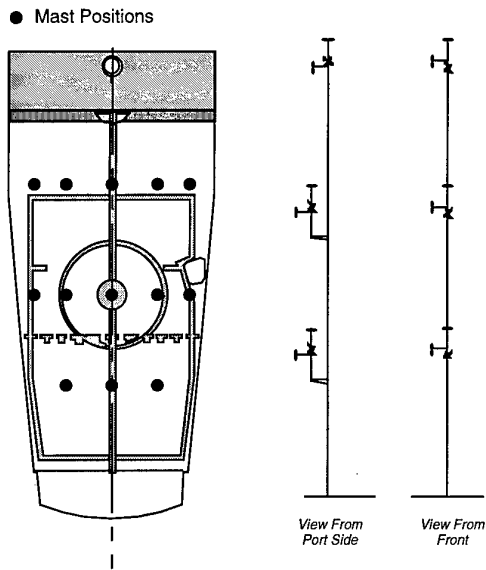


Figure 5; Australian full scale air wake trial – mobile mast layout and deck positions

In support of Canadian helicopter-ship integration, air wake measurements were made on the HMCS Halifax, a Canadian Patrol Frigate, in the summer of 1991. Measurements were made at fifteen locations on the flight deck at two heights above the deck, 5.5 metres and 9 metres. These measurements were made to verify earlier wind tunnel tests conducted prior to the commissioning of the ship. Correlations were poor in this case due to a number of superstructure configuration changes between the wind tunnel test model and the actual ship.

4.4.2 Wind tunnel measurements

An extensive wind tunnel experiment was conducted in the UK on a Type 23 frigate in which the testpoints were chosen to coincide with the data recorded on the full-scale ship. Limited model-scale tests are also conducted on each new ship entering service in an attempt to identify problems in the air wake before the ship is built. Recent tests have included the UK Royal Navy's Landing Platform Helicopter (LPH), Landing Platform Dock (LPD) and Auxiliary Oiler (AO) vessels. All of these tests contribute to a

database of air wake measurements which can be used throughout the TTCP community to validate models and improve understanding of the flow structure over a ship flight deck.

To complement the Australian full-scale trials, wind-tunnel measurements were made on a 1/64-scale model of an FFG-7 during the early 1990s [9]. For the wind tunnel tests, only mean flow could be measured and the measurement probe was limited to local flow deviations of less than about 40° , a serious deficiency in the recirculation region behind the hangar. Measurements were not corrected for blockage or interference.

Canadian wind tunnel tests were undertaken to provide wind tunnel air wake data for a configuration matching the as-built CPF. This work is discussed in detail in [2]. The measurements were undertaken to complement the parallel work conducted in the UK and Australia. There have been some attempts to collapse the air wake data from full-scale tests and wind tunnel tests, using the ship anemometer to normalise the velocities and the hangar height to normalise distances. Encouraging results were found for two distinct frigates for several wind angles. This type of approach is useful in providing a framework from which to build an air wake model.

4.4.3 Australian full-scale data representation

Initially, the purpose for obtaining both full-scale and wind tunnel air wake measurements by the Australians was to provide a model for use in simulation. Because of the deficiencies outlined above, it was concluded that the measurements obtained did not allow an adequate representation of the air wake covering the region surrounding the flight deck. The usefulness of the measurements is therefore considered limited to validation of models determined by other means, such as CFD techniques. The revised strategy adopted was to provide a separate mean disturbance flow and turbulence representation of the full-scale measurements in the form of a model valid only (a) for the nominal relative wind directions recorded, (b) within the measurement space domain for the mean flow, and (c) at the measurement grid points for the turbulence. Though a technique was successfully developed to remove ship motion effects from the measurements [8], it was found to make little difference to the results and so was not applied.

For a given nominal relative wind direction, the mean relative wind azimuth for each mast position showed some variation about the overall wind azimuth, which resulted in variations in velocity components recorded by the mobile mast anemometers in ship axes purely through vector rotation. This effect was removed by first resolving the components into wind axes. After normalising using free stream velocity,

different wind speeds at the same nominal azimuth (noting some significant deviations) were treated as duplicate cases, allowing the 'best' data set (in terms of measurement scope and standard deviation) to be chosen to represent measurements at that nominal azimuth.

For the mean disturbance flow, polynomials are used to curve fit the data. In the x (longitudinal), y (lateral), and z (height) directions, there were respectively three, five (but only three at aft of ship), and three anemometer locations. Hence, it was considered appropriate to use polynomials for representing u, v, and w of degree two, four, and two respectively for each wind direction of 0°, 30°, 60°, 90°, 135°, and 180°. This partial 4th degree polynomial representation had 27 terms.

The methodology adopted to represent turbulence was similar to that used at the Georgia Institute of Technology [10], who attempted to obtain a model using the Australian test data. In the Georgia Tech model, power spectral density is represented by an inverse power model with two constant coefficients obtained by fitting the model to auto-spectral power variations with frequency. This is done for the three velocity components at each location (i.e. 3 x 13 x 2 coefficients) for each wind direction case at a particular free stream wind velocity. To obtain a model over the flight deck, a spline fit was applied to each coefficient.

The Australian approach differed in that difficulties in obtaining consistency between coefficients for different wind speeds at the same nominal azimuth led to an abandonment of the prospect of a suitable model. Instead, the approach adopted was to represent the turbulence only at each grid point as an efficient way to archive the data for future use in validation. To represent the spectral density more faithfully, an additional coefficient was used in the inverse power model.

Using the coefficients obtained, the power spectral density can be calculated as a function of frequency and a simulated time history can be created using Shinozuka's algorithm [11].

4.5 Effect of helicopter-in-the-loop

The models described so far have attempted to predict the influence of the ship on the air flow as it passes over the superstructure and flight deck. However, the purpose of the modelling is to predict the behaviour of a helicopter operating in the air wake and so it is important that the effect on the air wake of the presence of the helicopter is also established. With the helicopter in the flow field, the air wake will be modified primarily by the downwash from the main rotor, but the tail rotor and body of the aircraft will also influence the flow structure. In

clear air, away from any surfaces or obstructions, these factors will not affect the performance or handling of the aircraft. In the presence of a horizontal or vertical surface, however, the flow is constrained and may recirculate through the main rotor, as shown in Figure 6. Furthermore, when hovering near the ground, the rotor downwash velocity is reduced and the pressure below the helicopter increases with a consequent reduction in the power required to hover, a factor known as ground effect.

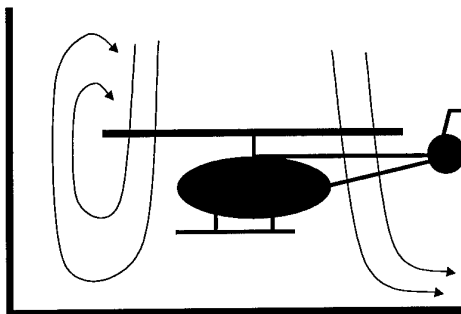


Figure 6; Recirculation effects

Ground effect and recirculation are both results of the rotor downwash influencing the freestream air flow, rather than the freestream influencing the helicopter, and may be expected to contribute to the performance of a helicopter operating over a ship flight deck. The degree to which each effect is present at the DI depends on a number of factors including the size of the ship and helicopter, the local wind speed and direction, and possibly ship motion. Ground effect is normally considered in terms of an infinite ground plane; for a finite surface, such as a ship flight deck, the ground effect can be expected to be reduced. Ground effect also diminishes with increasing wind speed as the area of increased pressure below the helicopter is effectively blown away, and a similar effect can be expected with recirculation. The area of the helicopter rotor in comparison to the size of the flight deck will also influence ground effect, and the dimensions of the hangar face will impact on the strength of recirculation. Ship motion will constantly alter the relative angle between the helicopter and the flight deck, as well as the effective area of the deck, and may influence both recirculation and ground effect.

4.6 Modelling the helicopter-in-the-loop

Modelling recirculation and ground effect presents a significant challenge, especially for real-time simulation. The whole flow field will change for every position of the helicopter relative to the ship. The angle of the rotor disc, the weight of the aircraft and the power applied will also have an influence on the flow structure. Initial attempts at real-time simulation of these effects may be based on the

empirical approach of the UK air wake model, so that a look-up table is used to approximate recirculation and ground effect at any point around the ship. This type of model would reside with the ship, but it seems likely that a higher fidelity representation of the helicopter-ship system will require integration of the rotor code with a real-time simulated air wake. Real-time calculations of this type cannot be expected in the foreseeable future, but off-line analysis is being conducted in the UK, US and Canada through the use of CFD codes.

4.6.1 UK research

In the UK research [3], a simple actuator disc technique has been used to represent the effect of the helicopter on the air wake. It is proposed that the effect of the modified air wake on the aircraft could be calculated by extracting the velocity field over the rotor disc from a CFD calculation and feeding it to a helicopter performance code. A modified loading over the actuator disc would then be applied as an input to the CFD calculation and an iterative process used to produce a representation of the complete flow field. As a precursor to this research, the UK has recently conducted a land-based trial in an attempt to determine the degree to which the presence of the helicopter influences the air wake over a flight deck. Air flow measurements, using a single laser anemometer, were taken around a helicopter hovering first behind a hangar and second in clear air. Both sets of data were recorded in nil wind conditions. The results were compared with a CFD analysis of the same conditions and initial comparisons were very encouraging [12]. However, perhaps the clearest indication of the influence of the helicopter and solid boundaries on the flow field is given by the pilots who consistently remarked on the difficulties of holding position behind the hangar in comparison to the hover in clear air.

4.6.2 Canadian research

Canadian work incorporating a numerical helicopter into an air wake was described by Syms and Zan [13]. In this work, the rotor module of the Sikorsky General Helicopter Flight Dynamics Simulation code GenHel [14 & 15] was "flown" through a numerical model of an air wake. The air wake in this case was obtained from cross-hot-film anemometer measurements made behind a model of a frigate in the IAR 0.9 metre wind tunnel, wherein an atmospheric boundary layer simulation was incorporated. Measurements were made of the three orthogonal mean and unsteady flow components. Simultaneous measurements from two anemometers permitted accurate measurements of the turbulence correlation between two physical points in the air wake region. A "flying" hot-film probe was also used in these tests to permit accurate measurements of velocities in the recirculation zone.

An algorithm to regenerate the unsteady characteristics (spatial and temporal) of the measured flow field was developed, and GenHel was then "flown" through this numerical air wake, with a thrust-to-weight ratio of unity. The spatial correlation in the generated turbulence could incorporate cross-spectra of either the streamwise or vertical velocity. No modelling of the lateral velocity cross-spectra or orthogonal component cross-spectra was attempted. This approach, while unparalleled in terms of accurate air wake modelling, is not able to model the coupling of the rotor downwash and air wake. The calculated rotor loads at a given point in space, as output from GenHel, were then analysed. It was reported that inclusion of spatial correlation effects increased the level of the unsteady rotor response. This is to be expected since the turbulence scales are of the same size as the rotor diameter. It was also found that the inclusion of the unsteady vertical velocity into the air wake model induced greater unsteady rotor loads than inclusion of an unsteady streamwise velocity.

In order to obtain quantitative information about the degree of coupling between the rotor downwash and the air wake as it affects the rotor, the IAR is conducting sub-scale wind tunnel experiments involving a frigate model and a sting-mounted rotor that is traversed into the air wake. The geometric scaling of the experiment is 1:50 and the rotor is powered by a small DC motor mounted on a six-component balance. In this case, correct scaling of the rotor aerodynamics, specifically advance ratio and thrust coefficient, will ensure the flow field coupling is correct. The rotor has the capability for arbitrary collective settings (up to stall); however, the capability for cyclic inputs is not possible at this scale. Thus the rotor is not trimmed, but can be operated at any fixed collective position for a given traverse. Ground effect is also inherently included in this experimental modelling.

These experiments will be followed by modification of the GenHel rotor to match the characteristics of the wind tunnel rotor and then this numerical rotor will be "flown" through the measured CPF air wake. With the numerical rotor validated against the wind tunnel rotor in uniform flow, changes in rotor loads determined from the experiment and the numerical model will indicate the importance of the downwash and air wake coupling.

Measurements of rotor loads in the wind tunnel experiment have been made for several onset wind speeds and directions as well as with changes in ship superstructure. It has been determined that for a fixed collective setting in a 35 knot wind, the time-averaged rotor thrust coefficient decreases about 10% for a rotor positioned 6 metres above the deck (full-scale) and over the centre of the flight deck as

compared to a rotor at 10 metres above the flight deck and displaced laterally by one rotor diameter. These positions represent the transition from alongside the ship to the low-hover, as practised by the British and Canadian navies. While a pilot will not hold a fixed collective during this manoeuvre, the results suggest the magnitude of quantitative corrective actions that a pilot must take during the landing. The pilot will, of course, decrease collective to execute the landing manoeuvre but these data suggest the rate of descent will be greater than if the same control strategy were implemented for a conventional ground-based landing. These effects may be overshadowed by the unsteady rotor loads arising from turbulence, or simply by the effort required to track the vertical and pitch deck motion in heavy seas. Whether the wind tunnel rotor can be used to extract dynamic loads arising from the unsteady components of the air wake remains to be determined.

4.6.3 US research

One US approach to modelling the rotor and air wake interaction has been reported by Landsberg *et al* [6]. The primary focus of the work was the modelling of exhaust gas concentrations in the vicinity of the flight deck as opposed to investigations of rotor aerodynamics and helicopter flight dynamics. An in-house developed unsteady-flow solver was used to compute the unsteady air wake and the ship stack exhaust gas trajectories for a DDG51 destroyer. Incorporated into the code was an actuator disc model to represent a 5000 kg helicopter with a 16.5 metre diameter rotor. This approach will result in a modified air wake due to the actuator disc; however, the modified air wake is not fed back into the actuator disc model, which would represent the fully-coupled case. The work included modelling of the atmospheric boundary layer to enhance accuracy of the boundary conditions. The CFD air wake prediction indicated that the predominant frequencies in the unsteady air wake are in a bandwidth likely to affect helicopter flight dynamics, and this echoes the experimental (wind tunnel) work reported by Sym and Zan [13].

4.7 Effect of the tail rotor

While the discussion so far has focused on the interactions of the main rotor and air wake, it is recognised that the tail rotor cannot be ignored. SHOL boundaries for beam winds are generally determined by limitations in tail rotor authority. Thus high-fidelity simulators used for training purposes or SHOL prediction must include suitably accurate modelling of the tail rotor aerodynamics.

5 PREDICTION OF SHOLS

5.1 Synchronised ship and helicopter measurements

As a first step in using analysis and simulation in determining SHOLs, the Australians obtained

synchronised ship and helicopter measurements for an S-70B-2 Seahawk helicopter operating from an FFG-7 frigate during a FOCFT in March 1994 [16]. A data acquisition system developed by the Australians was fitted to the ship, and another was fitted to the aircraft. Each system allowed up to 56 channels to be used, mostly analogue inputs, though synchro inputs were used for data recorded from normal ship instruments and some aircraft instruments. The ship was instrumented to record ship motion and wind velocity, and the helicopter was instrumented to record flight control positions and flight dynamic parameters. Duplication of some measurements from alternative sources allowed some redundancy, which was utilised when instrument failures occurred.

During these trials, though mean relative wind was measured using the mast-mounted ship and reference anemometers, the air flow distribution over the flight deck region and around the helicopter could not be measured. Hence, for relative wind headings where the ship hangar will significantly affect the air flow into the helicopter, the information is incomplete in attempting to duplicate the trials in a simulation using recorded pilot controls to drive the simulation.

5.2 Torque-limited SHOLs

In the absence of shielding of the air flow by the hangar, torque would be expected to decrease with increased airspeed up to about 80 knots. However, inspection of Australian FOCFT measurements showed that torque remained relatively constant as relative wind speed increased for headings where the ship hangar significantly affected the air flow. This indicated that the flow was being effectively blocked.

The blocking effect could be quantified in an off-line simulation by using GenHel without any allowance for ship air wake to predict torque for a trimmed aircraft behind the ship hangar. The ratio between the measured and predicted torque was obtained and plotted against relative wind speed for each 20 degree range of relative wind directions. Within this range, it was assumed that the physical characteristics of the flow were reasonably constant. In general, a good linear relationship between the torque ratio and relative wind speed was obtained for each region. An attempt was then made to use this relationship to predict torque-limited boundaries of the SHOLs. However, the boundaries did not match well with observations from the FOCFTs, primarily because of sensitivities of the boundaries to small changes in torque.

5.3 Piloted simulation

Piloted simulation offers a more promising method for recreating torque and pedal limited areas of the SHOLs. Additionally, more substantial areas limited by pilot workload can also be investigated. The main

obstacle to achieving a suitable model of the whole system is in representing the air wake. The most promising approach in the short term is to incorporate the UK look-up tables produced using the air wake model installed in the AFS. Initial trials at DERA have demonstrated the feasibility of this method [17] and Australia will shortly attempt to reproduce FOCFT test data using the look-up tables generated by the UK model. It should be noted, though, that in this air wake model, as with look-up tables produced by current CFD codes, no account is taken of the change in the air wake as a result of ship motion.

5.4 Pilot workload modelling

A critical factor in the development of a SHOL is the pilot workload. When the workload is too high due to the air wake effects, the pilot will be unable to consistently achieve safe and accurate landings and the SHOL boundary is reached. The UK is currently developing a modelling capability to assess and quantify the effects of the air wake on helicopter deck landing operations. The project is divided into two phases. The first phase uses a constrained simulation tool to estimate the control actions required to fly a helicopter model along a prescribed flight path that describes the deck landing task. The simulation incorporates a model of a human pilot with parameters to allow the pilot strategy to be varied. This prevents the prediction of unfeasibly large or rapid control inputs. The second phase utilises Wavelet Analysis to decompose the time histories of pilot control activity into discrete events which are then analysed to indicate the level of workload required.

The aim of the research is to enable the investigation of the mechanisms by which a helicopter performing a deck landing is influenced by the presence of an unsteady air wake and by ship motion. A piloted simulation trial is planned on the AFS at DERA Bedford to collect data for the assessment of the pilot model and to identify suitable modelling parameters for all stages of the deck landing task. The project will culminate with the production of predicted SHOLs which will be compared against equivalent data derived from piloted simulation.

6 CONCLUSIONS

This paper has shown how the modelling and simulation of ship air wakes offers substantial potential benefits to maritime helicopter operational availability through improved ship design, the development of new technologies and qualification techniques and more effective pilot training. Simulation allows any wind condition and ship motion to be investigated and enables exploration of areas of the flight envelope which may be dangerous in flight. By modelling the air wake, helicopter-ship interface issues can be explored and SHOLs estimated before a ship is built. High fidelity

simulation of the air wake remains, however, a significant challenge due to the complex and highly dynamic nature of the flow over the flight deck and the difficulties of obtaining validation data, at both full- and model-scale.

The paper has described how, under the auspices of TTCP, several organisations in the UK, Canada, Australia and the USA are working collaboratively to facilitate the development of air wake models with the aim of improving simulation of the DI. Each nation is using CFD techniques to calculate the air wake around a common SFS for various wind directions and comparing results against each other and against wind tunnel data generated by Canada. A more empirical approach is being pursued by the UK in an air wake model currently installed in the AFS and successfully used in trials aimed at supporting FOCFT with simulation. The model will be evaluated independently by Australia and the US in similar trials in the near future. The US has proposed inverse simulation as a means of deriving air wake data from aircraft position and pilot control activity. Each nation has been collecting air wake validation data through ship trials and wind tunnel experiments and distributing the results to other members of the group, forming a validation database.

The air wake models have already been applied to the prediction of operational limits using a variety of techniques, including piloted simulation and pilot workload modelling. It is anticipated that the synergy of effort achieved under TTCP will make considerable savings in the time and cost required to develop a high fidelity DI simulation and will significantly enhance the maritime operational capability of participating nations.

7 ACKNOWLEDGEMENTS

The research described in this paper results from the culmination of effort of perhaps forty individuals in the four nations. The authors gratefully acknowledge the substantial contributions of their colleagues without whom this work could not have progressed as reported here.

The Canadian wind tunnel work is a collaboration between the Institute for Aerospace Research and the Air Vehicle Research Section of the Department of National Defence.

8 GLOSSARY

AFS	Advanced Flight Simulator (DERA)
AO	Auxiliary Oiler
AOR	Auxiliary Oiler Replenishment
CFD	Computational Fluid Dynamics
DC	Direct Current
DERA	Defence Evaluation and Research Agency (UK)
DI	Dynamic Interface

DSTO	Defence Science and Technology Organisation (Australia)
FOCFT	First of Class Flying Trial
HMAS	Her Majesty's Australian Ship
HMCS	Her Majesty's Canadian Ship
IAR	Institute for Aerospace Research
LIDAR	Light Detection and Ranging
LPD	Landing Platform Dock
LPH	Landing Platform Helicopter
MOD	Ministry of Defence (UK)
NASA	National Aeronautics and Space Administration (USA)
NAWC	Naval Air Warfare Center (USA)
NRC	National Research Council (Canada)
SALTS	Shipboard Aircraft LIDAR Turbulence Sensor
SFS	Simple Frigate Shape
SHOL	Ship Helicopter Operating Limits
TTCP	The Technical Co-operation Programme
WOD	Wind Over Deck

9 REFERENCES

- 1 Jones, K.R.W., Reddy, K.R. & Toffoletto, R. 'CFD Studies of Ship Airwake, Computational Techniques and Applications', CTAC 97, University of Adelaide, 29 September to 2 October 1997.
- 2 Zan, S.J., Syms, G.F. & Cheney, B.T. 'Analysis of Patrol Frigate Air Wakes', in *Fluid Dynamics Problems of Vehicles Operating near or in the Air-Sea Interface*, RTO/AVT Symposium, Amsterdam, 5 to 8 October 1998, Paper 8.
- 3 Tattersall, P., Albone, C.M., Soliman, M.M. & Allen, C.B. 'Prediction of Ship Air Wakes over Flight Decks using CFD', in *Fluid Dynamics Problems of Vehicles Operating near or in the Air-Sea Interface*, RTO/AVT Symposium, Amsterdam, 5 to 8 October 1998, Paper 6.
- 4 Liu, J. & Long, L.N. 'Higher Order Accurate Ship Airwake Predictions for the Helicopter/Ship Interface Problem', 54th American Helicopter Society Annual Forum, Washington DC, May 1998.
- 5 Tai, T.C. 'Simulation and Analysis of LHD Ship Air Wake by Navier-Stokes Method', in *Fluid Dynamics Problems of Vehicles Operating near or in the Air-Sea Interface*, RTO/AVT Symposium, Amsterdam, 5 to 8 October 1998, Paper 5.
- 6 Landsberg, A.M., Boris, J.P., Sandberg, W. & Young, T.R., Jr. 'Analysis of the Non-linear Coupling Effects of a Helicopter Downwash with an Unsteady Airwake', AIAA-95-0047, 1995.
- 7 Woodfield, A.A. & Tomlinson, B.N. 'Ship Airwakes - A New Generic Model for Piloted Simulation', in 'Flight Simulation - Where are the Challenges?' AGARD CP 577, May 1995.
- 8 Arney, A.M., Blackwell, J., Erm, L.P. & Gilbert, N.E. 'A Review of Australian Activity on Modelling the Helicopter/Ship Dynamic Interface'. AGARD CP 509, Aircraft Ship Operations, Seville, Spain, 1991.
- 9 Matheson, N. 'Measurements of the Airflow about a 1/64 Scale FFG-7 Frigate Model and Correlation with Full Scale Results', 11th Australasian Fluid Mechanics Conference, University of Tasmania, Hobart, Australia, December 1992, pp. 655-658.
- 10 Mavris, D., Prasad, J.V.R. & Schrage, D.P. 'A Simulation Methodology for Modeling Ship-Airwake Turbulence', 25th Annual International Symposium of the Society of Flight Test Engineers, Washington, DC, August 1994.
- 11 Shinozuka, M. & Jan, C.M. 'Digital Simulation for Random Processes and its Application', Journal of Sound and Vibration, Vol. 25, No. 1, 1972, pp. 111-128.
- 12 Manning, A.P. & Allen, D.M. 'Comparison of Air Flow Measurements Around the Flight Deck of an AOR and Type 23 Frigate with CFD and Wind Tunnel Results', Unpublished DERA report, 1998.
- 13 Syms, G.F. & Zan, S.J. 'Analysis of Rotor Forces in a Ship Airwake', AGARD CP 552, August 1995, Paper 31.
- 14 Howlett, J.J. 'UH-60A Black Hawk Engineering Simulation Program: Volume I - Mathematical Model', NASA Contractor Report 166309, National Aeronautics and Space Administration, Ames Research Center, Moffett Field, California, USA, December 1981.
- 15 Howlett, J.J. 'UH-60A Black Hawk Engineering Simulation Program: Volume II - Background Report', NASA Contractor Report 166310, National Aeronautics and Space Administration, Ames Research Center, Moffett Field, California, USA, December 1981.
- 16 Arney, A.M., Fieldhouse, I. & Kenter, N.J. 'Australian Airborne Trials of the Sikorsky S-70B-2 Helicopter: Part III - FFG-7 First of Class Flight Trial Measurements', DSTO Technical Report 0660, Defence Science Technology Organisation, Department of Defence, Australia, April 1998.
- 17 Fitzjohn, D., Turner, G.P. & Padfield, G.D. 'The Use of Modelling and Simulation in Support of First of Class Flying Trials', 24th European Rotorcraft Forum, Marseilles, France, September 1998.

© British Crown Copyright 1998/DERA. Published with the permission of the Controller of Her Britannic Majesty's Stationery Office.

© 1998 National Research Council of Canada.

© Commonwealth of Australia 1998/DSTO.

Elements of this paper are declared the work of the US Government. The paper is not subject to Copyright protection in the US.

The experience of aerodynamic disturbances research behind an aircraft-carrier ship with elements for safe operation of ship-based aircraft

L.A.Maslov

N.O.Valuev

A.V.Zharinov

Gos NITs TsAGI, Moscow 107005
17, Radio Street, Russia

SUMMARY

An opinion about some reasons of relatively late appearance of the first aircraft carrier in the Soviet Navy is expressed. TsAGI's works for provision of aerodynamic compatibility of ship-based aircraft and carrier are described. The works were directed on development of methodology of estimation of wind flow disturbances over flight deck and behind carrier by model experiment in wind tunnel. Its aim was design and realization of measures of reduction of these disturbances and its gradients up to level required for takeoff landing operation safety.

Numerous model tests of different ship architecture variants allowed to study the mechanism of flow formation and to estimate the effects of motion ship kinematic parameters relative to wind and of some features of ship architecture on the flow structure.

Some recommendations were developed and created on aircraft-carrier cruiser «Minsk» for deck flow leveling. The range of relative wind angles was determined for safe landing on carrier «Admiral Kuznetsov».

INTRODUCTION

According to its geographical position Russia is the continental power. Therefore on many centuries its main defense task was to restrain an aggressor from west and south directions. The lack of oversee territories and restricted emergence to Baltic and to Black seas set before Russian naval fleet generally the tactic tasks of support of maritime flanks of overland armies on insignificant small distance from its shores. Such conception persisted up to 60th years of XX century.

Appearance in the stuff of the naval forces of the potential adversary of atomic submarines with ballistic rockets (ASBR) radically changed the views of soviet leadership on role and the place of navy, and principally - on its enlisted stuff of ships.

The boundaries of anti-submarine defense have moved on the thousands kilometers from coast, what demanded not only increase of autonomy and seaworthiness of ships, but also creation of principally new for the domestic navy ships with aircraft armament. Anti-submarine cruisers of project 1123, type of «Moskva», each equipped by 14 anti-submarine helicopters, put beginning of the application of deck aircraft in Soviet Navy.

For a long time Soviet Navy task forces have not in open ocean the air cover, which is very necessary for ensuring of combat stability. These functions was laid on anti-aircraft missile armament of the ships, and counteraction to aircraft-carriers of enemy was laid on coast-

based naval missile-carrier aviation and submarines, armed with winged missiles. In spite of the fact, that World War II showed leading role of aircraft-carriers among other classes of combat surface ships, «swimming aerodromes» had not found their place in USSR defense doctrine, which was not supposed conduct of war actions on alien territory. This circumstance and also economic difficulties of parallel creation of aircraft carriers and ASBR have lead to the fact, that prolonged time the soviet leadership at forming of programs of military shipbuilding gave absolute priority to ASBR, capable to decide the strategic tasks.

The development of marine strategic forces demanded with time the decisions of the tasks of protection of the positional areas of its deployment from anti-submarine means of antagonistically side. For this aim construction of heavy aircraft-carrier cruisers (HACC) of the projects 1143, 1143M and 11434, equipped with VTOL aircraft Jak-38, was deployed. The particular features of these ships applied architecture were a consequence of their functions.

An absence of experience of creation of such objects set before industry the quite a number of problems. Whereat one of principal tasks was found to be the provision of aerodynamic compatibility of ship-based aircraft and carrier-ship. With account of specifics of this problem, its decision was laid on Central Aerohydrodynamic Institute (TsAGI).

METHODIC AND RESULTS OF INVESTIGATIONS

As the first step there was the choice of methodology of experiment on receiving of physical picture of flow over the ship. Freeboard and super structures of aircraft-carrier from point of view of aerodynamics are typical bluff body with separated zones and vortex flow, fixed on sharp bends of form. Since in this case the inertia-type effects prevail over the effects of viscosity, the resulting flow picture practically does not depend on Reynolds number, and, consequently, on scale effect. This consideration allowed to go along the way of tests of models of aircraft-carriers in wind tunnels, giving for full-scale experiment the role of controlling instrument. Besides, this gave the possibility of realization of advanced investigations of perspective configurations.

The wind tunnel with open working part and nozzle diameter 2.2 m, having low level of turbulence, equal to 0.3%, was used. In 1971 here the experiment on study of pressure distribution on topside of HACC's hull for the project 1160 was made. The results did not give possibility to receive enough complete insight into the flow picture around ship.

The measurement of velocity fields around carrier-ship models became basic method of investigation. The five-tube air-pressure probes mounted on spatial coor-

dinating device became main instruments. Hot-wire anemometers for measurement of fluctuating velocity components also were included in the equipment. However the investigations of quasi-stationary picture of flow were main works. The measurements were complemented with visualization of flow around models in wind tunnel and towing tank. These tests allowed determining boundaries of zones of separated flow above deck and behind island qualitatively.

Measurements of parameters of perturbed airflow were carried out in transversal cross-sections above deck and in aerodynamic wake behind model, mounted both on even keel, and with static angles of heel and trim. Cartesian system of coordinates was used at the measurements; angle of relative wind β was counted between longitudinal centerline plane of model and vector of freestream velocity V_∞ .

Special series of methodic experiments in wind tunnel has shown, that tests of double mirror model for study of disturbed air flow in the wake behind ship is more correct to use for wind tunnel instead of model on screen. Influence of boundary layer, which is formed on motionless screen and does not correspond to real conditions, was eliminated in the case. Mounting model on horizontal flat screen, having less cost, was sufficient for flow measurement above deck.

Output data of information-measuring system of wind tunnel were the components of local disturbed velocity V_x , V_y , V_z , vector fields $V_{xz}=f(x,z)$ and $V_{yz}=f(y,z)$, and also distributions of angles of horizontal and vertical flow washes $\epsilon_H=f(y,z)$ and $\epsilon_V=f(y,z)$, $\epsilon_H=f(x,y)$ and $\epsilon_V=f(x,y)$. As longstanding practice has shown, such set of information permits to carry out exhaustive analysis of features of flow in wake behind ship. structure around aircraft-carrier and to determine quantitative characteristics of flow. Certain generalized picture of flow, received on base of tests of series of aircraft-carriers' models, forms of which correspond to classic configuration with displaced on the starboard side island and angled flight deck, is shown on Figs. 1 and 2 as an example.

Vortex system of flow around aircraft-carrier is the following. In front of carrier the undisturbed horizontal wind flow acquires vertical upwash due to which the flow separation occurs from windward edge of fore-deck. The vortex sheet is curtailed into large-scale vortex core, named further as «bow vortex», which propagates over flight deck. Vortex of analogous nature is formed on windward side edge of ship's sponson, on which angled deck is located. This vortex is found downstream up to distances behind the stern equal to 0.5-0.7L (where L - length of ship's hull). Bow vortex, as consequence of loss of its connection with feeding vortex sheet, is eroded gradually or joins with more intensive vortex, coming off from edge of sponson.

Third component of vortex system of aircraft carrier is the vortex, generated by island at angles ζ , which are different from zero. Intensity of this vortex is comparable with intensity of vortex, formed on edge of deck. Namely it exerts a crucial effect on parameters of airflow in zone of landing glidepath.

Extensive dead fluid zone behind the counter flat stern of ship is essential factor, determining flow in wake. The flow, closing behind the stern, obtains significant angles of vertical and horizontal washes, what leads to curving downward of trajectories of vortexes, coming from edges of deck and island.

The considered flow picture takes place at $\beta < 0$, i.e. at regimes, which are regarded as basic for realization of landing operations on carrier with angled deck sloped on the port side.

Vortex generations at $\beta=0$ occurs only on edges of fore-deck, where two symmetrical vortexes with opposite direction of rotation are formed. Velocity field behind island is vortexless. Flow is closed behind the symmetrical structure. Bow vortexes due to their small intensity are quickly destroyed, and velocity field in wake behind ship is formed under action of dead zone behind stern, diverting the resulting flow downwards (Fig. 2b).

At $\beta > 0$, when wind flow incomes on the starboard side, flow picture in bow part is similar to the picture at $\beta < 0$. However, encountering island on its way, bow vortex interacts with flow around this element of ship's architecture. Due to aerodynamic interference in wake behind aircraft carrier only one vortex is observed.

It is necessary to note that fixed flow separation zones are formed above surfaces of decks immediately behind its bow edges. Its heights are in the range 1-2 m. They do not exert considerable influence on resulting velocity field in wake, but it is necessary to take into account them at analysis of aircraft takeoff conditions.

Described above picture is principal structure of flow above flight decks and in wake behind aircraft carrier of the considered configuration. Both hull and island are flowed as thick wing of extremely small aspect ratio. The vortex system undergoes some changes quantitatively in dependence on absolute value of angle ζ , pitch and roll angles, and also on features of ship architecture, but qualitatively it remains practically unchanged. For example intensities of vortexes increase practically according to linear law at an increasing of absolute values (up to investigated range $-25^\circ < \beta < 25^\circ$).

Aircraft carrier in real conditions is subjected to rolling, pitching and heaving. However correct modeling of this process in wind tunnel with the aim of estimation of flow disturbances is impossible. The reason of this is in high-frequency oscillations of scale model, required according to kinematics criteria. The oscillations are close to vibration, what does not correspond to surveyed phenomenon. Therefore the investigations were restricted to estimation of influence of limiting static roll and pitch angles on characteristics of stationary flow fields around heeled or trimmed models. Such positions of ship are possible at presence of battle or operational damages.

Model experiment showed that heel on windward side on comparatively small angle $\theta = 3^\circ$ is accompanied with noticeable reduction of intensities of vortexes (approximately on 50-85%), coming from corresponding deck edges. Opposite effect is observed at heel on leeward

side (Fig. 3).

Influence of trim is more essential. So, intensity of edge vortexes at $\psi=1.5^\circ$ (trim by the stern) increases in 1.5-2 times and correspondingly decreases at $\psi=-1.5^\circ$. The dead fluid zone after stern grows exactly likewise at trim by the bow, because of it is observed more strong fall of path of vortexes, propagating in aerodynamic wake behind ship (Fig.4).

Vortex, generated by island, practically does not depend on angles of heel and trim. However the change of characteristics of another elements of vortex system leads to some change of resulting flow intensity picture in wake due to interaction.

There were made attempts of search of such shape-formations of island, at which vortex formation behind it was minimal. However since a use of radical means of aerodynamic improvement, as example spoilers and deflected flaps, in this case is impossible to create on practice, recommendations are reduced to requirement of decrease of aspect ratio and relative width of island.

Displacement of island to starboard from longitudinal plane and closer to the bow favorably effects on conditions of landing, since in these cases vortex, generated by it, removed from glide path.

How already it was noted, besides of kinematics parameters, there is a noticeable effect of some features of ship's architecture on quantitative characteristics of flow around it. For example the rise of foredeck bow part of HACC of the project 1143, type of «Minsk» effects on flow above deck like trim by the stern.

Just for this cruiser the first TsAGI experience was obtained in purposeful action on flow characteristic over its angled flight deck. That was in 1981 during the course of development of horizontal short-run takeoff of VTOL aircraft Jak-38 from «Minsk».

Aerodynamic tests have shown, that intensive vortex comes from windward side edge of risen foredeck. The vortex deflects by containers, located on its way just on flight deck. Moreover vertical front wall of large sponson leads to appearance of well-developed separated zone, covering up to 20% of runway. Flow in this zone is characterized with high deceleration of incoming flow (up to $0.65V_\infty$).

At the analysis of safety of above-mentioned takeoff the special requirements to parameters of air flow on take-off runway of given aircraft must be taken into account. These data became basic criteria of conformity takeoff conditions to required ones for safety. Study of data, received in wind tunnel has shown, that it is impossible to satisfy these criteria without modification of ships architecture, directed on air flow leveling. To decide this problem, TsAGI jointly with industry have carried out extensive research work, in process of which dozens of so-called leveling devices (LD) variants were tested.

As a result the such variant, was selected which reduced parameters of flow to correspondence with the

requirements from one side and was technologically and tactically acceptable from another side. The accepted composition of LD included three flat and one curved plates, as well as fairing on front wall of sponson

The flat plates turned the vortex flow into contoured passage between blast fence and curved plate, deviating it from flight deck. The fairing with symmetrical semi-elliptical profile practically removed separation zone over deck and decreased deceleration of flow to acceptable level. Whole complex LD reduced lateral, vertical and longitudinal disturbed velocities and its gradients over flight deck to required values, as it is shown on Figs. 5 and 6.

Full-scale measurements on HACC «Minsk» showed good convergence of the results with model experiment ones. The flight tests confirmed correctness of the accepted decisions. All ships of this type were equipped with developed LD complex, and there are no any takeoff accidents in process of long-term flight operation of aircraft Jak-38 due to external aerodynamic conditions.

The developed methodology allows easily to estimate the external aerodynamic condition on the first in USSR aircraft-carrier of classic type named now «Admiral Kuznetsov» (Fig.7) from point of view of safety problem of takeoff/landing operations on the design stage. Here, just like for Jak-38, the determination of requirements to parameters of air flow on trajectories of take-off and landing for ship-based fighters Su-33 and MIG-29K was as a point of departure.

Previous experience of satisfaction of demands to flow parameters along Jak-38 takeoff path needed in its evolution. There are high velocity of approach and limited deck section of touching by arrester hook. In comparison with ground-based aircraft the requirements to accuracy of nominal glidepath keeping are increased. This involve tightening of requirements to air flow parameters too. Besides, purposeful action on vortex system of wake becomes difficult due to an increase of scale of the phenomenon. Therefore one of the way of increase of landing safety was search of range of angles (, inside of which flow parameters would be conformed to the requirements.

Such range was found in process of model tests, results of which were confirmed subsequently by measurements on ship. As test pilots noted, simulation of landing outside the recommended of angle (range accompanied with vibration of aircraft, mushing and in isolated cases - with rolling-off. These phenomena, although are not catastrophically, presented certain hazard for operational pilot's. The necessity of additional controlling actions increased high psychophysical load on the pilot (Fig. 8).

Measurements of non-stationary component of disturbed air flow with help of hot-wire anemometers showed, that frequencies and levels of fluctuations over bow starting ramp and forward part of angled deck can lead to pumpage of compressor. Therefore TsAGI recommended to set profiled semi-elliptical fairing on bow and side edges of ships ramp and forward part of spon-

son. This permitted to eliminate formation of extensive separated zones, unfavourable influencing on conditions of flow around wing of aircraft at takeoff and on operation of its powerplant in consequence of high degree of non-uniformity of flow.

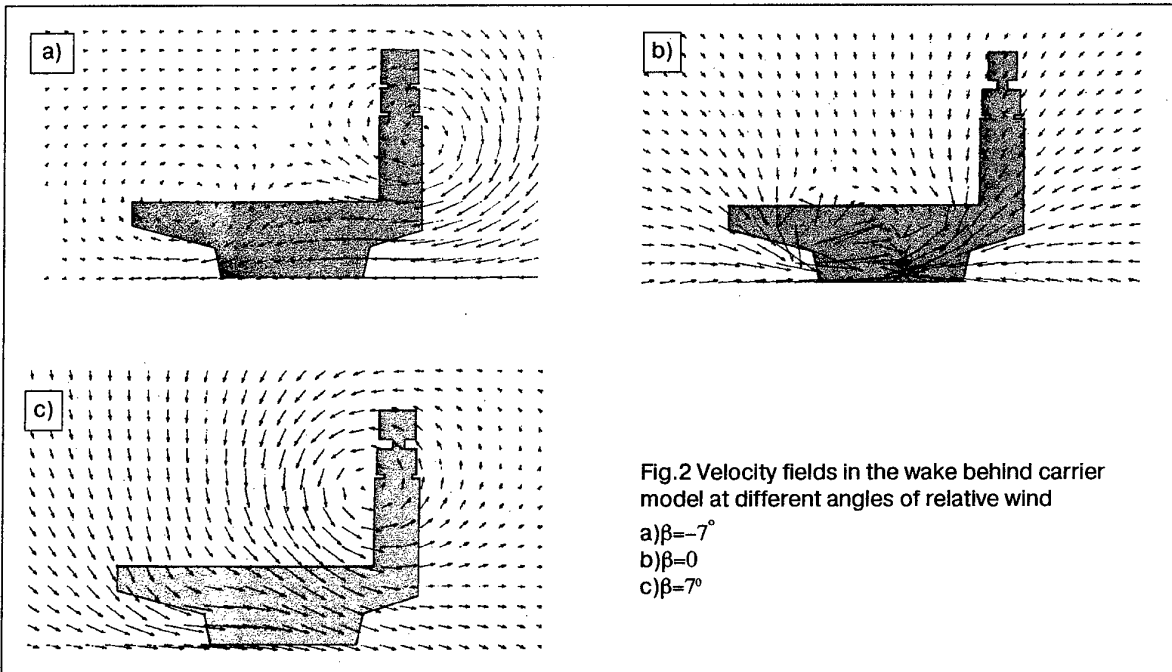
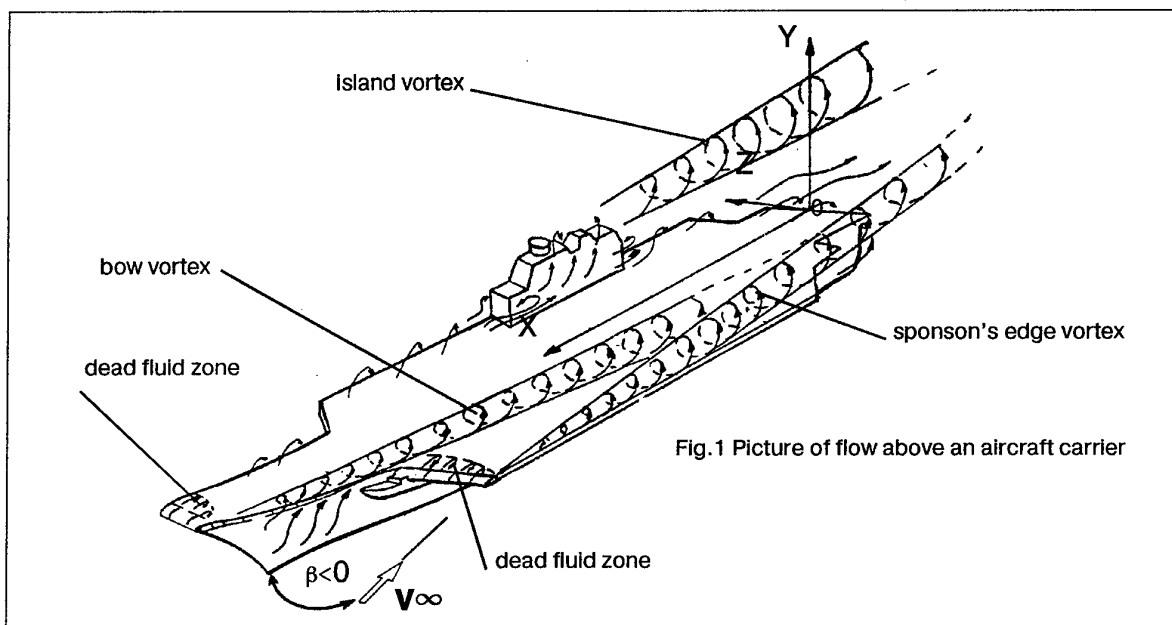
CONCLUSION

The developed methodology of investigations of disturbed air flow over deck and in wake behind aircraft carrier became important result of whole complex of the works. Some test facilities, software and model technology were created. Practical experience was obtained in development of measures for ensuring of flow parameters required for safe operation aircraft from concrete ships of given class.

Almost decennial experience of trouble-free drill operation of deck fighters Su-33 on aircraft-carrier «Admiral Kuznetsov» confirmed, in particular, correctness of recommendations of TsAGI, developed on base of model experiments.

Generalization of accumulated materials formed base for development of requirements to architecture of perspective aircraft carriers with group and single basing of aircraft.

Developed in TsAGI methodology of estimation and refinement of external conditions of basing of marine aircraft was used also at decision of the same questions, connected with operation of helicopters from military and civil ships and marine drilling platform.



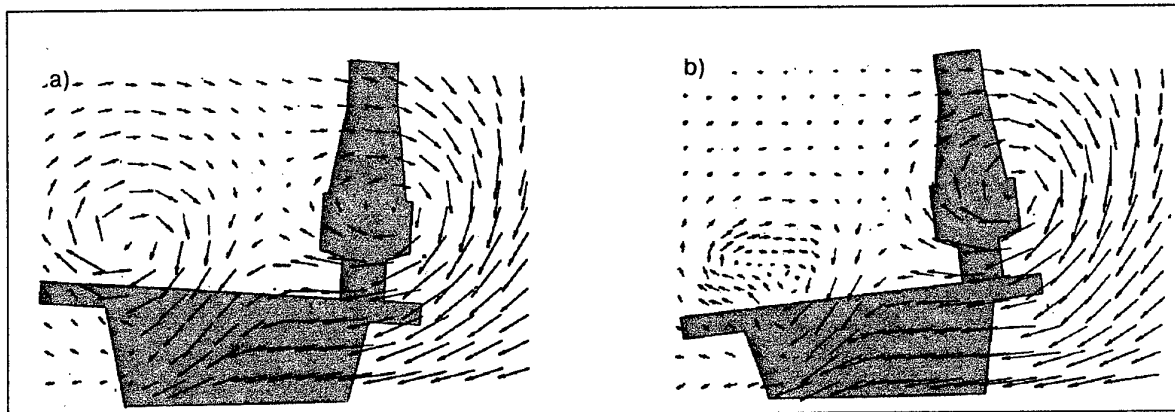


Fig.3 Velocity fields in cross-section at $X = -0.1L$ and $\beta = -7^\circ$
a) at heel on the starboard b) at heel on the port

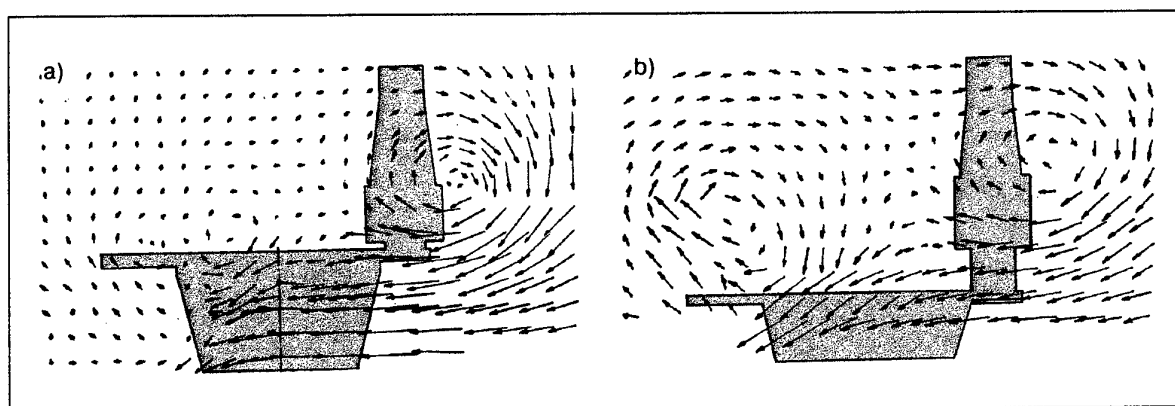


Fig.4 Velocity fields in cross-section at $X = -0.1L$ and $\beta = -7^\circ$
a) at trim $\psi = -1.5^\circ$ by the bow b) at trim $\psi = 1.5^\circ$ by the stern

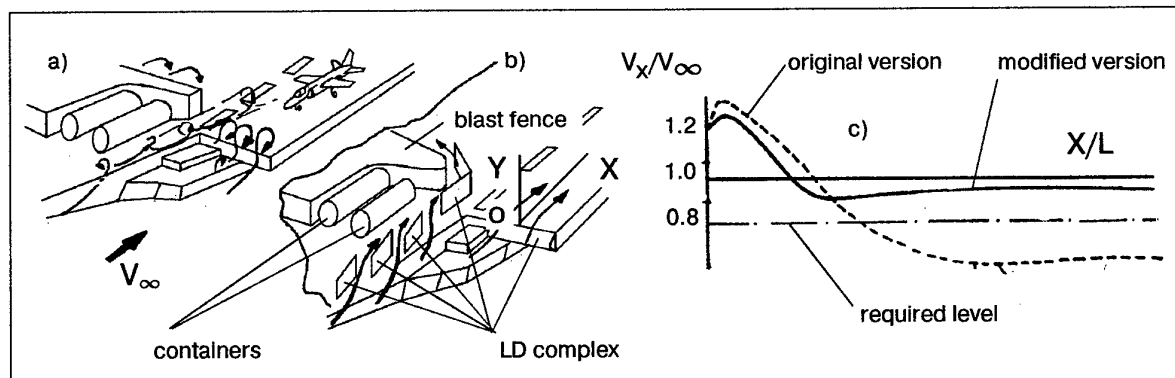


Fig. 5 Scheme of fore part of flight deck neighbourhood of HACC «Minsk»
a) original version, b) modified version, c) comparision of flow parameters over deck original and modified versions

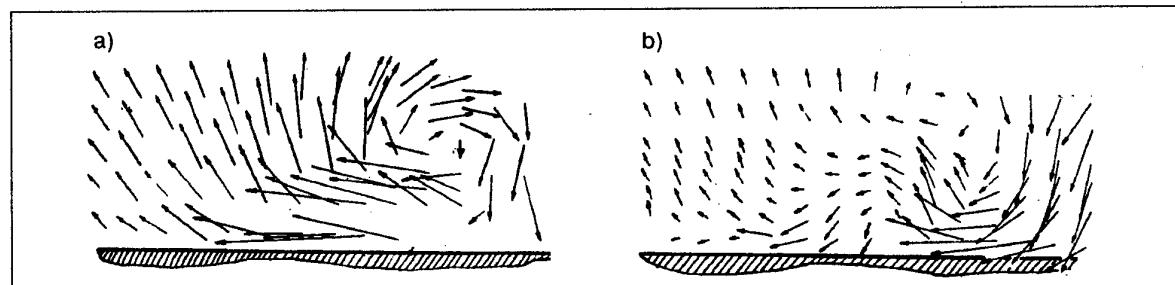


Fig.6 Flow field over flight deck of HACC «Minsk» model $\beta = -4^\circ$
a) original version b) modified version



Fig.7 Heavy aircraft carrier cruiser «Admiral Kuznetsov»

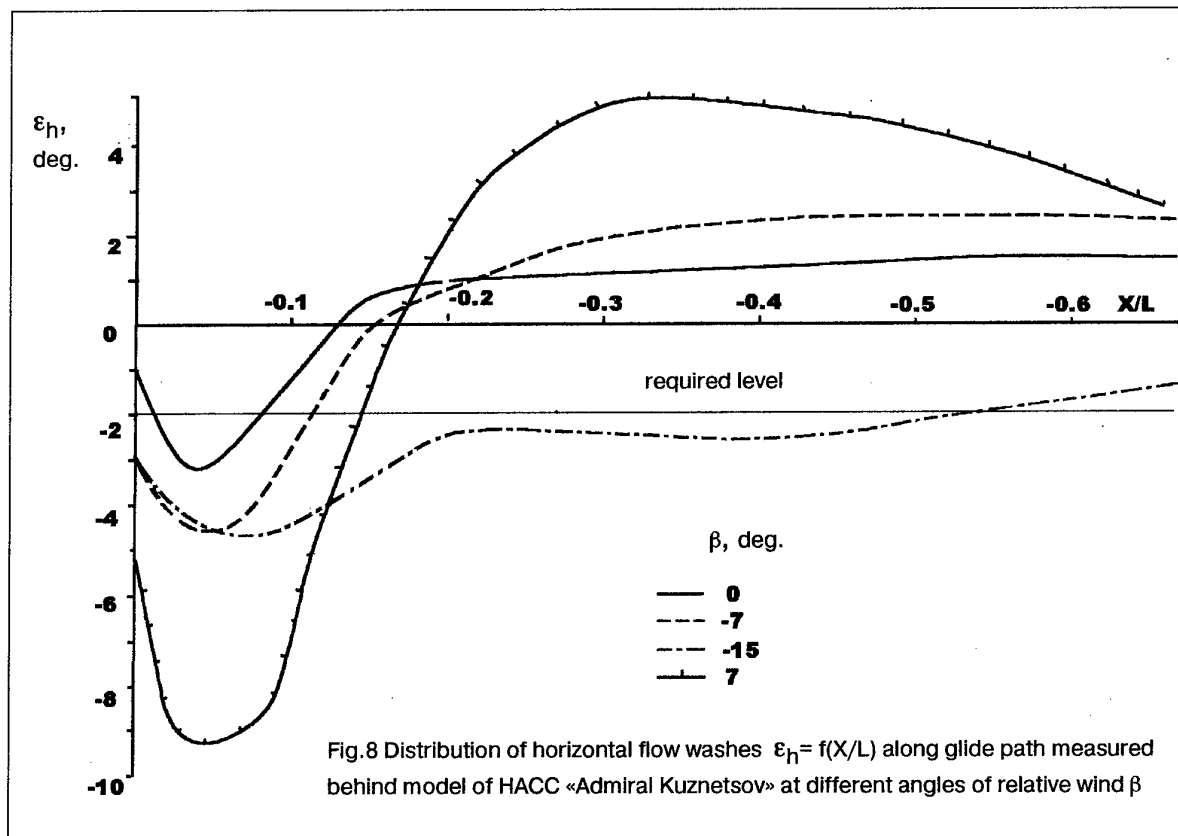


Fig.8 Distribution of horizontal flow washes $\epsilon_h = f(X/L)$ along glide path measured behind model of HACC «Admiral Kuznetsov» at different angles of relative wind β

Simulation Tools in the Calculation of Aircraft-Ship Interface Operational Limits

Application des outils de simulation pour le calcul des limites opérationnelles de l'interface dynamique aéronef-navire

Dr. Bernard de FERRIER
 Engineering Manager, Dynamic Interface Program
 Bombardier Services
 Arlington, Virginia U.S.A.

Bernard LANGLOIS
 Senior Test Engineer, Dept. 870 (UAV)
 Bombardier Services
 Mirabel, Québec Canada

Abstract

Helicopters operating from small ships are limited in the maritime environment by high winds and rough seas. In addition, man-made obstacles, such as, hangar wall generated turbulence, ship stack hot gas motor ingestion, inappropriate deck lighting and markings limit helicopters. Dynamic Interface (DI) is defined as the study of the relationship between an air vehicle and a moving platform. It is performed to reduce risks and maximize operational flexibility. Countries with a large number of platforms conduct DI testing as a matter of necessity. An analytic approach to helicopter/ship dynamic interface testing is presented.

A brief synopsis of the theory and calculation of the ship motion simulation program is presented. The Ship Motion Simulation (SMS) Model is derived from the relationship between the wave and ship motion spectrum. It incorporates seakeeping philosophy and applies various definitions of seaway spectral formulation. SMS defines a seaway, computes the hydrodynamic and hydrostatic forces imposed on a ship (defined as the product of its transfer function and the seaway) and calculates a resulting ship time history. The simulation is an extensive treatment of a floating object's response to the dynamic loads on its structure.

The application of ship motion simulation as a developmental operational tool is introduced. The primary application of the SMS is in operational simulation such as aircraft launch and recovery; deck handling; and flight readiness or availability. The Aircraft/Ship Interface Simulation (DI) is a mathematical description of conditions limiting the availability of an air vehicle. Factors affecting an air vehicle on a moving platform are primarily ship motion; wind-over-deck; ship airwake turbulence; and deck conditions (wet, dry, oily obstructed, etc). Sample helicopter/ship interface operational limits or envelopes are discussed. Spin-off projects into other fields of growth, such as visual aids, are developed.

Ferrier et Langlois sont diplômés de l'École Polytechnique de Montréal.

Sommaire

Le bilan de l'évolution d'une simulation du mouvement de navire et son application dans la simulation de l'interface dynamique aéronef-navire est ici présenté. Les opérations d'hélicoptères à bord de navires autres que les porte-avions sont limitées, en général, par des vents et de la houle. Ces deux facteurs sont la cause principale du mouvement irrégulier de la coque, mouvement à six degrés-de-liberté dont plusieurs peuvent être couplés. Sur le pont, il en résulte un écoulement extrême de l'air provoqué par des gradients de vitesse violents (rafales) et par la turbulence atmosphérique. Ces conditions climatiques maritimes sont à l'origine des contraintes opérationnelles et des facteurs de base des études de l'interface dynamique aéronef-navire. L'interface dynamique est définie comme étant les relations entre un véhicule aérien et une plate-forme en mouvement. Les études de l'interface dynamique sont réalisées afin de minimiser les risques opérationnels en maximisant la flexibilité tactique d'un système aéronef-navire.

Les facteurs pouvant limiter la disponibilité d'aéronef sont le mouvement du navire, la turbulence sur le pont, l'effet de sillage provoqué par l'écoulement autour de la superstructure et les conditions physiques du navire, soi les différents obstacles ou l'état du pont. La réponse du navire est définie par la résistance créée par la houle lors du passage du navire. La simulation du mouvement du navire est basée sur les caractéristiques spectrales du navire et de la mer. Le spectre de réponse est le produit des fonctions de transfert et du spectre de la mer définie dans le cadre du spectre rencontré. En simulation d'interface dynamique, une limite est définie au moment où un incident est identifié. L'incident est défini par un renversement en roulis ou en tagage de l'appareil, un glissement du train d'atterrissement sur le pont ou l'indication d'un décollage non contrôlé. Un incident peut être identifié au moment de l'atterrissement, du décollage ou du transfert de l'hélicoptère entre le hangar et l'extérieur. Des exemples du calcul des enveloppes opérationnelles sont présentés ainsi que d'autres applications telque les aides visuelles.

Introduction

Helicopters operating from small ships are limited in the maritime environment by high winds and rough seas. In addition, helicopters are limited by man-made obstacles, such as, hangar wall generated turbulence, ship stack hot gas motor ingestion, inappropriate deck lighting and markings. Dynamic Interface (DI) is defined as the study of the relationship between an air vehicle and a moving platform. It is performed to reduce risks and maximize operational flexibility [1]. Countries with a large number of platforms conduct DI testing as a matter of necessity. The American Navy matrix alone accounts for over a dozen VTOL/VSTOL manned and unmanned vehicles and more than 20 classes of aviation capable ships [2]. Recent and near future capital acquisitions by medium sized navies, such as in France, Britain and Germany, have increased interest in DI. The purpose of this paper is to present highlights of the analytic approach to dynamic interface testing and application.

Dynamic Interface Studies

Brief Overview

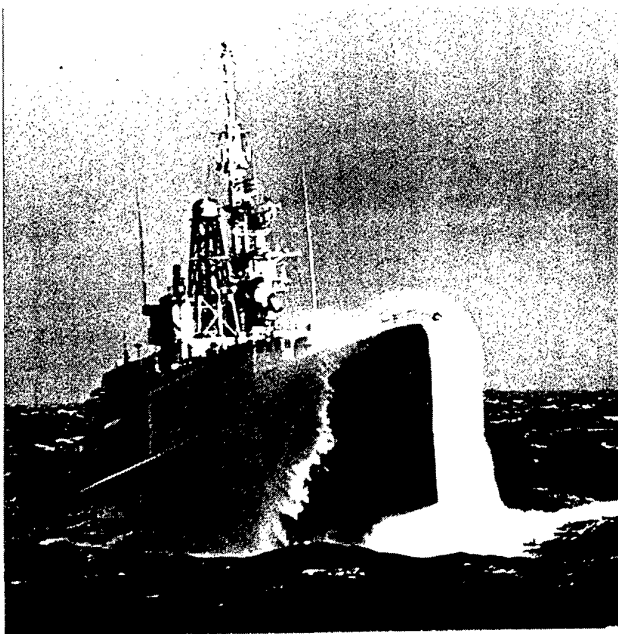
Dynamic Interface is divided into two broad categories: experimental or at-sea measurement and analysis, and analytical which is concerned with mathematical analysis and solution [3]. The methods are not mutually exclusive. Neither method alone can produce a comprehensive and timely solution of the DI problem.

The traditional approach is experimental DI. Experimentation investigates operational launch and recovery of vehicles, engage and disengage of rotors, vertical replenishment and helicopter in-flight refueling envelopes. "Shipboard suitability testing" assesses the adequacy, effectiveness, and safety of shipboard aviation. Testing methodologies and procedures have been standardized by laboratories, such as, Naval Air Warfare Center (Patuxent River, USA), DCN Toulon (France), and DRA Bedford (UK). While

experimental testing has numerous objectives, the primary activity is on launch and recovery envelope development and expansion. Launch and Recovery tests are rated by the pilot on an accepted scale, such as, the Pilot Rating Scale (PRS). The pilot assess workload resulting from aircraft control margins, aircraft flying qualities, and performance in the shipboard environment [4]. Other experimental analysis are (but not limited to): aviation facility evaluation and deck handling.

DI analytics use mathematical modeling and simulation to support flight testing. Simulation can be used to help define operational limits of any air vehicle/ship combination by:

1. simulating any kind of ship motion and ship motion condition.
2. simulating any kind of air vehicle over and on the deck.
3. simulating any kind of retention or handling system, such as, RAST and SAMAHE.
4. simulating any kind of environment natural and artificial (degraded modes).



While analytics may seem less taxing to the DI study process, it cannot replace experimentation. Envelope studies will always require physical verification.

Ship Motion Simulation

An important DI analytical tool is the Ship Motion Simulation (SMS) which was initially developed by Peter J.F. O'Reilly between 1973 to 1984 for the United States Navy. The program methodology uses spectral probabilities in order to produce deterministic synthetic time histories.

SMS Theoretical Synopsis

The Ship Motion Simulation (SMS) Model is derived from the relationship between the wave and ship motion spectrum [5]. It incorporates seakeeping philosophy and applies various definitions of seaway spectral formulation, such as, Bretschneider [6]. SMS defines a seaway, computes the hydrodynamic and hydrostatic forces imposed on a ship (defined as the product of its transfer function and the seaway) and calculates a resulting ship time history. The simulation is an extensive treatment of a floating object's response to the dynamic loads on its structure.

SMS is divided into two basic themes, spectral analysis and the calculation motion histories in the time domain. The SMS fundamental relationship is:

$$S_r = S_w(w) \cdot RAO \cdot f(V, m) \quad (1)$$

where:
 S_r : Ship response spectrum
 $S_w(w)$: Seaway spectrum
RAO: Ship transfer functions
 $f(V, m)$: Frequency mapping
 V : Velocity
 m : Relative wave angle

SMS can apply various definitions for the seaway. One of the most common is the definition called the Bretschneider, which is given by:

$$S_w(w) = \frac{483.5}{w^5 T_g^4} H_s^2 e^{-\frac{1994.5}{w^4 T_g^4}} \quad (2)$$

where:
 T_g : period (sec)
 w : wave frequency (rad/sec)
 $S_w(w)$: seaway spectrum ($m^2 \cdot sec$)
 H_s : significant wave height (m)

The spectral characteristic of a vessel is defined in the SMS by experimental or computational developed transfer functions termed Response Amplitude Operators

(RAO). The response amplitude operators define the dynamic ship responses for a specified load/operating condition [7].

The ship response spectrum is created as the product of the RAO and the driving sea spectrum (figure 1) over the entire range of frequencies. The response spectrum is reduced to sets of harmonic components for each degree-of freedom. Synthetic time histories are created stochastically by summing the harmonic components over a given time period. A typical time history equation is given by:

$$A_z = \sum_{n=1}^k (A_{zn} \cos(w_n t - e_{zn})) \quad (3)$$

where

A_z : DOF amplitude
 w : a circular frequency
 e : phase angle

Time histories are produced by the sum of 48 synthetic functions ($k=48$). Figure 2 displays a typical time history trace. In summary, the Ship Motion Simulation creates deterministic measures of ship motion from a probabilistic spectrum.

Aircraft/Ship Interface Simulation

The primary application of the SMS is in operational simulation such as aircraft launch and recovery; deck handling; and flight readiness or availability. The Aircraft/Ship Interface Simulation (DI) is a mathematical description of conditions limiting the availability of an air vehicle. Factors affecting an air vehicle on a moving platform are primarily ship motion; Wind Over Deck; Ship Airwake Turbulence; and deck conditions (eg: wet, dry, oily, obstructed).

An example of DI analysis involves deck handling. In DI the limitations can be defined as the point at which an aircraft/ship incident occurs. Incident means an occurrence of aircraft turnover, pitchback or on-deck slide at any point from touch-down to hangar stowage and back to launch. Deck handling studies determine turnover limits, sliding freedom, tiedown forces, traversing factors, and pitch back limitations.

DI Theoretical Synopsis

Motion of an aircraft on the flight deck is calculated in terms of ship motion as a function of the aircraft model. The aircraft model is considered an extension of the ship. The model is defined by its landing gear footprint; deck location and orientation; aircraft weight and inertias, center of gravity, lateral drag area and center of pressure. The aircraft experiences ship transferred forces and

moments which create rectilinear and angular accelerations on the air vehicle. The accelerations can be numerically integrated to determine the position and attitude of the helicopter relative to the ship as function of time, for various ship motions [8]. In essence, the aircraft is displaced as the sum of all forces to which it is exposed

The inertial loads at the helicopter center of gravity induced by ship motion is given by;

$$\begin{aligned} F_{ix} &= W * A_{Xcg} \\ F_{iy} &= W * A_{Ycg} \\ F_{iz} &= W * A_{Zcg} \end{aligned} \quad (4)$$

where,

$$\begin{pmatrix} F_{ix} \\ F_{iy} \\ F_{iz} \end{pmatrix} = \text{inertial forces due to ship motion}$$

W = aircraft weight

$$\begin{pmatrix} A_{Xcg} \\ A_{Ycg} \\ A_{Zcg} \end{pmatrix} = \text{accelerations}$$

In the longitudinal, lateral and vertical directions, these inertial loads become:

$$\begin{pmatrix} X \\ Y \\ Z \end{pmatrix} = \begin{pmatrix} T_{11} & T_{12} & T_{13} \\ T_{21} & T_{22} & T_{23} \\ T_{31} & T_{32} & T_{33} \end{pmatrix} \begin{pmatrix} F_{ix} \\ F_{iy} \\ F_{iz} + W \end{pmatrix} \quad (5)$$

where: $T_{ij} = T(\phi, \theta, \psi)$ (transformation matrix from ship's axis system to horizontal level/vertical axis system).

and

$$\begin{aligned} \phi &= \text{roll} \\ \theta &= \text{pitch} \\ \psi &= \text{yaw} \end{aligned}$$

Next, a wind force is added to the ship motion induced forces. In the Ship Motion Simulation, an unidirectional continuous wind model, whose vector is in the same direction as the seaway, is applied. The wind vector is defined by its magnitude (V_{wod}) and its direction (Ψ_{wod}). To compute the lateral force applied at the aircraft Center of Pressure due to the wind, the V_{wod} is resolved along the normal to the aircraft center line ($V_{w, long}$ and $V_{w, lat}$). The lateral component is used to compute the lateral force, as follows:

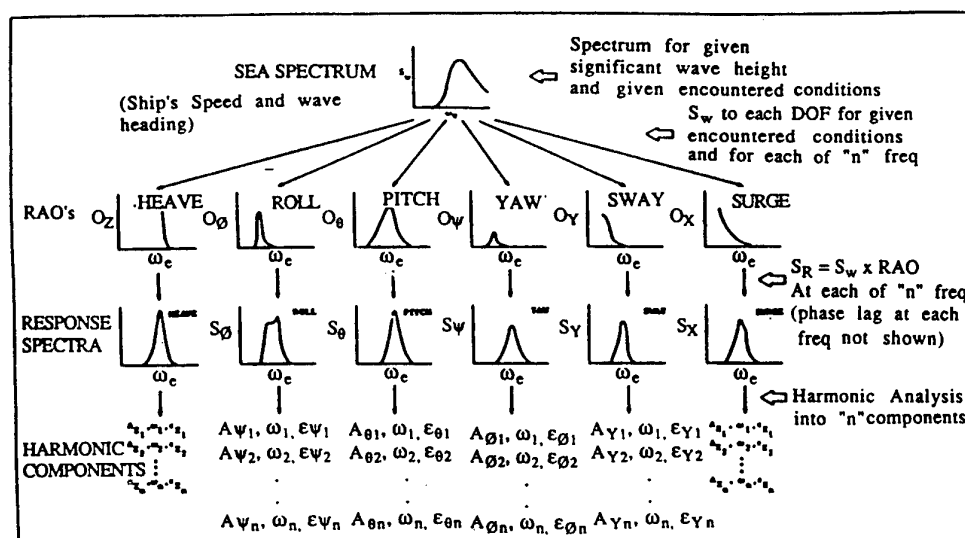


Figure 1 - Ship Motion Simulation Flow Diagram

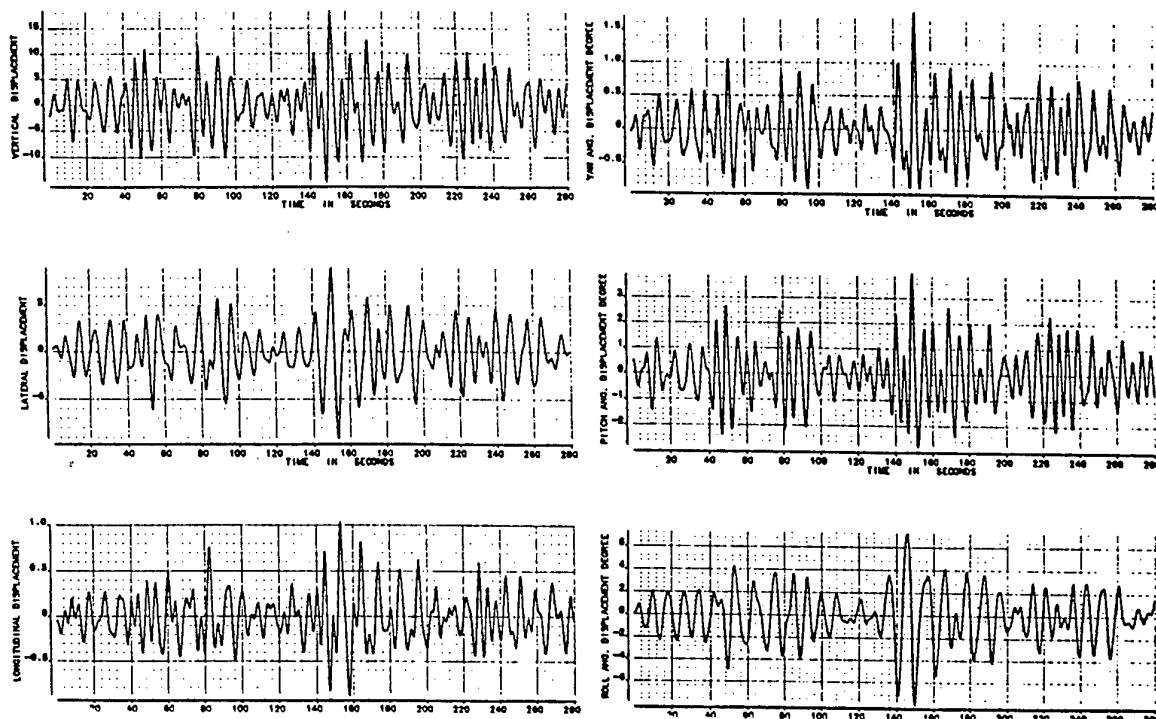
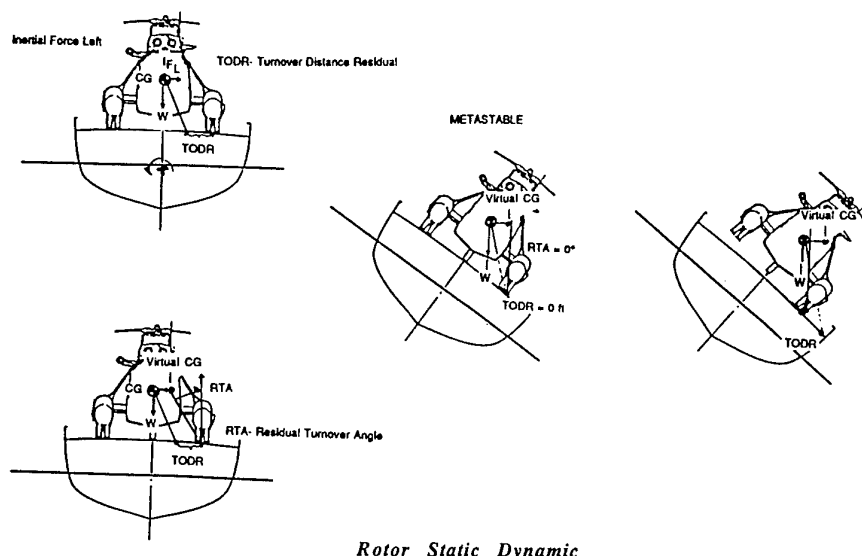


Figure 2 - Typical Time History Trace



*Rotor Static Dynamic
Turnover*

$$F_{W_y} = 3.5 A_y \left(\frac{V_{W_{lat}}}{100} \right)^2 \quad (6)$$

where: A_y = Aircraft projected area normal to the $V_{W_{lat}}$ component
 F_{W_y} = Lateral force applied at the aircraft center of pressure due to wind

The axial forces on the main landing gear due to the wind force F_{W_y} is given by:

$$FRMG_{WIND} = (F_{W_y}) \frac{(WL_{CP} - WL_G)}{(L_{BL} - R_{BL})} \quad (7)$$

where:
 $FRMG_{WIND}$ = Main Gear (right) axial force
 F_{W_y} = Wind lateral force component
 WL_{CP} = Center of pressure waterline
 WL_G = Ground waterline
 L_{BL} = Left wheel butteline
 R_{BL} = Right wheel butteline

The incremental aircraft roll due to the wind is given by:

$$\Delta\phi(WIND) = \tan^{-1} \left(\frac{FRMG_{WIND}}{(K)(L_{BL})} \right) \quad (8)$$

where: K = spring constant

Axial forces on the main landing gear due to aircraft inertial forces in the plane of the main gear, is given by:

$$FRMG_{(Inertie)} = Y \left(\frac{WL_{CG} - WL_G}{L_{BL} + R_{BL}} \right) \quad (9)$$

where:
 WL_G = Center of gravity waterline
 $FRMG_{(Inertie)}$ = Right main gear axial force due to the lateral inertial force Y defined in equation (5).

Assuming perfect rocking, the axial force on the left main gear is vectorially opposite to the force acting on the right main gear:

$$FLMG_{(Inertie)} = -FRMG_{(Inertie)} \quad (10)$$

where: $FLMG_{(Inertie)}$ = Left main gear axial force

The incremental aircraft roll due to inertial loads is determined by:

$$\Delta\phi_{(Inertie)} = \tan^{-1} \left(\frac{FRMG_{(Inertie)}}{(K)(L_{BL})} \right) \quad (11)$$

The simulation model assumes a constant wind, therefore, $\Delta\phi_{(wind)}$ is constant throughout the simulation run. However, $\Delta\phi_{(Inertie)}$ is continuously changing with ship motion. The total incremental change in the aircraft roll with respect to the ship is given by:

$$\Delta\phi_{(total)} = \Delta\phi_{(vent)} + \Delta\phi_{(inertie)} \quad (12)$$

Deck conditions, eg: dry or with substances, such as, water or oil, is a variable in the program. This parameter affects aircraft stability by changing the coefficient of friction between the aircraft landing gear and the deck. Aircraft handling systems are handled much in the same way. A maximum value of the encountered force load or geometric ship position is preprogrammed. When either force loading or ship angular position is greater than the manufacturer's design limits, an aircraft incident is registered. The aircraft operational limit is produced owing to the break-down of the aircraft handling system.

Scenarios are programmed for the "worst case" condition. For the greatest landing gear deflection, nose gears are modelled unlocked and castored for turnover. The model is lined up with the ship centerline and is rotated on the deck to find the least stable, but realistic, orientation (figure 3).

Referring to figure 3, the 'worst case' hinge line on the flight deck about which the aircraft will turnover are defined by Rto and Lto (right turnover and left turnover). Each line is computed from its main gear position to the nose gear swivelled for turnover. The azimuth of these two lines are then determined with respect to the ship's longitudinal axis, AZ_{Rto} and AZ_{Lto} .

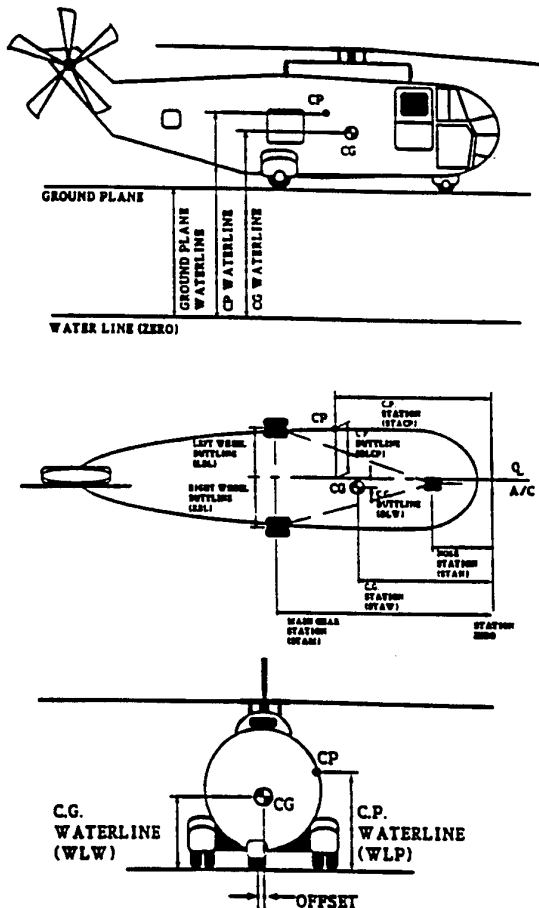
The distance from the aircraft center of gravity (CG) to each line is computed as $TODR$ and $TODL$ (right and left). They define the distance that the CG should move for a turnover to occur (right or left). These lines describe an angle TOR (right) or TOL (left). They are expressed as:

$$\leftarrow TOR = \tan^{-1} \left(\frac{TODR}{WL_W - WL_G} \right) \quad (13)$$

$$\leftarrow TOL = \tan^{-1} \left(\frac{TODL}{WL_W - WL_G} \right) \quad (14)$$

They describe the angle between a vector from the CG normal to the Rto and the Lto and the vertical.

Similar boundaries are computed for the pitchback condition. The hinge line about which the aircraft is likely to pitchback is the line which joins the right to left main gear. The distance from the CG to the hinge line is defined as PBD (pitchback distance) and expressed as:



$$PBD = (CG_x - MG_x) \quad (15)$$

where,

PBD = pitchback distance

CG_x = aircraft CG station

MG_x = aircraft main gear station

The associated pitchback angle or PBA is given by:

$$\text{PBA} = \tan^{-1} \left(\frac{MG_x - CG_x}{WL_w - WL_g} \right) \quad (16)$$

where,

WL_w = Waterline to the aircraft CG

WL_g = Waterline to the ship deck

Turnover incidents are static or dynamic in character. Static turnover is the same as on shore. The resolved weight vector migrates beyond either the friction forces causing the aircraft to displace or the reaction forces causing the aircraft to turnover. Dynamic turnover caused by the rotor disk (uneven loading of the rotor) or

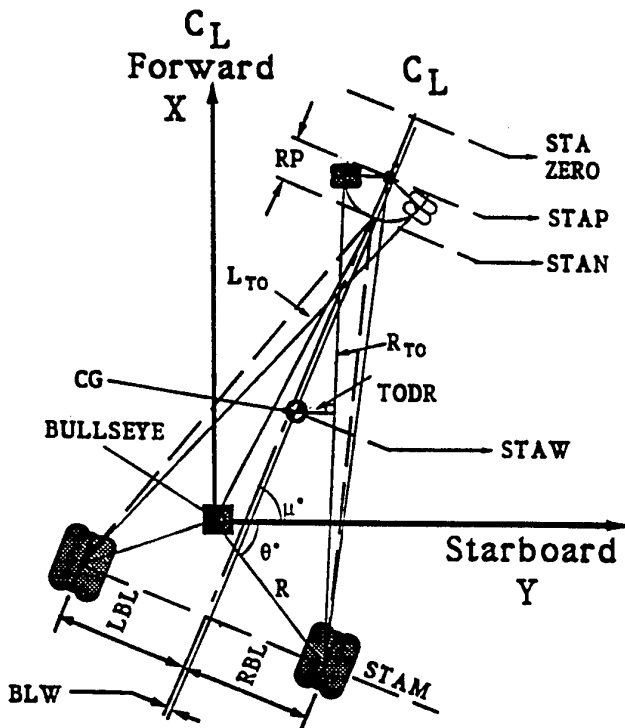


Figure 3 - Aircraft Model Definitions

by ship motion, the same phenomena occurs. The aircraft center of gravity is in motion. In the sum of forces, the weight vector is continually modified in response to inertial forces applied by either the rotor disk or ship motion or both. The distances TODR, TODL, and PBD essentially reflect system stability. At the point where a distance becomes negative, the system is unstable and will seek to find a more stable, but usually undesirable geometric solution. In similar fashion, when the landing gear friction values are exceeded by the combination of aircraft apparent weight and induced inertial forces, slippage will occur. Aircraft slide will continue until the aircraft frictional forces are greater than the disturbing inertial forces. Finally, when the vertical inertial force equals and opposes the aircraft weight, the deck friction goes to zero and an unintentional liftoff is indicated. The sum of these incidents trace aircraft-ship operational envelopes.

Calculation of Aircraft/Ship Operational Limits

The objective of analytic DI is to identify operational envelopes for launch and recovery, deck handling and general flight readiness or availability. The intention of analytical DI is not to replace experimental DI but to

compliment the activity. Once operational envelopes are calculated, DI test engineers would randomly verify selected data points in and out of the envelope. Ship speed, relative wave heading, significant wave height and modal period are the primary ship motion markers. A typical test matrix is furnished in table (1).

Ship Velocities:	05, 10, 15, 20 knots
Wave Angles:	0 - 180°, every 15 degrees
Sig. Wave Height:	1, 3, 6, 9 metres (Equivalent Sea State ~ 3, 5, 6, 7)
Modal Period:	5, 9, 11, 15 seconds
<i>additional matrix attributes</i>	
Deck Condition:	DRY and WET (water) (Coefficients) 0.8 0.5
Wind-Over-Deck:	0 - 50 knots

Table 1 - Typical Test Matrix

Several studies have been achieved by the Bombardier, Inc Canadair Defense Systems Division's Dynamic Interface Office for the Direction des Constructions Navales (DGA France). Several aircraft were modelled with high center of gravities and corresponding minimum mission weights. The air vehicles were modelled both secured and unsecured on the deck with rotors spread and free to rotate and fuselages unfolded and locked. The helicopters are modelled centered at the bullseye. The landing gear deflection and forward gears are modelled unlocked and castored for turnover. The aircraft are set on the ship's centerline and rotated to -20 degrees to provide the least stable orientation.

In the examples which follow, envelopes are based on limitations defined by the point at which an aircraft/ship incident occurs. Incident means occurrence of aircraft turnover, pitchback, ondeck slide or uncontrolled liftoff. At any point during a simulation analysis an incident is identified, the entire data point is declared out-of-limit. Interface testing is performed according to the test matrix indicated in table (1). Deck safety rondelles are created as a function of ship velocity and deck condition deck condition (figure 4). Areas within the shaded areas are inside operational limits. The bow of the ship is along the principal axis to the right out to 0 degrees relative wave angle. Each concentric ring relates a relative wave height and significant wave height. All cases are tested in seas ranging from 1 to 9 meters, 180 degrees in bearing (by symmetry 360 degrees) and a maximum of 50 knots wind-over-deck.

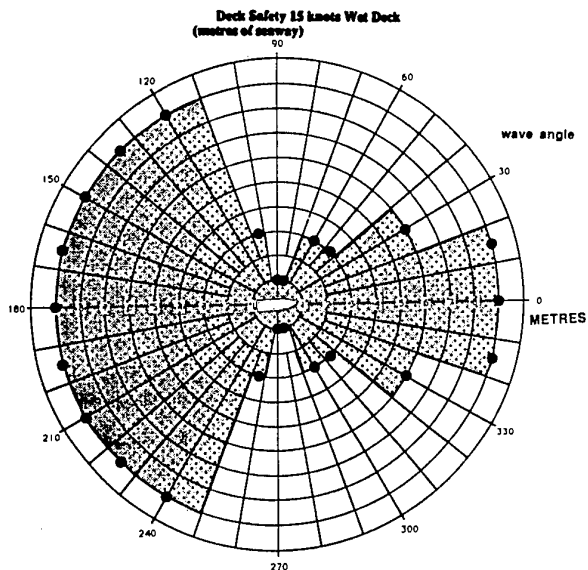


Figure 4 - Sample Deck Envelope

A comparative operational limit sample between various aircraft on the same ship is presented in figure (5). Here the models A and B show better limits than helicopter C for the same ship conditions.

Rondelles maybe used to indicate encountered loads as presented in figure (6). Here the shaded zone indicates air vehicle exposed force loads as a function of a given ship's velocity, and significant wave height. For example, the rondelle shows increased encountered loads at 75 degrees relative wave angle. In the following seas conditions, as one would expect, encountered loads are minimal.

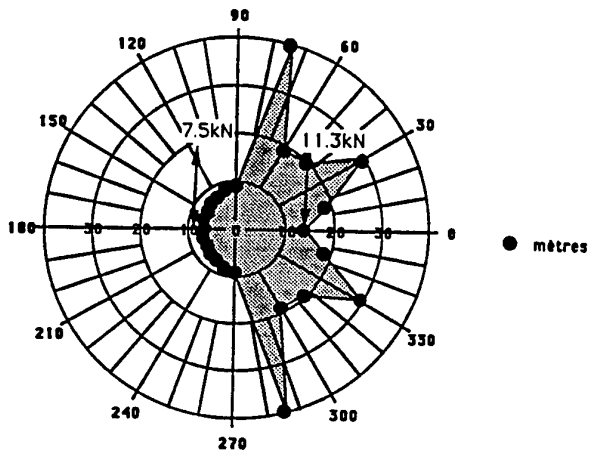


Figure 6 - Encountered force loads

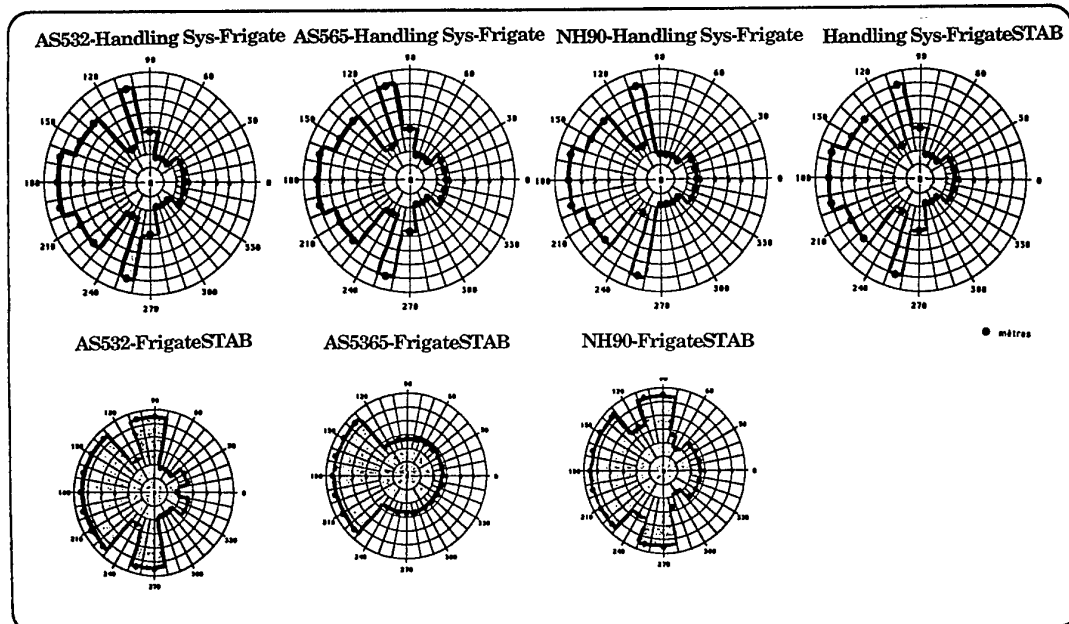


Figure 5 - Comparative Operational Limits

Real-Time DI Applications, Visual Aids
 Application of DI tools to the operational environment has produced numerous real-time improvements. One such improvement is the CL352 Landing Period Designator (LPD) helicopter landing aid. The LPD supplies real-time information about the motion of any vessel as a function of helicopter operational limits. The system furnishes this information about any kind of aircraft in any sort of sea condition on any sea vessel. LPD is designed to reduce pilot workload in completing ship interface activities by improving operational security in the reduction of helicopter hover time.

The LPD may show improved recovery opportunity from its ability to identify the onset of quiescent ship motion periods. This ability is based on ship motion as a function of the mechanical and dynamic limits of the helicopter. These limits are expressed by a scalar empirical formulation, termed, the energy index. The index identifies ship quiescence using displacement, velocity and acceleration terms. In short, the index furnishes information of the motion a ship must travel in the near-term future. This does not suggest that the index is predictive (using historical information to extrapolate into the future). Rather, it capitalizes on the rate at which a vessel can displace due to natural hydrodynamic forces as a function of the structural and dynamic characteristics of the approaching air vehicle.

The energy index is an empirical formulation designed to convert ship motion characteristics, aircraft structural dynamic limits, and user experience into a

meaningful value. The index is modular in design with the capacity of incorporating other parameters (e.g.: wind-over-deck module) to improve energy index significance and applicability. The Energy Index equation of LPD Mk III measures lateral, vertical velocities and accelerations as well as roll and pitch angular displacements and velocities weighted by dynamic coefficients. The equation in the Mk III is the sum of the squares of the various parameters and terms representing real-time ship/aircraft interface motion.

$$EI = a_1 \dot{y}^2 + a_2 \dot{x}^2 + a_3 \dot{z}^2 + a_4 \ddot{z}^2 + a_5 \dot{f}^2 + a_6 \dot{q}^2 + a_7 q^2 + a_8 \dot{q}^2 \quad (17)$$

(where a_1, a_2, \dots are weighted dynamic coefficients)

As indicated in equation 17, the index contains acceleration, velocity and displacement terms which determine the motion of the ship in the near future. The LPD code calculates the rate at which a vessel can displace due to natural hydrodynamic forces against the structural and dynamic operating limits of the matching air vehicle. The energy index uses eight parameters roll and pitch, their rates, lateral and vertical velocities and accelerations. All of the parameters are weighted by dynamic coefficients which are weighted according to the individual degree-of-freedom, the coupled degrees of freedom and normalized according to aircraft characteristics. The remaining two degrees of freedom (yaw and surge) are monitored for motion within certain limits and may be incorporated more actively later if warranted. The degrees of freedom, viz: roll, pitch, lateral, and vertical, are considered the most important for motion sensitive tasks (in particular launch and recovery of air vehicles).

Methodology for Coefficient Calculation

The calculation of dynamic coefficients is performed in three distinct steps executed simultaneously. In the first step, relative coefficients are established between each of the following four degrees of freedom and their derivatives. A relationship is derived for roll angle and roll rate, pitch angle and pitch rate, lateral velocity and lateral acceleration, and vertical velocity and vertical acceleration. These relationships are directly related to the ship's velocity, the relative wave angle, the significant wave height and the modal period.

$$A = \begin{bmatrix} A_1 \\ A_2 \\ A_3 \\ A_4 \\ A_5 \\ A_6 \\ A_7 \\ A_8 \end{bmatrix} = \left\{ \begin{array}{l} A_{11} \cdot A_{12} \cdot A_{13} \\ A_{21} \cdot A_{22} \cdot A_{23} \\ A_{31} \cdot A_{32} \cdot A_{33} \\ A_{41} \cdot A_{42} \cdot A_{43} \\ A_{51} \cdot A_{52} \cdot A_{53} \\ A_{61} \cdot A_{62} \cdot A_{63} \\ A_{71} \cdot A_{72} \cdot A_{73} \\ A_{81} \cdot A_{82} \cdot A_{83} \end{array} \right\} \quad (18)$$

The degrees-of-freedom that are considered highly coupled are roll and lateral motion and pitch and vertical motion. Coupled means that the degrees-of-freedom are directly related and can only occur independently in very special cases. Pitch and vertical motion usually occur together though rarely in phase. The phase lag between coupled degrees-of-freedom contribute to the stability of the energy index. A maximum in pitch will often occur some time, t , BEFORE the coupled peak in vertical displacement.

The third step compares the aircraft limitations scale completing the calculation of the appropriate weights of each degree-of-freedom. The product of the element coefficients A_{11}, A_{23} , (see eq.18) produces the energy index coefficients in real-time. The energy index is then calculated and compared to the established threshold (green, yellow, red) scale the results of which are communicated to the user.

The flow-chart of the energy index is presented on figure 7.

Methodology for Energy Index 'Motion Zone' Calculation

The meaning of the index value has been the object of much investigation. To be applicable, the quantity must reflect a physical state of the aircraft/ship combination in a given sea condition. For expedience, the scale is initially divided into four 'deck security' or 'availability' zones similar to the 'Pilot Rating Scale' (PRS) [9]. The definition of each deck security zone is normally refined during initial LPD sea trials.

The energy index value is analogous to the level of kinetic and potential energy contained in the ship.

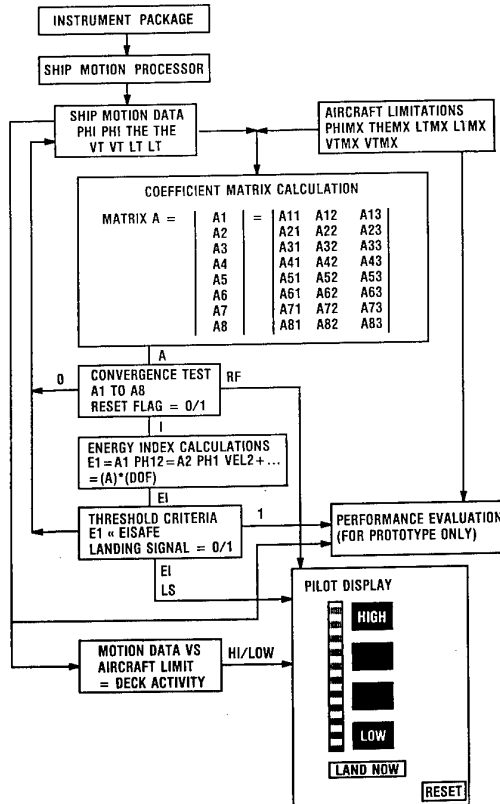


Figure 7 - Landing Period Designator Components

When the index is low the ship is stable and the ship motion is small. When the index value is below the danger threshold the landing deck motion is acceptable for aircraft activity. The ship can only displace from a stable to a high risk condition by the introduction of certain quantity of energy from the sea. For a given condition, time necessary to raise the deck from a stable to an unavailable condition can be derived experimentally from the calculation of the maximum Elmax. For the mass of a Destroyer class of ship, this measure is about 5 seconds. For a FFG-7 or Type 23 class ship, during normal environmental conditions, this minimum measure is about 4.5 to 5.0 seconds. Exceptions to this rule occur when encountering longitudinal propagating, high energy intensity wave fronts such as those created by an earthquake or weapon explosion.

The deck availability, as defined by the deck security zone criteria, is directly based on the ship characteristics (measured), aircraft limitations (defined), and pilot-in-loop factors (see figure 8). Deck motion security limits must be established for each combination of helicopter and ship. These limits may be measured

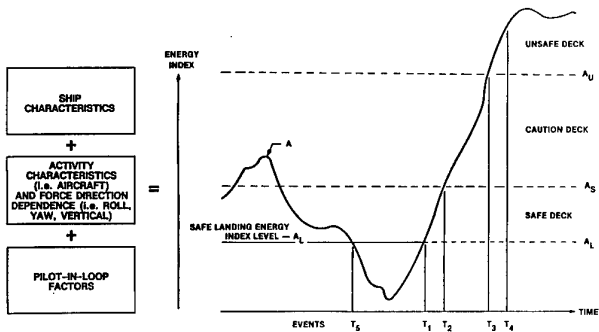


Figure 8 - Threshold Criteria

experimentally or calculated analytically. A limit is defined by the impact that a certain ship motion condition may have on the structural integrity or dynamic response of a given helicopter. If the condition exceeds an operational specification, a limit condition is identified. The sum of these limits produces a red line that is drawn on the energy index scale for a given ship.

All energy index values under the red line infer acceptable deck motions. The red line is absolute. In a red light helicopter recovery, one or more DOFs have exceeded acceptable aircraft limits. Therefore, deliberately assigning the red line several scalar points under the calculated absolute limit is a prudent if not conservative measure. The deck is available for aircraft activity under the red line. However, in order to capitalize on ship physical motion constraints, the operator must await a flashing green signal. The energy defined for a flashing green condition infers that the potential energy being transferred from the sea into the ship's structure is not sufficient to displace the ship into a red line condition in under some specified period of time.

Simulator and at-sea testing have been conducted by the US, British and German navies. The primary analysis after concluding that the LPD performed as per specification was to compare recoveries with and without the LPD. Figure 9 displays this result for both day and night, with and without the LPD.

Differences were detected between LPD day and night, and again between no LPD day and night calculated from a common way-point to the ship deck. Height over the deck and energy index traces were used (see Figure 4.3 for an example). From the data, night recoveries take on average about 50 seconds longer than day landings (other parameters held constant). During the day without the LPD, flights lasted on average almost as long as night recoveries with LPD. Night landings without the LPD took more than 25 seconds longer to complete than the same mission with the LPD.

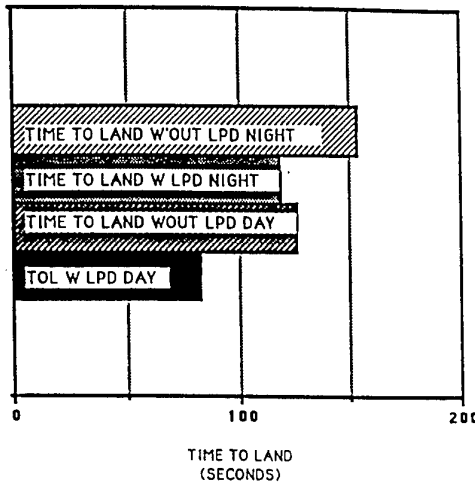


Figure 9 - Time to Land from Common Way-point

CONCLUSION

The overall objective of dynamic interface study is to determine the maximum safe air vehicle/ship platform operational limitations. Given an air/ship system and inherent operational limitations, DI strives to increase tactical flexibility for any set of environmental conditions. Analytic study is used to rapidly delineate system limitations. The calculated system limitations provide experimental DI with the necessary data to more effectively set testing strategy to probe the limiting conditions.

REFERENCES

- [1] Healey, J. Val (1986). Simulating the Helicopter-Ship Interface As An Alternative to Current Methods. NPS67-86-003. Naval Postgraduate School. Monterey.
- [2] Carico, D (1988). Proceedings of the First DI Working Group Meeting. DI-NAWC. Patuxent River.
- [3] Ferrier, B & Semenza, J (1990). NATC Manned Flight Simulator VTOL Ship Motion Simulation and Application. Proceedings of the AHS. Washington.
- [4] Ferrier & Semenza (1990).
- [5] St. Denis & Pierson, W (1953). On the Motions of Ships in Confused Seas. Transactions of SNAME. Vol 61. New York.
- [6] Bretschneider, C. L (1959). "Wave Variability and Wave Spectra for Wind-Generated Gravity Waves". Beach Erosion Board. U.S. Army Corps of Engineers. Technical Memo No: 118. Washington.
- [7] Baitis, A. E; Meyers, W. G; Applebee, T. R (1976). "A Non-Aviation Ship Motion Data base for the DD963, CG26, FF1052, FFG7 and the FF1040 Ship Classes". DTNSRDC Report. SPD-738-01. Washington.
- [8] Blackwell, J and Feik, R. A (1988). "A Mathematical Model of the On-Deck Helicopter/Ship Dynamic Interface (U)". Aerodynamics Technical Memorandum 405. Aeronautical Research Laboratory. Melbourne.
- [9] Ferrier & Semenza (1990).

Piloting of a VTOL-UAV to Shipboard Recovery

C. Reboulet(*) P. Mouyon(*) de Ferrier, Dr. B(**) Langlois, B. (***)

(*)ONERA/DCSD, 2 Av. Ed. Belin, 31055 TOULOUSE cedex(France)

(**)Bombardier Services Corporation, 1111 Jefferson Davis Hwy # 510
Arlington, Virginia 22202-4306 (USA)

(***) Bombardier, Canadair Defense Systems Division 10000 rue Cargo A4
Mirabel (Quebec) Canada J7N 1H3

Abstract

A system of guidance and control ensuring the safe recovery of a VTOL type unmanned air vehicle is described. The key ideas of the proposed approach are the estimation of the velocity/position with respect to the ship in a quasi-inertial coordinate frame and the guidance/control of the air vehicle to a virtual target (predicted position of the landing grid). The advantage of this guidance and control approach is the complete decoupling of the UAV from ship motions. The various methods used in each module of the whole recovery system are presented, including: tracking, filtering, and landing deck position prediction. Modul performances based on test results are discussed. Strategy chosen in the development of the whole automated recovery system is described. Finally, an assessment of the proposed concept obtained by simulation is provided. These results show that this approach is more robust than conventional motion sensitive techniques. The system promises to dramatically increase UAV operational limits and recovery efficiency. This activity is sponsored by the Délégation Générale de l'Armement (DGA France) and was accomplished within the framework of a Franco- Canadian collaboration project between ONERA-DCSD and Bombardier, Inc (Canadair).

1 Introduction

This article summarizes a study defining an automatic shipboard recovery system for a VTOL Unmanned Air Vehicle (UAV). A shipboard manual operator does not have all the information necessary to ensure secure vehicle recoveries. The operator can, for example, identify the effects of wind gusts only after the gust has displaced the vehicle. The operator can only interpret shipborne movements with some degree of accuracy. Experience has shown that manual recoveries are made with considerable difficulties in seas greater than sea state 3. In addition, data has demonstrated that

automatic recoveries are required in seas greater than sea state 4. Current automatic recovery systems generally use a tracking system to recover an air vehicle to the ship deck. The ship deck position being assessed only at the instant of recovery. These systems are driven by hardware solutions limited by the guidance system's capacity to judge accurately the relative position and velocity between the air vehicle and the ship. The guidance/piloting system's objective is to recover the air vehicle to the deck bullseye based on data received from the tracking system. The recovery system advantage is its basic simplicity. However, its performance is directly related to the sea condition. In essence, UAV accelerations are equal to or greater than that experienced by the ship. The UAV automatic pilot must be at least as rapid as sea generated perturbations. It is easy to understand why bullseye centred recoveries are difficult in agitated seas. As the seas become more agitated, recovery becomes increasingly difficult. In seas greater than sea state 5, practically impossible to have recoveries with a reasonable margin of safety. The system presented below attempts to avoid the problems described above by an approach considerably different than that of traditional systems.

2 Design of the system

The automatic recovery system concept proposed combines certain essential hardware and software elements. The system is based on two essential ideas (see figure 1).

In the first instance, the data being handled originates from the ship's inertial navigation system. This furnishes the information to characterize the vessel in the quasi inertial reference system. When resolved, it formulates a coordinate system describing the ships trajectory of movement. This is the reference system that is used in describing that data that is subsequently accumulated. The reference system is applied to UAV tracking, guidance and control. This requires that the state vector (which consists of a velocity vector and an

UAV positioning vector) be reassembled in the new reference system. The primary advantage of this system is to pilot the vehicle based on control laws unaffected by ship's random movement.

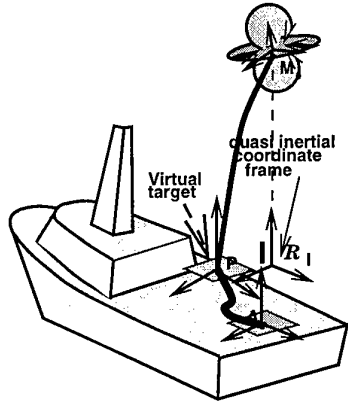


Figure 1: Proposed approach

The second essential element is a spatial definition of the bullseye which is used to guide the UAV to its centre. This is contrary to the instantaneous definition of the bullseyes used by traditional systems. The proposed system calculates the virtual position of the bullseyes which is independent of sea created ship perturbations. This methodology is described below.

An important advantage to this approach is that the guidance and the flight control modules are decoupled from the perturbations caused by ship motion. It is reasonable to assume that this approach can be considered more robust than that of the classic recovery systems. This approach, however, will have an important impact on the architecture of the system. The primary structural modification is the creation of various data streams coming from several data sources defining the deck attitude.

3 Tracking UAV

The technique of data fusion used is illustrated in figure 2. The illustration is of an autoland architectural system using a proposed sensor arrangement necessary for continuous vehicle tracking. Two optical sensor receivers provide angular positioning. The vehicle may be tracked using angular sensors.

Using only angular information in a similar way that radar is used, it is possible to determine the position of the UAV relative to the ship. This alone is insufficient. The definition must be converted to the quasi inertial reference system. It is for this reason that the information originating in the ship's inertial navigation system is combined with that from the UAV

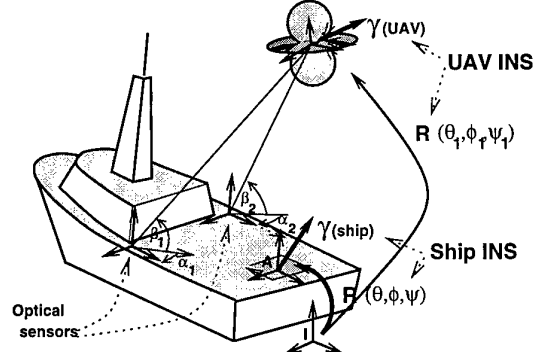


Figure 2: Sensor architecture

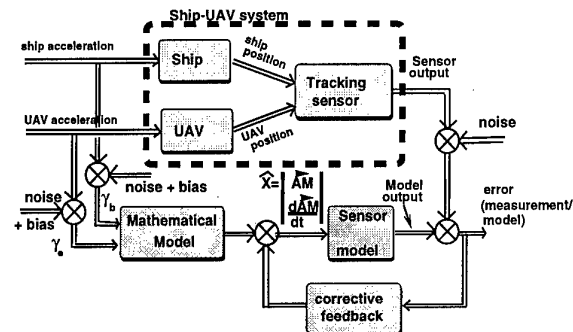


Figure 3: Data fusion method

inertial navigation system. INS data used are essentially accelerometric and vehicle orientation converted into the inertial reference system.

The problem is to determine the components, based on these data, of the AM vector and its derivative located in the inertial reference system (see figure 1).

Several methods may be used to track the vehicle. A method based on pseudo-measurement techniques was presented in [1], other techniques may, however, be used. The data handling methodology used is classic. This is illustrated in figure 3.

When the ship averaged accelerations are considered as input (originating from the inertial navigation system), the helicopter-ship system responds. The output is the definition of the relative position of the vehicle as function of the ship. The air vehicle position is measured by a device, such as, an optical or radar tracking system. The mathematical model which describes the system is composed of: model describing the state of the vehicle and ship (state variable model) and a model describing the tracking system. These calculated measurements are compared with actual measurements from the tracking system. The equations defining the position of the UAV are those of a classic

Kalman filter. At every step the state vector is corrected by true measures which are a function of the variation between calculated and measured values of the system.

It is known that the data provided by the tracking system (optical, for example) are excellent in the long term but are relatively noisy. On the other hand, the information provided by accelerometers are more accurate in the short term while drift is an important factor in the long term. Excellent results are produced when combining these two types of data collection systems. By using this technique, the reconstruction of the state vector is just as easily calculated in the ship's reference frame as in the inertial coordinate system. However, the latter is preferred since it allows decoupling of the vehicle command and control system from ship motions. Figure 4 is a flow diagram for the modelling of this system.

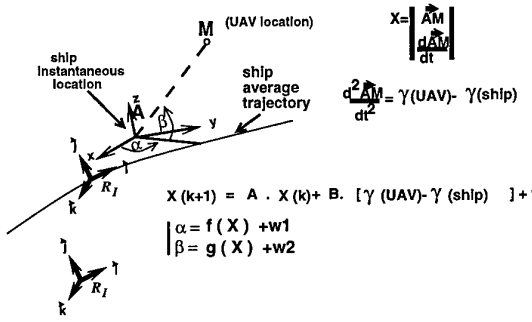


Figure 4: State representation

An Extended Kalman Filter is used to calculate the state vector used by this model. The results are displayed in figure 5. The first part of the curves are produced by vehicle tracking made by a relative GPS with a RMS of $0.5m$ and a sampling rate of $120ms$. The second part of the curves represent vehicle tracking made with 2 optical antennae providing a RMS of $0.002rd$. The noise from accelerometer signals is estimated to be $0.1m/s^2$.

All that remains is the calculation of the ship position in the inertial frame. A classic data filtering technique is used which provides the ship position as a function of the average R_I which is related to the trajectory. From the transformation of the R_I frame to the inertial frame (which may be accomplished as a first approximation) the position of the vehicle can be deduced as a function of R_I . It is this order of value what will be used in the vehicle piloting cycles.

4 Various strategies

Various strategies for vehicle shipboard recovery may be considered. Referring to figure 1. There are many

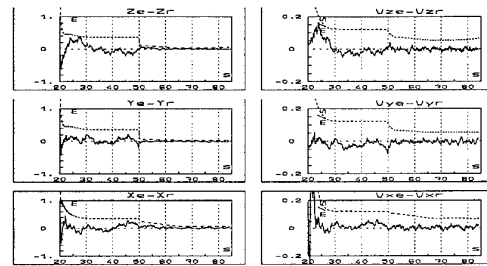


Figure 5: Kalman filter results

choices to make: the recovery point is defined as the terminal point of the guidance recovery trajectory. The optimal beginning of the final recovery phase must likewise be defined.

4.1 Choosing the virtual bull's-eye

As discussed earlier, the system does not use an instantaneous definition of the recovery bullseye. This definition is used by traditional recovery systems with limited performance results (particularly in higher sea states). The UAV is unable to follow the ship's motions in agitated seas. The purpose of this module is to predict the location and attitude of the bullseye at the moment of UAV touch-down. This decouple the calculation from random ship deck excursions.

Several methods may be considered in the calculation of the virtual bullseye. The simplest method is to take the average of the position of the bullseye over some period of time. This method was not selected since its precision is limited in higher sea conditions. Average motion calculations could in agitated seas produce amplitudes greater than the dimensions of the flight deck.

The strategy selected uses the unique characteristics of a VTOL particularly in its capability to hover over the deck. It is feasible to place the descending vehicle on station hold at various points during its recovery phase. It is possible to program the descent phase in advance. This last comment is important because this differentiates between the classical fixed wing UAV recoveries from that of a VTOL UAV. It is difficult to predict with precision the exact moment of recovery for a fixed wing UAV. For a VTOL UAV, it is possible to predetermine the length of time the recovery phase will be. It is also possible, using a control law, to predict the position of the virtual landing deck at the exact moment of recovery. It is difficult to implement but creates a much more preferable system.

4.2 Virtual bull's eye position prediction

The calculation methodology begins with a five minute ship motion time history in the x, y, z directions (surge, sway, heave). The autoregressive ship model (see figure 6) is derived from classic least squares techniques.

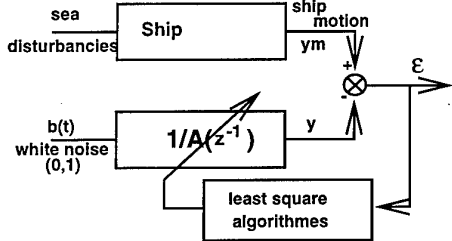


Figure 6: Identification scheme

This model is used to predict the location of the bullseye at the instant of recovery. The deck position is calculated with a model defining each of the three degrees-of-freedom mentioned earlier. Consider a discrete-time single-input-output plant governed by the equation:

$$y(k) = \frac{1}{A(q^{-1})} b(k)$$

where

y output sequence (ship motion)

b sequence of independent random variables

k current time

q forward shift operator $q^k y(m) = y(k + m)$ introduced by Astrom.

It is noted that the model $A(q^{-1})$ is valid at any given instance. This calculation must be completed 5 secondes prior to the beginning of the vehicle descent.

The position of the deck is given by $k + m$ where m is the position prior to the instant of recovery. This is given by the expression:

$$y(k + m) = \frac{1}{A(q^{-1})} b(k + m)$$

rewriting the equation

$$y(k + m) = X(q^{-1})b(k + m) + Y(q^{-1})y(k) \quad (1)$$

$X(q^{-1})$ and $Y(q^{-1})$ correspond to the minimal solution

with respect to X of the following polynomial equation:

$$A(q^{-1})X(q^{-1}) + q^{-m}Y(q^{-1}) = 1 \quad (2)$$

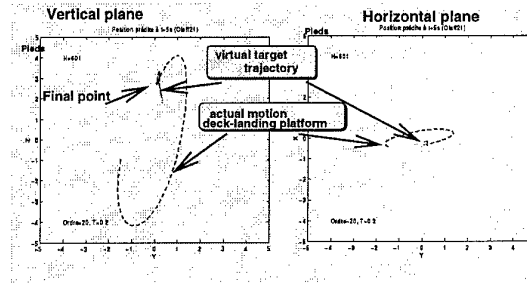


Figure 7: Virtual bull's-eye trajectory

The first term of the right side of equation 1 cannot be calculated since at k instance, the random sequence $b(k+1), \dots, b(k+m)$ is unknown. At the inverse the outputs $y(k), y(k-1), \dots$ have been already observed. Thus, considering the situation at time k , the best prediction for the output $y(k+m)$ is given by:

$$\hat{y}(k+m/k) = Y(q^{-1})y(k)$$

It is the term used to predict the location of the deck.

In summary, it is necessary to pre-calculate all the polynomial $Y(q^{-1})$. It is important to remark that each values of $Y(q^{-1})$ are only valid for a considered time m . The calculation may be made off-line based on ship motion characteristics.

Figure 7 displays the performance of this approach. The left portion represents motion in the vertical plane while the right part indicates motion in the horizontal plane. The dotted graph displays the flight deck motion while the heavy lined graph represents the virtual bullseyes trajectory during the landing phase.

4.3 Selecting the recovery moment

The second point consists of selecting the optimal instant that guarantees a safe recovery. A calculation is made using an energy index which determines the period where ship motion is below a level which ensures a safe deck. In brief the Landing Period Designator (LPD) is a helicopter recovery aid which calculates ship motion as a function of helicopter operational limits. The energy index collapses ship and helicopter limits into a scalar value while retaining the physical significance of the helicopter ship system. The energy index is constructed such that 4 energy states are described. The lowest energy state (very safe) guarantees the aircraft operator a quiescent flat deck for a delayed period of time consistent with basic principles of Newtonian mechanics. For more details on the LPD, please refer to [2].

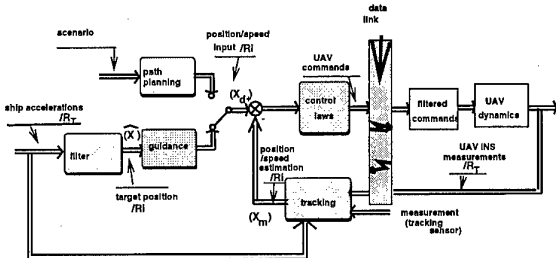


Figure 8: System general architecture

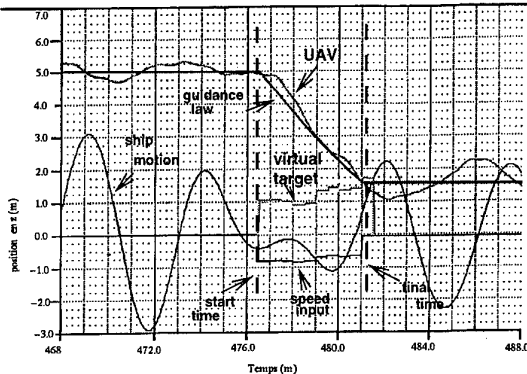


Figure 9: automatic deck-landing results

5 System general architecture

The system architecture is shown by figure 8. The tracking module reconstructs the state vector from information furnished by the ship and air vehicle inertial navigation system and a tracking system (such as GPS, radar, etc). This approximate state condition is used by the control laws module to map the vehicle in cartesian space.

The path planning module generates the flight path trajectory in the final approach phase. This module brings the air vehicle to the hover station at 400meters above the flight deck. From the hover station, the flight guidance module descends the air vehicle to the virtual bullseye's position. The inertial navigation data filter module has two functions:

- The first operational function is to detail the reference coordinate system related to the average ship trajectory. It is a reference coordinate system that can be regarded as quasi-inertial related to the duration of the landing phase (note R_I this reference coordinate system). The coordinate orientation is known from the ship inertial navigation system. There remains the calculation of its vertex. This is obtained by the use of a high pass filter.

The second function is to calculate the virtual bullseye in the R_I reference frame. This is based on

the prediction laws described above. The coordinate system defined by R_I is paramount in the autorecovery system. It serves to pilot the UAV to the predicted position of the deck.

Each of the modules described above were tested by simulation individually and assembled into a completed system. Figure 9 represents the strategy described earlier. At the onset of recovery the UAV is normally located in hover at 5m above the deck. At 476.5seconds the LPD signals that the deck is very safe and a quiescent period has begun. At that moment the motion predictor calculates the location of the virtual bull's-eye at the moment of touch-down. The guidance law fixes a descent trajectory which permits recovery within 5seconds. At each calculation update (several times/second), the virtual bull's-eye's position is corrected. The descent slope must be likewise corrected in order to respect the 5seconds recovery time.

It is noted that as the prediction time is reduced, the prediction is improved. The flight commands to the UAV are of paramount importance in the first instants. It is for this reason that the prediction estimates need to be good early in the process. After hundreds of simulation cases, the deck prediction error, even in the heaviest seas, rarely surpassed 50cm.

6 Autoland test results

Simulation studies of the entire system were performed using an AD-100 combined with a VAX3500 workstation. The program includes a six degree-of-freedom simulation model of the dynamic and mechanical definitions of the UAV. Transfer function models of various ship classes are included, as well. The simulation program contains an environmental model which defines shipmotion, winds and sea conditions.

The automatic recovery algorithms were programmed along with a model representing the Landing Period Designator (see reference 3 for details) which identifies shipmotion quiescent periods for vehicle recovery.

The simulation objective was to assess the performance of the entire system in various conditions of agitated seas. A test matrix was programmed showing seas from sea state 3 to 8. This included various mechanical conditions including loss of tracking system, and so forth.

The assessment of system was based on a set of criteria which examined UAV tilt on recovery, distance from the centre of the recovery grid, relative horizontal and vertical velocities. The statistical analysis of the results provided an estimate of the feasibility of an automatic recovery as defined above.

From the studies it can be concluded that safe recovery can be achieved in seas upto and including sea state 3. Between sea state 4 to 6, test results show that

the prediction technique well within acceptable parameters (none of the success criteria failed). In higher sea states, the only failed recoveries occurred owing to exceeded vertical velocities. This infers that a vertical rate predictor should be included in the final system.

7 Conclusion

The purpose of this article was to describe the design of an automatic recovery system for a VTOL type Unmanned Air Vehicle. From simulation results several tracking systems are possible. Two systems were considered. One tracking system used two optical receivers while the other used a radar tracking system. The results were comparably acceptable. Simulations results, however, favoured the optical tracking system, in spite of the known problems associated with its use in the maritime environment. Data handling fusion techniques from several optical receivers may adequately compensate for the deficiencies noted. An architecture using a redundant optical tracking system is an acceptable tracking technique. From simulation results optical tracking system failures may occur during the most critical phase of the vehicle recovery. Using redundant systems, it is highly unlikely that both tracking systems would fail at the same time. The costs involved, however, must be equally considered. In addition, unlike radar systems, optical tracking systems are not confronted with the problems associated by multipath. Careful trade-off analysis is necessary when deciding on the components of the autoland system.

What ever the technology chosen, data fusions techniques used in this study were achieved using Kalman filter applications. The Kalman filter application reduces the tracking error to under 20cm permitting the system to be a feasible solution.

The deck prediction module is considered indispensable to ensure safe recoveries in agitated sea conditions. The module calculates the virtual location of the recovery deck at the precise moment of touchdown. Simulation results supported deck recoveries under 50cm from the centre of bullseye. It is important to recall that the primary advantage of the autoland system proposed its robust character and its capability to operate even in agitated seas beyond sea state 6. Preliminary analysis has shown the system to be feasible. The task at hand validate the system is by assembling and testing the system at-sea.

References

- [1] B. de FERRIER, and C. REBOULET. "Conception et développement d'un système d'apportage maritime automatique d'un véhicule générique de type

VTOL" *AGARD CONFERENCE PROCEEDINGS 591*, pp 25/1-25/8, (1996).

- [2] B. de FERRIER, and J. SEMENZA. "Development, Simulation, and Testing of the Landing Period Designator (LPD) Helicopter Recovery Aid" *Proceedings of the American helicopter Society, May 1994, Washington*
- [3] B. de FERRIER, B. LANGLOIS, F. BERGERON, C. REBOULET, V. FUERTES, J-C. BARRAL. "The design and test using simulation techniques of an automated UAV-VTOL shipboard recovery system" *Proceedings of the American helicopter Society, May 1998, Washington*

Motions and Added Resistance due to Waves of Surface Effect Ships

Joost C. Moulijn
 Delft University of Technology
 Ship Hydromechanics Laboratory
 Mekelweg 2
 2628CD Delft
 THE NETHERLANDS

Summary

This paper presents a computational method for motions and added resistance due to waves of Surface Effect Ships. The computed added resistance only includes the added resistance of the air cushion. This added resistance component was believed to be the largest. The results of the computational method are compared to experimental results of MARIN and to results of new experiments which are carried out at the Ship Hydrodynamics Laboratory of Delft University of Technology.

The computed motions and cushion excess pressures agree well with the MARIN results. The computed added resistance is however much smaller than the added resistance that was measured by MARIN. This discrepancy was the major reason for the new experiments.

The aim of the new experiments is to get insight into the magnitude and origin of added resistance of SESs. The new experiments are still in progress at the time this paper had to be delivered. This paper presents therefore only some first results of these experiments. The new experiments show that the added resistance of the air cushion is not large. The new results for added resistance are reasonable agreement with the computational results.

1 Introduction

Up to now Surface Effect Ships (SESs) or air cushion supported catamarans were mainly operating in sheltered waters. In these days however both naval and civil operators show an increasing interest in large SESs sailing in open seas. The seakeeping of an SES is quite different from the seakeeping of a conventional ship. SESs appear to have a large speed loss when sailing in waves. The design of large SESs requires therefore an accurate prediction method for motions and added resistance due to waves.

A Surface Effect Ship is a hybrid of a catamaran and a hovercraft. An air cushion is enclosed by the side-hulls, the deck, the water surface and flexible seals at the bow and stern. Figure 1 presents a longitudinal cross section of an SES. Most of an SES's weight is carried by the air cushion. The remainder is carried by the buoyancy of the hulls. Some air will leak from the cushion through gaps under the seals. This leakage flow is compensated by a system of fans. Most SESs have a bag-type stern seal; a bag of flexible material which is pressurized at a slightly higher pressure than the air cushion. The bag is open to the sides where the seal plenum is closed by hulls. One or two internal webs restrain the aft side of the bag, thus dividing the bag into two or three lobes. The bow seal of SESs is usually of the finger type; a row of loops of flexible material which are open to the cushion side.

Several authors presented studies on motions of Surface Effect Ships. Kaplan and Davis[1] presented one of the first papers on motions of SES. Kaplan et al.[2] developed a non-linear six degree of freedom motion program. Doctors[3] presented an extensive overview of the hydrodynamics of hovercraft and SES. Sørensen[4], Steen[5] and Ulstein[6] published extensive studies of the high frequent motions of SES; the so called *cobblestone effect*. Nakos et al.[7] showed that these high frequent motions are caused by acoustic resonance of the air inside the cushion. The cobblestone effect causes SESs to have a poor ride quality. The present paper does not deal with the cobblestone effect.

Only very little literature can be found on the topic of added resistance due to waves of SESs. Faltinsen et al.[8] presented a comparative study on the speed loss and operability of a catamaran and an SES in a seaway. They did not however include the added resistance due to the air cushion. The result of the study is that the SES has a slightly larger speed loss than the catamaran. Ehrenberg[9] states however that an SES has much less speed loss in waves than a comparable catamaran. Kapsenberg[10] measured a large added resistance due to waves. He also showed that the usual quadratic rela-

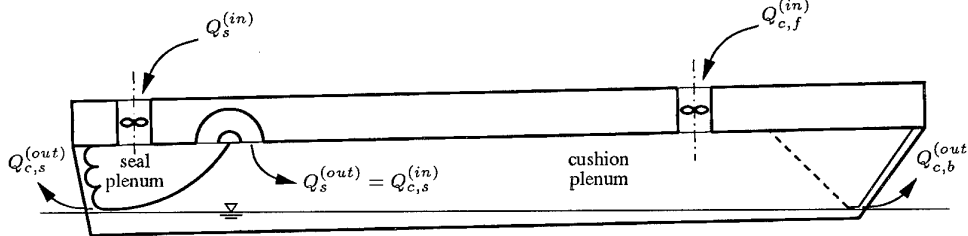


Figure 1: Longitudinal section of a Surface Effect Ship

tion of added resistance with wave height does not hold for an SES.

The main goal of the present PhD research project is to investigate how one can accurately compute the motions and added resistance due to waves of SESs. This paper presents results of a new computational method for motions and added resistance due to waves of SESs. These results are compared to the results of experiments that were carried out by Kapsenberg[11] at MARIN. The computational results are in good agreement with the MARIN experiments as far as motions and cushion pressure are concerned. The large added resistance due to waves that was measured at MARIN does not however follow from the computations. New experiments have been carried out at the Ship Hydromechanics Laboratory of Delft University of Technology. These experiments give new insights into the origin of the added resistance due to waves of SESs.

The next section presents a description of the new computational method for motions and added resistance due to waves of SESs. Section 3 describes the new experiments that were carried out at Delft University of Technology. Section 4 presents and compares the computational results, the experimental results of MARIN and some new experimental results.

2 Computational method

This section presents the computational method for motions and added resistance due to waves of Surface Effect Ships. Up to now the method is only suitable for head and following waves as only heave and pitch motions are considered. The effect of surge motion is neglected. Nevertheless most of the theory is presented for six degrees of freedom.

Consider an SES sailing in waves at a forward speed U . The vessel carries out small oscillatory motions which are superimposed to the translatory forward motion. These

small motions are defined by a small translation vector $\vec{\eta} = (\eta_1, \eta_2, \eta_3)^T$ and a small rotation vector $\vec{\Omega} = (\eta_4, \eta_5, \eta_6)^T$. The six small displacements, η_1, \dots, η_6 (i.e. surge, sway, heave, roll, pitch and yaw displacement) are the actual unknown motions that have to be solved. Next to these unknowns two additional unknowns occur: the excess pressure in the cushion plenum, p_c , and the excess pressure in the stern seal plenum, p_s . The excess pressures are assumed to be constant in space, so acoustic effects of the air inside a plenum cannot be resolved.

2.1 The equations of motion

The motions of the SES are assumed to be small. Then the equations of Euler for the motions of a rigid body can be linearized to the following system of differential equations:

$$\sum_{k=1}^6 M_{jk} \frac{d^2 \eta_k}{dt^2} = F_j \quad j = 1, \dots, 6 \quad (1)$$

where M_{jk} is the k^{th} component of the j^{th} row of the generalized mass matrix, F_1, F_2, F_3 are the forces which acts on the vessel in x -direction, y -direction, and z -direction, and F_4, F_5, F_6 are the moments which act on the vessel around the x -axis, y -axis, and z -axis. Each force is split up into the following components: a gravitational force, a propulsive force, a hydromechanic force, a force due to the air cushion and a force due to the seals. The propulsive force is balanced by the resistance of the vessel. The hydromechanic force is computed by means of a three-dimensional panel method. The force due to the air cushion follows from integration of the cushion excess pressure over the deck. The forces due to seals follow from the appropriate seal models.

2.2 The equations for p_c and p_s

Next to the equations of motion two additional equations for the additional unknowns p_c and p_s have to be formu-

lated. These equations follow from conservation of mass for the air in a plenum and the equation of state of the air in a plenum. The equation of state is taken to be the isentropic gas law. Figure 1 presents the system of plena and the air volume fluxes of an SES. The equations for p_c and p_s read:

$$\begin{aligned} \frac{V_c}{\kappa(p_c + p_a)} \frac{dp_c}{dt} &= (Q_c^{(in)} - Q_c^{(out)}) - \frac{dV_c}{dt} \\ \frac{V_s}{\kappa(p_s + p_a)} \frac{dp_s}{dt} &= (Q_s^{(in)} - Q_s^{(out)}) - \frac{dV_s}{dt} \end{aligned} \quad (2)$$

where V_c is the air cushion volume, V_s is the stern seal volume, p_a is the ambient pressure and κ is the ratio of specific heats of air; $\kappa = c_p/c_v \approx 1.4$. Furthermore $Q_c^{(in)} = Q_{c,f}^{(in)} + Q_{c,s}^{(in)}$ which is the sum of the flow through the cushion fan and the leakage flow from the stern seal, and $Q_c^{(out)} = Q_{c,b}^{(out)} + Q_{c,s}^{(out)}$ which is the sum of the leakage flow under the bow seal and the leakage flow under the stern seal. The cushion volume V_c depends on the heave and pitch displacement of the vessel, the geometry of the seals and the wave height in the air cushion. The stern seal volume V_s depends on stern seal geometry.

2.3 The fan system

The air volume flux through a fan into a plenum, $Q^{(in)}$ is approximated by the linearized steady fan characteristic. Durkin and Luehr[12], Sullivan et al.[13], Masset et al.[14] and Witt[15] show that fans respond in a dynamic way to oscillating back pressure. Sullivan et al.[13] show that the dynamic behavior of the fan has a damping effect on the heave motions of a hovering box. Moulijn [16] also showed that the fan has an important effect on the overall motions of an SES. Nevertheless all computational methods for seakeeping of SES, including the present method, use static fan characteristics. This is due to the absence of information on dynamic characteristics of lift fans.

2.4 Air leakage

Many authors (see for instance Nakos et al.[7], McHenry et al.[17], Masset et al.[14]) consider air leakage to be important and highly non-linear. Nevertheless, air leakage is often linearized or even neglected. Steen[5] showed the importance of air leakage for the cobblestone effect. Ulstein[6] carried out extensive air leakage computations using a non-linear panel method. He found that the following formula which follows from a stationary

one-dimensional analysis leads to good results:

$$Q^{(out)} = c_l A_l \sqrt{\frac{2\Delta p}{\rho}} \quad (3)$$

where c_l is the leakage coefficient which depends on the local geometry of the orifice, A_l is the leakage area, Δp is the pressure jump across the orifice and ρ is the density of air. The leakage areas under the seals follow from the seal models. The leakage area under a seal is highly non-linear in the local relative wave height. When the relative wave height at the seal is large, the seal will touch the water surface so the leakage area equals zero. When the relative wave height at the seal becomes smaller a leakage gap will occur suddenly, and afterwards grow linearly. This process cannot be captured by a linear formulation.

2.5 The stern seal

This subsection presents a brief descriptions of the stern seal model. A more complete description can be found in reference [18]. Lee[19], Steen[5] and Masset et al.[20],[14] presented similar seal models.

The following assumptions underlie the stern seal model. The model is two-dimensional in a longitudinal plane. This implies that the wave height is assumed to be constant in transverse direction. Therefore the seal model is most suitable for head and following waves. The gravitational and inertial forces that act on the seal canvas are neglected. Ulstein[6] developed a seal model which includes the inertial forces. He found that inertial effects are important for high frequent motions. When the seal does not touch the water surface air will leak from the cushion under the seal. This air flow will result in a dynamic pressure distribution under the seal which will reduce the air leakage gap. Lee[19] neglected this pressure distribution. In the present model and in the models of Steen[5] and Masset et al.[20],[14] a simple stationary one-dimensional modeling of the leakage flow is used. The seal canvas is assumed to have no bending stiffness; it only transmits tension.

For a given bag configuration the following parameters determine the bag geometry and the tension in the seal canvas: heave displacement, pitch displacement, cushion excess pressure, seal excess pressure, mean wave height at the seal and mean wave slope at the seal. When the bag geometry and the tension in the seal canvas are known, the seal volume and seal force can be computed easily. The seal may either touch the water surface or leave a leakage gap. In the bottom case the cushion pressure is larger than the seal pressure, which results in the concave cushion facing part of the seal.

2.6 The bow seal

The modeling of the finger-type bow seal is much more simple than the modeling of the bag-type stern seal. When the local deck height at the bow is smaller than the height of the seal, the lower part of the fingers is simply bent backwards at the water surface, and no air will escape under the seal. When the local deck height is larger than the height of the seal, the seal will leave a gap above the water surface, and air will escape from the cushion plenum. The bow seal model is also two-dimensional (in a longitudinal plane). Again the mean wave height and wave slope at the seal are used. The seal is represented by a flat boundary which roughly coincides with the foremost part of the fingers which actually closes the cushion plenum. The part of the seal that is bent backwards at the water surface is neglected. The frictional forces that act on the bow seal are neglected.

2.7 Hydromechanics

This subsection presents a brief description of the solution method for the hydromechanical problem of an SES sailing in waves. A more elaborate description of the method can be found in reference [21].

The hydromechanical problem is solved by means of a three-dimensional Rankine panel method. The water flow is assumed to be incompressible and non-rotational, so potential flow theory can be used. The boundary conditions on the free surface and on the hulls are linearized around the undisturbed flow. This leads to a Kelvin free surface boundary condition which includes some extra terms due to the presence of the air cushion, and a Neumann hull boundary condition. The hulls and a part of the free surface are paneled with flat quadrilateral panels. Each panel has a constant source and dipole distribution. The tangential derivatives of the unknown potential which occur in the free surface boundary condition follow from analytical differentiation of a bi-quadratic spline approximation of the potential. Nakos[22] also uses this spline scheme, but he also uses a quadratic singularity distribution on each panel. When the boundary value problem is solved, the pressure and the wave height can be calculated. The hydrodynamic forces which act on the hulls follow from integration of the pressure over the wetted part of the hulls.

The unsteady hydromechanic problem is solved in the frequency domain, thus avoiding a complicated time stepping algorithm and saving much computational time. The motions have to be solved in the time domain because of the non-linear cushion and seal dynamics. Therefore the theory of Cummins[23] and Ogilvie[24] is used to trans-

form the frequency domain results of the panel method to the time domain.

2.8 Added resistance due to waves

The added resistance due to waves of a ship is the time averaged resistance of the ship when sailing in a seaway minus the resistance of the ship when sailing in calm waters at the same speed. For convenience it is henceforth called added resistance. Most authors consider the added resistance of SESs to be large. Three components which contribute to the added resistance are distinguished:

1. the usual added resistance of the hulls,
2. the added resistance due to sinkage,
3. the added resistance of the air cushion.

The usual added resistance of the hulls is caused by the diffraction of the incident waves and the radiation of the waves due to the motion of the vessel. This added resistance component is also experienced by normal ships. It can be computed for instance by the method of Gerritsma and Beukelman[25].

The added resistance due to sinkage is basically an increase of the steady resistance of the hulls. When an SES sails in a seaway, the amount of air leakage increases because the ambient waves cause large leakage gaps under the seals. This results in a decrease of the mean excess pressure in the air cushion, so a larger part of the SES's weight has to be carried by the buoyancy of the hulls. The draft of the vessel will therefore increase, which leads to a greater resistance of the hulls. This greater resistance is partly caused by an increase of the frictional resistance due to the larger wetted area of the hulls. The rest of it is caused by an increase of the wave making resistance.

The resistance of the air cushion follows essentially from the following equation:

$$R^{(ac)} = p_c \cdot (\zeta_b - \zeta_s) \cdot B_c \quad (4)$$

where p_c is the cushion excess pressure, ζ_b is the wave height at the bow seal, ζ_s is the wave height at the stern seal and B_c is the width of the air cushion. Some extra terms which account for the momentum of leaking air should also be included. Then the *added* resistance due to the air cushion follows from:

$$R_{AW}^{(ac)} = \overline{R^{(ac)}}_{\text{(in waves)}} - \overline{R^{(ac)}}_{\text{(calm water)}} \quad (5)$$

where the over lining denotes that the time averaged value should be used.

The added resistance due to the air cushion should be by far the largest contribution to the total added resistance. Only a small part of the weight of an SES is carried by the buoyancy of the hulls. These hulls are usually very slender. The usual added resistance of the hulls should therefore be small. Kapsenberg[10] showed that the added resistance due to sinkage is relatively small too. He increased the RPM of the fans in order to compensate for the larger air leakage flow. This resulted in a reduction of the added resistance by only 6 percent. Therefore the major part of the added resistance must be attributed to the air cushion. The present computational method only computes the added resistance due to the air cushion.

The computational results do not however indicate a large added resistance due to the air cushion (see Section 4). The other components are not likely to be large either. Therefore new model tests have been carried out in order to get more insight into the magnitude and origin of the added resistance of SES. The next section describes the new model tests. Section 4 presents and compares the computational and experimental results.

3 New model experiments

This section presents a description of the new model experiments. The new experiments are still in progress at the time this paper has to be delivered. Therefore only a first part of the results is included in this paper.

The goal of the new model experiments is to get more insight into the magnitude and origin of the added resistance due to waves of Surface Effect Ships. An attempt is made to measure the three added resistance components that were distinguished by Section 2.8: added resistance of the hulls, added resistance due to sinkage and added resistance of the air cushion.

3.1 The model

The model was partly derived from the target vessel of the HYDROSES project, a large collective research project on seakeeping of SES. This enables comparison to the experimental results of Kapsenberg[26] that were carried out at MARIN. These experiments are a part of the HYDROSES project. Table 1 presents the basic dimensions of the model. This model will be referred to as DUTSES.

The air cushion plenum and the stern seal plenum are both pressurized by axial fans. The fans are mounted directly on the model. The RPM of the fans is controlled by a Computer. This ensures a very stable RPM of the fans.

L_{oa}	3.200 m
L_c	3.000 m
B_{plates}	0.549 m
B_{hulls}	0.745 m
B_c	0.525 m
T_0	0.100 m
T_{20}	0.050 m
p_c	300 Pa
p_s	306 Pa

Table 1: Main dimensions of the DUTSES model

The fans are kindly on loan from MARIN.

A flexible membrane is mounted on top of the air cushion. This membrane is called *diaphragm*. A diaphragm can be used to obtain a correct scaling of the stiffness of the air cushion. Kapsenberg[26] presented a paper on this diaphragm technique. Moulijn[27] also presented a more elaborate discussion on the topic of scaling of air cushion dynamics. In the present experiments the main purpose of the diaphragm is to prevent very large pressure amplitudes which might lead to a negative cushion excess pressure. When the cushion excess pressure becomes negative the seals will collapse, and air from outside the cushion will flow into the cushion. This is not a very realistic situation, which is effectively removed by the diaphragm.

Two versions of the model are tested. The hulls of the first version are very slender; in fact they are only 12mm thick plates. The forces that act on these plates are very small (in head and following seas). Therefore the forces that are measured during the testing of this version can be attributed almost entirely to the air cushion. This enables a measurement of the added resistance of the air cushion alone. This version of the model has almost no buoyancy. Therefore it is tested in a captive setup, where the model is connected rigidly to the carriage. Otherwise the model would capsize. This version of the model will be referred to as the model with plates.

The second version of the model is equipped with more realistic hulls. The difference between the results of this version and the version with plates provides an indication of the added resistance of the hulls. The second version of the model is also tested in a free sailing setup. An indication of the added resistance due to sinkage can be obtained from free sailing calm water test with a reduced fan RPM. This version of the model will be referred to as the model with hulls. The results of the model with hulls are not included in this paper, as the experiments were still in progress at the time this paper had to be delivered.

3.2 Experimental setup

The experiments are carried out at the #1 towing tank of the Ship Hydromechanics Laboratory of Delft University of Technology. This tank is 142m long, 4.22m wide and about 2.30m deep. The carriage is suitable for speeds up to 7m/s. A hydraulically driven flap-type wave maker, which can generate both regular and irregular waves, is installed at one end of the tank. The carriage can be equipped with an oscillator for forced oscillation experiments.

The model with plates is subject to two types of experiments: wave force measurements and oscillation experiments. The model with hulls is subject to three types of experiments: wave force measurements, oscillation experiments and free sailing experiments. During the wave force measurements the model is connected to the carriage by the two legs of the oscillator. The forces in the oscillator legs are measured and the model is restrained in its mean position while it is towed in waves. During the oscillation experiments the model is also connected to the carriage by the oscillator legs. Again the forces in the oscillator legs are measured. The model carries out an imposed oscillatory heave or pitch motion while it is towed in calm water. During the free sailing experiments the model is free in heave and pitch, while the model is towed in waves.

During the experiments several variables are measured. During captive experiments the vertical and horizontal forces in the oscillator legs are measured, while during free sailing experiments the heave and pitch displacement and the resistance are measured. Next to this the horizontal and vertical seal connection forces are measured. Further, the excess pressures in the cushion and stern seal plena, the flow through the fans and the wave height close to the bow and stern seals are measured. Finally the reference wave is measured.

4 Presentation and comparison of the results

This section presents and compares the computational and experimental results. First it presents computational and experimental results for the HYDROSES target vessel. Then the computational and experimental results for the DUTSES model are presented. Finally this section presents a discussion of the results for added resistance.

L_{pp}	153.00 m
L_c	144.00 m
B	35.00 m
B_c	26.00 m
P_c	11.11 kPa

Table 2: Main dimensions of the HYDROSES target vessel

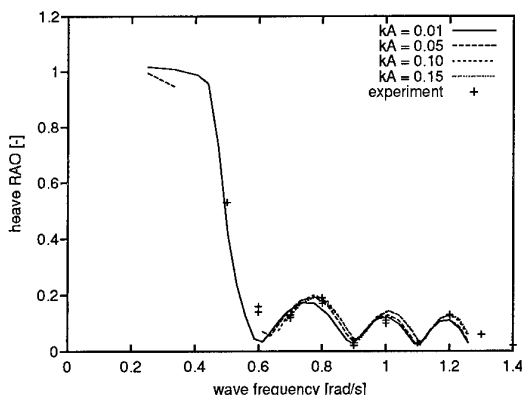


Figure 2: Heave RAO of the HYDROSES target vessel

4.1 The HYDROSES target vessel

The HYDROSES target vessel was designed as a car/passenger ferry by FINCANTIERI in Italy. It served as a study object in the HYDROSES project. Table 2 presents the main dimensions of the vessel. It is equipped with a tree-lobe bag-type stern seal and a finger-type bow seal. The lift to weight ratio of the vessel is about 0.85. The vessel's speed is 45 knots, and it sails in head waves. In the experiments the model was equipped with a diaphragm in order to obtain a correct scaling of the air cushion dynamics. The computations were carried out on full scale. All results are presented on full scale.

Figure 2 presents computed and measured heave Response Amplitude Operators (RAOs) as a function of the wave frequency. The RAOs follow from a harmonic analysis of the computed and measured time signals. Results for several levels of wave steepness are shown. The computations and experiments agree well. The effect of the non-linear cushion dynamics on the heave RAO is not very large. They manifest them self most prominently as sinkage and higher harmonics, as was shown in a previous paper by Moulijn[16].

Figure 3 presents the computed and measured pitch RAO as a function of the wave frequency. In the higher frequency range the computations and experiments agree

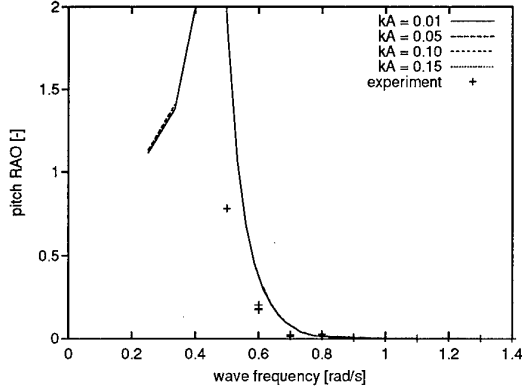


Figure 3: Pitch RAO of the HYDROSES target vessel

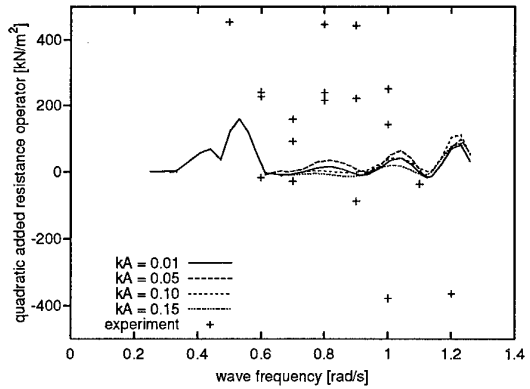


Figure 5: Quadratic added resistance operator for the HYDROSES target vessel

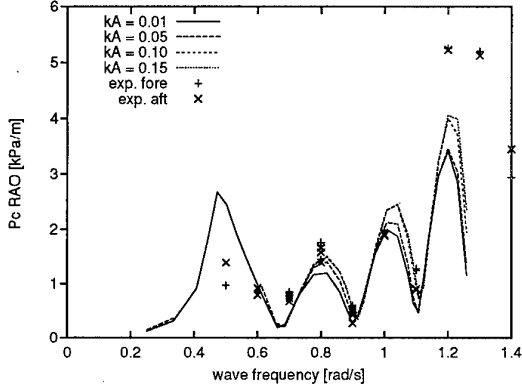


Figure 4: Cushion pressure RAO for the HYDROSES target vessel

well, but in the lower frequency range the computational results are larger than the experiments. It is not clear whether the computational method over predicts the pitch resonance, or whether the resonant frequency is shifted. This discrepancy is probably caused by the relatively harsh linearization scheme of the hydrodynamic problem. The effect of the non-linear cushion dynamics on the pitch RAO is negligible.

Figure 4 presents the computed and measured RAO for the cushion excess pressure. The pressure was measured at two locations: one at the fore side of the cushion and one at the aft side. The computations and experiments are in good agreement. The effect of the non-linear cushion dynamics on this RAO is larger, but still not really significant. In the high frequency range the experimental results are somewhat larger, while in the low frequency range the computational results are greater. The latter discrepancy is caused by the large computed pitch motions which cause air gap modulations under the seals. The Helmholtz resonant frequency of the air cushion is

located in the high frequency range. This resonance is very sensitive to for instance the behavior of the fan, and is therefore difficult to predict computationally (see reference [16]).

Figure 5 presents the computed and the measured added resistance divided by the wave height squared as a function of the wave frequency. MARIN measured added resistance values up to two times as large as the calm water resistance. In the case of conventional ships the added resistance is proportional to the incident wave height squared. The scattering of the experimental results indicates that this relation does not hold for an SES. The measured added resistance is negative in some cases. The computational results are much smaller than the experimental results. There even does not seem to be any correlation between the computed and measured added resistance. The computational results also indicate a non-quadratic relation of the added resistance with the wave height, although the scattering is much less severe. The discrepancy between the computed and the measured added resistance was the reason for the new experiments.

4.2 The DUTSES model

This section presents preliminary results of the new model experiments. These results are also compared to computational results. The experimental results have not been analyzed thoroughly yet. Nevertheless these results give some interesting new insights into the topic of added resistance of SESs. All results are for the model version with plates, and are presented on model scale. The model is towed in head waves at a speed of 3.72 m/s.

Figure 6 presents the measured and computed RAO for the wave force in heave direction. It displays results for

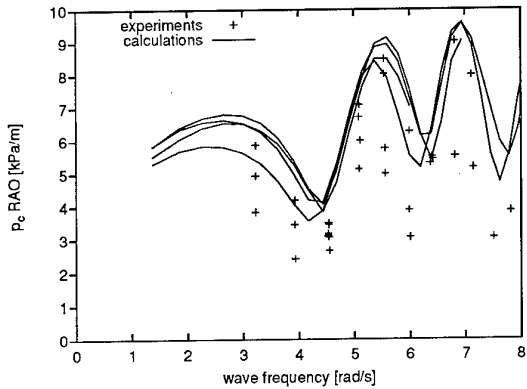


Figure 6: Heave force RAO for the DUTSES model

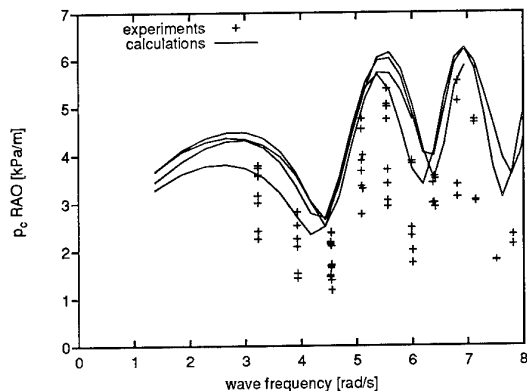


Figure 7: Cushion pressure RAO for the DUTSES model

several wave heights. The correlation is not fully satisfactory yet. The scattering of the experimental data indicate that the heave force is quite non-linear in the wave height. The computational data appear to behave in a much more linear way. Generally the correlation is better for higher waves.

Figure 7 presents the RAO for the cushion pressure during wave force experiments. The cushion pressure was measured on two locations: at the fore side of the cushion and at the aft side. These results are similar to the results for the heave force.

Figure 8 presents measured and computed quadratic operators for the added resistance of during (captive) wave force experiments. Both experimental and computational data indicate that the added resistance is not proportional to wave height squared. Contrary to the results for the HYDROSES target vessel, the results for the DUTSES model are of the same order of magnitude.

The computations do not include the usual added resistance of the plates. This added resistance should be small

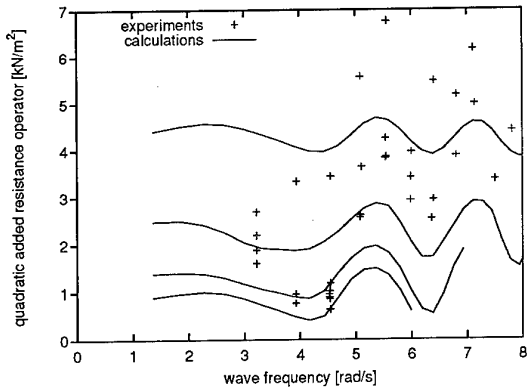


Figure 8: Quadratic added resistance operator for the DUTSES model

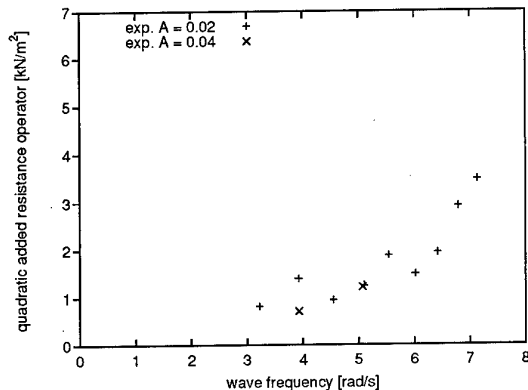


Figure 9: Quadratic added resistance operator for plates of the DUTSES model

as the plates are extremely slender. It was measured during wave force experiments without cushion pressure. Figure 9 presents the results of these experiments. The added resistance of the plates appears to be relevant when compared to the total added resistance as presented by Figure 8.

The added resistance of the air cushion can be calculated by subtracting the added resistance of the plates from the total added resistance. This way of computing the added resistance of the air cushion implies that interaction of the air cushion with the plates is neglected. The added resistance of the plates was assumed to have a quadratic relation with wave height. This assumption is approved by one of the $A = 0.04$ measurements (A is wave amplitude). The other $A = 0.04$ measurement does not approve a quadratic relation (see Figure 9).

Figure 10 presents the thus calculated experimental added resistance of the air cushion. The results are *not* divided by wave height squared. The calm water resistance

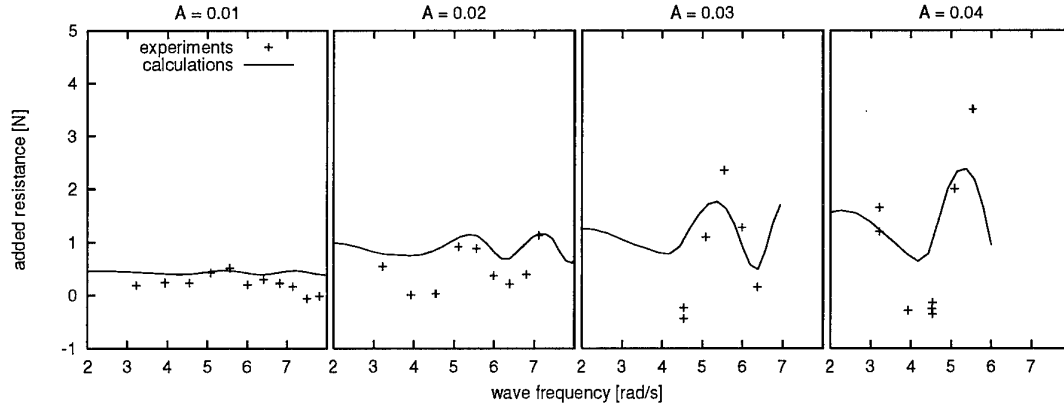


Figure 10: Added resistance of the air cushion; the experiments follow from the total added resistance minus the added resistance of the plates

of the vessel was about 27 N. The computed and measured added resistance of the air cushion are in reasonable agreement. The magnitude is about the same, and the trends do also agree.

The added resistance due to the air cushion can also be calculated from the horizontal seal connection forces. The resistance of the air cushion follows from:

$$R^{(ac)} = -F_{xs} - F_{xb} - p_c \cdot A_d \cdot \eta_5 \quad (6)$$

where F_{xs} is the horizontal stern seal connection force (positive in forward direction, hence the minus sign), F_{xb} is the horizontal bow seal connection force, p_c is the cushion excess pressure, A_d is the deck area and η_5 is the pitch displacement angle. The *added* resistance of the air cushion follows again from Equation 5.

Figure 11 presents the added resistance of the air cushion, where the experimental results were calculated from the seal forces and the cushion pressure. Again the results are in reasonable agreement. The results of both methods for calculating the experimental added resistance of the air cushion agree quite well (compare Figure 10 with Figure 10).

4.3 Discussion

This section presents a discussion on the topic of added resistance. There is an obvious difference between the experimental results of MARIN and the new experimental results. There are however many differences between both experiments.

The model was free in heave, pitch and surge during the MARIN experiments, while the model was rigidly connected to the carriage during the new experiments. The

cushion pressure amplitude is much larger during a wave force experiment than during a comparable free sailing experiment. Therefore one might expect to find a larger added resistance during wave force experiments. This is not however the case.

The MARIN model has realistic side hulls instead of plates. If this is the reason for the large added resistance, the major part of the added resistance should be attributed to the hulls. This is not very likely as the realistic hulls are still very slender.

The added resistance was measured in two quite different ways. The MARIN model was self-propulsing by means of model water-jets. The added resistance was determined from a propulsion increase of the water-jets, which follows from a measurement of the flow through the water-jet. In some cases an extra towing force was added because the model could not reach the desired speed. The DUTSES model is always towed. The added resistance follows from an increase of the towing force. This method is, according to the author, more simple and more reliable than the method adopted at MARIN. The MARIN results might be affected by a decrease of the efficiency of the water-jet propulsors.

The large speed loss of SES might also be caused by a decrease of the thrust of the water jets. This would explain the large added resistance measured at MARIN. It would also explain the statement of Ehrenberg[9] that an SES has much less speed loss in waves than a comparable catamaran, as his experience follows from an SES which is propelled by means of surface piercing propellers.

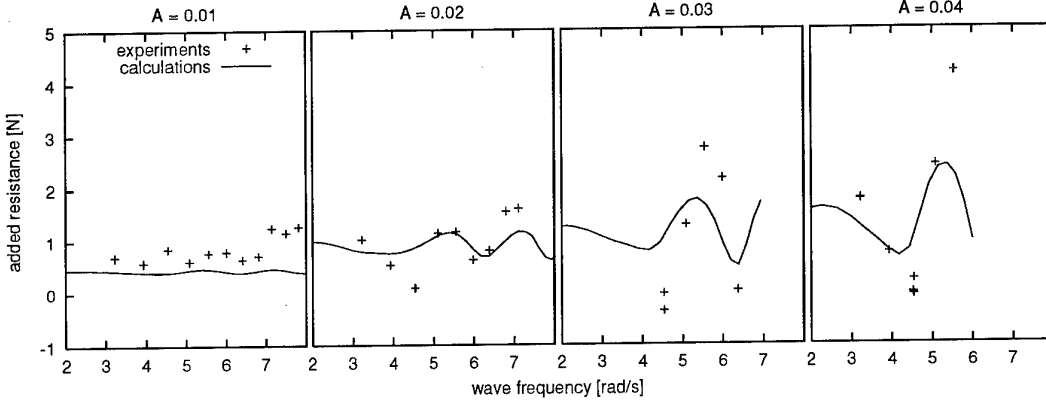


Figure 11: Added resistance of the air cushion, the experiments follow from the seal forces and the cushion pressure

5 Conclusions

The results of the computational method that was presented by Section 2 are in good agreement with the experimental results of MARIN, as far as motions and cushion pressure are concerned. The computational results for added resistance are however much smaller than the added resistance that was measured at MARIN. New experiments, which were carried out at Delft University of Technology, lead to a much smaller added resistance which is in reasonable agreement with the computations. There were however many differences between both experiments.

At this stage it is not possible yet to say if SESSs have a large added resistance. It can however be concluded that the added resistance due to an air cushion is relatively small. The added resistance of the hulls and the added resistance due to sinkage will follow from the experiments that are in progress at the time this paper is written.

Acknowledgments

I would like to thank the Royal Netherlands Navy and MARIN for their financial support of my PhD-project. MARIN is also acknowledged for providing the experimental results for the HYDROSES target vessel, and for providing a lot of equipment for use in the new experiments.

References

[1] P. Kaplan and S. Davis. A simplified representa-

tion of the vertical plane dynamics of ses craft. In *AIAA/SNAME Advanced Marine Vehicles Conference*, AIAA Paper No.74-314, 1974.

- [2] P. Kaplan, J. Bentson, and S. Davis. Dynamics and hydrodynamics of surface effect ships. In *Transactions of SNAME*, volume 89, pages 211–247, 1981.
- [3] L.J. Doctors. The use of pressure distribution to model the hydrodynamics of air cushion vehicles and surface effect ships. In *Intersociety High Performance Marine Vehicle Conference and Exhibit (HPMV'92)*, Arlington, VA, 1992.
- [4] A.J. Sørensen. *Modelling and Control of SES in the Vertical Plane*. PhD thesis, The Norwegian Institute of Technology, 1993.
- [5] S. Steen. *Cobblestone Effect on SES*. PhD thesis, The Norwegian Institute of Technology, 1993.
- [6] T. Ulstein. *Nonlinear effects of a flexible stern seal bag on cobblestone oscillations of an SES*. PhD thesis, The Norwegian Institute of Technology, 1995.
- [7] D.E. Nakos, A. Nestegård, T. Ulstein, and P.D. Sclavounos. Seakeeping analysis of surface effect ships. In *Fast Conference, Trondheim*, 1991.
- [8] O.M. Faltinsen, J.B. Helmers, K.J. Minsaas, and R. Zhao. Speed loss and operability of catamarans and ses in a seaway. In *First International Conference on Fast Sea Transportation (Fast'91)*, Trondheim, Norway, 1991.
- [9] H.D. Ehrenberg. *Das Verhalten von Luftkissenkatamaranen (SES) im Seegang*. PhD thesis, Institut für Schiffbau der Universität Hamburg, 1996.

- [10] G.K. Kapsenberg. Seakeeping behaviour of a ses in different wave directions. In *Proc. Second International Conference on Fast Sea Transportation (FAST'93)*, Yokohama, Japan, 1993.
- [11] G.K. Kapsenberg and P. Blume. Model tests for a large surface effect ship at different scale ratios. In *Proc. Third International Conference on Fast Sea Transportation (FAST'95)*, Lübeck-Travemünde, Germany, 1995.
- [12] J.M. Durkin and L. Luehr. Dynamic response of lift fans subject to varying backpressure. In *AIAA/SNAME Advanced Marine Vehicles Conference, AIAA Paper No.78-756*, 1978.
- [13] P.A. Sullivan, F. Gosselin, and M.J. Hinchee. Dynamic response of an air cushion lift fan. In *HPMV '92 Conference, Washington*, 1992.
- [14] J.F. Masset, J.P. Morel, and G.K. Kapsenberg. Large surface effect ship (ses) air cushion dynamics: An innovative methodology for theoretical modelling validation. In *Proc. Third International Conference on Fast Sea Transportation (FAST'95)*, Lübeck-Travemünde, Germany, 1995.
- [15] K.C. Witt. Lift fan stability for ses. In *Second International Conference on Fast Sea Transportation (FAST'93)*, Yokohama, Japan, 1993.
- [16] J.C. Moulijn. Non-linear motions of surface effect ships. In *International Conference on Air Cushion Vehicles (ACVs), RINA*, London, 1997.
- [17] G. McHenry, P. Kaplan, F. Korbjn, and A. Nestegård. Hydrodynamic analysis of surface effect ships: Experiences with a quasi-linear model. In *Fast Conference, Trondheim*, 1991.
- [18] J.C. Moulijn. A model for flexible bag stern seals. Technical Report 1082-O, Delft University of Technology, Ship Hydromechanics Laboratory, 1997.
- [19] G.J. Lee. On the motions of high speed surface-effect-ships in waves. *Journal of Hydrospace Technology*, 1(2):13–35, 1995.
- [20] J.F. Masset and J.P. Morel. A test rig for the analyses of a large surface effect ship seals dynamics: design, manufacturing and results. In *NAV'94 proceedings*, volume 1, 5-7 October 1994.
- [21] J.C. Moulijn. Motions of surface effect ships. Technical Report 1051-O, Delft University of Technology, Ship Hydromechanics Laboratory, 1996.
- [22] D. E. Nakos. *Ship Wave Patterns and Motions by a Three Dimensional Rankine Panel Method*. PhD thesis, M. I. T., 1990.
- [23] W. E. Cummins. The impulse-response function and ship motions. *Schiffstechnik*, 9(47):101–109, 1962.
- [24] T. F. Ogilvie and E. O. Tuck. A rational strip theory for ship motions -part i. Technical Report 013, Department of Naval Architecture and Marine Engineering, University of Michigan, USA, 1969.
- [25] J. Gerritsma and W. Beukelman. Analysis of the resistance increase in waves of a fast cargo ship. Technical Report 169s, Netherlands Ship Research Center TNO.
- [26] G.K. Kapsenberg. Added mass and damping coefficients for a large ses including an appreciation of scale effects. In *Proc. NAV'94*, volume 1, 1994.
- [27] J.C. Moulijn. Scaling of aircushion dynamics. Technical Report 1151, Delft University of Technology, Ship Hydromechanics Laboratory, 1998.

COBBLESTONE EFFECT ON SES

Tore Ulstein and Odd M. Faltinsen
 Department of Marine Hydrodynamics
 Norwegian University of Science and Technology
 N-7034 Trondheim, Norway

SUMMARY

Wave induced vertical accelerations (cobblestone oscillations) of a SES in small sea states is studied. Resonant spatially uniform and nonuniform dynamic cushion variations are then important. A nonlinear time domain solution is used. The nonlinearities are mainly due to the flexible stern seal bag behaviour. It is demonstrated that both the spatially varying pressure underneath the flexible stern seal bag and the impact between the bag and the water are important for the vertical accelerations of the vessel. The influence of main parameters characterizing the stern seal bag is discussed.

1. INTRODUCTION

A problem with a Surface Effect Ship (SES) is high vertical accelerations in small sea states. This represents a comfort problem for passenger transportation. The phenomenon is often referred to as the cobblestone effect and is a resonance effect due to the compressibility of air in the air cushion. The cobblestone effect is excited because the water waves dynamically change the air cushion volume. The resonance phenomenon occurs at high frequencies relative to the resonance frequencies for the rigid body motions of displacement ships of similar length. The two lowest resonance frequencies in the air cushion of a 30-35 m long SES are approximately 2 Hz and 5-6 Hz. Due to the frequency of encounter effect there are waves with sufficient energy in small sea states that excite these resonance oscillations. The eigenfunction for the dynamic air cushion pressure is constant in space for the lowest eigenfrequency and represents acoustic wave resonances for the higher eigenfrequencies. [1] demonstrated the importance of the lowest eigenfrequency. [2], [3] and [4] showed that acoustic standing wave effects must also be included. [5] and [6] give simplified introductions to cobblestone oscillations. [2] documented by full scale measurements onboard a 35 m long SES the importance of the two lowest eigenfrequencies (see Fig. 1). Since the lowest eigenmode is constant in space, it affects mainly heave accelerations. The second eigenmode, which corresponds to the lowest acoustic resonance frequency, has a node approximately midships. It can be

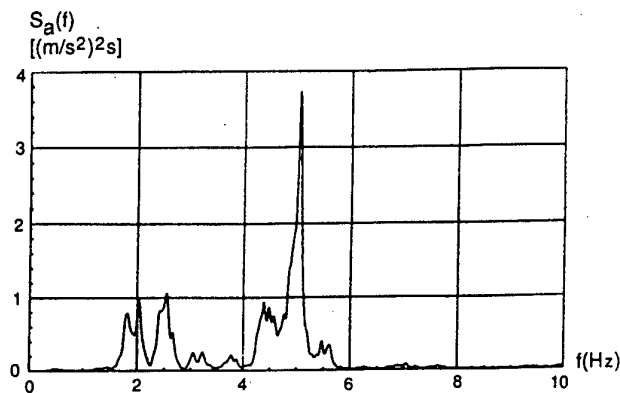


Fig. 1 Full scale measured spectrum $S_a(f)$ of vertical accelerations at bow of 35 m SES. Flexible stern seal bag. 45 knots. Head sea. $H_{1/3} = 0.3\text{-}0.4 \text{ m}$. f=frequency. Ref. [2].

approximated by a sinusoidal function. The modal wave length is roughly twice the ship length. It means that the second eigenmode affects mainly the pitch accelerations. Fig. 2 gives an overview over

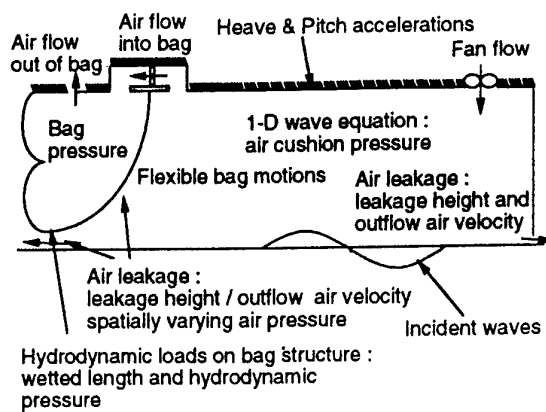


Fig. 2 Investigated physical effects.

investigated subproblems. Important damping mechanisms of the cobblestone oscillations are due to the air flow into the air cushion through the fans and the air leakage underneath the seals and through louvers

that are part of a ride control system. The placement of the louver system is essential. For instance if the louver system is placed midships, it will have a negligible effect on the acoustic resonance mentioned above. The reason is simply that the acoustic pressure component has a small amplitude midships, while it has its maximum absolute value at the ends of the cushion. Fig. 3 shows a proposed ride control system by [7]. A louver system consisting of two vent valves in the front

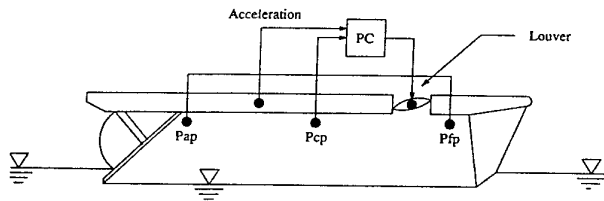


Fig. 3 Ride Control System. Ref. [7].

of the air cushion is used. The opening and closing of the vent valves control the air flow from the air cushion and cause damping of the cobblestone oscillations. Three pressure sensors were used in the air cushion and one accelerometer on the vessel as part of the ride control system. By properly filtering the signals from the measurement units and using a mathematical model for the behaviour of the SES, the control system can give the correct signals to the louver system. In order to construct a ride control system, a simplified but rational mathematical model is needed ([4]). This study focus on the nonlinear effects of the flexible stern seal bag. The cobblestone oscillations do not Froude scale. For instance resonance periods are approximately proportional to the ship length. This makes comparisons with model tests difficult. Full scale validation is needed.

2. THEORY

Head sea longcrested waves are assumed. A right-handed coordinate system that moves with the forward velocity U of the SES and is fixed to the mean oscillatory position of the vessel, is used. Here the X -axis points upstream in the direction of the forward velocity, and goes through the center of gravity (CG). The Y -axis points to the port side and the Z -axis is upwards. Both goes through CG. The equations of coupled heave (η_3) and pitch (η_5) motions are formulated in the time domain as

$$(M + A_{33}^h)\ddot{\eta}_3 + B_{33}^h\dot{\eta}_3 + C_{33}^h\eta_3 + A_{35}^h\ddot{\eta}_5 + B_{35}^h\dot{\eta}_5 + C_{35}^h\eta_5 = F_r^h(t) + F_3^{ac}(t) \quad (1)$$

$$(I_5 + A_{55}^h)\ddot{\eta}_5 + B_{55}^h\dot{\eta}_5 + C_{55}^h\eta_5 + A_{53}^h\ddot{\eta}_3 + B_{53}^h\dot{\eta}_3 + C_{53}^h\eta_3 = F_5^h(t) + F_5^{ac}(t) \quad (2)$$

t is the time variable and dot stands for time derivative. M is the structural mass and I_5 is the structural mass moment of inertia around the Y -axis of the SES. A_{ij}^h , B_{ij}^h and C_{ij}^h are hydrodynamic infinite frequency added mass, damping and restoring coefficients of the two side-hulls. F_i^h is the linear hydrodynamic excitation force on the side-hulls and F_i^{ac} is the nonlinear force acting on the SES due to integrated unsteady excess pressure in the air cushion in direction i . The nonlinearity in F_i^{ac} is mainly caused by nonlinear effects related to the flexible stern seal bag. The hydrodynamic loads on the hull are expressed by strip theory ([8]). This is not an important part of the cobblestone analysis.

2.1 Global Air Cushion Model

The air cushion is analyzed in two steps. First a global flow model is studied. The air cushion is then approximated as a box. Air flow through fans, air leakage and the velocities of the bounding surfaces are accounted for. The global flow is later connected to a detailed model around the bag. The global model describes the air flow by the wave equation

$$\frac{\partial^2 \phi}{\partial t^2} - v_s^2 \nabla^2 \phi = 0 \quad (3)$$

Here ϕ is the velocity potential, v_s is the velocity of sound in air and ∇^2 is the Laplacian operator. The linear dynamic pressure \hat{p}_c can be expressed as $-\rho \partial \phi / \partial t$. Boundary conditions have to be imposed. Formally we can write that $\partial \phi / \partial n$ is equal to the normal velocity $\vec{V}(\vec{x}, t) \cdot \vec{n}$ on the surface Γ that encloses the air cushion volume. The normal vector \vec{n} to Γ is positive out of the air cushion. Since it is sufficient to consider a one-dimensional flow in the longitudinal direction, the normal velocities at the stern and seal regions are averaged over the height of the air cushion. For instance at the stern of the air cushion there is a combined effect of the flow between the inside of the bag and the air cushion, the motions of the air bag, and the leakage below the air bag. The motions of the air bag have an important effect on the lowest acoustic spatially varying natural mode of the air cushion. The boundary condition at the free water surface follows from the kinematic free surface condition. Only incident waves are considered. The boundary condition at the rigid part of the wetdeck follows from the heave and pitch velocities. The normal velocity at the fan is expressed by the steady fan characteristics. The Finite Element Method has been used to solve the problem. Eq. (3) is combined with the boundary conditions and written as

$$\int_{V_c} N^T (\nabla^2 \phi - \frac{1}{v_s^2} \frac{\partial^2 \phi}{\partial t^2}) dV_c \quad (4)$$

$$-\int_{\Gamma} N^T \left(\frac{\partial \phi}{\partial n} - \mathbf{V}(\vec{x}, t) \cdot \mathbf{n} \right) d\Gamma = 0$$

Here N^T is the transposed of the trial function matrix N . The first term in Eq. (4) is rewritten by Green's theorem as

$$\int_{V_c} N^T \nabla^2 \phi dV_c = \int_{\Gamma} N^T \frac{\partial \phi}{\partial n} d\Gamma - \int_{V_c} \nabla N^T \cdot \nabla \phi dV_c \quad (5)$$

The analyzed domain is broken down into N_{el} small 1-D elements in the longitudinal direction. It is assumed that $\phi(\xi, t) = N(\xi) \{\phi(t)\}$ where $\{\phi(t)\}$ is a vector containing the node point values of the velocity potential of the air flow. A linear variation is used over each element. [9] verified the numerical method by comparing with the Finite Difference Method and by using an analytical solution based on mode superposition.

2.2 Local Air Cushion Model at the Stern

It is now focused on the details at the stern bag seal. A 2-D problem is solved in the longitudinal plane of the SES. The pressure is assumed spatially constant inside the bag. This pressure can be related to the pressure in the air cushion by using continuity of mass flow in and out of the bag. The air inside the bag is assumed compressible and an adiabatic relationship is used between the pressure and the air density. The bag structure is modelled as a cable in the cross-sectional plane. In the static case the bag is not touching the water, but the leakage height underneath the bag is assumed to be initially zero in the time domain solution procedure. The aerodynamic pressure force acting on the bag is an order of magnitude larger than the gravity force. The dynamic contributions from gravity will appear as restoring terms and can be neglected compared to the tension terms. The bag structure is therefore modelled as a weightless but not massless cable. The studied bag geometry is a typical 2-loop bag configuration (see Fig. 4). The static bag geometry is

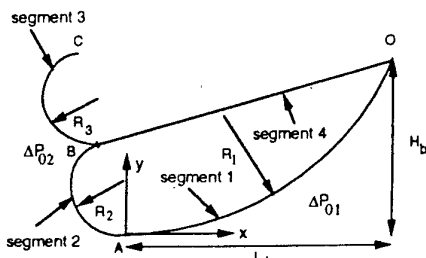


Fig. 4 Static geometry of 2-loop flexible bag seal.

approximated by 3 cable segments with constant radius of curvature R . This implies spatially uniform static difference pressure over each segment. The tensions in segments 1 and 2 are constant and equal. There are equal static difference pressures across segments 2 and 3, i.e., $\Delta P_{02} = \Delta P_{03}$.

The equations of motions for the flexible bag are derived by a linear perturbation of the static solution. Compatibility gives the relationship between tension and the motions in the transverse and the longitudinal directions. Since the radius of curvature R is constant for each cable segment, the equations of motions can be set up separately for each segment. Afterwards these cable segments are linked together with the boundary conditions. The equations of motions for a cable segment are finally written as

$$M_m \ddot{\eta}_n = T_0 \frac{d^2 \eta_n}{ds^2} + \frac{(T_0 + EA)}{R} \frac{d\eta_n}{ds} - \frac{EA}{R^2} \eta_n + \Delta P_u \quad (6)$$

$$M_m \ddot{\eta}_l = EA \frac{d^2 \eta_l}{ds^2} - \frac{EA}{R} \frac{d\eta_l}{ds} \quad (7)$$

Here η_n and η_l are the motions in the transverse and longitudinal directions. M_m is the structural mass per unit length of the cable. E is the elasticity modulus of the material. A is the cross dimensional area of unit width and T_0 is the static tension in the cable segment. s is the longitudinal coordinate along the cable segments (see Fig. 4) and ΔP_u is the unsteady difference pressure across the cable. The structural boundary value problem is solved by "dry" mode superposition. We can write

$$\eta_n(s, t) = \sum a_i(t) \phi_i^n(s) \quad (8)$$

$$\eta_l(s, t) = \sum a_i(t) \phi_i^l(s) \quad (9)$$

Here $a_i(t)$ is the principal coordinate of vibration mode number i and ϕ_i^n and ϕ_i^l are the mode shape functions in the transverse and longitudinal directions. A finite number of modes is used. Eqs. (8) and (9) are substituted into Eqs. (6) and (7). The two equations are multiplied with ϕ_j^n and ϕ_j^l , respectively and integrated over the length L_{cs} of all the cable segments. The two coupled equations of motions are added and give

$$M_j \ddot{a}_j + C_j a_j = \int_{L_{cs}} \Delta P_u \phi_j^n ds \quad (10)$$

where

$$\int_{L_{cs}} \Delta P_u \phi_j^n ds = \int_{L_1} \hat{P}_{cal} \phi_j^n ds \quad (11)$$

$$- \hat{P}_b \int_{L_1 + L_2 + L_3} \phi_j^n ds + \int_{L_1} p(s, \eta_n, t) \phi_j^n(s) ds$$

Here \hat{p}_b is unsteady pressure inside the bag. $p(s, \eta_n, t)$ is the unsteady hydrodynamic pressure. L_i is the length of bag segment number i . Since the hydrodynamic pressure is dependent on the bag deformations, the problem is hydroelastic. \hat{p}_{cal} is the unsteady spatially varying air cushion pressure underneath the flexible stern seal bag. This is present when there is a gap between the lowest point of the bag and the free water surface.

We will show how \hat{p}_{cal} and p are evaluated. We assume first the bag is not touching the water and $p=0$. A 2-D problem is analyzed. This information is used as a basis for a 1-D approximation. The flow is assumed quasi-steady and incompressible. The air is inviscid. Since the important wave lengths in the acoustic air cushion problem is much longer than the cross-sectional length dimensions of the air bag, the assumption of incompressibility is consistent from that point of view. However, when the air gap becomes very small, the local Mach number is high. The assumption of quasi-steady flow and inviscid air may also then be questioned. Since viscous effects are neglected, the separation point of the air flow must be chosen. The lowest point of the bag is used. The geometry and the coordinate system are defined in Fig. 5. Origo is placed at the steady free water surface. The x -axis is parallel to the undisturbed free water surface and is pointing towards the stern of the SES. The y -axis is pointing upwards. The velocity potential ϕ of the local air flow satisfies the 2-D Laplace equation. The kinematic condition on the free air surface is

$$\phi_y(x, y) = \phi_x(x, y)\zeta_x(x) \quad \text{on} \quad y = \zeta(x) \quad (12)$$

implies that

$$\phi_s(x, y) = V_a \quad \text{on} \quad y = \zeta(x) \quad (13)$$

The subscript s denotes the tangential derivative at the free air surface and V_a is the constant air flow velocity at the free air surface as indicated in Fig. 5. There are no normal velocity on the "walls". A Kutta condition is prescribed at the separation point (lip). It expresses that the tangential velocity and aerodynamic pressure are continuous at the lip. The horizontal uniform inflow velocity is assumed known and constant over the height of the air cushion. The outflow velocity V_a is assumed constant through the air jet. The velocity potential ϕ for the incompressible air flow inside the fluid domain is represented by Green's second identity, i.e.

$$2\pi\phi(\vec{x}_1) = \int_{S(\vec{x})} \left[Q(\vec{x}, \vec{x}_1) \frac{\partial\phi(\vec{x})}{\partial n(\vec{x})} - \phi(\vec{x}) \frac{\partial Q(\vec{x}, \vec{x}_1)}{\partial n(\vec{x})} \right] dS(\vec{x}) \quad (14)$$

Here S is the surface that encloses the air flow volume. The normal vector \vec{n} to S is positive into the air flow domain. Further $Q = \log|\vec{x}_1 - \vec{x}|$. When the field point approaches a point on the boundary, an integral equation of Fredholm type is obtained. The geometry is discretized into straight elements. The velocity potential and the normal velocity are assumed constant over each element. A set of linear equations follows from the discretization. To get a correct representation of the velocity potential on the lip of the bag, the equation that satisfies no normal velocity on the last element on the lip is exchanged with an equation that prescribes atmospheric pressure at the trailing edge. This implies that the tangential velocity at the separation point must be equal to V_a (see Eq. (13)). To establish this equation the local behaviour of the tangential velocity of the air flow near the lip is used. The unknowns are the normal derivative of the velocity potential on the free air surface and the velocity potential on the inflow and the wall surfaces. The solution procedure is as follows. First a jet contraction coefficient $k_a = \zeta(x \rightarrow \infty)/h_L$ (see Fig. 5) is guessed. A free air surface is generated based on this guess. This surface is described by an exponential function in the first iteration. The unknown coefficients in this function are determined from the approximation of the jet contraction coefficient and the fact that the tangent to the free air surface is equal to the tangent of the bag at the lip. An outflow velocity can be found from the jet contraction coefficient by mass conservation. The potential on the free air surface can now be found from the dynamic free surface condition defined in Eq. (13), since now both the velocity potential at the outflow surface and the tangential velocity at the free air surface are known. Green's second identity can then be used to find the normal derivative of the velocity potential on the free air surface. When this velocity is known, the

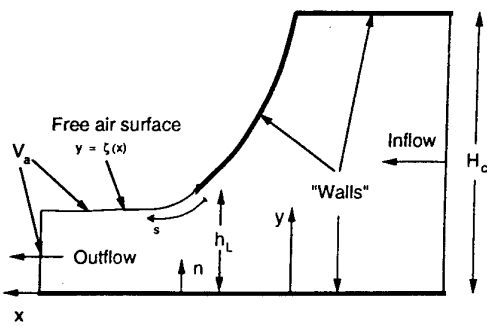


Fig. 5 Air flow underneath stern seal bag.

Here $\zeta(x)$ is the air surface coordinate defined in Fig. 5. The subscripts x and y denote the x - and y -derivatives. The dynamic condition states that the pressure on the free air surface is equal to the atmospheric pressure. This

kinematic free surface condition is used to generate a new free air surface (see below), and the procedure is repeated until there is no updating of the free air surface or that the error estimate obtained from the conservation of momentum is below a chosen value (e.g. 1%). One important point is how the kinematic free surface condition is rewritten into an iterative scheme to update the free air surface. To obtain a stable and accurate solution, the kinematic free surface condition defined in Eq. (12) is rewritten into the following iterative scheme

$$\zeta_x^{N_u+1} = \frac{\zeta_x^{N_u} \phi_s^{N_u} + \phi_n^{N_u}}{\phi_s^{N_u} - \zeta_x^{N_u} \phi_n^{N_u}} \quad (15)$$

It is used that $\zeta_x = -n_1/n_2$, $\phi_x = n_1\phi_n + n_2\phi_s$ and $\phi_y = n_2\phi_n - n_1\phi_s$. Here $n = (n_1, n_2)$. The slope of the first element on the free air surface is set equal to the slope of the last element on the lip, and is not updated by the algorithm described above. The reason is the Kutta condition, that ensures a smooth flow at the separation point of the bag. Now both the velocity potential and its normal derivative are known on the whole enclosing surface. The air pressure is found from Bernoulli's equation. The method has been verified against analytical solutions based on conformal mapping ([9]). Since a more simplified method is beneficial in a ride control system, 1-D approximations have been studied. It has been found that the pressure distributions can be well described by

$$\frac{p(x) - p_a}{0.5\rho_a V_a^2} = 1 - \left(\frac{k_a h_L}{h(x)}\right)^2 \quad (16)$$

Here $h(x)$ is the local vertical distance between the water free surface and the bag. h_L is the value of h at the lowest point of the bag. The jet-contraction coefficient k_a is determined a priori by a 2-D analysis for a given bag. V_a is found by setting p equal to p_c upstream.

Water impact loads

The behaviour of a planing bag bouncing on the free water surface is analyzed as a water entry problem, assuming a large forward speed of the SES relative to the relative vertical velocity between the bag structure and the water surface. Gravity can be neglected. The wetted length of the bag will vary strongly through the impact on the free water surface. The hydrodynamic loading will be much larger than the aerodynamic loading due to the relatively low pressure in the air cushion and inside the bag. This implies that the immersion of the bag is low. The body boundary conditions can therefore be transferred to a straight horizontal line. This together with the free surface conditions leads to a square root singularity in the hydrodynamic pressure at the spray root in the planing problem. The modal hydrodynamic

force defined by the last integral on the right hand side of Eq. (11), will not be affected by the detailed behaviour of the flow around the spray. The vertical global motions of the bag and the effect of the vertical motions due to incident waves are considered. A right-handed local xy -coordinate system that moves with the forward speed U of the vessel is used. The origin is fixed at the lowest point of the static bag configuration. The x -axis is positive towards the upstream direction of the undisturbed water flow and the y -axis is positive upwards. The undisturbed free stream velocity U is in the negative x -direction relative to this coordinate system. Since potential flow is assumed, the separation point must be determined a priori. The lowest point of the bag is chosen. The body boundary conditions are transferred to a straight horizontal line that corresponds to the x -axis ($y=0$) defined above (see Fig. 6). The total

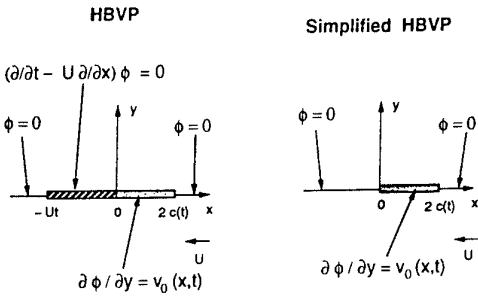


Fig. 6 Hydrodynamic boundary value problems (HBVP) for water entry of bag.

velocity potential is defined as $\Phi(x,y,t) = -Ux + \phi_i(x,y,t) + \phi(x,y,t)$ where $\phi_i(x,y,t)$ is the incident irregular wave potential and $\phi(x,y,t)$ is the velocity potential for the water flow caused by the bag. ϕ is found by a quasi-steady approach in the simplified Hydrodynamic Boundary Value Problem (HBVP). The dynamic free surface condition is approximated by $\phi=0$ on $x < 0$ and $x > 2c(t)$. Here $2c(t)$ is the wetted length. At the wetted surface of the bag the following vertical velocity is prescribed

$$v_0(x,t) = \dot{\eta}_3 + \frac{L}{2}\dot{\eta}_5 + \frac{\partial \eta_{bag}}{\partial t} - U \frac{\partial \eta_{bag}}{\partial x} - \frac{\partial \phi_i}{\partial y} \quad (17)$$

Here η_{bag} describes the unsteady geometry of the bag, that is the vertical distance between a point on the bag and a horizontal line defined by $y=0$. An approximation of the wetted length is found from

$$h_{L0} + \eta_{bag}(2c(t),t) = \zeta(-\frac{L}{2},t) - \eta_3(t) - \frac{L}{2}\eta_5(t) \quad (18)$$

Here h_{LO} is the vertical distance between the lowest point of the bag and the free water surface at $t=0$ and ζ defines the incident wave profile. L is the length of the air cushion and the flexible bag is located at $X=-L/2$. Pile-up of water is neglected. A more correct way to define the HBVP is shown in Fig. 6. [10] and [11] solved this HBVP and did also include pile-up of water upstream the wetted part of the bag. This represents a more complicated procedure. Numerical studies by [9] showed that the errors using the simplified solution are not important.

3. RESULTS

Unsteady air cushion pressures and vertical accelerations of a SES are studied at AP, CG and FP. Here AP is located at $X=-L/2$, CG at $X=0$ and FP at $X=L/2$. The SES is described in Table 1. Head sea longcrested waves are assumed. A modified Pierson Moskowitch wave spectrum with peak period $T_p=1.8$ s is used. This spectral period is realistic for small sea states. The peak period is chosen so that there are significant vertical accelerations in the frequency domain around the first spatial pressure resonance of the air cushion. There is negligible wave energy at the lowest eigenfrequency. The results are organized so that the simplest simulation model is presented first. Different effects are then added, so the importance of each effect can be quantified. The results are presented in terms of response spectra as a function of frequency of encounter.

Table 1. Main particulars of SES

Weight (M)	140 000 kg
Air cushion length (L)	28 m
Air cushion height (H_c)	2 m
Air cushion beam (B_c)	8 m
Mean side-hull beam	1.5 m
Mean side-hull draft	1.0 m
Mean air cushion pressure (p_{c0})	510 mmWc
Mean fan flow rate (two fans) (Q_{i0})	2.8 m ² /s
Linear air cushion fan slope (two fans) ($\frac{\partial Q}{\partial p}\right)_0^c$	-0.00104 m ² s/kg
Linear bag fan slope (two fans) ($\frac{\partial Q}{\partial p}\right)_0^c$	-0.00063 m ² s/kg
Longitudinal position of fans (X_f)	12 m
Forward speed (U)	23 m/s

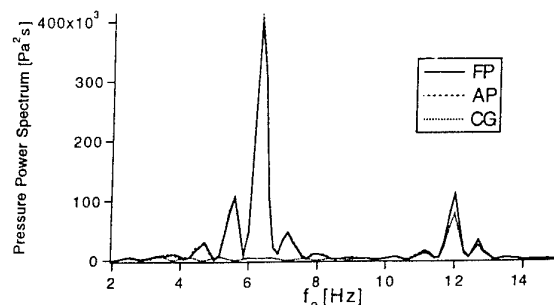


Fig. 7 Spectra of air cushion pressures. Air leakage neglected. Rigid stern seal. Head sea. $T_p=1.8$ s. $H_{1/3}=0.15$ m.

Fig. 7 shows the unsteady air cushion pressure when the stern seal is rigid and air leakage underneath the seals is neglected. The spectra have an oscillatory behaviour with many peaks. This is caused by amplification and cancellation effects in the volume pumping of the air cushion due to the incident waves. If the cancellation effect is disregarded, there are two main spectral peaks at approximately 6 and 12 Hz. These frequencies correspond to the two first spatial pressure resonances of a rectangular box, with length $L=28$ m. The spectral values around 6 Hz are nearly the same at AP and FP and nearly zero at CG. The reason is that the first eigenfunction for acoustic resonance in a rectangular box is equal to -1, 0 and 1 at AP, CG and FP. Around 12 Hz there is significant response also at CG. The reason is that the second eigenfunction for acoustic resonance is equal to -1, 1 and -1 at AP, CG and FP. Vertical accelerations at AP, CG and FP are presented in Fig. 8. The accelerations and the air cushion pressures have a similar behaviour, except that the accelerations around 12 Hz is negligible. Fig. 8 illustrates that the linear hydrodynamic wave excitation forces and moments on the side-hulls are negligible.

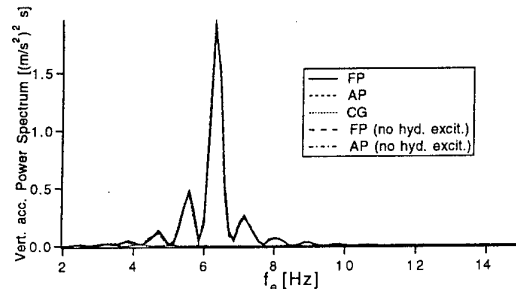


Fig. 8 Spectra of vertical accelerations. Air leakage neglected. Rigid stern seal. Head sea. $T_p=1.8$ s. $H_{1/3}=0.15$ m.

In order to illustrate possible deformation patterns of the stern seal bag, the static and the first four mode shapes of a 2-loop flexible stern seal bag are represented in Fig. 9. These mode shapes are the first four used (see Eqs. (8) and (9)) to describe the deformation of the flexible stern seal bag structure.

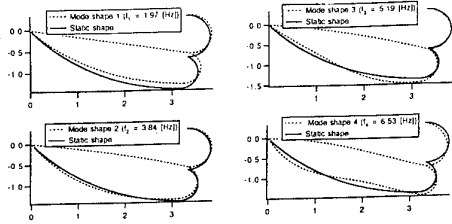


Fig. 9 Static configuration and first four mode shapes of flexible stern seal bag. Static difference pressures: $\Delta P_{01} = 500 \text{ Pa}$. $\Delta P_{02} = 5500 \text{ Pa}$. Bag length $L_b = 3.16 \text{ m}$. Bag height $H_b = 1.4 \text{ m}$. $EA = 0.6 \cdot 10^6 \text{ N}$. $M_m = 4.3 \text{ kg/m}$.

Vertical accelerations at AP, CG and FP with a flexible stern seal bag are presented in Fig. 10. The air leakage underneath the seals is neglected. If Fig. 8 is compared with Fig. 10, some differences are observed. First one notes that the main spectral peak is shifted from approximately 6 Hz down to about 5 Hz. This is due to the flexible behaviour of the stern seal bag. The mechanism may be explained as follows; the flexible bag is deformed due to the unsteady air cushion pressure so that the deflected volume is in phase with the unsteady air cushion pressure. This leads to an equivalent horizontal velocity at the bag, due to the assumption of uniform pressure over the height of the air cushion. A simplified model can illustrate this phenomenon. Assuming harmonic time dependence $e^{i\omega_e t}$ and neglecting damping, the following eigenvalue problem can be defined

$$\begin{aligned} -\omega_e^2 \Psi_{bsp} - v_s^2 \Psi_{bsp,x'x'} &= 0 \\ \Psi_{bsp,x'} &= 0 \quad \text{at } x'=0 \\ \Psi_{bsp,x'} &= \frac{dV_c}{dp_c} \frac{\rho_{co} \omega_e^2 \Psi_{bsp}}{H_c B_c} \quad \text{at } x'=L \end{aligned} \quad (19)$$

Here i is the complex unit and $\Psi_{bsp} e^{i\omega_e t}$ is the velocity potential of the air flow in the air cushion due to the motion of the bag. H_c and B_c are the cushion height and beam. ρ_{co} is the steady mass density of air in the air cushion. dV_c/dp_c is a measure of the change in air cushion volume V_c due to bag deformation. It can be evaluated by noting that the right hand side of the boundary condition at $x'=L$ is a longitudinal velocity u' averaged over the

cross-section of the air cushion. This can be expressed as

$$u' e^{i\omega_e t} H_c B_c = \frac{dV_c}{dt} = \frac{dV_c}{dp_c} \frac{dp_c}{dt}$$

Here $p_c = -\rho_{co} i \omega_e \Psi_{bsp} e^{i\omega_e t}$ is the dynamic pressure in the air cushion at $x'=L$. dV_c/dp_c can be estimated by a static analysis of the bag. The solution of the eigenvalue problem is $\Psi_{bsp} = \Psi_{bsp} \cos rx'$ where $\omega_e = v_s r$ and

$$\tan rL + \frac{\gamma_s p_{co}}{H_c B_c L} \frac{dV_c}{dp_c} rL = 0 \quad (20)$$

Here r is the wave number of the standing pressure waves in the air cushion. Eq. (20) is the dispersion relation of the acoustic pressure waves inside the air cushion. When dV_c/dp_c is zero, $rL = \omega_e L/v_s = n\pi$, $n=1, 2, \dots$. This is a well known result for standing pressure waves in a long tube with rigid ends. Since $dV_c/dp_c > 0$ for a flexible stern, the resonance frequency is reduced relative to rigid ends. The actual value depends on L, H_c, B_c , the ratio of specific heat of air γ_s and the steady excess pressure p_{co} in the cushion.

Second one notes that the spectral peaks of the vertical accelerations at AP and FP in Fig. 10 are reduced with approximately 40% and 20% relative to Fig. 8. This reduction is explained by the flexible behaviour of the stern seal bag and the coupling between the bag pressure and the air cushion pressure at the bag. The differences between the vertical accelerations at AP and FP presented in Fig. 10, may be explained by the mode shape function of the pressure waves. If the previous simplified solution of Ψ_{bsp} is used, then the variation in the longitudinal direction is given by $\cos rx'$. The ratio of Ψ_{bsp} between AP and FP is $\cos rL$. Since rL is less than π , the absolute value of the ratio is less than 1. Fig. 10 shows that the flexible bag increases the accelerations in the region just above 10 Hz. This increase is mainly explained by the volume change of the air cushion due to the deformation of the flexible stern seal bag.

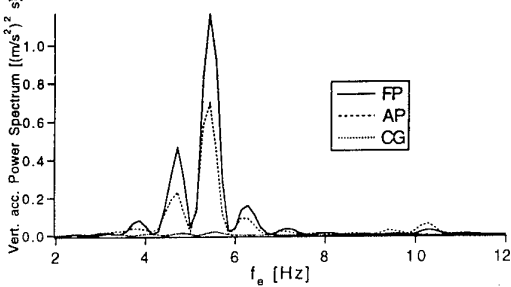


Fig. 10 Spectra of vertical accelerations. Air leakage neglected. Flexible stern seal bag. Head sea. $T_p = 1.8 \text{ s}$. $H_{1/3} = 0.15 \text{ m}$.

The effect of a constant leakage height underneath the stern seal bag can be studied by comparing Fig. 10 and 11. The vertical accelerations in Fig. 11 are decreased with approximately 10% relative to Fig. 10 around the first spatial pressure resonance frequency. The reason is additional damping caused by the air leakage underneath the stern seal bag.

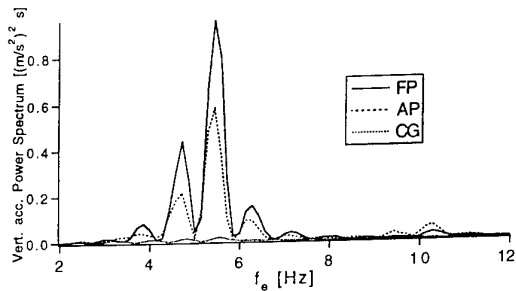


Fig. 11 Spectra of vertical accelerations. Constant leakage heights: 0 m (bow); 0.02 m (stern). Flexible stern seal bag. Head sea. $T_p = 1.8$ s. $H_{1/3} = 0.15$ m.

Vertical accelerations at AP, CG and FP accounting for variable leakage height underneath both the bow and stern seal are presented in Fig. 12. The variable leakage height underneath the seals is dependent on the relative motion between the seal and the water surface. The spatially varying pressure underneath the flexible bag is also accounted for. The static leakage height (h_{LO}) is set equal to -0.1 m and 0.02 m at the bow and the stern. The negative static leakage height at the bow means that the relative motion between the bow skirt and the water surface must be 0.1 m before air leakage at the bow occurs. These values of the static air leakage height are used through the remaining part of this section.

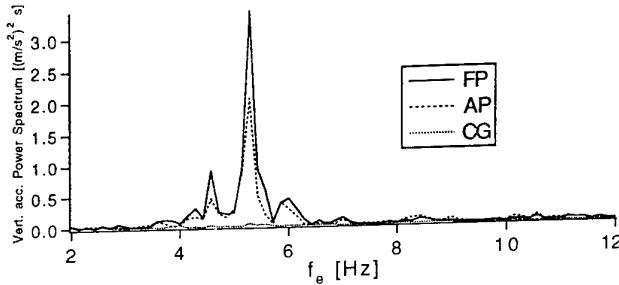


Fig. 12 Spectra of vertical accelerations. Variable air leakage. Spatially varying pressure underneath flexible stern seal. Head sea. $T_p = 1.8$ s. $H_{1/3} = 0.15$ m.

When vertical accelerations presented in Fig. 12 are compared with Fig. 11, one observes an increase of approximately 85% in the vertical accelerations around the first spatial pressure resonance frequency. An important reason is reduced damping due to smaller leakage height underneath the flexible stern seal bag. The spatially varying pressure underneath the bag forces the flexible bag to reduce the leakage height. There is also a change in the excitation of the air cushion pressure caused by the flexible bag motion.

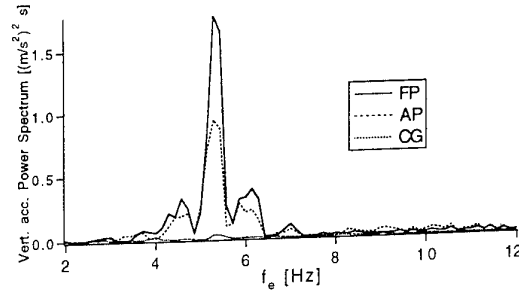


Fig. 13 Spectra of vertical accelerations. Variable air leakage. Spatially varying pressure underneath flexible stern seal. Water impact on bag. Head sea. $T_p = 1.8$ s. $H_{1/3} = 0.1$ m.

Vertical accelerations predicted by the complete model are presented in Fig. 13. The effect of air leakage underneath the seals is included together with hydrodynamic impact forces from the contact with the water. $H_{1/3}$ is reduced from 0.15 to 0.10 m in these calculations. This is necessary to avoid too large deformations of the bag structure and not contradict the assumption of a linear elastic model. These deformations are mainly caused by the interaction between the spatially varying pressure underneath the flexible bag and the hydrodynamic impact loads from the water. Since the bag structure is close to being horizontal in the impact region, a small increase in the immersion of the bag results in large increase in the wetted length. This causes large impact loads that punch the bag structure out of the water. On the other hand the spatially varying air pressure is in a way forcing the bag structure to reduce the leakage height underneath the bag. Many modes are needed to describe the dynamic behaviour of the bag during water impact. Improved convergence was achieved by introducing a bending stiffness term $-EI\partial^4\eta_n/\partial s^4$ on the right hand side of Eq. (6). The mode shapes corresponding to $EI=0$ were used. EI was set equal to 4.0 Nm^2 . It was controlled that the global response was independent of this particular choice of EI as long as EI was small and larger than 3 Nm^2 .

To evaluate the effect of the hydrodynamic impact between the flexible stern seal bag and the water, an analysis is made with the same model and data as described in Fig. 13, but without the effect of water impact. The results are presented in Fig. 14. The

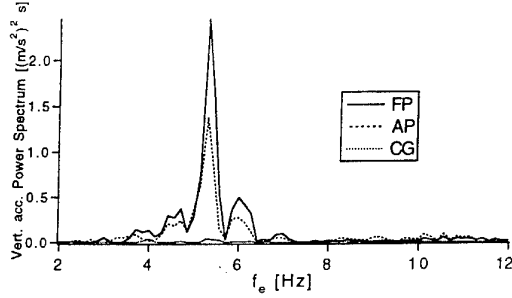


Fig. 14 Spectra of vertical accelerations. Variable air leakage. Spatially varying pressure underneath flexible stern seal bag. No water impact. Head sea. $T_p=1.8$ s. $H_{1/3}=0.1$ m.

largest differences between Figs. 13 and 14 occur in the frequency region around the first spatial pressure resonance of the air cushion (≈ 5 Hz). Spectral values for vertical accelerations are increased about 20% relative to the results in Fig. 13. One possible explanation is that the motion of the stern seal bag induced by the water impact affects the air cushion pressure similarly as a piston at the end of a long tube and may in this way cancel a part of the pressure variation in the air cushion. A probably more important reason is that the hydrodynamic impact punches the bag out of the water immediately after the initial impact so that an air leakage is recovered. The air leakage introduces damping and therefore reduces the vertical accelerations.

Since the results in Figs. 12 and 14 are obtained by the same physical model, but with different values of $H_{1/3}$, it illustrates that vertical accelerations are nonlinearly dependent on $H_{1/3}$. If the vertical accelerations had a linear behaviour, spectral value of the vertical accelerations at FP at the highest peak of the spectrum should be approximately $5.4 (m/s^2)^2 \cdot s$ for $H_{1/3}=0.15$ m when the corresponding spectral value is $2.4 (m/s^2)^2 \cdot s$ at $H_{1/3}=0.10$ m. Fig. 12 shows instead a value of $3.4 (m/s^2)^2 \cdot s$ at $H_{1/3}=0.15$ m. This means that cobblestone oscillations of a SES can be overpredicted if linear transfer functions are used.

The airgap underneath the lowest point of the static bag configuration are presented as function of time in Fig. 15. The complete model is used. The significant difference between the two curves is due to the dynamic deformation of the lowest point of the bag. Fig. 15 illustrates that the

flexible stern seal bag is “following” the water surface. A main reason is that the spatially varying pressures caused by the air leakage reduce the leakage. This behaviour is a characteristic feature of a flexible stern seal bag.

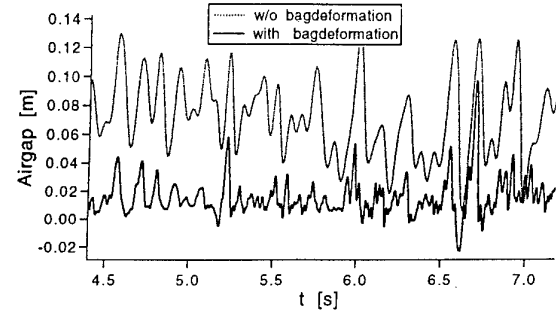


Fig. 15 Airgap underneath lowest point of static bag configuration as function of time. Effect of dynamic bag deformations. Full simulation model. (see also Fig. 13).

The previous analysis has in particular focused on the dynamics of the flexible stern seal bag and its effect on the vertical accelerations. An important parameter from a design point of view is the height to length ratio of the flexible stern seal bag. Fig. 16 shows vertical accelerations

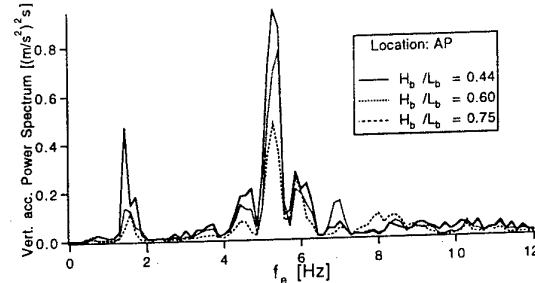


Fig. 16 Spectra of vertical accelerations at AP for different height to length ratios of flexible stern seal bag. Data and model as in Fig. 13.

at AP for three different height to length ratios of the flexible stern seal bag. When the height to length ratio is increased, the vertical accelerations are reduced. Similar results are obtained at FP. Fig. 16 shows also that the frequency region of the uniform pressure resonance is affected. The uniform pressure resonance frequency is approximately 1.6 Hz. Since the linear wave loads are negligible in this region due to the assumed wave spectrum, the response is due to nonlinear effects. One possible explanation for the reduced accelerations is that increased height to length

ratio of the flexible stern seal bag reduces the effect of the spatial pressure variation underneath the bag caused by the air leakage. This reduction may be explained as follows. The effect of the spatial pressure variation underneath the bag is mainly important in the region where the ratio between the leakage height and the height at the actual position is most influenced by the motion of the bag, that is the region near the lowest point of the bag. In the present case where the height to length ratio is increased, this implies that the length of this region is reduced and the effect of the spatial pressure variation as a result is reduced.

4. CONCLUSIONS

Cobblestone oscillations are theoretically studied in the time domain. Focus is on the influence of flexible stern seal bags and how the associated aero-hydroelastic problem can be simplified. It is shown by a case study that:

- The flexible stern seal bag reduces the lowest spatial resonance frequency of the air cushion. The elastic bag deformations are important for cobblestone oscillations.
- The spatially varying pressure caused by air leakage underneath the bag reduces the air leakage. This effect is important and increases the cobblestone oscillations.
- Hydrodynamic impact on the bag matters and reduces the vertical accelerations.
- Hydrodynamic wave induced loads on the side hulls are not important.
- Increased height to length ratio of the bag reduces the vertical accelerations.
- Vertical accelerations have a nonlinear dependence on significant wave height.

The analysis assumes that the incident waves pass undisturbed through the air cushion. The influence of the change in air cushion volume and leakage area due to diffraction of the incoming wave system by the presence of the side hulls, cushion pressure and bow seal should be studied. This includes interaction with the steady flow field. A quasi-steady analysis of the fans is used. [12] reports that dynamic fan effects may significantly reduce the spatially uniform pressure response in the air cushion.

Since the cobblestone oscillations are difficult to study in model scale [1], the theory needs to be validated by full scale results.

References

1. Kaplan, P., Bentson, J., Davis, S., "Dynamics and Hydrodynamics of Surface-Effect Ships", Trans. SNAME, Vol. 89, 1981, pp. 211-247.
2. Steen, S., "Cobblestone Effect on SES", Dr.ing. Thesis, Dept. Marine Hydrodynamics, Norw. Univ. of Science and Technology, Trondheim, Norway, 1993.
3. Steen, S., Faltinsen, O.M., "Cobblestone Oscillations of a SES with Flexible Bag aft Seal", J. Ship Res., Vol. 39, No.1, March 1995, pp. 25-41.
4. Sørensen, A.J., Steen, S., Faltinsen, O.M., "SES Dynamics in the Vertical Plane", Schiffstecknik, Bd 40, 1993, pp. 71-84.
5. Faltinsen, O.M., "Sea Loads on Ships and Offshore Structures", Cambridge University Press, 1990.
6. Faltinsen, O.M., "Hydrodynamics of High Speed Vehicles", Ch. 3 in Advances in Marine Hydrodynamics (Ed. M. Ohkusu), Computational Mechanics Publications, Southampton, Boston, 1996.
7. Sørensen, A.J., "Modelling and Control of SES Dynamics in the Vertical Plane", Dr.ing. Thesis, Dept. of Engineering Cybernetics, Norw. Univ. of Science and Techn., Trondheim, Norway, 1993.
8. Salvesen, N., Tuck, E.O., Faltinsen, O.M., "Ship Motions and Sea Loads", Trans. SNAME, Vol. 78, 1970, pp. 250-287.
9. Ulstein, T., "Nonlinear Effects of a Flexible Stern Seal Bag on Cobblestone Oscillations of a SES", Dr.ing. Thesis, Dept. Marine Hydrodynamics, Norw. Univ. of Science and Techn., Trondheim, Norway, 1995.
10. Ulstein, T., Faltinsen, O.M., "Hydroelastic Analysis of a Flexible Bag-Structure", 20th Symp. on Naval Hydrodynamics, University of California, Santa Barbara, USA, 1994.
11. Ulstein, T., Faltinsen, O.M., "Two-Dimensional Unsteady Planing", J. Ship Res., Vol. 40, No. 3, Sept. 1996, pp. 200-210.
12. Sullivan, P.A., Gosselin, F., Hinchen, M.J., "Dynamic Response of an Air Cushion Lift Fan", Proc. HPMV'92, Conference and Exhibits, ASME, Flagship Section, Arlington, VA, USA, 1992, pp. ACV39-ACV47.

Heel compensation for the Charles de Gaulle aircraft carrier : principles and control structure

S.KUMMER

DGA/DCN INGENIERIE - Surface Ship Department
8 boulevard Victor
00303 - PARIS ARMEES (France)
Tél. +33.01.40.59.15.79 - Fax +33.01.40.59.16.15
emel : dcning@cedocar.fr

G.HARDIER, C.LAMBERT

ONERA - System Control & Flight Dynamics Department
2 avenue Edouard Belin
31055 TOULOUSE Cedex 4 (France)
Tél. +33.05.62.25.27.77 - Fax +33.05.62.25.25.64
emel : hardier@cert.fr

Abstract

To improve the seakeeping performances of the french nuclear aircraft carrier Charles de Gaulle, with respect to its predecessors Clémenceau and Foch, DCN has developed a platform motion control system, called SATRAP, which reduces the ship motions while ensuring navigation capability. This system involves a centralized computer which controls three subsystems: two pairs of stabilizing fins, a set of rudders and a moving-mass system (athwart ship) for heel compensation, the Cogite system. Originally conceived for situations where the stabilizing fins would be otherwise saturated (steady heel from wind or heavy weights displacements), Cogite has evolved into a system which also improves the operational capability of the ship by limiting the heel during sharp turns, permitting non-stop handling and preparation of aircrafts. This paper presents the results of the studies which led to the development of a performing mode of operation for SATRAP, where the helmsman has full control of the rudders while the fins and Cogite system automatically reduce the ship motions. The following points are discussed in this paper: operational requirements in terms of performances, SATRAP system architecture and principles chosen for the control laws (task allocation for the actuators, feedforward-feedback controllers).

Résumé

Pour améliorer la tenue à la mer du porte-avions nucléaire Charles de Gaulle (en comparaison des porte-avions Clémenceau et Foch de l'ancienne génération), la DCN a mis au point un système de contrôle des mouvements de plate-forme, le SATRAP, qui stabilise le navire et assure les fonctions d'un pilote automatique traditionnel. Ce système coordonne, par l'intermédiaire d'un calculateur centralisé, l'action des différents organes: deux paires d'ailerons stabilisateurs, l'appareil à gouverner, un système de masses mobiles en transversal pour Compenser la Gîte (Cogite). Conçu à l'origine pour suppléer l'action des ailerons lorsqu'ils sont inefficaces (gîtes permanentes induites par le vent ou le chargement), le système Cogite permet désormais d'augmenter les capacités opérationnelles du navire en compensant la gîte durant les manœuvres, ce qui facilite et accélère la mise en oeuvre des aéronefs. Ce papier présente le résultat des études qui ont abouti à la mise au point d'un fonctionnement "transparent" pour le SATRAP, où l'homme de barre a toute liberté d'action sur l'appareil à gouverner, tandis que les ailerons et le système Cogite assurent une stabilisation automatique des mouvements du

navire. Les points suivants sont abordés dans ce papier: besoins opérationnels au niveau des performances, architecture du SATRAP, principes des lois de commande (répartition des tâches entre les actionneurs, commandes boucle ouverte et boucle fermée).

1. Operational requirement for the Charles de Gaulle aircraft carrier

Aircraft carriers are especially designed to integrate aircraft and ship constraints. The ship must be a real airport, even if smaller, with landing runway, parking area, hangar, maintenance devices, traffic control, etc.... However, shipboard aircraft operations remain complex and need a highly trained crew, even on calm seas : so, what about operations in rough weather conditions ?

At the early stages of the Charles de Gaulle design, DCN and the French Navy took special care of these weather constraints. In fact, due to ship motions, the three aircraft main operations (handling, take-off and landing) become hazardous. Thus, the 40 000 tons displacement CdG-CVN is required to reach, in rough weather conditions, the shipboard aircraft operational capability of a 90 000 tons US Navy CVN, which means aircraft operations up to sea state 5, instead of up to sea state 4 for the Clemenceau class former CV.

To achieve this requirement, DCN designed a new system called SATRAP (Système Automatique de Tranquillisation et de Pilotage, i.e. Steadyng and Piloting Automatic System), which controls "horizontal" ship motion, i.e. roll, yaw and lateral displacement at the arresting gear area.

1.1 Main aircraft operations

The SATRAP is mainly designed to ease the most dangerous aircraft operations such as take-off and landing. During these phases, the ship is on straight course, with enough speed to generate sufficient wind over deck ; so, active lifting surfaces (rudders and stabilization fins) give the best trade-off between cost and efficiency.

As the horizontal ship motions are physically coupled, the rudders and fins control laws of this "steadiing system" have a multivariable structure, different from the classical monovariable laws used for a classical piloting or stabilizing system.

To achieve heel requirements, without degrading the stabilization fins dynamic efficiency, a specific heel control system was designed, which is the third mechanical component of SATRAP. In the first design step, it was made of sea water ballasts and transfer pumps located in sponsons, just under the flight deck, to get the maximum righting lever arm. After an optimization stage, a better solution was chosen, involving solid mass transfer.

Even during straight courses, the heel control is essential for CdG-CVN (figure 1):

- due to the larger flight deck beam, the wind heeling moment is bigger on Charles de Gaulle than on former Foch CV, as shown by aerodynamical scale model testing,
- also due to the larger flight deck beam and to the increase of shipboard aircraft weight (11 tons Super Etendard versus 20 tons Rafale), aircraft handling create higher heeling moment ($\times 1.8$) than on former French CV.

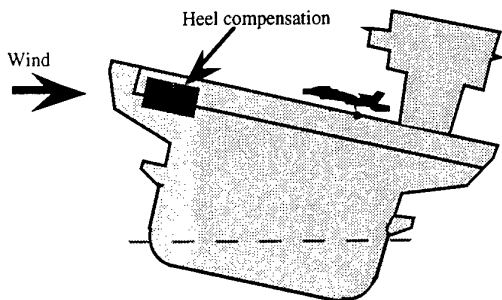


Figure 1

To achieve Foch CV heel performances, an increase of ship righting moment could have been chosen, which means a high transversal stability module. But high stability module induces unacceptable architectural constraints, and much higher natural roll motion. The ship would have been difficult to stabilize or unacceptable fins surfaces would have been induced. DCN chose to develop an active heel compensation system instead.

1.2 Reducing the mission preparation stage

Heel control is also useful to reduce the mission preparation phase. Most of the time, an aircraft carrier has to change course to come to head wind, which allows to carry out take-off and landing operations. The course changing delay is an operational constraint which has to be taken into account for aircraft launch.

On Clemenceau class CV, two ways are available to decrease this delay :

- by choosing a small rudder angle which results in a low induced heel, and allows aircraft handling,
- by choosing a high rudder angle to quickly reach the operational heading, but in this case aircrafts have to be tied down during the course changing, due to the heel induced by a high yaw rate.

For the CdG-CVN, it was decided to use the heel compensation system for reducing heel during gurations in

order to decrease the course changing duration while carrying aircraft handling (see figure 2).

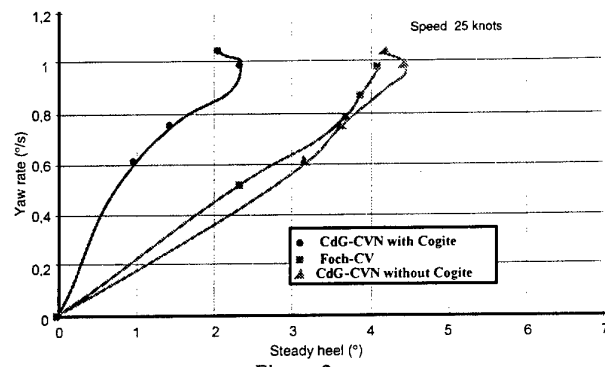


Figure 2

The associated criteria are :

- roll less than 3 degrees (max. value), while course keeping or course changing,
- heel (i.e. low frequency part of the roll) less than 1 degree in straight courses.

1.3 Operational course changing management

Aboard a classical ship, the Officer of the Deck (OOD) can learn quickly how to associate the giration steady heel with ship speed, rudder angle and wind speed. With an automatic heel compensation system, the behaviour of Charles de Gaulle CVN becomes non-linear. Indeed, most of the time the ship sails with zero heel, but when the heel compensation device reaches its limits, the ship turns into a classical ship and the heel increases.

There are several means to carry out course changing while keeping the heel operational limits :

- full automatic course changing with the mass transfers pre-computed (before course changing). This solution allows to check that the heel won't be above the operational limit all along the manoeuvre ; however, changing the giration parameters while turning is very demanding, and if the OOD decide to switch to manual steering, heel constraints could no more be ensured.
- real time computation of mass transfers permitting manual or automatic course changing. In this mode, the OOD has the ability to change the giration parameters at any time, but the maximum heel reached during the manoeuvre will be unknown in advance.

As an aircraft carrier has to find quickly the best heading according to the wind, and as wind characteristics (speed and direction) can also vary quickly, it must be always possible for the OOD to correct easily and safely the giration parameters. So the second option was chosen, and a heel prediction algorithm (predicted over about one min) has been developed too. It increases the safety by giving the OOD information in advance for changing the giration parameters.

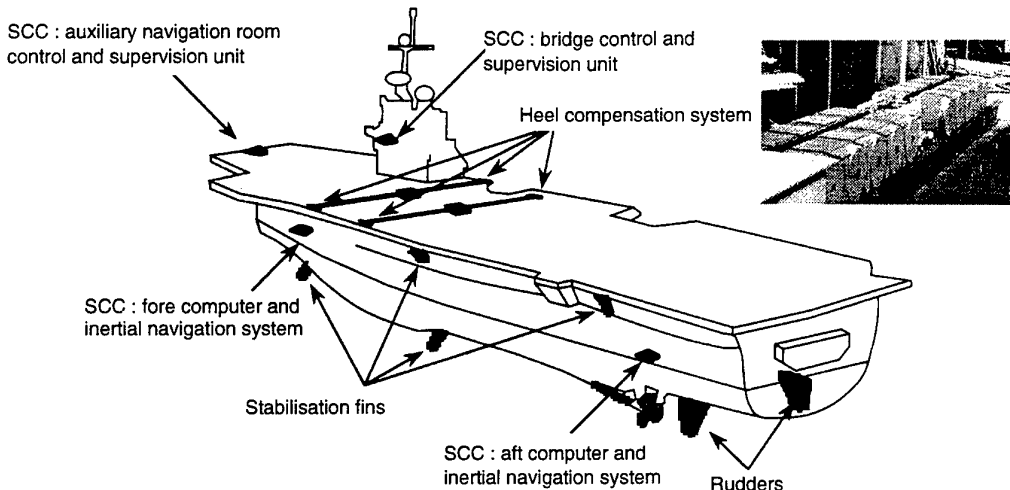


Figure 3

2. SATRAP system : architecture and functions

To ease control of the sub-systems, all of them acting on physically bound phenomena, SATRAP is a very integrated system which fully performs three functions :

- steadyng horizontal ship motions
- steering control (course changing and course keeping)
- heel compensation (in straight courses or during course changing).

The SATRAP system is fitted with the following subsystems (see figure 3) :

- two 19 m^2 rudders, with a $12^\circ/\text{s}$ deflection rate, developped and built by NFM,
- four 12 m^2 stabilization fins, with a $10^\circ/\text{s}$ deflection rate, developped and built by ACH Engineering,
- the heel compensation device, called "COGITE" by Technicatome which developed it,

- a redundant high level control and supervision unit which takes ship motion data from the "Integrated Navigation System" (inertial system) and wind data (speed and heading) from the "wind network", and which elaborates subsystems control orders. This system is usually operated from the bridge, but a redundant device located in the Auxiliary Navigation Room allows to operate SATRAP if the bridge is destroyed. Thomson ISR developped and built this controller subsystem, which integrates the control laws described in this paper.

3. COGITE system

3.1 Mechanical principles

This SATRAP subsystem is equipped with twelve independant 22 tons moving masses (trains), running athwart ship under the flight deck, from side to side (figure 4).

Four speeds are available ($0.2, 0.4, 0.6$ and 0.8 m/s) : the last one allows a complete transfer in less than one minute, the lower speeds being suited for smoother transfers.

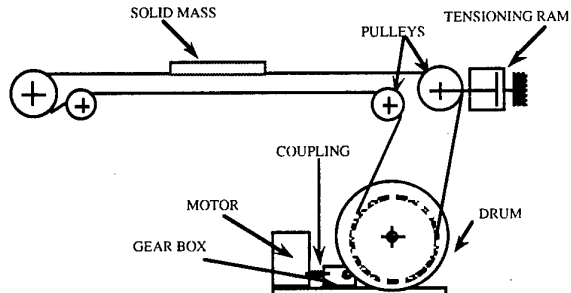


Figure 4

The "solid mass" choice induces 20% weight, 30% cost, 40% volume and 50% electrical power reduction compared with the liquid solution. It is also more precise and easier to design with high reliability constraints.

3.2 Reliability of Cogite device

On rough seas, the SATRAP system is essential for allowing the CdG-CV to perform aircraft operations. In case of failure, take-off may become impossible and landing crash may occur. To avoid failure, SATRAP has been designed to comply with a very high reliability and availability requirement, and so do

the Cogite subsystem, thanks to the following characteristics :

- two separate systems (two sub-groups of six trains) in two separate rooms, to avoid loosing all the devices contributing to a given function.
- system designed to survive to the first failure, for any part of the system and associated ancillaries, i.e. for control units (3 redundant processors), mechanical actuators, motor cooling, electrical power ... The reconfigurations can happen even during a transfer and are fully automatic. In case of damage for one electro-mechanical element, the train is coupled to the adjacent one, and nominal performances are still available.
- high level of reliability and availability even in the fully redundant state, i.e. insensitive to the first failure.
- very secure manual mode in case of several serious troubles.

4. Principles of heel compensation and roll stabilization

On the roll axis, the control system aims at minimizing the effects of the different disturbances acting on the ship, i.e. sea, wind, on-board masses displacements (aircrafts handling), likewise the outcomes of ship manoeuvres (course-changing for instance). To fulfil this requirement, according to the previously mentioned trends, SATRAP disposes of two types of actuators, namely :

- the fins devoted to the control of high frequency disturbances (sea waves). In fact, their static efficiency is low, and using them all over the frequency range would produce a bias in case of steady heel : due to the limitation of control deflections, it should result in a dissymmetrical reduction of the sea disturbances, which is certainly not desirable.

- the moving masses of the Cogite device devoted to the compensation of the whole low frequency motions. In fact, Cogite response time makes it unsuited to oppose the roll fast motions and, on the other hand, overheating and wear electro-mechanical constraints are not consistent with ceaseless displacements of the masses.

It should be observed that a classical water-ballasting system still subsists on the CdG-CVN, and is available for manually compensating the heel variations induced by different ship load conditions.

The control scheme of figure 5.a is derived from satisfying these constraints, and from the frequential complementarity of the two actuators. The specific actions of the fins and Cogite are frequency uncoupled, because of the controllers structure (roll rate and acceleration feedback for the stabilization system, and heel proportional-integral feedback for the compensation system), and by means of appropriate filtering.

However, by taking into account the desired operational performances (residual heel less than one degree), and the care for preventing any ill-timed motion of Cogite (which implies a safety filtering with regard to the lowest frequency seas), this classical feedback scheme is not sufficient by itself. It can be improved by introducing a feedforward component (figure 5.b), which will allow to anticipate the foreseeable heel motions induced by the wind and rudders deflection (helmsman or automatic piloting), especially during the transient phase. This feedforward control action makes use of a simplified ship modeling, permitting to derive a continuous estimation of the heeling moment acting on the roll axis. The predictable moving-masses speed can thus be deduced, necessary for preventing the ship from heeling. The advantages of this approach are manifold :

- the control is directly issued from the hydrodynamic and aerodynamic effects on the heeling moment ; therefore, no delay comes from the integration of these effects through the ship own dynamics.

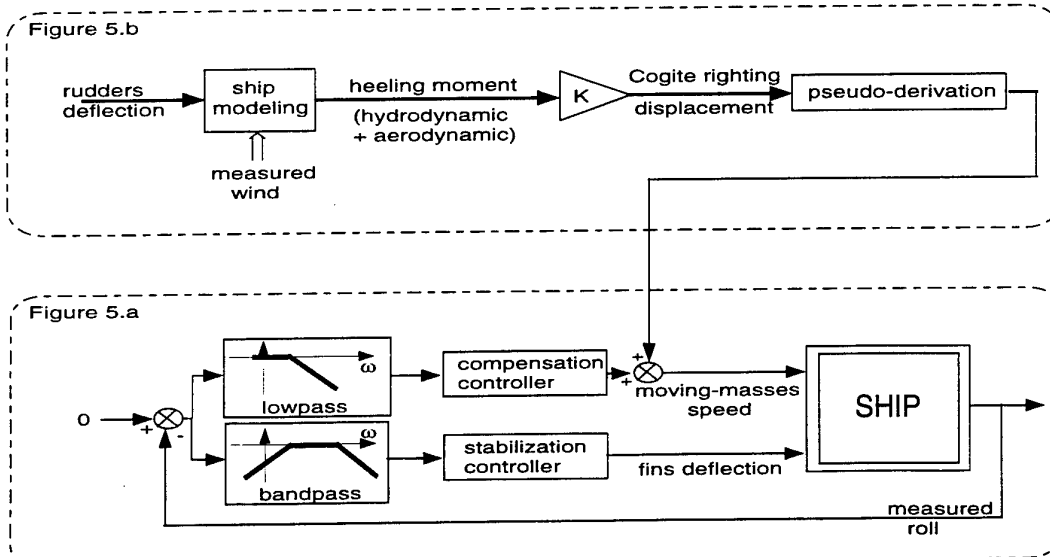


Figure 5

- the modeling naturally disregards the high frequency disturbances induced by the sea ; so, the control orders produced through it are “clean” ones, and do not require the same kind of filtering as their feedback counterparts.
- since we get a model with a ship state vector (synchronously estimated) at our disposal, it is easy to take advantage of them to predict the ship behaviour by simulation, over a short receding horizon (some secondes) ; so, by using past, present and future informations, it is possible to implement a non-causal derivator filtering to produce a moving speed without any additional phase lag with respect to the desired righting displacements. After synthesis from an ideal frequency shaping, this FIR filter is described by the (finite) series of its impulse response coefficients, permitting to compute the feedforward control action by straightforward convolution with the sequence of estimated displacements.

Regarding the drawbacks, introducing an explicit modeling into the control scheme could prove to be detrimental to the robustness. In the present case, this is not crucial since using a model is mainly motivated by the search for early starting or stopping of Cogite (more generally, anticipating any speed level change). In practice, this trend information proves to be unsensitive to the modeling errors, as confirmed by many simulations intending to check the robustness of the method. In the extreme, even a simplistic modeling could be useful to predict how the ship is going to heel in terms of the steering angle, and therefore to determine the way the moving masses have to start for opposing this effect. However, in view of the coupling existing between the different axes and of the nonlinearities induced by the physical limits of the masses motions, it would be irrelevant to leave the model internal state free, without taking care of its fitting and consistency with the real ship. This question will be addressed in §5, but implies to go further into the structure of the internal model first.

5. Consistency of the internal model state

The internal model is of the traditional manoeuvrability modeling type, the different components of which have been identified from sea tests on scale models (for the hydrodynamic and propelling parts), and from wind tunnel tests (for the aerodynamic part). Later on, the hydrodynamic coefficients will be improved from real sea tests to be performed soon aboard the Charles de Gaulle. The modeling structure obey the following equations :

$$\left\{ \begin{array}{lcl} M_u \ddot{u} - M v r & = & F_x^H + F_x^A + F_x^P \\ M_v \dot{v} + M u r & = & F_y^H + F_y^A \\ \dot{\phi} & = & p \\ I_\phi \ddot{p} + Mg \overline{GM} \sin \phi & = & M_\phi^H + M_\phi^A + M_\phi^C [+\Delta M_\phi] \\ \dot{\psi} & = & r / \cos \phi \\ I_\psi \dot{r} & = & M_\psi^H + M_\psi^A [+\Delta M_\psi] \end{array} \right. \quad (1)$$

where the superscripts H, A, P, C represent the forces (F) or the moments (M), respectively of hydrodynamic, aerodynamic, propelling type and induced by Cogite displacements. u and

v correspond to the longitudinal and lateral components of the ship speed. ϕ is the roll, ψ the heading. \overline{GM} the athwart stability modulus, and M the ship mass : M_u , M_v , I_ϕ and I_ψ represent the masses and inertia of their corresponding axes, including added masses and inertia. The hydrodynamic part can be developed in the following form :

$$\left\{ \begin{array}{l} F_x^H = \frac{1}{2} \rho S V^2 \left[C_{xu2} \bar{u} | \bar{u} | + C_{x\delta_2} \delta^2 + C_{xv2} \bar{r}^2 + C_{xvv} \bar{r} \bar{v} \right] \\ F_y^H = \frac{1}{2} \rho S V^2 \left[C_{yu} \bar{v} + C_{yr} \bar{r} + C_{y\delta} \sin \delta + C_{yv2} \bar{v} | \bar{v} | \right] \\ M_\phi^H = \frac{1}{2} \rho S L V^2 \left[C_h \bar{v} + C_{\delta h} \sin \delta + C_{lp} \bar{p} + C_{\delta p} \bar{p} / V \right] \\ M_\psi^H = \frac{1}{2} \rho S L V^2 \left[C_m \bar{v} + C_{mr} \bar{r} + C_{n\delta} \sin \delta \right] \end{array} \right.$$

by denoting L and S the ship length and reference surface. ρ the water density, V the speed modulus. δ the rudders angle, and the adimensional states as :

$$\bar{u} = \frac{u}{V}, \quad \bar{v} = \frac{v}{V}, \quad \bar{p} = \frac{pL}{V}, \quad \bar{r} = \frac{rL}{V}.$$

The coefficients involved in the aerodynamic forces are computed as a function of the relative wind parameters (speed and direction), which are measured on board by the wind sensors. During the prediction stages with the internal model, these parameters are calculated by using the latest estimation of the real wind and the course changes of the ship trajectory.

Following the structure of equations (1), several ways are used to make sure of the relevance of the trends issued from the feedforward component (figure 6) :

- The thrust F_x^P is expressed in terms of u and propeller revolutions T_h through the propeller advance ratio. As far as the internal modeling is concerned, the propeller number of revolutions is not measured, but is used as a control variable for keeping the model longitudinal speed u close to the ship measured one. In other words, the working of the propelling model is fictitious and not linked with the real one ; it is only used for balancing some of the modeling errors and for ensuring the consistency between the ship and model speed variations.
- the ΔM_ϕ term squares with an estimate of the aggregate modeling error on the roll moment. It is evently and asynchronously readjusted for taking into account the nonlinear effects induced by the masses displacement limit (± 20 m). The goal is to allow the model heeling when the real Cogite device is saturated (beyond the righting capability), and to integrate this compensation shortage when the control is on the point of unsaturating the system. This adjustment is calculated in terms of the moving masses position (d^{CS}), and possibly of the difference between the model and ship heels.

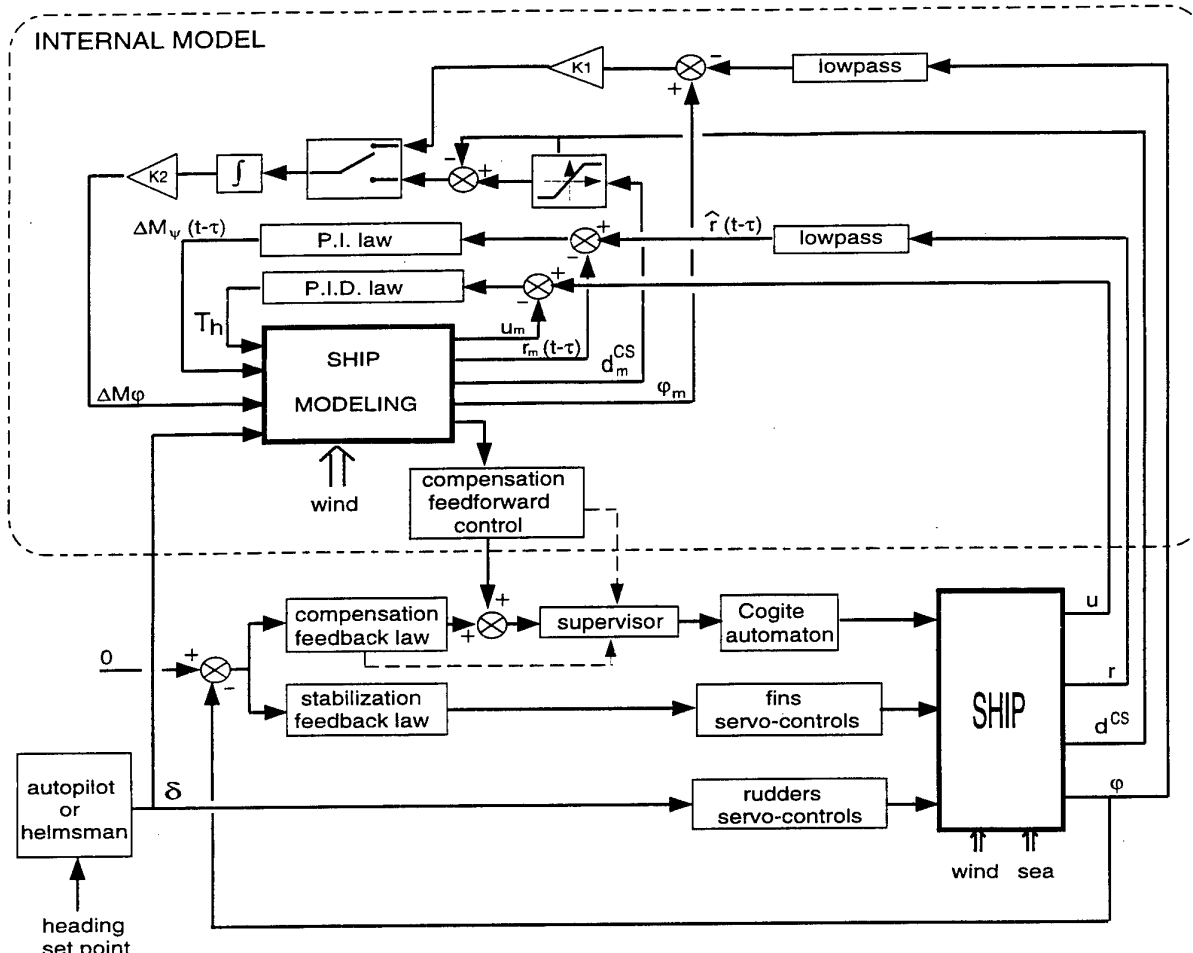


Figure 6

- the ΔM_ψ term represents an estimation of the modeling error on the yaw moment. It is used to be sure that the model trajectory stays in agreement with the ship one (especially the yaw rate). To this end, a servomechanism involves the model and measured yaw rate with the variable ΔM_ψ as a control input. Since it is imperative not to introduce high frequency disturbances into the modeling, this yaw rate has to be filtered first, and therefore it is a delayed model (delay τ corresponding to the filter propagation time) which is servocontrolled. Then, a predictive simulation permits to recover this delay and to get synchronous informations about the modeling state.

To achieve describing the working of the feedforward component, it can be stated that the rudders angle used during the simulation stages is associated either to the helmsman set point for manual steering, or to a reconstruction of the autopilot orders from heading set points and internal variations of the model states.

6. Problems induced by quantifying the control

The feedforward and feedback control components, mentioned up to now, were continuous variables, added for obtaining the final order to be sent to the compensation device. However, this order has first to be quantified (following the aforesaid 9 speed levels - see § 3) before being used by Cogite automaton. It explains the appearance of a "supervisor" unit in the scheme of figure 6. Its function is to quantify the control output by means of a standard threshold logic, while avoiding over-delayed decisions of speed level changes, and obviously ill-timed startings which could result from a too strict quantifying. For achieving this, in addition to the instantaneous orders delivered by the feedforward and feedback modules, the supervisor uses a very short-term prediction (4 seconds) of these two components, permitting to smooth the decisions to be taken. The feedforward component prediction is easily obtained by model simulation, and the feedback control prediction is issued from a closed loop simulation of an Auto-Regressive modeling, build and periodically adjusted with recent signal samples.

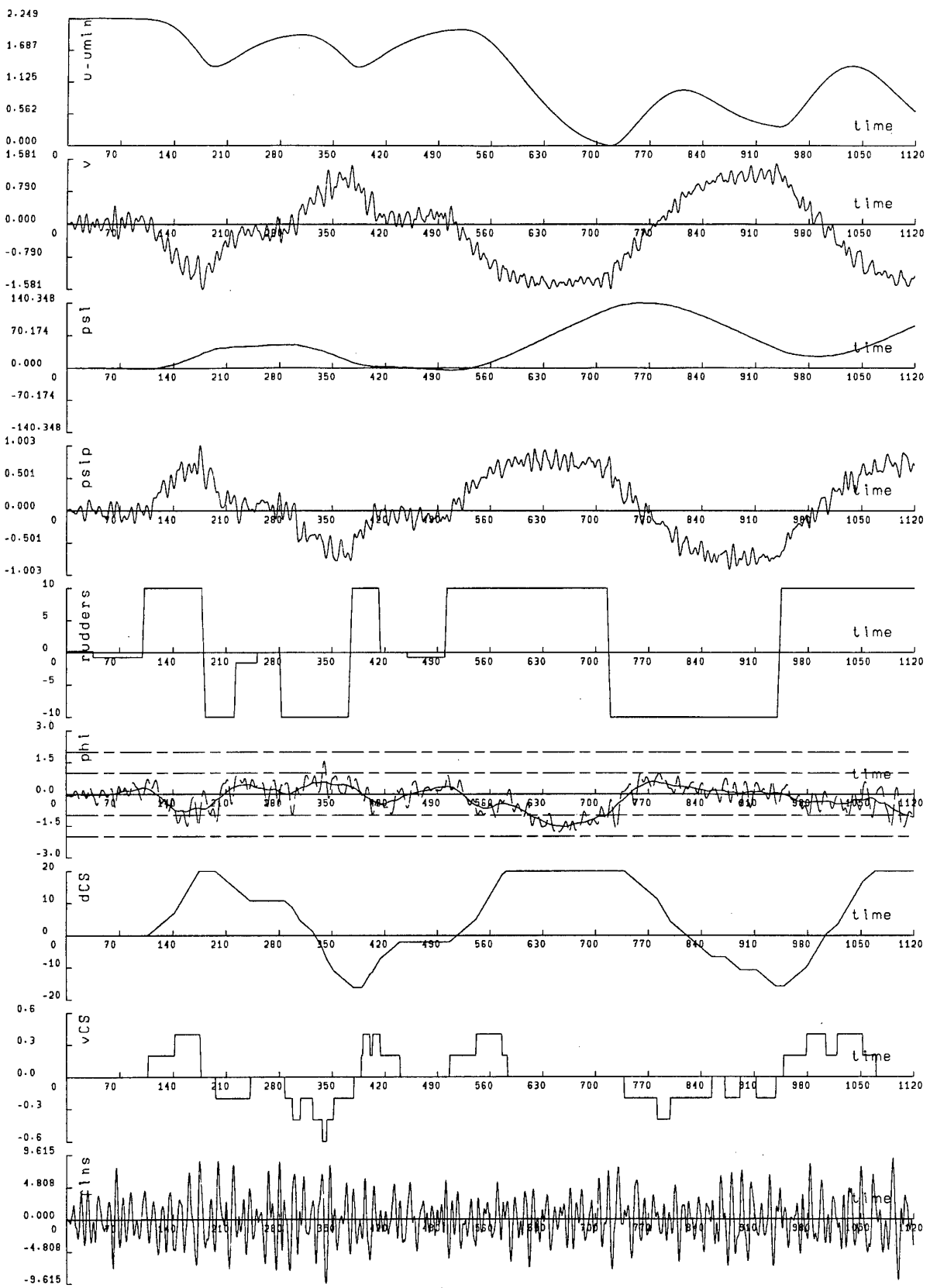


Figure 7

On the other hand, because of the dead zone around 0 induced by the lowest speed levels (± 0.2 m/s), a weak heel residue could remain in steady state since the static gain of the feedback component is limited. To cancel it, under some circumstances, the integrator of the closed loop must have the capability of ordering a moving masses displacement, a posteriori converted into a speed command during the convenient lapse of time. This function is devoted to the supervisor too.

7. Validation of the approach by simulation

Figure 7 displays the results obtained during hard manoeuvres, the ship moving forward at the initial speed of 20 knots, with variable wind conditions (rear wind at time $t=0$) between 30 knots (at the beginning) and 20 knots (at the end of the simulation). The sea disturbances correspond to a sea state 5, and fluctuate during the test as a function of the ship encounter angle. The notations used for distinguishing the different plots of figure 7 are defined as :

- ($u-u_{min}$) in m/s denotes the variations of the longitudinal speed from its initial value of 20 knots.
- v in m/s, the lateral component of the speed.
- ψ in degrees, the heading.
- $\dot{\psi}$ in deg/s, the yaw rate.
- δr in degrees, the rudders angle.
- ϕ in degrees, the roll of the ship (in dotted lines, an estimate of the heel being superimposed in solid lines).
- dCS in meters, the displacement of the 12 moving masses of Cogite.
- vCS in m/s, the displacement speed (according to the 9 available levels).
- $fins$ in degrees, the deflection of the stabilization fins.

The manoeuvres carried out during this simulation can be read as a series of course-keeping and course-changing stages, followed by emergency manoeuvring at the end of the sequence. The robustness issue is also addressed by means of large hydrodynamic modeling errors, i.e. the ship model used for the main simulator is different from the internal one used for computing the feedforward control component.

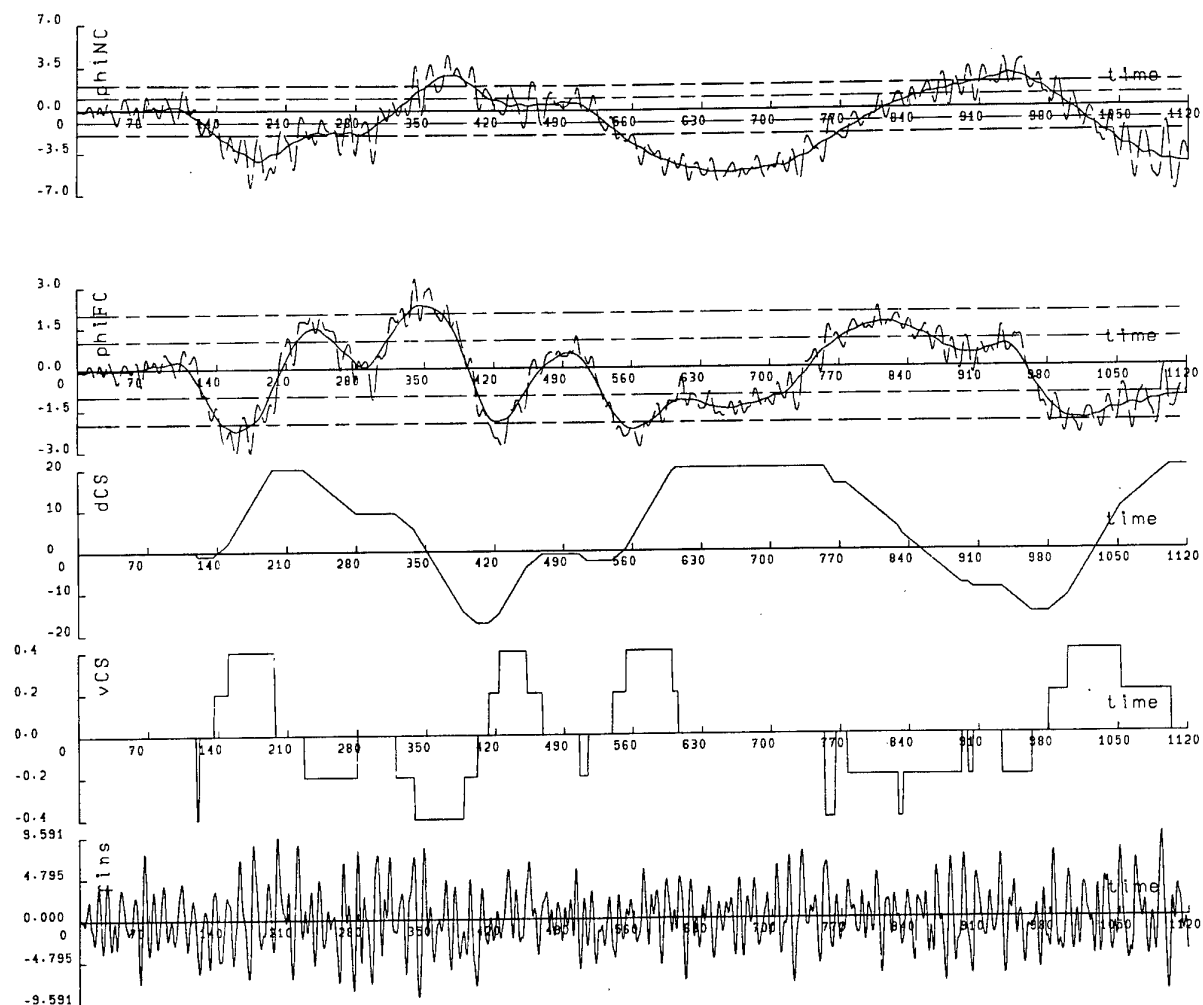


Figure 8

Figure 7. where both feedforward and feedback components are active, give an idea of the performances which can be obtained in realistic conditions, as the requests rate of the compensation system. Outside the zones where Cogite is saturated (± 20 meters in displacement), the residual heel remains below one degree, and the control proves to be weakly sensitive to high frequency sea disturbances.

By comparison, figure 8 depicts the roll motion when the stabilization and compensation systems are not available (ϕ_{INC}), as the roll (ϕ_{IFC}) and Cogite control order when the feedback component is active alone. The latter curves allow to quantify the contribution of the feedforward component : it is easy to see that, in both cases, the masses displacements are identical in the aggregate, but that adding the feedforward action is useful for anticipating the speed demands for about thirty seconds. In the end, this is translated into about 1.5° gain on the transient heel, which permits to fulfil the required performances.

More generally, a number of simulations were performed to check the performances in all operational conditions, stressing the transient stages of heeling. The robustness has been tested too, by resorting to many types of modeling errors, as well hydrodynamic as aerodynamic, and by simulating various unknown damage conditions on the actuators. However, about this, it must be stated that the system is provided with automatic reconfiguration facilities, in many damaged situations of the actuators (moving masses locked or coupled, steering trouble) or sensors (loss of informations from wind channel), as far as they are recognized by the acquisition and processing system.

8. Conclusions

From the operational requirements of an aircraft carrier, this paper has shown how the design stage has ended in defining and realizing an innovating and high-performance heel compensation device, the Cogite system. On the other hand, it has been shown, too, why the control laws structure was mostly conditioned by the actuators peculiarities and the desired performances. In the present case, the use of a feedforward component in addition to the classical feedback control has settled the trade-off between transient performances and insensitiveness to sea disturbances.

With regard to side advantages, disposing of an internal modeling allows to provide the OOD with a prediction of the future heel on a receding horizon (of about one minute), thus balancing the drawbacks induced by the discontinuous behaviour of the ship heeling.

Moreover, it must be highlighted that the working of the feedforward and feedback control components is completely uncoupled. So, in highly damaged situations where an extended loss of sensors signals prevents from safely using the feedforward action, the Cogite system will continue to be piloted by the feedback structure only, the ship keeping the benefits of automatic heel compensation.

Regarding future prospects, real tests, aboard the Charles de Gaulle, will be held at sea next winter. They are considered confidently, in view of the high level of performances and reliability achieved by the Cogite device, in addition to the control structure which turns the device capacities to the best account. Besides, US Navy, within the framework of CVX studies, and British Navy, within the framework of

developments for her next aircraft carrier, take a great interest in this new concept of compensation which improves the safety and operational capability of the carrier-borne aircraft. Likewise, an adaptation to others types of vessels, or navy devices, could be considered without too many difficulties.

References

- H.Quintin
PA CdG : rapport de sûreté de l'environnement navire
Attitudes de plate-forme. Rapport DCN ING/AN/BS/
PACDG/Sûreté / RPS 2/19, vol. 1, 2 et 3 - Version 2.0
Juillet 1996
- E.Jenn, V.Lalumia, D.Ferrand
Etude définitive de sûreté de fonctionnement du système
Cogite. Rapport Technicatome DI/SCE/ 9505250 - 1995
- S. Kummer
PA CdG - SATRAP : Girations optimisées interruptibles
Spécification technique de besoin - Rapport DCN ING/
AN/BS N° 364/96 - Octobre 1996
- S. Kummer
SATRAP V2 : Procédures de comparaison des lois de
giration - Rapport DCN ING/AN/BS/PACDG/SATRAP/
PG - n° 2 - Octobre 1996
- S. Kummer
SATRAP V2 : Synthèse de la comparaison des lois de
giration - Rapport DCN ING/AN/BS/PACDG/SATRAP/
PG n° 3 - V1.0 - Février 1997
- P.Perdon
Manœuvrabilité du PAN - girations stabilisées
Rapport du Bassin d'Essais des Carènes - Etude 2341 -
Pièce n° 11 - Mars 1991
- J.P.Jung, G.Hardier, M.A.Grandclément, P.Riot
Integrated control of warship's steering and stabilizing
system - 10th Ship Control Systems Symposium,
Ottawa - 1993
- C.Lambert, G.Hardier
Compensation de gîte du SATRAP : girations
optimisées et interruptibles - Rapport DCSD-T
1/7996.20 - Mars 1997
- C.Lambert, G.Hardier
Définition des lois de commande et du logiciel du
système Cogite du Charles de Gaulle -Rapport DCSD-T
2/7997.24 - Février 1998
- A.Le Pourhet, G.Hardier
Porte-avions Charles de Gaulle : identification de la
maquette de Castillon - Rapport DCSD-T 1/7997.42
Juin 1998

New advances in Sailing Hydrofoils

François Lefauzeux

Délégation générale pour l'armement
BP 20-92211 SAINT-CLOUD CEDEX

1. Abstract

Two sailing hydrofoils projects are currently in progress in France. The objective of the first one, *Techniques Avancées*, is to establish a new all categories world speed record (now belonging to *Yellow Pages Endeavour* with more than 46 knots).

The objective of the second, *L'Hydroptère*, is even more ambitious; it is to establish a new record for the eastward crossing of the Atlantic Ocean.

The two boats have been built and they sail regularly, a lot have been learnt from those experiments and they are quite successful. *Techniques Avancées* holds the world speed record in its size category, *L'Hydroptère* sails regularly at 35-37 knots and it has been recorded at 39 knots.

This paper presents, first, a brief history of hydrofoil sailing, starting with *Monitor*, a very successful project dating from the end of the fifties. After this introduction to hydrofoil sailing, it concentrates on the two main design advances which explain the success of those two ships.

- The first deals with the lateral stability of hydrofoils sailing ships which have to counter the strong lateral force and heeling moment due to the action of the wind on the sails.
- The second deals with the problem of the general longitudinal stability of an ocean-going first generation hydrofoil in strong seas: how to avoid the dangers of fast changes in the flow angle of incidence on the main foils with the risks of negative lift and subsequent "hard landing".

2. HISTORY

Sailors and naval architects have soon realised that the wake was the main speed limiting factor and that it would be of interest to extract the hull from the water. The first patent for an hydrofoil craft—a rowing boat—has been applied for in 1869 [Mr. Fargot french patent].

The first successful hydrofoil motorboat has been constructed by an Italian, Forlanini. The photo ① has been taken at Monaco in 1908. As can be seen, this ship is running at medium speed fully level and it looks stable on its foils.

First sailing hydrofoils are said to have been tried in the thirties, but I don't have any documentation on those experiments. The first successful and well documented hydrofoil sailing boat is *Monitor* (photo ②), designed and built by Baker in the late fifties with the full support of the US Navy (David Taylor Model Basin). From all I know on this boat, it is clearly apparent that a full aero-hydrodynamic model

has been devised and several very interesting innovations incorporated in the design. This ship is said to have sailed consistently at more than thirty knots. So, what is difficult to understand is why there was no more interest for this technique and no follow-on design, either experimental or commercial. *Williwaw* (photo ③) is the only known other sailing hydrofoil in the States during this period. It was a small ocean going vessel and it crossed from Sausalito to Hawaii, foil borne at moderate speed. The next development for the US Navy are the well known fast hydrofoils patrol boats made by Boeing and also made under licence for the Italian Navy and the Japanese one (photo ④). The only recent well known American sailing hydrofoil is the very innovative *Long Shot* built at the beginning of the nineties and, for a time, the holder of the world speed record in its category with 43.5 knots. He is the third second generation (i.e. with fully submerged main foils) sailing hydrofoil, the first being *Force 8* and *Philfly* built in the seventies (photo ⑤).

Most of the modern research work on small sailing hydrofoils have been made in England during the sixties and the seventies, the incentive was the speed week of Weymouth (in fact Portland harbour).

The most successful entries were able to sail foil borne in a stable manner but the speed of those boats have generally been quite a deception for their builders and owners.

These bad results have long been a mystery for me: the design of these boats was clearly correct. It took all the experience accumulated those last ten years to understand some of the reasons for this lack of performance.

The deception was such in England that the enthusiasm for hydrofoil sailing has decreased a lot in the eighties.

The technique was nearly unknown in France in the seventies, when a team of Dassault engineers discussed with Eric Tabarly, the well known French sailor, and convinced him to try hydrofoils. Tabarly was not interested by small inshore waters boats, but by ocean going ships. He asked the Dassault engineers to work with a naval architect; this explains my permanent involvement in this very specific field.

A model, about the size of the English boats, but approximately one third scale of an ocean going vessel, was built in 75-76. It was easy to handle and the transition to foil borne operation was soft (Eric Tabarly is shown on-board on photo ⑥). The boat speed, again, was quite limited. Nevertheless, Eric Tabarly asked for the preliminary design of an ocean going ship able to compete efficiently in the big transatlantic races which were then very important events with a lot of interest in the general public, at least in France.

When we tried to develop the real ship we came to the conclusion that the material most widely used then, i.e. naval aluminium alloy, was not strong enough to build the most solicited parts of the ship, namely the foils roots.

So we came out with an hybrid design — what is sometimes call a foiler — that is to say a boat with small foils to assist in the transversal stability but with no possibility to come foil borne. This boat is *Paul-Ricard* (photo ⑦). It finished second, five minutes behind the winner, in the 1979 double Atlantic crossing race non stop. After some modifications, it succeeded in beating by more than two days the very old Eastward Atlantic crossing record of Charlie Barr with the well named schooner *Atlantic*.

Starting in 1987 two new projects were independently developed in France.

One is an Engineers School students project “*Techniques Avancées*” (photo ⑧) whose ambition was to beat the *Crossbow II* world record of about 36 knots.

The second, the dream of a young sailor named Alain Thebault, was to finalise the idea behind *Paul-Ricard* of an ocean going sailing hydrofoil racer.

Due to circumstances, they are now closely linked together and they benefit of the same scientific and technical team.

Techniques Avancées (the name is coming from the Engineering School named “École Nationale Supérieure des Techniques Avancées”), has been sailing regularly since 1991 and it has beaten in 1997 the world speed record for its size class with 42.6 knots.

Before the drawing of its ocean going vessel, Alain Thebault and our team made a lot of sea trials with a scale model about seven metres long (photo ⑨) and a lot of model basin and wind tunnel tests have been also undertaken; the fast and very long towing tank of Centre d'Études Aéronautiques de Toulouse (CEAT), belonging to DGA, has been particularly appreciated. The decision to go full scale has been taken in 1992 after the scale model had proven its ability to sail at more than thirty knots in waves of up to nearly one metre high.

The full scale boat, *L'Hydroptère*, has finally been launched in 1994, it sailed during all the winter season 94-95. In June 95, during a race with the French Navy frigate *Surcouf*, the starboard arm broke in pieces with no apparent reason at about thirty knots. It took us a long time to understand the real reasons of the accident. Finally we redesigned several important pieces of the boat, we made it quite more stronger and, building on our at sea experience, we made some more modifications in order to have an even faster boat. The rebuilt ship has been launched at the end of September 97 (photo ⑩). I allowed it to go progressively faster; at the beginning of December it was allowed to sail at up to thirty six knots when Alain Thebault rushed her up to thirty nine knots by a graceful day. More interesting for the architects and engineers, it encountered the same day really harsh seas and, as two dozens of strain gauges were continuously recorded, this allowed us to verify most of our assumptions and computations. Photo ⑪ was also taken that day, the speed at the time of the shot is about thirty seven knots.

With *Techniques Avancées* as well as with *L'Hydroptère* those performances were not obtained easily. At sea experience, theoretical interpretation of the problems encountered, modifications to the boats and, then, new sea trials, a lot of such loops were necessary to understand the physics behind the observed phenomena.

Several aspects of hydrofoil sailing theory have been revisited and it is the goal of this paper to present two of them.

The first one to be presented is the dependence of lateral stability on the general shape of the main foils.

The second to be discussed is the importance of main foil twist on longitudinal stability.

Before to go in those details I will quickly explain the general stability of an hydrofoil sailing craft.

3. GENERAL STABILITY OF AN HYDROFOIL SAILING BOAT.

There are two main differences between an aeroplane and a sailing hydrofoil:

- one is the strong lateral force due to the action of the wind on the sails. With fast sailing boats, apparent wind is generally “close hauled” and the resultant lifting force on the sail has a lateral component greater, and sometimes a lot greater, than the longitudinal, useful, one. To give an idea, this force is in the order of the boat displacement.

- propulsive forces and drag forces are not at all in the same plane, the distance between the forces generates important moments (up to eighty kdn.m for *L'Hydroptère*) and these moments have to be countered either by classical righting moment of an archimedian hull or by the lifting forces differential on the foils.

To deal with those problems, two main types of hydrofoils boats have been designed:

- first generation hydrofoils are designed with a specific geometry and V shaped surface piercing foils so as to give the ship self stability characteristics for flight altitude, pitch and roll; the pilot has only to control the course with the rudder. These ships have more or less the same reactions as normal boats. Most of the motor hydrofoils (which are quite numerous and are mainly used as fast passengers boats) are entering this category.

- second generation hydrofoils have fully submerged lifting foils. Such a geometry has not a self stability characteristic and, so, needs appropriate attitude and altitude sensors and the associated control loops.

Most sailing hydrofoils are of the first type, but *Long Shot*, for instance, is of the second type, the control loops being fully mechanical.

This lecture deals only with first generation hydrofoils.

After experimentation with a lot of different foils configurations, there is now unanimity to consider that the best foils disposition is with two main forward foils, as distant laterally as possible, supporting most of the ship weight and an horizontal fully submerged stabilising aft foil.

On quiet waters this aft foil controls very precisely the longitudinal trim.

Transverse equilibrium is far more complex to deal with and it is the subject of the next paragraph.

4. TRANSVERSE EQUILIBRIUM

As for all mechanical equilibria one must have zero resultant forces and zero resultant moments.

Here we deal with four forces, the two hydrodynamic forces on the foils, the transverse component of the aerodynamic force on the sail and, finally, the weight.

Classical hydrofoils boats have straight foils, lift is perpendicular to the wing middle axis, so the two hydrodynamic forces converge at a fixed point. I call this point M because it has some resemblance with the metacentre of a classical hull.

The simplest hydrofoils theory (see fig. 1) stipulate that the two other forces are also passing through this point. This is obviously true for the gravity force when there is no heel, but it is more difficult to defend for the aerodynamic force which depends on the size, the twist, the angle of attack, etc. of the

sail. Anyway, this theory is quite simple. It says that the lateral component of the aerodynamic force induces an angle of leeway, so changing the angle of incidence on the main foils, increasing the down wind one and decreasing the up wind one, until to obtain equilibrium direction, the amplitude being automatically adjusted by the change in the flight altitude. With this configuration of forces there is no roll effect.

A more realistic theory is as follow (fig. 2): point M is still a fixed point in the median plane of the ship, aerodynamic force and the weight converge at the point P which change with roll angle. Roll angle adjust itself so that the resultant

of the aerodynamic force and the displacement passes through point M and, as in the first theory, the leeway and the flight altitude adjust themselves so that the hydrodynamic resultant is exactly opposite to the sum of the two other forces.

It can be shown that this equilibrium is stable if M is lower than P, that is to say under the aerodynamic center of effort, and the equilibrium is unstable if M is above P.

All classical sailing hydrofoils have been built on that theory.

For a practical reason, we have been obliged to adapt a vertical winglet at the tip of the main foil. This reason is easy to understand: with very wide multihulls hydrofoils, the lateral aerodynamic force component can be greater than the ship weight; as the dihedral angle of the main foil is always quite near to 45° , in that condition the leeward foil generates a vertical force greater than the displacement and so it "climbs" out of the water, the wetted useful surface decreases, hydrodynamic charge by unity of surface increases and, finally, through stall phenomenon or an other phenomenon specific to hydrofoils, ventilation, the lift decreases brutally,

there is a violent side slip, the transverse equilibrium is destroyed and there is an immediate hard landing!

To avoid this very annoying phenomenon we have added a vertical winglet; if there is a stall on the main foil surface, the side force is maintained and the equilibrium is generally automatically recovered before landing!

When taking into account the presence of this winglet into the equilibrium equations, one can see that this winglet enhances considerably the stability of the equilibrium and the range of conditions in which the equilibrium is possible; practice confirms this finding.

This point can be explain graphically (fig. 3).

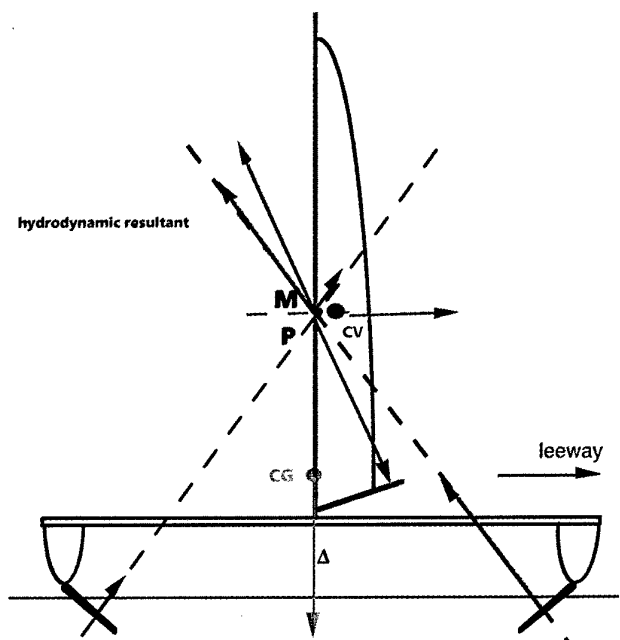
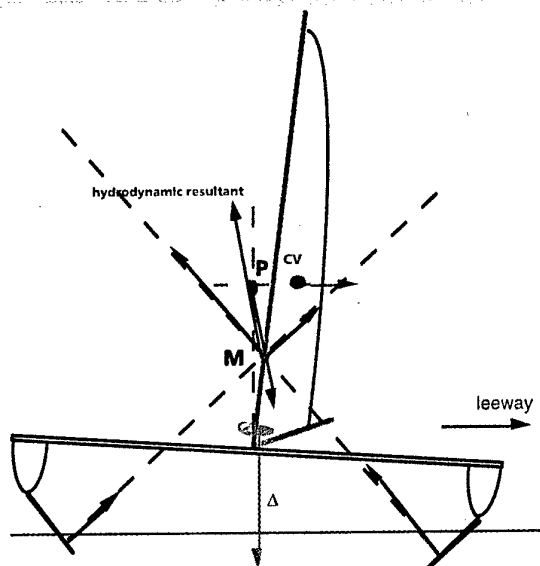
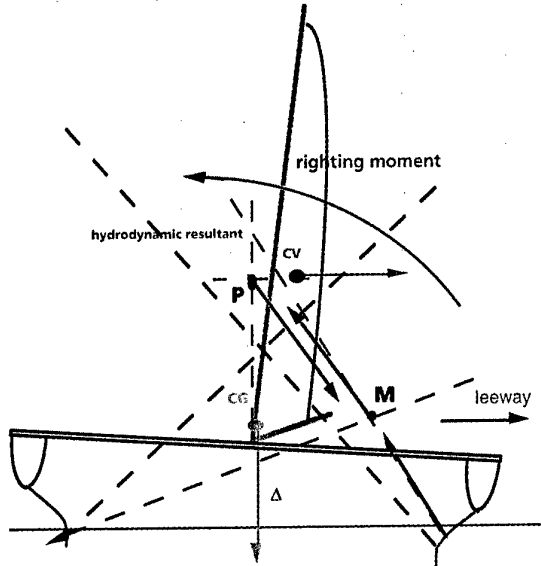


Fig. 1 Lateral stability Simplified theory



**Fig. 2 Lateral equilibrium
Standard theory**



**Fig. 3 lateral stability
virgule foils**

With classical straight foils, the point M is a fixed one. With a vertical winglet the direction of lift on the foil is not fixed, it depends on the wetted surface of the main foil and on the leeway angle, because this leeway angles modify the incidence angle on the vertical winglet faster than on the main foil ($\cos 45^\circ$ effect).

For instance, if there is an increase in roll angle, with no change in leeway, the M point is shifting leeward, P is shifting windward and this creates immediately a righting moment which can be at least twice as important than with no vertical winglets.

One can show that the increase in the stability domain is such that the situation with the centre of aerodynamic effort below the M point can also be stable if the distance is not too big.

This is very important for a sea going hydrofoil like *L'Hydroptère*. With strong winds, the sail area is greatly decreased (reefs on the main sail are five metres apart); combined with a small foresail the aerodynamic centre can be quite low in these conditions. Photo 11 of *L'Hydroptère* illustrates perfectly this situation.

The use of such a vertical winglet has been for us a real breakthrough, allowing the crews to push the two boats far more harder than before with, as a result, a tremendous increase in speed.

There is no theoretical differences between the straight main foil with a vertical winglet and the so-called "virgule" foil; the stabilising effect is the same. The advantage of the virgule foil is a significant drag reduction.

Techniques Avancées is equipped with a virgule starboard foil (this ship, as most of the speed record ships, is asymmetric); this is not yet the case for *L'Hydroptère* due to cost considerations: her main foils are six metres long and new virgule foils will be quite expensive to manufacture; so we have decided to experiment as much as possible with the existing foils, so to be sure we have the best design before going on ...

5. OCEAN GOING HYDROFOILS SPECIFIC PROBLEMS

It is first useful to describe the open seas waves to be encountered. The classical model of sea waves is the so called trochoidal model by Gerstner. It is represented by figure 4

Water particles are describing a circle of fixed centre at constant speed.

To make a record eastward crossing of the Atlantic *L'Hydroptère* will needs winds in the range 20-25 knots. This means sea state 5-6. For an established wind of 25 knots, the parameters of the trochoidal model are typically:

$$\lambda = 100 \text{ m}$$

$$H = 6 \text{ m}$$

$$V = 24 \text{ Kt. (wave speed)}$$

$$v = 2.5 \text{ ms}^{-1} \text{ (water orbital speed)}$$

$$\alpha = 10.6^\circ \text{ (maximum slope)}$$

The orbital speed of the water is one of the most important characteristics of ocean waves. Horizontal speed is backward in the trough, forward at the crest; this can induce surging in the speed of the boat, but this is not a problem.

The real problem is with vertical speed at mid height of the wave, particularly at its back where the speed is downward.

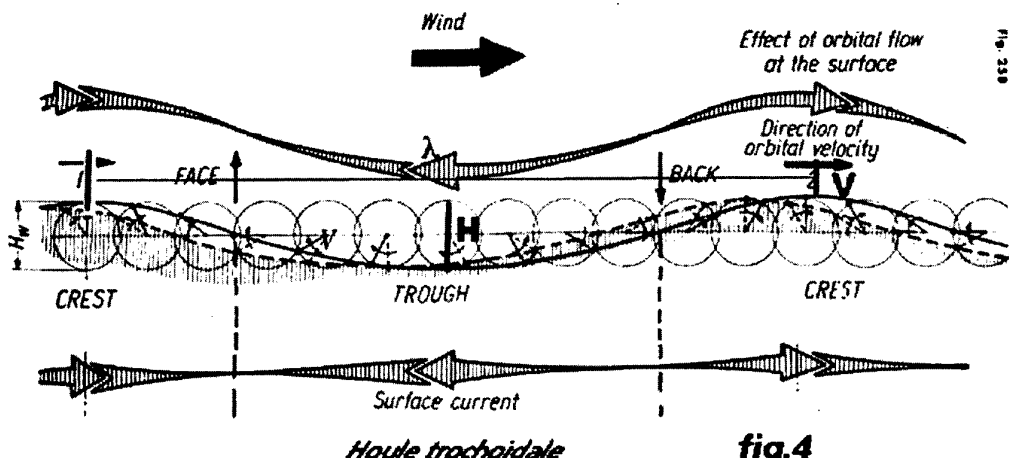


fig.4

Supposing the speed of the boat is thirty knots, this represent a variation of the angle of attack on the main foils of about

$$\alpha = \tan^{-1} \frac{2.5}{15} = 9.5^\circ$$

This is not the only component in the variation of the angle of attack, the two others are the vertical speed of the boat itself when climbing up or down the waves and, finally, its pitch angle.

The real problem with sea going hydrofoils is to limit as much as possible the risk of apparition of a negative hydrodynamic angle of attack and, in consequence, of a negative lift on the main foils. If a main foil is in the situation of negative lift, the flight altitude decreases, the wetted surface of the foil increases and the negative lift increases; a hard landing is unavoidable.

As any sailor knows, problems are quite different going windward close hauled, against the sea, or reaching in following seas. The difference is even greater with fast hydrofoils boats.

Close hauled, against the sea, negative incidence angles on the main foils are not really anticipated. Time of reaction can be a problem as period of encounter of the waves can be as small as two seconds. Risks are limited to violent vertical positive and negative accelerations and even to "take-off" behind the crest of the wave. The bow can, may be, enter the water when just beginning the wave ascent.

The risk, reaching in following seas, is to lose lift or, even, to pass in regions of negative lift on the main foils. If the ship goes faster than the sea — and he will normally try to do so — he will ascend the back of the wave. He will encounter there negative vertical orbital speed of water particles, himself having a positive vertical speed: the two effect converge to produce negative incidence angles and lift. The aft foil will modify the pitch to recover a positive incidence (which needs an absolute pitch angle greater than the wave slope), but there can be a delay because vertical orbital speed can be less aft of the ship than forward and also because of pitch rotation inertia of the ship. The needed

efficiency of the aft foil in that situation determines its surface, but the risk will stay, real seas being quite complex.

The first idea to reduce this risk is to work with a great nominal angle of attack on the main foils, but this is, alas, non practicable. For a ten degrees hydrodynamic angle of incidence and thirty knots, the lift coefficient is about 1 and the lift per square metre on the foil would theoretically be:

$$F = 1/2 \rho V^2 = 11 \text{ kN.m}^{-2}$$

far too much compared with the limitations imposed by ventilation and cavitation.

So, to adopt a nominal angle of attack more than a few degrees would increase significantly the drag and be contrary to the objective of hydrofoils which is to reduce drag as far as possible. Experience has effectively shown that performance was very sensitive to the value of the nominal angle of attack, the best angle being 2° or less.

The proposed solution is then two folds:

- first, to twist significantly the foil between the nominal "water line" and the root of the foil,
- second, to have a significantly tapered foil, giving thus a greater surface to the high angle of attack parts than to the nominal angle of attack ones.

The general aspect of such a foil will resemble the sketch of fig. 5.

The goal is to recover as fast as possible an important global positive lift when the tip of the foil encounters a negative hydrodynamic angle of attack (fig. 6). This solution has of course its own penalty: a momentary sharp increase in drag, but a lot less than the one corresponding to a full hard landing.

The only other solution is to abandon the first generation concept and to adopt the second generation concept with incidence controlled foils; this is what has been done for the military patrol hydrofoils. Mechanical control solutions exists for sailing hydrofoils; they have been validated for inner waters boats, not yet for ocean-going ones, but I don't foresee insurmountable problems to adapt the inner waters

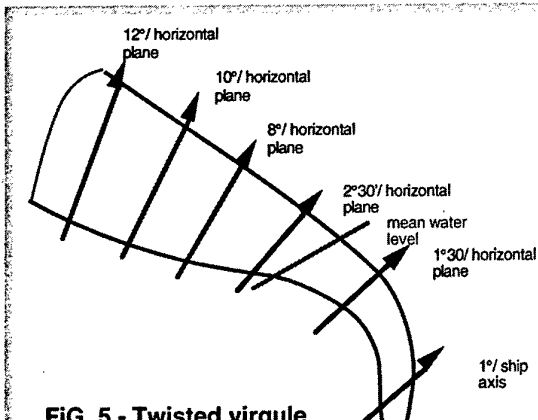


Fig. 5 - Twisted virgule foil
(indicative values not for real use)

solutions to the high seas conditions; such systems have been computed. The only possible drawback of the fully submerged main foils corresponding to that type of architecture is an overall mean drag slightly more important than with the surface piercing hydrofoils (due to the fact that the total surface is always wetted), but this solution is probably the next step for even faster ocean going racers. It is also, of course, the obvious solution for fast military patrol boats.

7. CONCLUDING REMARKS

The developments presented here can seem very specific. I am in fact convinced that at least some of the results of this work can help to design better motor hydrofoils ships, either for commercial or for military purposes.

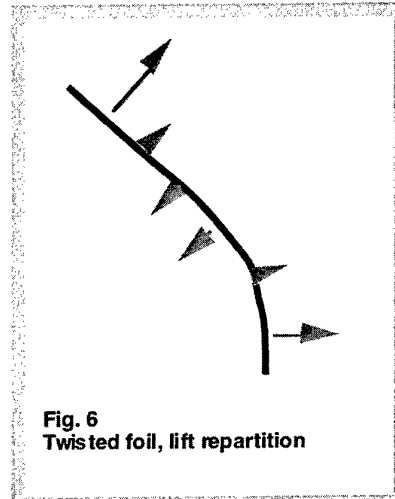


Fig. 6
Twisted foil, lift repartition

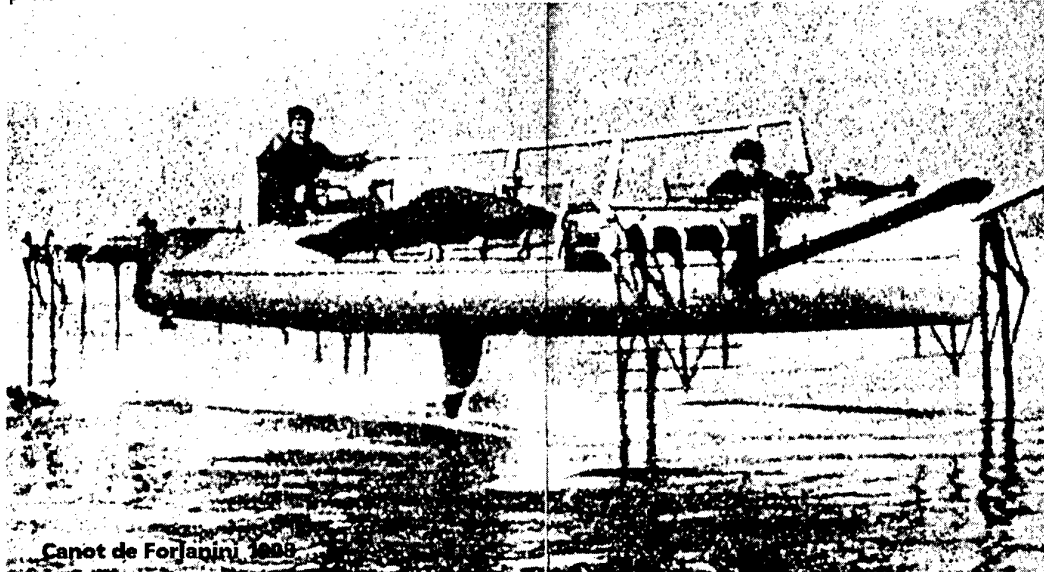
As an example, the market for fast ferries is booming. Of course, fully flying hydrofoils cannot be thought of for the bigger types, but even for very big ferries foils can enhance a lot their performances, reducing hull wave drag and stabilising the platform, either along the roll axis or the pitch axis. In the military domain, true hydrofoils fast patrol boats, of a more advanced design than the PH from Boeing which are now nearly thirty years old, are clearly possible, capitalising on light carbon construction, lower consumption gas turbine and foil design advances. fast patrols boats of up to 200-300 tons capable of sustaining a speed of fifty knots in sea state 4, with a good radius of action at that speed and with an interesting armament capability are a real possibility.

*François Lefaudoux
January 26, 1998*

Bibliography	photographies
<p>1. A Alexander; J. Grogono; D. Niggs Hydrofoil Sailing Juanita Kalerhi, 1972.(ISBN 0-903238-00-4)</p> <p>2.B. Smith, The forty knots sailboat Grosset & Dulap, New-York</p> <p>3. J. Grogono Icarus, the boat that flies Adlard Coles limited, ©J. Grogono 1987 (ISBN 0-229-11803-8)</p> <p>4. Ira H. Abbot & Albert E. Von Doenhoff Theory of Wing Sections Dover Publications (ISBN 0-486-60586-8)</p>	<p>1. published by Daniel Charles in Les chasseurs de futur, Éditions maritimes et d'Outre-mer ;1991 ISBN 2 7373 0577 2</p> <p>2. et 3 photographies published in <i>Hydrofoil Sailing</i></p> <p>4. Flottes de Combat 1996 (photo Ships of the world 1994)</p> <p>5. published in <i>Icarus, the boat that fly</i></p> <p>6. Éditions du Pen Duick</p> <p>7. François Lefauzeux</p> <p>8. Xavier Linck</p> <p>9. anonymous</p> <p>10. François Lefauzeux</p> <p>11. Guillaume Plisson</p>

L'Hydroptère crew François Brillant Michel Desjoyeaux Jean Le Cam Alain Thebault Olivier Wroczinski Jean Abribat (flight test engineer) François Mer (CEA) test engineer	Technical team (L'Hydroptère) Alain de Bergh (Dassault) Michel Fontayne (Aérospatiale) Vincent Lauriot-Prevost (naval architect) Philippe Perier (Dassault) Marc Van Peteghem (naval architect) Maurice Prat (Aérospatiale) André Sournat (Dassault) Hugues de Turckheim (hydrodynamicist & naval architect) J.C. Veber (Dassault) François Lefauzeux (DGA)
Techniques Avancées crew Gerard Navarin Christian Colombeau	Technical team (Techniques Avancées) Association Vecteur Vitesse (École des techniques avancées students association) Hugues de Turckheim François Lefauzeux

photo ①



Canot de Forlanini 1900

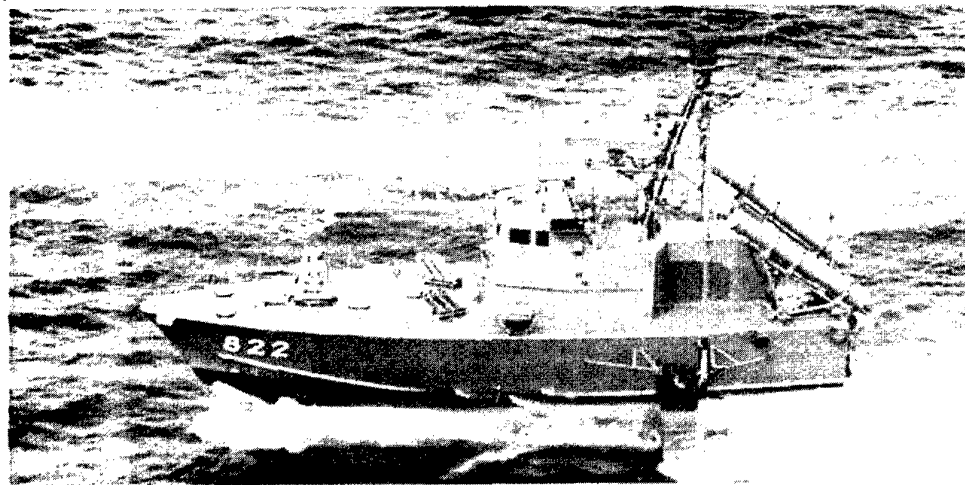
photo ②



photo ③



photo ④



PG 02 (822)

Photo Ships of the world 1974

photo ⑤

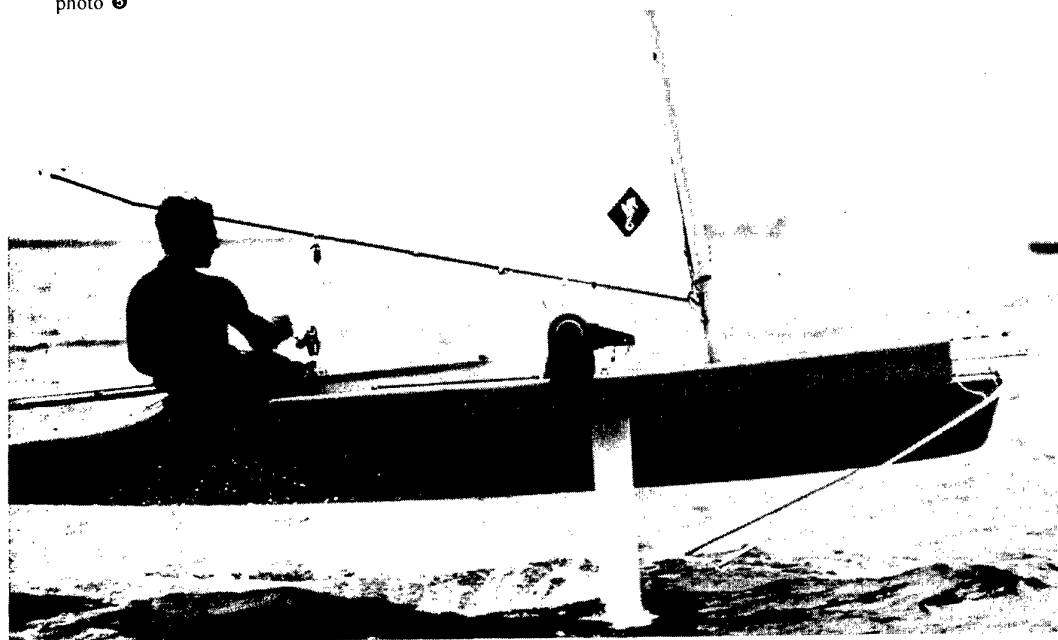
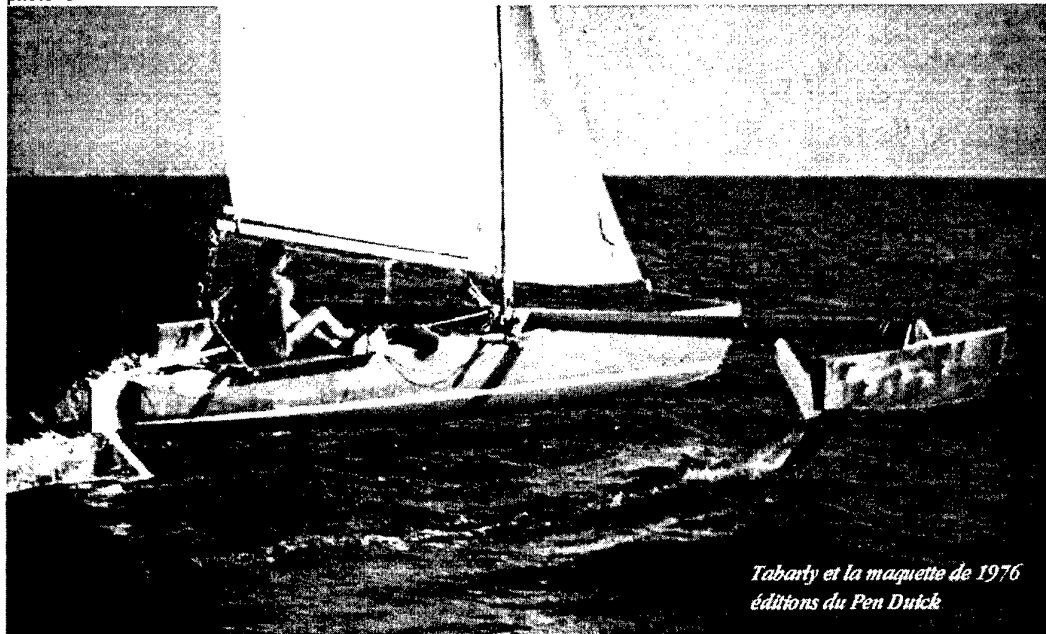


photo 6



*Tabarly et la maquette de 1976
éditions du Pen Duick*

photo 7



François Lefauzeux

photo ③

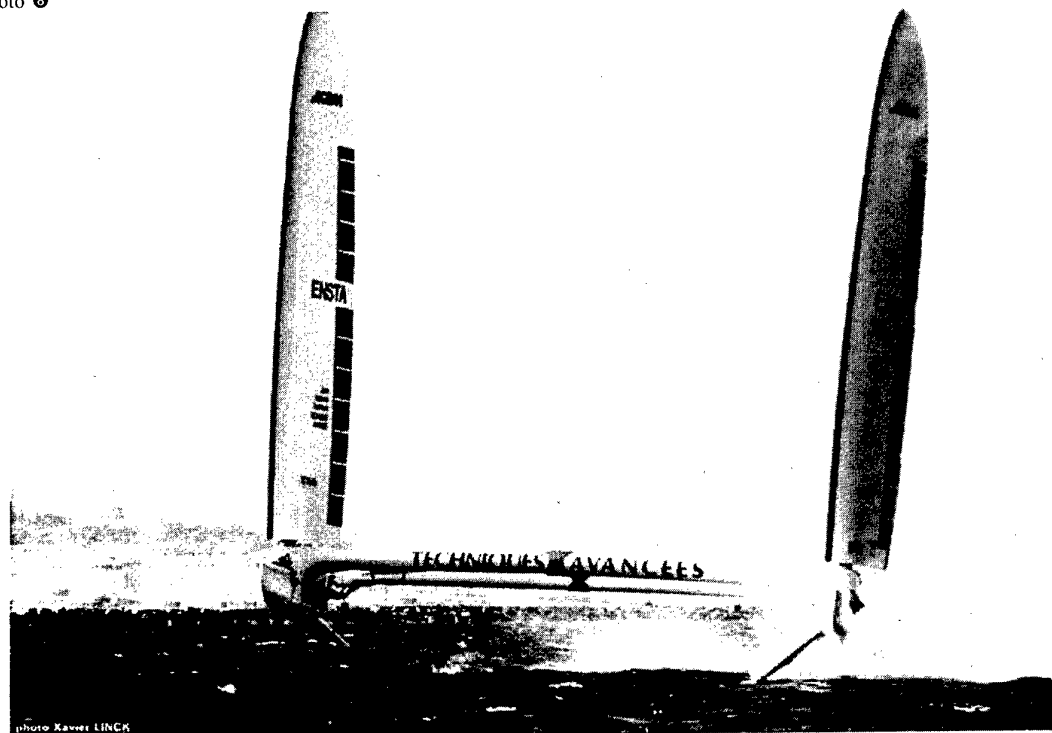
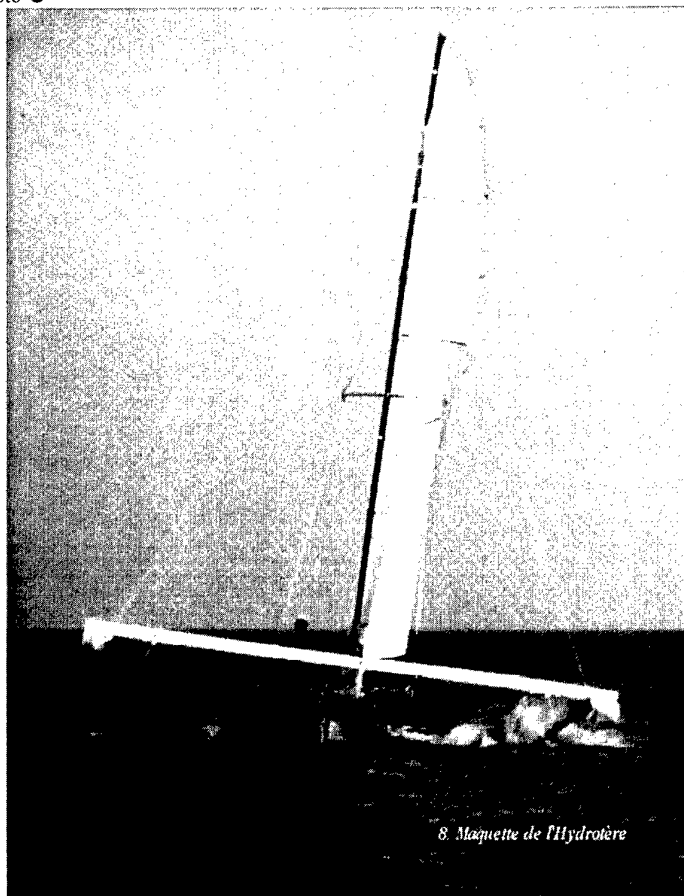


photo Xavier LINCK

photo ⑨



8. Maquette de l'Hydrotère

photo ⑩

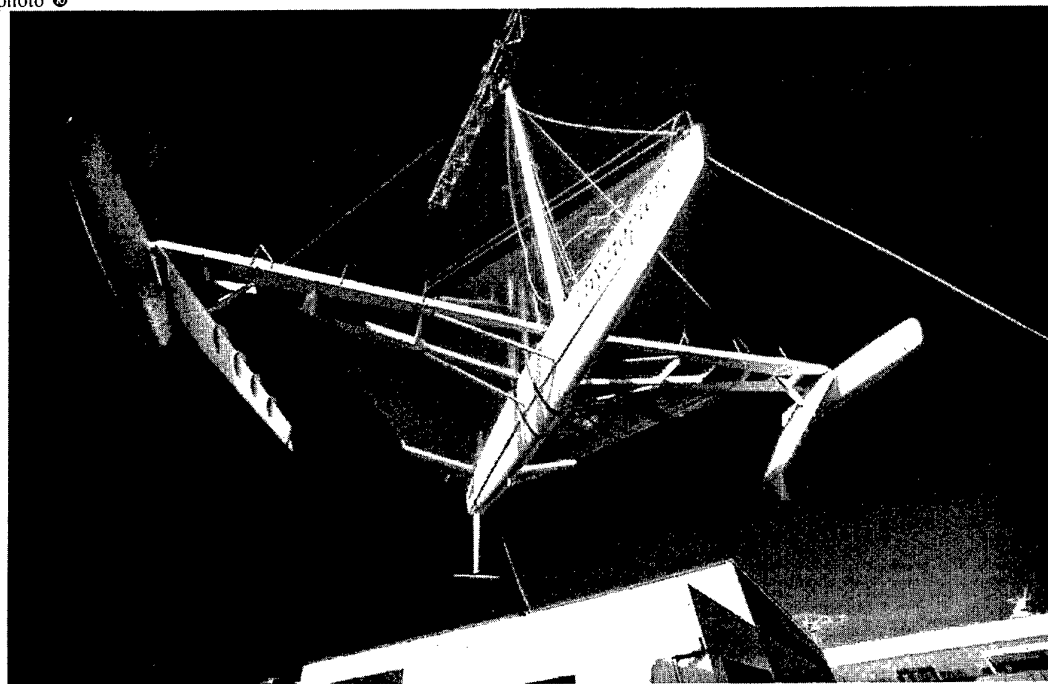
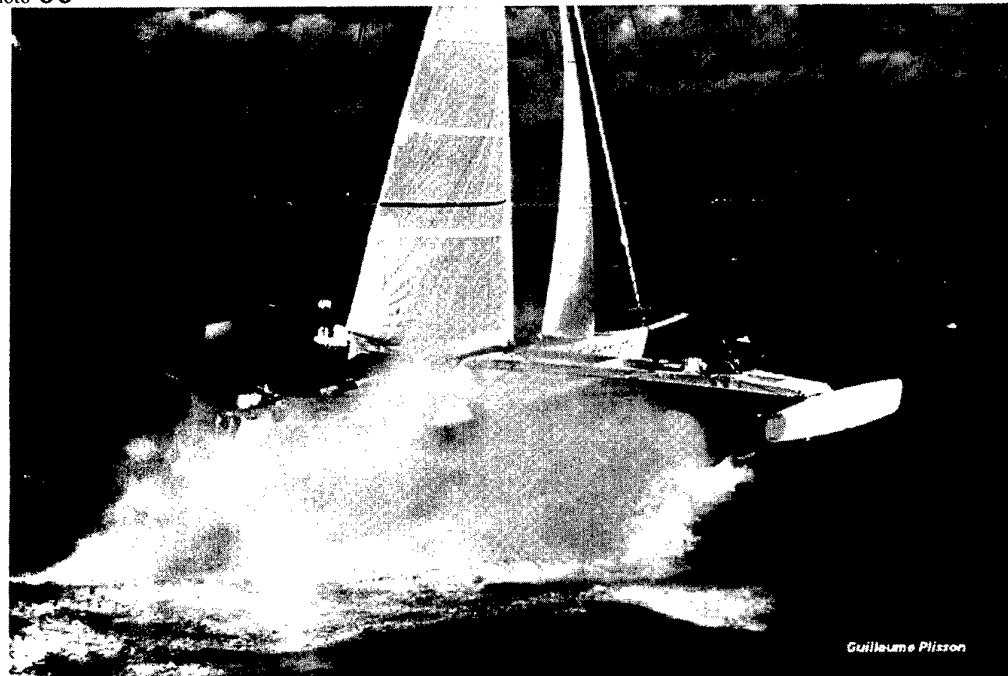


Photo ⑪



Unsteady flow around a hydrofoil beneath waves

U.P. Bulgarelli, M. Greco, M. Landrini, C. Lugni

INSEAN, Italian Ship Model Basin

Via di Vallerano 139, 00128 Roma – Italy

SUMMARY

A general model for studying the unsteady free surface flow generated by a hydrofoil moving beneath a wavy free surface is presented. The flow field is assumed irrotational everywhere except for a thin wake shed from the trailing edge. A boundary integral formulation for the velocity field is introduced and integral equations for the unknown velocity components are solved by an accurate as well as efficient method. The solution is stepped forward in time by evolution equations for the free surface and the wake.

Test cases are solved for which experimental results are available. Both foils with and without angle of attack are considered and experimental wave profiles are successfully recovered. Drag and pressure coefficients on the hydrofoil satisfactorily compare with the experiments. The ability to handle highly nonlinear behaviours of the free surface is shown by computing breaking waves generated by a foil slightly immersed with a large angle of attack.

List of symbols

\mathcal{R}_f	inertial frame of reference
\mathcal{R}	moving frame of reference
\mathcal{H}	hydrofoil
\mathcal{F}	free surface
\mathcal{W}	wake
c	hydrofoil chord length
d	depth of submergence from mid-chord profile
U	stream velocity
q	fluid velocity in the moving frame
\mathbf{u}_s	Stokes velocity field
\mathbf{u}	perturbation velocity field
g	gravity acceleration
G	free space Green function
η	wave elevation
$\mathbf{P} - \mathbf{O}$	vector position in the moving frame
ν	unit normal vector to the boundary
τ	unit tangent vector to the boundary
α	angle of attack
γ	vorticity strength
Γ	circulation
ρ	water density
p	pressure
C_p	pressure coefficient
F_n	Froude number

1. Introduction

Lifting bodies are largely employed in naval hydrodynamics both as control devices of the hull motions, and as main sustaining system of the entire vessel. In both cases, ambient waves, vehicle's motions and, generally speaking, out-of-design conditions render the flow unsteady. Moreover, as a result of small immersion or large amplitude motions, the flow field around the hydrofoil is significantly affected by the air-water interface.

Therefore, several authors attacked the problem and we limit ourselves in mentioning those papers relevant for the two-dimensional problem dealt with via inviscid models. In this framework, Giesing and Smith (1967) gave one of the first numerical solutions of the linearized steady problem by us-

ing boundary integral equations. The steady nonlinear problem is solved in [9] by a suitable iterative procedure. In both cases a (steady) Kutta condition provides the uniqueness of the (numerical) solution. Coleman (1986) firstly solved the unsteady nonlinear free surface problem by discretizing the Euler equations and linearizing the wake dynamics. Unsteady free surface flows with embedded concentrated vorticity are discussed by Casciola & Piva (1990) by using an integral representation for the velocity field coupled with suitable evolution equations. On that ground, solutions for the fully nonlinear inviscid-rotational problem were presented in [4].

In this paper we present, §2., a general time-domain model for the two-dimensional flow around a slightly submerged hydrofoil arbitrarily moving beneath incoming waves. Once large separation phenomena and cavitation are ruled out, the flow field can be well described in terms of inviscid-rotational fluid mechanics in which a thin vortical layer mimics the hydrofoil's wake and a suitable unsteady Kutta condition provides the mechanism for vorticity generation. The velocity field is described through an integral representation derived from the Poincaré identity. Free surface boundary conditions which hold in the general rotational case are derived from the Euler equations and the nonlinear free surface dynamics is fully retained.

The resulting model is able to capture qualitatively and quantitatively several features of the phenomenon and successful comparisons with experimental results are presented in §3.. In particular the waves generated by foils with zero and non-zero angle of attack are well reproduced and the related wave drag is reasonably predicted. Consistently, the pressure distribution on the foil satisfactorily compares with measured data.

2. Mathematical statement of the problem

2.1 The continuous problem

Notation and kinematics The unsteady motion of the fluid generated by a hydrofoil \mathcal{H} advancing beneath the free surface \mathcal{F} is considered (v. fig. 2). The main motion of the hydrofoil is a translation but arbitrary oscillations in heave, surge and pitch are allowed. We consider an inertial frame of reference $\mathcal{R}_f(x_1, x_2)$ such that the fluid at infinite depth is at rest. A Stokes wave train possibly exists far from the body, say at $x_1 = -\infty$. In this case, for finite times, the wave elevation η and the velocity field \mathbf{u}_s are expressed in terms of truncated Fourier series

$$\begin{aligned}\eta &= \sum_{k=1}^M a_k \cos(k(x_1 - ct)) \\ \mathbf{u}_s &= \nabla \left\{ \sum_{k=1}^M b_k e^{kx_2} \sin(k(x_1 - ct)) \right\}\end{aligned}\quad (1)$$

while, closer to \mathcal{H} , the fluid velocity \mathbf{Q} is decomposed as the sum of the known Stokes velocity field \mathbf{u}_s and an unknown perturbation velocity field \mathbf{u} .

A frame of reference $\mathcal{R}(x, y)$ moving with respect to \mathcal{R}_f with a time dependent velocity $-\mathbf{U}(t) = -U(t)\mathbf{e}_1$ is also considered. In \mathcal{R} the fluid velocity is $\mathbf{q} = \mathbf{U} + \mathbf{u}_s + \mathbf{u}$, where the proper time dependence for \mathbf{u}_s can be inferred from (1) by introducing $x_1(\hat{t}) = x - \int_0^{\hat{t}} U(t)dt$, which relates the two frames \mathcal{R} and \mathcal{R}_f .

In the general case with non-zero heave, surge and pitch motions of the foil, the velocity \mathbf{V} and the acceleration \mathbf{A} of a point $\mathbf{P} \in \mathcal{H}$ in \mathcal{R}_f are

$$\begin{aligned}\mathbf{V}(\mathbf{P}, t) &= -U(t)\mathbf{e}_1 + \underbrace{\mathbf{V}(\mathbf{O}, t)}_{\text{heave-surge}} + \underbrace{\Omega(t) \times (\mathbf{P} - \mathbf{O})}_{\text{pitch}} \\ &= -U(t)\mathbf{e}_1 + \mathbf{v}(\mathbf{P}, t) \\ \mathbf{A}(\mathbf{P}, t) &= -\frac{dU}{dt}\mathbf{e}_1 + \mathbf{A}(\mathbf{O}) + \frac{d\Omega}{dt} \times (\mathbf{P} - \mathbf{O}) \\ &+ \Omega(t) \times \Omega(t) \times (\mathbf{P} - \mathbf{O}) = -\frac{dU}{dt}\mathbf{e}_1 + \mathbf{a}(\mathbf{P}, t)\end{aligned}\quad (2)$$

where \mathbf{O} is the center of rotation moving with velocity $\mathbf{V}(\mathbf{O}, t)$ and $\Omega(t)$ is the angular velocity. Consistently with the introduced notation, $\mathbf{a}(\mathbf{P}, t)$ and $\mathbf{v}(\mathbf{P}, t)$ are the corresponding quantities in \mathcal{R} .

Equations of fluid motion In the moving frame \mathcal{R} , the flow is described by the Euler equations in the form

$$\nabla \cdot \mathbf{q} = 0 \quad \frac{D\mathbf{q}}{Dt} = -\frac{1}{\rho} \nabla p + \mathbf{g} + \frac{d\mathbf{U}}{dt} \quad (3)$$

where $D/Dt = \partial/\partial t + \mathbf{q} \cdot \nabla$ is the substantial derivative, \mathbf{g} is the gravity and p is the pressure of the fluid with density ρ . The term $d\mathbf{U}/dt$ accounts the non-inertial character of \mathcal{R} . Observing that \mathbf{u}_s and \mathbf{U} are solenoidal vector fields and that

$$\frac{D\mathbf{q}}{Dt} = \frac{D\mathbf{u}}{Dt} + \frac{D\mathbf{u}_s}{Dt} + \frac{d\mathbf{U}}{dt},$$

the field equations are recast in terms of the perturbation velocity

$$\nabla \cdot \mathbf{u} = 0 \quad \frac{D\mathbf{u}}{Dt} = -\frac{1}{\rho} \nabla p + \mathbf{g} - \frac{D\mathbf{u}_s}{Dt} \quad (4)$$

Body boundary condition In the frame of reference \mathcal{R} , the standard impermeability condition holds in the form

$$(\mathbf{u} - \mathbf{v}(\mathbf{P})) \cdot \boldsymbol{\nu} = -(u_s + U) \cdot \boldsymbol{\nu} \quad (5)$$

where the unit normal vector $\boldsymbol{\nu}$ points into the body.

Free surface evolution equations The free surface equations follow from the kinematic condition that the fluid does not cross it and the dynamic constraint that the pressure is atmospheric on \mathcal{F} [21]. These requirements are fulfilled if the motion of the free surface points $\mathbf{P}(\xi, t)$ are described through

$$\left\{ \begin{array}{l} \frac{\partial \mathbf{P}(\xi, t)}{\partial t} = \mathbf{w} = q_\nu \boldsymbol{\nu} + w_\tau \boldsymbol{\tau} \\ \frac{\partial u_\tau(\xi, t)}{\partial t} = \boldsymbol{\tau} \cdot \left\{ (\mathbf{w} - \mathbf{q}) \cdot \nabla \mathbf{u} + \mathbf{g} - \frac{1}{\rho} \nabla p_a - \frac{D\mathbf{u}_s}{Dt} \right\} \\ \quad + \mathbf{u} \cdot \frac{\partial \boldsymbol{\tau}(\xi, t)}{\partial t} \end{array} \right. \quad (6)$$

In these equations $\boldsymbol{\nu}$, $\boldsymbol{\tau}$ are the unit normal and tangent vectors to \mathcal{F} and $\frac{\partial}{\partial t}$ is the derivative following the motion of the point $\mathbf{P}(\xi, t)$ of the free surface \mathcal{F} . The first equation states that \mathbf{P} moves with velocity \mathbf{w} : the normal component $\mathbf{w} \cdot \boldsymbol{\nu}$ is fixed by the corresponding component $q_\nu = \mathbf{q} \cdot \boldsymbol{\nu}$ of the fluid below, while the tangential one, w_τ , can be arbitrarily chosen. Anyway, regardless the actual value of w_τ , the tangential velocity component u_τ of the fluid evolves according to the second equation, which follows from the tangential projection of the Euler equation.

Wake evolution equations We consider the vorticity to be confined in a narrow wake \mathcal{W} downstream the hydrofoil which is modeled by a zero thickness vortex layer of local strength

$$\gamma_{\mathcal{W}} = \gamma_{\mathcal{W}} \mathbf{k} = (\mathbf{q}_+ - \mathbf{q}_-) \times \boldsymbol{\nu} = [q_\tau] \mathbf{k}, \quad (7)$$

In (7), $[q_\tau] \equiv [u_\tau]$ is the jump of the tangential component of the fluid velocity across \mathcal{W} while the normal component q_ν is continuous by virtue of mass conservation [10]. The Lagrangian behaviour of the wake is described by

$$\frac{\partial \mathbf{P}(\xi, t)}{\partial t} = \mathbf{w}(\xi, t) \quad \frac{\partial J \gamma_{\mathcal{W}}}{\partial t} = 0 \quad (8)$$

which take into account the kinematics and the dynamics of the wake, respectively. In particular, a wake point $\mathbf{P}(\xi, t)$, labelled by the Lagrangian coordinate ξ , moves with a velocity 'defined' as $\mathbf{w}(\xi, t) = \frac{1}{2}(\mathbf{q}_+ + \mathbf{q}_-)$. Consistently, $\frac{\partial}{\partial t}$ is the rate of change of a quantity seen by an observer moving with a wake point. Hence, the second equation, where $J(\xi, t) = \left| \frac{\partial \mathbf{P}}{\partial \xi} \right|$, describes the time evolution of the density $\gamma_{\mathcal{W}}(\xi, t)$ of the vortex layer according to the Kelvin theorem. In the present initial value problem it is assumed that the vorticity is continuously shed from the trailing edge where the density γ_{TE} of the 'nascent' wake element is determined by an unsteady Kutta-like condition. A zero-thickness vortex wake cannot sustain a pressure jump and, in the limit of $x_w \rightarrow x_{TE}$, the assumption of zero trailing edge loading appears a reasonable hypothesis. Consistently, from the Euler equation written in a frame of reference fixed with respect to the hydrofoils, it follows

$$\frac{d\Gamma}{dt} = \left[\frac{1}{2} \alpha^2 \right] = -\mathbf{w} \cdot \gamma_{TE} \quad (9)$$

which relates the rate of change of the circulation around the hydrofoil, $\frac{d\Gamma}{dt}$, to the flux $-\mathbf{w} \cdot \gamma_{TE}$ of vorticity $\gamma_{TE} = (\alpha_{TE}^+ - \alpha_{TE}^-)$ injected in \mathcal{W} with velocity $\mathbf{w} = \frac{1}{2}(\alpha_{TE}^+ + \alpha_{TE}^-)$. In (9), α is the fluid velocity for an observer attached to the hydrofoil. On physical ground the above condition states that the vorticity created and convected in the boundary layer leaves the hydrofoil at the trailing edge to enter into the wake region.

Hydrodynamic forces For computing the forces

$$\mathbf{F} = \int_{\mathcal{L}} p(s) \boldsymbol{\nu} dl \quad \mathbf{M} = \int_{\mathcal{L}} p(s) \mathbf{r} \times \boldsymbol{\nu} dl \quad (10)$$

acting on the hydrofoil during its motion, the pressure $p(s, t)$ has to be evaluated. The tangential projection

$$\frac{\partial \alpha}{\partial t} + \frac{1}{2} \frac{\partial \alpha}{\partial \tau} = -\frac{1}{\rho} \frac{\partial p}{\partial \tau} + \mathbf{f}_a \cdot \boldsymbol{\tau} + \mathbf{g} \cdot \boldsymbol{\tau} \quad (11)$$

of the Euler equation in a body-fixed frame of reference \mathcal{R}_b is then considered, where the apparent forces

$$\begin{aligned}\mathbf{f}_a = & - \left(-\frac{dU}{dt} \mathbf{e}_x + \mathbf{A}(\mathbf{O}) + \frac{d\Omega}{dt} \times (\mathbf{P} - \mathbf{O}) \right. \\ & \left. + \Omega(t) \times \Omega(t) \times (\mathbf{P} - \mathbf{O}) \right)\end{aligned}\quad (12)$$

per unit of mass are introduced and $\alpha = \alpha\tau$ is the total fluid velocity in this frame of reference. By integrating (11) along the body surface the pressure

$$\begin{aligned} p(s, t) - p(s_0, t) &= -\rho \int_{s_0}^s \dot{\alpha} d\ell - \frac{1}{2} \rho \alpha^2 |_{s_0}^s \\ &\quad + \rho \int_{s_0}^s (\mathbf{f}_{ap} + \mathbf{g}) \cdot \boldsymbol{\tau} d\ell \end{aligned} \quad (13)$$

is finally obtained. The reference pressure $p(s_0, t)$, say the pressure at the trailing edge, is undetermined. Clearly the loads (10) are not affected by its actual value, while the pressure distribution on the foil at different time instants are comparable except for a constant time dependent shift. We discuss this point later.

The initial value problem The mathematical statement of the problem is completed by prescribing suitable initial conditions. To the purpose we assume that the hydrofoil starts to move from rest in an initially quiescent fluid. Then the problem will consist in computing the disturbance \mathbf{u} with respect to the uniform stream $\mathbf{U}(t)$.

Dealing with incoming waves, it is assumed that the foil suddenly appears beneath a regular wave system ranging from $x_1 = -\infty$ to $x_1 = \infty$. Again, the presence of the moving foil will cause a perturbation \mathbf{u} and a change in the wave height η with respect to the unperturbed η_s . Although the transient stage is non-physical, this procedure avoids the need of a numerical wave maker to generate the incoming waves and simplify the damping of outgoing signals (see Landrini et al. (1998)).

2.2 The numerical procedure

General description of the algorithm In the following we consider only those cases for which the motion of the hydrofoil is *a priori* known. Let us now assume that at a given time instant t_0 the flow field is completely known. In this case, without solving the field equations, a Cauchy problem can be formulated for the boundary geometry and some of the fluid dynamic variables that can be prolonged up to the time $t_0 + \Delta t$. In fact

- the body motion fixes in advance the normal component $u_\nu|_{\mathcal{H}}$ of the fluid velocity (cfr. eq. (5)).
- the free surface geometry \mathcal{F} can be updated by the first of (6), while the tangential component $u_\tau|_{\mathcal{F}}$ of the fluid velocity can be prolonged by the second one.
- the knowledge of the velocity field on the hydrofoil allows computing the newly generated vorticity γ_{TE} , while \mathcal{W} changes according to (8).

Apparently, the normal component $u_\nu|_{\mathcal{F}}$ and the tangential component $u_\tau|_{\mathcal{H}}$ are still required for a complete knowledge of the flow field at the time $t_0 + \Delta t$, and it is not possible to prolong the solution further in time.

Dealing with free and moving boundaries, one can expediently recast the problem in the form of boundary integral equations, a method introduced by Longuet-Higgins (1976) and Faltinsen (1977) for fully potential free surface flows. For rotational flow fields, following Casciola & Piva (1990), the unknown velocity components are evaluated by solving the kinematic problem

$$\nabla \cdot \mathbf{u} = 0 \quad \nabla \times \mathbf{u} = \zeta \quad (14)$$

through a boundary integral equation approach. In the present paper the vorticity ζ reduces to the wake vorticity γ while the more general case with vorticity distributed over a finite area is discussed by Landrini et al. (1998) for the case of a circular cylinder beneath incoming waves.

The solution of the kinematic problem with boundary data

$$u_\tau \text{ on } \mathcal{F} \quad u_\nu \text{ on } \mathcal{H} \quad \gamma_{\mathcal{W}} \text{ on } \mathcal{W}$$

provides all the information requested to step forward in time the solution according to the procedure summarized in figure 3. In particular, both the free surface evolution equations and the wake evolution equations are integrated in time by a fourth order Runge-Kutta scheme.

Integral formulation of the velocity field In the moving frame of reference \mathcal{R} , $\mathbf{q} \rightarrow \mathbf{u}_s + \mathbf{U}$ as $|\mathbf{x}| \rightarrow \infty$ and, for finite times, the perturbation velocity field \mathbf{u} is asymptotically zero far from the hydrofoil. Then, under quite weak hypotheses [1], \mathbf{u} can be represented by the Poincaré Formula

$$\begin{aligned} \mathbf{u}(\hat{\mathbf{P}}) &= \nabla_{\hat{\mathbf{P}}} \int_{\mathcal{F} \cup \mathcal{H}} \mathbf{u} \cdot \boldsymbol{\nu} G dS_P + \nabla_{\hat{\mathbf{P}}} \times \int_{\mathcal{F} \cup \mathcal{H}} \mathbf{u} \times \boldsymbol{\nu} G dS_P \\ &\quad + \nabla_{\hat{\mathbf{P}}} \times \int_{\mathcal{W}} \gamma_{\mathcal{W}} G dS_P \end{aligned} \quad (15)$$

where the first two terms take into account the presence of the free surface and the hydrofoil and the Biot-Savart integral represents the effect of the thin rotational wake \mathcal{W} .

The direct use of (15) to solve the kinematic problem leads to some numerical difficulties. It can be shown, in fact, that an eigensolution related to the circulation Γ around the hydrofoil exists [1] and that a singular value decomposition technique has to be adopted in order to solve the discretized boundary integral equations [5]. A different approach to the problem is here developed. By introducing a fictitious velocity field

$$\mathbf{v}(\hat{\mathbf{P}}) = -\nabla_{\hat{\mathbf{P}}} \int_{\mathcal{H}} \mathbf{v} \cdot \boldsymbol{\nu} G dS_P - \nabla_{\hat{\mathbf{P}}} \times \int_{\mathcal{H}} \mathbf{v} \times \boldsymbol{\nu} G dS_P \quad (16)$$

inside the body \mathcal{H} , the hybrid velocity representation

$$\begin{aligned} \mathbf{u}(\hat{\mathbf{P}}) &= \nabla_{\hat{\mathbf{P}}} \int_{\mathcal{F}} \mathbf{u} \cdot \boldsymbol{\nu} G dS_P + \nabla_{\hat{\mathbf{P}}} \times \int_{\mathcal{F}} \mathbf{u} \times \boldsymbol{\nu} G dS_P \\ &\quad + \nabla_{\hat{\mathbf{P}}} \int_{\mathcal{H}} \sigma G dS_P + \frac{\Gamma}{\mathcal{L}} \nabla_{\hat{\mathbf{P}}} \times \int_{\mathcal{H}} \mathbf{k} G dS_P \\ &\quad + \nabla_{\hat{\mathbf{P}}} \times \int_{\mathcal{W}} \gamma_{\mathcal{W}} G dS_P \end{aligned} \quad (17)$$

can be deduced by summing (15–16) and requiring

$$\sigma = [\mathbf{u} - \mathbf{v}] \cdot \boldsymbol{\nu} \quad \frac{\Gamma}{\mathcal{L}} \mathbf{k} = -[\mathbf{u} - \mathbf{v}] \times \boldsymbol{\nu} \quad \Gamma = \int_{\mathcal{H}} \mathbf{u} \cdot \boldsymbol{\tau} d\ell \quad (18)$$

In (17) the body effects are represented through a simple layer potential $\int \sigma G dS$ and a vorticity layer distributed on \mathcal{H} . The source density σ accounts the discontinuity in the normal direction of the two vector fields across \mathcal{H} and the integral of the vortex layer with uniform strength $-[\mathbf{u} - \mathbf{v}] \times \boldsymbol{\nu}$ equals the total circulation Γ around the hydrofoil. Being the body circulation explicit, the integral equations following from (17) are free from eigensolutions and fast iterative solvers can be successfully applied.

Discretized integral equations For the purpose of discussion it suffices to recall that, by introducing $N_{\mathcal{F}}$ points on the free surface and $N_{\mathcal{H}}$ (second order) panels on the hydrofoil, an algebraic system of the form

$$\underbrace{\begin{bmatrix} \mathcal{F} \rightarrow \mathcal{F} & \mathcal{H} \rightarrow \mathcal{F} \\ \mathcal{F} \rightarrow \mathcal{H} & \mathcal{H} \rightarrow \mathcal{H} \end{bmatrix}}_{\mathcal{A}} \begin{Bmatrix} u_{\nu} \\ \sigma \end{Bmatrix} = \boldsymbol{\tau} \quad (19)$$

is obtained for the unknown normal velocity component and the source strength. In (19) the matrix coefficient \mathcal{A} follows by assembling the self-influence and the cross-influence of the free surface and the hydrofoil, while the right hand side

$$\begin{aligned} \boldsymbol{\tau} = & \begin{bmatrix} \mathcal{F} \rightarrow \mathcal{F} \\ \mathcal{F} \rightarrow \mathcal{H} \end{bmatrix} \{ u_{\tau} \} + \frac{\Gamma}{\mathcal{L}} \begin{bmatrix} \mathcal{H} \rightarrow \mathcal{F} \\ \mathcal{H} \rightarrow \mathcal{H} \end{bmatrix} \\ & + \begin{bmatrix} \mathcal{W} \rightarrow \mathcal{F} \\ \mathcal{W} \rightarrow \mathcal{H} \end{bmatrix} \{ \gamma_{\mathcal{W}} \} \end{aligned} \quad (20)$$

takes into account the known free surface contribution due to the tangential velocity component u_{τ} , the influence of the body circulation Γ and the wake vorticity $\gamma_{\mathcal{W}}$, respectively. Clearly, for not deforming bodies, the self-influence matrix $[\mathcal{H} \rightarrow \mathcal{H}]$ can be computed once and for all, as well as the self induced velocities. The solution of (19) is rapidly evaluated by means of an iterative solver while for the influence of wake vortices a fast summation algorithm based on multipole expansion is employed. An enhanced solver for (19) based on fast summation of multipoles expansion coupled to an iterative solver was developed by Graziani & Landrini (1998). A deeper discussion of the numerical method can be found there and in Landrini et al. (1998) for the specific problem at hand.

Numerical treatment of the free surface A truncated computational domain has to be used and, in general, both the velocity components u_{τ} and u_{ν} and the wave height η do not vanish at the edges, at least for long enough evolution time. Therefore, unphysical reflections and numerical errors due to unbalanced edge singularities may occur. This drawback is avoided by artificial damping layers which force the tangential velocity component and the wave disturbances to vanish when approaching the outer portions of \mathcal{F} . In particular, modified free surface evolution equations can be written by introducing a damping function $\mu(x)$, zero everywhere except within the damping regions, which multiplies u_{τ} and η in the dynamic and kinematic free surface equations, respectively. The length of the damping layers and the maximum damping coefficient have been heuristically determined. The accuracy of the computation is eventually maintained under control by comparing different solutions for increasing domain lengths.

Finally, in order to handle the mean horizontal motion $\mathbf{U}(t)$ in the frame of reference \mathcal{R} of the free surface points, a fixed computational window is considered and those points dropping out downstream are thrown away and new markers are inserted upstream.

The sawtooth instability, that usually sets in for long enough evolutions, are removed by high order filtering procedures.

Numerical treatment of the wake The wake is a vortex sheet continuously emanated from the trailing edge of

the hydrofoil. In the computations, the wake is replaced by a set of point vortices with circulation Γ_k fixed at the time of shedding according to (9). Hence, the Kelvin theorem (8) implies that Γ_k stays constant during the following motions. Consistently, the Biot-Savart integral in (17) is replaced by the sum of the velocity $\Gamma_k \nabla_{\hat{P}} G(\hat{P}, P_k) \times \mathbf{k}$ induced by the point vortices embedded in the flow field. For long time evolution, to prevent irregular motions and instabilities discussed by Krasny (see [12] and the literature cited therein), the kernel is desingularized by convolution with a cut-off function which, in practical terms, implies a finite velocity induced on near vortices and a zero self-induced velocity. An additional difficulty in modeling the wake appears when dealing with large deformations of the wake. In particular the distance can increase or decrease too much. In these circumstances, at the expense of an approximation, vortices are splitted or merged, respectively, by enforcing the conservation of the total circulation and of the center of vorticity. Finally, the computational effort becomes larger and larger as time passes. A significant reduction has been obtained by using multipoles expansion with fast summation techniques both for computing the self induced velocity and evaluating the influence of the vorticity field on the other fluid boundaries.

3. Discussion

After the transient stage, the flow field can attain a quasi-steady regime: the wave profile is constant in a body-fixed frame of reference and the hydrodynamic loads reach constant values. In these circumstances it is easier to compare the numerical results with the experimental data available in literature. For clarity, we firstly discuss the flow around hydrofoil at zero geometrical incidence and then the case with non zero angle of attack.

Hydrofoil at zero incidence In [17], [18] Salvesen gave the very first attempt to analyze the nonlinearities in wavy flows generated by a submerged foil. He performed a wide set of experiments, [17], by using a mathematically generated profile. Later, [18], he developed a second order theory in which i) the thickness and the chord are comparable and ii) the free surface is far enough to assume the disturbance on \mathcal{F} one order lower in the perturbation expansion scheme. Here we reproduce some of the Salvesen experimental conditions. We start from figure 4 where, for the larger immersion $d/c = 1.37$ shown on the left-plots, the wave forms are reported for increasing forward speed (from top down $F_n = U/\sqrt{gc} = 0.422, 0.590, 0.759, 0.928$, respectively). The foil is placed at zero incidence with the trailing edge at $x/c = 0, y/c = -1.37$. The non dimensional horizontal coordinate x/c is scaled by F_n^{-2} so that, at the first order, the same number of crests are plotted for each case. Although the physical dimensions of the adopted computational domains are different, the discrete parameters for each case are refined enough to have results of comparable accuracy. Finally, if not stated otherwise, a smooth acceleration up to the final forward speed is used to reduce the oscillatory behaviour characteristic of the transient stage.

Regular wave systems are obtained for all cases and, at first sight, the measured wave height denoted by symbols compares well with the numerical profile (solid lines). Increasing the forward velocity, the troughs are eventually underestimated. A wave profile shift is detected for the case $F_n = 0.759$.

The results reported in the right-plots of figure 4 for the

smaller immersion $d/c = 1.14$ allow a clearer analysis of nonlinearities. Because of the smaller depth of submergence, amplitudes are larger with respect to the previous cases but the overall agreement is still satisfactory. Actually greater discrepancies in hollows appear as the Froude number increases. The wavelength is rather well predicted also in the worst case $F_n = 0.928$. Exactly for this speed (third right-plot in fig. 4) we compare our results with Salvesen second order theory (dashed line). The improvement is apparent both in capturing the correct wave height and predicting the wavelength. Salvesen himself, in fact, developed a (non-consistent) third order correction (dotted line) which nicely reproduces the experimental data and agrees better with the present numerical results.

In spite of the good prediction of wave forms, the computed loads are no more than acceptable. The wave drag deduced by the Salvesen formula $D = \frac{1}{4}\rho g H^2$ is no more than a global measure of the wave pattern because, as Salvesen discussed, the measured drag is significantly affected by viscous effects which varies with the immersion for the geometric scale here adopted. In figure 5, the wave drag deduced by the measured wave height H is compared with the numerical results obtained by direct pressure integration (denoted by \bullet) and using the Salvesen formula. In some cases, Salvesen used the first wave peak which is apparently affected by local effects due to the hydrofoil. Therefore we used both the first peak, Δ , and the wave amplitude far from the hydrofoil, ∇ , to determine the wave-drag. For both the immersions but more clearly for the lowest one, we can observe an increasing under prediction as the Froude number increases which is the 'signature' of the increasing difficulties in capturing the measured wave-height. For the smaller d/c (bottom plot in figure 5) we also report the theoretical second order result (dashed line), in good agreement for all cases but for $F_n = 0.759$.

Hydrofoil with an angle of attack In this case the foil is placed beneath the free surface with a geometrical incidence α different from zero and, regardless the law $U(t)$ adopted to reach the steady-regime forward speed, a more vigorous vortex shedding γ_{TE} is expected in the initial stage. Consistently, a circulation Γ around the body grows and together with the lift force component (see figure 6).

Eventually steady state is reached and the predicted wave pattern is here compared with data measured by Duncan (1983). A NACA0012 profile with chord c at an angle of attack $\alpha = 5^\circ$ is considered. In this case, the immersion d/c is measured from the mid-chord profile to the undisturbed water level and results for the three values $d/c = 1.2857$, 1.1626 and 1.0345 are reported in figure 7, from top down respectively.

More precisely, the present results (solid lines) are compared both with the measured wave profile, \diamond , and the numerical predictions obtained by other numerical methods. Namely, a steady solver [19] based on a boundary integral formulation for potential flow with lifting effects, \diamond , and a finite volume code [15] to solve the Reynolds averaged Navier-Stokes equations, \bullet .

For all the computational methods considered, tests are performed to check the invariance with respect to further refinements of the discrete solution. In the RANSE code, the part of the geometry which embeds the free surface is systematically refined using three different grids, the numerical grid around the hydrofoil is kept unchanged. The numerical tests show that the grid refinement around the profile is not so im-

portant for the formation of the free surface as around the free surface itself where numerical diffusion could quickly damp the generated waves. To rule out the uncertainty due to the graphic manipulation, the Lagrangian free surface markers are simply connected with straight segments. For all the cases shown, quite reasonable wave patterns can be observed. For the deepest submergence (upper plot) only the present solution is contrasted with the Duncan data: the first trough just above the profile is well predicted as well as the two following peaks.

For $d/c = 1.1626$ some differences appear. In particular, the trough induced above the suction side is under-predicted by all methods. Steady BEM, \diamond , and RANSE, \bullet , solutions give roughly the same values while a deeper depression is predicted by the present unsteady solver which is placed half-way from the actual data. This feature is repeated for hollows more downstream. The two inviscid rotational models capture the first and second experimental wave humps well, while the third crest is rather underestimated. Also a sort of 'shift' of the wave forms can be detected and it may require an analysis of the discrete dispersion relation. As the RANSE code prediction is concerned, wave height is significantly under predicted although the wavelength is correctly captured. The reason for this disagreement has to be investigated, but recent results in [20] indicate that the assumption of turbulent flow over the whole foil may be one contributing factor.

This behaviour is, in some sense, magnified for the shallowest immersion (bottom plot in fig. 7). In particular the free surface deformation above the hydrofoil is by far more pronounced in the experiments. Following the Duncan suggestion, in the first computations performed the bottom of the basin was not taken into account because of the deep water regime of the generated waves. On the other hand, the 'ground-effect' on the hydrofoil should increase the actual body circulation which might explain the reduced depression predicted. Anyway, although RANSE computation takes the bottom effect, the same disagreement is observed. For the sake of completeness, we eventually included the bottom effects by the method of images and the steady regime results obtained are practically identical.

The last point to mention is the experimental uncertainty. No error bar is reported in Duncan paper and he generally claimed 'distances were measured to an accuracy of about ± 0.3 cm', which can explain the differences between the experiments and the reported numerical results only partly.

Pressure distribution on the foil We like to discuss in more detail the pressure computation. Once again, we can use experimental data to validate the method. In [16], the flow around a NACA 0012 with $\alpha = 5^\circ$ placed at a depth $d/c = 0.8$ has been considered and for the case $F_n = 0.35$ the authors reported the measured pressure coefficients on the foil surface. Consistently with the Duncan observations, in spite of the small d/c , the reduced speed allows for obtaining a non-breaking solution which is reported in figure 8 for $tU/c = 30$. As discussed, the pressure is obtained by the equation (13) and to compare with experiments the instantaneous reference pressure $p_0(s, t)$ has to be determined. Fortunately, the contribution $-\rho \int_{s_0}^s \dot{\alpha} d\ell$ eventually disappears in steady regime and the reference pressure is simply $-\frac{1}{2}\rho(\alpha_0^2 - U^2)$. Once this is taken into account, the pressure coefficient $C_p(s, t) = (p(s, t) - p_a)/\frac{1}{2}\rho U^2$ (dashed line) on the foil for $tU/c = 30$ is compared with the measured values (symbols) in figure 9. Although the method is relatively

crude, the overall agreement is quite satisfactory and it appears suitable to discuss, at least from a qualitative point of view, the pressure behaviour in more complex flow conditions.

Formation of breaking waves As the immersion decreases the amplitude of the generated wave system increases, and for a small enough value of d/c the appearance of breaking waves is expected. Duncan found [8] that a non breaking wave profile can be still obtained for a NACA 0012 placed at $d/c = 0.9507$ but, by perturbing the free surface, he observed the formation of a spilling breaker at the first crest past the foil. Here, we consider the sudden start of the foil to obtain the results of figure 10. Symbols refer to the non-breaking experimental wave profile and nicely agree with the present solution. In the enlarged view the emission of a tiny jet at the first crest is clearly detected and, eventually, the simulation stops. We are not able to prolong further in time the present computations: the coupling with the model for steady breakers proposed by Cointe & Tulin (1994) may be the possible way to overcome this difficulty.

Finally, we like to show some refined computations of the growth of a larger plunging breaker past a NACA 0012 slightly immersed, $d/c = 0.25$, with an angle of attack $\alpha = 10^\circ$. The left plots of figure 11 show the wave motion due to the sudden start of the foil, as well as the starting vortex. Time passes from top down and it is clearly seen that, in spite of the large breaker just behind the foil, the free surface just above it becomes soon stationary. The pressure on \mathcal{H} at the same time is plotted on the right. It is interesting to observe that at the very beginning of the phenomenon the C_p distribution still resembles that one typical of a foil with positive incidence and, actually, during the first stage the lift (not reported) sharply increases. As time passes the free surface becomes highly deformed and the pressure on the upper side decreases. Unlike, the pressure on the lower side seems quite unaffected and, eventually, the lift after an initial peak decreases. The simulation stops a bit after and we are not able to give a steady regime value of the lift. Anyway, it is well known from experimental data that the reducing of d/c lowers the lift, that can become negative even for positive angles of attack. The late details of the plunging breaker are shown in a natural scale in the figure 12.

4. Conclusions and perspectives

An unsteady model for the inviscid flow generated by a hydrofoil moving beneath a free surface has been presented. Rotational effects are modeled by a thin wake embedded in a otherwise irrotational flow and shed from the trailing edge. An efficient and accurate numerical procedure is developed. Several examples to discuss the validity of the physical model and the performances of the developed algorithm have been presented. Specifically, we have considered those flows characterized by a non-breaking steady regime. Resulting wave forms are compared with experimental results given by Salvesen [17] for a foil with zero geometrical incidence and by Duncan [8] for a NACA 0012 at an angle of attack. The agreement in all cases is satisfactory.

For the same cases, drag predictions computed by pressure integration fit well the experimental wave resistance. The pressure acting on the foil has been compared with that one measured in [16].

Finally, refined computations in breaking cases are presented to show the ability of the numerical technique in handling

highly nonlinear free surface flows.

In spite of the simplicity of the model, the quantitative agreement appears good enough to consider the present model a valuable theoretical tool for analyzing more general conditions. In fact, arbitrary body motions and incoming waves are, in principle included in the present model, are actually discussed in [14].

Further extensions are presently under analysis. If massive separation occurs, the method can be generalized following Landrini et al. (1998) in which an operator splitting technique to solve the Navier-Stokes equations is coupled to the unsteady nonlinear free surface model. Also, as discussed in Bulgarelli et al. (1997), the model can be modified to deal with the flow generated by an aerofoil moving *above* the air-water interface to analyze the unsteady flow of WISES-concept vehicles.

Acknowledgments

The research was supported by Italian *Ministero del Trasporto e della Navigazione* through INSEAN Research Program 1997-99.

References

- [1] P. BASSANINI, C.M. CACIOLA, M.R. LANCIA, R. PIVA, 1991. *A boundary integral formulation for kinetic field in aerodynamics. Part I: Mathematical analysis. Part II: Applications to unsteady 2D flows*. Eur. J. Mech. B/Fluids. **10**, 6 and **11**, 1.
- [2] BERTRAM, V., MUZAFERIJA, S.; PERIĆ, THIART, G., 1998. *A comparison of free surface viscous and inviscid methods to compute the flow about a submerged hydrofoil*. SACAM '98, Capetown.
- [3] U. B. BULGARELLI, M. GRECO, M. LANDRINI, AND C. LUGNI, 1997. *A simple model for the aero-hydrodynamics of Ekranoplans*. AGARD Workshop on "High Speed body motion in water", Kiev.
- [4] C. M. CACIOLA AND M. LANDRINI, 1991. *Inviscid flows about a slightly submerged oscillating hydrofoil*. First European Fluid Mechanics Conference, Cambridge.
- [5] C.M. CACIOLA AND R. PIVA, 1990. *A boundary integral approach in primitive variables for free surface flows*. Proc. 18.th Symp. on Naval Hydron., Ann Arbor.
- [6] R. COINTE & M.P. TULIN (1994). *A theory of steady breakers*. J. Fluid Mech., **276**.
- [7] R.M. COLEMAN, 1986. *Nonlinear calculation of breaking and non-breaking waves behind a two-dimensional hydrofoil* 16th Symp. on Naval Hydrodynamics, Berkeley.
- [8] J. DUNCAN, 1983. *The breaking and non-breaking wave resistance of a two dimensional hydrofoil*. J. Fluid Mech. **126**.
- [9] L. K. FORBES, 1985 A numerical method for non-linear flow about a submerged hydrofoil. J. Eng. Math. **19**
- [10] K.O. FRIEDRICH, 1966. Special Topics in Fluid Mechanics New York, Gordon and Breach.
- [11] J.P. GIESING & A.M.O. SMITH, 1967. Potential flow about two-dimensional hydrofoils. J. Fluid Mech. **28**.

- [12] R. KRASNY, 1991. Vortex sheet computations: roll-up, wakes, separation. *Lectures in Applied Mathematics*, Vol. 28.
- [13] M. LANDRINI, M. RANUCCI, C. M. CACCIOLA AND G. GRAZIANI, 1998. *Viscous effects in wave-body interaction*. Int. J. Off. and Polar Eng..
- [14] M. LANDRINI, C. LUGNI, M. GRECO, 1998. *Unsteady flow around an oscillating hydrofoil beneath waves*. Submitted.
- [15] MUZAERIJA, S.; PERIĆ (1997), *Interface-tracking and interface-capturing methods for viscous free-surface flows*, 5th Symp. on Nonlinear and Free-Surface Flows, Hiroshima
- [16] K. H. MORI AND M. S. SHIN, (1988). *Sub-breaking wave: its characteristics, appearing conditions and numerical simulation*. Proc. of 17th Symp. on Naval Hydrodynamics.
- [17] N. SALVESEN, 1966. *Second order wave theory for submerged two-dimensional bodies* in Proc. of 6th Symp. on Naval Hydrodynamics, Washington.
- [18] N. SALVESEN, 1969. *On second order wave theory for submerged two-dimensional bodies* J. Fluid Mech. **38**.
- [19] THIART, G.; BERTRAM, V. (1998), *Staggered-grid panel method for hydrofoils with fully nonlinear free-surface effect*, submitted to International Shipbuilding Progress.
- [20] TZABIRAS, G.D. (1997), *A numerical investigation of 2d, steady free surface flows*, Int. J. Num. Methods in Fluids 25, pp. 567-598
- [21] G.B. WHITHAM, 1974. *Linear and nonlinear waves*, 1974. John Wiley & Sons.

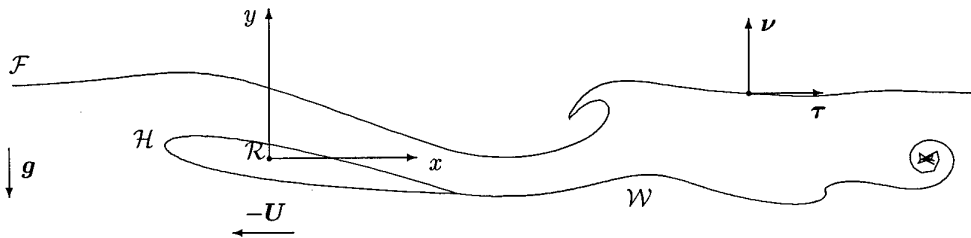


Figure 2: Sketch of the problem and adopted nomenclature.

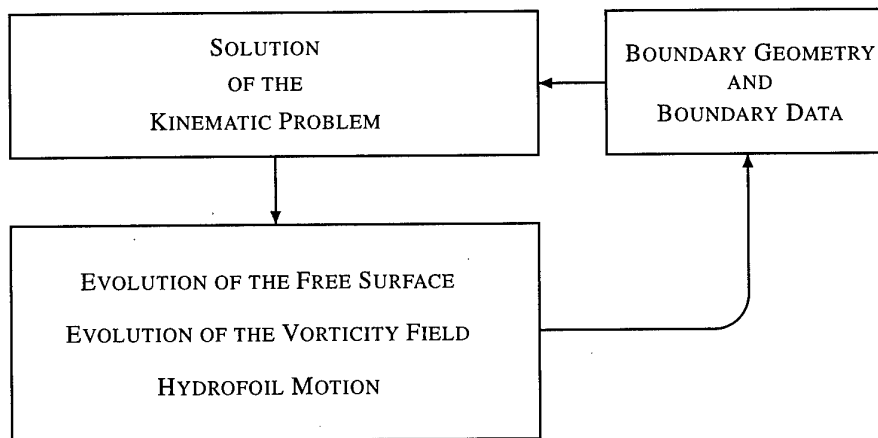


Figure 3: Schematic description of the numerical procedure.

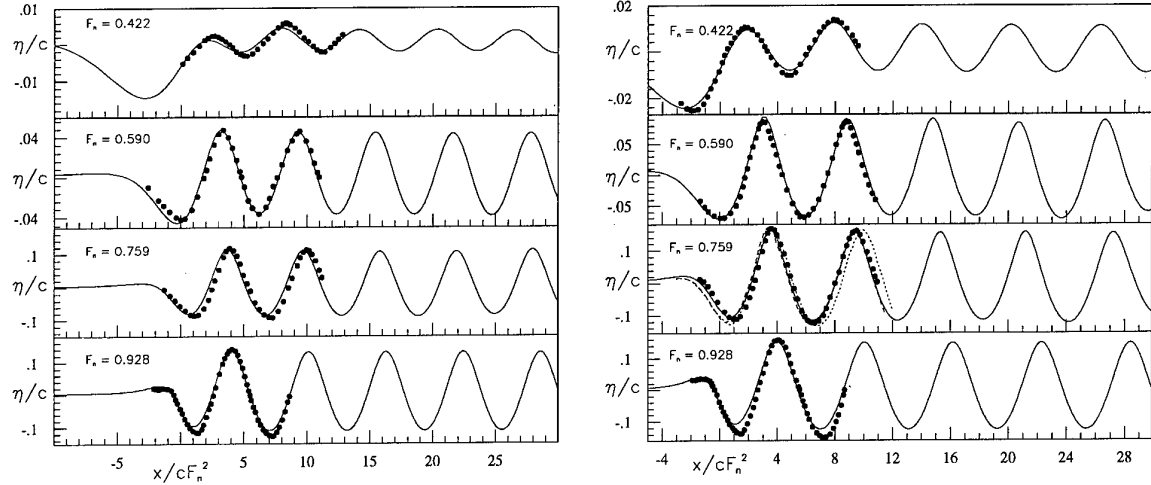


Figure 4: Hydrofoil at zero incidence. The Froude number $F_n = U/\sqrt{gc}$ increases from top down. Present numerical results (solid lines) are compared with experimental data, \bullet , from [17]. Left: The trailing edge is located at $(x = 0., y = -d/c = -1.37)$. Right: The trailing edge of the foil is located at $(x = 0., y = -d/c = -1.14)$. For this depth of submergence and $F_n = 0.759$, second and third order results (dashed and dotted lines respectively in the third right-plot) are taken from [18].

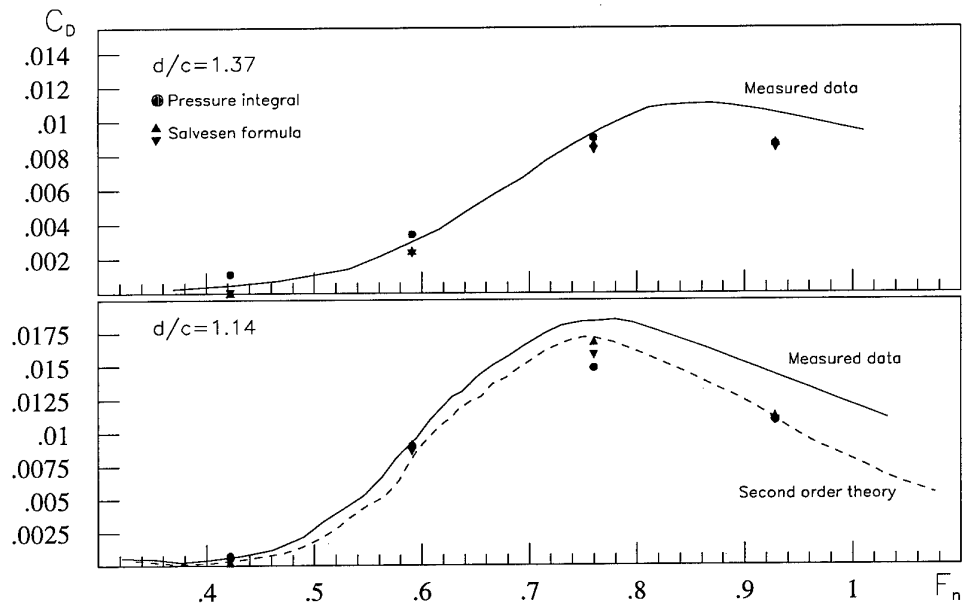


Figure 5: Hydrofoil at zero incidence. Drag coefficient $C_D = D/\frac{1}{2}\rho U^2 c$ in steady regime for the same cases of figure (top plot: $d/c = 1.37$, bottom plot: $d/c = 1.14$). Wave resistance from measured wave height is taken from [17]. The numerical C_D is obtained both by direct pressure integration, \bullet , and by applying the Salvesen formula to predicted wave height Δ , ∇ . Second order theory (dashed line in the upper plot) is taken from [18].

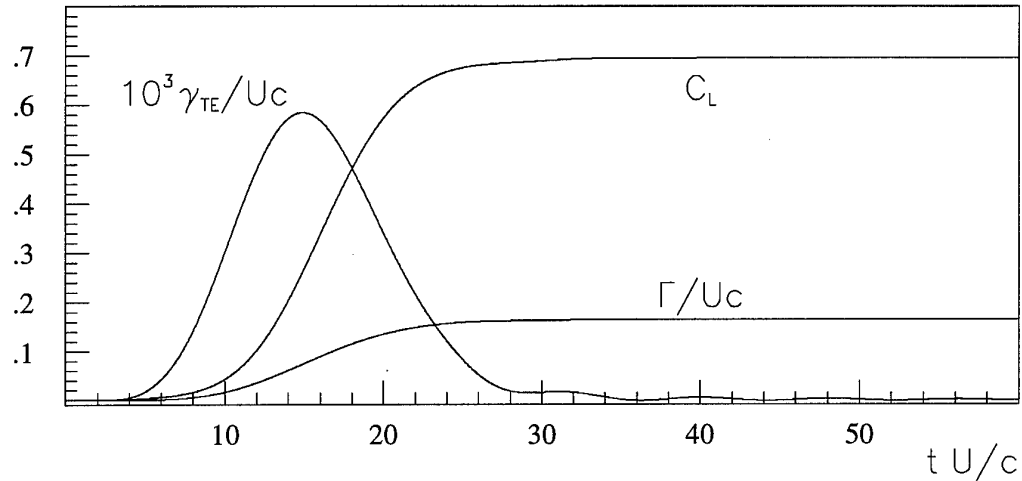


Figure 6: Histories of the lift coefficient C_L , body circulation Γ and vortex shedding γ_{TE} for a NACA0012 starting from rest ($\alpha = 5^\circ$, $d/c = 1.28$, $F_n = U/\sqrt{gc} = 0.5669$).

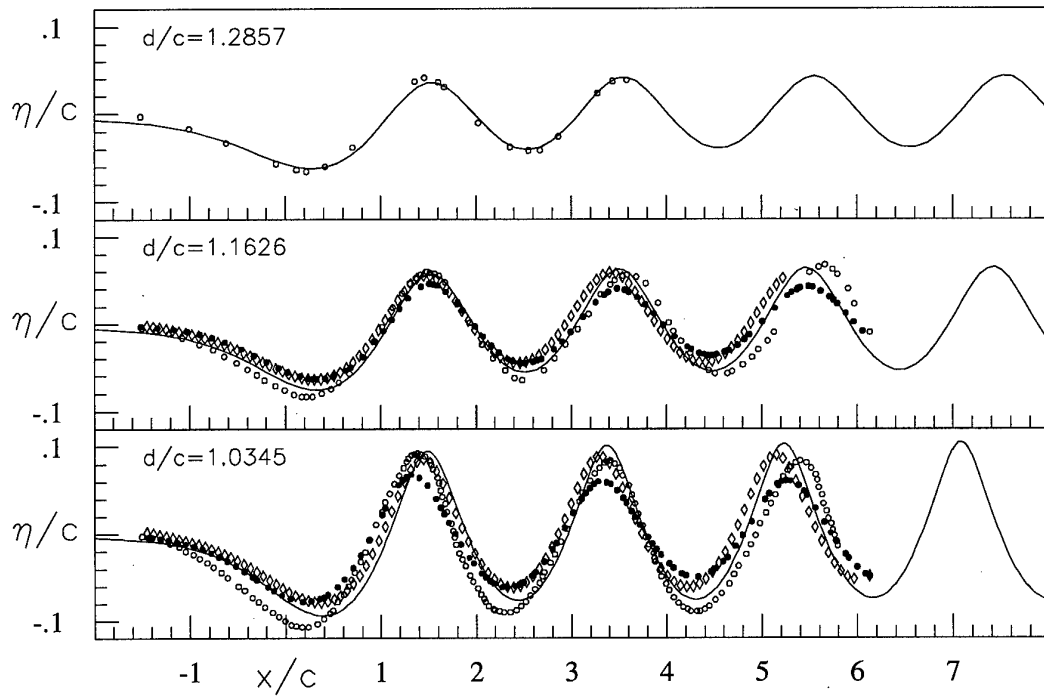


Figure 7: Hydrofoil at incidence. Wave height η/c past a NACA 0012 ($F_n = U/\sqrt{gc} = 0.567$, $\alpha = 5^\circ$). Submergence d/c measured from the mid-chord point decreases from top down. Solid lines: present unsteady results, \circ measurements, \bullet viscous results from [2], \diamond steady inviscid results from [2].

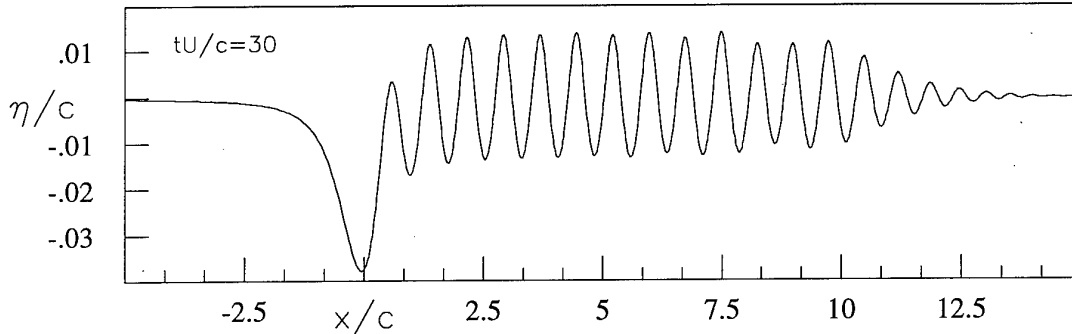


Figure 8: Wave profile past a NACA0012 foil ($\alpha = 5^\circ$, $d/c = 0.8$, $F_n = 0.35$). Discrete parameters: $N/\lambda = 10$, $N_b = 120$, $\Delta t = \frac{1}{50}c/U$

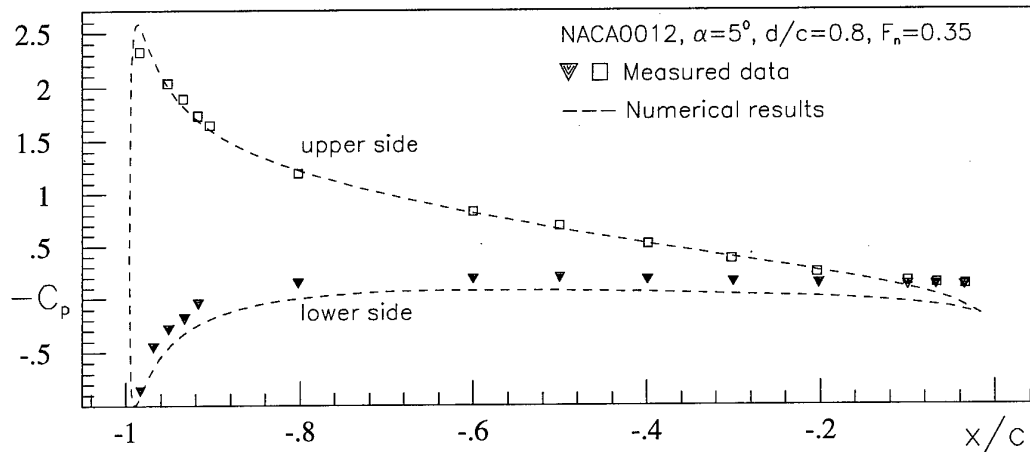


Figure 9: Comparison of measured and predicted pressure coefficient. Symbols: measured data from [16]. Dashed line present numerical results. Flow conditions: NACA0012 profile, $\alpha = 5^\circ$, $d/c = 0.8$, $F_n = 0.35$. Discrete parameters: $N/\lambda = 10$, $N_b = 120$, $\Delta t = \frac{1}{50}c/U$

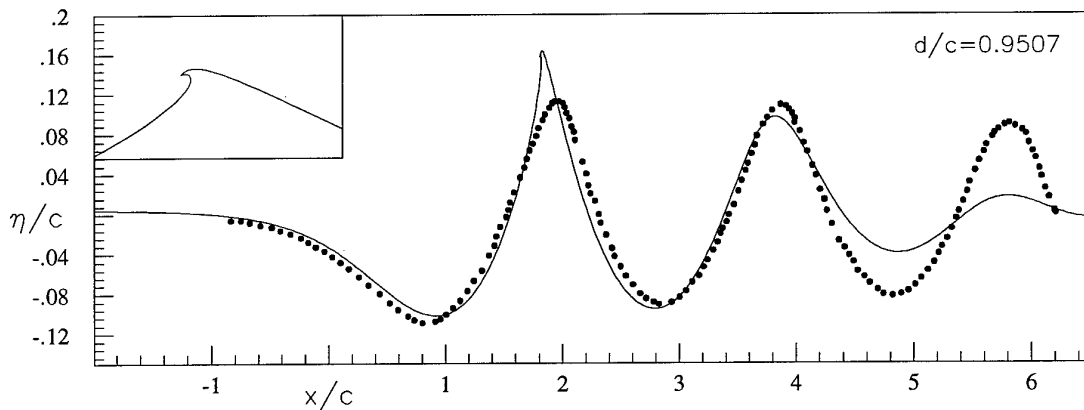


Figure 10: Formation of a spilling breaker past a NACA 0012, $\alpha = 5^\circ$, $F_n = 0.5669$, $d/c = 0.9507$, $tU/c = 11.5279$ after the sudden start. Experimental data, ●, from [8]. Top left: detail in natural scale of the spilling crest.

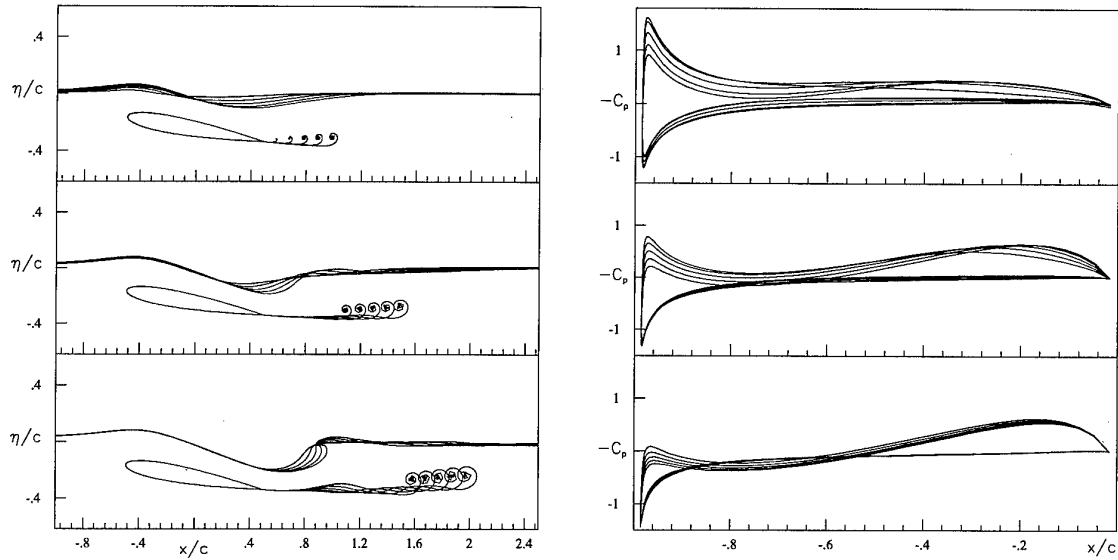


Figure 11: Evolution toward breaking of the first crest past a NACA 0012, $\alpha = 10^0$, $F_n = 0.5669$, $d/c = 0.25$. Left: wave profile from $tU/c = 0.1133$ up to $tU/c = 1.7007$ time step $\Delta tU/c = 0.1133$ Right: unsteady pressure coefficient at the same time instants.

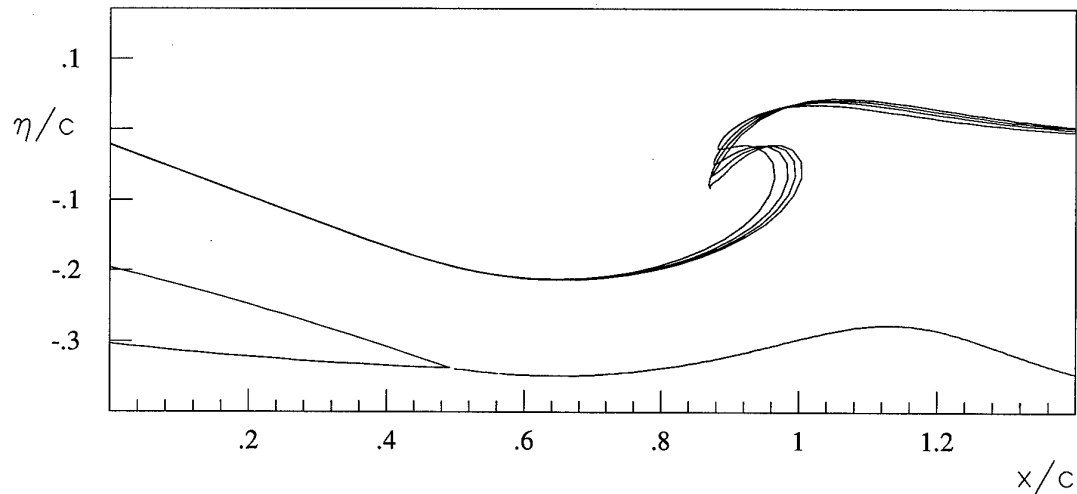


Figure 12: Details of the plunging breaker past a NACA 0012, $\alpha = 10^0$, $F_n = 0.5669$, $d/c = 0.25$, $tU/c = 1.7007$, 1.7544 , 1.7856 , 1.8125 .

Hydrodynamic Characteristics of Rudders Operating in Air-Sea Interface

V.T.Savchenko

Inst. of Math. Mach. & Systems Problems
UNAS, 42, Glushkova Prospect
252187 Kiev, Ukraine

SUMMARY

Results of experiments with a series of rectangular and triangular (in plane) foils are described. These foils have a wedge profile and function nearly a solid body. Three conditions of flow around the foil were being guaranteed: a continuous, a cavitating and continuous with a gas-liquid layer (Gll) at the body. The research permitted us to find some effects and to design a special foil operating effectively at the body with a gas layer.

LIST OF SYMBOLS

Gll	gas-liquid layer (abbr)
P	free stream static pressure
Pc	pressure in cavity
Q	volume of airflow rate
Cq	airflow rate coefficient
Py	lifting force
Px	drag force
Cy	lifting force coefficient
Cx	drag force coefficient
Cyk	lifting force coefficient of insulated foil
Fr	Froude number
Re	Reynolds number
We	Weber number
σ	cavitating number
α	angle of attack
f	concentration of gas in Gll
Z	thickness of near wall layer
A	aspect ratio of foil
c	chord of foil
S	foil area
L	model length
R	radius of body of revolution.

1. INTRODUCTION

A great number of experimental as well as theoretical works explore hydro- and aerodynamic characteristics of protruding elements of the bodies, for instance, the bodies of revolution. The results of many of them describe the inseparable flow and have been summarized in monographs (Ref. 1, 2, 3). If conditions of exploiting bodies are more

complicated, the hydrodynamic forces acting on the protruding elements of a body have to be thoroughly explored in every concrete case. For instance, investigation of a high-speed water entry of a body required to solve two complicated problems. One of them was protecting the protruding elements from overloads. They are rather significant due to the increase in the medium density (in 800 times more) and the high speeds. The second problem was preserving the adequate function of controllability of rudders and stabilizers in various streamline regimes. A series of works conducted at the Institute of Hydromechanics UNAS are devoted to finding solutions of these problems (Ref. 4).⁵

The problem on functioning of the protruding elements of the body in conditions, when a gas component (phase) of various concentration is present in the stream, is not less interesting and very practical.

The elements of the bodies, which move near the boundary of the two mediums, as well as the cavitating bodies, are in such conditions. For instance, the system of lifting foils, which compensates for the loss of buoyancy of a body in a cavity, is among these bodies too. It is known that in such conditions cavitating and supercavitating profiles are used. The theory of cavitating foils has been developed in detail, e.g. Tulin, Kinnass, Egorov, Basin and other (Ref. 6, 7, 8, 9, 10, 11).

The experimental works carried out in the laboratory of the Institute of Hydromechanics are devoted to the systematic investigation of GLL influence on the hydrodynamic characteristics of various types of rudders. They are partially presented in this paper.

2. TEST CONDITIONS

When the hydrodynamic characteristics of bodies are being investigated, the bodies are usually put into the middle part of the hydrotunnel's stream. If the foil operates near the body of revolution, the experiments can be carried out using semi-body of revolution. This semi-body should be mounted on a

flat solid wall in the hydrodynamic tunnel (HDT) (Fig.1).

The HDT has a 2000 mm long working part with the open free surface and rectangular 340×330 mm cross-section. The contour of the model was chosen that its main parts correspond to the profiles of vehicles being usually used (Fig.2). The head part of it was shaped as a parabola while the main part was as a extended cylinder. The total length of a model was 387 mm, the radius of the cylinder part was 30mm. The foil was inserted into a special clamp 30 mm away from the model's stern. It could be rotated and fixed at the required angles to the flow.

There were two ring slits at the front of the cylinder part of the model. The first one was intended to separate the fluid stream directly in front of it. The gas for forming either a developed cavitation flow around the model or a two-phase near wall layer of liquid is supplied into the stream through the second ring slit. The 5 orifices with diameter 2 mm were made in the slit particularly for this purpose. There was an orifice to measure the pressure in the cavity P_k in the middle part of the model.

3. BASIC PARAMETERS

The experiments were carried out with a series of rectangular and triangular in plane foils with the symmetric wedge profiles. The 12 types of rudders have been tested as a whole. Aspect ratio of this series was being altered within the limits of $0.9 \leq A = S/c^2 \leq 4$ (S is the area of a foil, c is the foil's chord). There was a series of rudders with the equal lateral surface. It was convenient for evaluating their hydrodynamic characteristics.

The angle α between the plane of foil's symmetry and the plane of the semi-model's symmetry was being altered within the limits of $|\alpha|=15^\circ$ with the step $|\Delta\alpha|=3^\circ$. The tests were carried out at the velocity of free stream $V = \text{const} = 9 \text{ m/s}$. For the described model this corresponded to the non-dimensional parameters as follows (Ref. 12):

Reynolds number $Re = VL/v = 3.2 \cdot 10^6$; v is the kinematic coefficient of viscosity,

Froude number $Fr = V/\sqrt{gL} = 4.6$; g is the acceleration due to gravity,

Weber number $We = c\rho V^2/\xi = 1.5 \cdot 10^3$; ξ is the coefficient of surface tensions, ρ is the mass density, R is the radius of the cylinder part of the model.

The cavitation number depending on the flow regime was changed within the limits of $0.015 \leq \sigma = 2(P-P_0)/\rho V^2 \leq 0.045$.

Airflow rate Q for gas supply into the near wall layer was $Q_1 = 1.2$, $Q_2 = 0.6$, $Q_3 = 0$ (liter/sec). This corresponded to the three flow regimes:

1. The regime with the air layer between the foil and the body. The cavity is closed behind the foil.
2. Gll forms between the foil and the body. The cavity is closed in front of the foil.
3. The regime of continuous flow about the foil.

The coefficient of airflow rate was calculated according to the following formula $C_Q = Q / \pi R^2 V$. Air concentration in Gll f was determined depending on the airflow rate Q and a thickness of the layer Z

$$f = \frac{C_Q}{\left(1 + \frac{Z}{R}\right)^2 - 1} \quad (1)$$

Parameters for regime 1 were: $Z_1 = 3 \pm 4 \text{ mm}$, $\sigma = 0.015 \pm 0.02$.

Parameters for regime 2 were: $Z_2 = 5 \text{ mm}$, $f = 0.095$, $\sigma = 0.04 \pm 0.045$.

The components of hydrodynamic forces P_x and P_y , acting on the foil, were measured during the experiment. P_x force acts along the up-running stream (a drag force), while P_y acts across a plane of a body's symmetry (a lift force of the foil).

The tests were carried out in order to estimate the value and the type of changes of hydrodynamic forces acting on the rudders which operate near the body of revolution in each of the three flow regimes: continuous flow, Gll between the hull and the rudder, and the air layer between the rudder and the hull.

4. TEST RESULTS

The results of the tests are represented as a dependence of coefficients of hydrodynamic forces C_x and C_y on the angles of attack at flow regimes described above. The typical regimes of flow about the model are displayed in figure 3 (photo a,b,c,d,e).

If the experiment is carried out in conditions described above, stable dependencies $C_x(\alpha)$ and $C_y(\alpha)$ take place in presence of a developed cavity (regime 1) or in presence of the Gll (regime 2). To show it better, figures 4, 5 display the measurement results at deviations of rudders once in positive and once in negative directions.

The characteristics of foils $C_x(\alpha)$ and $C_y(\alpha)$ in the flow regime 1 and in continuous flow regime 3 are shown in figures 6, 7. The jumps discontinuity (the 1st type) appear in the third regime. They usually

shown in figures 6, 7. The jumps discontinuity (the 1st type) appear in the third regime. They usually occur when air is bursting from the main cavity towards the foil. This situation are determined for each case by conditions of the experiment.

Fig. 8 displays polars of the same foil for flow regime 3 once with and once without flow separation. Formation of a cavity behind a foil reduces the hydrodynamic forces almost twice. We found even smaller forces in the first flow regime (fig. 9). Such decrease of the hydrodynamic forces, which takes places when the continuous flow regime changes into the developed cavitation regime, is due to the loss of interference.

As seen from the experiments the GII with air concentration $f \leq 0.1$ ($Z=5\text{mm}$) weakly influences on the $C_x(\alpha)$ and $C_y(\alpha)$ dependencies and does not reduce the interference between a foil and a body.

Presence of rudders sometimes influences on the character of flow around a model. It is seen in photo (Fig. 3) that in practically all the cases of a local cavity is formed nearby a rudder. It does not disappear when a rudder is in its neutral position $\alpha = 0$ and it increases if α increases. Dimensions of such cavity are comparable in regimes 1 and 2 when the rudder has a angle of attack $\alpha > \alpha_{cr}$ ($\alpha_{cr} \approx 6^\circ$ for this considered case). When this angle $\alpha < \alpha_{cr}$ the length of a local cavity in the second regime is in 10 times smaller than in the first regime. We should note also that a rudder creates a support to a cavity on a body and when $\alpha > \alpha_{cr}$ its dimension decreases significantly.

5. SOME QUANTITATIVE ESTIMATIONS

A comparison of the lifting force coefficient from experiments $C_{yexp} = 2Py(\alpha)/\rho V^2 S$ for third regime with corresponding calculations at the unbounded stream $C_{yk}=2\pi/(1+2/A)$ shows for small angles (when there is no separation):

$$C_{yk}^\alpha = 4.2; 4.0; 3.14; 2.1; 2.0$$

$$C_{yexp}^\alpha = 5.3; 4.7; 4.2; 2.8; 2.0$$

We can see the derivative C_{yexp}^α is considerably more than the theoretical C_{yk}^α . This fact may be explained by the foil-hull interference. The foil operates in conditions close to conditions of presence of a solid wall. Based on calculation estimations of the hull interference on foil's lifting force Pyk for aspect ratios $A \leq 2/3$ give us: $K = Py/Pyk = 1.6$ (Ref. 1, 13).

If there is a cavity around a hull, the foil operates in conditions of intersection of the free surface. The

estimation of the free surface influence (Ref. 14) shows:

$$\frac{C_{yk}^\alpha - C_{yk^{Fr=\infty}}^\alpha}{C_{yk}^\alpha} \approx 0.1 \quad (2)$$

The lift force value reduces almost 10% [14].

In the experiment we have observed the value of lift force reduction almost twice if an air layer formed there between the hull and the foil. This phenomenon can be explained only by taking into account all losses: the interference lose, the free surface influence, and the partial loss of the area of the foil $\Delta S = c \cdot Z$. To unload the weight of the aft part of the cavitating object we have suggested a special shape of the foil in plan. This gave a possibility to reduce the loss of hydrodynamic quality down to the value of 0.12. The loss of quality for rectangular foils was of the order of 0.4.

CONCLUSIONS

1. Conducting the investigations on flow about the series of protruding elements (of foils, rudders) nearby the bodies of revolution has given us an opportunity to find the significant, more than twice, reduction of hydrodynamic forces on rudders if an air layer between a hull of a body and a rudder was present. This phenomenon is explained by taking into account the three factors: the complete loss of foil-hull interference, the partial loss of the effective area of a foil and influence of the free surface of the air layer (cavity).
2. Existence of the air phase in the near hull layer of a concentration $f \leq 0.1$ does not reduce the value of hydrodynamic forces on the rudders.

REFERENCES

1. Krasnov, N.F., "Aerodynamics", Moscow, SU, Bishaya shkola Press, 1971, 420-446pp. (in Russian).
2. Eshli,X., Lendal,M."Aerodynamics of Foils and Hulls of Vehicles", Moscow, SU, Mashinostroenie Press, 1969, 318p.(in Russian).
3. Ivanov, A.N., "Hydrodynamics of developed cavitating flows", Leningrad, SU, Sudostroenie Press, 1980, pp.162-181. (in Russian).
4. Savchenko, V.T., Putilin, S.I., Savchenko, Y.N. (1992) "Aerohydrofoil", A.C. 1710445 USSR, ICI 5B54C 3/14, Inform. Bull. 5, 1992 (in Russian).
5. Savchenko, V.T., "Reduction of Overload on a body Entering Water at High Speed", in "High

Speed Body Motion in Water", AGARD-R-827,
September 1997, Paper 29.

6. Tulin, M.P., "Supercavitating flow past foils and struts", In: Proc. 1955 MPL Simp. On Cavitation in Hydrodynamics, Paper 16, HMSO, London, 1955.
7. Kinnas, S.A., "Analysis of the flow around supercaviting hydrofoils with midchord and face cavity detachment", J. Ship Res., 35, 3, 1991, pp. 198-209.
8. Egorov, I.T., Sadovnikov, Yu.M., Isaev, I.I., Basin, M.A., "Artificial Cavitation", Sudostroenie Press, Leningrad, SU, 1971, 280p. (in Russian).
9. Basin, M.A., Shadrin V.P., "Hydroaerodynamics of Foil near the Boundary of Medium Separate", Liningrad, SU, Sudostroenie Press, 1980, 340p.(in Russian).
10. Uhlman, J.S., "The Surface Singularity Method Applied to Partially Cavitating Hydrofoils", J. Ship Res., 31, 2, 1987, pp.107-124.
11. Semenenko, V.N., "Calculation of unsteady hydrodynamic characteristics of ventilated hydrofoil near the wave water surface", J. Hydromechanics, 48, 1983, pp.6-10, Kiev, UKR, (in Russian).
12. Epshtein, L.A. "Methods of Theory of Dimensionality and Similarity in Problems of Ship Hydromechanics" Leningrad, SU, Sudostroenie Press, 1970, 205p.(in Russian).
13. Nilsen, Dj., "Aerodynamics of Controled Shells", Moscow, SU, GNTI Oborongiz Press, 1962, pp. 134-135. (in Russian).
14. Borisuk, M.N., "Problem on vertical hydrofoil", J.Hydromechanics of High Speeds, Kiev, UKR, 1966, pp.59-74. (in Russian).

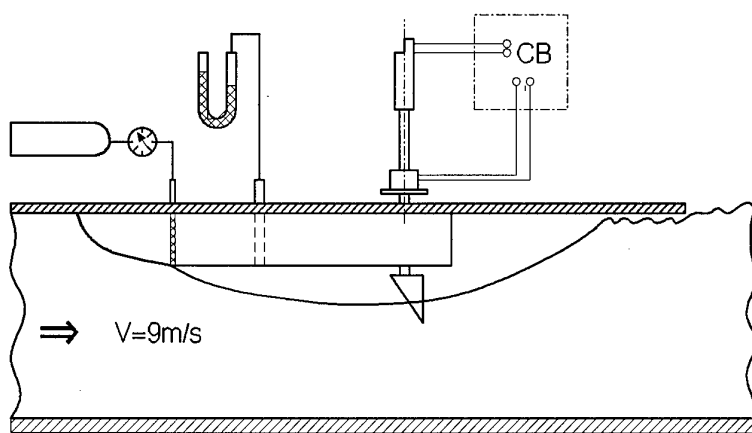


Fig. 1. Scheme of experimental installation

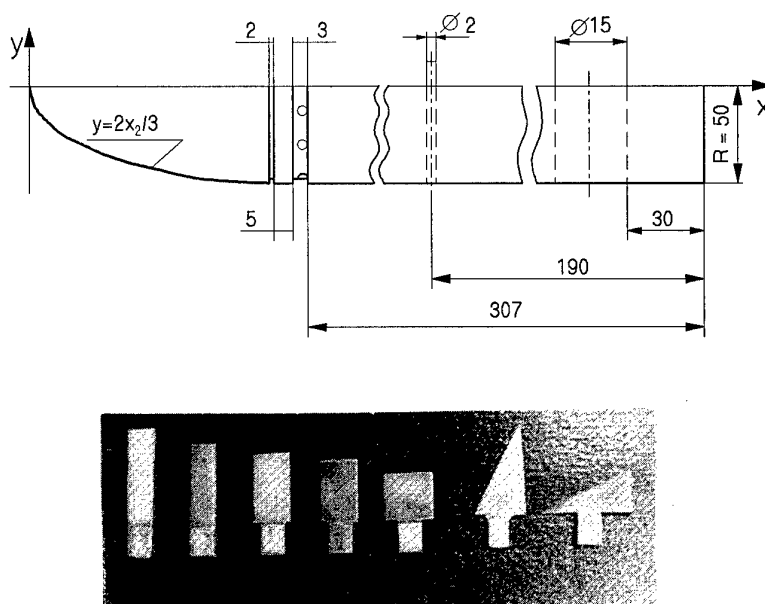


Fig. 2. Main parameters of model (mm) and foto of typical rudders

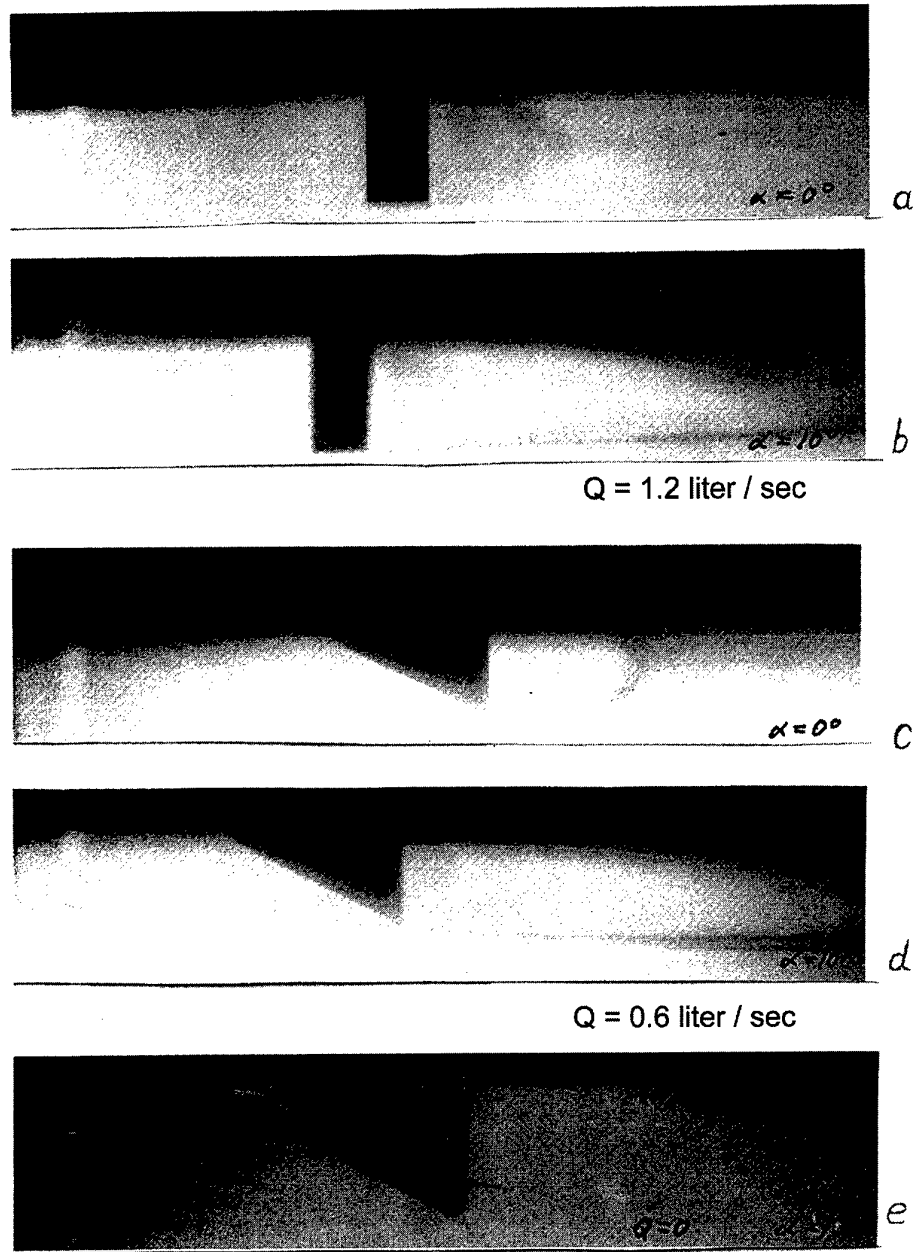


Fig. 3. Typical regimes of flow about rudders

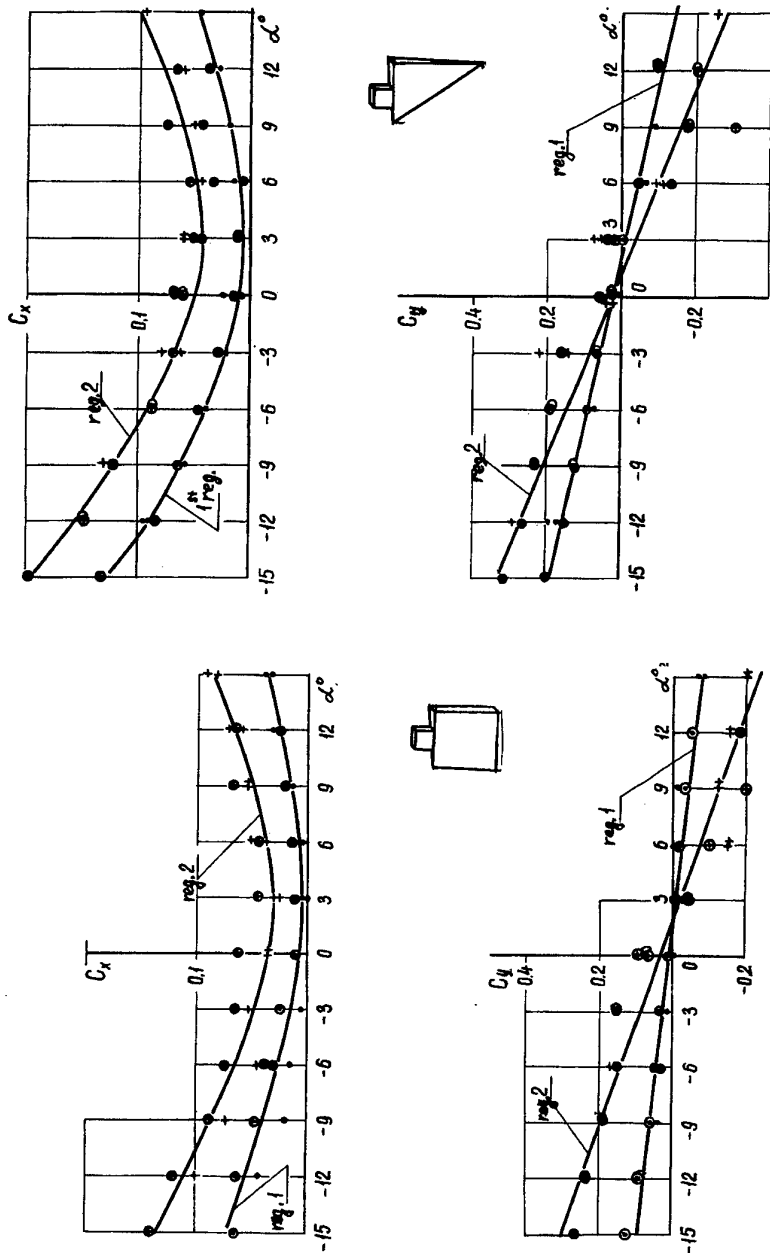


Fig. 4. Graphs of hydrodynamic force coefficients C_y , C_x for flow regimes 1 and 2 (rudder N 9)

Fig. 5. Graphs of hydrodynamic force coefficients C_y , C_x for flow regimes 1 and 2 (rudder N 11)

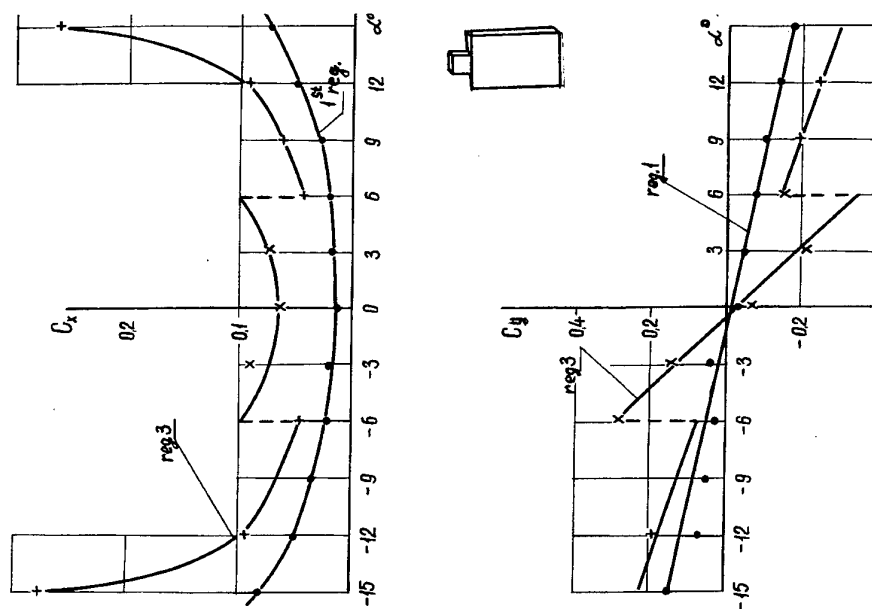


Fig. 6. Graphs of hydrodynamic force coefficients C_y , C_x
for flow regimes 1 and 3 (rudder N 8)

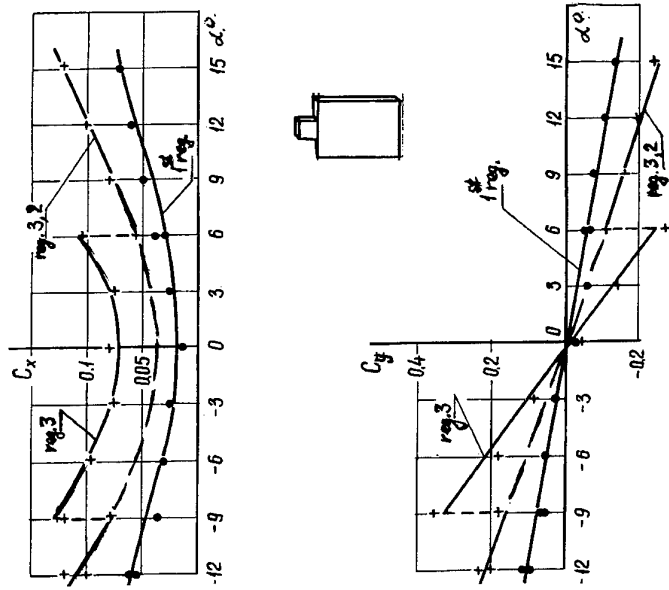


Fig. 7. Graphs of hydrodynamic force coefficients C_y , C_x
for flow regimes 1, 3 and 2 (rudder N 6)

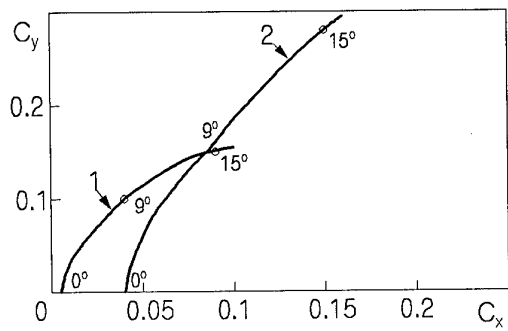


Fig. 8. Foil polars with (1) and without (2)
flow separation

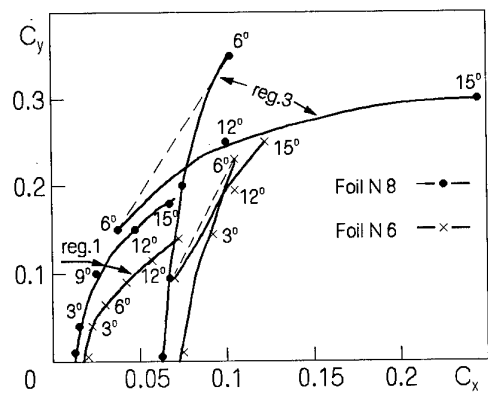


Fig. 9. Foil polars in flow regimes 1 and 3

Hydrodynamical Characteristics of an Ekranoplane Wing Flying Near the Wavy Sea Surface

V.G.BYELINSKY
P.I.ZINCHUK

Institute of Hydromechanics,
Ukrainian National Academy of Sciences
Zhelyabov Street 8/4
252057 Kyiv, Ukraine

SUMMARY

Some results of experimental studies conducted at the Institute of Hydromechanics of Ukrainian National Academy of Sciences applicable to the problem of ekranoplane creation are presented in this paper. The aim of these research works was to determine the influence of proximity of the flat and wavy screen upon aerodynamics of the ekranoplane's wing. Experimental installation and procedure of the experiment are described. Instantaneous values of lift, drag and position of centre of pressure for a wing moving above the flat and wavy screen have been defined. It has been determined the influence of the angle of attack, the aspect ratio, the distance to a flat and wavy screen as well as the wave length and wave height of a wavy screen on the wing lift. The measurement results of forces and moments on the wing moving above the oblique waves are given.

LIST OF SYMBOLS

v_0 - wing velocity,
 ℓ - wing span,
 b - wing chord,
 S - wing area,
 $\lambda = \ell/b$ - aspect ratio of a wing,
 θ° - angle of attack of a wing,
 h - non-dimensional distance from a rear edge of wing to a screen,
 H - non-dimensional distance from a rear edge of hydrofoil to a free surface of a liquid,
 $C_y, C_x, C_{mz}, C_{mx}, C_{my}$ - coefficients of lift, drag, pitching moment, rolling moment and yawing moment,
 $K = C_y/C_x$ - coefficient of lift/drag ratio,
 x_c - centre of pressure coefficient,
 λ_b - wave length of a wavy screen,

H_b - wave height of a wavy screen,
 c - wave velocity,
 σ - apparent frequency of wing's contact with a wave,
 $P = \frac{2\pi \cdot b}{\lambda_b}$ - Strouhal number,
 γ - deviation angle of waves crests.

1. INTRODUCTION.

In many countries of the world the attempts were taken during last decades to develop new means of transportation on water - ekranoplanes. Ekranoplanes, as it is known, are vehicles intended for the flight in the immediate proximity to a water surface. They are based on using so-called "screen effect". The essence of this effect lies in the sharp increase of a wing lift and its lift/drag ratio on flying at the low altitudes above the sea surface. Lately, numerous experimental models of ekranoplanes have been created in different countries. However, only a few of them produced encouraging results. The most successful achievements in this field were gained in the former Soviet Union. Substantial scientific and manufacturing personnel were enlisted for the development of ekranoplanes. As a result of a common efforts, under the guidance of the prominent designer Mr.P.E.Alexeev a number of especially large ekranoplanes with a great takeoff weight and a high flying speed had been designed, produced and field tested [1].

However, it should be admitted that, regardless of some successes, the creation of ekranoplanes is still the subject for investigations for the most countries of the world. Many scientific and technical papers and articles have been dedicated to the creation of ekranoplanes.

As an example, we would like to make reference to survey works on this problem [2, 3, 4]. Nevertheless, it still remains many indistinct and insufficiently studied problems in this field. One of the problems is the effect of a wavy sea surface on the ekranoplane.

In this paper, some experimental results on this problem obtained at the Institute of Hydromechanics of Ukrainian National Academy of Sciences are given. In the Institute a special experimental installation was created to research into aerohydrodynamics of ekranoplanes in late 70-es. Great volume of works pertaining to the research into the movement of ekranoplanes' models and their wing systems in the near to a flat and wavy screen had been carried out in this installation. On fulfilling these studies, only one experimental work connected with the movement of wing above a wavy screen was known to us [5].

In this paper, however, it was considered one specific case of a wing's motion above the waves of only one certain length and height. Our studies were conducted in compliance with a larger-scale programme. This allowed to produce data on the influence of a sufficiently wide spectrum of characteristics of the wavy screen upon hydrodynamic characteristics of the wing moving above it. The results of our studies were partially published in the articles [6,7,8,9,10]. Tests results of separate wings on their movement above a flat and wavy screen are presented below.

2. EXPERIMENTAL INSTALLATION AND PROCEDURE.

Experimental installation represents a hydrodynamic channel with the following dimensions: length - 140.0 m, width - 4.0 m, depth - 1.2 m. The channel is equipped with two towing carriages: slow-moving with the towing speed up to 6.0 m/sec and fast-moving up to 25 m/sec. The channel is also fitted with a wave maker - a generator of surface waves. In this installation, it is possible to carry on the towing tests of ekranoplanes' models with the wing spans up to 2.0 m above a free water surface as well as the tests of separate airfoils and hydrofoils at Reynolds numbers $R = 10^6$. The tests of airfoils above the calm surface of water made possible to receive the results with sufficiently pinpoint accuracy. But on testing airfoils above a choppy surface of

water the accuracy of the results obtained was less accurate. This was caused by the following factors: high speeds of towing of comparatively massive models; small absolute values of aerodynamic forces to be measured; relatively low natural frequency of the measuring installation. In order to overcome these difficulties and to increase the accuracy of the measurements, the hydrodynamic method for the research into aerodynamics' problems was applied. This method was substantiated and tested in TsAGI [11, 5]. It amounts to the fact that a wing in the experiment was moving in a water medium instead of air. In so doing, a liquid flat or wavy screen was replaced with a solid flat or wavy screen. Changing from the air medium to the water medium is quite possible as, under conditions of the given experiment, the compressibility effects can be disregarded. Such replacement is expedient as it allows: to obtain relatively high forces to be subjected to a measurement; to attain fairly big Reynolds numbers (up to $2 \cdot 10^6$) at relatively low speeds of towing (up to 5-6 m/sec). In this particular case, the replacement of a liquid screen with the solid one is possible because the tests of wings were carried on at high Froude numbers $Fz = 4$. As this takes place, the disturbances of flow, caused by a wing movement, reach the screen surface at a sufficiently great distance beyond the wing and do not affect the results of the experiment. The error out of such replacement does not exceed 1% [12]. It should also be pointed out that on replacing of a real moving wavy surface with a stationary wavy screen, the speeds of air, caused by the movement of a water surface, are not taken into consideration in the experiment. These speeds can be determined from the following formula [13]

$$v = A \cdot \sqrt{\frac{2 \cdot \pi \cdot g}{\lambda_b}} e^{-2\pi \frac{z}{\lambda_b}} \cdot \cos 2\pi \left(\frac{x - x_0}{\lambda_b} \right) \quad (1)$$

where A - wave amplitude;

λ_b - wave length;

x and z - longitudinal and vertical coordinates. However, compared to the velocity of a wing movement, these velocities, in many cases, amount to the value (1-2 %) and they can be ignored. The inherent velocity of a real wave movement at its replacement in the experiment with the solid wavy screen can be considered in the following way (discussed the

case, when velocities of a wing movement and a wave coincide by a direction or are directly opposite).

Apparent frequency of the wing contact with a wave is equal to:

$$\sigma = \sigma_0 \pm \sigma_1 = \frac{2\pi}{\lambda_b} \cdot v_0 \pm \frac{2\pi}{\lambda_b} c = \frac{2\pi}{\lambda_b} \cdot (v_0 \pm c) \quad (2)$$

where: σ_0 - frequency of the wing contact with a stationary wave of the screen;

σ_1 - wave frequency;

c - wave speed.

Strouhal number, which characterizes the process considered will have the following form:

$$Sh = \frac{\sigma \cdot b}{v_0} = \frac{2\pi \cdot b}{\lambda_b} \cdot \frac{(v_0 \pm c)}{v_0} = P \cdot \frac{(v_0 \pm c)}{v_0} \quad (3)$$

$$P = \frac{2\pi \cdot b}{\lambda_b} \quad (4)$$

where: b - wing chord;

P - Strouhal number, which characterizes the wing movement with respect to the stationary wavy screen.

Thus, in the experiment, the results have been obtained, which are characterized by Strouhal number (4), which is a special case of Strouhal number (3) at $c=0$.

To correct for the mobility of the real wavy surface, Strouhal number P should be supplemented with the factor:

$$(v_0 \pm c) / v_0$$

At the high speeds of a wing movement, when $v_0 \gg c$ it can be accepted that $Sh=P$.

With due regard for the above-mentioned, the underwater solid screen was built at the bottom of hydrodynamical channel. The screen consisted of separate sections of a flat and wavy form. The wavy sections were composed of separate groups of the sinusoidal waves of various length and height. Waves crests of the screen were located perpendicularly to the channel's axis and were on the same horizontal level. Above the channel, it was moving a towing carriage equipped with a vertical hydrodynamical blade of a variable height. At an underside of the blade, it was placed a strain-measuring dynamometer to which the tested wing was attached. Screen and the wing

were positioned in the channel at a sufficiently high depth so that the influence of a free water surface was eliminated. All tested wings had a rectangular form in plan and the same profile "TsAGI SR-16-6M" with a thickness ratio 6 % and the chord $b=160-250$ mm. Wings of various aspect ratios $\lambda = l/b$ from $\lambda=0.5$ to $\lambda=5.0$ were tested, where l - wing span. The length of flat sections of the screen was $24 \cdot b$. Waves' length of the wavy screen varied in the range from $\lambda_b=20 \cdot b$ up to $\lambda_b=b$. Waves' height of the screen at different wavy sections ranged from $H_b=\lambda_b/20$ to $H_b=\lambda_b$. The overall length of an underwater screen was equal to 70.0 m. On a wing passing above the wavy screen, the following range of Strouhal numbers was covered:

$$P = \frac{2\pi \cdot b}{\lambda_b} = 0,201 \div 6,28$$

General scheme of the experimental installation is presented in Fig.1.

All the results presented below pertaining to the movement of a wing above the flat screen had been produced in accordance with "A" and "B" schemes, which are given in this Figure. Results on a wing movement above the wavy screen were obtained according to "B" scheme. On tests, it was measured the instantaneous values of a lift, drag and pitching moment of a wing relative to its leading edge. The velocity of a wing's movement was also determined and a wing's position relative to the screen was noted at every given moment of time.

The results were presented in the form of non-dimensional coefficients of a lift, drag, and pitching moment

$$C_y = \frac{2Y}{\rho v_0^2 \cdot S}; C_x = \frac{2X}{\rho v_0^2 \cdot S}; C_{mz} = \frac{2M_z}{\rho v_0^2 \cdot S \cdot b}; \quad (5)$$

where: S - wing area.

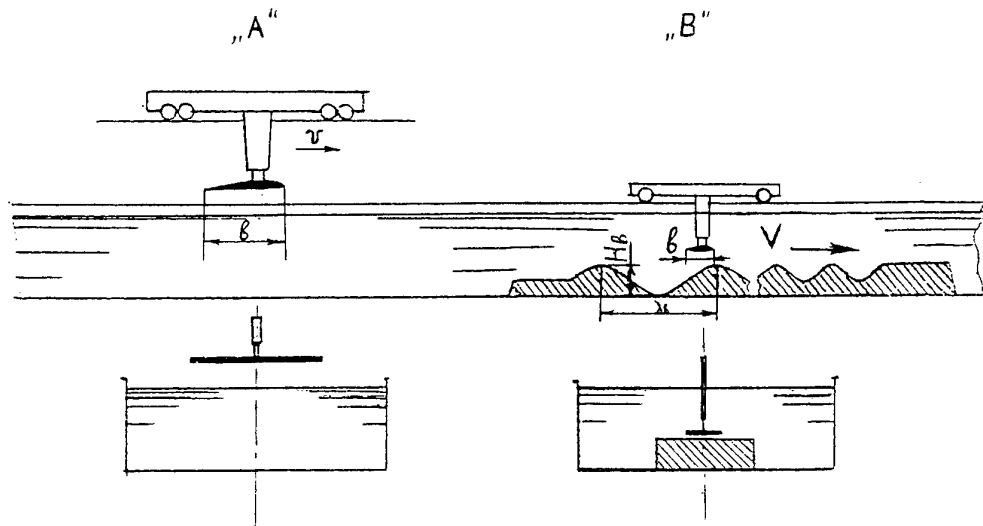


Fig.1

3. TESTS OF WINGS ABOVE THE FLAT SCREEN.

Results pertaining to the movement of a wing above the flat screen are illustrated by the following data given below.

Dependence of a lift coefficient C_y upon an angle of attack θ for the wing with aspect ratio $\lambda=2$ is shown in Fig.2.

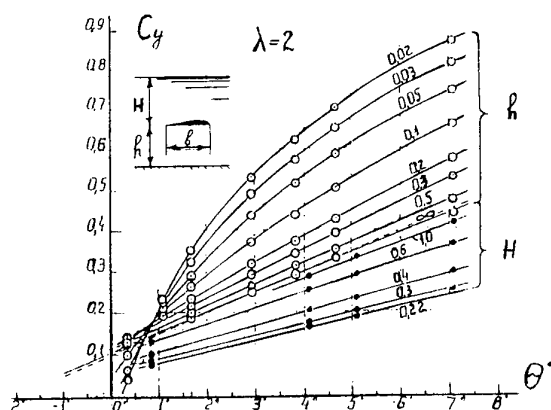


Fig.2

This dependence is given for various distances from the rear edge of a wing to the

flat screen "h" and also to a free surface of liquid H . As seen from the graph, the lift force of a wing increases on approaching to the screen from above (the case of wing movement above the screen) and decreases on approaching of a wing to a free surface of liquid from below (the case of hydrofoil movement).

At small angles of attack ($\theta < 1^\circ$) and at little distances to the screen ($h < 0.2$) there comes a phenomenon of negative influence of the screen upon the lift force of a wing. In case of a wing movement under a free surface of liquid at $H < 0.2$, the partial uncovering of an upper surface of wing is observed. On further " H " reduction there starts the transition of a wing movement to a gliding regime. As this takes place, C_y of a wing tends to the half of its value on infinity.

Dependence of the drag coefficient of a wing C_x upon an angle of attack θ for the various distances of " h " and " H " is presented in Fig.3. Here it is important the fact that screen influence on a wing drag is different at little and high angles of attack. At $\theta < 3^\circ$, the proximity of the screen somewhat reduces a wing drag. At $\theta > 3^\circ$, a wing drag increases on approaching to the screen. On wing's approaching to a free surface of liquid its drag decreases in the whole range of studied angles of attack. This result has been obtained at Froude numbers $F_r = 3.8$.

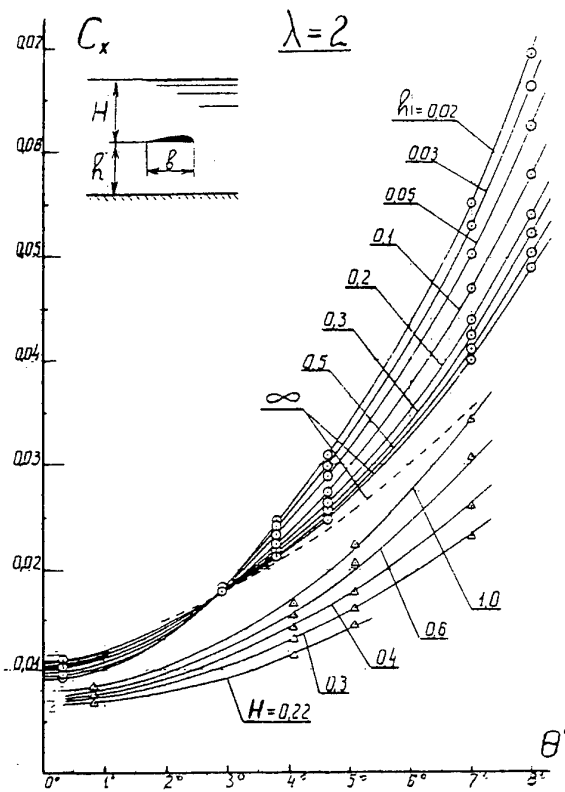


Fig.3

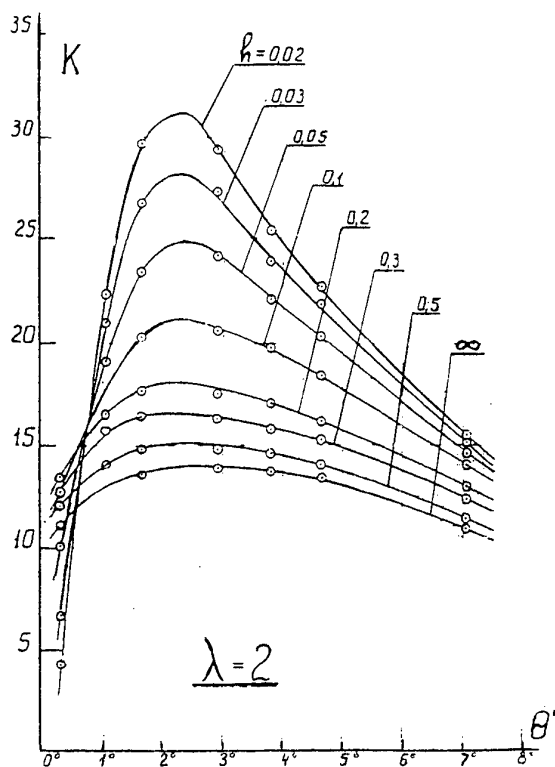


Fig.4

Fig.4 shows the dependence of the lift/drag ratio of a wing "K" on the angle of attack " θ " for various distances "h".

$$K = \frac{C_y}{C_x} \quad (6)$$

This dependence has a clearly defined maximum in the area of angles of attack $\theta = 2.0^\circ - 2.5^\circ$. At such angles of attack and at low "h" values, the hydrodynamical lift/drag ratio of a wing can be doubled in comparison with a wing movement far away from the screen. At the angles of attack equal to $\theta < 2^\circ$, a sharp decrease in the value of "K" is observed and at low values of "h" it can attain zero and even negative values. At the angles of attack equal to $\theta > 2.5^\circ$, the value "K" smoothly diminishes with the growth of an angle of attack.

Figure 5 shows the dependence of a coefficient of wing's centre of pressure upon the distance "h" for various angles of attack θ .

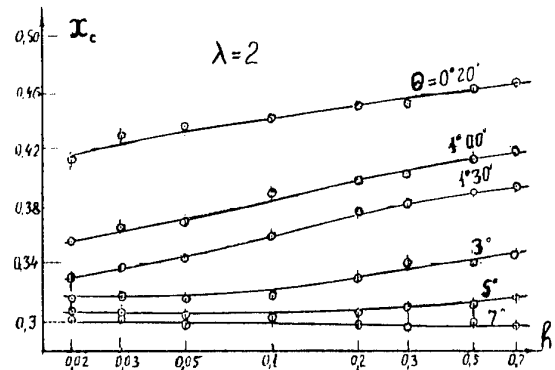


Fig. 5

$$x_c = \frac{C_{mz}}{C_y} \quad (7)$$

Here x_c - dimensionless coordinate of a wing's centre of pressure reckoned from the leading edge of a wing. At high angles of attack ($\theta > 3^\circ$), the position of a centre of pressure has little dependence upon "h". At minor angles of attack, the centre of pressure moves to the leading edge of a wing, when a wing is approaching to the screen. About the

influence of the wing aspect ratio on the lift one can judge from Fig.6.

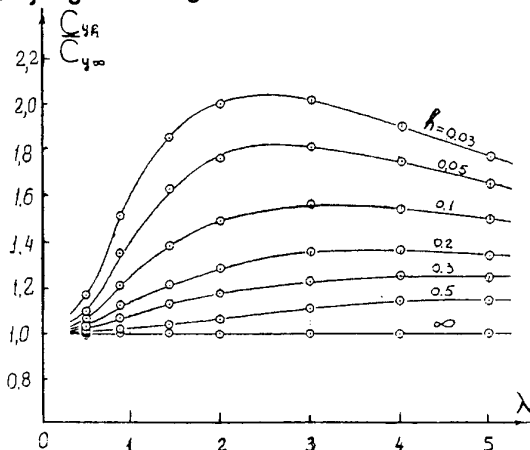


Fig.6

In this Figure, the test results of seven wings with different aspect ratios from $\lambda=0.5$ to $\lambda=5.0$ are presented. In the graph, it is given the ratio of a coefficient of wing lift near the screen " C_{y_h} " to its value in the infinity " C_{y_∞} " depending on the wing aspect ratio " λ " for different values of " h ". It is evident from this graph, that the most growth of the wing lift has been attained at the wing aspect ratios from $\lambda=2$ to $\lambda=3$.

Therefore, the most optimal, from the viewpoint of a growth of the lift force near the screen, is a wing with the aspect ratio in the range of $\lambda=2\div 3$.

Figure 7 shows the ratio of maximum lift/drag ratio of a wing near the screen " K_{maxh} " to its value in the infinity " $K_{max\infty}$ " depending on the wing aspect ratio " λ " for different values of " h ".

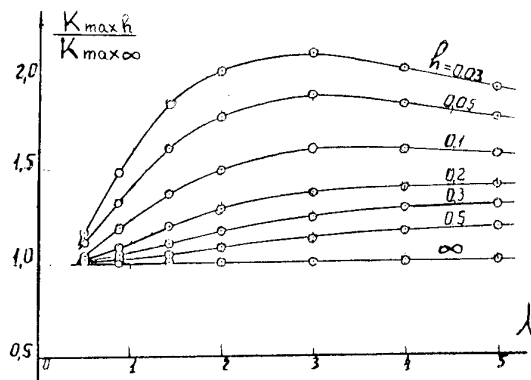


Fig.7

It is clear from this graph that optimal, from the standpoint of the maximum lift/drag ratio of a wing near the screen, is a wing with aspect ratio of $\lambda=3$.

Comparison of the test results of two similar wings: airfoil and hydrofoil is presented in Figure 8.

The airfoil was tested near undisturbed surface of water (scheme "A" in Fig.1).

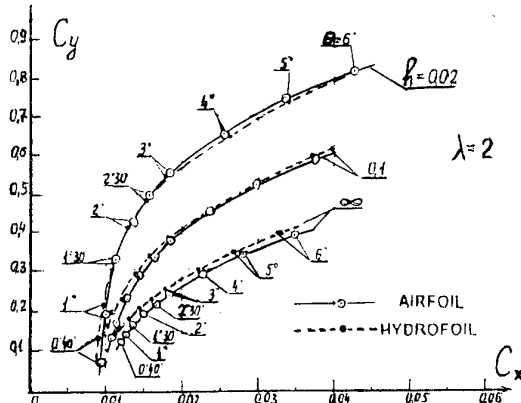


Fig.8

The hydrofoil was tested near the solid screen (scheme "B" in Fig.1). The airfoil had the absolute dimensions 1500 X 750 mm and was tested at the speed 18 m/sec, and the hydrofoil - 500 X 250 mm and 6 m/sec, respectively. Wing polars $C_y=f(C_x)$ of these wings are given for different distances " h ". The consideration of these dependences shows a complete qualitative agreement between the results of both air and underwater tests. The minor quantitative discrepancies are within the accuracy of measurements. These results indicate a practical equivalence of two discussed methods of wing tests near the screen.

4. TESTS OF WINGS ABOVE THE WAVY SCREEN.

Let us pass to the consideration of test results of a wing moving above the wavy screen (scheme "B" in Fig.1). Figure 9 shows the patterns of oscillograms with the continuous recording of instantaneous values of a lift force, drag, and pitching moment of a wing with the aspect ratio $\lambda=4$, when it moves above

the screen's sinusoidal waves of different length from $\lambda_b=5.0$ m up to $\lambda_b=0.25$ m.

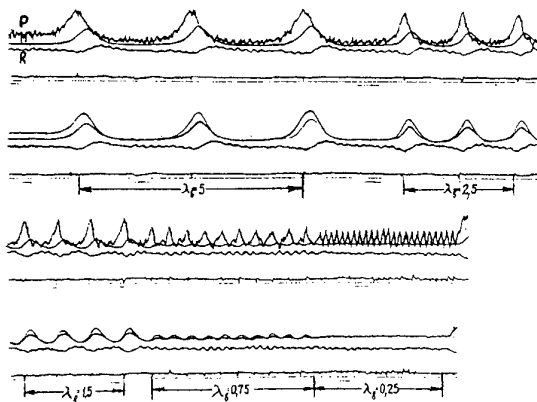


Fig.9

The movement occurred at a distance $h_i=0.03$, which was measured from the rear edge of a wing to the level of waves crests.

Figure 10 illustrates the curves of a variation of instantaneous values of coefficients of the lift force $C_{yh}/C_{y\infty}$, drag $C_{xh1}/C_{x\infty}$, and centre of pressure $x_{ch1}/x_{c\infty}$ of a wing with the aspect ratio $\lambda=2$, when a wing moves at varying distances from wave crests of the screen h_i and at Strouhal number (4) equal to $P=0.314$.

Along the axis of abscissae, the profile of a wavy screen is plotted (vertical scale is increased). Analysis of given curves demonstrates that on moving above the sinusoidal screen, the values C_y , C_x , and x_c do not vary in compliance with the sinusoidal law.

The maxima of curves C_y and C_x and the minima of curves x_c take place earlier than the leading edge of a wing reaches a wave crest. Curves are asymmetrical relative to the vertical lines passing through the extremal dots of these curves. In so doing the left branches of curves, which correspond to approaching of a wing to a wing crest, are more complete.

All curves of instantaneous values of coefficients of a lift force obtained during the experiment, were subjected to the harmonic analysis.

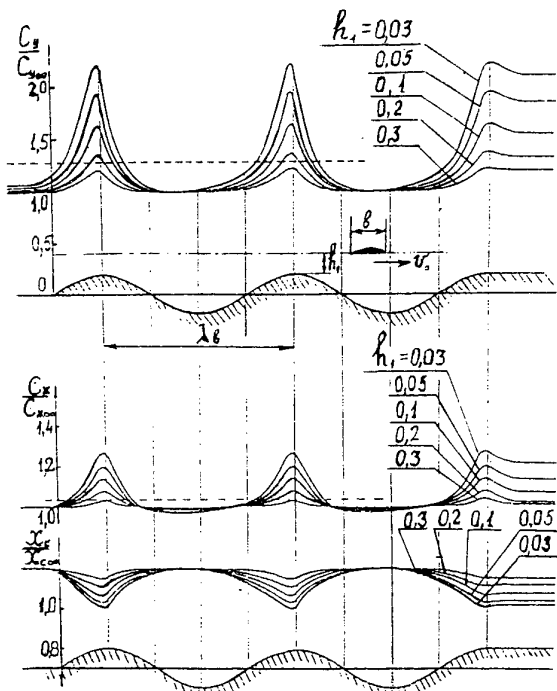


Fig.10

It had been derived the mean for the period values of the lift force coefficient and the coefficients at the first six harmonics of Fourier series.

$$C_y(\varphi) \approx a_0/2 + \sum_{k=1}^6 a_k \cdot \cos k\varphi + \sum_{k=1}^6 b_k \cdot \sin k\varphi \quad (8)$$

where: φ - phase angle of the lift force curve;
 $a_0/2$ - mean for the period value of the lift force coefficient;
 a_k and b_k - coefficients of Fourier series.

The set of these data represents the material by which using the formula (8) it can be reproduced the curve of instantaneous values of the lift force coefficient for any values of wing parameters and the wavy screen from the range considered in this paper.

Below, based on these data, the influence of some parameters of a wing and the wavy screen on the curve of instantaneous values of a lift force coefficient is discussed. The following characteristics of this curve will be considered:

- instantaneous values of a lift force coefficient above a wave crest C_{y1} ;
- the same above a trough of wave C_{y3} ;
- mean for the period value of lift force coefficient C_{y22} .

These values of a lift force coefficient will be compared with those its values, which it assumes:

- above the flat screen at the level of waves crests C_{y01} ;
- above the flat screen at the level of a wave center line C_{y02} .

With the same indices ($i=1,01,02, 3$) we shall mark the corresponding distances (dimensionless) from a wing's rear edge to the flat or wavy screen:

- to the crest and to the trough of wave h_1 and h_3 ;
- to the flat screen at the level of crests h_{01} ;
- to the flat screen at the level of a wave center line h_{02} .

Figure 11 gives characteristics of the lift force curve C_{y1} , C_{y3} and C_{y22} depending on the angle of attack of a wing. Difference of ordinates ($C_{y1} - C_{y3}$) determines the amplitude of oscillation of a wing lift above the wavy screen. It is seen that with the increase of an angle of attack the amplitude is growing and it becomes commensurable with a wing lift above the flat screen at the level of a wave center line (curve C_{y02}).

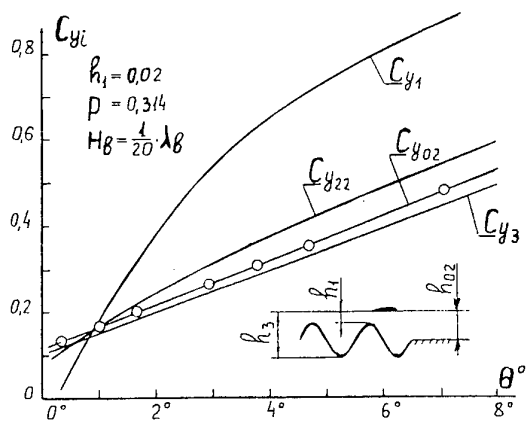


Fig 11

This circumstance gives the idea of a scale of the wavy screen influence on the ekranoplane's dynamics. At small angles of attack ($\theta \leq 1^\circ$), the difference of ordinates ($C_{y22} - C_{y02}$) becomes negative. In so doing, a wing loses its lift force and this could result in an impact of a wing upon the wave crest. Excess of the curve C_{y22} over the curve C_{y02} reflects one important fact that mean for the period value of the lift force is higher than on a wing's movement over the flat screen at the level of a wavy center line. This condition also has a considerable effect on the ekranoplane's dynamics.

Figure 12 presents characteristics of the lift curve C_{y1} , C_{y3} , and C_{y22} depending on the distance of a wing to the screen h_1 .

It is evident that the influence of a screen is practically not found at $h_1 > 0.7$. It is also apparent that at $h_1 < 0.7$ the amplitude of oscillation of the lift force above the wavy screen increases on approaching of a wing to waves crests. This increase takes place mainly due to the rise of the lift force above a wave crest (C_{y1}).

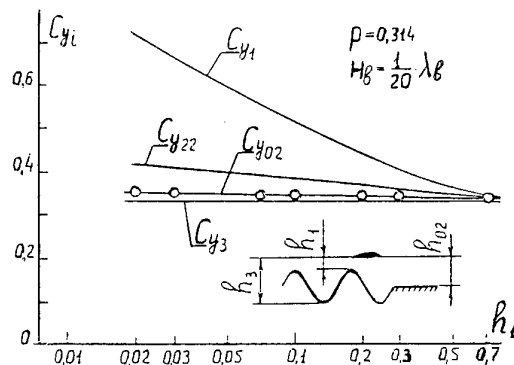


Fig 12

The lift force above a wave trough (C_{y3}) has only little dependence upon a wing's distance to the screen. Increment of the wing lift above the wavy screen (in comparison with the flat screen at the level of a wave center line) is expressed by the difference of ordinates ($C_{y22} - C_{y02}$). It is seen that this increment rises on a wing's approaching to waves crests. At $h_1 = 0.02$, this increment amounts to a value in the region of 20 %.

Figure 13 demonstrates characteristics of the lift curve C_{y1} , C_{y3} and C_{y22} depending on the wing aspect ratio. It is evident that with the increase of a wing aspect ratio, the amplitude of the lift curve is growing and it attains a maximum for a wing with the aspect ratio $\lambda=3$.

The amplitude decreases on further growth of the wing aspect ratio. So far as the increment of a wing lift above the wavy screen ($C_{y22} - C_{y01}$), it is of a little dependence from the wing aspect ratio.

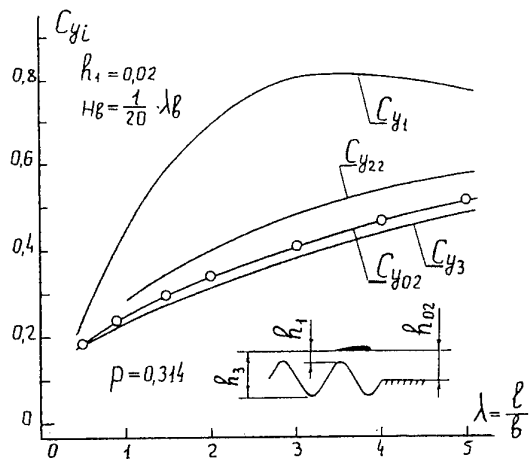


Fig 13

Figure 14 illustrates the influence of a wave length of the screen λ_b on the lift of a wing.

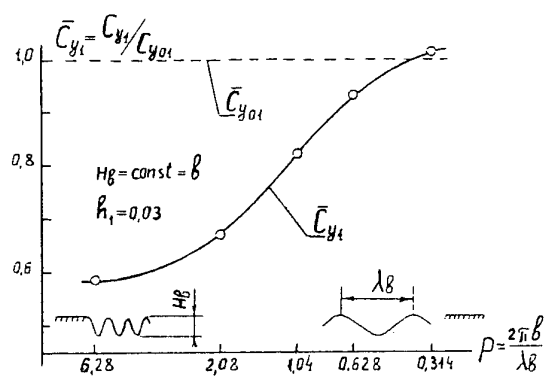


Fig 14

In this graph, Strouhal numbers P , which are a function of a wave length of the screen, are plotted on the abscissas. The ratio of a wing lift coefficient above the waves crests C_{y1} to its value above the flat screen at the level of waves crests C_{y01} is plotted as ordinates. In this case, it has been selected and plotted only those values C_{y1} which correspond to waves of different length λ_b , but of the same height $H_b = b$. This gives the opportunity to follow the influence of the screen's wave length in the pure state. It is obvious, that above the long waves of the screen ($P=0.314$), C_{y1} differs too little from C_{y01} . But with the reduction of a wave length ($P \rightarrow 6.28$), the wing lift above wave crests C_{y1} considerably decreases.

The influence of a wave height H_b upon the wing lift is shown in Figure 15.

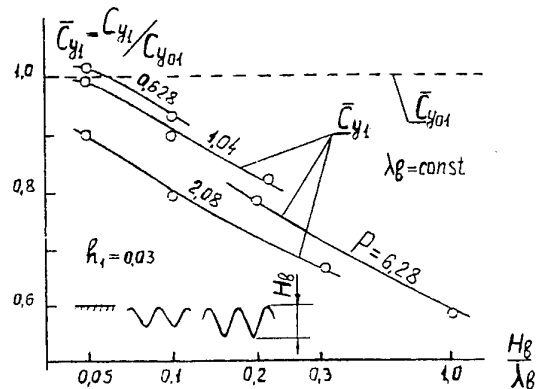


Fig 15

Here, the scale of ratios of waves' height H_b to a wave's length λ_b is plotted on the abscissas. Extreme left value on this scale corresponds to the standard wave approved for shipbuilding calculations, for which $H_b/\lambda_b = 1/20$. Extreme right value conforms to the case, when a wave height is equal to a wave length. On the graph, lines of equal values of Strouhal numbers P are plotted. This is analogous to equal values of a wave length of the screen. It is evident from the graph, that at the fixed value of Strouhal number, the wing lift above waves crests drops when a wave height of the screen goes up.

Figures 16, 17, and 18 illustrate characteristics of the lift curve C_{y1} , C_{y3} and C_{y22} depending on Strouhal number P .

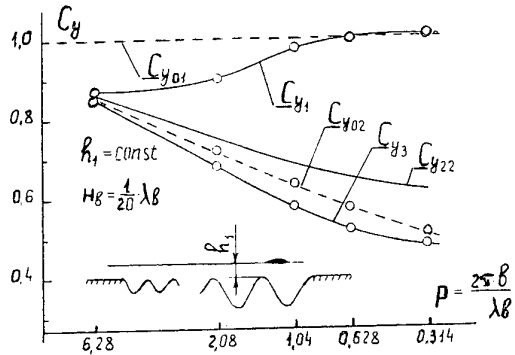


Fig 16

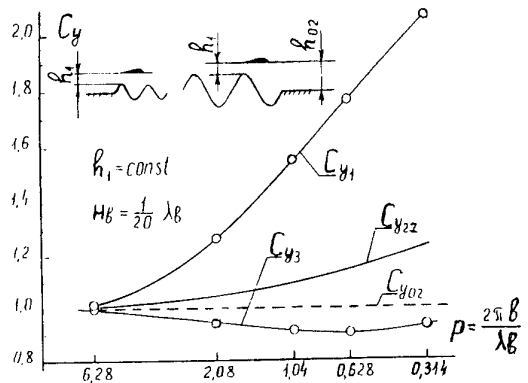


Fig.17

In all three cases, it is considered the movement of a wing above the wavy screen, which consists of standard waves of a different length. Common to these Figures is the fact that the amplitude of oscillation of the lift curve (C_{y1} — C_{y3}) increases on falling of Strouhal number. The increment of a wing lift above the wavy screen (C_{y22} — C_{y02}) also rises as Strouhal number goes down that is evident from Figures 16 and 17.

The difference of these three mentioned Figures lies in the following. In Figure 16, characteristics C_{y1} , C_{y3} and C_{y22} are compared with the wing lift above the flat screen at the level of waves crests C_{y01} . The case is considered, when a wing moves at a constant height above waves crests h_1 . It is obvious, that all these characteristics are less than C_{y01} .

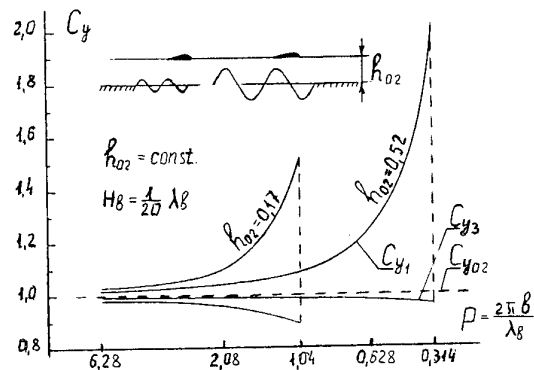


Fig 18

The exception makes the wing lift above waves crests. The wing lift, in the range of Strouhal numbers of $P=0.628-0.314$, can exceed to some extent the lift above the flat screen at the level of waves crests.

In Figure 17, characteristics C_{y1} , C_{y3} , and C_{y22} are compared with the wing lift above the flat screen at the level of a wave's center line of the screen. Here, we also discuss the case, when a wing moves at a steady height above waves crests h_1 . It is seen that C_{y1} and C_{y22} exceed C_{y02} . It is natural that the lift value above waves' trough C_{y3} is less than C_{y02} .

Figure 18 presents the case when a wing, which at first was moving above the flat screen, then starts to move above the wavy screen. In the beginning, small waves start to appear under a wing (big Strouhal numbers) and then the dimensions of waves increase (the movement to the side of small Strouhal numbers). In so doing, the distance from a wing to the flat screen and to a center line of the wavy screen remains constant all the time. Such movement is possible until a wing starts to touch waves crests. For example, at $h_{02}=0.5$ such moment will occur at $P=0.314$ and at $h_{02}=0.15$ this moment will take place at $P=1.04$. In the Figure, it is shown for these two cases, how rises the amplitude of oscillation of the wing lift (C_{y1} — C_{y3}) with the increase of the screen's waves dimensions (while Strouhal numbers going down). One can see that in the first case, the amplitude of oscillation of the wing lift in a limit attains the value approximately two times greater than the wing lift above the flat screen at the level of

wave's center line. In the second case this increase amounts to the value in the order of 60 %. The results, presented in this Figure, give once again an idea of the scale that the wavy screen influences on the ekranoplane's dynamics.

The foregoing results pertaining to the movement of a wing above wavy screen refer to the case, when a wing is moving perpendicularly to the direction of waves crests. Below, it is also discussed the case of a wing movement above oblique waves, when a wing does not move perpendicularly to the direction of waves crests. Figure 19 shows the experimental installation for the research into the movement of a wing above oblique waves.

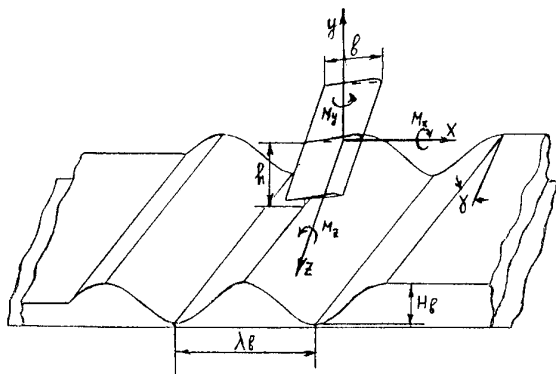


Fig 19

This installation makes possible to change the angle "γ" between the direction of waves crests and the axis "z" in the range of "γ"=0-30°.

It can be noted the following peculiarities of an influence of the angle "γ" upon hydrodynamical characteristics of a wing moving above oblique waves.

As the angle "γ" increases, the symmetry of distribution of the wing lift and the drag along a wing span is disturbed. This initiates the rolling moment M_x and the yawing moment M_y on a wing. These moments change their direction each time when a wing moves above the crest or the trough of a wave. They can exert influence on the rolling and yawing stability of the ekranoplane movement.

Figure 20 illustrates dependence of the coefficient of a wing lift above waves crests C_{y_1}

and the coefficient of a rolling moment C_{mx} upon the deviation angle of waves crests "γ".

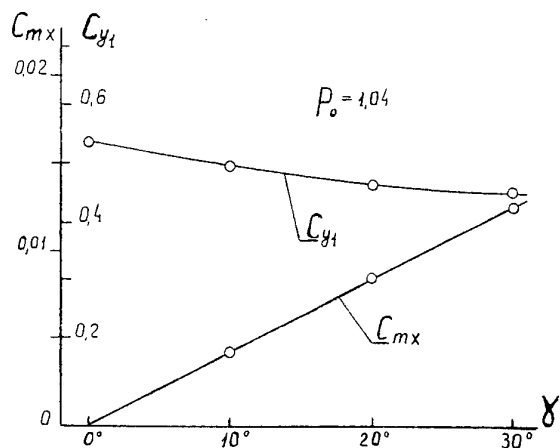


Fig 20

These results are generated for the wing with aspect ratio $\lambda=2$ and Strouhal number $P_0=1.04$.

CONCLUSION

At the Institute of Hydromechanics of the Ukrainian National Academy of Sciences, the special experimental installation has been devised for the research into hydroaerodynamics of ekranoplanes and their wing systems. The portion of results obtained in this installation, which refer to the movement of a wing above the flat and wavy screen has been presented in this paper. Generated hydrodynamical characteristics of a wing can be used on designing of ekranoplanes and on analysing of their movement above a calm and rough surface of a sea.

REFERENCES

1. Belavin N.I. Superlarge wing-in-ground effect vehicles by chief designer R.E.Alexeev. J.Sudostroenie, N 1, 1993, pp.3-7 (in Russian).
2. Belavin N.I. Ekranoplanes. Leningrad. Sudostroenie. 1977, pp. 230 (in Russian).
3. Stephan F.Hooker. A review of current technical knowledge necessary to develop large-scale wing-in-surface effect craft.// Intersociety advanced marine vehicles

- conference.Arlington, VA/
June 5-7, 1989. pp. 367-429.
4. Ollila R.G. Historical Review of WIG Vehicles.J of Hydronautics. 1980, v.14, N 3, pp.65-77.
 5. Grebeshov E.P., et. al. Aerodynamical Characteristics of Wing Profile Near Flat and Wavy Screen.// TsAGI Proceedings, Moscow,1976, Issue 1725, pp.31-58 (in Russian).
 6. Byelinsky V.G., et. al. Maximum and Mean Value of the hydrodynamic Characteristics of a Wing Moving Above an Uneven Surface.// Gidromechanika. N29. 1974. Kyiv. Naukova Dumka. pp.43-45 (in Russian).
 7. Byelinsky V.G., et.al. Effect of the Form of a Non Planar Screen on the Hydrodynamic Characteristics of a Foil Traveling Above it.// Gidromechanika. N31.1975. Kyiv. Naukova Dumka. pp.28-32 (in Russian).
 8. Byelinsky V.G., et.al. Effect of Strouhal Number on Foil Characteristics Near a wavy Screen.// Gidromechanika. N31.1975.Kyiv. Naukova Dumka. pp.32-35. (in Russian).
 9. Byelinsky V.G., Orishychev V.A. On the Flap Efficiency Near Solid Wall. // Gydromechanika. N52. 1985. Kyiv. Naukova Dumka. pp. (in Russian)
 10. Byelinsky V.G. About Movement of a Wing Above Wavy Surface of Water. AGARD Report 827. Workshop on High Speed Body Motion in Water. Kyiv. 1-3 September 1997. pp.17.1-17.9.
 11. Epstein L.A. Hydrodynamical Methods of Problems Investigation In Aerodynamics.// TsAGI Proceedings. Moscow.1980.Issue 2035. 28 p. (in Russian).
 12. Panchenkov A.N. Hydrodynamics of the Underwater Wing. Kyiv. Naukova Dumka. 1965. 552 p. (in Russian).
 13. Voytkunskiy J.I. Theory of Wave and Wave Drag. Leningrad. LKI. 1959. 230 p. (in Russian).

THEORETICAL ANALYSIS OF DYNAMICS OF A WIG VEHICLE IN EXTREME GROUND EFFECT

K.V. Rozdestvensky

Professor

Saint-Peterburg State Marine Technical University
3, Lotsmanskaya, 190008 Saint-Petersburg
Russia

ABSTRACT

The paper discusses asymptotic form of the equations of longitudinal motion of ekranoplan in extreme ground effect, i.e. for very small relative ground clearances h . Derivation of "quartic" and "quintic" characteristic equations of unsteady perturbed motion is presented. One-dimensional unsteady nonlinear theory of a simple flying wing with endplates, moving in close proximity to the ground, is used to determine derivatives of major aerodynamic coefficients with respect to perturbations of height and pitch as well as asymptotic behaviour of these derivatives for vanishing h . Asymptotics of perturbed equations of motion is derived for distances of the order of the chord from the moment of perturbation. It is shown that in very close proximity to the ground parameters of stability and motion of the lifting system depend on ratios of design pitch angle and curvature of the lower side of the wing to relative ground clearance h as well as on a "reduced" density of the vehicle. The analysis also shows that at distances of the order of the chord from the moment of perturbation the vehicle performs corresponding induced motions in height and pitch, its speed remaining almost the same. At distances of the order of chord/ h there takes place variation of speed mostly driven by height and pitch perturbations. At distances of the order of chord/ h^2 variation of speed of the craft is due to speed perturbation proper.

1. INTRODUCTION

Analysis of dynamics of wing-in-ground effect vehicles has always been practically important. First of all, due to necessity to secure stability of motion, and, secondly, to provide data for assessment of controllability and ride comfort of the craft under

development. Analysis of linearized equations of motion of wing-in-ground effect vehicles has been carried out by Irodov [1] and further on investigated by Kumar [2] and Staufenbiel [3,4]. A thorough study of dynamics of WIGs, incorporating stability analysis with special reference to design, was carried out by Zhukov [5].

Irodov considered linearized equations of perturbed longitudinal motion in terms of variation of angle of attack and ground clearance. Assuming the the speed of the vehicle remains constant, he derived a characteristic polynomial equation of the fourth order. Applying Gurvitz-Ruth criteria of stability he came to the conclusion that aperiodic static stability is ensured when aerodynamic center in height is located upstream of that in angle of attack, which was very important practical result. According to Irodov (1970), to secure oscillatory stability of the vehicle one has to provide an appropriate location of the center of gravity. Irodov also stated that the account of variation of cruise speed practically does not modify the abovementioned conditions of static aperiodic stability.

Kumar studied dynamics of a wing-in-ground effect vehicle for both longitudinal and lateral motion cases, incorporating effects connected with perturbation of speed of forward motion. His stability analysis was based on a quintic characteristic equation. Staufenbiel also employed quintic equation and discussed nonlinear effects.

In this paper an attempt is made to derive asymptotic form of the equations of motion of a wing-in-ground effect vehicle in extreme ground effect, i.e. for vanishing relative clearances between the lifting surface and the ground. First of all, a derivation is given in terms of perturbations of relative ground clearance h and pitch angle θ of the linearized equa-

tions of motion without (*à la* Irodov) and with (*à la* Zhukov) account of perturbation of forward speed. Then orders of magnitude of the terms are made and assumed on the basis of a simplified nonlinear unsteady theory of extreme ground effect [6]. Eventually, an asymptotic form of the equations of motion is derived for $h \rightarrow 0$ and small periods of time from the moment of perturbation. The cases of larger time scales are discussed.

2. LINEAR EQUATIONS OF DYNAMICS

Here, the linearized versions of equations of longitudinal motion will be deduced, corresponding to what is known as "quartic" and "quintic" description of dynamics of wing-in-ground effect vehicles. In other words, linearized equations of motion and corresponding characteristic equations are written with and without account of perturbation of forward speed. Instead of representative kinematic parameters α (angle of attack) and h (relative ground clearance) utilized by Kumar and Staufenbiel, parameters θ (pitch angle) and h (relative ground clearance) will be employed. In what follows all unsteady aerodynamic derivatives will be incorporated.

The pair of parameters θ, h is more practical in aerodynamics of ground effect vehicles than that of α, h . Use of θ, h was first proposed by Treshkov (1970) and since had been adopted in most of the Russian developments on WIGs.

2.1. "Quartic" equations

Consider first the case when the cruise speed remains constant in the otherwise perturbed motion. In what follows all quantities and functions will be rendered nondimensional with respect to cruise speed U_o and root chord C_o of the main wing of the vehicle. In this case the equations of perturbed uncontrolled motion of the WIG can be written as

$$\mu \frac{d^2\tilde{h}}{dt^2} = \tilde{c}_y \quad (1)$$

$$\mu i_z \frac{d^2\tilde{\theta}}{dt^2} = \tilde{m}_z \quad (2)$$

where μ is relative density of the vehicle defined by the formula

$$\mu = \frac{2M}{\rho S C_o} \quad (3)$$

In (27), (28) \tilde{c}_y, \tilde{m}_z are perturbed lift and moment coefficients, $\tilde{h}, \tilde{\theta}$ represent perturbed relative ground

clearance and pitch angle, M is the vehicle's mass in cruise, S is a wing's reference area, ρ is specific density of air and i_z is a coefficient of the longitudinal moment of inertia of mass, determined by means of a relationship

$$i_z = \frac{I_z}{M C_o^2} \quad (4)$$

where I_z is the longitudinal moment of inertia of mass with respect to the center of gravity. To track the relationship between dynamic stability of the vehicle with its cruise speed it is sometimes convenient to use the following obvious equation

$$\mu = Fr_c^2 c_{y_o}, \quad Fr_c = \frac{U_o}{\sqrt{g C_o}} \quad (5)$$

where Fr_c and c_{y_o} are correspondingly the cruise Froude number and cruise lift coefficient. With account of (1), (2) and (5) the (two) equations of motion with respect to perturbations of pitch and ground clearance can be written in an alternative form as

$$Fr_c^2 c_{y_o} \frac{d^2\tilde{h}}{dt^2} = \tilde{c}_y \quad (6)$$

$$Fr_c^2 c_{y_o} i_z \frac{d^2\tilde{\theta}}{dt^2} = \tilde{m}_z \quad (7)$$

Using representation of perturbed lift and moment coefficients in terms of derivatives with respect to principal kinematic parameters θ, h one can write

$$\tilde{c}_y = c_y^\theta \tilde{\theta} + c_y^h \tilde{h} + c_y^{\dot{\theta}} \dot{\tilde{\theta}} + c_y^{\dot{h}} \dot{\tilde{h}} \quad (8)$$

$$\tilde{m}_z = m_z^\theta \tilde{\theta} + m_z^h \tilde{h} + m_z^{\dot{\theta}} \dot{\tilde{\theta}} + m_z^{\dot{h}} \dot{\tilde{h}} \quad (9)$$

Now one can re-write equations (8), (9) in the following form

$$\mu \frac{d^2\tilde{h}}{dt^2} - c_y^h \frac{d\tilde{h}}{dt} - c_y^{\dot{h}} \tilde{h} = c_y^{\dot{\theta}} \frac{d\tilde{\theta}}{dt} + c_y^\theta \tilde{\theta} \quad (10)$$

$$\mu i_z \frac{d^2\tilde{\theta}}{dt^2} - m_z^{\dot{\theta}} \frac{d\tilde{\theta}}{dt} - m_z^\theta \tilde{\theta} = m_z^{\dot{h}} \frac{d\tilde{h}}{dt} + m_z^h \tilde{h} \quad (11)$$

Excluding \tilde{h} or $\tilde{\theta}$ from equation set (10),(11), one comes to the following fourth order (quartic) characteristic equation of the system

$$D^4 + A_1 D^3 + A_2 D^2 + A_3 D + A_4 = 0 \quad (12)$$

where the coefficients $A_i (i = 1, 2, 3, 4)$ are

$$A_1 = -\frac{1}{\mu i_z} (m_z^{\dot{\theta}} + i_z c_y^{\dot{h}}), \quad (13)$$

$$A_2 = -\frac{1}{\mu^2 i_z} [c_y^{\dot{\theta}} m_z^{\dot{h}} - c_y^h m_z^{\dot{\theta}} + \mu (m_z^\theta + i_z c_y^h)], \quad (14)$$

$$A_3 = \frac{1}{\mu^2 i_z} (m_z^\theta c_y^h + m_z^\theta c_y^h - c_y^\theta m_z^h - c_y^\theta m_z^h), \quad (15)$$

$$A_4 = \frac{1}{\mu^2 i_z} (m_z^\theta c_y^h - c_y^\theta m_z^h) \quad (16)$$

The last coefficient can be re-written to be expressed in terms of abscissas of aerodynamic centers in height x^h and in pitch θ

$$A_4 = -\frac{c_y^h c_y^\theta}{\mu^2 i_z} (x^h - x^\theta) \quad (17)$$

The stability of motion in the case of the fourth order equation will be ensured if

$$A_1, A_2, A_3, A_4 > 0$$

and

$$A_2 A_3 - A_1^2 A_4 - A_3^2 > 0 \quad (18)$$

It can be shown from consideration of the formulae (13)-(17) that conditions $A_1 > 0$, $A_2 > 0$ and $A_3 > 0$ always hold. Hence the requirements of stability in proximity of the ground can be reduced to two inequalities $A_4 > 0$ and $A_1 A_2 A_3 - A_1^2 A_4 - A_3^2 > 0$. Satisfaction of the former condition provides an aperiodic stability of the craft, i.e. absence of positive real roots of characteristic equation). Meeting the latter requirement ensures oscillatory stability, i.e. absence of positive real parts of complex roots of characteristic equation). It follows immediately from these considerations and observation of (17) that to secure aperiodic stability of the wing-in-ground effect vehicle one should select such an aerodynamic configuration of the craft which results in location of the center in height upstream of the center in pitch, i.e. $x^h - x^\theta > 0$ (note that here x axis is directed upstream).

2.2. "Quintic" equations

If one accounts for the perturbation of speed of forward motion, the corresponding equations can be written as

$$\mu \frac{dU'}{dt} = (c_t^{\bar{U}} - 2c_{x_0}) U' - c_x^\theta \tilde{\theta} - c_x^h \tilde{h} - c_x^\theta \dot{\tilde{\theta}} - c_x^h \dot{\tilde{h}} \quad (19)$$

$$\mu \frac{d^2 \tilde{h}}{dt^2} = 2U' c_{y_c} + c_y^\theta \theta + c_y^\theta \dot{\tilde{\theta}} + c_y^h \tilde{h} + c_y^h \dot{\tilde{h}} \quad (20)$$

$$\mu i_z \frac{d^2 \tilde{\theta}}{dt^2} = y_t (2c_{x_0} - c_t^{\bar{U}}) U' + m_z^\theta \tilde{\theta} +$$

$$m_z^h \tilde{h} + m_z^h \dot{\tilde{h}} + m_z^\theta \dot{\tilde{\theta}} \quad (21)$$

In the above equations U' represents a relative perturbation of cruise speed, $c_t^{\bar{U}}$ is a derivative of the thrust coefficient with respect to relative speed of forward motion, c_x is a static drag coefficient¹, y_t is vertical distance of the thrust line from the vehicle's center of gravity. As earlier, all quantities are rendered nondimensional with use of cruise speed U_0 and root chord C_0 . Drag coefficient is related to instantaneous cruise speed $U_0(1+U')$. Excluding two of the three unknown parameters one comes to the following fifth order (quintic) characteristic equation of the perturbed system

$$\begin{bmatrix} \mu D - (c_t^{\bar{U}} - 2c_{x_0}) & c_x^h D + c_x^h \\ -2c_{y_c} & (\mu D^2 - c_y^h D - c_y^h) \\ -y_t (2c_{x_0} - c_t^{\bar{U}}) & -(m_z^h D + m_z^h) \\ c_x^\theta D + c_x^\theta \\ -(c_y^\theta D + c_y^\theta) \\ (\mu i_z D^2 - m_z^\theta D - m_z^\theta) \end{bmatrix} = 0 \quad (22)$$

Write the quintic characteristic equation (22) as

$$D^5 + B_1 D^4 + B_2 D^3 + B_3 D^2 + B_4 D + B_5 = 0 \quad (23)$$

Corresponding necessary and sufficient requirements for stability of the system will be

$$B_i > 0 \quad (i = 1, \dots, 5), \quad B_1 B_2 - B_3 > 0; \quad (24)$$

$$(B_1 B_2 - B_3)(B_3 B_4 - B_2 B_5) - (B_1 B_4 - B_5)^2 > 0. \quad (25)$$

Coefficients B_i can be found in the Appendix.

3. UNSTEADY AERODYNAMICS OF A SIMPLE FLYING WING CONFIGURATION IN EXTREME GROUND EFFECT

In order to produce a qualitative description of dynamics for the case when relative ground clearance becomes very small one can employ a simplified mathematical model of the lifting flow in extreme ground effect. In what follows an unsteady nonlinear one-dimensional formulation of [6] will be used to derive that for unsteady perturbed flow, linearized with respect to nonlinear steady-state flow.

¹Incorporating both viscous and induced drag

3.1. One-dimensional nonlinear unsteady formulation

In [6] there was derived a one-dimensional equation of nonlinear, unsteady aerodynamics of a simple flying wing configuration in form of a rectangular wing with thin endplates. Essentially, a possibility to reduce initially three-dimensional problem to that in one-dimension is a result of two effects. On one hand, when a wing flares very close to an underlying surface, the prevailing contribution to its aerodynamics comes from the *channel flow* underneath. On the other hand, when the gaps under tips of endplates decrease, the sideward leakage from under the wing diminishes. Consequently, the channel flow becomes "almost" one-dimensional. Corresponding nonlinear unsteady flow problem has the form, [6]

$$\frac{\partial}{\partial x} \left[h^*(x, t) \frac{\partial \varphi}{\partial x}(x, t) \right] + \frac{2\delta_{ep}(x, t)}{\lambda} \text{sign } p(x, t) \sqrt{|p(x, t)|} = -\frac{\partial h^*}{\partial t} \quad (26)$$

where $h^*(x, t)$ is an instantaneous distribution of local relative ground clearance, φ is the channel flow velocity potential of relative motion, $\delta_{ep}(x, t)$ is a distribution of gap between the tip of endplate and the ground, λ aspect ratio of the wing, $p(x, t)$ - nondimensional pressure in the channele flow. Note, that both velocity potential and pressure distributions are averaged spanwise. *Signum* function in front of the square root indicates direction of sideward leakage (inward in the case of local suction, outward - in the case of local pressure). Here and further on, all quantities and functions are rendered nondimensional with use of the chord C_o and cruise speed U_o of the wing. Coordinate system is Cartesian one with x -axis directed forward, y -axis directed upward and z -axis directed to the starboard. Abscissas are measured from the trailing edge of the wing. Equation (26) should be solved with two boundary conditions

$$\varphi(1, t) = 0, \quad \text{at the leading edge} \quad (27)$$

$$p(0, t) = 1 - \left(\frac{\partial \varphi}{\partial x} \right)^2 - 2 \frac{\partial \varphi}{\partial t} = 0, \quad (28)$$

at the trailing edge. From physical viewpoint the former condition can be interpreted as that of no vorticity upstream of the leading edge whereas the latter one is similar to Kutta-Zhukovsky condition. In the steady-state case the relationships (26), (27) and (28) yield

$$\frac{d}{dx} \left[h_o(x) \frac{d\varphi_o}{dx}(x) \right] + \frac{2\delta_{ep}(x)}{\lambda} \text{sign } p_o(x) \sqrt{|p_o(x)|} = 0$$

$$\varphi_o(1) = 0, \quad \frac{d\varphi_o}{dx} \Big|_{x=0} = -1.$$

3.2. Perturbed flow analysis

For analysis of linear dynamics of a lifting configuration in ground effect one needs derivatives of aerodynamic coefficients with respect to relative ground clearance h , pitch angle θ and their rates \dot{h} and $\dot{\theta}$. In order to determine these derivatives, consider small unsteady perturbations of a nonlinear steady-state flow. Such an approach enables to retain nonlinear dependence of the derivatives under discussion upon basic steady state parameters, e.g. adjusted pitch angle, cruise relative ground clearance, etc. Represent velocity potential, local ground clearance distribution and gap under the endplates in the following way

$$\varphi(x, t) = \varphi_o(x) + \tilde{\varphi}(x, t),$$

$$h^*(x, t) = h_o(x) + \tilde{h}(x, t)$$

$$\delta_{ep}(x, t) = \delta_{ep}(x) + \tilde{\delta}_{ep}(x, t)$$

Substituting perturbed quantities into (26) and accounting for the description of the steady state flow problem, one comes to the following equations for the perturbed unsteady flow potential

$$\frac{\partial}{\partial x} \left[h_o(x) \frac{\partial \tilde{\varphi}}{\partial x}(x, t) \right] + \frac{\partial}{\partial x} \left[\tilde{h}(x, t) \frac{d\varphi_o}{dx} \right] + \frac{\tilde{h}(x, t)}{\lambda} \text{sign } p_o(x) \sqrt{|p_o(x)|} = -\frac{\partial \tilde{h}}{\partial t} \quad (29)$$

$$\tilde{\varphi}(1, t) = 0, \quad \tilde{p}(0, t) = 2 \left(\frac{\partial \tilde{\varphi}}{\partial x} - \frac{\partial \tilde{\varphi}}{\partial t} \right) \Big|_{x=0} \quad (30)$$

Making use of the steady flow equation, one can obtain an alternative equation for the perturbed unsteady velocity potential

$$\frac{\partial}{\partial x} \left[h_o(x) \frac{\partial \tilde{\varphi}}{\partial x}(x, t) \right] + \frac{\partial}{\partial x} \left[\tilde{h}(x, t) \frac{d\varphi_o}{dx} \right] - \frac{\tilde{h}(x, t)}{\delta_{ep}(x)} \frac{d}{dx} \left[h_o(x) \frac{d\varphi_o}{dx} \right] = -\frac{\partial \tilde{h}}{\partial t} \quad (31)$$

Having fulfilled linearization of a perturbed unsteady flow in vicinity of a nonlinear steady state flow, one can consider separately two required cases of height perturbation and pitch perturbation.

3.2.1. Height perturbation

In the case of height perturbation $\tilde{h}(x, t) = \tilde{h}(t)$. Perturbation potential can be represented as

$$\tilde{\varphi}(x, t) = \tilde{\varphi}^{\tilde{h}}(x) \tilde{h}(t) + \tilde{\varphi}^{\dot{\tilde{h}}}(x) \dot{\tilde{h}}(t) \quad (32)$$

Assume that the gap under the tips of the endplates is constant chordwise $\delta_{ep} = \text{const}$. Corresponding equations for the components of the perturbed solution can be derived in the form

$$\frac{d}{dx} \left[h_o(x) \frac{d\tilde{\varphi}^h}{dx} \right] + \frac{d^2 \varphi_o}{dx^2}(x) - \frac{1}{\delta_{ep}} \frac{d}{dx} \left[h_o(x) \frac{d\varphi_o}{dx} \right] = 0, \quad (33)$$

$$\frac{d}{dx} \left[h_o(x) \frac{d\tilde{\varphi}^h}{dx} \right] = -1 \quad (34)$$

Imposing conditions at the leading edges, one arrives at the following boundary conditions at $x = 1$ for the equations (33) and (34).

$$\tilde{\varphi}^h(1) = 0, \quad \dot{\tilde{\varphi}}^h(1) = 0 \quad (35)$$

Applying Kutta-Zhukovsky condition, one has

$$\frac{d\tilde{\varphi}^h}{dx} \tilde{h} + \frac{d\tilde{\varphi}^h}{dx} \dot{\tilde{h}} - \tilde{\varphi}^h \dot{\tilde{h}} - \tilde{\varphi}^h \ddot{\tilde{h}} = 0 \quad (36)$$

Neglecting second derivative of perturbation in height in (36), which implicitly would imply that Strouhal numbers are small, one arrives at the following boundary conditions at $x = 0$.

$$\frac{d\tilde{\varphi}^h}{dx}(0) = 0, \quad \left(\frac{d\tilde{\varphi}^h}{dx} - \varphi^h \right)_{x=0} = 0 \quad (37)$$

Integration of the equations (33)-(34) gives the following expressions for the corresponding perturbation velocities and potentials

$$h \frac{d\tilde{\varphi}^h}{dx} = v_o(x) \left[\frac{1}{\delta_{ep}} - \frac{1}{h_o(x)} \right] + \frac{c_1}{h_o(x)} \quad (38)$$

$$h\tilde{\varphi}^h = \int_1^x \left\{ v_o(x) \left[\frac{1}{\delta_{ep}} - \frac{1}{h_o(x)} \right] + \frac{c_1}{h_o(x)} \right\} dx \quad (39)$$

$$h \frac{d\tilde{\varphi}^h}{dx} = -\frac{x}{h_o(x)} + \frac{c_2}{h_o(x)} \quad (40)$$

$$h\tilde{\varphi}^h = \int_1^x h \frac{d\tilde{\varphi}^h}{dx}(\xi) d\xi \quad (41)$$

In the above expressions h is relative ground clearance defined as the ratio of the trailing edge ground clearance to the chord, $\bar{\delta}_{ep} = \delta_{ep}/h = O(1)$, $h_o(x) = h_o(x)/h = O(1)$, $v_o(x) = d\tilde{\varphi}_o/dx$ span averaged channel flow velocity. The constant c_1 and c_2 are given by the formulae.

$$c_1 = \frac{1}{\delta_{ep}} - 1, \quad c_2 = h\tilde{\varphi}^h(0)$$

It can be seen from equations (38)-(41) that both derivatives of perturbation velocity and potential with respect to kinematic parameters are inversely proportional to relative ground clearance in cruise, i.e. are of the order of $O(1/h)$. Derivatives of perturbed pressure with respect to perturbation in height \tilde{h} and rate of variation of height $\dot{\tilde{h}}$ can be determined in the form

$$p^h(x) = -2 \frac{d\tilde{\varphi}^h}{dx} \frac{d\varphi_o}{dx} = -2v_o(x) \frac{d\tilde{\varphi}^h}{dx} \quad (42)$$

$$p^{\dot{h}}(x) = -2 \left(v_o(x) \frac{d\tilde{\varphi}^h}{dx} + \tilde{\varphi}^h \right) \quad (43)$$

3.2.2. Pitch perturbation

In the case of pitch motions around the center of gravity $\tilde{h}(x, t) = \tilde{\theta}(t)(x - x_{cg})$ the perturbation potential of unsteady flow can be represented as

$$\tilde{\varphi}(x, t) = \tilde{\varphi}^{\tilde{\theta}} \tilde{\theta} + \tilde{\varphi}^{\dot{\tilde{\theta}}} \dot{\tilde{\theta}} \quad (44)$$

Derivatives of unsteady perturbed velocity potential with respect to perturbation in pitch $\tilde{\theta}$ and rate of pitch $\dot{\tilde{\theta}}$ are governed by the following equations

$$\frac{d}{dx} \left[h_o(x) \frac{d\tilde{\varphi}^{\tilde{\theta}}}{dx} \right] + \frac{d}{dx} \left[(x - x_{cg}) \frac{d\varphi_o}{dx} \right] - \frac{(x - x_{cg})}{\delta_{ep}} \frac{d}{dx} \left[h_o(x) \frac{d\varphi_o}{dx} \right] = 0 \quad (45)$$

$$\frac{d}{dx} \left[h_o(x) \frac{d\tilde{\varphi}^{\dot{\tilde{\theta}}}}{dx} \right] = -1. \quad (46)$$

The boundary conditions at the leading and trailing edges for the equations (45) and (46) are

$$\tilde{\varphi}^{\tilde{\theta}}(1) = 0, \quad \tilde{\varphi}^{\dot{\tilde{\theta}}}(1) = 0. \quad (47)$$

$$\frac{d\tilde{\varphi}^{\tilde{\theta}}}{dx}(0) = 0, \quad \left(\frac{d\tilde{\varphi}^{\tilde{\theta}}}{dx} - \tilde{\varphi}^{\tilde{\theta}} \right)_{x=0} = 0 \quad (48)$$

Solution of the equations (45) and (46) is straightforward and leads to the following formulae

$$h \frac{d\tilde{\varphi}^{\tilde{\theta}}}{dx} = -\frac{(x - x_{cg})}{h_o(x)} \frac{d\varphi_o}{dx} + \frac{(x - x_{cg})}{\bar{\delta}_{ep}} \frac{d\varphi_o}{dx} - \frac{1}{\delta_{ep} h_o(x)} \int_0^x \bar{h}(\xi) \frac{d\varphi_o}{dx}(\xi) d\xi + \frac{c_3}{h_o(x)} \quad (49)$$

$$h\tilde{\varphi}^{\tilde{\theta}}(x) = \int_1^x \frac{d\tilde{\varphi}^{\tilde{\theta}}}{dx}(\xi) d\xi \quad (50)$$

$$h \frac{d\tilde{\varphi}^{\dot{\tilde{\theta}}}}{dx} = -\frac{x}{h_o(x)} + \frac{c_4}{h_o(x)},$$

$$h\tilde{\varphi}^{\dot{\theta}} = \int_1^x \frac{d\tilde{\varphi}^{\dot{\theta}}}{dx}(\xi) d\xi \quad (51)$$

The constants c_3 and c_4 can be calculated with help of the formulae

$$c_3 = x_{cg} \left(1 + \frac{1}{\delta_{ep}} \right), \quad c_4 = h\tilde{\varphi}^{\dot{\theta}}(0) \quad (52)$$

Derivatives of pressure distribution induced by unsteady variation of pitch can be determined by means of the following expressions

$$\tilde{p}^{\dot{\theta}} = -2v_o(x) \frac{d\tilde{\varphi}}{dx}, \quad \tilde{p}^{\dot{\theta}} = -2 \left(v_o(x) \frac{d\tilde{\varphi}^{\dot{\theta}}}{dx} + \tilde{\varphi}^{\dot{\theta}} \right) \quad (53)$$

3.2.3. Determination of aerodynamic coefficients and their derivatives

Derivatives of lift and moment (around the center of gravity $x = x_{cg}$) coefficients can be obtained through integration of derivatives of corresponding pressure distributions.

$$c_y^{\tilde{h}, \dot{\tilde{h}}, \tilde{\theta}, \dot{\tilde{\theta}}} = \int_0^1 \tilde{p}^{\tilde{h}, \dot{\tilde{h}}, \tilde{\theta}, \dot{\tilde{\theta}}}(x) dx \quad (54)$$

$$m_z^{\tilde{h}, \dot{\tilde{h}}, \tilde{\theta}, \dot{\tilde{\theta}}} = \int_0^1 (x - x_{cg}) p^{\tilde{h}, \dot{\tilde{h}}, \tilde{\theta}, \dot{\tilde{\theta}}}(x) dx \quad (55)$$

Now, one can pass over to determination of drag coefficient c_x and its derivatives with respect to height and pitch perturbations. The drag coefficient can be written as

$$c_x = c_{x_i} + c_{x_f} \quad (56)$$

with c_{x_i} and c_{x_f} representing correspondingly induced drag and viscous drag. For turbulent regime of the flow the latter can be determined as (mostly) friction drag with use of the formula

$$c_{x_f} = \frac{S_{wet}}{S} \frac{0.455}{(\log Re)^{2.58}} \quad (57)$$

where S_{wet} and S are wetted area of the configuration and main wing's reference area respectively. Reynolds number is based on chord of the wing. Further on it will be assumed that viscous part of the drag does not vary with small perturbation of ground clearance and pitch angle.

Induced drag coefficient can be obtained by means of the formula, derived in [6]

$$c_{x_i} = c_{x_p} + c_s \quad (58)$$

where c_{x_p} is part of the induced drag coefficient due to longitudinal component of pressure forces, c_s is

a suction force contribution. For the case of flat ground c_{x_p} can be written as

$$c_{x_p}(x, t) = h \int_0^1 p(x, t) \frac{d\bar{h}^*(x)}{dx} dx \quad (59)$$

Substituting $h^*(x, t) = h_o(x) + \tilde{h}(t) + \tilde{\theta}(t)(x - x_{cg})$ and perturbation expansion of pressure $p(x, t)$ into (59), one comes to the following expressions for the derivatives of c_{x_p} in height and pitch

$$c_{x_p}^{\tilde{h}, \dot{\tilde{h}}, \tilde{\theta}, \dot{\tilde{\theta}}} = h \int_0^1 \tilde{p}^{\tilde{h}, \dot{\tilde{h}}, \tilde{\theta}, \dot{\tilde{\theta}}}(x) \frac{d\bar{h}_o(x)}{dx} dx \quad (60)$$

The steady state pressure contribution to induced drag is equal to

$$c_{x_{po}} = h \int_0^1 p_o(x) \frac{d\bar{h}_o(x)}{dx} dx \quad (61)$$

Consider the suction force contribution to induced drag coefficient. According to [6] it can be determined as

$$c_s = -h \bar{h}^*(1, t)[1 + v(1, t)]^2 = \\ -h(\bar{h}_o + \tilde{h}(1, t))[1 + v_o(1) + \tilde{v}(x, t)]^2 \quad (62)$$

where $\tilde{v}(x, t) = \partial \tilde{\varphi} / \partial x$. Expanding (62) to the first order, one has

$$c_{s_o} = -2h\bar{h}_o(1)[1 + v_o(1)]^2 \quad (63)$$

$$c_s^{\tilde{h}, \dot{\tilde{h}}, \tilde{\theta}, \dot{\tilde{\theta}}} = -2h\bar{h}_o(1)[1 + v_o(1)] \frac{d\tilde{\varphi}^{\tilde{h}, \dot{\tilde{h}}, \tilde{\theta}, \dot{\tilde{\theta}}}}{dx}(1) \quad (64)$$

It can be seen from (60) and (64) that for $h \rightarrow 0$ induced drag coefficient is of the order of $O(h)$. Because $h\tilde{\varphi}^{\dot{\theta}} = O(1)$, it follows from (60) and (64) that derivatives of induced drag coefficient in extreme ground effect are of the order of $O(1)$.

4. ASYMPTOTIC FORM OF EQUATIONS OF MOTION IN EXTREME GROUND EFFECT

4.1. Order estimates and assumptions

In this section asymptotics is derived of the "quintic" equations of motion for $h \rightarrow 0$. So far, order estimates have been obtained for all major aerodynamic coefficients on the basis of a mathematical model of a simple flying wing configuration, flaring in immediate proximity of the ground. In particular, for adjusted angle of pitch (in radians) and

curvature of wing sections of the order of $O(h)$, one has

$$c_{y_o}, m_{z_o} = O(1), \quad c_{x_{io}} = O(h) \quad (65)$$

As per previous analysis the derivatives of aerodynamic coefficients have the following order of magnitude

$$(c_y, m_z)^{\tilde{h}, \dot{h}, \tilde{\theta}, \dot{\theta}} = O\left(\frac{1}{h}\right) \quad (66)$$

$$c_{x_i}^{\tilde{h}, \dot{h}, \tilde{\theta}, \dot{\theta}} = O(1) \quad (67)$$

In order to evaluate the order of magnitude of the coefficient c_t^U which represents derivative of the thrust coefficient with respect to relative speed, it is assumed that drop of the thrust versus cruise speed is linear, so that the thrust T of the engines can be expressed in terms of relative speed of motion, installed thrust T_m and cruise thrust T_o as

$$T = T_m - \bar{U}(T_m - T_o), \quad \bar{U} = \frac{U}{U_o} \quad (68)$$

where U_o is design cruise speed. Introducing the thrust coefficient as

$$c_t = \frac{2T}{\rho U_o^2 S} = \frac{2T_m}{\rho U_o^2 S} - \frac{U}{U_o} \frac{2(T_m - T_o)}{\rho c_{y_o} U_o^2 S}$$

wherefrom the derivative of the thrust coefficient with respect to relative speed is equal to

$$\begin{aligned} c_t^U &= -\frac{2(T_m - T^*)}{\rho U_o^2 S} = -\frac{2c_{y_o}(T_m - T_o)}{\rho c_{y_o} U_o^2 S} = \\ &= -c_{y_o} \left(\frac{T_m}{W} - \frac{T_o}{W} \right) = -c_{y_o} \left(c_{T_m} - \frac{c_x}{c_{y_o}} \right) = \\ &= c_x - c_{y_o} c_{T_m} \end{aligned} \quad (69)$$

where $c_{T_m} = T_m/W$ is the installed thrust-to-weight ratio, characterizing relative power capacity of the vehicle.

Recalling previous order estimates, and assuming additionally that installed thrust-to-weight ratio $c_{T_m} = O(h)$ one finds

$$c_t^U = c_x - c_{y_o} c_{T_m} = O(h) \quad (70)$$

It seems rational to consider magnitude y_t as that of the order of $O(h)$. In other words such an assumption means that the ordinate of the thrust line is comparable with ground clearance.

Another convention to be adopted is related to the density factor μ , entering the equations of motion. Based on the statistics on existing and projected wing-in-ground effect craft, see [7], one can assume that the product of the vehicle's density and relative ground clearance is of the order of $O(1)$. In this case, it is appropriate to introduce instead of μ a new quantity $\bar{\mu} = \mu h = O(1)$, which can be called *reduced density*.

4.2. Derivation of asymptotic form of the equations of motion for $h \rightarrow 0$

Employing the above estimates and conventions about the orders of magnitude (in terms of h) and neglecting terms of the order $O(h)$ and higher, one can reduce the equations (19)-(21) to

$$\bar{\mu} \frac{dU'}{dt} = 0 \quad (71)$$

$$\bar{\mu} \frac{d^2\tilde{h}}{dt^2} = a_1 \tilde{h} + a_2 \dot{\tilde{h}} + a_3 \tilde{\theta} + a_4 \dot{\tilde{\theta}} \quad (72)$$

$$\bar{\mu} i_z \frac{d^2\tilde{\theta}}{dt^2} = b_1 \tilde{h} + b_2 \dot{\tilde{h}} + b_3 \tilde{\theta} + b_5 \dot{\tilde{\theta}} \quad (73)$$

where $a_1 = h c_y^{\tilde{h}}, a_2 = h c_y^{\dot{\tilde{h}}}, a_3 = h c_y^{\tilde{\theta}}, a_4 = h c_y^{\dot{\tilde{\theta}}}$. Coefficients $b_i, i = 1 \dots 4$ are given by the formulae

$$b_1 = h m_z^{\tilde{h}}, b_2 = h m_z^{\dot{\tilde{h}}}, b_3 = h m_z^{\tilde{\theta}}, b_4 = h m_z^{\dot{\tilde{\theta}}}.$$

Note that coefficients a_i and b_i are of the order of unity, because for each of the above derivatives one has

$$\text{coefficient}^{\tilde{h}, \dot{\tilde{h}}, \tilde{\theta}, \dot{\tilde{\theta}}} = O\left(\frac{1}{h}\right) \quad (74)$$

The system of equations (72) and (73) has the structure similar to (10) and (11), i.e. corresponds to Irodov's assumption of no perturbation in speed. It gives birth to a "quartic" characteristic equation (12) with the coefficients identical to $A_i, i = 1 \dots 4$, though written somewhat differently

$$A_1 = -\frac{1}{\bar{\mu} i_z} (b_4 + i_z a_2) \quad (75)$$

$$A_2 = -\frac{1}{\bar{\mu}^2 i_z} [a_4 b_2 - a_2 b_4 + \bar{\mu} (b_3 + i_z a_1)] \quad (76)$$

$$A_3 = -\frac{1}{\bar{\mu}^2 i_z} (a_2 b_3 - a_4 b_1 - a_3 b_2) \quad (77)$$

$$A_4 = \frac{1}{\bar{\mu}^2 i_z} (a_1 b_3 - a_3 b_1) \quad (78)$$

The advantage of the formulation presented above is in reduction of number of parameters on which depend A_i . In particular, for $h \rightarrow 0$ relative clearance h does not enter the coefficients of the quartic equation explicitly. Thus, the coefficients of the quartic depend (nonlinearly) only on reduced density $\bar{\mu}$ and ratios ε/h , characterizing design geometrical and kinematic parameters of the vehicle. Parameter $\varepsilon = O(h)$ can be adjusted angle of pitch θ or maximum curvature c of the lower side of the wing, related to h .

Variation of speed can be analysed introducing "large time" $t = O(1/h)$ and "very large time"

$t = O(1/h^2)$. It can be shown that on the scale of "large time" variation of speed of the vehicle is mostly driven by perturbations in height and pitch, whereas on the scale of "very large time" variation of speed is determined by perturbation of speed proper. In the latter case perturbed equation for speed is completely uncoupled from those for height and pitch and has the form

$$\bar{\mu} \frac{dU'}{d\tau_2} = (\bar{c}_t^U - 2\bar{c}_x) U' \quad (79)$$

where $\tau_2 = h^2 t$ is "squeezed" time variable, $\bar{c}_t^U = c_t^U/h$ and $\bar{c}_x = c_x/h$ are quantities of the order of unity.

5. CONCLUSIONS

In the present paper an attempt has been made to derive asymptotic form of the equations of motion of a lifting configuration in extreme ground effect through formal estimate of orders of magnitude of different terms when $h \rightarrow 0$. It has been shown that on (nondimensional) time scale $t = O(1)$, which corresponds to distances of the order of the chord from the moment of perturbation, the equations of motion correspond to "quartic" formulation of Irodov [1], i.e. the speed of the vehicle remains almost constant. As different from Irodov, the asymptotic form of the equation, valid for vanishing h , does not depend explicitly on relative ground clearance, but rather on reduced density $\bar{\mu} = \mu h$ and ratios of design pitch and curvature of the lower surface to h , i.e. number of parameters is less by one. On larger time scales of the order of $1/h$ and $1/h^2$ variation of speed is first driven by height and pitch perturbations and, later is determined by the speed perturbation proper. The latter conclusion confirms results, derived by Zhukov [5].

6. REFERENCES

- [1] Irodov, R.D., "Criteria of Longitudinal Stability of Ekranoiplan", Uchenye Zapiski TSAGI, Moscow, Vol. 1, No. 4, 1970, pp. 63 - 74.
- [2] Kumar, P.E., "Some Stability Problems of Ground Effect Vehicles in Forward Motion", Aeronautical Quarterly, Vol. XVIII, Feb. 1972, pp. 41-52.
- [3] Staufenbiel, R. W., "On the Design of Stable Ram Wing Vehicles", in Proc. Symposium "Ram Wing and Ground Effect Craft", The Royal Aeronautical Society, London, 19 May 1987, pp. 110-136.

[4] Staufenbiel, R., Kleineidam, G., "Longitudinal Motion of Low-Flying Vehicles in Nonlinear Flowfields", in Proc. of the Congress of the International Council of the Aeronautical Sciences, Munich, FRG, 1980, pp. 293-308.

[5] Zhukov, V.I., "Peculiarities of Aerodynamics, Stability and Controllability of an Ekranoiplan", Izdatelskiy Otdel Tsentralnogo Aerogidrodinamicheskogo Instituta im. N.E. Zhukovskogo, Moscow, 1997, 81 p.

[6] Rozhdestvensky, K.V., "An Effective Mathematical Model of the Flow past Ekranoiplan with Small Endplate Tip Clearances in Extreme Ground Effect", in Proc. of the International Workshop on "Twenty-First-Century Flying Ships", The University of New South Wales, Sydney, Australia, 7-9 November 1995, pp. 155-178.

[7] Rozhdestvensky, K.V., "Ekranoiplans - The GEMs of Fast Water Transport", Trans. Institute of Marine Engineers, Vol. 109, Part 1, 1997, pp. 47-74.

7. APPENDIX

Formulae for the coefficients B_i , $i = 1 \dots 5$

$$B_1 = \frac{1}{\mu i_z} [(2c_x - c_t^U - c_y^h)i_z - m_z^\theta] \quad (A1)$$

$$B_2 = \frac{1}{\mu^2 i_z} [(c_t^U - 2c_x)(i_z c_y^h + m_z^\theta - y_t c_x^\theta) + i_z(2c_y c_x^h - \mu c_y^h) + c_y^h m_z^\theta - c_y^\theta m_z^h - \mu m_z^\theta] \quad (A2)$$

$$B_3 = \frac{1}{\mu^3 i_z} \left\{ (c_t^U - 2c_x)[y_t(c_x^\theta c_y^h - c_x^h c_y^\theta) - c_x^h m_z^\theta] + \mu(m_x^\theta + i_z c_y^h) + c_y^\theta m_z^h - c_y^h m_z^\theta] + 2c_y(c_x^\theta m_z^h + c_x^h \mu i_z - c_x^h m_z^\theta) + \mu(c_y^h m_z^\theta + c_y^h m_z^\theta - c_y^\theta m_z^h - c_y^\theta m_z^\theta) \right\} \quad (A3)$$

$$B_4 = \frac{1}{\mu^3 i_z} \left\{ (c_t^U - 2c_x)[y_t(c_x^\theta c_y^h - c_x^h c_y^\theta - c_x^h c_y^\theta + c_x^\theta c_y^h) - c_y^h m_z^\theta + c_y^\theta m_z^h + c_y^\theta m_z^h - c_y^h m_z^\theta] + 2c_y(c_x^\theta m_z^h - c_x^h m_z^\theta + c_x^\theta m_z^h - c_x^h m_z^\theta) + \mu(c_y^h m_z^\theta - c_y^\theta m_z^h) \right\} \quad (A4)$$

$$B_5 = \frac{1}{\mu^3 i_z} \left\{ (c_t^U - 2c_x)[c_y^\theta m_z^h - c_y^h m_z^\theta + y_t(c_x^\theta c_y^h - c_x^h c_y^\theta)] + 2c_y(c_x^\theta m_z^h - c_x^h m_z^\theta) \right\} \quad (A5)$$

Coefficients can be rearranged to show the influence of different criteria (e.g. static stability margin as

$x^h - x^\theta$) somewhat more explicitly. For example, the coefficient B_5 can be re-written in the following form, coinciding with account of difference in nondimensionalization with Zhukov (note that here x -axis is directed upstream)

$$B_5 = \frac{c_y^h c_y^\theta}{\mu^3 i_z} \left\{ (x_h - x_\theta)(c_t^U - 2c_x + 2c_y \frac{c_x^\theta}{c_y^\theta}) + \left(\frac{c_x^\theta}{c_y^\theta} - \frac{c_x^h}{c_y^h} \right) [y_t(c_t^U - 2c_x) + 2c_y x^\theta] \right\} \quad (A6)$$

LONGITUDINAL STABILITY OF EKRANOPLANS AND HYDROFOILS SHIPS

V.I. Korolyov

Institute of Hydromechanics of Ukrainian National Academy of Sciences,

8/4 Zelyabov str. 252057, KIEV, UA

SUMMARY

Longitudinal stability of ekranoplans and hydrofoil ships, that have two carrying hydrofoils separated by some distance along the length of hull, "tandem" system, is considered in the paper. Longitudinal stability is characterized by the value of metacentric height, which is used in the practice of ship-building. An expression is given for the definition of this value depending on the main geometric and aerodynamic parameters. A link is determined between the metacentric height and frequency of the free angular movements of ekranoplans. A parameter investigation is fulfilled and recommendations are obtained for the choice of combinations of the carrying system basic elements.

LIST OF SYMBOLS

C_y	wing-lift coefficient
C_y^h, C_y^α	derivatives of the wing-lift coefficient for the relative distance from the screen and for the angle of attack
$C_i = C_{y_i}^h/C_{y_i}^\alpha$	hydrodynamic characteristic of i-hydrofoil
α	angle of attack with account of zero lifting force angle
$\Delta\alpha$	increment of the angle of attack
$K = C_y/C_x$	hydrodynamic quality of hydrofoil
V	movement speed of ekranoplan (hydrofoil ship)
h	distance between the back hydrofoil edge of ekranoplan and the screen and between the front edge of hydrofoil and the water surface for hydrofoil ship
$\bar{h}_i = h_i/b_i$	
S_i	wing area
$\lambda_i = S_i/b_i$	relative lengthening of rectangular wing
P_i	lifting force of i-hydrofoil
ρ	air density (for ekranoplan), water density (for hydrofoil ship)
D	object weight
l	distance between the centres of pressure of hydrofoils
l_1	arm of lifting force of the back hydrofoil relating to the

$l_{b_1} = l/b_1$	mass centre characteristic of the object lengthening relative chord of back wing
m	mass of the object
g	gravity acceleration
r	longitudinal radius of inertia of the object masses
H	full longitudinal metacentric height of the object
H_∞	metacentric height in the boundless flow
H_h	component of metacentric height conditioned by influence of the screen (free surface of water)

1. INTRODUCTION

Creation of high-speed marine transport means is possible on the base of use of dynamic lifting force of the carrying surfaces, that move close to the boundary between air and water (ekranoplans, hydrofoil ships). According to this development of effective carrying systems, that ensure high aerohydrodynamic quality K and the necessary stability of movement, becomes actual.

The problem of stability is especially urgent for ekranoplans. Their efficiency considerably increases with the decrease of distance between the carrying elements and a screen. Optimum exploitation gaps between the back edge of the carrying wing and the screen constitute not more than 10% of the wing chord. At movements in such conditions deviations, that lead to the strokes against water, are inadmissible. This circumstance causes strict requirements on the object stability, thus limiting amplitudes of the vertical motion of its elements by the mentioned limits.

Characteristic feature for both types of transport means is the sharply expressed non-linear dependence of the dynamic lifting force on hydrofoils on the distance between the hydrofoil and boundary surface (screen). See Figure 1.

Gradients of the dynamic lifting force near this boundary ensure an emergency of restorative forces and moments at the wing's deviation from the regimes of the set in movement. This permits to create objects with the natural stability (self-stabilization). This is evident from the experience of construction and exploitation of ship with the little sink underwater hydrofoils /1/.

The longitudinal static stability of the objects with two carrying wings separated by some distance, which is determined by the length of hull, "tandem" system (Figure 1) is being investigated in the present work.

2. DERIVATION OF THE MAIN DEPENDENCE.

At the calculated conditions the object moves at a rate V with the given fit - defined angles of the hydrofoil attack α_i and their distance from the boundary of separation h_i . It is possible for wings to have different chords b_i , relative distances from the boundary of separation $h_i = h_i/b_i$, relative lengthenings $\lambda = S_i/b_i$. Here at the analysis of the main dependences we consider wings with the rectangular plan form, but this method can be used for wings with arbitrary form, if there is information about the aerohydrodynamic characteristics. At every change of the fit, i.e. position of wings relatively to the boundary of separation, caused by external forces, carrying forces on the wings change, this leads to the appearance of the longitudinal moment, which can be both restoring and destabilizing. Value and sign of this moment can be determined taking into account the following considerations. Change of the carrying force on the back wing at the change of the attack angle by the value $\Delta\alpha$ (turn of the ekranoplane about transverse axis that goes across centre of mass) can be determined as follows /2/:

$$\Delta P_1 = \frac{\partial P_1}{\partial \alpha} \Delta\alpha + \frac{\partial P_1}{\partial h} \Delta h = \frac{\rho V^2}{2} S_1 \left(\frac{\partial C_{y_1}}{\partial \alpha} \Delta\alpha + \frac{\partial C_{y_1}}{\partial h} \Delta h \right) \quad (1)$$

It is possible to obtain from the condition of statics:

$$P_1 = D(1 + \bar{l}_1) \quad (2)$$

$$P_2 = -D\bar{l}_1 \quad (3)$$

(Marked at Fig. 1). Taking into account that $\Delta h_1 = \bar{l}_1 \Delta\alpha$ we shall obtain:

$$\Delta P_1 = D(1 + \bar{l}_1) \left(1 + \frac{C_{y_1}^h}{C_{y_1}^\alpha} \bar{l}_1 l_{b_1} \right) \frac{\Delta\alpha}{\alpha_1} \quad (4)$$

where $l_{b_1} = l/b_1$. Increment of the carrying force on the front wing is determined by analogy:

$$\Delta P_2 = -D\bar{l}_1 \left[1 + \frac{C_{y_2}^h}{C_{y_2}^\alpha} (1 + \bar{l}_1) l_{b_2} \right] \frac{\Delta\alpha}{\alpha_2} \quad (5)$$

$$l_{b_2} = l/b_2$$

Moment, conditioned by the change of the carrying forces on wings, is determined in the form:

$$\Delta M = D\bar{l}_1(1 + \bar{l}_1) \left\{ (1 + C_1 \bar{l}_1 l_{b_1}) \frac{1}{\alpha_1} - \right.$$

$$- \left[1 + C_2(1 + \bar{l}_1) l_{b_2} \right] \frac{1}{\alpha_2} \} \Delta\alpha \quad (6)$$

$$C_i = C_{y_i}^h / C_{y_i}^\alpha \quad (7)$$

For the wings with the rectangular plan form

$$P_i = C_{y_i} \frac{\lambda_i l_i^2 \rho V^2}{l_{b_i}^2} \quad (8)$$

Using (2) and (3) we shall obtain

$$\frac{C_{y_1} \lambda_1 l_{b_1}^2}{C_{y_2} \lambda_2 l_{b_2}^2} = \frac{1 + \bar{l}_1}{-\bar{l}_1} \quad (9)$$

Taking

$$\frac{C_{y_1} \lambda_1}{C_{y_2} \lambda_2} = p \quad (10)$$

we shall obtain

$$l_{b_2} = l_{b_1} \sqrt{\frac{1 + \bar{l}_1}{-p\bar{l}_1}} \quad (11)$$

Putting (11) into (6) we shall obtain resulting:

$$H = \frac{\Delta M}{\Delta\alpha} \frac{1}{Dl} = \bar{l}_1(1 + \bar{l}_1) \left\{ (1 \pm C_1 \bar{l}_1 l_{b_1}) \frac{1}{\alpha_1} - \right. \\ \left. - \left[1 + C_2(1 + \bar{l}_1) l_{b_2} \right] \sqrt{\frac{1 + \bar{l}_1}{-p\bar{l}_1}} \frac{1}{\alpha_2} \right\} \quad (12)$$

The value Hl - coefficient of the restoring moment by the angle of deviation $\Delta\alpha$ - is analogous to the longitudinal metacentric height, which is used in the shipbuilding practice. Unlike the analogous characteristic for the tonnage ships, metacentric height, that corresponds to the stable regime of ekranoplans's movement must be negative, as well as the moment that emerges at the positive increment of the attack angle $\Delta\alpha$. So, H can be called as the dimensionless metacentric height. Equation (12) structure permits to divide the metacentric height at two components - aerodynamic component - for the wing in the infinite flow and screen component.

$$H_\infty = \bar{l}_1(1 + \bar{l}_1) \left(\frac{1}{\alpha_1} - \frac{1}{\alpha_2} \right) \quad (13)$$

$$H_h = \bar{l}_1(1 \pm \bar{l}_1) l_{b_1} \times$$

$$\times \left[C_1 \bar{l}_1 \frac{1}{\alpha_1} - \frac{C_2(1 + \bar{l}_1) \sqrt{\frac{1 + \bar{l}_1}{-p\bar{l}_1}}}{\alpha_2} \right] \quad (14)$$

(12 - 14) equations are obtained for ekranoplans. Analogous expressions are applicable for the hydrofoil ships. The equations differ only by signs, in equations (12) and (14) for the hydrofoil ships the positive sign is replaced by the negative. It is necessary to note, that when the wing system deviates by the angle $\Delta\alpha$, not

only a moment appears, but also an additional force, which is defined by the expression

$$\frac{\Delta D}{D} = \left\{ (1 + \bar{l}_1)(1 + C_1 \bar{l}_1 l_{b_i}) \frac{1}{\alpha_1} - \right. \\ \left. - \bar{l}_1 \left[1 + C_2(1 + \bar{l}_1)l_{b_i} \sqrt{\frac{1 + \bar{l}_1}{-p l_1}} \right] \frac{1}{\alpha_2} \right\} \Delta \alpha \quad (15)$$

or, in other words, the inclinations are non-equilibrium. The change of the lifting force is determined by calculations and has the order of

$$\frac{\Delta D}{D} \cong 0.5 \frac{\Delta \alpha}{\alpha_1} \quad (16)$$

Therefore it is necessary to correct the fit of the object in order to preserve D value constant for the calculation of the recoveral moments at essential deviations ($\Delta \alpha$).

In majority of cases it is necessary to know the initial values H for small deviations, which do not need correction. In particular, such characteristic is important for determination of parameters of aerodynamics scheme of apparatus, which ensure its stability. It is particularly actual taking into account the absence of experience in construction of ekranoplans of the discussed scheme. In the work /3/ an expression was obtained for the determination of the own frequency of the longitudinal angular oscillations of ekranoplan. In the dimensional form it looks like:

$$\omega_2 = \left\{ \frac{-\rho V^2}{2mr^2} \left[\left(\sum_{i=1}^2 C_y^h \frac{S_i l_i^2}{b_i} + \sum_{i=1}^2 C_y^\alpha S_i l_i \right) - \right. \right. \\ \left. \left. - \frac{1}{4mr^2} \left(\frac{\rho V^2}{2} \sum_{i=1}^2 C_y^\alpha S_i l_i^2 \right)^2 \right] \right\}^{1/2} \quad (17)$$

The second term in the formula (17) usually constitutes small part of the first one (3–4%) and can be neglected. Taking into account this circumstance it is possible to obtain the following dependence, which links the metacentric height with the own frequency of longitudinal angular oscillations (pitching oscillations):

$$\omega_2 = \sqrt{\frac{-gl}{r^2} H} \quad (18)$$

Dependence (18) is absolute similar to the corresponding dependence for the tonnage ships.

3. ANALYSIS OF INFLUENCE OF DIFFERENT FACTORS ON EKRANOPLAN STABILITY

The resulting expression (12) depends on geometric l_1 and aerodynamic (C, p) characteristics. Analysis of the formula (12) shows that the main contribution into the recoveral moment is made by the back wing. This contribution is defined by the term $I + C_l l_1$. Indeed, the

stabilizing moment appears when the attack angle increment on the back wing is positive. This moment is conditioned by approach of the wing to the screen and by the attack angle increase. Sign of the moment on the front wing is determined by that parameter, which more influence the change of the lifting force – increase of the relative distance to the screen h_2 or of the attack angle α_2 . Therefore, in order to obtain the maximum value of H , the attack angle α_2 must be as big as possible. (This condition determines also the negative value H_∞). The value $l_{b_i} = l/b_i$, which characterizes the relative lengthening of the object unambiguously determines the main component of H – screen H_h , which value is proportional to l_{b_i} . Next main factor, that influence the value of H is the characteristic $C = C_y^h/C_y^\alpha$. Its increase leads to the increase of the metacentric height. For calculation of C values dependences of C_y on the lengthenings and other parameters were used. These dependences were obtained for the profile ЦАГИ СР-16-6М [4,5]. C values, calculated according to these data in the lengthening range $\lambda = 2 - 4$, attack angles $\alpha = 2^\circ - 6^\circ$, distances from the screen $h = 0.05 - 0.2$ for the wings of rectangular form with the relative profile thickness $\delta = 0.06$ are given at Figure 2. C value weakly depends on lengthening λ , greatly increases while approaching the screen and in the attack angle range $0^\circ - 6^\circ$ has approximately linear dependence on the attack angle. Analysis of the influence of the above mentioned factors is fulfilled by calculations.

H value is calculated according to formula (12) at their change in the following limits: $\lambda_i = 2 - 4$, $\alpha_i^\circ = 2^\circ - 6^\circ$, $h_i = 0.05 - 0.2$. Relative lengthening of the object $l_{b_i} = l/b_i$ is taken 5. Influence of this factor is unambiguous, its increase leads to the increase of H . Influence of centering (position of the mass centre along the length) was determined by calculation of every variant of scheme at four centerings. (And the static condition was observed by variation of b_2 value.)

Calculation results show, that the value of H is mainly dependent on attack angles α_1 and α_2 , value h_1 and on the position of mass centre (\bar{l}_1). In every case increase of H is facilitated by the increase of α_1/α_2 ratio. Reduction of this ratio sharply decreases stability and can lead to its loss. At Figure 3 the generalized results are given for the absolutely symmetric scheme ($\lambda_1 = \lambda_2$, $\alpha_1 = \alpha_2$, $b_1 = b_2$, $\bar{h}_1 = \bar{h}_2$, $\bar{l}_1 = -0.5$), and at Figure 4 the maximum values of H are given together with the corresponding of their determining parameters. In every case the lengthening and attack angles for the back wing (λ_1, α_1) were minimum, and for the front – (λ_2, α_2) – maximum. Influence of the distance between the screen and the back wing h_1 is small and ambiguous. h_2 value, on the contrary, greatly influence the value of H (increases at the decrease of h_2). And the mass centre in every case must be closer to a stern ($l_1 = 0.2 - 0.35$) (Figure 5).

Carried out at the Institute of Hydromechanics model

experiments confirmed received results.

We do not consider the questions of compatibility of stability and aerodynamics requirements (K quality), of possibility for the practical realization of the small values of h and other peculiarities, connected with implementation of the obtained results in practice. These questions are to be solved when the aerodynamic schemes of the definite projects are developed, on the base of definite information – aerodynamic characteristics of wing with the account of their mutual influence, influence of fuselage and other elements, form of wing in plane and so on. The given data are of approximate character. Nontheless these data give definite enough view of the influence of main factors, permit to analyse the possibilities of different compositions.

4. STABILITY OF HYDROFOIL SHIPS

In the former Soviet Union a series of projects for the ships with the little sink underwater hydrofoils was developed /1/. Hydrodynamic scheme of these ships is analogous to the aerodynamic scheme of ekranoplan with the "tandem" system of hydrofoils (Figure 1). Stability problems of their movement were solved by empiric method – the optimum combinations of hydrofoil system parameters, which ensure high hydrodynamic quality and stability were found as a result of numerous experiments. So, all the constructed hydrofoil ships have good stability and can serve as some standard when new projects are estimated. Analysis of the main parameters of the carrying systems of these ships shows, that the definite enough ratios are characteristic for them:

- position of the mass centre along the length is determined by the value $\bar{l}_1 \cong 0.48$;
- lengthening $l_{b_1} = l/b_1 \cong 25$;
- chord ratio of the bow and stern hydrofoils $b_2/b_1 = 0.9$;
- ratio of the lengthening of hydrofoils was in the limits $\lambda_2/\lambda_1 = 1.1 - 1.35$, in majority of cases the attack angles of the stern hydrofoil were less, than that of the bow hydrofoil ($\alpha_1 < \alpha_2$);
- dipping of the bow hydrofoil in every case is more, than that of the stern hydrofoil ($h_2 > h_1$).

Here are given the average values of parameters. Their variability can be explained by the influence of numerous factors, which are not taken into account – hydrofoil deadrise and hydrofoil sweep, profile form, influence of form of wing in plane, position of the struts, hydrodynamic influence of the front hydrofoil on the back one and other individual peculiarities of the projects. However, general tendencies, that determine influence of principal factors, manifest themselves quite clearly. In this connection comparison of these data with the calculation results according to formula (12) are interesting. Calculations were fulfilled in the real range of parameters, which was developed in the practice of exploitation of such ships. The ratio λ_2/λ_1 changed in

narrow limits, where influence of λ on C_i is small so, in every case $\lambda_2/\lambda_1 = 1.1$ and relative lengthening of the object $l_{b_1} = 25$ were taken. Attack angles (with account of the angles of zero lifting force) $\alpha = 2^\circ - 4^\circ$, relative dippings $h_i = 0.4 - 1.6$. Calculations were provided at several values of l_1 for determination of the value l_1 (centering), which corresponds to the maximum value of H . Condition of statics was observed automatically, for the value b_2 was determined in the course of calculations.

Hydrodynamic characteristic of hydrofoils – parameter $C_i = C_y^h/C_y^\alpha$ (Figure 6) was determined according to the data from the book /6/ – values $C_y^\alpha = f(h, \lambda)$, obtained theoretically for the plane rectangular hydrofoil. Influence of thickness and curvature of the axial are of the profile on C_y was accounted for by the change of the angle of zero lifting force. Calculation results, corresponding to the greatest values of H are given at Figure 7. As it is seen from the table, correspondence of the influence of ratios α_i and h_i of the calculation results and practice is quite unambiguous. Dependences of H on mass centre position (\bar{l}_1) for the variants of calculations with the greatest values of H are given at Figure 8. In every case the value of \bar{l}_1 changes in narrow enough limits (approximately 0.4 – 0.5), this also corresponds to the results from practice. The carried out comparison shows that the influence of the factors α_i , h_i , l_i on the value of H is determining; the developed method of H calculation quite objectively reflects the link of metacentric height with these factors.

5 SOME ESTIMATIONS AND DEDUCTIONS

Ekranoplan must satisfy two main requirements – to have high aerodynamic efficiency and high level of safety, particularly stability of movement. Taking into account the scale of damages due to inadequate efficiency or stability, when conflicting requirements are to be observed, the problem must be solved by way of compromise, with the priority of requirements, that ensure safety. One of the advantages of the two-support scheme, that was considered above, is that the requirements for optimum choice of parameters for wings from the point of view of quality and stability in some cases coincide. Thus the main (back) wing, carrying 65 – 70% of the load, must have, according to both requirements, small attack angle $\alpha_1 = 2^\circ - 2.5^\circ$. Aerodynamic scheme of the stabilized ekranoplan is more efficient in principle, that the scheme with control, for it excludes appearance on the control elements – stabilizers – of the control "sinking" forces.

Stability on the vertical travel for ekranoplans and hydrofoil ships of "Tandem" scheme is ensured in every case at the account of appearance of restoring force, which is defined by the value C_y^h .

Besides, for the scheme, that is asymmetric relating to the mass centre (such scheme of "tandem" system is the most stable), at vertical travel the restoring mo-

ment appears, which facilitate the system's return to the initial position. Increase of this scheme's stability can be facilitated by using the proposed in the article /6/ application of two consequently located wings, that are rigidly links to each other, as the front carrying element. This construction has the negative derivative C_y^α and permits to increase sufficiently the value of H and to widen the range of heights for the stable flight. Comparison of stabilities for ekranoplans and hydrofoil ships shows that the values of H in both cases are of approximately the same order. This permits to consider, that the static stability, which is necessary for creation of self - stabilizing ekranoplan, can be ensured.

More valid opinion is possible to obtain on the base of detail study of dynamic reaction of ekranoplan to the external disturbances. As every marine transport means, ekranoplan will have restrictions on external conditions. The most important disturbances, which define the possibility of ekranoplan application in the real conditions are the disturbances, that are initiated by:

- movement over the long waves and, in particular, on the oblique courses;
- movement in the conditions of intensive turbulence in the lower atmosphere layer (wich the height up to 25 m over the sea level). In both cases the positive influence on the flight safety is exerted by speed increase. At flight over the choppy sea this increases the frequency of meetings with the waves and removing off the resonance conditions, and in the conditions of turbulence - decreases the influence of turbulent pulsations due to the relative decrease of the increment of pulsating forces.

6. CONCLUSION

Expression (12), determining the metacentric height and giving dependence between geometric and aerohydrodynamic characteristics of ekranoplan and hydrofoil ship permits to solve the following problems:

- rational choice of the carrying system elements, that secure maximum longitudinal static stability of the object at full speed;
- determination of stability characteristics at different regimes of the object movement (speeding - up, braking);
- determination of stability characteristics of the object with the given elements of the carrying system.

Estimation of stability of hydrofoil ships on the base of metacentric height H permits to make a conclusion about applicability of this method for the estimation of stability of the carrying system with "tandem" scheme. Comparison of stability characteristics for ekranoplans and hydrofoil ships of the similar scheme gives ground to consider, that it is possible to construct self - stabilizing ekranoplan according to the scheme, which is analogous to that of the hydrofoil ships.

REFERENCES

1. Zaytcev M.A., Maskalik A.I., "National hydrofoil ships", Moscow: Sudostroyeniye, 1967. 362 p.
2. Korolyov V.I., "Longitudinal static stability of the apparatus with two carrying hydrofoils", in: "Hydrodynamics of the carrying surfaces", Kiev: Naukova Dumka, 1966, pp. 216-222.
3. Korolyov V.I., "Movement of the apparatus with air carrying hydrofoils over the choppy sea surface", in: "Hydrodynamics of high speeds", Kiev, Naukova Dumka, 1966, pp. 75-80.
4. Belynsky V.G. et al "Effect of the Form of a Non Planar Screen on the Hydrodynamic Characteristics of a Foil Traveling Above it", Gidromechanika N 31, 1975
5. Belynsky V.G., About movement of a wing above wavy surface of water, High Speed Body Motion in Water, AGARD Report 827, UNAS, Kiev, Ukraine, 1-3 Sept. 1997.
6. Egorov I.T., Sokolov V.T. "Hydrodynamics of high-speed ships", Moscow: Sudostroyeniye, 1971. 424 p.
7. Gusev I.N., "Improvement of the exploitation possibilities of ekranoplan of "Utko" scheme", Izv. VUZov, "Aviation engineering", 1995, N2, Kazan'-State Technical University, p. 9-13.

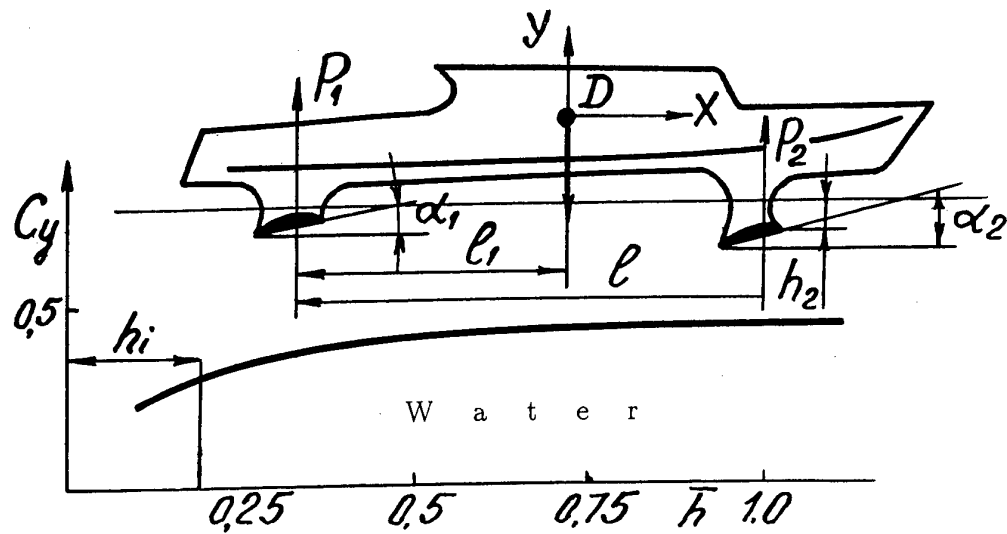
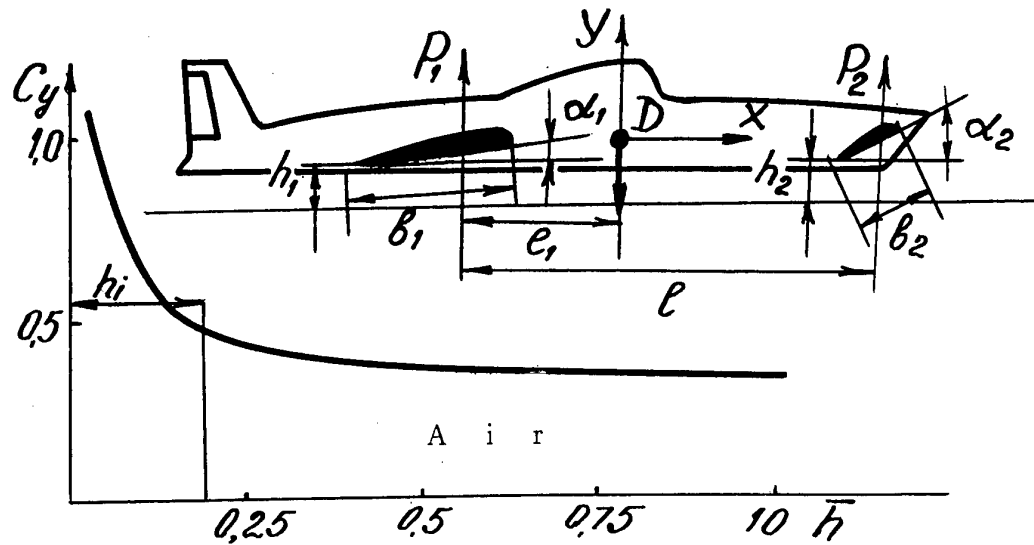


Fig.1. "Tandem" scheme of ecranoplan and hydrofoil ships.

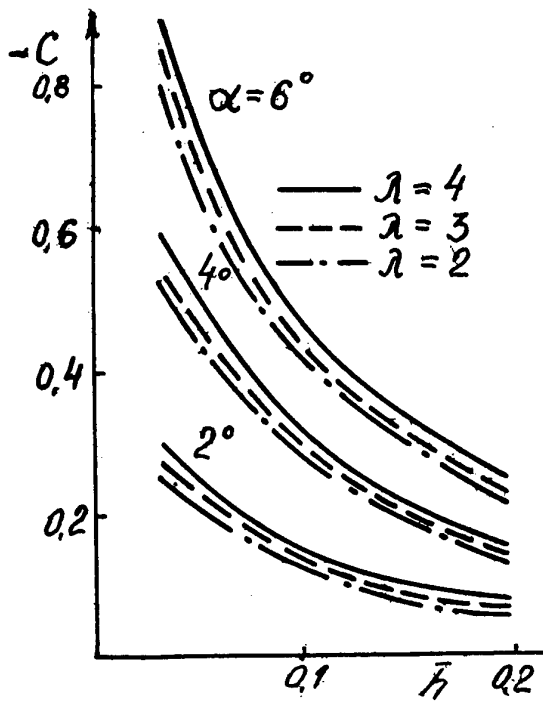


Fig. 2. Aerodynamical wings characteristics of ekranoplan.

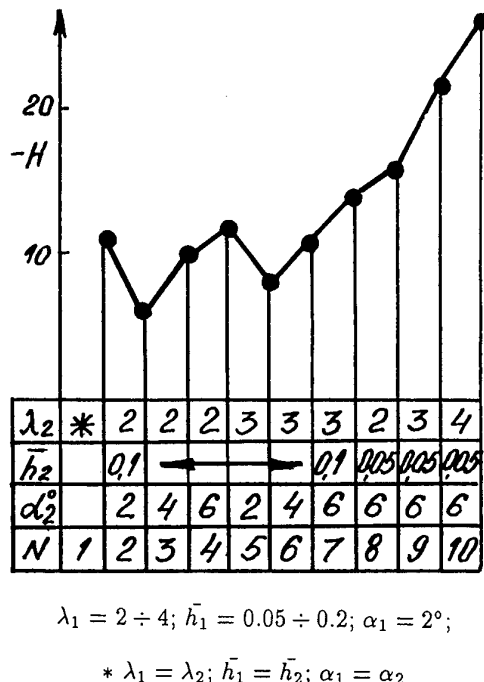


Fig. 4. Dependence of H on main parameters of ekranoplan.

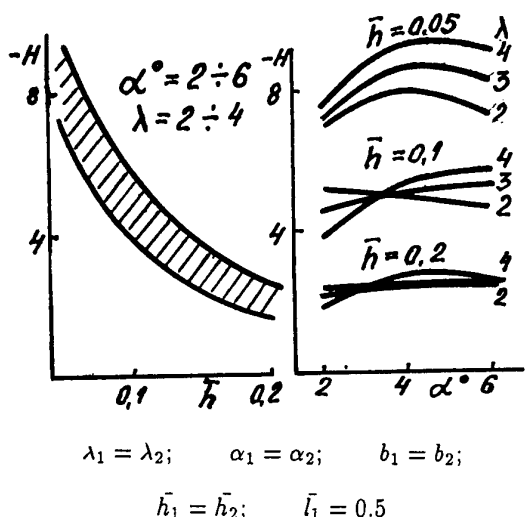


Fig. 3. Stability characteristics of ekranoplan with identical forward and after wing.

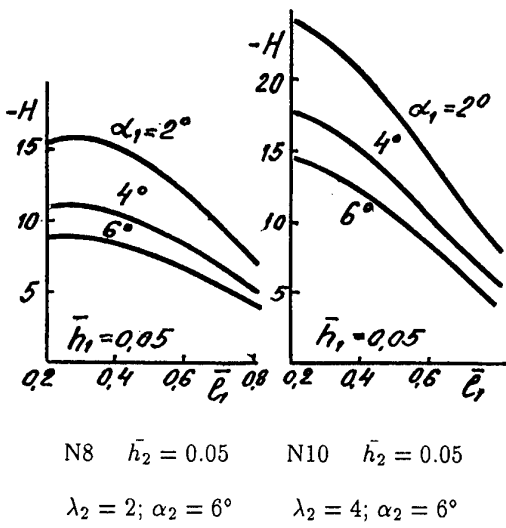


Fig. 5. Dependence of H on mass center of position ekranoplan.

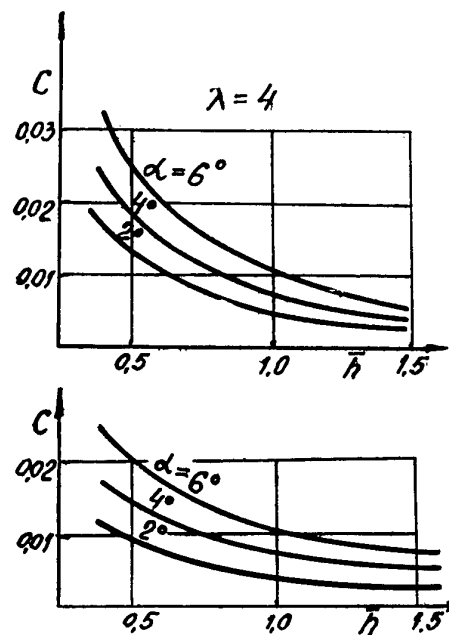
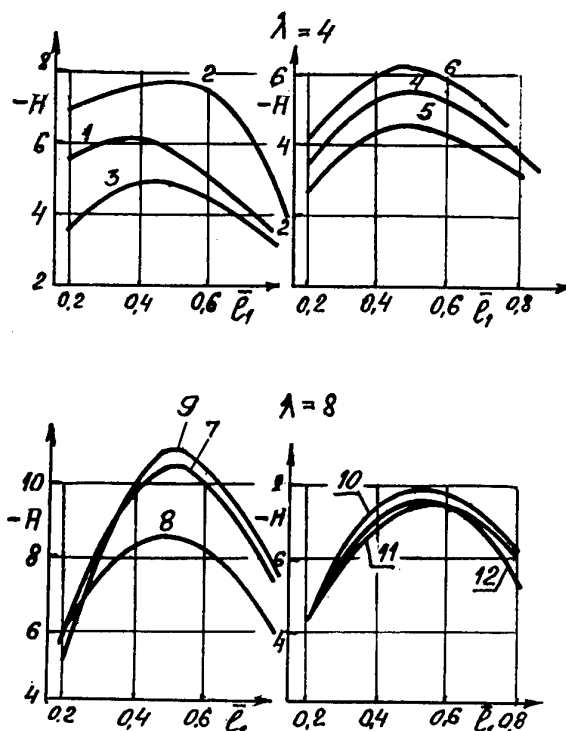
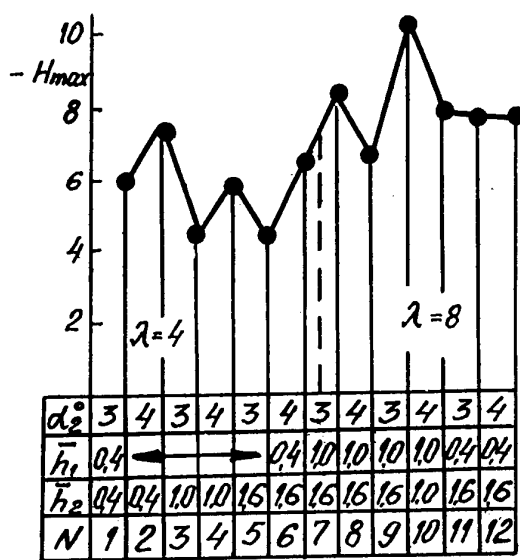


Fig. 6. Hydrodynamical characteristics of hydrofoils.

Fig. 8. Dependence of H on mass center position of hydrofoil ships.

$$\alpha_1 = 2^\circ$$

Fig. 7. Dependence of H on main parameters of hydrofoil ships.

AERODYNAMIC SCHEME OF EKRAPOANE OPTIMIZATION WITH REFERENCE TO NEW AREAS OF APPLICATION¹

A.V. Nebylov

State University of Aerospace Instrumentation,
67 Bolshaya Morskaya, St. Petersburg, 190000 Russia.

E.Th. Zhigalko

Faculty of Mathematics and Mechanics, St. Petersburg State University,
P.O.Box 154, St. Peterhof, 198904 Russia.

SUMMARY

Opportunities of a choice of the expedient scheme of a large scale ekranoplane (LE) which would ensure the self-stabilization of an angle of attack and the controllability and would improve its properties required, for example, in using LE as a booster for an aerospace plane or as a sea rescue carrier are considered herein. The treated arrangement differs from known ones by utilizing less amount of aircraft elements which are not fully effective in flight of this type.

1. INTRODUCTION

There is no doubt that the expansion of space programs will be accompanied by perfecting technical means, in particular, reusable aerospace planes (ASP). Due to utilization of reusable application boosters with horizontal start, start from equatorial region and other innovations further raise of profitability of space systems in terms of the cost of payload delivery to an orbit is expected. It have not still an engineering solution due to a number of reasons: insufficiency of technologies and materials development, other difficulties.

Basing on prospects for technological progress up to 2005 the Japanese specialists indicate an optimal solution which make it possible for ASP with an initial mass of 600 ton and initial horizontal velocity 0.6 M to deliver 7 ton payload to the low earth orbit. There is no transport tool to carry mass of 600 ton at velocity of

220 m/sec; however, large ekranoplanes are capable to solve this problem. Besides, they are likely to be just the means for docking a returning ASP without heavy undercarriage (HLHL systems).

2. PARAMETERS OF EKRAPOANE, INTENDED FOR ASP LAUNCHER

Only a few designs of WIG (from a known common number of tens) have indicated the expected properties. They are X-112, X-113, some modern small class ekranoplanes, and put into practice large ekranoplanes "Orlionok" and "Lun". The reason is that most constructors did not take into account all requirements to the design. There is no essential practicable utilization of an ekranoplane as yet. Other transport tools appears to withstand a competition in broad application in basic indexes, in the ultimate load on a wing, in the mass response and cost prices of ton-kilometer, however, the practical interest to unique properties of ekranoplanes (the greatest size and mass of load unit, low height of flight, amphibiouguity) is still insufficient.

Prospects of application of a WIG plane as a launcher-carrier of ASP for a HLHL system, are promising since the conditions of reaching the highest possible velocity of driving and single mass of load are the most essential, while the profitability of transportation recedes to the background.

¹ The work was executed under support of Russian Foundation for Basic Researches according to the project 96-01-00010.

There are numerous functions directly or implicitly ensured by aerodynamic properties of LE. They are: a lift capability, a property of the self-stabilization of flight (on a height, load change, pitch and bank angles), controllability (on a velocity, altitude, pitch, course, roll) providing with maneuvers (take-off from water, landing) buoyancy and stability in sailing, basing of ASP, joint with ASP maneuvers (start, landing, emergency), alternative application. There are other functions apart from the transport ones affecting the realizability of the project, for example, a safety, a manufacturability and interaction with an environment.

When estimating the take-off weight of ASP is chosen as 600 tons, the landing weight is 60 tons, a square of a wing is 600 m^2 . The booster velocity is 0.6 M that covers a range of 3000 km. Basing on parameters of known machines and using extrapolation one can calculate that the ekranoplane valid for the booster function own mass will reach 1500 tons while a chord and a square of the main wing are 60 m and 3000m^2 correspondingly.

The scale increase of a flying apparatus erects new problems on the design, for example, conjugated with necessity of the arrangement of a sufficient number of drives of a limited single power. The most appropriate among existing at the moment is the Russian drive NK-44, and the Russian company AO NTK "Engines NK", has declared readiness to produce it in lots.

3. PECULIARITIES OF ARRANGEMENT OF EKRAPOANE, POSSESSING PROPERTY OF SELF-STABILIZATION

A lift force F_y for a profile (whose chord is b), flying at a small altitude $y \approx b$ above a basic surface, can be a monotonously decreasing nonlinear function of y at a proper choice of the form of the wing profile and of the attack angle. The relative increase of the proper lift to drag

ratio can with a drop to a basic surface achieve two. This property together with the effect of altitude self-stabilization (see Fig.1,

$F_y > G$, the gravity force, when $y < h_k$) distinguishes an ekranoplane from an airplane and is important enough for making the concept of WIG plane attractive, even at its known basic shortages. The most important among these is the problem of an ekranoplane flight stability, under which its ability is understood to independent (without interference of a pilot or system for automatic motion control, SAMC) return to the initial condition of driving after random perturbation.

The solution of the problem may be provided with the proper choice of the glider form and the mass center location. The importance of the question for ekranoplane results from the altitude of its flight being too small for a piloting error correction.

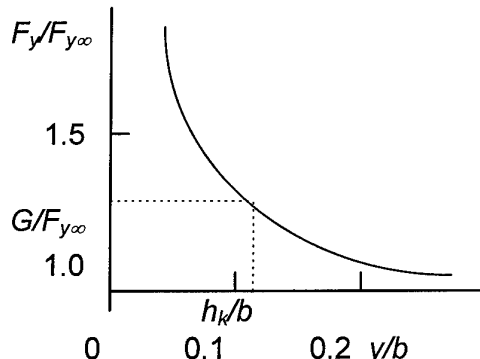


Fig. 1. Typical lift dependency on flight altitude

Traditionally heavy WIG planes have been designed, leaning upon schemes of a construction of airplanes providing flights on different altitudes including these above the zone of WIG-effect. However, flight dynamics of a WIG and of an airplane in a free flight is different as well as requirements on a stability and controllability.

At perturbation of normal flight of a wing about a basic surface there are the forces

and moment M , regenerating an altitude of flight, but neutral, or worsening in relation to a deviation of the pitch angle, and neutral, or weakly regenerating in relation to bank angle.

The experimental researches and theoretical analysis indicate conditions that must be taken into account at ekranoplane designing. A mutual association of arguments hampers the analysis of a WIG plane stability, since relative altitudes of the machine parts are measured in different dials, the modification of a pitch results in a modification of altitudes, etc. Therefore general conclusions on stability are received by methods of an analytical mechanics [5]. Reduced to the most primitive form they tell that the angle of attack focus (the point where the lift force $F_{y\alpha}$ is applied due to the angle of attack α perturbation) should be placed behind the gravity center GC as well as the height focus (Irodov' criteria [4]).

Fig. 2 illustrates conditions of the self-stabilization of a combination of two WIG profiles in tandem in a longitudinal plane. The leading profile 1 exercised an altitude perturbation (positive increment of pitch angle). The moment will be stabilizing, if

$$\partial M_z / \partial \alpha < 0, \text{ i.e.,}$$

$$(x_{F\alpha 1} - x_{GC}) \Delta F_{y\alpha 1} + (x_{Fh1} - x_{GC}) \Delta F_{yh1} + (x_{F\alpha 2} - x_{GC}) \Delta F_{y\alpha 2} < 0,$$

and, for recovery $x_{GC} - x_{F\alpha} > 0$ (this residual is called sometimes the surplus of centering).

It is not easy to satisfy these conditions at a LE glider design since simultaneously usual demands are actual for the craft

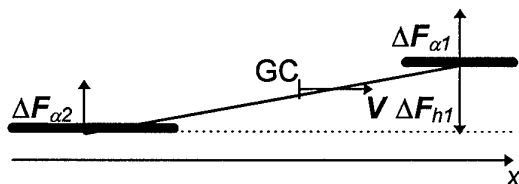


Fig.2. Resulting forces at h_1 change.

mass centering as both an airplane and a hydroplane.

The goals were achieved for known successful designs. The small Lippisch' ekranoplanes (X-112, etc.) have the reverse V-figurative wing, that allows to place a mass center near the leading edge of a wing and to use end washers of the wing as floats. These ekranoplanes and large ones, "Orlionok", "Lun", have a T-figurative tail of an airplane type but of a far larger square (about 30 % of square of the main wing at X-112, 40 % at "Orlionok", at 20% at an airplane). It is located above the operative range of the WIG-effect, therefore plays a role of a stabilizer in a longitudinal plane irrespective of an altitude. Therefore, the position of a height focus x_{Fh} , is defined by the WIG-effect of a basic wing only. Besides, an elevated horizontal stabilizer is removed away from the wake of the basic wing and the control becomes sufficiently monotonous. The surplus of a static stability in a longitudinal plane (product of horizontal stabilizer square on an arm from GC, divided by a product of square of the wing on an average aerodynamic chord) is equal to 1.3 in case "Orlionok" at about 1 at X-112 and 0.6 at airplane. The refusal from the elevated (that means, remote from a screen) tail horizontal stabilizer, will require another organ of the WIG stabilization in a longitudinal plane.

For an ekranoplane it is also important to possess the property of the self-stabilization on the roll angle. In case of an airplane it is not essential owing to sufficiency of control.

The minimal configuration on ekranoplanes, including three elements, located at vertexes of an isosceles triangle, whose axis of a symmetry is directed along the trajectory, has a property of the self-stabilization on altitude, pitch and roll angles.

4. PARAMETERS OF FLIGHT OF HEAVY EKRAPOANE AND CONTROLLABILITY

A heavy ekranoplane trajectory ought be almost rectilinear. Maneuvers as take-off or landing are also restricted. The pilot detailed control over the ekranoplane, should be entrusted to rather reliable systems AMC. The restrictions on admissible values of parameters of driving in case of an ekranoplane are more numerous, than these for another FA. It is necessary to respect a restriction on a value of lowering velocity as the excess of some limit at a limited altitude of flight cannot be compensated by action of self-stabilizing moments only.

Existence of a critical velocity of lowering can be easily seen if combine the elementary model of the WIG-effect

$$F_y = F_{y\infty} \left(1 + \left(\frac{G - F_{y\infty}}{F_{y\infty}} \right)^{\frac{y}{h_k}} \right),$$

and the equation of vertical motion. After integration with y_0 , $v(y_0)$ one can get that if $v(y_0) \leq v_*(y_0)$ (see formula1), collision will happen. If $v(y_0) > v_*(y_0)$, the falling will be suspended before a tangency of a screen and will be turned in elevation. There exist also similar limitations for angular velocities of pitch and roll.

Resources of control on a velocity, course, attack and roll that are custom in aircraft construction, are accompanied by other ones specific for ekranoplane. Among the first are maneuver by a thrust, mechanics of wings, vertical course control surfaces and fuel swapping. To second group refer

beneath blow engines and wing terminal washers. In a floating position hydrodynamic control surfaces and screws are active. The control is carried out under monitoring of an automatic tracking and traffic control system preferred before the manual control.

In lengths, comparable to a chord of a wing, the ekranoplane at a basic surface is equivalent to a thin blunt body. It is known, that a flow about a body of this class as well as damping of perturbations can be considered in scales, comparable to its thickness, though it is known also, that some effects, of jet or rotational nature are transferred on significant distances. The ekranoplane involves an air in motion. The field of induced flow is inhomogeneous: a slot jet emanates at a trailing edge from under an ekranoplane along a basic surface. It is subsonic as related to the plane, hence has even a smaller velocity to a basic surface. The slot jets expire also from under terminal washers of WIG-wing. Here the configuration of boundaries stimulates a fly-off current and twisting of jets in a rotational braid. This flow is observed at a flight of an ekranoplane. Such observations can at insufficiency of systematic data be taken into account at the judgment about perturbations, brought in an environment by an ekranoplane. The observers unanimously consider these perturbations being smaller, than expected comparing with driving of ground vehicles. However, it is known that hydrofoil ships also few revolt a water surface and air medium.

$$v_*(y) = -\sqrt{\frac{2}{M} \left[(F_{y\infty} - G)y + h_k F_{y\infty} \left(\ln \left(\frac{G - F_{y\infty}}{F_{y\infty}} \right) \right)^{-1} \left(\left(\frac{G - F_{y\infty}}{F_{y\infty}} \right)^{\frac{y}{h_k}} - 1 \right) \right]} \quad (1)$$

5. EXAMPLES OF LE DESIGN

Probably, it is better to consider separately LE designs for the ASP carrier, a launching booster and a landing means purposes. Each of them determines the general transport performances its own way. At actual premises these three functions may be overlapped.

Approximate parameters of a LE, intended for the carrier-launcher can be received, basing on the well-approved "Orlionok", in extrapolation with methods, used in aircraft construction, combining the laws of a similarity ("square-cubic") and realistic evaluations.

A glider, similar to "Orlionok", preserving a specific wing load and a surplus of static stability, would have sizes, enlarged in 3.6 times (length of 220m.), a higher cruiser velocity and smaller relative altitude of flight. However, performing the booster function by this LE, is rather hampered.

Bearing of an exterior freight of a commensurable mass changes centering of mass and aerodynamic forces. If ASP is to be placed above the GC of LE, then the normal function of the tail stabilizer will be broken, besides an essential displacement of the GC upwards will reduce a stability and self-stabilization of the integrated flying apparatus on roll angle, and also stability in sailing conditions. A displacement of ASP ahead will change normal sailing ability while backward - will reduce the surplus of centering and will displace the flight altitude focus. If to assume, that ASP will land on such LE, then the tail vertical and horizontal planes will interfere with the landing aircraft.

The use of a two-body arrangement (a^0) liberates the take-off-landing approaches

(Fig.3). It makes worse the aerodynamics, but preserves a stability in a longitudinal plane, and increases a stability on roll. It is possible, proceeding from performances of a large ekranoplane "Orlionok", to make evaluations of parameters of a booster design, combining WIG planes. The arrangement (b^0) could represent a two-fuselage frame with a fore-part stabilizer and second, a basic WIG-wing of $S_2=3000\ m^2$. Such arrangement does not provide a general self-stabilization in a longitudinal plane. In flight automatic and manual control should ensure a stability.

The arrangement (c^0) can represent a two-fuselage frame with a front basic WIG-wing $S_1=3000\ m^2$, and second WIG-wing - stabilizer $S_2=0.25\ S_1$, composed of two consoles outside the frame. At extremities of fuselages there are two tail vertical stabilizers.

The front wing has a middle longitudinal spacer, ensuring the adequate self-stabilization of the fore-part of arrangement on roll. The left- and right-hand back half-ekranoplanes ensure the sufficient self-stabilization of a back part of arrangement on a roll in view of a possible high disposition of the mass center of ASP (together with the stabilizing contribution of the aerodynamic elements of ASP). In a front part of fuselages are located power and navigational systems. The center of masses of LE (without ASP) is at the center of a forward wing. The center of masses of an integrated craft is between a center of a forward wing and its trailing edge. The fuselages possess a buoyancy and ensure centering of the LE in a sailing position. The spacers of back consoles are floats and ensure stability of an integrated apparatus in a sailing position. The glider may be classified as a sectioned flying wing.

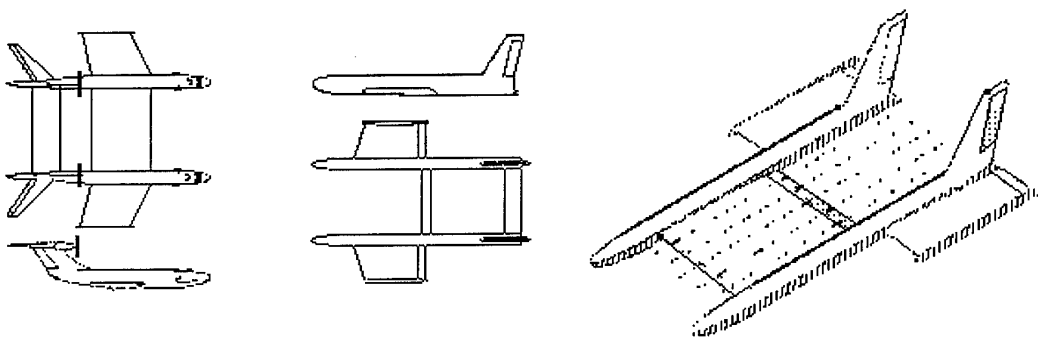


Fig.3 Arrangements of ekranoplanes

Before a take-off and after landing, the ASP, possessing an aerodynamic quality, makes the third aerodynamic element of an integrated craft. It has its own adequate lift force. It is better to bear charged ASP low above the center of mass of the LE. From here it can produce a low start. The light ASP can land on the second part of the tandem as well. At such tactics, it due to own aerodynamics, actually compensates the displacement of the GC after landing.

A partial autonomy of the main three FA parts on both the dynamics and control, is a key point of the given project. Every part, the forward WIG-wing, the back WIG-wing and the ASP (in an integrated phase), possess its own possibilities of the position stabilization, at least partial. Such approach unloads in a norm the links between elements of this massive arrangement. It erects before control systems new problems, let solvable basically, and raises on a more high level a role of a control system in this new engineering solution.

6. COMPARISON OF AERODYNAMIC PROPERTIES OF ARRANGEMENTS

Three considered arrangements meet the applicability requirements, though to various extend. Different are ways for

providing of a longitudinal stability. In cases b^0, c^0 both planes of tandems perform an altitude self-stabilization while the tail stabilizer of a^0 creates a regenerating moment in dependency on an angle of attack and is not sensitive to an altitude. Every of arrangements is capable to bear charged ASP and to ensure its start at an approaching choice of such parameters, as square of wings and potency of engines, the minimum of values of which corresponds to an optimum of a choice of arrangement.

Comparison of properties of arrangements in joint driving with ASP. The symmetry of arrangements a^0, b^0, c^0 , and a separating effect of fuselages reduce an unfavorable influence of trailing vortexes on dynamics of the carrier, therefore here it is neglected, in view of outcomes of estimations and preliminary own experiments in an aerodynamic tube. Dynamics of ASP in the excited field is still under study.

The take-off from a front part creates a favorable elevating impulse, from a back part (except a^0) an unfavorable diving impulse.

Table 1. Dynamics of LE and mounted ASP at flight

1	Aerodynamic interference	Arr-t	Charged ASP			Empty ASP		
			At front		At rear	At front		At rear
			a^0	b^0	c^0	a^0	b^0	c^0
Fore-wing		1*	-		-	x		
		2*				x		
		3*		+		x		
Rear wing		1*				x	-	
		2*	-	-	-	x		
		3*			+	x	++	
ASP ¹⁾			-	+		x	-	+
2	Displacement of GC	Hor.	+	+	+	x	-	-
		Vert.	+	+	+	x	-	-
			-		-			

¹⁾ In this line the sign "+" shows presence of adequate aerodynamics.

Various schemes of landing ASP on the mobile carrier are possible. Eventually the LE can fly under the lowering ASP. The landing on a front part creates unfavorable diving impulse while on a back part - a favorable elevating impulse.

The aerodynamic effects of a combined flight of LE with ASP are shown in the Table 1.

In this table the following labels are used:
 1 * - modification of aerodynamics of a flow about the upper surface of a wing,
 2 * - general modification of aerodynamics of a wing (f.e. in a turbulized wake),
 3 * - modification of end effects of a wing.
 The signs "+" and "-" designate the favorable and unfavorable contributions, they are doubled, if the modification is essential. An effect, comparable with a main value, is considered being essential. The unacceptable arrangement is designated with "x".

Observing the data in Table 1, it is possible to make a common inference about validity of arrangements for performing of required functions, by considering total numbers of favorable and unfavorable effects. They are (+3,-12), (+7,-8), (+11,-4), for arrangements a^0 , b^0 , c^0 , correspondingly. Obviously, the arrangement " c^0 " has indisputable advantage over arrangements " a^0 " and " b^0 " in the considered application. The given conclusion is scholastic to some extent, besides it is limited by an actual incommensurability of various "-" and "+" in these tables. Nevertheless, it can hardly be neglected, as it distincts arrangements essentially, and the amount of effects, put in a basis, is rather significant.

As an additional conclusion from the comparison we shall specify that using the arrangement " c^0 " a charged ASP is to be mounted on a front wing of an ekranoplane while an empty one is placed at any point of a centerline.

The suggested variant of the ekranoplane tandem configuration - ASP carrier can be compared to another variant of ekranoplane - catamaran (Fig.2) described in [1]. It is closer to the airplane configuration and allows to flight both in the WIG-effect action zone and outside it. However, it is possible to consider the last function which is superfluous for examined ekranoplane's application. Without tandem arrangement, this variant could be aerodynamically more favorable, but it has smaller margin of stability in comparison with variant "c⁰", and with "Orlionok" that forces to increase essentially the load to aerodynamic control elements and to increase the responsibility of automatic stabilization and damping systems up to the top. The final conclusion about advantage of any considered variants can be made only on the basis of detailed research and simulation in view of all set of essential circumstances.

7. CONCLUSION

The proper choice of arrangement of an ekranoplane can ensure its high properties: the carrying capacity and velocity. Properties are ensured of the self-stabilization of a flight altitude as well as of pitch and roll angles. Applied criteria have been proved by practice of use of large Russian ekranoplanes "Orlionok", "Lun". The self-stabilization is combined well in flight with a SAMC action which is attribute of the control circuit for ekranoplane. A heavy ekranoplane can be

a booster-carrier for ASP horizontal start and landing and do the similar operations in other fields.

REFERENCES

1. Tomita, M., Ohkami,Y., Nebylov A.V., Sokolov V.V., "The concept of heavy ekranoplane use for aerospace plane horizontal take off and landing", WIGs RINA International Conference, London, UK, 1997.
2. Tomita, M., Tsurumaru D., Saotomi T., Ohkami,Y., Nebylov A.V., Sokolov V.V., "Feasibility study of a rocked powered HLHL SSTO with ekranoplane as a take off assist", 7th AIAA International Aerospace Planes and Hypersonic Technologies and Systems Conference, Norfolk, Wa, USA, 1996.
3. Nebylov, A.V. "Measurement of Parameters of Flight close to the Sea Surface", Publication of SAAI, St. Petersburg, 1994, in Russian with summary in English.
4. Diomidov, V.B. "Automatic Control of flight of ekranoplanes", Elektropribor, SPb, Russia, 1996, in Russian.
5. Zhukov, V.I. "Peculiarities of Aerodynamics, Stability and Handling of Ekranoplanes", RINA, International Conference on WIGs. London, UK, 1997.

Conceptual bases of WIG craft building: ideas, reality and outlooks

E.A.Aframeev
 Krylov Shipbuilding Research Institute
 44, Moskovskoe Shosse
 Saint Petersburg, 196158
 Russia

SUMMARY

WIG craft (ekranoplans) building has sufficiently long history but till now there is no any established view on their technical appearance and place in the system of transport means. It was assumed that technical and economical characteristics of WIG craft wittingly exceeded those of competitive transport means - aircraft (and hydroaeroplanes) because of the high lift-to-drag ratio value (aerodynamic efficiency). However in reality they don't a priori provide the superiority over the aircraft (hydroaeroplanes). Now it is necessary to revise the conceptual base of WIG craft building.

The idea of creation of second generation ekranoplans on the base of the A-conception, suggested by the author in 1977, assumes that they are created as marine transport means with high ship features when sailing (air transport means, including hydroaeroplanes, doesn't possess such features), i. e. as two-mode vehicles.

Realization of this conception puts the ekranoplans out of competition as compared with other classes of engineering in the cases when it is necessary to stay at sea for a long time. At the same time such ekranoplans have the incomparably high level of safety when using for the transportation of passengers and cargo.

In the near-term future the sphere of WIG craft application can be significantly expanded and include not only the transportation but such important missions as the creation of global sea rescue system or sea launch of space vehicles. In the more remote future it may be possible to realize the trans-ocean transportation, however this mission requires the creation of superheavy ekranoplans what in turn requires the solution of some complicated technical problems.

LIST OF SYMBOLS

M	total takeoff weight
Mhl	weight of hull
Mw	weight of wings
Mh	weight of horizontal empennage
Mv	weight of vertical empennage
P	weight of payload
F	weight of fuel
E	weight of power plant
T	adjusting engines thrust
H	ground clearance
b	middle chord of wing
S	total surface of construction
Sw	horizontal projection of surface of wings
L	range
Kmax	max lift-to-drag ratio (flight)
Kmin c	min lift-to-drag ratio in calm sea (takeoff)
Kmin r	min lift-to-drag ratio in rough sea (takeoff)
h3%	3% provision wave height
v	takeoff acceleration

1. INTRODUCTION

The appearance of the new type of transport means - ekranoplans - can be considered as the natural consequence of intensive and accelerating process of humanity development of sea and ocean space.

By now the ekranoplans building has sufficiently long history, large amount of R&D works has been carried out. In essence, all main scientific-technical problems in the spheres of hydro- and aerodynamics, strength, power plants, building technology, special equipment have been solved. However in spite of this even the specialists have no clear view of the ideas which must serve as a basis for creation of ekranoplans, their rational technical appearance and the perspectives of introduction into the system of transport means. In many respects it is explained with unsufficient experience of their practical realization and operation,

which is limited with solitary examples of large ekranoplans application in Russian Navy and some small ones in other countries.

Meanwhile the important qualitative conclusions can be made from the available R&D and design works, experience of ekranoplans creation and operation. These conclusions will allow to outline the conceptual base for ekranoplans building for the present time and more remote future: the aims of the creation, technical appearance, ways of practical introduction into the system of transport means.

The complex works in the sphere of future ekranoplans were carried out in Russia in 1970-1980 at Krylov Shipbuilding Research Institute under the guidance of the author with participation of design and research organizations of shipbuilding and aircraft industries. In the process of these works the author suggested and grounded the idea of the transition to the creation of the second generation ekranoplans with high ship features. The proper author's conception (A-conception) of two-mode ekranoplans was developed. Later on the subsequent R&D of the second generation ekranoplans and the transport system on their base were carried out [1].

The fundamental theses of the above stated author's conception are presented in this paper on the base of the analysis of real experience of creation and operation of the available ekranoplans and development of perspective ones. The suggestions concerning the development of ekranoplans and their immediate practical application are stated.

In accordance with the author's classification the ekranoplans are divided into superlight (takeoff weight up to several tons), light (up to several tens of tons), middle (up to 100-500 tons), heavy (up to 800-1500 tons) and superheavy (up to several thousands of tons). The principal theses of this paper are dedicated to the middle and large ekranoplans, however in many respects they are correct for the lighter ones too.

2. THE IDEAS

Now as before the ekranoplans building needs the ideas determining the technical appearance of the ekranoplans and the spheres of their application.

Aspiration for reaching the high lift-to-drag ratio (aerodynamic efficiency) of ekranoplan wings owing to its movement near the underlying surface was, as it is well known, a pioneer technical idea, starting the appearance of the ekranoplans. It was assumed that high aerodynamic efficiency would provide the advantage of the ekranoplans even over the air transport means in respect of such features as thrust-to-weight ratio and fuel consumption, i. e. eventually in respect of the economical efficiency.

In the majority of the countries developing the ekranoplans this idea is considered now so important that their arrangement, in essence, provides only the aspiration for reaching as high aerodynamic efficiency as possible to the detriment of providing some other necessary features. Such particular approach can be considered as appropriate one for the development and experimental stages of research when the aims of ekranoplans practical introduction into the system of transport means are not so urgent. However on the stages of practical realization of the ekranoplans the more detailed consideration of all diversity of the factors connected with both the creation of the ekranoplans (parameters of structure materials, the engines for the power plant, technology of building and so on) and their operation (tasks, conditions of sailing and basing, economical factors of the operation and so on) is necessary.

Unfortunately, in the most of investigations carried out the impact of the real factors of creation and operation of the ekranoplans upon their technical appearance isn't taken into account properly. The design is unsufficiently attended with economical research which moreover are excessively general and rough.

As regards the ideas connected with the spheres of ekranoplans applications it is necessary to say that they aren't very diverse. As a rule, the use as the passenger transport mean in civilian sphere or for the troops and armament transportation, in particular, the forces of quick deployment in military one are considered. The lack of widespread view on the modern and future needs of mankind in marine means doesn't allow to determine the requirements upon the technical

appearance of the ekranoplans and to evaluate their real potentialities.

The development of the ekranoplans in Russia was carried out on the order of the Navy and the further increase of the speed of marine combat means compared with that achieved for the hydrofoils and air cushion vehicles was the main idea. This idea was confirmed with the considerations of low detectability of the ekranoplans owing to the small altitude of flight, quick dispersing from their bases in a threat period, facilitation of the basing problems at the expense of their amphibious properties and so on. In connection with the specific formulation of the problem of the realization of the ekranoplans in Russia most attention has been concentrated on the problems of their practical building and operation, but the aspiration for increasing the lift-to-drag ratio value in every possible way and for exceeding this parameter as compared with aircraft also made the foundation for determining the arrangement of the vehicles.

Unfortunately, the idea of the creation of the ekranoplans as marine means aimed to the prolonged presence in sea and ocean space (and correspondingly with high values of seakeeping) wasn't the key one in Russia too. One of the consequences of such approach was the transition from the designing of the ekranoplans of large weight (the takeoff weight of ab. 450 tons was achieved on the full-scale ekranoplan KM) to the creation of relatively small ones (the ekranoplan "Orlyonok" with takeoff weight of ab. 110 tons). Such transition must be recognized as a mistake with respect to the strategic line of the progress.

The ideas of civil use of the ekranoplans in Russia were in the background for a long time. Nevertheless the practical realization of the ekranoplans in Russia in many respects promoted the development of this new class of the engineering as a whole.

3. THE REALITY

The creation and operation of the ekranoplans in reality allowed to solve some new technical problems and also revealed their strong and weak aspects.

3.1. The principal achievements

- The possibility of flying near the underlaying surface with high

aerodynamic efficiency has been proved in practice.

- The idea of using the engines stream blowing under the lifting surfaces for the considerable increase of the hydrodynamic efficiency when taking off has been developed and realized.
- The possibility of providing the amphibious properties of the ekranoplans for landing on the not-fitted shore and going out of it with the use of blowing has been proved.
- Higher safety of the ekranoplans as compared to the aircraft owing to the possibility of emergency landing on water has been confirmed actually.

3.2. Main shortcomings

- The superiority over the aircraft (hydroaeroplanes) in respect of the aerodynamic efficiency hasn't been achieved in real conditions of the operation.
- The relative level of seaworthiness in respect of takeoff and landing doesn't essentially exceed that of the modern hydroaeroplanes.
- The use of blowing leads to the complication of power plant construction, additional weight expending, reducing of aerodynamic efficiency and the stability of the flight.
- The use of amphibious properties is advisable only for the light ekranoplans, at the same time the loss of the payload is considerable.
- The complicity of the control of the ekranoplans takeoff, particularly at rough sea, the necessity for qualified pilot team and their constant training.
- The need for new avionic systems, in particular, the sensors of low altitude of the flight, automatic pilot of takeoff-landing taking account of the sea surface state; navigation systems of obstacles detection (including low-detectable ones) and so on.
- The aerodynamic "aircraft" arrangement which is used now has no prospects.

3.3. The aerodynamic efficiency

The aerodynamic efficiency achieved for the ekranoplans in conditions of calm sea is at the same level as for the modern heavy aircraft. In the case of the higher altitude of the flight (for example, because of rough sea) the aerodynamic efficiency will be considerably

lower [Fig1]. The range considerably decreases too [Fig2].

The use of blowing when taking off in conditions of calm and rough sea allows to achieve the high values of hydrodynamic efficiency which are not lower than that for the modern hydroaeroplanes [Fig3].

As a whole, for the first generation ekranoplans with "aircraft" arrangement the forced reduction of wing lengthening because of the use of blowing in a great extent levels the effect achieved owing to the "ground" effect. The deviation from the optimal parameters of the lifting surfaces and the restricted possibilities of wing mechanization decrease the competitiveness of the ekranoplans as against the aircraft in respect of aerodynamic efficiency.

3.4. Seakeeping

The seakeeping of the ekranoplans is determined with the height of the waves allowing their takeoff and landing. In spite of the use of blowing the level of ekranoplans seakeeping is essentially the same as that of the modern hydroaeroplanes using the powerful wing mechanization when taking off [Fig3].

3.5. The problems of weight perfection

3.5.1. The level of weight perfection

The level of weight perfection of the ekranoplans is determined with their full weight efficiency showing the share of possible payload (i. e. the sum of load and fuel) in the total weight of the vehicle.

It is advisable to compare the full weight efficiency of the available first generation middle ekranoplans having the takeoff weight up to 450 tons and the perspective second generation heavy ekranoplans having the weight of 700-800 tons with that of the heavy aircraft. The full weight efficiency of the first generation ekranoplans is a several times smaller as compared with the aircraft and the competitive parameters are achieved only for the second generation heavy ekranoplans [Fig4].

The analysis of the relative weight of the main glider units for the ekranoplans and aircraft shows that their empennage weight are equal to each other and the weight of the hull and wings of the ekranoplans is considerably greater than that of the aircraft [Fig5].

3.5.2. The potentialities of the optimization

The comparison of the ekranoplans and the aircraft in respect of the "weight efficiency" - the specific index of the weight of unit square of surface of the construction - shows that the ekranoplans and aircraft constructions have the same level of perfection [Fig6].

The potentialities of the weight optimization of the ekranoplans consist in the selection of rational arrangement (for example, including the hull into the lifting surfaces analogically to the aircraft of "flying wing" type) or increase the loads on the wing. The characteristic feature of the ekranoplans is the small loads on the wing [Fig7], i. e. there are some reserves in respect of the weight perfection, but the increase of these loads is restricted with the difficulty of mechanization of low-arranged wings.

As a whole, in spite of some available reserves of the weight optimization it should be considered that the weight perfection of the ekranoplans would be not higher than that for the aircraft because of the contacts of their construction assemblies with the water when taking off and landing.

3.6. The problems of the power plant

As a rule, the power plant of the ekranoplans are completed with converted aircraft engines, i. e. they aren't optimized for the permanent work at low altitudes. It is necessary to place the engines in the bow of the ekranoplan with sufficient advancement before the wing for providing the effective blowing. Such arrangement leads to the increase of hull dimensions, the appearance of massive pylon carrying the engines, difficulties in vehicle centering, danger of engines flooding when sailing and taking off and so on. The special equipment for the deflection of the engines streams under the wing or for turning the engines as a whole is also required what complicates and increases the weight of the power plant. The above stated has a negative effect on the parameters of the aerodynamic and weight perfection of the ekranoplans.

3.6.1. Thrust-to-weight ratio

The total thrust-to-weight ratio of the ekranoplans representing the specific value of required adjusting engines thrust is sufficiently similar to that of the heavy aircraft because of using the takeoff with

blowing [Fig8]. It seems impossible to decrease the thrust-to-weight ratio essentially because it leads to the delay of the takeoff and to increasing of construction loads.

3.6.2. Fuel efficiency

Fuel efficiency is characterized with fuel consumption for the transportation of payload unit for the distance unit. Fuel efficiency for the first generation ekranoplans is essentially lower than that for the aircraft [Fig9]. Fuel efficiency for the second generation ekranoplans may be equal to that for the aircraft because of simultaneous increase of weight efficiency and more effective use of the "ground" effect.

3.6.3. Potentialities of the optimization

The optimization of the power plant may be realized owing to the rational selection of the engines type and combination of blowing and march systems. The potentialities of the optimization are available, but are restricted, what may be illustrated with the fact of the impact of the engines type and different blowing schemes upon the power plant weight and flight range when providing the equal takeoff accelerations [Fig10].

3.7. The economic factors

The results of economic investigations carried out as applied to some specific lines of operation of the various types of the ekranoplans in wide range of takeoff weight (up to superheavy ones with the weight of ab. 2700 tons on the transoceanic routes) show that there is no success in providing their a priori superiority in respect of the transportation cost as compared with air transport means, and in some cases, with the other classes of high-speed water transport means too.

From the other side, it should be not expected that the cost of the creation and operation of the ekranoplans would be considerably higher than that for aviation means.

Depending upon the specific conditions of operation, length of the lines, value and constancy of passengers and cargo traffic, availability of the other transport means, possibilities of creation of the required infrastructure and service and so on, the use of the ekranoplans can be turn out profitable or not competitive.

The economic analysis of the profitability of the ekranoplans always has to precede not only the approving of their creation, but the determination of main parameters of their technical appearance as applied to the specific missions and operation areas.

3.8. The military factor

The military use of the first and second generations ekranoplans seems to be not advisable. The military-economic investigations show that raising of naval forces efficiency is achieved only in the case of large-scale building of the ekranoplans and their considerable amount in the Navy.

Taking into account the armament available in developed countries one can say than the combat systems on the base of the ekranoplans are redundant (especially as such systems don't exclude the need in other classes of the armament). Application of superheavy ekranoplans for the forces of quick deployment is difficult to realize in connection with the technical reasons which will be said about below.

As a whole, the military factor as an incentive of ekranoplans building development must be excluded.

4. THE PROSPECTS

Thus the ekranoplans have no a priori and considerable advantages over such classes of high-speed transport means as aircraft or hydroaeroplane in respect of neither the parameters of technical perfection nor economic efficiency. Nevertheless they have good prospects. There is no alternative for them in the sphere of high-speed marine transport means for the expanding ocean operation areas.

4.1. The need for the change of the fundamental conception

From the above stated it follows that the pioneer technical idea of achieving the ekranoplans advantages owing to the high value of aerodynamic efficiency can't be determinative for their practical realization. The basic ideas for the perspective ekranoplans must be found not in the sphere of competition with aircraft or hydroaeroplanes in respect of aerodynamic efficiency. The ekranoplans created up to now essentially as the kind of aviation engineering can't win in a competition with

the representatives of this kind of engineering.

From the other side, the idea of the creation of the ekranoplans as the kind of especially marine engineering opens the wide possibilities in connection with the following reasons:

- all types of the ships moving in direct contact with water surface have the rigid restrictions of their technical characteristics, which don't allow to create the transport means with the speed more than 130-150 km/hour providing the quick transportation at a great distance away from the point of departure,
- aviation transport means having great speed and range of the flight can't fulfil all necessary missions at sea. It concerns the hydroaeroplanes too, which are to a great extent arranged for carrying out the marine tasks, but their main operation mode nevertheless is the flight far from the sea surface and the ship features are provided to a minimum extent.

Thus there is a technical recess between the high-speed craft and hydroaeroplanes (aircraft) for the means having, from one side, high values of ship features and from the other side, the speed common to the aircraft. The ekranoplans must be exactly such means. They can be realized as the kind of the engineering only if they have the specific features which other kinds of transport doesn't possess or which considerably distinguish them when operating.

4.2. A-conception of the ekranoplans technical appearance

The essence of A-conception of the ekranoplans technical appearance suggested by the author for the advanced development is formulated as follows:

- the ekranoplans must be the marine means having two equivalent operation modes;
- the mode of sailing providing all spectrum of ship features,
- the mode of flying in proximity to free water surface in the zone of the positive influence of the supporting surface on their aerodynamic characteristics.

The pointed order of accents placing isn't accidental. The flying mode remains as a main transport mode of the ekranoplans

operation, however, the problem of high value of the aerodynamic efficiency is moved to the background as compared to the problem of ship features providing. Thus the foundation of the conception is the provision of two modes of ekranoplans operation - above the sea surface similar to ships and in the flight similar to aircraft.

Two-mode operation which is not common to the first generation ekranoplans must be the basic sign, determining the transition to the new generation in the ekranoplans building.

As the result of two-mode operation, the level of the safety for passengers and cargo will be cardinally increased and become incomparably greater than that of aircraft transport means.

The conception of the second generation ekranoplans as two-mode transport means logically determines all their construction parameters. In accordance with the conception the ekranoplans when sailing are bound to have the high level of such characteristics as floatage, stability, unsinkability, seaworthiness and controllability.

The floatage, stability and unsinkability of the ekranoplans are bound to correspond the requirements being imposed upon the ships and warships. Because of this it is necessary to use hull shapes and the other technologies providing the pointed features which are traditional for the shipbuilding taking into account the high speed of ekranoplans takeoff and landing.

The seaworthiness and controllability of the ekranoplans must provide them the possibility of any required manoeuvres at the sea surface and the movement in accordance with preset heading for a long time in wind and rough sea conditions, and their power plant must provide them the ability to arrive, if necessary, in the sailing mode to the port-shelter from any point of operation area (in particular, in the case of impossibility of further flight because of rough sea, icing, fault of equipment and so on). From this it follows that it is necessary to include the ship-borne engines in the composition of the ekranoplans power plant and to use hydrodynamic propulsors and steering gears.

The demand of sailing for a long time leads to corresponding arrangement of the hull, power plant, lifting surfaces and flight control systems which ought to be dry, not damaging with the waves and floating objects, not exposing to corrosion and so on.

After fulfilling the conditions of sailing in the process of ekranoplans designing all measures must be taken for increasing of their flight characteristics, including the aerodynamic efficiency, owing to the "ground" effect. At the same time the requirements of efficient takeoff and landing must be considered.

The above stated determines the solutions concerning the aerodynamic arrangement of the hull and lifting surfaces, power plant and the takeoff and landing systems, in particular, the transition to the "compound wing" arrangement of the lifting surfaces for the second generation ekranoplans.

The approving of the stated conception gives the ekranoplans so specific qualities that they in truth become the new marine transport means, differing from the analogues with its technical appearance, performance, areas of application and so on. The ekranoplans safety level will be incomparably greater than that of other types of aircraft.

The conception of two-mode operation is suitable at one or another extent to all classes of the ekranoplans, from superlight till superheavy ones (in spite of the possibility of the latter to have the advantages over the aircraft in respect of the aerodynamic efficiency).

4.3. The next step in the development of the ekranoplans

It is obvious that all classes of the ekranoplans will be developed and improved. It is also obvious that they will not replace the other types of high speed marine craft and aircraft (hydroaeroplanes) even in the future, but will be the addition to the available transport means. Having the possibility of two-mode operation superlight ekranoplans will occupy the technical receipt between small boats and small hydroaeroplanes, light and middle ones – between the other types of high speed craft and hydroaeroplanes up to the largest ones, heavy ekranoplans will represent the class of high speed marine transport means which have no real fleet and aviation analogues, superheavy ones will be,

probably, the single type of high speed transport means of so great weight using above the water surface. The ekranoplans will be applied in the spheres requiring the quick transportation of passengers and cargo along the water areas when it isn't advisable or unprofitable to use the aircraft or hydroaeroplanes, sailing for a long time (including the sailing in conditions of rough sea), fulfillment of various works on the sea surface; superheavy ekranoplans will be applied for transoceanic transportation of passengers and cargo with high level of comfort and safety, transportation of large-sized cargo and so on.

It is obvious that the greatest potentialities of the ekranoplans building are in the sphere of large vehicles in full measure realizing the possibilities of two-mode operation in conditions of rough sea and saving no rivals among the transport means. Therefore in the course of ekranoplans development it is necessary to aim at the realization of the vehicles of as great as possible weight what is really possible at the present level of aircraft and ship power engineering, construction materials, instrument – building, building technology and so on.

The next step in the ekranoplans building development at the present level of engineering will be the creation of the heavy ekranoplans with the takeoff weight of 700-800 tons, what is practically can be realized just now. As it is evident from the illustrations of the previous part, the basic technical characteristics of such ekranoplans already will be at the level of those of the heavy aircraft.

As the result of the above mentioned complex works carried out in 1970-1980 years the completely technically grounded design of the 750 tons ekranoplans is available in Krylov Shipbuilding Research Institute. The share of the payload and fuel reserves for this ekranoplans is about 250-300 tons, what provides the range of operation up to 3000 – 4000 km. The takeoff, landing and cruising flight are possible at sea states not less than 5 balls (waves height of 3% ensuring up to 3,5 m). The speed of the flight – 400-450 km/h, the sailing speed – ab. 25 km/h. The ekranoplans fully complies with the requirements of two-mode operation providing both the sailing for a long time in conditions of rough sea and the returning to

the port – shelter from any point of its operation area in the sailing mode driving with the diesel engines of low speed.

Because of hight technical characteristics of the heavy ekranoplans the sphere of these application is wide. For example, it may be the commercial passenger and cargo transportation (including the use as a car – passanger ferry), patrol – guard duties (including the constant duty in the economical zones), rescue operations, tourism and so on. It seems' unquestionable that with the advent of heavy two-mode ekranoplans another, not mentioned above spheres of their application will be determined.

The real creation of such ekranoplans will be the important event in the development of marine transport means and will allow the marking to solve some problems which were difficult to solve before.

4.4. Creation of global international sea rescue system based on the heavy ekranoplans is the challenge for the international community

The challenge of the effective rescue of people and technical facilities in the case of disaster at sea is one of the burning world problems. It connects with total considerable intensification of mankind activity on the world ocean areas, growth of passenger and cargo shipping traffics (in particular, the oil and chemical product), wide air transportation over the seas and oceans, fishing development, intensive developing of marine zones of minerals resources extraction.

As estimated, about 1200-1300 lives are lost aboard the sea-going ships and about 400 ships with total capacity of about 1,5 million register tons are lost annually. Financial losses of ships-owners caused only with the loss of the ships are equal to 1-2 billion dollars, the losses of consignee are not less. Disasters and losses of the ships transporting the oil or oil-chemical products lead to hard ecological consequences.

However in spite of the above stated some kind of integral international rescue systems which can render emergency aid in catastrophes at sea is absent till now. Primarily it is connected with the lack of the transport means which can quicly arrive to

the point of emergency. Experience has proven that the use of aircraft or hydroaeroplanes doesn't solve all problems connected with the rescue and is often unefficient in unfavorable hydrometeorological conditions, because of some accident-related reasons or because of their own limited capabilities. The use of helicopters is limited to coastal areas. The ships and vehicles that happen to be near accident sites remain the main rescue means as before. However, most of them don't have the special rescue equipment and is little suited for rescue operations.

The use of above mentioned heavy two-mode second generation ekranoplans with weight of 750 tons provides the basis for effective marine rescue system organization. Such global international rescue systems should be intended to rescue crews and passengers of ships,submarines and aircraft, personnel of oil drilling platforms and other technical facilities at sea and technical facilities themselves and render emergency aid in environmental catastrophes at sea.

It should be emphasized that the effective rescue may be carried out if two components are available: quick notification about the catastrophe and quick arriving of the rescue means to the point of distress.

Now the international community already use the COSPAS-SARSAT satellite communication and navigation system created by Russia, the United States, Canada and France for rescue operations at sea. This system is being intensively modernized for providing the immediate reception of distress signals and information about the emergency object location, circumstances of accidents and weather conditions in the area of the accident.

The ekranoplans – rescuer, designed by Krylov Shipbuilding Research Institute on the base of above mentioned heavy ekranoplan with weight of 750 tons, may be the second component of the rescue system. This vehicle can quickly deliver the wide range of rescue equipment, from rafts and motor boats to a boom defense ship, a bathyscaph and a helicopter, to an accident site. Owing to the possibility of two-mode operation such ekranoplan can sail and manoeuvre at sea for a long time even in conditions of very rough sea and rescue the people and render the aid

in rescue of emergency technical facilities by means of transportation the repair teams and special equipment or even towing the emergency vehicle to the port-shelter. On board of the ekranoplans-resquer disaster victims are provided with necessary conditions of living and can receive any medical aid.

The use of such ekranoplan in the case of environmental catastrophes at sea allows to localize the disaster area quickly and deliver the emergency teams and special equipment there, in particular, for restriction of oil flood and areas of pollution.

As a whole, the rescue system may consist of 12 bases at ports in the Far East, SouthEast Asia, Africa, Europe and North and South America, where 50 heavy-class ekranoplans will be stationed (3-4 units per each base [Fig11]). The zone of ekranoplans operation will enable the global rescue system to cover all areas of world shipping, fishing, oil extraction and so on [Fig12].

According to the preliminary estimations, the total cost of creation of 50 ekranoplanes and the infrastructure of the rescue system will be of 10 billion dollars, what is quite affordable for the international community.

For the purpose of gradual development of the resque system and investments its creation may be started from the organization of 2-3 ports and building of 8-10 heavy ekranoplans. A cut in expenditure can be achieved at the expense of using of the exsisting ports, ekranoplans constant basing at the floating terminals and so on.

The author of this paper suggests to begin the practical realization of the global international rescue system just now. The efforts in the development of heavy two-mode rescue ekranoplan, building and operation the series of them and the system as a whole can be joined within the framework of an international consortium of the shipbuilding and aircraft companies and with the financial support of the project by all countries interested in rescue at the sea.

The creation of suggested system really may become the "design of century".

4.5. The remote prospects

Besides the expanding of ekranoplans applications in the commonplace spheres the remove prospects of their practical use are connected with the further including of ocean space into the sphere of versatile man's activity. Such activity will require the availability of high-speed means capable both to transport the considerable amounts of persons and cargo and carry out the various works in the distance from the shore.

As an example we refer to ekranoplan use as the boosters for the air-space vehicles with horisontal launch. This kind of sea launch make it possible to impart the certain initial speed to the air-space vehicle and thus decrease its launch weight. In addition, sea launch system using the ekranoplans allows the launch from the equatorial latitudes what also descreases the launch weight of space vehicles; launching of space vehicles from the ekranoplanes in the distance from the shore essentially eliminates the hazardous influence upon the environment.

The analyses shows that the space systems with sea launch can be created even on the base of heavy-class ekranoplans and such problem may be raised just now.

At present it seems to be enough justified that building of superheavy-class ekranoplanes with takeoff weight of 3-5 thousands tons is the ultimate aim of their creating because they will be capable to carry out transoceanic transportation of passengers and cargo and provide the main needs of mankind in the high speed means for working in the open seas and oceans.

However the creation of such ekranoplanes is real only in the remote future.

The estimations and analysis of superheavy ekranoplan show that in principle, it is possible to create them on the base of the available construction materials and prospective conventional and nuclear power plants. Therewith the use of nuclear power plants is more preferable in respect of their weight and dimensions because during the service life of the reactor's cores the essentially unlimited endurance is provided with the same cargo-capacity. The demands of environmental safety of operation of so great hight-speed transport means are met if the nuclear power plant is functioning

normally. The state-of-the-art scientific and technical level make it possible to start the real development of such power plants just now, but its complication and high cost don't allow to put it on the agenda.

It is possible that the further development of superheavy ekranoplans may lead to the encouraging results in respect of its real creation. For example, the hopeful future of creation of efficient and safe power plants for them is connected with using of hydrogen as a fuel for gas-turbine engine. From technical point of view it is possible to start the development of such conception just now.

5. CONCLUSION

It is obvious that the stages of ekranoplans building development will be corresponded with the total level of world engineering and economy and will be determined by real needs of mankind in high-speed marine

transport means. Now it can be said with assurance that the ekranoplans inevitably will be a part of the total system of marine transport means and the technical feasibility of the ekranoplanes of all classes is sufficiently clear.

REFERENCES

1. Aframeev, E.A., "Will the WIG Craft Become Transport of the Future?", in "Navy and Shipbuilding Nowadays", Krylov Shipbuilding Research Institute, International Conference Proceedings, February 1996, ppA1-22-1-A-1-22-6.
2. Aframeev, E.A., "Heavy-class Ekranoplans to Make up Global Rescue System at Sea", J. Military Parade, №4(28), July-August 1998, pp93-95

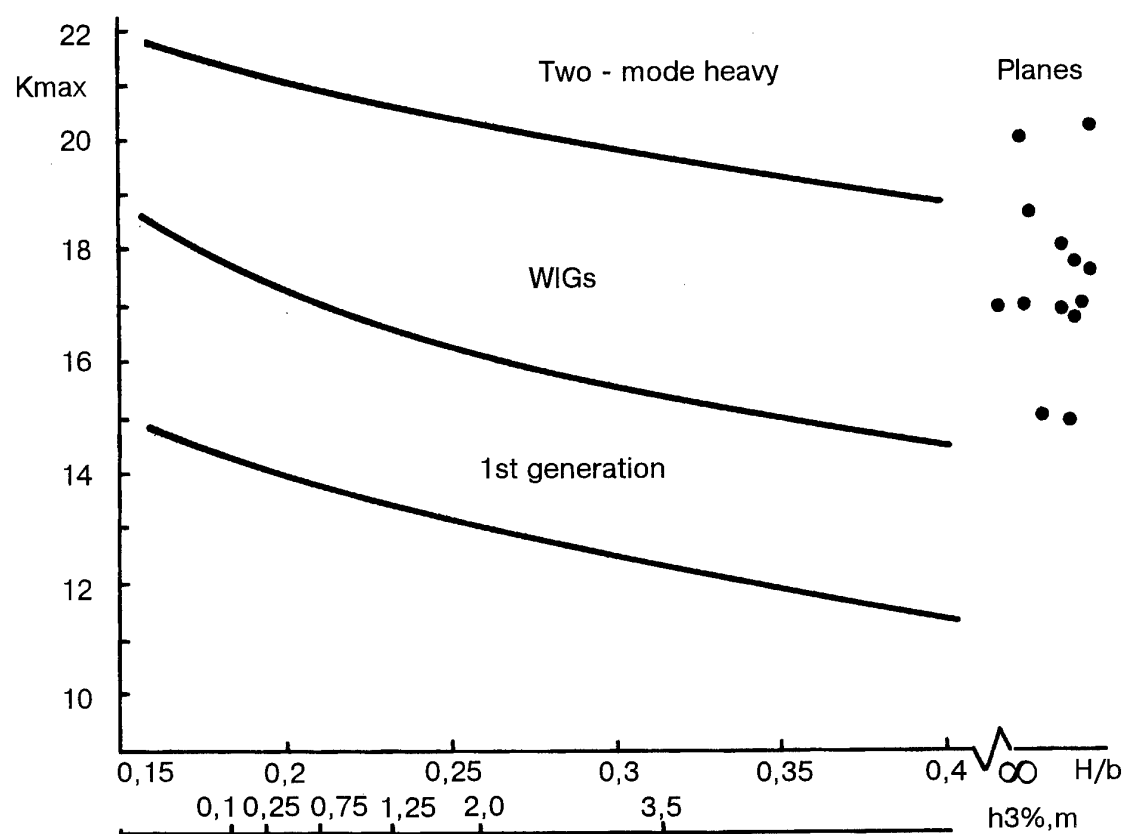


Fig 1. Flight lift-to-drag ratio of WIGs and planes.

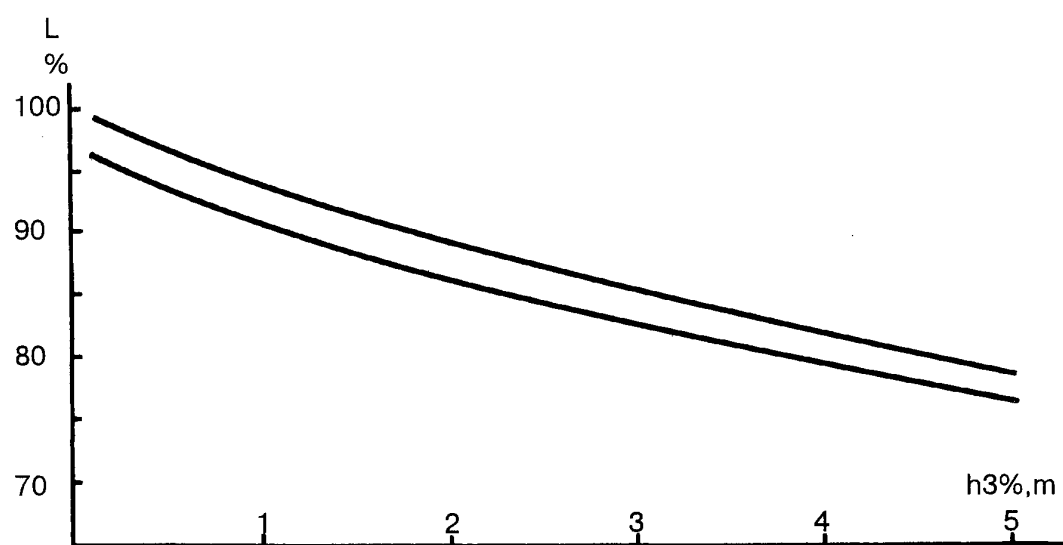


Fig 2. Influence of waves upon flight range of WIGs.

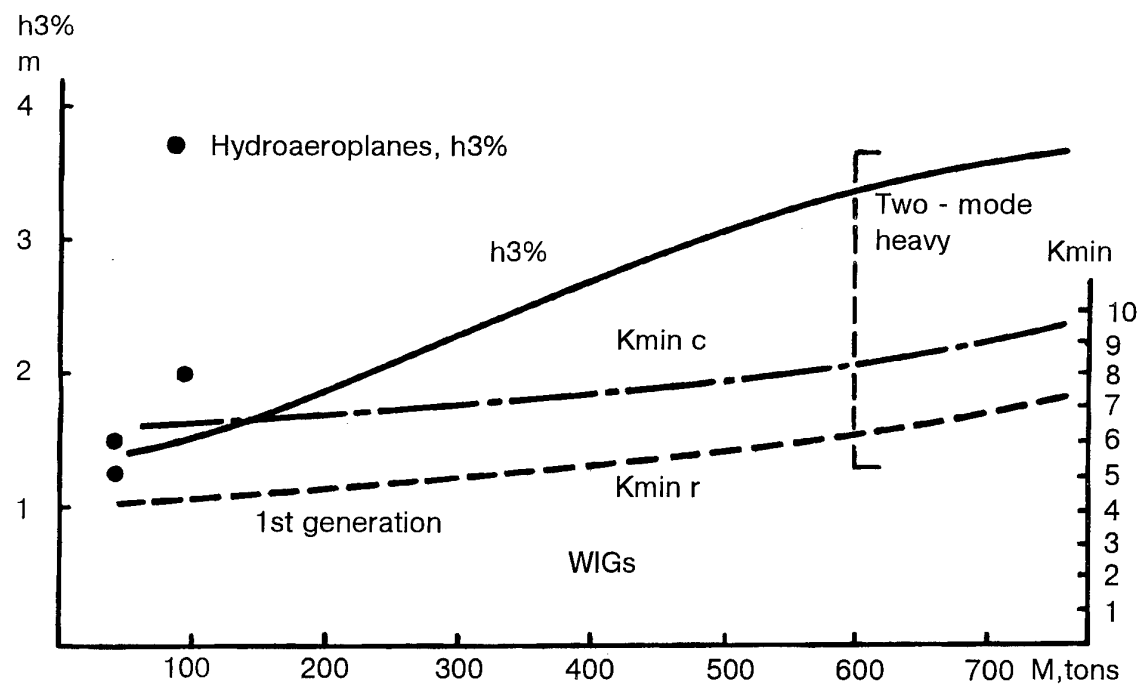


Fig 3. Seaworthiness and takeoff lift-to-drag ratio of WIGs.

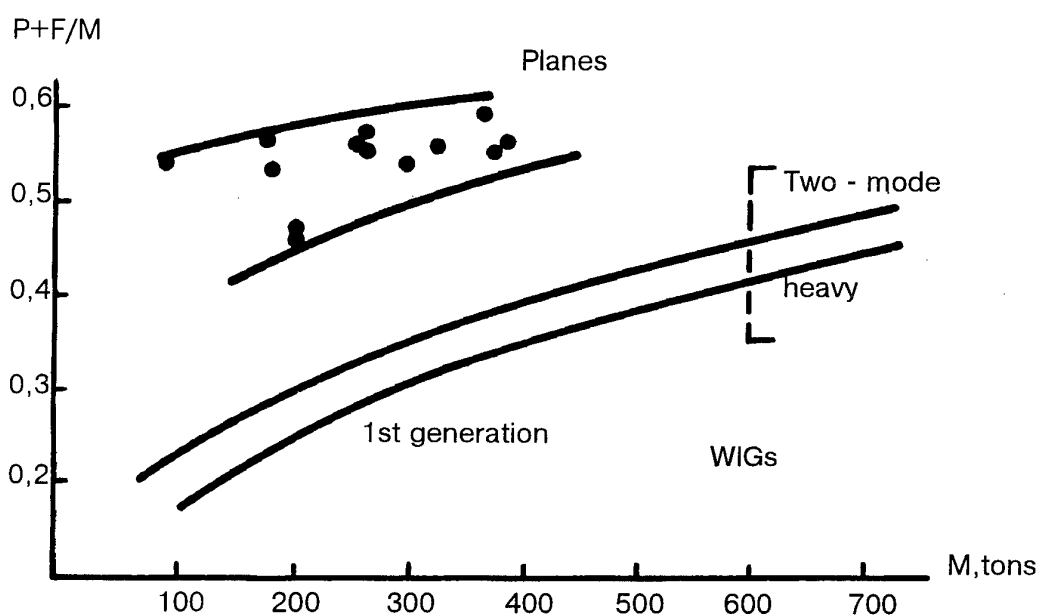


Fig 4. Full weight efficiency of WIGs and planes

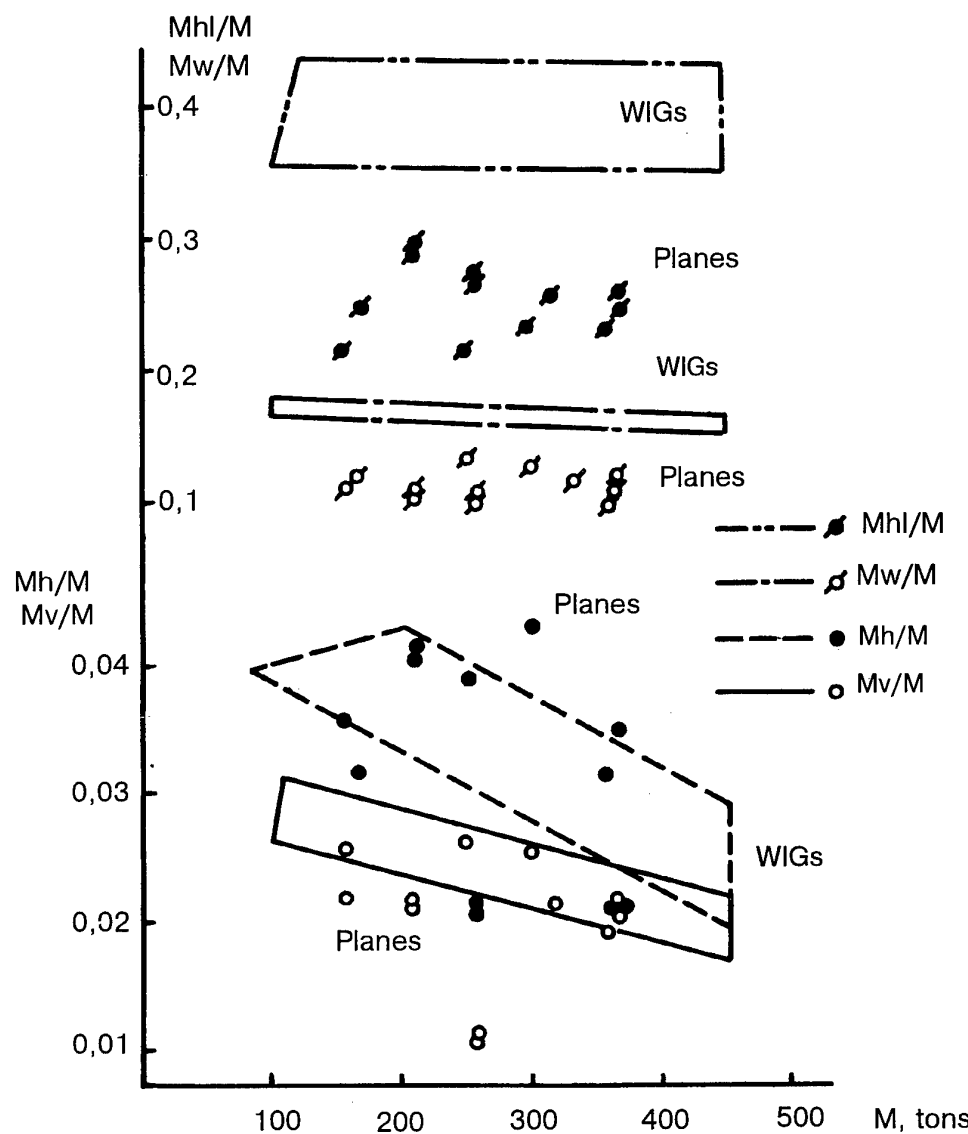


Fig. 5. Main weight components of construction of WIGs and planes.

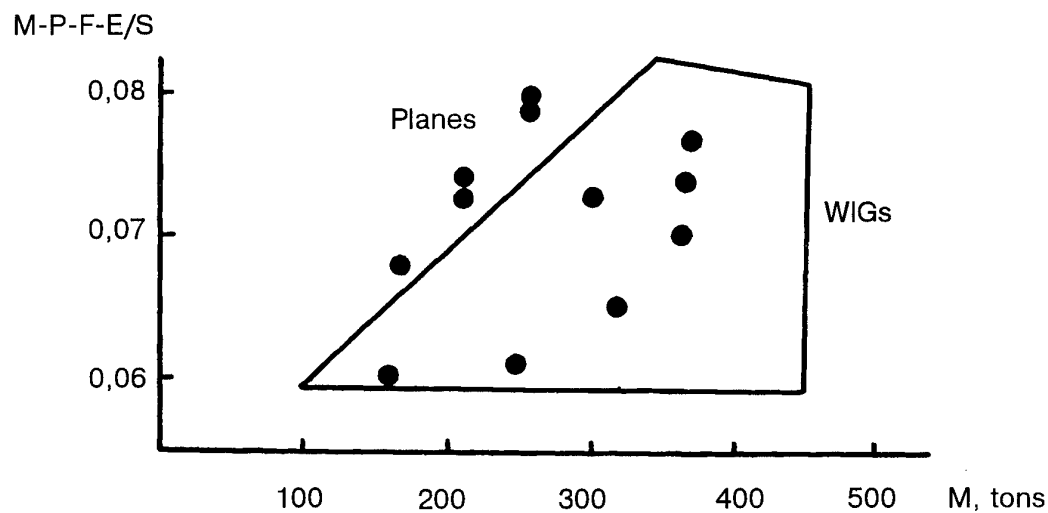


Fig. 6. Weight-to-surface ratio of construction of WIGs and planes.

Mw/M

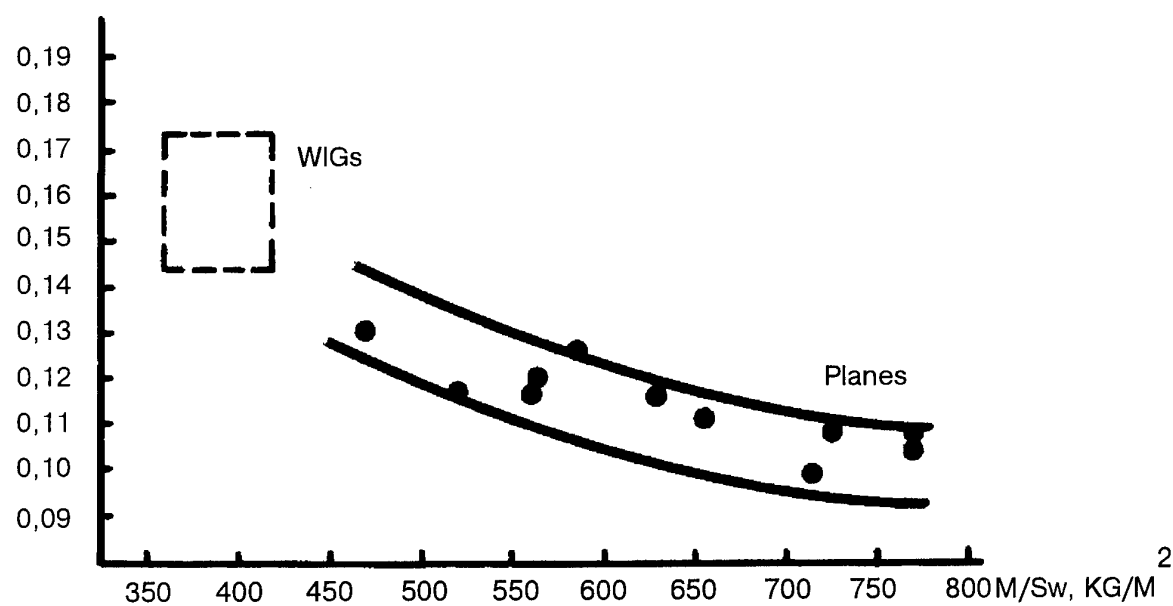


Fig 7. Influence of wing load upon weight of wings of WIGs and planes.

T/M

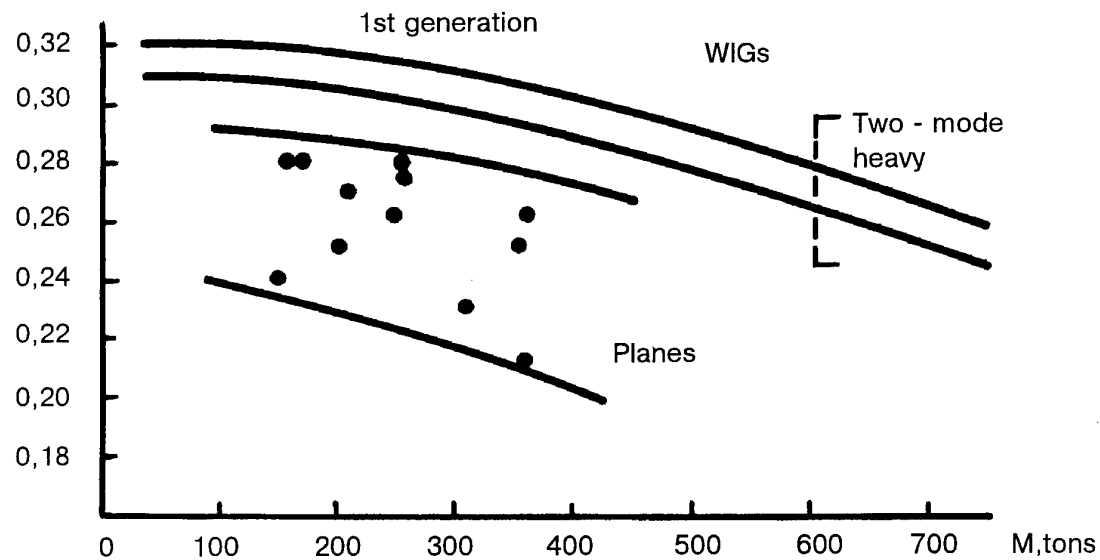


Fig 8. Thrust-to-weight ratio of WIGs and planes.

F/P·L, KG/t·km

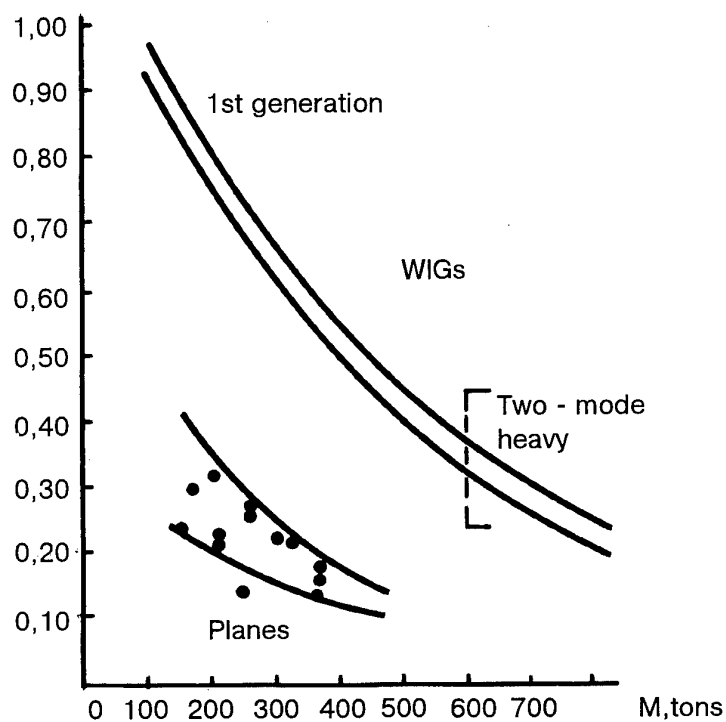


Fig 9. Fuel efficiency of WIGs and planes

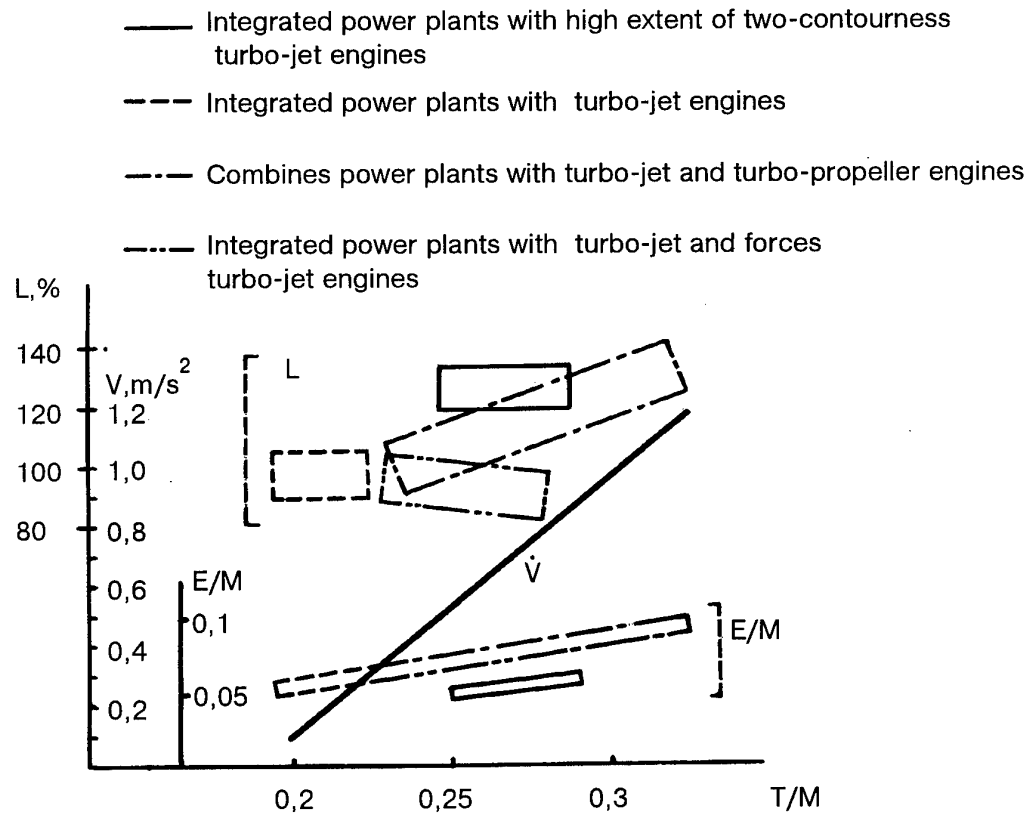
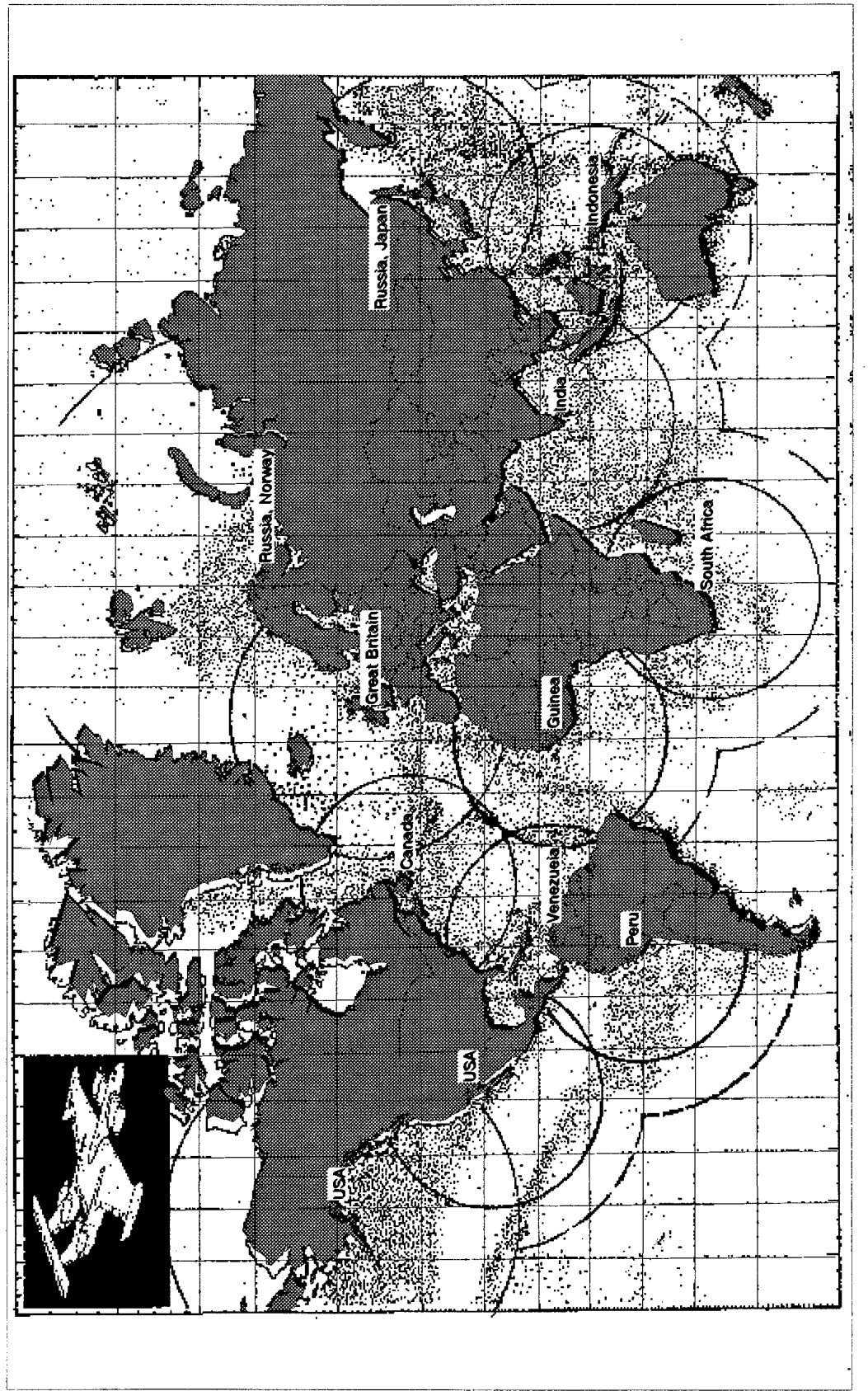


Fig 10. Influence of power plant type upon characteristics of WIGs.

E K R A N O P L A N	Takeoff weight, ton	750
	Dimensions: lenght*width*height, m	95*85*17
	Speed of the flight, km/h	400
	low speed, km/h	30
	Range of the flight, km	6500
	at low speed, km	9500
	Takeoff wave height	3,5-4,0
	Payload, ton	70
	Actual square, m ²	1200
	Technical facilities	Helicopter Motor semiffatable boats Tug – boat of oil barrage Rescue rafts Underwater vehicle
SYS TEM	Cost, including the technical facilities, mln. dol.	120
	Number of basing points	12
	Number of the ekranoplans	50
	Total cost, bil. dol.	10

Fig 11. Characteristics of Global Sea Rescue System.

FIG 12. RANGE OF OPERATION OF EKRANOPLANS



**PROGRESS REPORT ON AERODYNAMIC ANALYSIS OF A SURFACE PIERCING
HYDROFOIL-CONTROLLED WING-IN-GROUND EFFECT SEABUS CONFIGURATION ***

C.M. van Beek and B. Oskam
 National Aerospace Laboratory NLR
 Anthony Fokkerweg 2
 1059 CM Amsterdam
 The Netherlands

and

G. Fantacci
 Intermarine S.p.A.
 Via Alta
 19038 Sarzana (La Spezia)
 Italy

SUMMARY

Preliminary design investigations are presented for a Wing-In-Ground effect craft (SEABUS) in the framework of a European project on technology development for this type of vehicle. The concept of the craft features hydrodynamic control surfaces and a water jet propulsion system.

A computational tool is developed and used to investigate the static equilibrium of lift, drag and pitching moment on the complete configuration over the entire speed range by taking the aerodynamic, hydrodynamic and propulsion contributions into account at the same time. Hydrodynamics turns out to be one of the key factors. At cruise speed the total drag of the presently proposed configuration is dominated by the hydrodynamic contributions of the submerged components.

Limited effort has been spent on the design of the wing and the high lift system. Aerodynamic analysis of this design shows fair correspondence in terms of lift with the required lift values obtained from the preliminary design method. Ground effect trends on performance are correctly calculated. Optimization of the wing and high lift system has to be pursued.

1 INTRODUCTION

Recent industrial needs of shipbuilders and shipoperators are focussed on increasing efficiency and economy of shipping operation. An important aspect in this matter is the speed of the vehicle. Efforts are therefore made worldwide to increase this speed, while keeping safety at an acceptable level. This has led to new concepts for transporters cruising at speeds beyond the limit of conventional high-speed ships. Also improvement has been made of already existing concepts of, for example, hydrofoil boats, hovercrafts, catamarans and trimarans.

One of these new configurations is the Surface Piercing, Hydrofoil-Controlled Wing-In-Ground Effect vehicle. It is basically a large wing operating in ground effect just above the water surface for favourable wing performance; the ground ef-

fect increases the lift-drag ratio.

However, flight at an extremely low altitude obviously carries with it a considerable risk, since the time of aerodynamic manoeuvres is relatively large in relation to the short time available at low altitude. The manoeuvrability of the craft is rather limited, since banking in turning operations is hardly possible. A solution to this limitation might be the application of hydrodynamic control through the use of hydrofoils. Due to the much higher density of water compared to air, the response time of the control system is shorter. For the proposed configuration, the hydrofoils are positioned in a trimaran arrangement and are connected to the wing by vertical, water surface piercing struts. An additional aspect is that longitudinal stability of the craft can be obtained by the hydrofoils which implies the redundancy of aerodynamic tail planes.

Separate V-shaped take-off hydrofoils are critical elements of the vehicle to assist in generating lift forces on the configuration and thereby decrease the take-off speed at which the floating hulls of the configuration rise from the water.

In order to continue the development of this concept beyond the conceptual phase, research activities in several technological areas have to be performed in order to obtain a configuration layout which will meet the required control of the craft and also meets the safety regulations. Probably the most important problem to be solved is the cavitation phenomenon on the hydrofoils which occurs at speeds above approximately 40 knots. The availability of hydrofoils for safe and reliable operation in this speed regime is of prime importance for the successful development of the concept.

Intermarine has taken the lead of a European consortium of 13 companies and research institutes to perform research in a number of these areas. The work is performed in the "Brite-Euram III" Programme of the European Commission under the project name SEABUS-HYDAER (HYDrodynamics/AERodynamics); the configuration studied in the project is adopted under the name SEABUS. The project started in December 1997 and will have a duration of 3 years. The main operational requirement of

*The SEABUS configuration is internationally patented by Intermarine S.p.A.; the concept has been established by Admiral Prof.Dr. S. Roccotelli.

the present configuration is to carry 800 passengers and 100 cars at a cruise speed of 120 knots over a distance of 850 km. The emphasis in the present project is on hydrodynamics, aerodynamics and their interaction, on high-speed waterjet propulsion, on the optimization of thick composite structures and on obstacle detection systems.

As project co-ordinator, Intermarine is involved into all aspects of the SEABUS-HYDAER project. As a partner in the project, NLR is involved in the aerodynamics of the wing of the craft. Activities in the aerodynamics field have been defined in the analysis of the wing and its high lift system in ground effect. However, since the performance of the complete vehicle is strongly related to the stability and control of the complete vehicle, it is not meaningful to consider the wing isolated from the hydrodynamic components and the propulsion system. At the start of the project, such an integrated approach has not yet been pursued. Therefore it was imperative to perform a preliminary design study into the controllability of the complete configuration and postpone the detailed wing design until constraints on the wing design goals have been achieved from a preliminary design study.

2 BACKGROUND

From the beginning of the 20th century it was noted that a wing flying in close proximity to the ground experiences an increase of the lift and a reduction of the induced drag. This phenomenon, called ground effect, has been studied since then, because it complicated the take-off and landing of aircraft. Already in 1912 Betz sought to discover what lay behind this phenomenon, see Hooker (Ref. [14]). A historical overview of several projects for Wing-In-Ground (WIG) effect craft until 1980 has been presented by Ollila (Ref. [18]).

Wing-In-Ground (WIG) effect craft have been under development in various countries, such as China, Germany, Italy, Japan, Russia and the United States. From the 1960's Russia put large efforts in the development of "ekranoplans" (Russian for Wing-In-Ground effect vehicles). The central role was played here by Rostislav Alexeyev from the Hydrofoil Design and Construction Bureau. They developed several large ekranoplans (take-off weight from 120 to 550 tonnes). Nowadays there is an extensive amount of open literature available on their research. Examples are: Chubikov et al. (Ref. [6]), Rozhdestvensky (Ref. [21]) and Kirillovikh (Ref. [16]). These papers show that many aspects, such as aerodynamics, propulsion, stability and control, have to be taken into account in close interrelation in order to obtain an efficient transport vehicle. From a United States point of view, the same conclusion was also put forward by Balow et al. (Ref. [3]).

Also smaller scale WIG craft have been developed and built. An example is the work performed by Jörg in Germany since the early 1960's on several small craft (Ref. [15]).

In the future an increasingly important role for WIG craft is envisaged, mainly for civil applications. This prophecy is expressed in many publications, see for example Rozhdestvensky and Synitsin (Ref. [22]). Development of commercial WIG craft is in progress in Russia, Australia, Germany, China and Korea.

A wide variety of techniques have been employed to study the aerodynamics of WIG vehicles. Ando (Ref. [1]) gave a short summary of empirical methods, classical theoretical methods

and the Split Orifice Flow Model for the prediction of the lift-to-drag ratio of WIG vehicles. Rozhdestvensky (Ref. [20]) presented one- and two-dimensional mathematical models for the non-linear aerodynamics of lifting surfaces in ground effect. Other methods apply the lifting line theory, matched asymptotic expansions and various implementations of the vortex lattice method, see Hooker (Ref. [14]). A more recent example of the vortex lattice method approach can be found in Day and Doctors (Ref. [9]).

Also panel methods have been used for the calculation of the flow around three-dimensional wings near the water surface. Goetz et al. (Ref. [12]) used the PANAIR panel method for calculations on a low aspect ratio rectangular wing with end plates and trailing edge flap deflection. Chun and Park (Ref. [7]) performed steady and unsteady panel method calculations; the latter showed that the ground effect for a wing above waves is lower than above flat ground. Kühmstedt and Milbradt (Ref. [17]) presented an application of several two- and three-dimensional potential flow methods to the airfoil and wing design of a WIG craft. Chun et al. (Ref. [8]) presented results of panel method calculations not only for wing configurations, but also for a complete WIG craft. Correspondence with experimental results for the wing configurations are shown to be good, except for situations where the wing is in close proximity to the ground. This conclusion has also been drawn in the other panel method references.

With the continuing development and application of Euler and Navier-Stokes codes, these methods have started to be used also in the analysis of WIG configurations; Hirata and Kodama (Ref. [13]) applied a Navier-Stokes solver for calculations on a three-dimensional wing with end-plates in ground effect.

As for cruising conditions, the ground effect plays also an important role at lower speeds in take-off and landing high lift conditions. Steinbach and Jacob (Ref. [23]) conducted a combined experimental and theoretical investigation into a high lift airfoil configuration. They presented the opposite effects of ground influence on lift for two-dimensional airfoils with deflected high lift systems (lift decrease due to the "forward-wash" effect) and for low aspect ratio three-dimensional wings in high lift condition (lift increase due to the image trailing vortices). Filippone and Selig (Ref. [10]) investigated with a panel method the ground effect on a thin and a thick airfoil. They showed opposite effects in extreme ground effect on the thin airfoil (lift increase) and on the thick airfoil (lift decrease). The reason for this is a different balance of the "forward-wash" effect and the "ram" (stagnation) effect. They also studied three-dimensional effects of the flow about low aspect ratio wings by VSAERO panel method calculations; these effects are responsible for the much lower lift coefficients compared to the two-dimensional case.

Most methods for aerodynamic calculations on WIG configurations consider the water surface as not deformable. However, the non-uniform pressure field which is created by the wing, alters the water surface and generates a specific wave pattern. In this sense the aerodynamic flow-field and the hydrodynamic flow-field are strongly coupled. Bulgarelli et al. (Ref. [5]) presented a mathematical model to describe the unsteady flow about a wing moving in the proximity of the air-water interface. As the air-water density ratio is very small, the usual assumption is to neglect completely the free surface deformation and to

consider the WIG craft in flat ground effect. The aerodynamic flow-field and the hydrodynamic flow-field are then assumed to be decoupled.

As already indicated, stability and control of WIG craft is an important aspect which needs careful consideration. Studies into this subject are not as numerous as into the performance of these vehicles. Gera (Ref. [11]) discussed the static and dynamic stability characteristics of wingships.

The present paper presents the status of the limited preliminary design of the complete craft and of the aerodynamic analysis of the wing in ground effect. The next section presents the layout of the configuration, as it is defined at the start of the project by Intermarine. Section 3 deals with the preliminary design investigations. Section 4 shows first results of the wing aerodynamic analysis. Finally, section 5 contains preliminary conclusions on the results obtained up to now.

3 THE SEABUS CONFIGURATION

The initial configuration of the SEABUS has been developed and defined by Intermarine. It is shown in figure 1.

The wing features a low aspect ratio in order to take advantage of the ground effect. The outer parts of the wing can be folded to reduce the span for manoeuvring operations in harbours. The high lift system of the wing consists of a full-span trailing edge single-slotted Fowler flap. Passengers and cargo are accommodated inside the inner part of the wing. The absence of a fuselage is favourable for achieving a high lift/drag ratio of the configuration.

Three hulls are connected in a trimaran configuration to the lower surface of the wing; one hull in a forward position in the plane of symmetry, the two others in an aft starboard and port position. The main purpose of the three hulls is to provide buoyancy during floating operations at low speed in harbours and in take-off and re-entry operations.

The complete speed range is subdivided into three subranges:

- the planing hull state or the hullborne state (0-30 knots)
- the foilborne state (30-70 knots)
- the airborne state (70-120 knots)

The speed between hullborne state and foilborne state is defined as the take-off speed. The speed between foilborne state and airborne state is defined as the minimum airborne speed.

The SEABUS features a set of V-shaped take-off hydrofoils which is separate from the control hydrofoils. The V-shaped take-off foils generate additional lift in the foilborne state of the flight between the take-off and the airborne state, i.e. the operation state where the weight of the craft is fully carried by the wing. These take-off foils are partially submerged in the foilborne state and are above the water in the airborne state.

Control hydrofoils are used for longitudinal controllability of the craft in the foilborne and airborne state. These control foils are non-movable and do not feature flaps. Control is accomplished by the blowing of air from the upper or lower side of the

foils at the mid-chord location.

The take-off foils are vertically positioned in such a way that they are fully submerged in the planing hull state in order to generate maximum lift to decrease the take-off velocity as far as possible. Applying take-off hydrofoils will allow the take-off at a lower speed than in case the configuration only features an aerodynamic wing to generate lift. After take-off the vehicle rises with increasing speed due to the lift force generated by the take-off hydrofoils and the wing, such that just after take-off the hulls are already well above the surface surface. Also the V-shaped take-off foils become decreasingly submerged with increasing speed. At the speed where the vehicle becomes fully airborne the take-off foils are no longer submerged, therefore not contributing to the hydrodynamic drag in the airborne speed regime. The control foils are located at the bottom of the struts and remain submerged over the entire speed range of the craft. An example of an existing WIG craft with hydrofoils is the Lipisch X-114H.

Propulsion of the vehicle is provided by a waterjet, located just under the wing at the end of the front hull. The water jet nozzle can be tilted from a horizontal position towards a 10 degrees downward position. In this way the thrust can also assist in the generation of the required lift force during take-off. The water inlet is located at the bottom of the front strut. The inlet duct runs through this strut upwards to the pump which is located in the front hull. The thrust is generated by a gas-turbine, also placed inside this hull, which is connected by a gearbox to the pump.

The main characteristics of the SEABUS configuration are:

- weight:
 - take-off: $W_{to} = 500 \text{ ton}$
 - payload: $W_p = 266.5 \text{ ton}$
- cruise speed: $U_\infty = 120 \text{ kts}$
- wing:
 - span: $b = 111.92 \text{ m}$
 - mean aerodynamic chord: $\bar{c} = 48.64 \text{ m}$
 - taper ratio: $\lambda = 0.5$
 - aspect ratio: $A = 2.38$
 - area: $S = 5254 \text{ m}^2$
 - non-dimensional span of prismatic center section: $b_{pr}/b = 0.4465$
 - dihedral angle of outer wing part: $\Gamma = 5.22^\circ$
 - straight quarter-chord line
- front strut:
 - 30 % thick, base vented, parabolic profile
 - span: $b = 7.60 \text{ m}$
 - chord: $c = 4.70 \text{ m}$
 - forward sweep angle: $\Lambda = 30^\circ$

- aft strut:
 - 20 % thick, base vented, parabolic profile
 - span: $b = 7.40 \text{ m}$
 - chord: $c = 3.33 \text{ m}$
 - sweep angle: $\Lambda = 0^\circ$
- front take-off hydrofoil:
 - 6 % thick, base vented, curved, parabolic profile
 - straight-tapered, taper ratio: $\lambda = 0.5$
 - aspect ratio: $A = 8.26$
 - area: $S = 40 \text{ m}^2$
 - V-shaped, dihedral angle: $\Gamma = 30^\circ$
- front control hydrofoil:
 - 6 % thick, NACA 16006 profile
 - airfeed at 50 % chord on the upper and lower side, for lift variation for control purposes ($\Delta c_{l,profile} = \pm 0.15$)
 - straight-tapered, taper ratio: $\lambda = 0.39$
 - aspect ratio: $A = 5.36$
 - area: $S = 10 \text{ m}^2$

The two aft take-off hydrofoils feature each only half of the front take-off hydrofoil: at the starboard-side aft strut only the starboard-side of the front foil, $S = 20 \text{ m}^2$, at the port-side aft strut only the port-side of the front foil, $S = 20 \text{ m}^2$. Each of the two aft control hydrofoils features half of the front control hydrofoil area: $S = 5 \text{ m}^2$, at the same values of the other foil parameters.

In summary we have:

- total take-off foil area: $40+20+20=80 \text{ m}^2$
- total control foil area: $10+5+5=20 \text{ m}^2$

4 THE PRELIMINARY DESIGN CALCULATIONS

A limited preliminary design for the SEABUS configuration has been performed. The aim was to determine the performance of the vehicle and the amount of propulsive power required for obtaining static equilibrium with regard to lift, drag and pitching moment. Also it has to provide the design lift coefficients for the wing, the wing pitching moment limitations in both cruise and high lift configurations and the angle of attack limitations, which will be used in the detailed design of the wing and the high lift system of the wing. This section presents several aspects of the preliminary design and results of calculations.

4.1 Aspects of the preliminary design

The lift and drag data over the entire speed range for the hydrodynamic components of the SEABUS configuration are provided to NLR by the partners in the SEABUS-HYDAER consortium which are responsible for the design, testing and validation of the hulls, struts, take-off foils and control foils. Data on the propulsion (water inlet and water jet) has also been supplied to NLR by the partner responsible for this subject. These data itself

are not discussed in the present paper. It has to be realized that these data are a first iteration. The hydrodynamic behaviour of struts and foils at the speed range in which the SEABUS is intended to operate is an unknown area in which super-cavitation phenomena play a dominant role. It is exactly one of the goals of the present project to obtain hydrodynamic data up to speeds of 120 knots. The same holds for the propulsion; the flow in the inlet at high velocities is also strongly influenced by cavitation. This will also be investigated in the project.

The aerodynamic characteristics of the wing and the high lift system are calculated with well-established preliminary design methods, taken from Ref. [24]. It also includes corrections for the lift, drag and pitching moment due to the ground effect. The effect of the deformable water surface has not been taken into account.

Beside the geometrical data already discussed, a number of additional data has also to be defined to perform the static analysis. The wing profile characteristics are defined in such a way that, at the cruise speed of 120 kts, the wing lift for zero angle of attack, plus the component in lift direction of the pressure related part of the force on the water inlet, equal the weight of the craft. The inlet features an inclination angle of 30 degrees with respect to the vertical axis. The wing lift coefficient in cruise equals: $C_{L,wing,cruise} = 0.39$. The wing planform, as specified in the previous section, has been used. The flap/wing chord ratio has been selected at 0.35. No attempts have been made to optimize this ratio. The center of gravity and its range are defined; the average location is at 30 % of the wing root chord from the leading edge.

The height of the wing above the water surface and its angle of attack depend on the phase of the flight. From zero up to take-off speed the craft is in the planing hull state where it is planing on the three hulls. The height above the surface is selected at 2.4 meter. In the foilborne state from the take-off velocity up to the fully airborne velocity the height increases with increasing speed. The height is determined by the extent of submergence of the take-off hydrofoils which is required to generate, in combination with the lift on the wing, the total lift on the vehicle. The total lift equals the weight of the configuration. Therefore the height in the foilborne state results from the calculations. In the airborne state the height is defined at 9 meter, such that the take-off foils are above the water surface. This implies that the craft is flying at a relative flight height of 18.5 % of the mean aerodynamic chord length. A wing with an aspect ratio between 2 and 3, flying at a relative flight height of 20 % of the mean aerodynamic chord length is considered acceptable for an efficient transport vehicle, see Kirillovikh (Ref. [16]). Rozhdestvensky (Ref. [20]) states that the relative ground clearance should be in the range of 5-10 % of the mean chord for obtaining efficient WIG craft from the viewpoint of aerodynamics. The seastate (waveheight) comes also into the picture, requiring a larger percentage.

The minimum take-off velocity is determined by the condition that the take-off hydrofoils and the wing carry the vehicle (the front and two aft control foils together are assumed to generate no net lift); the value of this velocity is therefore a result from the calculations. The minimum airborne velocity is determined by the condition that the wing fully carries the vehicle; the value of this velocity is also a result from the calculations.

Finally, the angle of attack of the craft in the planing hull state and the foilborne state can only be chosen within strict limits. Restrictions are the requirements that the wing trailing edge does not touch the water surface and that the water inlet and, at the take-off velocity, the take-off foils remain properly submerged. A limited angle is also a requirement to avoid shifting of the cars in the cargo-space, since it will be in practice impossible to fasten all cars sufficiently to the floor. In the present preliminary design calculations the angle of attack has been set at zero degrees. In the airborne state the angle of attack results from the analysis by the condition that at all speeds in this state the wing generates a lift force which equals the weight of the vehicle.

The hydrodynamic, propulsion, aerodynamic and additional data are combined in a computer program in order to calculate the performance over the entire velocity range, for minimum required power, of the complete vehicle based on static equilibrium of the lift, drag and pitching moment, i.e. only starboard/port-side symmetric conditions are considered. All calculations are made for the take-off weight of the vehicle and for the average location of the center of gravity.

4.2 Results of preliminary design calculations

Calculations have been performed in order to establish the inputs for the detailed aerodynamic design of the SEABUS configuration. The results of the calculations are summarized for a number of velocities in the tables 3 and 4.

The take-off velocity is 30 knots; the presently calculated minimum airborne velocity is 70 kts. At the latter speed the vehicle can change the foilborne state into the airborne state by simultaneously increasing the height above the water surface and increasing the angle of attack. After take-off the increased height above the water surface enables to deflect the wing trailing edge flap to 10 degrees, and above 45 knots to 15 degrees.

In the foilborne state the lift force on the take-off hydrofoils decrease with increasing speed, while the wing increasingly takes over the function of lift generation device. This is also presented in Fig. 2 in which the total lift coefficient of the vehicle for static equilibrium is plotted; also shown are the lift coefficient of the take-off hydrofoils (front and two aft together) and the wing. All coefficients are based on the dynamic pressure of the airflow and the planform area of the wing (to allow addition).

Figure 3 presents the lift coefficient of the wing and the angle of attack over the speed range; also the trailing edge flap deflection angles are indicated. In the planing hull and foilborne state the angle of attack has to remain zero degrees. In the airborne state the angle of attack varies with speed in order to achieve at all speeds equilibrium of forces and pitching moment, while fluctuations of the flap deflection angle, which is at its maximum of 15 degrees at 70 kts, are avoided, such that the flap can be retracted smoothly with increasing speed until the high lift system is no longer required at 100 kts.

Table 4 shows the drag on the components and on the entire configuration. Clearly the hydrodynamic components account for the largest portion of the drag. The drag contribution of the wing is 15 per cent at 120 knots. This is also illustrated in Fig. 4 where the drag of the various components is given as percentage of the drag of the entire vehicle.

Fig. 5 presents the installed power over the speed range. As for "conventional" WIG craft, the power required reaches a local

maximum at the take-off speed due to the wave-making drag of the hulls which are no longer submerged in the foilborne state. In the foilborne state the power required is nearly constant, because the hydrodynamically wetted area decreases with increasing speed due to the increased height of the vehicle above the water surface. As shown in Table 4, the drag of the configuration decreases in the foilborne state with a factor two, while the speed doubles from 35 to 70 knots. In the airborne speed range, being at a constant height of 9 meter, the power required approximately increases up to the overall maximum of 90 MegaWatt at 120 kts. This is in contrast to conventional WIG craft without submerged components above the take-off speed for which the overall maximum power required is determined by the wave-making drag at the take-off speed.

The high value of the maximum installed power required affects the operational efficiency in an adverse way. Ando (Ref. [2]) devised the non-dimensional "Modified Effective Lift-Drag Ratio" parameter: $(WV/P)M_{cr}$, where W is the weight, V the cruise velocity, P the installed power and M_{cr} the Mach number at cruise. Ando presented plots for this parameter based on the gross-weight W_g and on the payload W_p for a wide range of transport vehicles. For the present SEABUS configuration the numbers are: $W_g = 500 \text{ ton}$ (gross-weight), $W_p = 266.5 \text{ ton}$ (payload), $V_{cr} = 120 \text{ kts}$, $P_{in} = \pm 90 \text{ MegaWatt}$ and $M_{cr} = 0.18$. These data result in two values of the efficiency parameter $(WV/P)M_{cr}$:

1. one based on gross-weight; this value of the SEABUS configuration equals the value for an efficient helicopter in comparison with various other transport vehicles, as presented by Ando.
2. one based on payload; this value of the SEABUS configuration exceeds that of helicopters, and equals the value for a passenger car and, although operating in a higher speed range, the value for less efficient jet aircraft.

5 THE DETAILED DESIGN CALCULATIONS

Detailed wing design activities have recently been started. This section describes the work performed on the wing profile and trailing edge flap profile design and on the analysis of the performance of the three-dimensional wing and the high lift system.

5.1 Wing and flap profile design

Recently, detailed analysis of the performance of the wing has been started. Based on the lift coefficients for the wing, obtained from the preliminary design calculations, wing profile design can be performed. Initially, Intermarine has chosen the Göttingen 1020 profile for the SEABUS wing. A first iteration in this profile design has been executed. Using a two-dimensional panel method with ground effect capability, coupled with a boundary layer method, see Ref. [19], a profile with enhanced lift capability has been designed during an earlier design iteration, allowing for larger angles of attack up to seven degrees. Modifications to the original profile relate to the upper side near the nose and the adoption of a flat lower side, see Fig. 6, where the profiles are shown at airborne height.

The trailing edge flap profile is based on the single-slotted flap of a three element airfoil. The flap/wing chord ratio is 0.35. The geometry of the flap has been modified in order to integrate it in

retracted position smoothly in the wing profile. The flap/wing chord ratio has been kept the same. Fig. 7 shows the flap profile in retracted and deflected position at a foilborne height.

Since wing analysis is performed with a non-viscous potential flow method, a modification to the wing profile with relation to the flap cove has to be made in case of calculations on the wing with deflected flap in order to prevent unrealistic results in the cove. To simulate flow separation in the potential flow calculations, the cove has been faired smoothly from the profile lower side to the trailing edge, see Fig. 7.

It is mentioned that the two-dimensional wing and flap profile design, which has been performed up to now, is of limited scope. Complete wing design activities would require several iteration loops of preliminary design calculations, as presented in the previous section, two-dimensional profile design and three-dimensional detailed design, as is presented in the next subsection.

5.2 Wing-In-Ground effect calculations

A number of aerodynamic calculations on the SEABUS wing have been performed. The calculational method is the PDAERO panel method, see Ref. [4]. This method is capable of the calculation of the three-dimensional inviscid, subsonic potential flow on arbitrary aeronautical configurations. The method includes an option for (undeformable) ground effect calculations.

The geometry of the wing is based on the planform which has been defined by Intermarine and which is presented in section 2. The wing and flap profile are discussed in section 4.1. The flap/wing chord ratio is constant in spanwise direction.

Calculations have been performed at one foilborne and two airborne conditions (all conditions are starboard/port-side symmetric):

1. $U_\infty = 50 \text{ kts}, \alpha = 0^\circ, \delta_f = 15^\circ$
2. $U_\infty = 85 \text{ kts}, \alpha = 2.1^\circ, \delta_f = 5^\circ$
3. $U_\infty = 120 \text{ kts}, \alpha = 0^\circ, \delta_f = 0^\circ$

The full-span, single-slotted trailing edge flap is of the Fowler type. The chord extension due to the translation of the flap in backward direction is set at 30 % flap chord at 5° flap deflection and at 50 % flap chord at 15° flap deflection. The extension percentages are constant in spanwise direction. For both deflection angles, the gap between wing and flap is 2 per cent of the wing chord without flap deflection, again constant in spanwise direction.

The panel distribution is shown in Fig. 8 and 9 for the wing with retracted flap and in Fig. 10 for the wing with flap deflection. Fig. 11 shows details of the wing and flap paneling, including their wakes, near the wing trailing edge. The wake of the main wing, trailing off in downstream direction over the deflected flap, is taken parallel to the upper surface of the flap up to the trailing edge of the flap.

At each condition calculations have been performed with and without ground effect in order to investigate this phenomenon. The number of panels for the clean wing geometry is: 2700 (in ground effect effectively 5400), for the wing with deflected flap: 4500 (in ground effect effectively 9000). The calculations have been executed on the NEC SX-4 supercomputer of NLR. Run times vary from 55 seconds for the clean wing without ground

	$h[m]$	$U_\infty[\text{kts}]$	$\alpha[^{\circ}]$	$\delta_f[^{\circ}]$	C_L	C_D	L/D
1a	∞	50	0	15	0.8376	0.0300	28
1b	6.15	50	0	15	1.2668	0.0156	81
2a	∞	85	2.1	5	0.5705	0.0267	21
2b	9	85	2.1	5	0.7803	0.0165	47
3a	∞	120	0.1	0	0.2780	0.0160	17
3b	9	120	0.1	0	0.3939	0.0104	38

Table 1: Wing lift and wing drag coefficients at three conditions from the preliminary design calculations

	$h[m]$	$U_\infty[\text{kts}]$	$\alpha[^{\circ}]$	$\delta_f[^{\circ}]$	C_L	C_{D_i}	L/D_i
1a	∞	50	0	15	0.8357	0.0900	9
1b	6.15	50	0	15	1.4511	0.0670	22
2a	∞	85	2.1	5	0.5971	0.0460	13
2b	9	85	2.1	5	0.9055	0.0429	21
3a	∞	120	0	0	0.3027	0.0119	25
3b	9	120	0	0	0.3824	0.0093	41

Table 2: Wing lift and wing induced drag coefficients at three conditions from the PDAERO calculations

effect calculation to 250 seconds for the calculation on the wing with deflected flap including ground effect.

Pressure distributions over the wing and flap, for two spanwise locations ($\eta=y/(b/2) = 0.2$ and 0.7) and spanwise lift distributions are presented in Fig. 12 through 19. At all conditions, the ground effect increases the pressure at the lower side of the wing, while the distribution at the upper side remains relatively unchanged. The ground effect is most prominent at the foilborne condition where the wing is closest to the ground.

The results for lift and drag are given in table 1 and 2. Table 1 contains the lift and total drag from the preliminary design calculations, table 2 the lift and induced drag from the PDAERO calculations. In both tables results without and with ground effect are presented. Comparison of lift coefficients shows that without ground effect the lift values are in fair correspondence. With ground effect larger differences occur for the two high lift conditions.

Comparison of drag coefficients shows that the panel method values, consisting of induced drag only, are higher than the values resulting from the preliminary design calculations in the two high lift conditions, but lower at cruise condition.

These wing analysis results should be regarded as results in progress for the SEABUS configuration. The generally fair correspondence between the results on lift from the preliminary design calculations and from the wing analysis indicate that the wing design can be developed further from the present layout. Design of the wing and the high lift system (flap gap and overlap) is possible through modification of several parameters, such as wing leading edge curvature, which define a complete, three-dimensional wing.

6 CONCLUSIONS

A description has been presented of a preliminary design investigation into the SEABUS WIG concept which features hydrodynamic control surfaces and a water jet propulsion system. A computational tool has been developed allowing to calculate static equilibrium states with relation to lift, drag and pitching

moment in a rapid manner, taking severe operational limitations in terms of the angle of attack into account. The preliminary design results indicate a drag level dominated by hydrodynamic contributions and as a consequence a large installed power. The resulting operational efficiency of the SEABUS, based on gross-weight, equals the value of efficient helicopters; the operational efficiency of the SEABUS, based on payload, equals the value of passenger cars and, although operating in a higher speed range, the value of less efficient jet aircraft. These efficiencies indicate the need for further design iterations to reduce the hydrodynamic drag level of the SEABUS concept, by reducing the size of the struts and the control foils, to increase the operational efficiency.

7 REFERENCES

- [1] Ando, S., "Note on Prediction of Aerodynamic Lift/Drag Ratio of WIG (Wing-In-Ground) at Cruise", Proc. of FAST'93, Yokohama, Japan, Dec. 13-16, 1993, pp. 1561-1572.
- [2] Ando, S., "Some Topics on WIG (Ekranoplan) Design", Trans. of the Japan Society for Aeronautical and Space Sciences, Vol. 39, No. 124, Aug. 1996, pp. 184-198.
- [3] Balow, F.A., Guglielmo, J.G. and Sivier, K.R., "Design and Evaluation of a Midsize Wing-in-Ground Effect Transport", AIAA 93-3952, AIAA Aircraft Design, Systems and Operations Meeting, Monterey, CA, Aug. 11-13, 1993.
- [4] Beek, C.M. van, Piers, W.J. and Oskam, B., "Aerodynamic Analysis of Slipstream/Wing/Nacelle Interference for Preliminary Design of Aircraft Configurations", AGARD-CP-498, Paper No. 6, 1992.
- [5] Bulgarelli, U.P., Greco, M., Landrini, M. and Lugni, C., "A Simple Model for the Aero-Hydrodynamics of Ekranoplans", Proc. of the AGARD Fluid Dynamics Panel Workshop on High Speed Body Motion in Water, Kiev, Ukraine, Sept. 1-3, 1997, AGARD-R-827, Paper 16.
- [6] Chubikov, V., Pashin, V., Treschchevsky, V. and Maskalik, A., "Ekranoplan: A High-Speed Marine Vehicle of a New Type", Proc. of FAST'91, Vol. 1, June 1991, pp. 641-648.
- [7] Chun, H.H. and Park, I.R., "Analysis of Steady and Unsteady Performances for 3-D Airwings in the Vicinity of the Free Surface", Proc. of a Workshop on Twenty-First Century Flying Ships, Sydney, Australia, Nov. 7-8, 1995, pp. 23-46.
- [8] Chun, H.H., Park, I.R., Chung, K.H. and Shin, M.S., "Computational and Experimental Studies on Wings In Ground Effect and a WIG Effect Craft", Workshop Proc. of Ekranoplans and Very Fast Craft, Sydney, Australia, Dec. 5-6, 1996, pp. 38-59.
- [9] Day, A.H. and Doctors, L.J., "A Study on the Efficiency of the WIG Concept", Proc. of a Workshop on Twenty-First Century Flying Ships, Sydney, Australia, Nov. 7-8, 1995, pp. 1-22.
- [10] Filippone, A. and Selig, M.S., "Low Aspect-Ratio Wings for Wing-Ships", AIAA 98-0761, 36th Aerospace Sciences Meeting and Exhibit, Reno, NV, Jan. 12-15, 1998.
- [11] Gera, J., "Stability and Control of Wing-In-Ground Effect Vehicles or Wingships", AIAA 95-0339, 33rd Aerospace Sciences Meeting and Exhibit, Reno, NV, Jan. 9-12, 1995.
- [12] Goetz, A.R., Osborn, R.F. and Smith, M.L., "Wing-In-Ground Effect Aerodynamic Predictions Using PANAIR", AIAA-84-2429, AIAA Aircraft design systems and operations meeting, San Diego, CA, Oct. 31 - Nov. 2, 1984.
- [13] Hirata, N. and Kodama, Y., "Flow Computation for Three-Dimensional Wing in Ground Effect Using Multi-Block Technique", Journal of the Society of Naval Architects of Japan, Vol. 177, June 1995, pp. 49-57.
- [14] Hooker, S.F., "A Review of Current Technical Knowledge Necessary to Develop Large Scale Wing-In-Surface Effect Craft", Intersociety Advanced Marine Vehicles Conf., Arlington, VA, June 5-7, 1989, pp. 367-429.
- [15] Jörg, G.W., "History and Development of the "Aerodynamic Ground Effect Craft" (AGEC) with tandem wings", Proc. of the Symposium "Ram Wing and Ground Effect Craft", The Royal Aeronautical Society, London, England, May 19, 1987, pp. 87-109.
- [16] Kirillovikh, V.N., "Russian Ekranoplans", Proc. of a Workshop on Twenty-First Century Flying Ships, Sydney, Australia, Nov. 7-8, 1995, pp. 71-117.
- [17] Kühmstedt, T. and Milbradt, G., "Aerodynamic Design of Wing in Ground Effect Craft", Proc. of FAST'95, Lübeck-Travemünde, Germany, Sept. 25-27, 1995, Vol. 1, pp. 597-608.
- [18] Ollila, R.G., "Historical Review of WIG vehicles", Journal of Hydraulics, Vol. 14, No. 3, July 1980, pp. 65-76.
- [19] Oskam, B., Laan, D.J. and Volkers, D.F., "Recent Advances in Computational Methods to Solve the High-Lift Multi-Component Airfoil Problem", AGARD-CP-365, Paper No. 3, 1984; also NLR MP 84042 U, 1984.
- [20] Rozhdestvensky, K.V., "Nonlinear Aerodynamics of Ekranoplan in Strong Ground Effect", Proc. of FAST'95, Lübeck-Travemünde, Germany, Sept. 25-27, 1995, Vol. 1, pp. 621-630.
- [21] Rozhdestvensky, K.V., "Ekranoplans - Flying Ships of the Next Century", Proc. of a Workshop on Twenty-First Century Flying Ships, Sydney, Australia, Nov. 7-8, 1995, pp. 47-70.
- [22] Rozhdestvensky, K.V. and Synitsyn, D.N., "State-of-the-Art and Perspectives of Development of Ekranoplans in Russia", Proc. of FAST'93, Yokohama, Japan, Dec. 13-16, 1993 pp. 1567-1670.
- [23] Steinbach, D. and Jacob, K., "Some Aerodynamic Aspects of Wings near Ground", Trans. of the Japan Society for Aeronautical and Space Sciences, Vol. 34, No. 104, Aug. 1991, pp. 56-70.
- [24] Torenbeek, E., "Synthesis of Subsonic Airplane Design", Delft University Press and Martinus Nijhoff Publishers, 1982.

W = vehicle weight

SEABUS - lift force											
U_∞ [kts]	h $\alpha=0$	hulls		take-off foils		wing			state		
		lift force		lift force		lift force		α			
		[ton]	% W	[ton]	% W	[ton]	% W	$C_{L_{wing}}$	[deg]		
0	2.40	500	100.0	0	0	0	0	0	0	hullborne	
10	2.40	438.4	87.7	43.6	8.7	7.0	1.4	0.8066	0	0	hullborne
20	2.40	291.4	58.3	174.3	34.9	28.0	5.6	0.8066	0	0	hullborne
30	2.40	46.3	9.3	392.1	78.4	62.9	12.6	0.8066	0	0	hullborne
35	4.24	0	0	364.9	73.0	135.1	27.0	1.2698	0	10	foilborne
40	5.00	0	0	340.2	68.0	159.8	32.0	1.1517	0	10	foilborne
50	6.15	0	0	223.5	44.7	276.5	55.3	1.2668	0	15	foilborne
60	6.88	0	0	116.9	23.4	383.1	76.6	1.2092	0	15	foilborne
70	7.86	0	0	3.0	0.6	496.9	99.4	1.1523	0	15	foilborne
70	9.00	0	0	0	0	490.9	98.2	1.1560	0.8	15	airborne
80	9.00	0	0	0	0	491.0	98.2	0.8853	0.6	9	airborne
90	9.00	0	0	0	0	490.4	98.1	0.6986	0.8	5	airborne
100	9.00	0	0	0	0	485.5	97.1	0.5602	2.6	0	airborne
110	9.00	0	0	0	0	488.6	97.7	0.4659	1.1	0	airborne
120	9.00	0	0	0	0	491.5	98.3	0.3939	0.1	0	airborne

Table 3: Lift force distribution

SEABUS - drag force							
U_∞ [kts]	hulls	struts	take-off foils	control foils	wing	conf.	state
	drag	drag	drag	drag	drag	drag	
	[kg]	[kg]	[kg]	[kg]	[kg]	[kg]	
0	0	0	0	0	0	0	hullborne
10	7000	125044	1292	1858	90	135283	hullborne
20	20000	127435	5168	7336	354	160293	hullborne
30	51000	131087	11630	16394	788	210898	hullborne
35	0	87696	13653	22260	1464	125073	foilborne
40	0	73450	15051	24085	1816	114402	foilborne
50	0	55415	13073	23935	3379	95802	foilborne
60	0	46794	7944	24531	5177	84446	foilborne
70	0	35309	300	25041	7599	68249	foilborne
70	0	22302	0	23535	8800	54637	airborne
80	0	24384	0	25360	9070	58813	airborne
90	0	28004	0	27437	9545	64986	airborne
100	0	37170	0	28101	14201	79473	airborne
110	0	35980	0	28712	13324	78016	airborne
120	0	36241	0	35276	12997	84513	airborne

Table 4: Drag force distribution

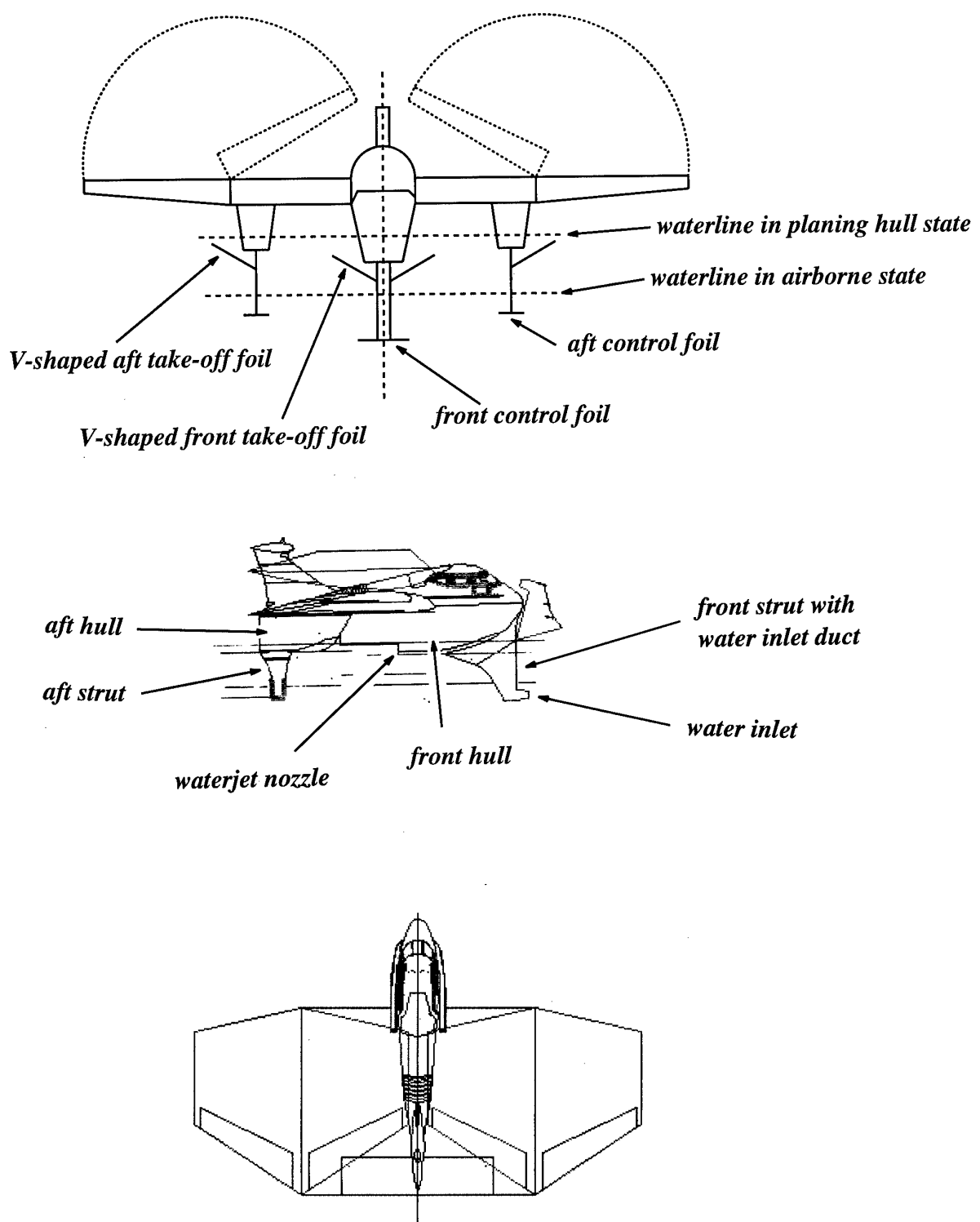


Figure 1: The SEABUS configuration (on scale of the Technology Demonstrator)

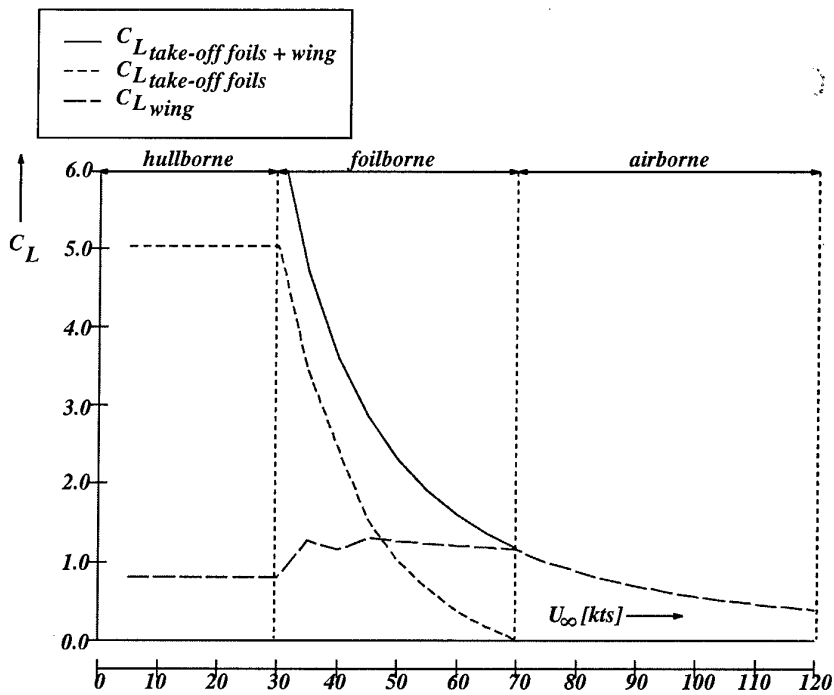


Figure 2: Lift coefficients for static equilibrium over the speed range

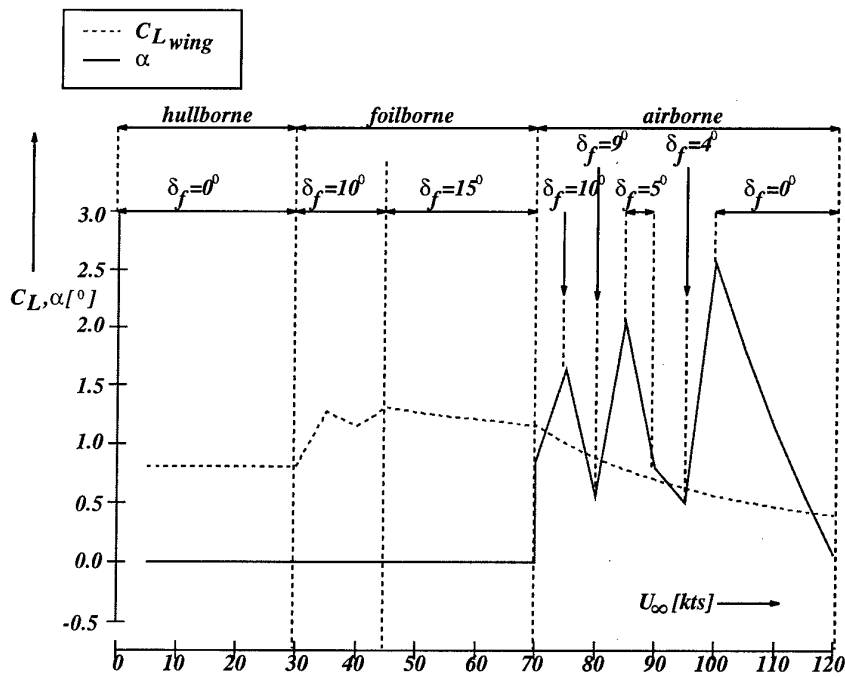


Figure 3: Wing lift coefficient and angle of attack for static equilibrium over the speed range

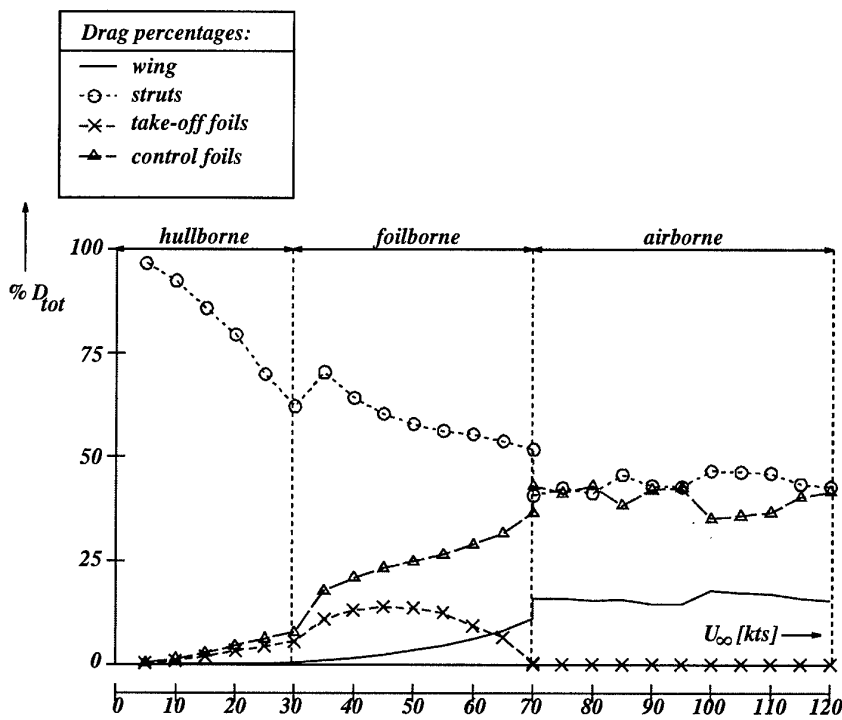


Figure 4: Drag of various configuration components as percentage of the total drag at static equilibrium over the speed range

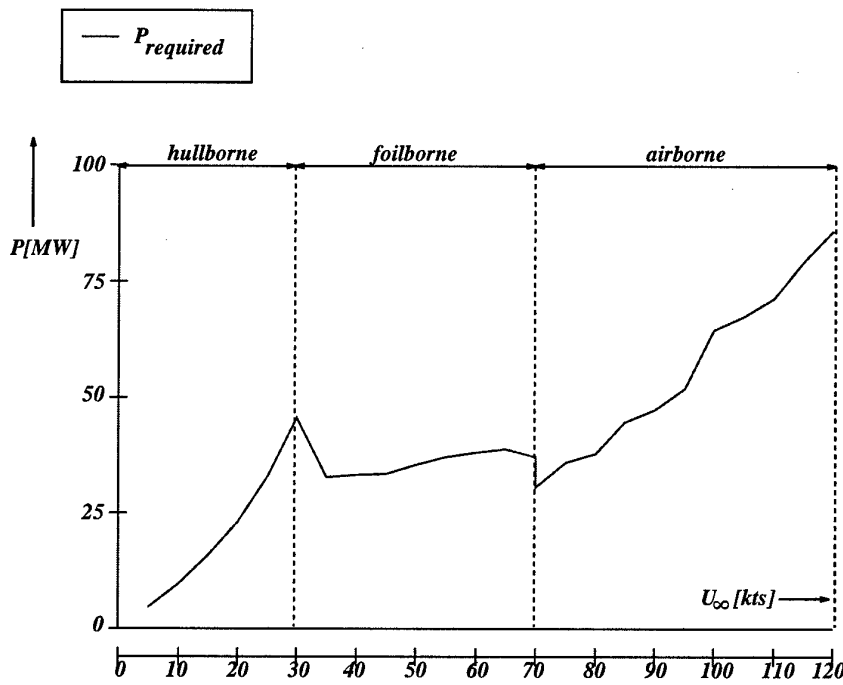


Figure 5: Installed power required at static equilibrium (lift, drag and pitching moment) over the speed range

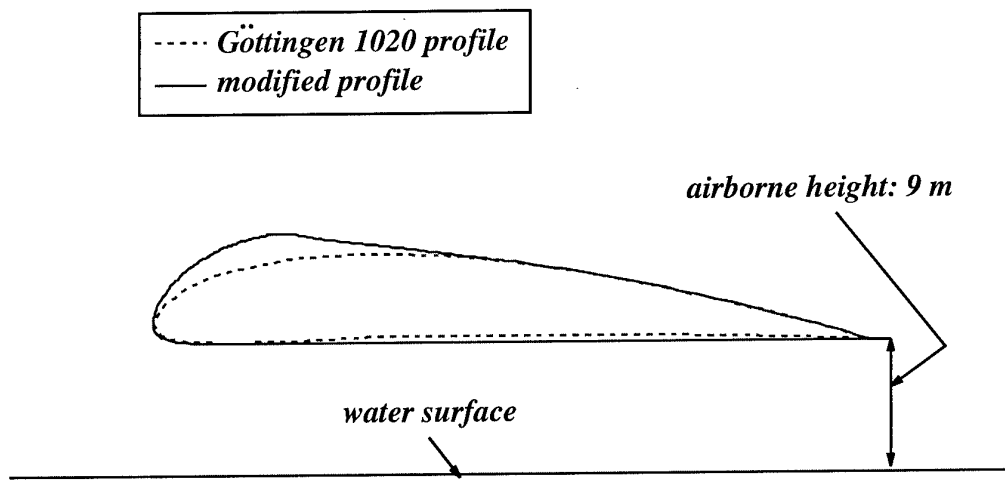


Figure 6: The initial and modified wing profile (of earlier design iteration, allowing angles of attack up to seven degrees) in airborne state

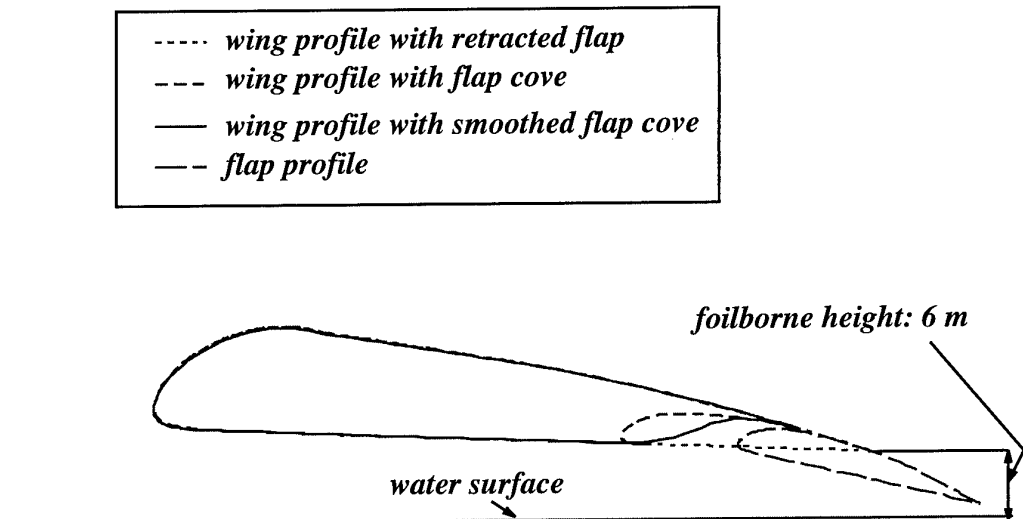


Figure 7: The wing profile (of earlier design iteration) and the trailing edge flap profile in foilborne state

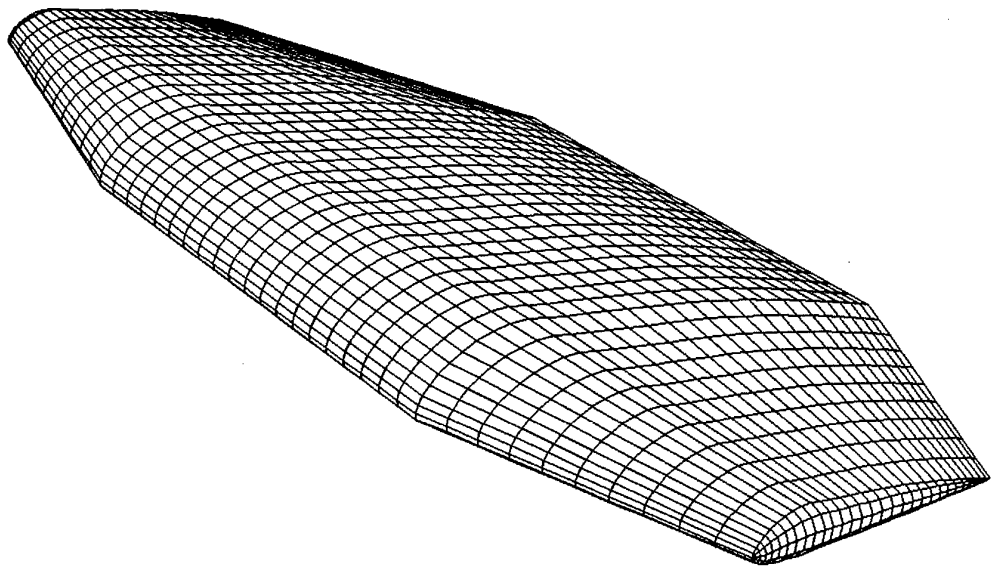


Figure 8: *Panel distribution over the wing*

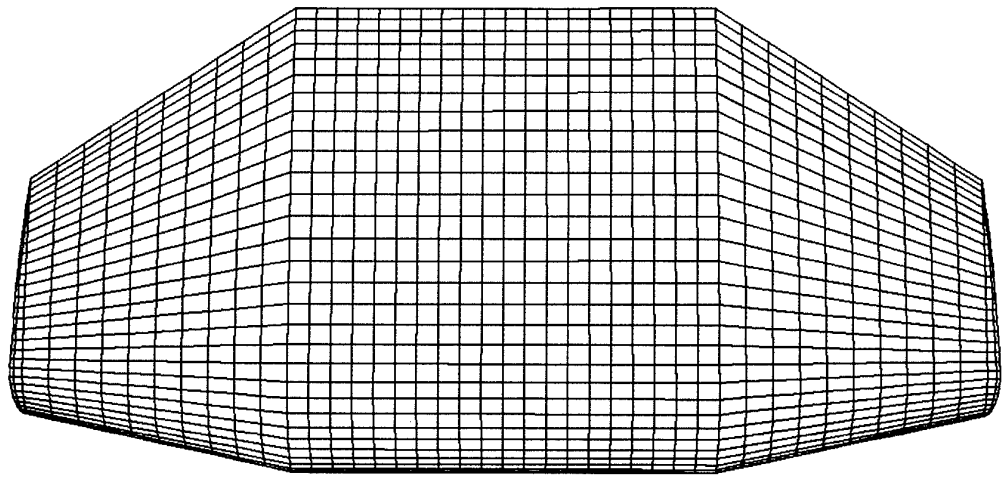


Figure 9: *Panel distribution over the wing; top view*

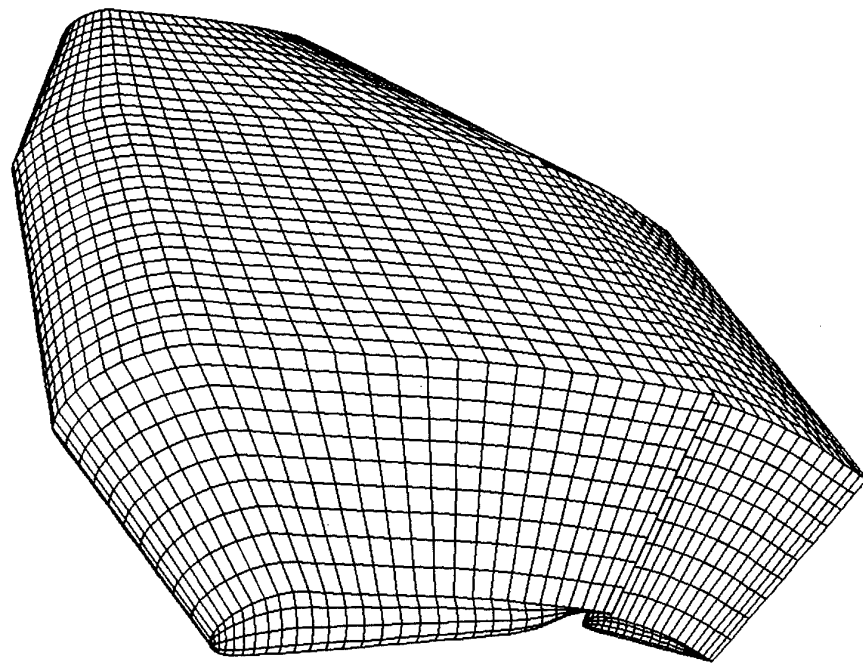


Figure 10: *Panel distribution over the wing with extended flap*

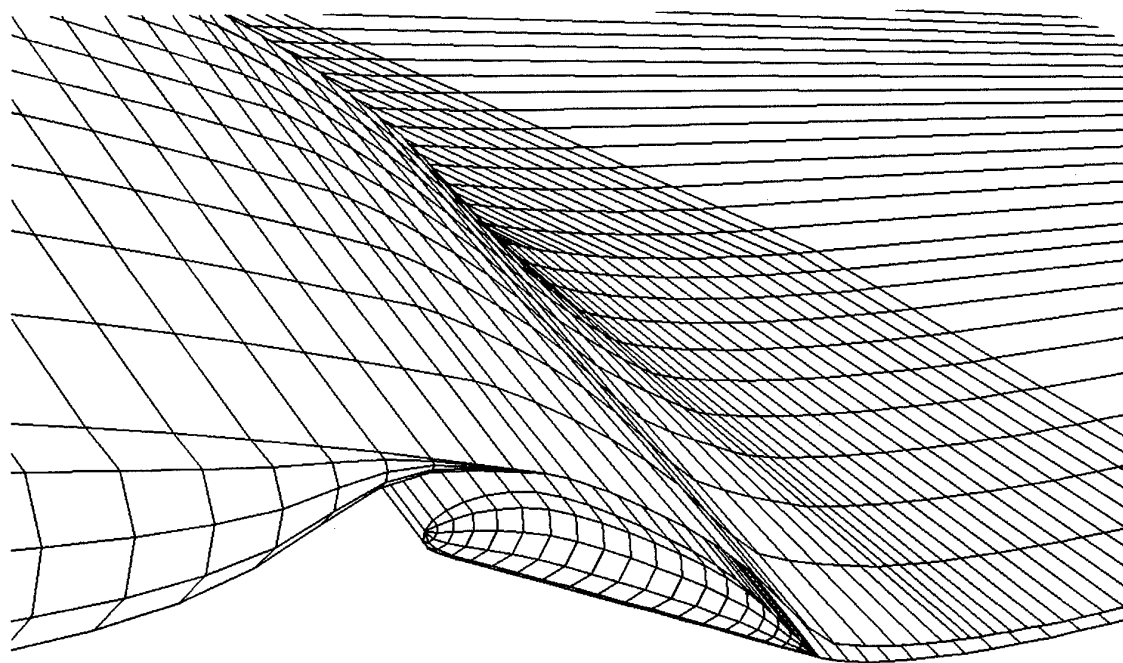


Figure 11: *Panel distribution over the wing with extended flap and the wakes; detail near the flap*

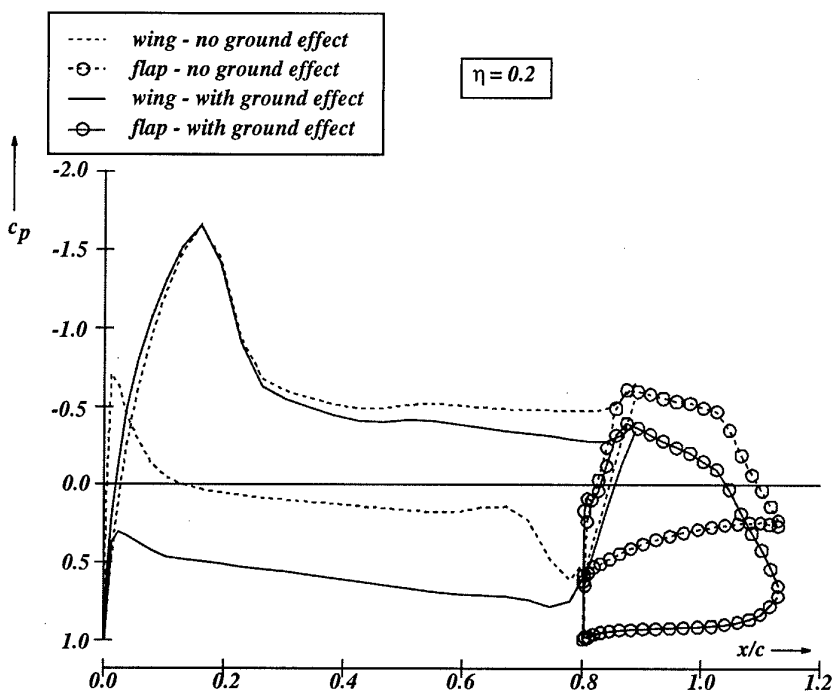


Figure 12: Pressure distributions over the wing and flap at $\eta = 0.2$ for $U_\infty = 50\text{kts}$, $\alpha = 0^\circ$, $\delta_f = 15^\circ$, foilborne state

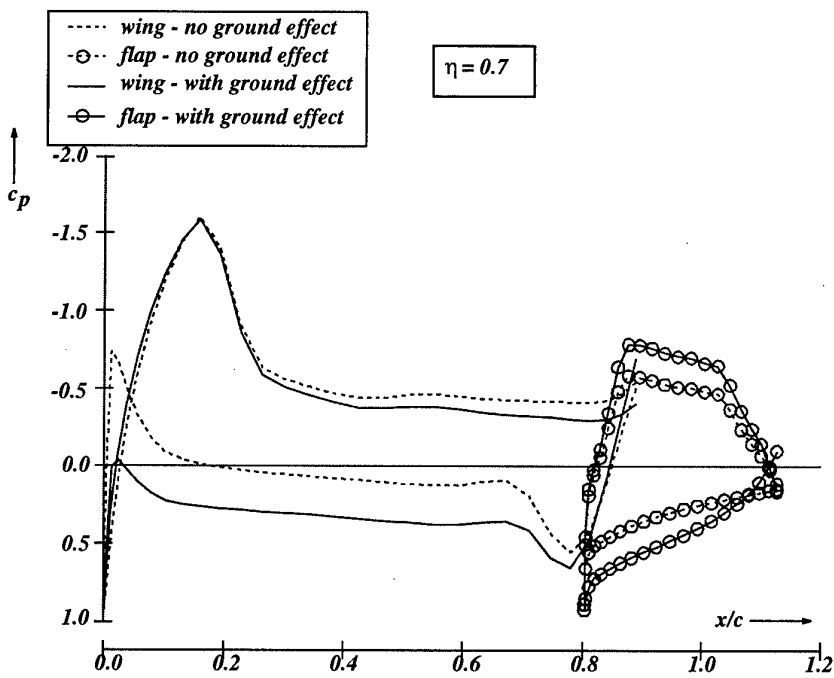


Figure 13: Pressure distributions over the wing and flap at $\eta = 0.7$ for $U_\infty = 50\text{kts}$, $\alpha = 0^\circ$, $\delta_f = 15^\circ$, foilborne state

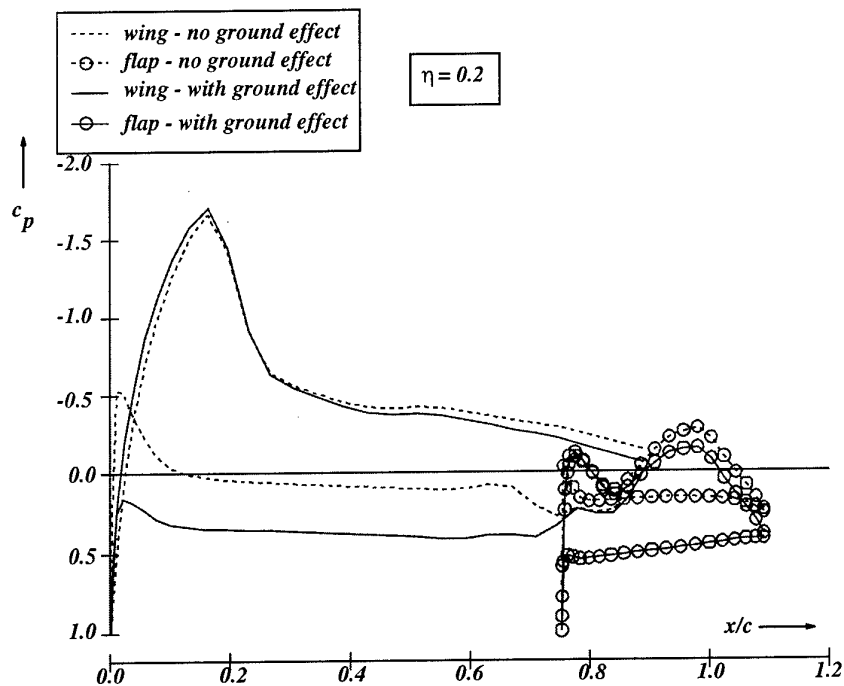


Figure 14: Pressure distributions over the wing and flap at $\eta = 0.2$ for $U_\infty = 85\text{kts}$, $\alpha = 2.1^\circ$, $\delta_f = 5^\circ$, airborne state

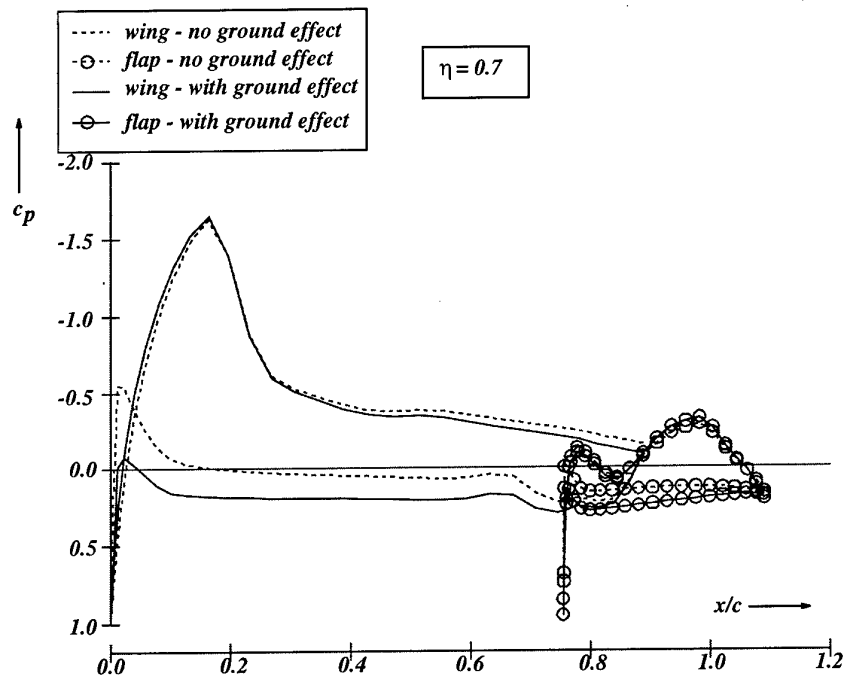


Figure 15: Pressure distributions over the wing and flap at $\eta = 0.7$ for $U_\infty = 85\text{kts}$, $\alpha = 2.1^\circ$, $\delta_f = 5^\circ$, airborne state

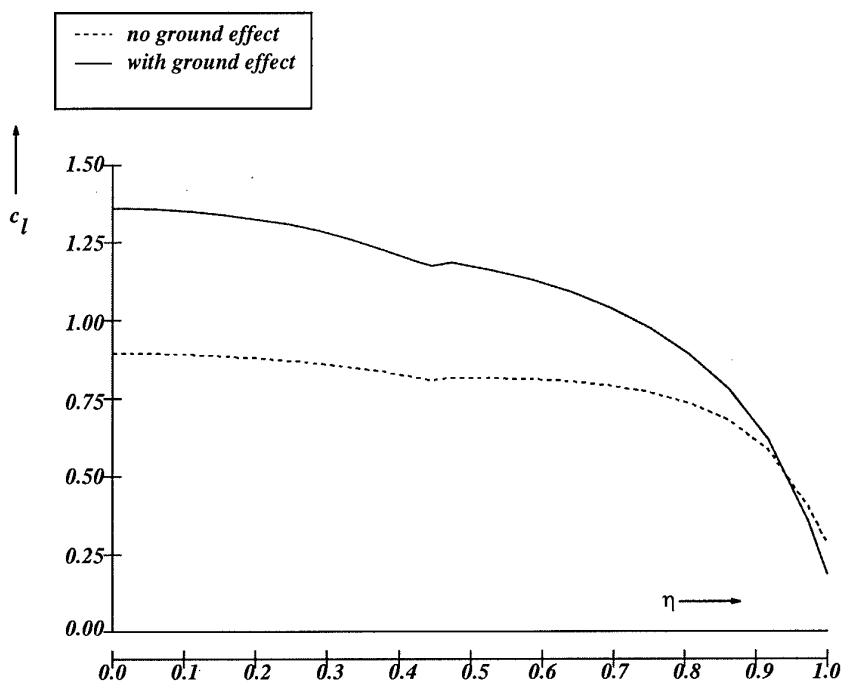


Figure 16: Spanwise lift distribution over the wing for $U_\infty = 50\text{kts}$, $\alpha = 0^\circ$, $\delta_f = 15^\circ$, foilborne state

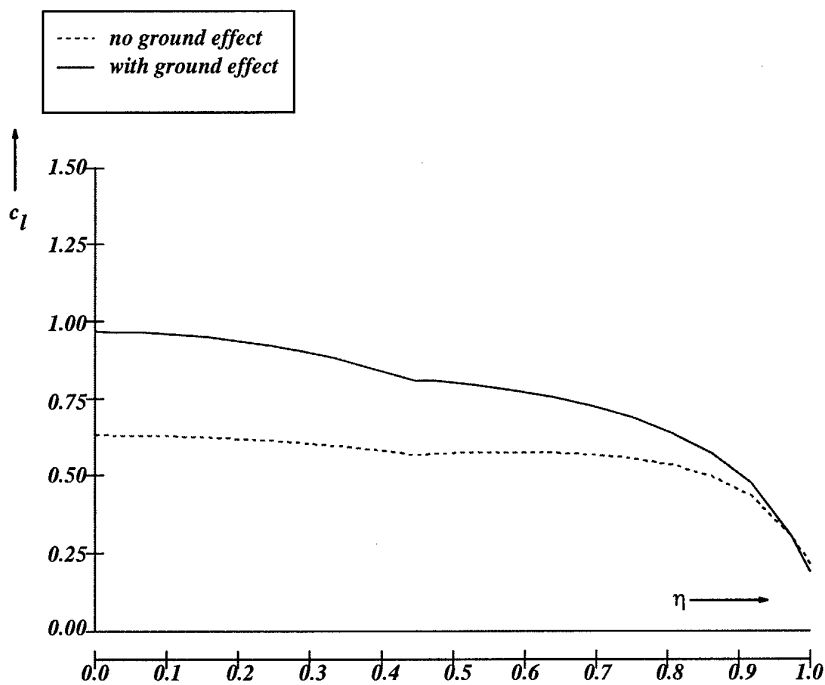
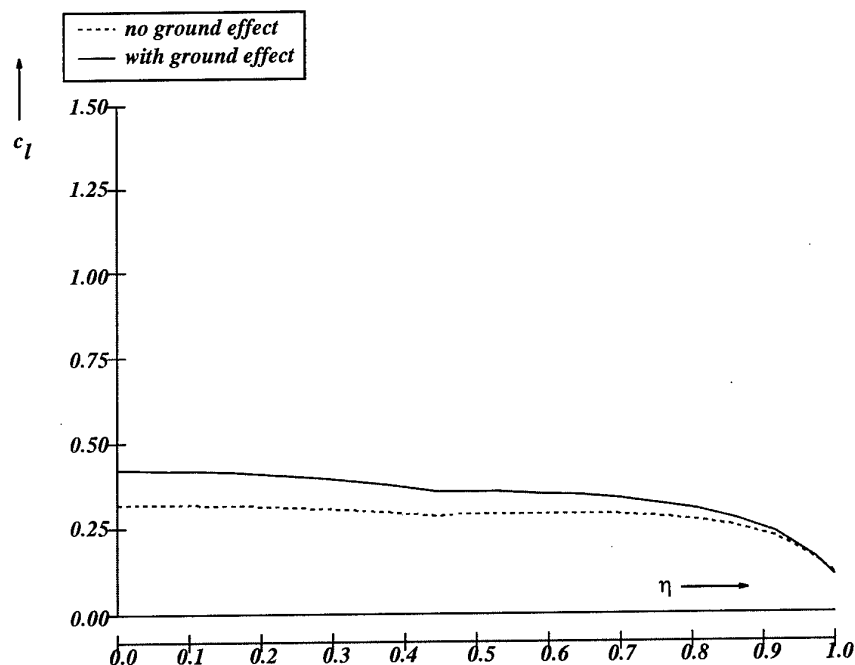
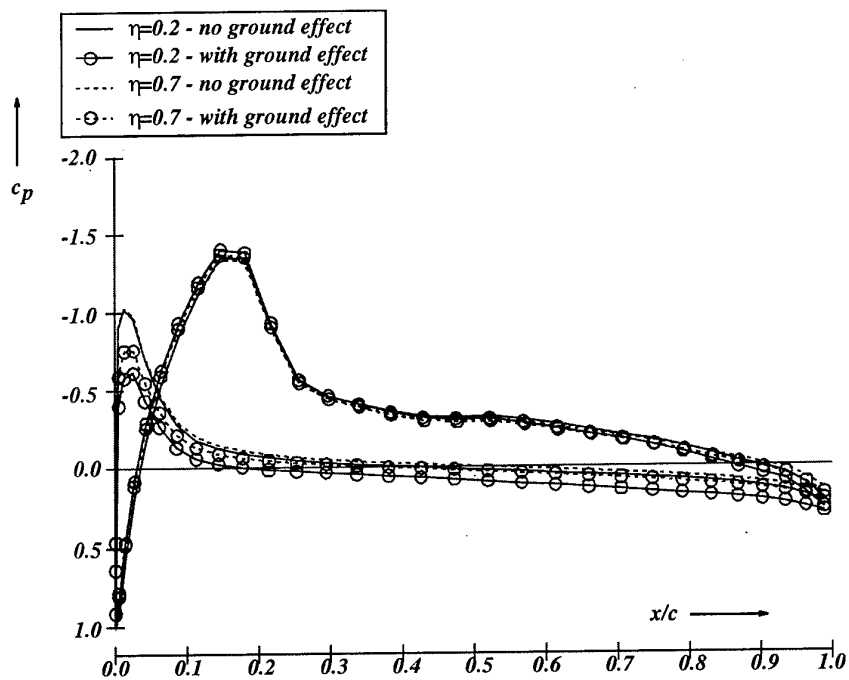


Figure 17: Spanwise lift distribution over the wing for $U_\infty = 85\text{kts}$, $\alpha = 2.1^\circ$, $\delta_f = 5^\circ$, airborne state



The first commercial ekranoplan "Amphistar" and prospects for the development of passenger ekranoplans

Dr. D.N. Sinitsyn

Dr. A.I. Maskalik

Technologies & Transport JSC

Sormovskoye Shosse 1-a

603603 Nizhny Novgorod, RUSSIA

Summary

The background and evolution of ekranoplan development in Russia is described in the paper. The data are given on the developed ekranoplans including the first civilian ekranoplan "Amphistar". The whole range of marine passenger ekranoplans (MPE) developed by the Russian "Technologies & Transport" JSC is shown. The description of the Marine Passenger Ekranoplan MPE-200 is presented together with conclusions concerning prospects for the development of passenger ekranoplans.

On 26 December 1997 the Russian Maritime Register of Shipping issued Certificate no.97.0222.130 for a sea-going dynamic air-cushion boat -ekranoplan "Amphistar" ("Amphibian star"), developed and built by a Russian company - "Technologies & Transport" JSC (Fig.1)*.

Thus the world civilian high-speed craft was for the first time enriched with extremely fast passenger boat based on a new concept - using the aerodynamic force of a wing in proximity of a screen.

This happened almost 40 years after R.E. Alexeyev, an outstanding Russian designer of high-speed sea-going vehicles, an author of "Volga", "Raketa", "Meteor", "Komet" and other hydrofoil craft well-known in Russia and abroad, commenced developing new craft-ekranoplans, using the so called "screen" effect for their movement.

R.E. Alexeyev's initiative to create ekranoplans was supported in the late 1950's by the Russian Navy, on the assignment of which during the 60-70's under R.E. Alexeyev's supervision the Nizhny Novgorod Central Hydrofoil Design Bureau developed a wide range of ekranoplan projects. These projects are based on a conceptually new aerohydrodynamic configuration of "a small-aspect-ratio wing with a lifting stabilizer" (Fig.2).

* The authors have got a video film about the "Amphistar" (10 minutes) that will be shown after the paper presentation.

The configuration is based on a small-aspect-ratio wing ($\lambda \leq 3$) with end plates, on an "under-wing air-jets" blowing system providing high take-off/landing and amphibian properties and on a stabilizing system consisting of a horizontal and a vertical tail planes that provide longitudinal and lateral stability together with controllability.

During 1960-1964 under Alexeyev's supervision some experimental ekranoplans (self-propelled models - CM) weighting up to 8 tons were built and thoroughly and successfully tested in still waters and with waves up to 1 meter at speeds up to 200 km/h in proximity to the screen (Fig.3). The tests proved the ability of the designed aerohydrodynamic configuration to solve the main task - ensure movement stability of an ekranoplan in extreme proximity to the "screen" and its natural "binding" to the water surface.

The consummation of the 1st generation ekranoplan aerohydrodynamic configuration worked out in the 60's became the largest of ekranoplans - KM (craft - model), designed under Alexeyev's guidance during 1964-1966. Its weight was about 500 tons, cruising speed - 500 km/h and seaworthiness corresponding to wave height of more than 3 m [1, 2]. During 1966 - 1969 the ekranoplan was successfully tested and the authoritative Government commission stated its high tactical and technical achievements.

The results of development and operation of the self-propelled ekranoplan models and the KM craft were incarnated while creating the first practical ekranoplan prototypes for the Russian Navy: landing troop carrier "Orlyonok" and missile-carrier "Lun" [1, 2].

Table 1 presents the basic data on the 1-st generation ekranoplans, designed under R.E.Alexeyev supervision [1].

During the 70's R.E. Alexeyev guided extensive scientific research and development on further perfection of ekranoplan aerohydrodynamic configuration. The main task of these activities was improvement of ekranoplan economic effectiveness, seaworthiness and amphibian capabilities.

The aerohydrodynamic configuration of the 2-nd generation ekranoplan was designed under Alexeyev's supervision by the end of the 70's (Fig.4).

It is based on a composite wing of a large extension ($\lambda=4-6$) with functional subdividing of its area into "lifting" and "blowing-under" parts. Such a wing and maximum reduction of the stabilizing surfaces area allowed to achieve the aerodynamic quality of 25 - 30, that is two times higher as compared to the 1-st generation ekranoplans; this also helped to substantially improve ekranoplan seaworthiness and amphibian capabilities.

The adoption of the new configuration implies a range of problems to be resolved, for instance provision of high precision and safe operation of automatic damping and stabilization systems. At the beginning of the configuration implementation we developed the first stage of the aerohydrodynamic configuration of the 2-nd generation ekranoplan, which still retains stabilizers system, though with significantly reduced area (Fig.5).

On the basis of the described configuration the "Technologies & Transport" Joint-Stock Company involved in development of passenger ekranoplans and formerly constituting a part of the Central Hydrofoil Design Bureau worked out a wide range of passenger ekranoplans, see Table 2[1], the first specimen of which (the boat-ekranoplan "Amphistar") was successfully built and certified by the Russian Maritime Register of Shipping.

In passenger ekranoplan design the company "Technologies & Transport" made use of flexible pneumo-cylinders as hydrodynamic elements of an ekranoplan. As compared to the stiff analog used in the 1st generation ekranoplans the flexible pneumo-cylinders show higher weight efficiency in providing floating and gliding as well as give an opportunity to substantially decrease overloads in take-off / landing modes and provide a wide range of amphibian capabilities.

In figure 6 there is shown a range of tasks that include optimization of all ekranoplan elements from the point of view of technical capabilities, as well as prospective commercial application.

On the basis of the defined design tasks we worked out a scale range of passenger ekranoplans of the 2-nd generation. Figure 7 shows their tactical and technical data. This range consists of ekranoplans with a displacement from 10 up to 500 tons, passenger capacity from 20 to 500 persons, seaworthiness - up to 3.5 m wave height and range - up to 6000 km.

The level of technical perfection of these ekranoplans, their transport, fuel and weight efficiency in comparison to other vehicles is shown in figures 8 - 10. On the conventional Gabrielli - Kármán diagram ekranoplans have their own application "niche", where they are unrivaled in transport efficiency. In terms of fuel and weight

efficiency the 2-nd generation ekranoplans are just as good as the modern subsonic passenger aircraft.

Thus, at the end of the 20th century it became possible for the mankind to implement a new type of perspective transport means that can be used in all seasons - ekranoplans that ensure highly efficient and safe transfer of passengers at speeds exceeding 600 km/h, at low (screen) flight altitudes over water (wave height up to 3m), ground, snow and ice; besides they possess amphibian capabilities and ability to come out directly to the shore, to move and to be based on it.

Besides the "Amphistar" ekranoplan the "Technologies & Transport" JSC has developed the Marine Passenger Ekranoplan MPE-200 (Fig.11). The aerohydrodynamic configuration of this ekranoplans is given in Fig.12. It consists of a body (1), a lifting wing with intermediate plates (2) and a twin-fin tail with high set horizontal tail plane (3). In the bow of the ekranoplans there is a starting power unit (4) consisting of two high-bypass-ratio turbofan home produced engines NK-87 with steering nozzles (5).

At the intersection of tail fins and horizontal tails there is a flight power unit (6) consisting of two turboprop engines NK-15 with coaxial propellers AV-90.

To support the craft in amphibious modes and to reduce the structure workload in take off / landing modes the body and the intermediate end plate lower surfaces are equipped with pneumo-cylinders acting as shock absorbers (7).

The wing of the craft is mechanized with deflecting flaps (8).

To control the ekranoplans the upper part of the wing panel is equipped with spoiler-ailerons (9), tail fins - with jar rudders (10,11) and the horizontal tail - with an elevator (12).

General layout of the ekranoplans is given in Fig. 13. In the bow there are a starting power unit, starting equipment and switch gear compartment, towing and anchor - handling gear, aerial post of the radar anti-collision station, wheel compartment and radio room.

The wheel compartment has working places for a commander, second pilot, flight engineer and navigator.

In the bow passenger cabin section the seats are placed on two decks. The upper deck is equipped with 81 airplane seats and toilets. The main deck bow section is divided into two cabins: the first one with 32 passenger seats, a kitchen and a buffet and the second - with 43 seats.

In the central part of the craft close to the center wing section there are domestic and auxiliary compartments (toilets, luggage, kitchen, buffet, provision and water compartments, etc.).

The stern passenger cabin section is also double-decked. The platform cabin is equipped with 51 seats, the main deck cabin - with 43 seats.

The stern part has auxiliary power unit section, electrical equipment, ventilation and heating equipment section and life rafts.

The horizontal tail is equipped with the stern power unit. Fuel is held in four fuel tanks in the center wing section.

The undertaken research works testify that exploiting these craft for passenger conveyance is effective and highly promising not just owing to their high speed, seaworthiness properties and economic efficiency, but also due to the safety aspect. High passenger conveyance safety as compared to aviation is provided in an emergency by the ability of an ekranoplan flying low over the water to execute "soft" landing at any moment.

The prospects for the future development of passenger and cargo ekranoplans depend, on the one hand, upon general acceptance of the second generation aerohydrodynamic configuration and on the other hand, upon further development of its potential to increase weight efficiency, economic ratio, safety, seaworthiness, to improve overall strength and effectiveness of engines, to provide control system reliability, to decrease the craft weight etc.

In particular, Russian researchers expect that a possible increase in ekranoplan range considered as the integral economic ratio could reach 25-30%. Thus, the range of the MPE-200 would be more than 4000 km.

Illustrations

I List of Figures

Fig.1. The "Amphistar" ekranoplan moving in proximity to the screen, speed - 150 km/h.

Fig.2. The 1st generation ekranoplan aerohydrodynamic configuration.

Fig.3. Self-propelled model of the 1st generation ekranoplan

Fig.4. The 2nd generation ekranoplan aerohydrodynamic configuration.

Fig.5. First stage 2nd generation ekranoplan aerohydrodynamic configuration.

Fig.6. The problems to be solved while designing ekranoplans.

Fig.7. The 2nd generation civilian ekranoplans.

Fig.8. Gabrielly -Karman diagram.

Fig.9. Ekranoplan fuel effectiveness.

Fig.10. Ekranoplan weight effectiveness.

Fig.11. Marine passenger ekranoplan MPE-200.

Fig.12. Aerohydrodynamic configuration of the MPE-200 ekranoplan.

Fig.13. General layout of the MPE-200 ekranoplan.

II Tables

1. The 1st generation ekranoplans.

2. The 2nd generation passenger ekranoplans (General Designer D.N. Sinitsyn).

References

1 D.N. Sinitsyn, A.I. Maskalik «The Ekranoplan is a New Type of High Speed Water Transport which can be used in all Seasons», Workshop Proceedings of Ekranoplans & very fast craft, 5-6 December, 1996, Sydney, Australia, p.p.152-162.

2 V.N. Kirillovikh «Russian Ekranoplans», Proceeding of the International Workshop on «Twenty - First Century Flying Ships», held in the University of New South Wales, Sydney, Australia, 7-9 November, 1995, p.p. 71-117.

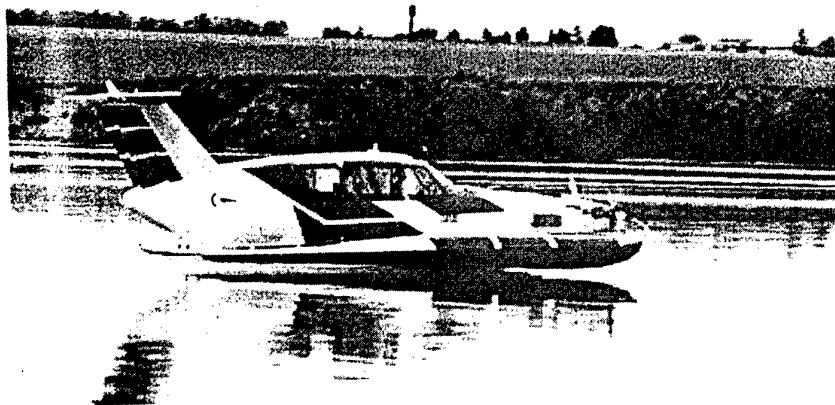


Fig. 1

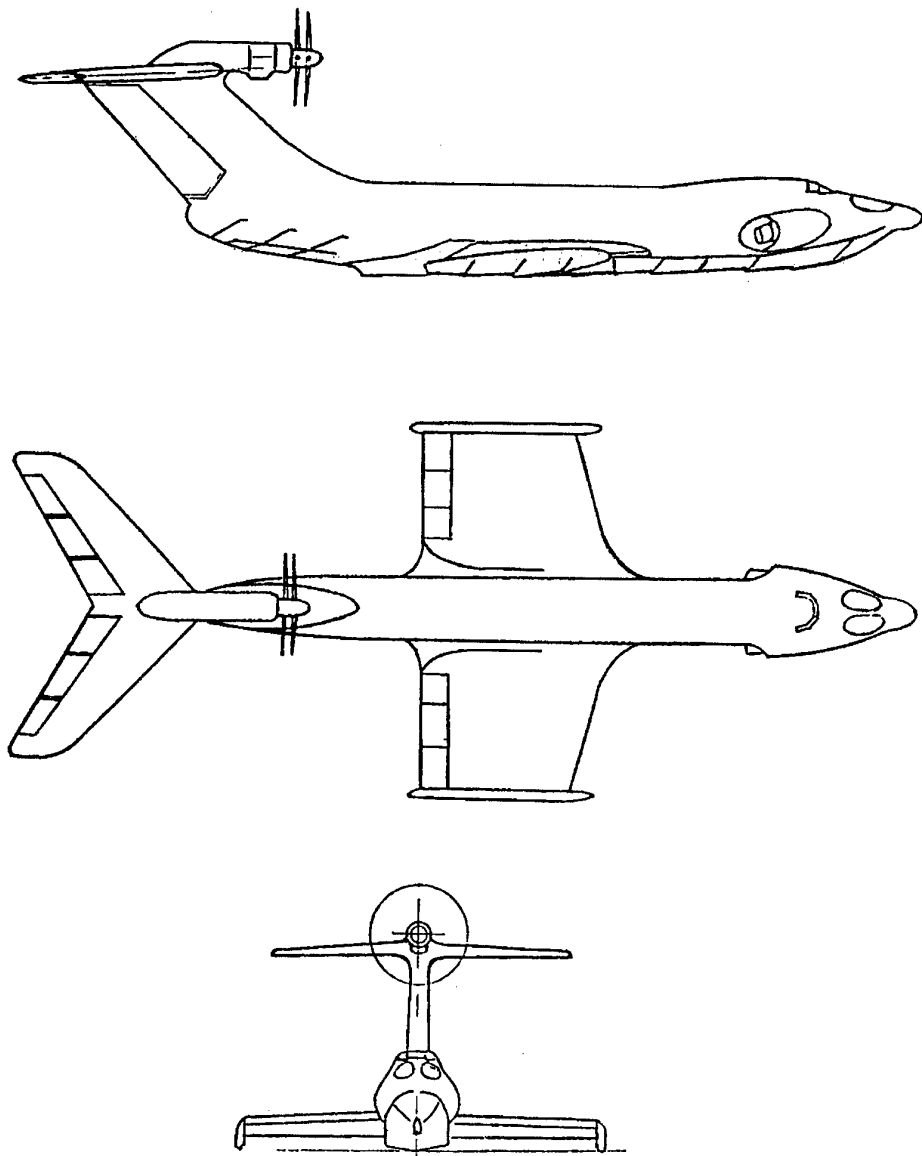


Fig. 2

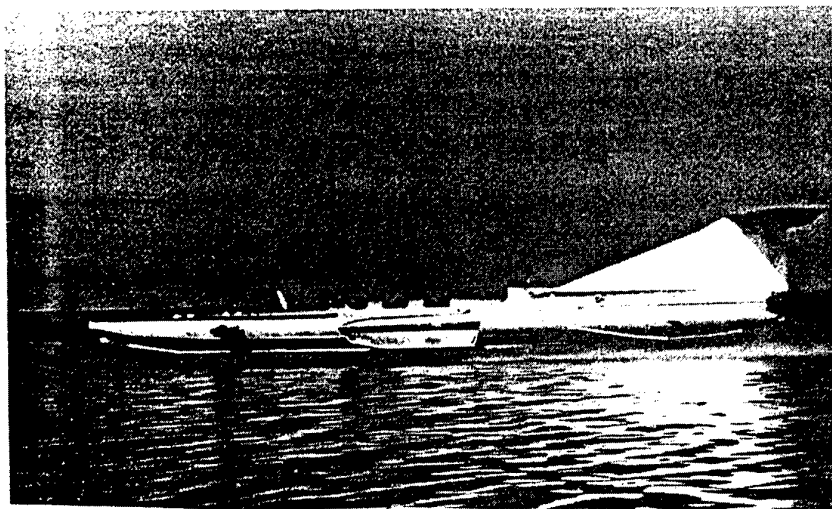


Fig. 3

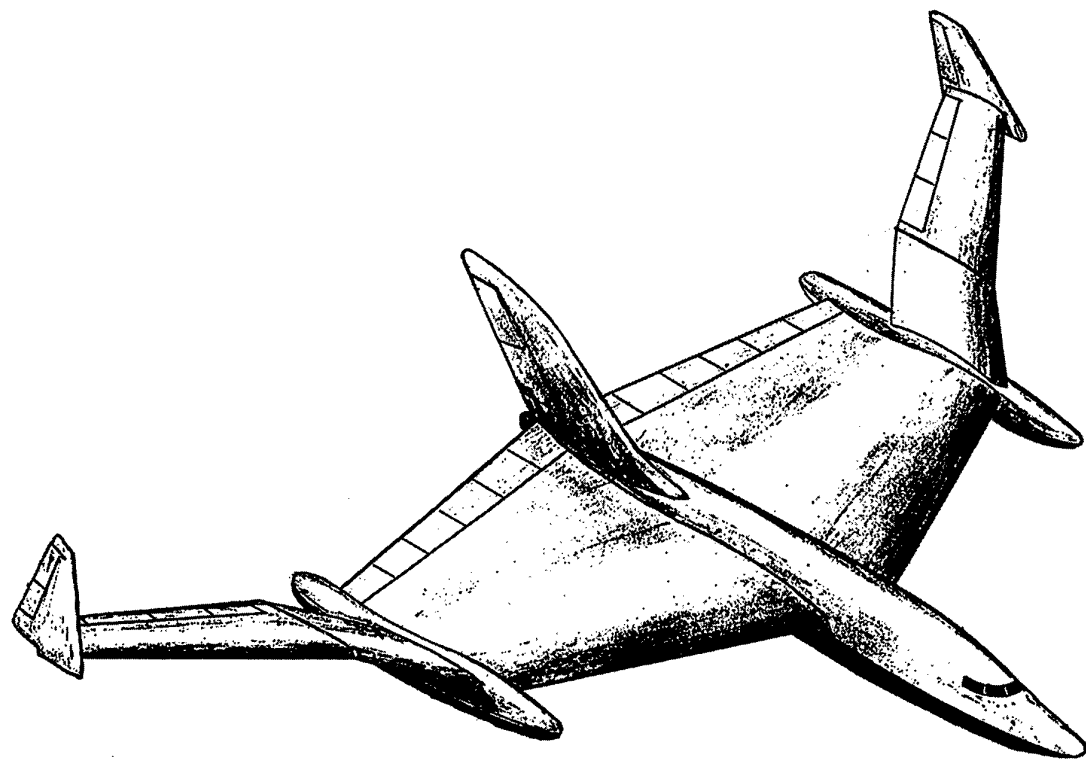


Fig. 4

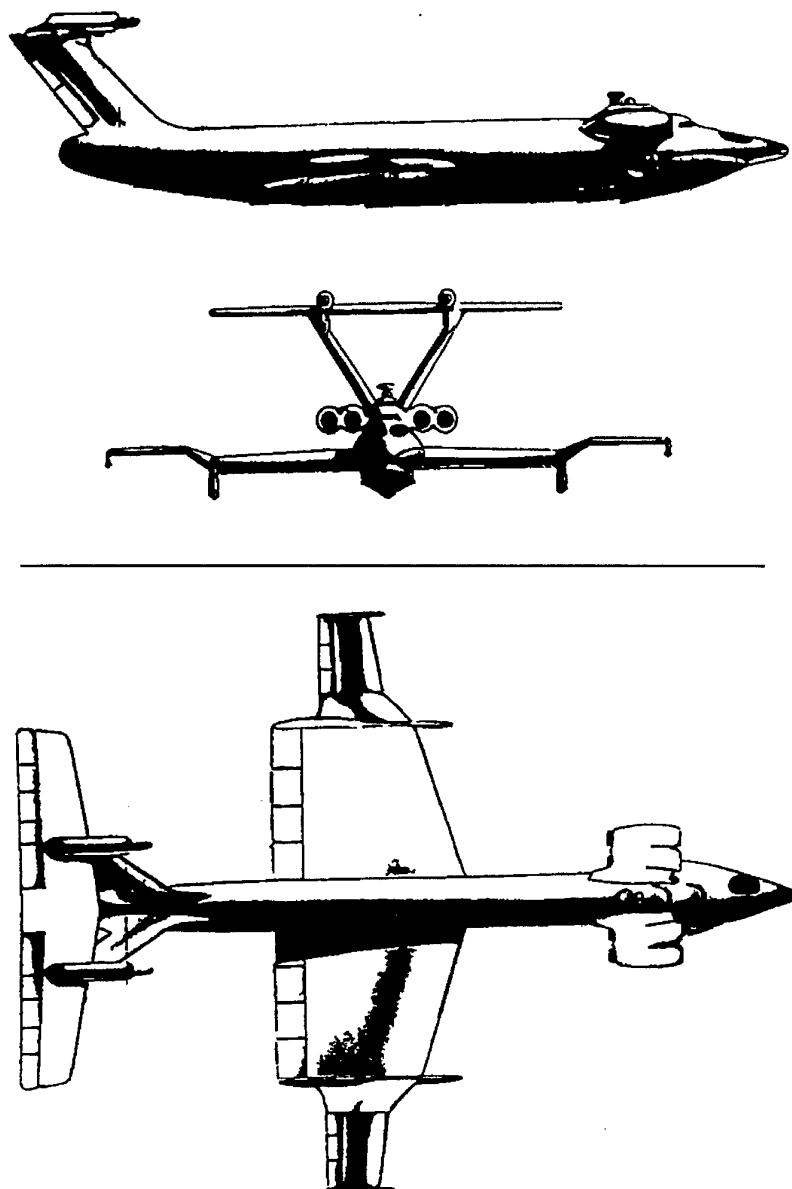
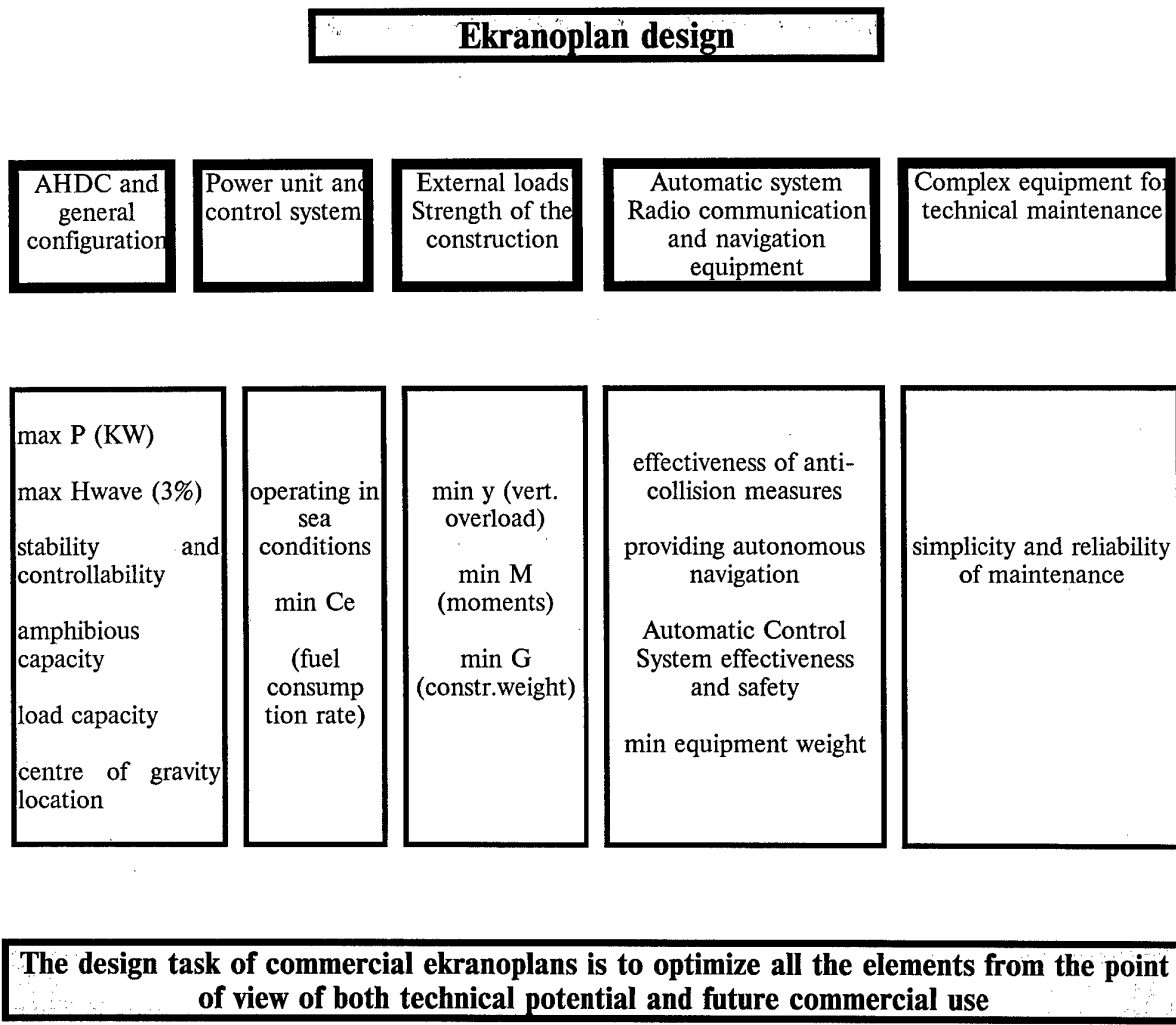


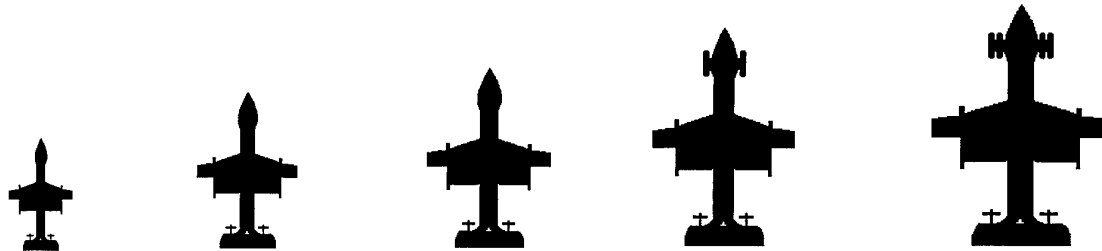
Fig. 5

**Fig. 6**

The second generation civilian ekranoplans

Basic Technical Data (specifications)

Range (km)				
1000	1800	3000	4500	6000
Wave height at take off (m)				
1.0	1.5	2.0	2.5	3.0
Cruising speed (km/h)				
250	320	400	450	500
Passenger capacity				
18	150	250	340	460
Displacement (t)				
10	90	210	300	470
MPE-10	MPE-100	MPE-200	MPE-300	MPE-400



Integrated aerohydrodynamic configuration
 Unified engines
 Base navigation-handling complex

Fig. 7

The level of technical perfection
of ekranoplans in comparison
with conventional vehicles

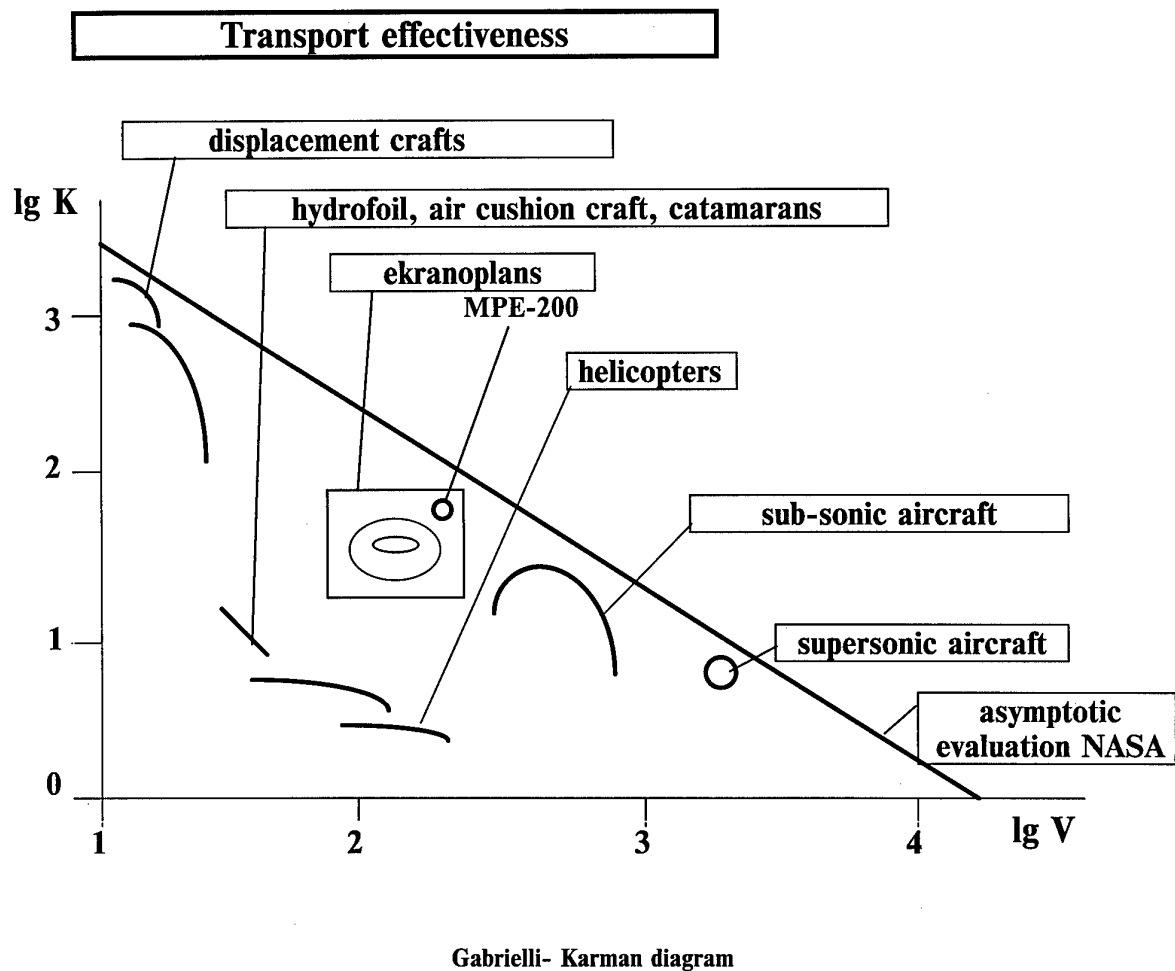


Fig. 8

**Technical comparison of
ekranoplans with conventional
vehicles**

Fuel consumption effectiveness

Q pass.= 1 gram of fuel / 1 passenger 1 km

fuel consumption in order 1
passenger x 1 km

Qt load = 1 gram of fuel / 1t of load 1 km

fuel consumption in order 1t of
load x 1km

Qt weight = litres of fuel / 1t of weight 100 km

fuel consumption in order 1t of
total weight x 100 km

Type of a vehicle	Q pass	Qt load	Qt weight
Boeing 707-320C	31.3	334	8.54
Aerobus A 310-300	33.9	339	4.98
Aerobus A 300 B4	34.0	329	8.54
MPE-200	47.0	466	7.71

**The second generation ekranoplan fuel consumption transporting 1t of total
weight is comparable to subsonic aircraft**

Fig. 9

The level of technical perfection of ekranoplans in comparison with conventional vehicles

Weight effectiveness

G useful.	G hull.	
G vert.tail=-----	G hull.=-----	G useful. = G comm. + G t
--	--	
G total.	G total.	

Type of vehicle	Gtotal.	Guseful. %	Ghull. %	Gvert.tail	Ghull.
The first generation ekranoplans "Orlyonok"	140	37.5	64.9	26.8	46.4
The second generation ekranoplans MPE-200	210	72.8	65.6	34.7	31.2
Modern aeroplanes					
IL-86	206	91.5	62.9	44.4	30.5
AN-22	225	105.9	70.0	47.1	36.0
DC-10	195.2	90.1	57.2	46.1	29.3
Boeing 707-320C	148	85.7	35.4	57.9	23.9

The second generation ekranoplans have relative hull weight on the level of modern aeroplanes, but they are inferior in weight efficiency due to the installation of equipment for safety in sea operations

Fig. 10

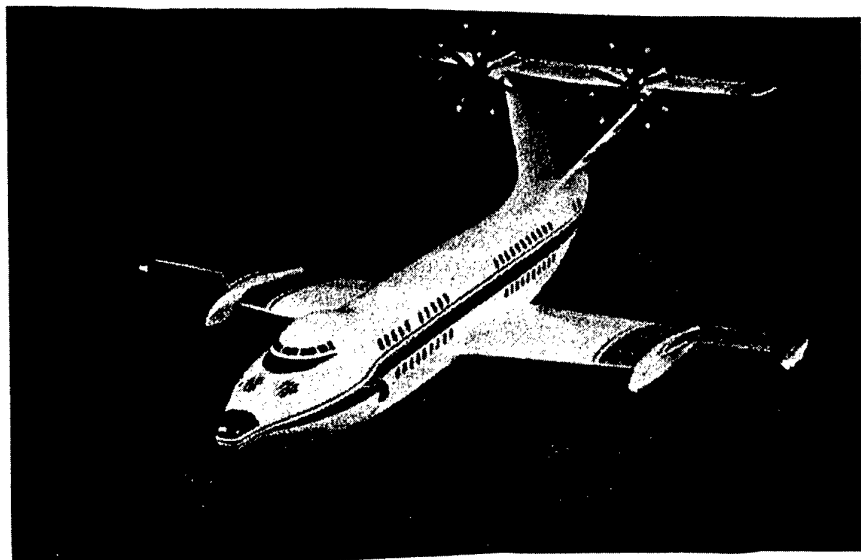


Fig. 11

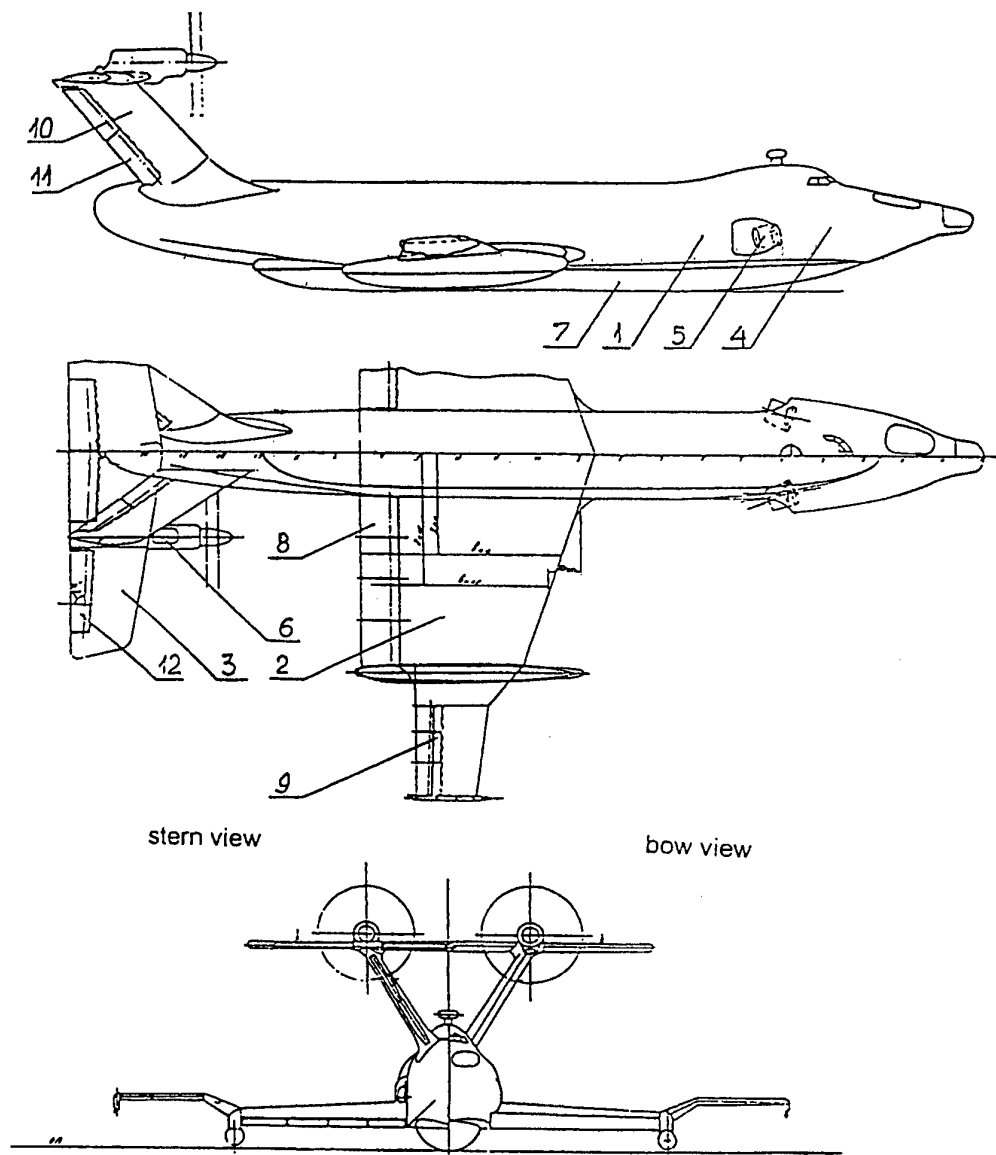


Fig. 12

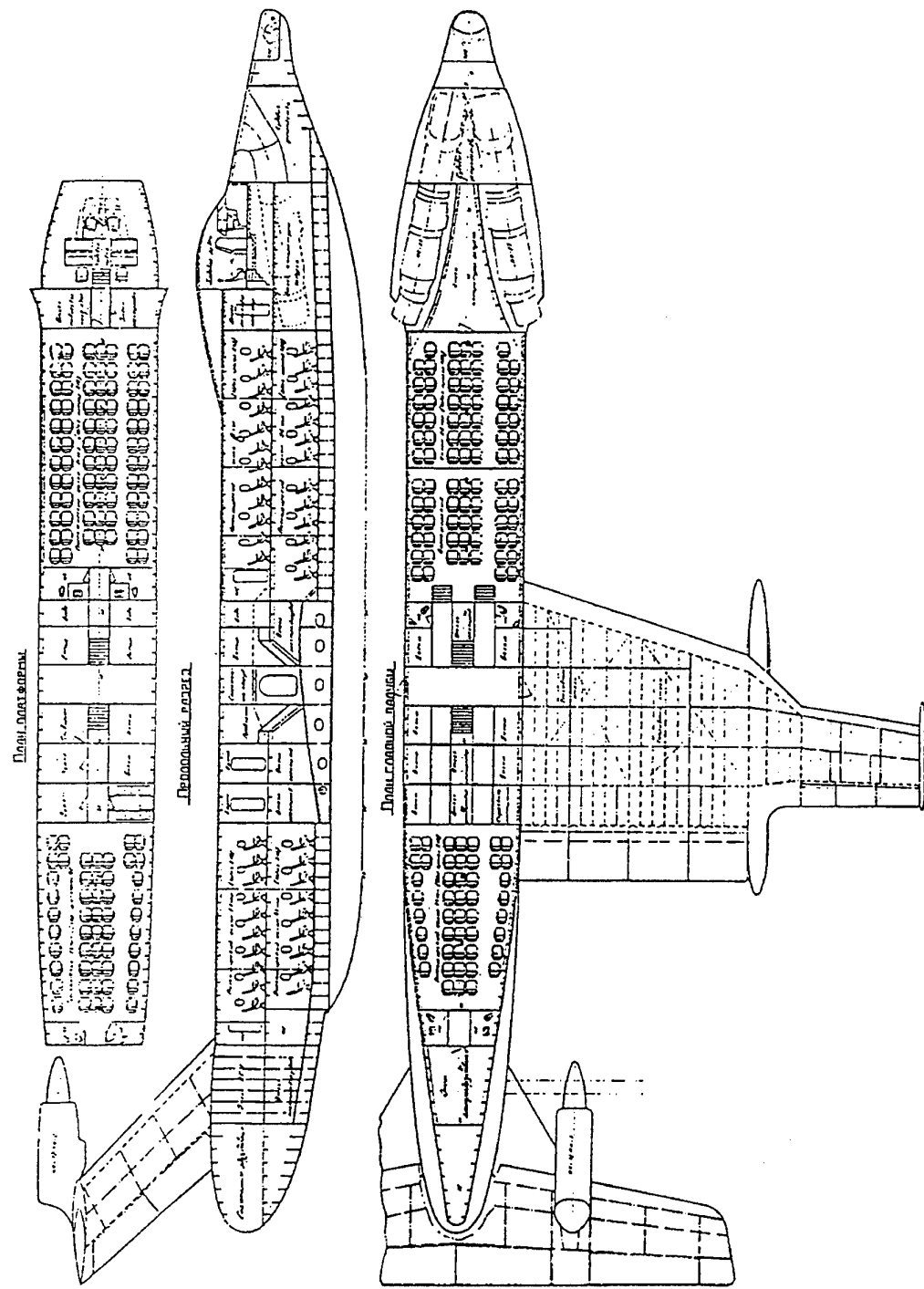


Fig. 13

Table 1
The first generation ekranoplans

	Ekranoplan type	The AHDC scheme	Max displacement (take off weight), t	Overall dimension LxBxH	The wing aspect ratio B=bow S=stern	Power unit type	Max thrust (power), t, (h,p)	Max speed km/h	Seaworthiness Hwave 3%, m
1	SM-1	biplane	2.8	20.0x1.0x1.4	$\lambda_{bow}=1.26$ $\lambda_{stern}=1.35$	4xTS-12	P= 4x0.12	250	0.5
2	SM-2	biplane	3.2	20.0x0.9x1.5	$\lambda_{bow}=1.73$ $\lambda_{stern}=2.0$	2xRU-19-300	P= 2x0.9	250	0.5
3	SM-2P7	monoplane +lifting stabiliser	6,3	19,4x0.9x1.6	$\lambda=2.0$	KR7-300	P=2,0	300	1,0
4	SM-3	"	3.5	14.5x0.9x1.3	$\lambda=0.48$	RU-19-300	P=1.0	200	0.5
5	SM-4	"	4.8	20.0x0.9x1.96	$\lambda=2.0$	B:KR7-300 S:RU-19-300	PB=2.0 PS=1.0	300	0.7
6	SM-5, SM-8	"	8.0	24.5x9.5x5.5	$\lambda=2.0$	B:KR7-300 S:KR7-300	PB=2.0 PS=2.0	300	12
7	KM	"	500	98x35x22	$\lambda=2.0$	B:8xVD-7 S:2xVD-7M	PB= 8x9.5 PS=2x10.5	550	3.5
8	SM-6	"	26.5	31.0x14.8x7.9	$\lambda=2.8$	B:2xRD-9B S:AI-20	PB=2.1 PS=(3750)	300	1.0
9	UT-1	"	0.9	9.7x5.4x2.0	$\lambda=22$	M332	N= 140	170	0.3
10	The landing troop carrier "Ortyonok"	"	140	58.0x31.5x16.0	$\lambda=3.0$	B:2xNK8-4 S:NK-12	PB=2x10.5 PS=15.0	400	1.5

Table 2
Second generation passenger ekranoplans
(General Designer Sinitsyn D.N.)

Ekranoplan type	Passenger board	The AHDC scheme	Max displ (t/o weight),t	Overall dimension	Wing Aspect ratio	Power unit type	Max thrust (power) t(h,p) B=bow S=stem	Cruising speed km/h	Cruising range km	Seaworthiness in take off and landing modes Hwave (3%)
1 Amphistar	4	low-set lifting wing small aspect ratio	2.4	11.0x5.9x3.2	0.8	Mercedes-benz N=240 h,p		165	400	0.3
2 Marine passenger MPE-100	150	composite wing	80-100	41x30x12	4.5	B:2xD-30 S:D-27	PB=2x6.8t PS=14t	380	1800	1.3-1.5
3 Marine passenger MPE-200	250	composite wing	180-210	57x42x15	4.5	B:2xNK-87 S:2xNK-15	PB=2x13.5t PS=2x15t	400-430	3000	1.8-2.0
4 Marine passenger MPE-300	340	composite wing	300-350	68x48x17	4.5	B:4xNK-87 S:2xNK-15	PB=4x13.5t PS=2x15t	450	4500	2.0-2.5
5 Marine passenger MPE-400	460	composite wing	450-500	73x53x20	4.5	B:6xNK-87 S:2xNK-15	PB=6x13.5t PS=2x15t	500	6000	2.5-3.0

A VIEW OF THE PRESENT STATE OF RESEARCH IN AERO - AND HYDRODYNAMICS OF EKRANOPLANS

A.I. Maskalik

Deputy Director General

JSC "Technologies & Transport"

K.V. Rozhdestvensky

Saint-Peterburg State Marine Technical University

3, Lotsmanskaya, 190008 Saint-Petersburg

D.N. Sinitsyn

Director General and Principal Designer

JSC "Technologies & Transport"

1a, Sormovskoye shosse, Sormovo

603603 Nizhniy Novgorod

Russia

ABSTRACT

Ekranoplans as a novel very high-speed craft is one of the promising transportation alternatives of the next millennium. The paper presents a viewpoint upon present state of research relevant to development of ekranoplans with focus on Russian achievements in this field. More information on the corresponding developments on the international scene can be found in (Ref. 11-14). Discussed are the problems of aerodynamics, hydrodynamics and dynamics of ekranoplans with particular attention to the matters related to use of power augmentation and peculiarities of static and dynamic stability.

conceived under guidance of R.E Alekseev and served as a basis in development of ekranoplans "Orlyonok" and "Lun", comprises main wing of moderate aspect ratio $\lambda = 2-3$ with a special foil section and one sided endplates, and a sizable lifting highly mounted horizontal tail unit. An inseparable part of this configuration was a lift-off power augmentation system, designed for the purpose of blowing the engine exhaust under the main wing.

1. INTRODUCTION

Development and construction of ekranoplans necessitated solution of challenging problems of aerodynamics of vehicles, advancing near interface of two media : water (snow, ice, ground) and air.

During the period of development of practical prototypes of ekranoplans "Orlyonok", "Lun", "Amphistar" (Ref. 1-5) in Russia there were created basics of theory of motion of these vehicles as well as experimental facilities and installations for the purpose of solution of principal problems of aerodynamics and hydrodynamics of ekranoplans. At present time, when the first Russian commercial ekranoplan "Amphistar" (principal designer D.N. Sinitsyn) has been built (Ref. 5), the state of the art in aero- and hydrodynamics of this high-speed craft can be characterized in the following way

2. AERO-HYDRODYNAMIC CONFIGURATION (AHC)

Aero-hydrodynamic configuration of ekranoplans of the first generation (Figure 1), which was

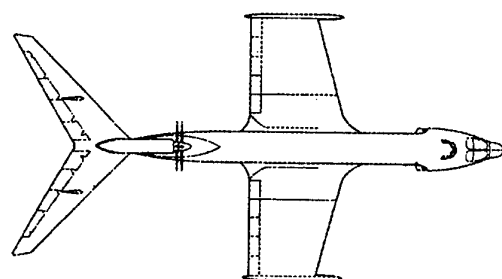
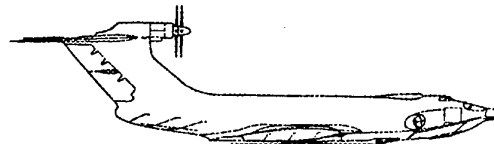


Fig. 1 Aerodynamic configuration of ekranoplan of the 1st generation

Implementation of this AHC secured the following principal features of ekranoplan:

- Detachment from water (snow, ice, ground) with further acceleration into a cruise flight;
- Stable (without use of automatic control system) cruise flight in ground effect;
- Lift-to-drag ratio $L/D = 15 - 17$;
- Seaworthiness (as capacity to take-off and land in conditions of rough seas) up to $h_w 3\% = 2.5 - 3.0 m$;
- Good characteristics of steerability and maneuverability in all modes of motion;
- Amphibious capacity, in particular, capability of climbing onto a beach, as well as moving and basing on it, and returning to water.

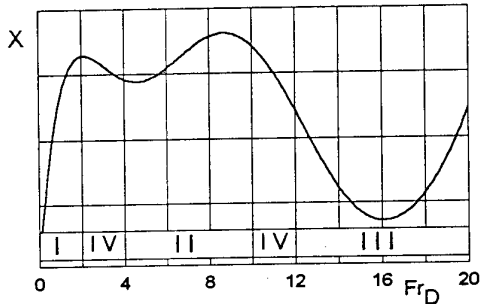


Fig. 2 Characteristic drag curve of ekranoplan of the 1st generation (I - floating, II - planing, III - flaring in ground effect, IV - intermediate regimes)

Figure 2 presents characteristic drag curve of an ekranoplan of the first generation plotted versus displacement Froude number Fr_D .

In the seventies R.E. Alekseev proposed an aerohydrodynamic configuration of ekranoplan of the second generation (Ref. 1) of the "flying wing" type, see Figure 3. Due to increase of the aspect ratio up to $\lambda = 4 - 6$ and use of S-shaped wing sections lift-to-drag ratio of such a configuration can be augmented up to $K = L/D = 25$. Therewith the ekranoplan based on such a configuration can operate far from the underlying surface (out-of-ground effect) still retaining sufficiently high lift-to-drag ratios of 10-12. During development of the "flying wing" configuration there were encountered serious problems of hydrodynamics and take off (landing) which still await their solutions.

In the eighties D.N. Sinitsyn proposed an AHC of an ekranoplan of the first stage of the second generation (Ref. 1,4), see Figure 4. This AHC employs a scheme of a "composite wing" with functional subdivision of wing area into a "lifting" and "power augmented" parts. Introduction of such a concept enabled to considerably reduce the area of horizontal stabilizer (tail) as compared to the ekranoplans of the first generation, increase lift-to-drag ratio up to 20, improve seagoing and amphibious properties of the craft.

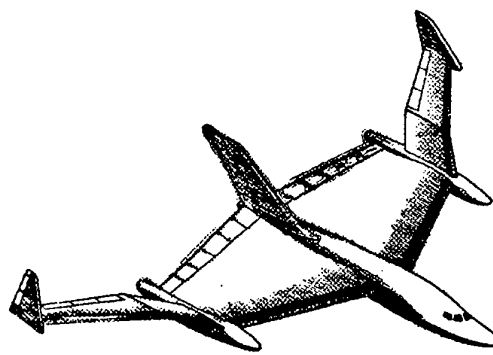


Fig. 3 Alekseev's flying wing configuration.

On the basis of the aforementioned AHC the Joint-Stock Company "Technology and Transport" developed a scale series of commercial ekranoplans with technical parameters as presented in Table 1. One can see from this table that the ekranoplan of the second generation MPE-400, comparable in its main dimensions to the ekranoplan of the first generation "Lun" at a similar cruise speed of 500 km/h will have range about 6000 km (against 2000 km of "Lun") and (take-off) seaworthiness of $2.5-3.0 \text{ m}$ wave height (against 2 m of "Lun").

3. AERODYNAMICS

Developed as a result of large effort of Russian and foreign researchers (Ya. M. Serebriysky, R.E. Alekseev, Ya. I. Voitkunsky, G.A. Pavlovets, V.K. Treshkov, A.N. Panchenkov, V.N. Treschevsky, L.D. Volkov, K.V. Rozhdestvensky, V.P. Shadrin, T. Nishiyama, S. Widnall *et al.*) the theory of wing motion in ground proximity enables (at conceptual and preliminary stages of design) to solve practical tasks of choice of the geometry and reciprocal location of lifting elements of the AHC of ekranoplan as well as

other tasks related to determination of aerodynamic characteristics of these wing elements.

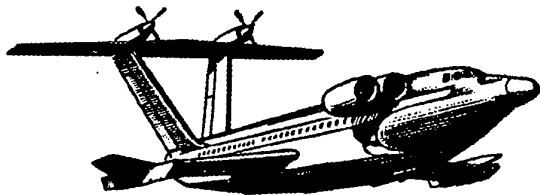


Fig. 4 Aerodynamic configuration of ekranoplan of the first stage of 2d generation (MPE-400)

Oftentimes, use of very simple close form expressions can provide sufficient information at first stages of design. For example, an estimate of the influence of the ground upon lift coefficient of a wing can be made with acceptable accuracy using the formula (Ref. 6),

$$c_y = \frac{dc_y}{d\alpha} (\alpha + \Delta\alpha - \Delta\alpha_o), \quad (1)$$

where α_o , angle of zero lift of the foil in unbounded fluid, $\Delta\alpha_o$, correction to α_o accounting for the influence of the ground, $\Delta\alpha_o = \alpha_o \theta_c(\bar{h})$, \bar{h} relative ground clearance, defined as the ratio of the ground clearance to the chord of the main wing, function $\theta_c(\bar{h})$ characterizes variation of α_o due to the curvature of the foil, see Figure 5.

With account of thickness and curvature of the foil

$$c_y = \left(\frac{dc_y}{d\alpha} \right)_{h=\infty} \cdot \theta_\alpha(\bar{h})(\alpha + \Delta\alpha - \Delta\alpha_o), \quad (2)$$

where

$$\Delta\alpha_o = \theta_\delta(\bar{h}) \frac{8\delta}{1 + \delta^2} + \theta_c(\bar{h})\alpha_o,$$

and δ is relative thickness of the foil, $\theta_\delta(\bar{h})$ corresponding *thickness function*

Many practical analytical results, relating aerodynamic performance of a wing in close proximity to an underlying surface with its geometry and kinematics, have been obtained with use of the theory of a lifting system in extreme ground effect (Ref. 7). These formulae are useful as the first approximation when carrying out preliminary design of the vehicle.

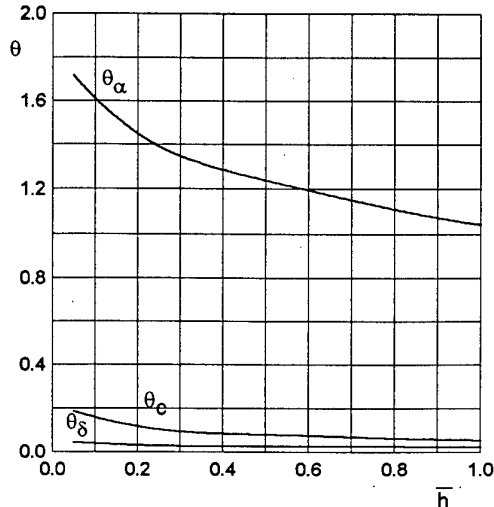


Fig. 5 Parameters θ_α , θ_c and θ_δ versus relative height of the foil above the ground.

Second approximation is usually obtained on the basis of experimental investigation with use of facilities for physical modelling of the ground effect. Among those developed in Russia, one can mention wind tunnels with reproduction of ground effect by means of different reverse flow technique (mirror image, still ground board, still ground board with suction of boundary layer, moving ground (belt)) as well as test facilities realizing direct motion of the wing (in a hydrochannel, above a "dry" track or by means of a catapult). Among the most important results, obtained on the basis of theoretical and experimental research of aerodynamics of the wing in ground proximity one can list the following

- The influence of the ground features considerable increase of its lift and lift-to-drag ratio with almost no variation of total drag versus ground clearance
- Among geometrical parameters, the aspect ratio has the most significant influence upon aerodynamic characteristics of a wing in ground effect; decrease of the aspect ratio results in decrease of the lift and lift-to-drag ratio, this decrease being more pronounced than for a wing in unbounded fluid. Putting lower one-sided endplates on the tips of the wing considerably enlarges effective aspect ratio by way of reducing lateral leakage of the flow from under the wing (so called end losses are reduced).

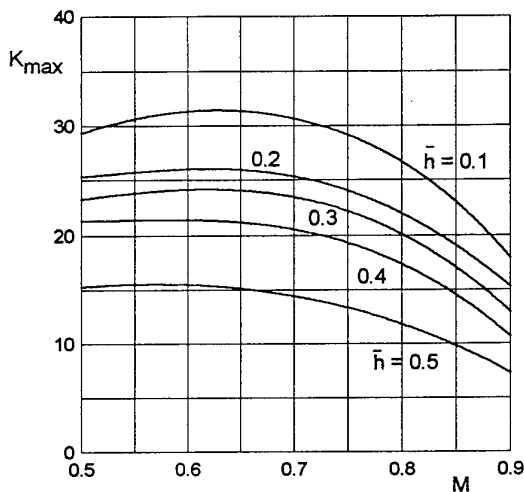


Fig. 6 Lift-to-drag ratio of a rectangular wing versus Mach number ($\lambda = 2$).

- Augmentation of thickness of the foil, moving near the ground at small angles of attack, leads to reduction of lift coefficient c_y and its derivative with respect to ground clearance c_y^h , and to increase of derivative of the lift coefficient with respect to angle of attack. Simultaneously, parasite drag increases.
- Increment of curvature of the foil out of ground effect entails augmentation of lift coefficient c_{y_0} , corresponding to zero angle of attack, with almost no variation of c_y^α . In ground effect the increment of c_{y_0} is more noticeable, although magnitude of c_y^α diminishes. Drag of the wing at c_{y_0} varies insignificantly when closer to the ground, although with large curvature $c > 9\%$ the ground exerts favourable influence upon flowfield, the wing's drag being reduced.
- Displacement of maximum thickness of the foil in chordwise direction serves to change lifting properties of the wing in ground effect. Maximum magnitudes of derivatives c_y^h and c_y^α are associated with location of maximum thickness, close to the leading edge ($\approx 20\%$ of the chord). The same location corresponds to maximum lift-to-drag ratio.
- Prevailing contribution to lifting capacity in ground effect is due to lower surface of the wing, whereas the upper one plays insignificant role. Character of dependence of derivative c_y^α on the form of the lower side of the

wing in ground effect is a function of the aspect ratio and the angle φ_{ep} of installation of lower endplates. For example, for $\lambda = 2$ and $\varphi_{ep} = 0$ the derivatives c_y^α are practically the same for a flat and curved foil. With increase of φ the derivative c_y^α diminishes. When $\varphi_{ep} = 90^\circ$ the derivative c_y^α of a curved foil is much smaller than that of a flat one. For $\lambda = 1$ the curvature of the wing section has but insignificant influence upon c_y^α . The magnitude of the derivative c_y^h decreases with increase of curvature of the lower side of the wing.

- Influence of the ground proximity upon unsteady characteristics of a wing displays itself in the following way. Aspect ratio λ has similar effect upon all rotatory derivatives, namely with increase of λ these derivatives increase in magnitude. Form of the foil, operating near the ground, essentially influences derivatives with respect to parameter h and have less effect upon derivatives with respect to speed of rotation $\dot{\theta}$. Derivatives in parameters h and $\dot{\theta}$ are close in magnitude. Rotatory derivative c_y^h is dominated by added mass, which considerably increases as the wing approaches to the ground. Other derivatives with respect to parameters h and $\dot{\theta}$ are small.

Derivatives c_y^h and m_z^h grow in magnitude when the wing comes closer to the ground, but to lesser degree than positional derivatives.

Derivative c_y^h increases near the ground more rapidly for wings of small aspect ratios. Rotatory derivative of the moment grows more intensively for wings of large aspect ratio.

- When the wing is moving above wavy underlying surface, the magnitudes its aerodynamic characteristics are oscillating near their average values $c_{y_0}, m_{z_0}, m_x = 0$, corresponding to the wing's motion above flat ground. For a fixed relative ground clearance \bar{h} the amplitudes of these oscillations increases with growth of the wave amplitude. For a fixed wave amplitude decrease of \bar{h} entails growth of increments of c_{y_0} and m_{z_0} .
- Favourable influence of the ground upon aerodynamic characteristics is maintained up to Mach numbers $M \approx 0.7$ (see Figure 6). Then its lift-to-drag ratio decreases quite considerably

The influence of the angle of attack α_o at large distances from the ground has but a weak effect upon derivatives c_y^θ and m_z^θ ; for smaller ground clearances augmentation of α_o results in reduction of c_y^θ ; derivative m_z^θ increases with increase of α_o for wings of large aspect ratio and diminishes for wings of small aspect ratio.

β_g ratio of momentum of gas blown under the wing to that in the jets under the wing.

4. HYDRODYNAMICS

On the basis of research, conducted by Russian researchers (R.E. Alekseev, A.I. Maskalik, V.K. Dyachenko, E.A. Kramarev, E.I. Privalov *et al.*) there was created theoretical and experimental knowledge base relevant to modes of motion of ekranoplan in contact with water, which can be assigned to "hydrodynamics" of wing-in-ground effect craft. As a matter of fact, according to the concept of motion of the developed ekranoplans, power augmentation (blowing under the wing) is enabled before they start to move, i.e. at zero speed.

Presence of jets of the engines under the wing changes the character of interaction of the ekranoplan with the underlying surface. Among the most important results, obtained from theoretical and experimental investigations of ekranoplan's mode of motion in contact with water, one can single out the following

Generation of considerable lift upon the wing subject to power augmentation by means of blowing the exhaust of the engines underneath (Figure 7) is largely due by stagnation of the engine jets, blown between the wing and the ground.

Figure 8 shows dependence of nondimensional magnitude of average pressure under the wing $p/\rho u^2$ (u velocity of gas at the engine nozzle exit) upon relative (equivalent) ground clearance

$$\bar{h}_{eq} = 0.42 \frac{b}{l} \left[\frac{h}{b} + 1.89 \cdot 10^{-4} \frac{\varphi b}{h} + \frac{\Delta S}{bl} \right] \quad (3)$$

where ΔS excess of the area of cross section under the leading edge of the wing over the area of the jets of the engines.

Total forces, acting upon ekranoplan in power augmentation mode, with account of engine thrust can be expressed by the formulae

$$Y = T \sin \theta_e (1 - \beta_g) + p l b \quad (4)$$

$$X = T \cos \theta_e [1 - (1 - \varepsilon) \beta_g] \quad (5)$$

where T is total thrust of engines, θ_e angle of inclination of the engine axis with respect to horizon,

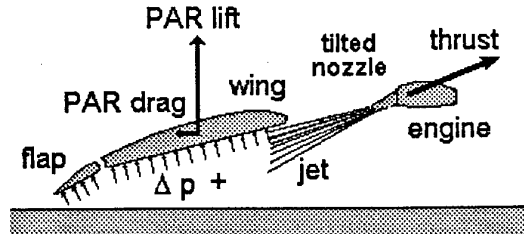


Fig. 7 Scheme of generation of lift force in power augmentation mode.

Using the above formulae one can evaluate the efficiency of power augmentation as a function of the geometry of the wing (l, b), angle of inclination of the wing with respect to the hull (φ), position of the engines (θ_e, β_g), location of the flap above the ground (h), number of functioning engines n and mode of their operation (T, u), pitch angle of ekranoplan φ . Magnitude of real lift-to-drag ratio in PAR mode of the developed ekranoplans is $K = Y/X = 16 - 17$.

Development of mathematical models of motion of an ekranoplan in this mode requires knowledge of its hydrodynamic characteristics with account of blowing ($H + B$)

$$c_{y_{HB}} = \frac{2Y_{H+B}}{\rho V^2 S}, \quad c_{x_{HB}} = \frac{2X_{H+B}}{\rho V^2 S}, \quad (6)$$

$$m_{z_{HB}} = \frac{2M_{z_{H+B}}}{\rho V^2 S b} \quad (7)$$

These coefficients are determined by means of towing tank tests of models of ekranoplan, equipped with special power augmentation devices, in the towing tank or with use of special aerohydrodynamic testbeds.

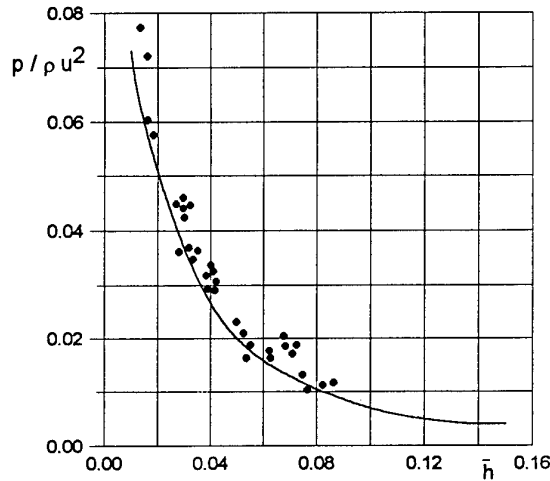


Fig. 8 Average pressure $p / \rho u^2$ in PAR generated cushion versus equivalent ground clearance \bar{h}_{eq}

Hydrodynamic components of these coefficients can be written as

$$c_{yH} = c_{y_{H+B}} - \bar{Y}_B \cdot c_t \quad (8)$$

$$c_{xH} = c_{x_{H+B}} - \bar{X}_B \cdot c_t \quad (9)$$

$$m_{zH} = m_{z_{H+B}} - \bar{M}_{z_B} \cdot c_t \quad (10)$$

where

$$\bar{X}_B = \frac{X_B}{T}; \quad \bar{Y}_B = \frac{Y_B}{T};$$

$$\bar{M}_{z_B} = \frac{M_{z_B}}{T} \quad (11)$$

are correspondingly nondimensional drag, lift and longitudinal moment due to power augmentation,

$$c_t = \frac{2T}{\rho V^2 S} \quad (12)$$

coefficient of thrust (T) of the engine.

Figure 8 shows nondimensional hydrodynamic coefficients versus clearance. With increase of the ground clearance h magnitudes of hydrodynamic forces vanish. The factors influencing c_{yH} , c_{xH} , m_{zH} are parameters h and φ which determine the wetted area of the ekranoplan. Investigated in the wide range of variation were the influence of position of the nozzles of PAR engines, aspect ratio of the wing and loading of the power augmented area of the wing upon efficiency of the blowing under the wing, in particular, upon lift-to-drag ratio in PAR

mode. Research covered wide range of thrust-to-weight ratios ($T/G = 0.15 - 0.25$) and relative distances of the wing's leading edge from the ground ($h/\sqrt{S} = 0.25 - 0.6$).

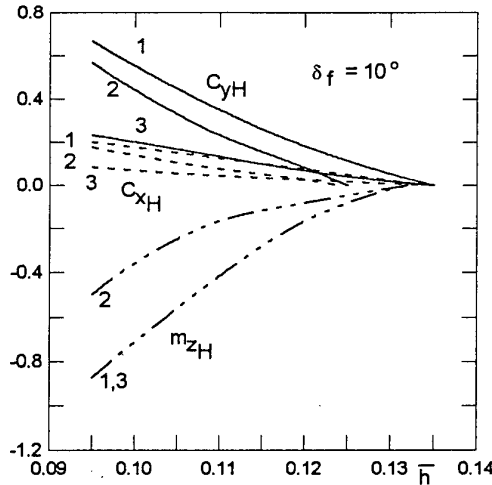


Fig. 9 Dependence of hydrodynamic coefficients upon relative height ground clearance (1 - $\varphi = 1^\circ$, 2 - $\varphi = 2^\circ$, 3 - $\varphi = 5^\circ$; $G_{model} = 4.8 \text{ kg}$, $c_t = 1$, $\delta_{nozzle} = 22^\circ$)

The methodology of research enables to devise an optimal power augmentation system for an ekranoplan in each particular case. The efficiency of power augmentation is, to a considerable extent, determined by achievable minimum speed of detachment of the ekranoplan from water. Reduction of the speed of detachment of the craft from water brings about reduction of maximum external loads acting upon an ekranoplan, i.e. eventually the vehicle's economic efficiency and seaworthiness.

Figure 10 presents dependence of detachment speed of ekranoplan on its take-off mass for different efficiencies of power augmentation. It can be seen that more efficient blowing (at $\delta_f = 10 - 15^\circ$) reduces magnitude of the speed of detachment from water.

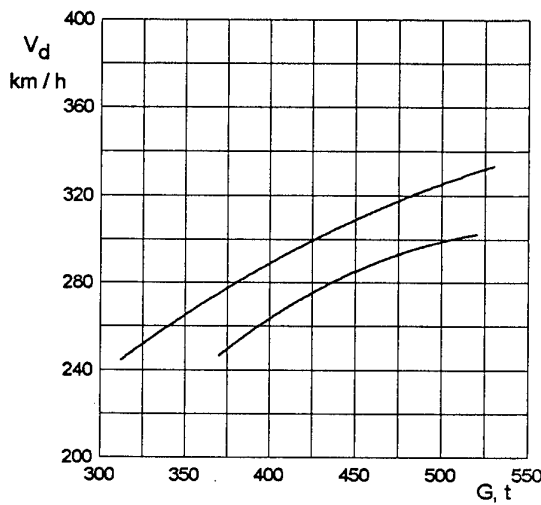


Fig. 10 Speed of detachment of ekranoplan from water versus take off weight G ($1 - \delta_{fl} = 6^\circ - 10^\circ$, $2 - \delta_{fl} = 10^\circ - 15^\circ$)

5. STABILITY AND CONTROLLABILITY

Based on results of research of Russian scientists (R.E. Alekseev, A.I. Maskalik, D.N. Sinitsyn, V.I. Zhukov, G.V. Aleksandrov and others) there are established at present time fundamentals of the theory of stability and controllability of ekranoplans (Ref. 8). Principal peculiarity of ekranoplan consists in dependence of its aerodynamic characteristics not only on pitch angle but also on ground clearance. Therewith these dependences have quite pronounced nonlinear character. That is why development of a theory of stability of ekranoplan required application of new approaches.

5.1. Longitudinal motion of ekranoplan

Characteristic equation, corresponding to a system of differential equations, describing longitudinal motion of ekranoplan, has the form

$$\begin{aligned} F(\lambda) &= \lambda^5 + A_1 \lambda^4 + A_2 \lambda^3 + \\ &A_3 \lambda^2 + A_5 = 0 \end{aligned} \quad (13)$$

where the coefficients $A_i, i = 1 \dots 5$ are expressed in terms of concrete aerodynamic characteristics of ekranoplan and their derivatives, depending upon relative ground clearance. The following condition

of longitudinal static stability of ekranoplan in height was obtained (Ref. 8)

$$\left(\frac{dc_y}{d\bar{H}} \right)_{m_z=0, \delta^*=const} = c_y^{\bar{H}} \frac{\bar{x}_{F_\theta} - \bar{x}_{F_H}}{\bar{x}_{F_\theta} - \bar{x}_T} > 0 \quad (14)$$

In order to secure longitudinal static stability of ekranoplan in pitch and in height it is necessary to fulfil the following inequalities

$$\bar{x}_{F_\theta} > \bar{x}_T, \quad \bar{x}_{F_\theta} > \bar{x}_{F_H} \quad (15)$$

which basically means that for a statically stable vehicle the aerodynamic center in height should be located upstream of the aerodynamic center in pitch. Note, that here the x -axis is directed downstream.

The following conditions stipulate longitudinal static stability of ekranoplan as a flying craft

$$A_1 > 0; \quad A_2 > 0; \quad A_3 > 0; \quad (16)$$

$$A_4 > 0; \quad A_5 > 0, \quad (16)$$

$$A_1 A_2 - A_3 > 0 \quad (17)$$

$$\begin{aligned} R_5 &= (A_1 A_2 - A_3)(A_3 A_4 - A_2 A_5) - \\ &(A_1 A_4 - A_5)^2 > 0. \end{aligned} \quad (18)$$

The boundary of oscillatory stability is determined by the equality $R_5 = 0$. The boundary of aperiodic stability is determined by equality $A_5 = 0$. The requirement of aperiodic stability for an ekranoplan ($A_5 > 0$) has the form (Ref. 8)

$$\begin{aligned} m_z^{c_y} < \frac{k_2 \Delta \bar{x}_{F_H}}{K(c_x^\theta / c_y^\theta - c_x^{\bar{H}} / c_y^{\bar{H}})} + \\ \frac{\bar{y}_t}{K} \left(1 - \frac{c_t^{\bar{V}}}{2c_{x_0}} \right) \end{aligned} \quad (19)$$

where

$$k_2 = 1 - \frac{c_t^{\bar{V}}}{2c_{x_0}} - K \frac{c_x^\theta}{c_y^\theta} \quad (20)$$

$$c_t^{\bar{V}} = \frac{2T^V}{\rho SV} \quad (21)$$

and c_t is thrust coefficient,

$$\bar{y}_t = \frac{y_t}{b} \quad (22)$$

ordinate of thrust axis.

Condition of oscillatory stability of ekranoplan $R_5 > 0$:

$$(\Delta \bar{x}_{F_H})_{min} < \Delta \bar{x}_{F_H} < (\Delta \bar{x}_{F_H})_{max} \quad (23)$$

5.2 Lateral motion of ekranoplan

A distinguished feature of ekranoplan as compared to the airplane in lateral motion is considerable dependence of lateral moment coefficient m_x on ground clearance h , see Figure 11.

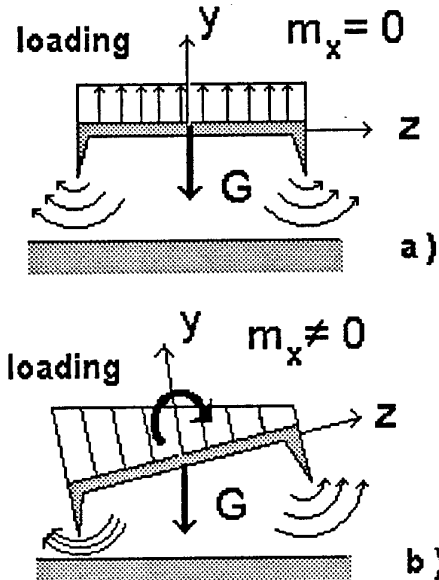


Fig. 11 Principle of natural lateral stability of ekranoplan in heel when moving near the underlying surface (a - without heel, b - with heel)

As a consequence, ekranoplan, differently from the airplane, has natural self-stabilization capability near the ground.

The following expression was obtained for the derivative m_x^γ

$$m_x^\gamma = \lambda \frac{c_y}{12} \quad (24)$$

Equations of lateral motion of ekranoplan have the following form

$$\begin{aligned} \gamma'' - \frac{m_x^{\bar{\omega}_x}}{i_x} \gamma' - \frac{\mu}{i_x} \left(m_x^\gamma - m_x^{\bar{\omega}_x} - \frac{c_y}{2\mu} \right) \gamma - \\ \frac{m_y^{\bar{\omega}_y}}{i_x} \beta' - \frac{\mu}{i_x} m_y^\beta \beta = 0 \\ \beta'' - \left(\frac{m_y^{\bar{\omega}_y}}{i_y} + \frac{c_z^\beta}{2} \right) \beta' - \frac{\mu}{i_y} m_y^\beta \beta - \\ \left(\frac{m_y^{\bar{\omega}_x}}{i_y} + \frac{c_y}{2} \right) \gamma' - \frac{\mu}{i_y} \left(m_y^\gamma - m_y^{\bar{\omega}_x} - \frac{c_y}{2\mu} \right) \gamma = 0 \quad (25) \end{aligned}$$

These equations can be used when solving practical problems of lateral dynamics of ekranoplan. Conditions of lateral stability of ekranoplan at small relative ground clearances have the form

$$m_y^\beta < 0 \quad (26)$$

condition of oscillatory course stability

$$\frac{m_y^{\bar{\omega}_y}}{i_y} + \frac{c_z^\beta}{2} < 0 \quad (27)$$

condition of oscillatory stability in slipping

$$m_x^\gamma - m_x^{\bar{\omega}_x} \frac{c_y}{2\mu} < 0 \quad (28)$$

condition of static stability in heel

$$m_x^{\bar{\omega}_x} < 0 \quad (29)$$

6. EXPERIMENTAL METHODS

When in design stage, the problems, related to stability of motion of ekranoplan, are solved with application of both theoretical and experimental methods.

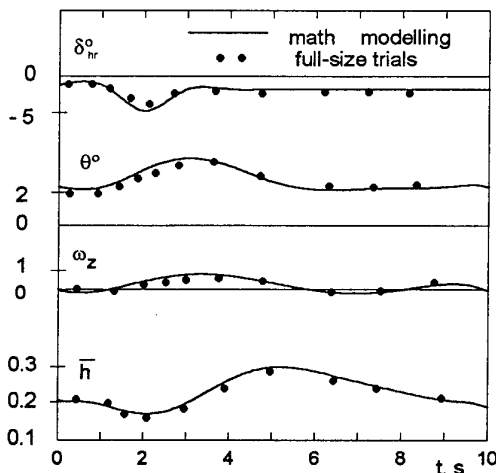


Fig. 12 Transitional processes due to perturbation of longitudinal motion of an ekranoplan of 120 t.

Among experimental methods of investigation of stability those making use of radio controlled and piloted self-propelled models as well as full-size tests are viewed as the most reliable. Radio controlled models provide an opportunity of collecting necessary data without endangering the lives of test pilots. When making use of such models, controlled

from accompanying cutters, for different positions of the center of gravity and parameters of motions in the process of testing are excited perturbations through channels of longitudinal and lateral motion (by means of height rudder, course rudder, flap, engine thrust, etc.). Corresponding perturbed motion of the ekranoplan is registered versus time.

Using the time history data of perturbed motion of the ekranoplan, corresponding to different channels (pitch, heel, ground clearance, etc), one can evaluate parameters of stability.

The same methods are employed when investigating stability and controllability on self-propelled models and full size ekranoplans. Only after formal determination of characteristics of stability and controllability of the ekranoplan by the crew a conclusion is made on acceptability of these characteristics from viewpoint of comfort of passengers and crew.

Figure 12 gives dependences of parameters of longitudinal perturbed motion of ekranoplan of mass 120 t after excitation by means of a height rudder. For comparison, in the same Figure there are plotted results of mathematical modelling of this perturbed motion of ekranoplan.

7. CERTIFICATION OF EKRANOPLANS

During several years a team of Russian scientists and engineers (D.N. Sinitsyn, A.I. Maskalik, A.I. Bogdanov, V.I. Evenko, A.N. Novichenko *et al*) has been working on development of a Safety Code for Ekranoplans (Ref. 9, 10) Main results of this work have been released as a Draft of such a Code and discussed, preliminarily, in Committees and Sub-Committees of the International Maritime Organization (IMO) In the year 2000 it is envisaged to consider the draft of this Code at the General Assembly of the IMO. Keeping in mind that the draft of the Safety Code of Ekranoplans is based upon High-Speed Craft Safety Code and operational experience of Russian ekranoplans, one can be sure that the Code will be approved by the Assembly.

Simultaneously, the same team of experts has developed "Temporary Rules of Classification of Provision of Safety of Small A-Type Ekranoplans", considered and endorsed by the Russian Register of Shipping in 1998. On the basis of these Rules the Russian Register of Shipping has released certificates for the world's first passenger ekranoplans of "Amphistar" type which are at present undergoing operational testing.

8. REFERENCES

- [1] Maskalik, A.I. ed., Proc. 1st International Conference on Ekranoplans, St. Petersburg, "Sudostroenie", 1993.
- [2] Rozhdestvensky, K.V., Sinitsyn,D.N., "State of the Art and Perspectives of Development of Ekranoplans in Russia", in Proc. FAST 93, Vol. 2, 1993, pp. 1657 - 1670.
- [3] Kirillovikh, V.N., "Russian Ekranoplans", in Proc. of the International Workshop on "Twenty-First Century Flying Ships", The University of New South Wales, Sydney, Australia, 7-9 November 1995, pp. 71-117.
- [4] Sinitsyn, D.N., Maskalik, A.I., Litinsky, L.O., "The Present Day State and Prospect for the Development of Commercial Ekranoplans", in Proceeding Workshop EKRANOPLANS & VERY FAST CRAFT, The University of New South Wales, Sydney, Australia, 5-6 December, 1996, pp. 163-176.
- [5] Sinitsyn, D.N., "Summary of the Construction of the First Commercial Ekranoplan "Amphistar", in Proceedings of the International Workshop EKRANOPLANS & VERY FAST CRAFT, The University of New South Wales, Sydney, Australia, 5-6 December, 1996, pp 146-151.
- [6] Basin, M.A., Shadrin, V.P., "Hydrodynamics of a Wing near Interface", St. Petersburg, "Sudostroenie", 1980, 304 p.
- [7] Rozhdestvensky, K.V., "Method of Matched Asymptotic Expansions in Hydrodynamics of a Wing", St. Petersburg, "Sudostroenie", 1979, 213 p.
- [8] Zhukov, V.I., "Peculiarities of Aerodynamics, Stability and Steerability of an Ekranoplan", Izdatelstvi Otdel Tsentralnogo Aerogidrodinami cheskogo Instituta im. N.E. Zhukovskogo, Moscow, 1997, 81 p.
- [9] Bogdanov, A.I., Sinitsyn, D.N., "New IMO High-Speed Craft Code and the Problems of Ekranoplans' Certification", in Proc. FAST'93, Vol. 2, pp. 1457-1465.
- [10] Bogdanov, A.I., Maskalik, A.I., "Some Results on the Civil Ekranoplans Certification Works", in Proc. of a Workshop EKRANOPLANS & VERY FAST CRAFT, The University of New South Wales, Sydney, Australia, pp. 177-185.
- [11] Prandolini, L., ed., Proc. of a Workshop on TWENTY-FIRST CENTURY FLYING SHIPS, The University of New South Wales, Sydney, Australia, November 7 and 8, 1995, 244 p.

9. ADDITIONAL BIBLIOGRAPHY

[12] Prandolini, L.J., ed., Proc. of a Workshop EKRANOPLANS & VERY FAST CRAFT, The University of New South Wales, Sydney, Australia, 5 and 6 December, 1996, 300 p.

[13] Prandolini, L.J., ed., Proc. of a Workshop "WISE up to ekranoplan GEMs", The University of New South Wales, Sydney, Australia, 15 and 16 June, 1998.

[14] Proc. International Conference on WING-IN-GROUND EFFECT CRAFT (WIGs), Royal Institution of Naval Architects, London, 4 and 5 December 1997.

Table 1: Second generation of ekranoplans

Vehicle	Amphistar	MPE-10	MPE-23	MPE-55	MPE-100	MPE-200	MPE-300	MPE-400
Aerodynamic configuration	low set lifting wing of small aspect ratio	composite wing	composite wing	composite wing	composite wing	composite wing	composite wing	composite wing
Take off mass (t)	2.1	9-10	23-25	55-60	80-100	180-210	300-350	450-500
Number passengers	4	18	48	72	150	250	340	460
Main particulars L x B x H m x m xm	10.5 x 5.9 x 3.4	21 x 15 x 7	30 x 21 x 8	40 x 28 x10	45 x 30 x12	57 x 42 x16	68 x 48 x17	73 x 53 x21
Area of the wing S sq. m	43.5	50	98	174	200	392	512	624
Aspect ratio	0.8	4.5	4.5	4.5	4.5	4.5	4.5	4.5
Maximum wing loading kg/ sq. m	48	200	255	345	500	536	684	800
Power plant PAR engine	Mercedes Benz 240 hp PAR+ cruise	AI-25TL thrust 1.9 t	2 x MK861-49 2.4 t thrust	NK-8-2U 10.5 t of thrust	2 x D30 2 x 6.8 t thrust	2 x NK-87 2x 13.5 t thrust	4 x NK-87 4x 13.5 t thrust	6 xNK-87 6 x 13.5 thrust
Cruise engines	-----	two TVD-1500 2 x 1300 hp	2 x 2500 hp 2 x 2.42 t	2 x MK21-22 2 x 4550 kW	2x D27 14 t thrust	2 x NK-15 2x 15 t thrust	2 x NK-15 2x 15 t thrust	2 x NK-15 2x 15 t thrust
Cruise speed km/h (knots)	150 (81)	250 (135)	300 (162)	350 (189)	320 (173)	400-430 (216 - 233)	450 (243)	500 (270)
Seaworthiness (wave height h 3%, m) Take off /landing cruise								
	0.3 0.5	0.8-1 1.25	0.8 1.25	1.2 2.0	1.3-1.5 3.5	1.8-2.0 3.5	2.0-2.5 6.0	2.5-3 6.0
Range (km)	400	1000	1000	1500	1800	3000	4500	6000

On the Prediction of Nonlinear Free-surface Flows past Slender Hulls using $2D + t$ Theory: the Evolution of an Idea.

E. Fontaine, M.P. Tulin

Ocean Engineering Laboratory,

University of California, Santa Barbara, CA93106-1080.
USA

SUMMARY

The basis, evolution and applications of the $2D + t$ nonlinear slender body theory are described through a review of the literature. Attention is focussed on practical problems, where nonlinearities, such as spray and wave breaking, play an important role. Examples of computations are provided to illustrate the capability of the method.

1. INTRODUCTION

Free-surface flows in the vicinity of a piercing body often exhibit a strong nonlinear character, which is experienced as jet generation and wave breaking. The modelling of such violent motion of the free-surface in the immediate vicinity of a body remains a challenge even within the simplest framework of potential flow theory.

In view of the difficulties in dealing with the exact nonlinear free-surface conditions in practical three-dimensional situations, numerous studies have recently been carried out using a "parabolic" approximation of the equations, also called $2D + 1/2$ or $2D + t$ theory. The present work describe the basis, the evolution and the applications of this theory through a survey of the literature.

2. SLENDER BODY THEORIES

2.1 Thin Bodies

The earliest example of approximation theory for the flow about a body was the thin ship theory of Michell (1898), who assumed the beam of the ship to be much thinner than either its draft or length; the separate Froude numbers based on length and water depth were the parameters. The resulting wavy perturbation flow was proportional to the beam. This first-order "linearized" theory was followed about twenty years later by two-dimensional thin-airfoil theory (the Göttingen school), and later by the linearized theory of finite wings, i.e., the so-called lifting surface theory. The aerodynamic applications were very successful because of the actual thinness of wings, but the original application to ships did not prove quantitatively successful, largely because ships are not sufficiently thin.

2.2 Axially Symmetric Slender Bodies

For bodies with axial symmetry the situation becomes more complicated than for thin bodies, with a distinctive difference between the separate cases of purely axial and purely transverse flows for slender bodies. That is, for smooth bodies with $D/L \ll 1$, where D is the maximum diameter, and L its length.

2.2.1 Axial flow about slender bodies

This flow is complicated by two factors: (i) the strong nature of the source-like singularity which prevails in the vicinity of the body, and (ii) the long range axial interaction between the parts of the body distributed over its length. As a result of (i), the flow perturbation is not linear in the small parameter D/L ; for practical bodies, where $D/L = 0(10^{-1})$, it behaves more like $(D/L)^2$. As a result of (ii), an axial flow is induced along the body representing the cumulative effects of the body volume distribution. This behavior was already understood circa 1950 and was documented, for example, by Ward (1949) and Adams and Sears (1953), for both subsonic and supersonic Mach numbers. See also Ashley and Landahl (1965), Chapter 6.

2.2.2 Transverse flow about slender bodies

In the case of transverse flow, a new simplicity results because of the symmetry which caused the flow potential to be zero in a plane through the body and normal to the far field motion. In this case the flow is dipole-like not only in the far field but also locally near the body.

For slender bodies the mutual interference between transverse dipoles at different points along the body may be neglected, and the local dipole field treated as 2D in the transverse plane. This situation was first described and utilized by Max Munk (1924), resulting in "Munk's Slender Airship Theory," allowing the calculation of transverse loads on an airship inclined in a stream. In this beautiful theory, the first $2D + t$ theory, the local loads are given in terms of the added mass of transverse sections and their rate of axial change.

2.3 Impact and Planing

Subsequently, Theodore Von Karman (1929) realized that the flow about a nearly flat body impacting a horizontal water surface at high speed was also essentially dipole-like in the near field, and expressed the vertical loads, like Munk, in terms of added mass variation in time. This comprised the first water impact theory. Wagner (1932) justified formally Von Karman's work and pointed out that the impact theory could be applied to slender planing surfaces (a narrow delta, for example), thereby combining the ideas of Munk and Von Karman, in the process neglecting the generation of waves by the planing surface. This kind of planing theory was used by flying boat hydrodynamists in the US during W.W.II, where seaplanes played a distinctive role. Its feasibility depended on the very high forward speed of the seaplane.

On a slender planing surface, part of the energy put into the water (drag · forward speed) is due to lift and is lost in the wake, and another part is lost in the spray. Tulin (1957), used $2D + t$ theory for slender planing surfaces and showed how to minimize the energy lost to spray through camber of the surface, he also showed that for a flat or presumably slender surface, the energy loss in the wake and due to spray were always equal, but not in general when the body is cambered. The theory included consideration of non-linear effects at the wet chine, where a singularity appears in Von Karman's model, but which bifurcated into a stagnation line (inboard of the chine), and a spray jet (outboard of the chine) in Tulin's model. Similar approaches based on $2D + t$ theory, including the advantages of high resolution numerical computation are still in use today: Takagi & Niimi (1990), Vorus (1996), Zhao et al (1997), Fontaine & Cointe (1997). Gravity is neglected.

2.4 Slender Wings Including Separation

The use of Munk's $2D + t$ model was also extended to slender wings, fully wetted, like deltas, following W.W.II, including supersonic flows, by R.T. Jones (1946) of NACA Langley, and somewhat later, Clinton E. Brown, also of Langley, introduced a model with a vortex above each of the two leading edges of the delta, on the lee side, in order to model the effect of the flow separation which was commonly observed on the delta. In a related problem, Tulin (1959) used the $2D + t$ theory to approximate the effect of leading edge cavitation for slender delta wings operating at high speed in water, a flow already studied experimentally by Reichardt at Göttingen.

2.5 High Speed Displacement Ships

In principle, the problem of displacement ships in the high speed limit (very high Froude number) can be treated by $2D + t$ theory, and this was undertaken by Tulin and Hsu (1986) specifically to

study the effect of the aft lines and transom shape on the resistance of fast naval ships, for which high speed data (substantially beyond the wavemaking peak) existed for David Taylor Model Basin Hull Series (64). They were able to predict high speed resistance very well, and showed that it was related to a vortex wake produced in the shadow of the maximum beam of the ship. This wake is akin to the wake which originates at the trailing edge of an extended delta wing, i.e. a slender wing on which the trailing edges are swept back from the maximum span, creating a backward facing extension to the rear of the wing. This problem had been treated by aerodynamicists using slender wing theory in the 40's and 50's. In their work, Tulin and Hsu satisfied exactly the boundary conditions on the hull in each transverse plane, but the free surface condition was only satisfied in the linear approximation on the horizontal plane in each 2D section.

2.6 Slender Bodies Maneuvering

In all of the cases mentioned above, except impact, the bodies are considered in a steady homogeneous flow and in a fixed orientation. But these restrictions are not always necessary, and by the early 60's hydrodynamicists and aerodynamicists interested in the stability and control of slender bodies like planing surface, projectiles, missiles, submarines, and torpedoes, had applied the Munk theory to the calculation of stability derivatives which arise during turning, maneuvering, and oscillations.

2.7 Ships in Waves; Strip Theory

In the early 50's, in a very fruitful application, Korvin-Kroukovsky (1956) and Lewis (1955) of the Stevens Institute applied cross flow theory to the prediction of the load induced by the passage of ships through waves. In this theory, the flow at each transverse section is treated as 2D with the transverse velocity due to the wave providing the dynamic excitation. This has always been called "strip" theory. The transverse forces calculated on this basis include hydrostatic (Froude-Krylov), added mass and damping due to the generation of 2D beam-wise waves. This $2D + t$ (strip) theory, ignoring the interaction between different parts of the ship, has been applied now for about fifty years, very successfully, and has only lately been supplanted by more advanced analytic and numerical theories. Its success is extraordinary, considering that it is also based on the linearizing assumption of small waves and small motion. In the conventional strip theory, the forward motion of the ship enters the theory only through the kinematical effects created by the ship's encounter with wave trains, where the relative motion of the ship and waves determines the frequency of forcing, etc. The very visible and important effects created locally at the bow of the ship as waves are first encountered depend on the widening of the hull; this effect is specifically

neglected in comparison to that due to waves and wave induced motion of the ship. In this respect strip theory is more approximate than $2D + t$ theory in its treatment of forward motion effects.

2.8 Bow Interaction with Waves; Deck Wetting; Non Linear $2D + t$ Theory.

In practice, the visual motion of a ship in stormy weather is comparable to the ship draft, and the effects of this motion combined with large waves requires non-linear theory for the wave response near the hull. In the late 80's, H. Maruo, then at the Ocean Engineering Laboratory, UCSB, showed the applicability of a non-linear $2D + t$ theory involving approaching waves at the bow, ship motion, and appropriate non-linear boundary conditions in the free surface, including the effect of gravity, Maruo (1990). This method was subsequently implemented successfully, Mauro & Song (1993; 1994) and Wu (1997), utilizing high speed, high resolution numerical computation.

2.9 Early Effects with Gravity

The work of Maruo et al, did not represent the earliest attempts to include gravity effects in $2D + t$ calculations. The flow around a wedge shaped bow of a very small angle, was treated analytically using the $2D + t$ approach and linearizing the free surface condition, Ogilvie (1972); and Chapman (1975) again used the linearization to study a surface piercing plate oscillating in yaw and sway, with good experimental agreement. He went on, Chapman (1976), to calculate the steady loads on a plate at incidence, but using the full non-linear boundary conditions within the $2D + t$ approximation, again with good agreement with experiments.

2.10 Ship Waves

The idea of applying $2D + t$ theory to the prediction of wave generation by a shape (calm sea) was taken up in the early 50's by W. Cummins of the David Taylor Model Basin in his Ph.D. dissertation at American University in Washington. He concluded that only the divergent waves could in this way be simulated. This opened up the prospect to treat high Froude number wavemaking effects, dominated by divergent waves, using $2D + t$ theory. Even this, however, has taken a very long time to be realized.

For normal ships, the transverse waves (crests normal to the ship's direction) are responsible for most of the ship's wave resistance, and effective non-linear methods exist for their computation. The divergent waves have been and still are much more poorly understood. Since they are waves of higher frequency, it is natural that they arise from regions of rapid change in the flow field, notably the region of the ship bow for fine ships. Here non-linear complexity abounds. It has been known for some time that the mathematical solution is non-uniformly convergent near the bow, see the

review of Tulin (1976). This means that there is a small region of the flow centered about the bow, within which the behavior of the flow is very different from the more regular flow surrounding both it and the rest of the ship. This region grows with increasing speed. For a fine ship at low speed its size scales with the wave number g/U^2 , where U is the ship speed, Tulin & Wu (1996), and when its size approaches the ship's draft, h , it more likely scales as hU/\sqrt{gh} , Fontaine & Cointe (1997).

2.11 Splash and Divergent Waves.

The splash commonly seen at the bow of fine ships is the central physical feature arising in the region of flow non-uniformity. This splash would seem to be an impact-like phenomena, already observed in the case of slender planing surface and treated there by the $2D + t$ theory in the absence of gravity. In the case of ship splash, the rising water is eventually halted by the action of gravity and falls, in the process creating a divergent wave crest which radiates out away from the body. This may then be followed by at least one more divergent crest. The entire process has been mapped out using high resolution $2D + t$ numerical computations, Wu (1997), Tulin & Wu (1996). The theory seems highly applicable both near the bow and for the entire divergent wave pattern, as the divergent features calculated in this way match in great detail the same features as calculated by general ship wave codes, the notable difference being that the $2D + t$ calculations can follow the divergent waves through to breaking, while breaking never occurs in the low resolution general codes, Tulin & Wu (1996).

There were earlier pioneering attempts to use $2D + t$ to study the splash on a hull. Fritts et al (1988) and Calisal & Chang (1989) used a fully non-linear numerical method; they partially succeeded, but did not have sufficient resolution to accurately predict this splash.

2.12 High Speed Ships and the Future

As the ship speed increases, the entire inner flow is occupied by splash and its consequences, wave breaking, the appearance of a wake behind the maximum beam, and the appearance of a rooster tail behind the ship, as mapped out by Wu (1997), see Figure 4. The missing transverse waves become insignificant in the near field. At this stage the use of $2D + t$ theory to predict the resistance and motions of high speed ships comes into its own, Faltinsen & Zhao (1991), Fontaine & Cordier (1997). Its use for slamming loads, including hydroelastic effects, has begun, Magee & Fontaine (1998), and would seem most appropriate.

As the ship speed increases, the region of greatest interest in the flow shrinks down to the immediate region of the hull and the wake beyond it. Very high numerical resolution is required to map out the processes in this region, see figures 4-10. In

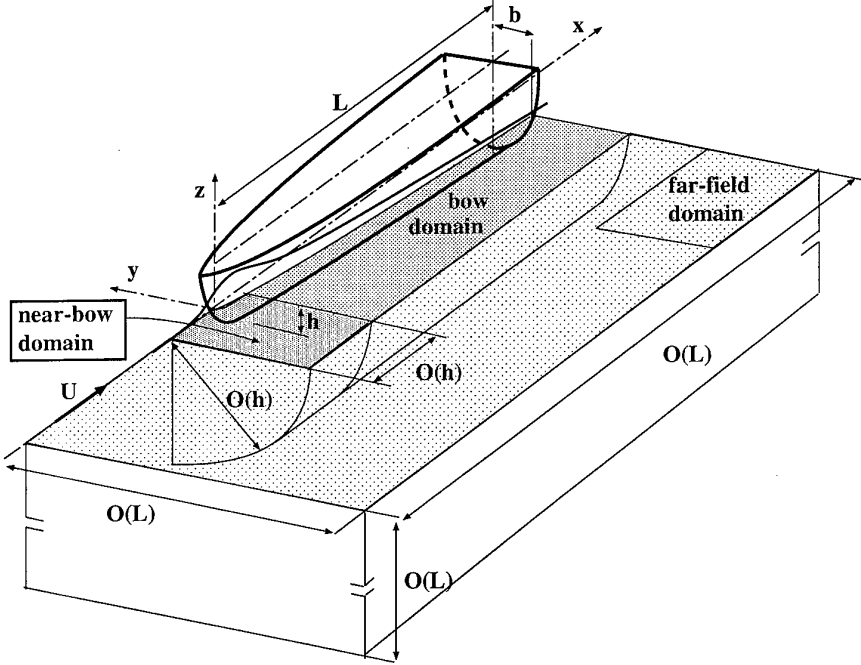


Figure 1: Illustration of the different domains of the composite solution.

these calculations the equivalent of 10^6 grid points were used. This is very far beyond the capability of today's 3D ship codes, which are therefore unable to accurately resolve splash and breaking. The situation worsens for 3D codes if the ship's motion is unsteady or into waves, whereas the $2D + t$ calculation is not basically modified, Maruo (1990). It seems increasingly obvious that the $2D + t$ method will become heavily utilized for the study of a wide variety of problems connected with the growing subject of high speed ships, and especially since the prediction of hydrodynamic loads grows in importance.

3. THE FORMAL MATHEMATICAL APPROACH TO $2D + t$

3.1 Formal Asymptotics

The history of approximation theories in aerohydrodynamics is marked by the successful application to engineering problems of ad hoc approximate theories at the hands of highly skilled innovators, for example: Michell, the Göttingen School, Munk, Von Karman, Wagner, and later Korvin-Kroskovsky, Dawson, Maruo, and others. The validity of these theories has always rested on comparison with experiments, as in the entirety of science. It has to be added that even when not suitably correct, approximation theories have often led to enormous physical and often mathematical insight into the actual mechanics of the flow processes.

There are at least two common difficulties with ad hoc theories: (i) it is difficult sometimes to know the best, most consistent form of theory; (ii) it is often very difficult to improve the approximation

in a rational way. To improve the situation, formal small perturbation expansions came into use, and eventually the development of formal asymptotic methods as described by the CalTech school in the early books of Cole (1968) and van Dyke (1975). An example of the successful use of small perturbation expansions in hydrodynamics is in the case of supercavitating flows in 2D, Tulin (1964), where engineering results of considerable utility were given through second order. Later, formal asymptotic methods were used to great effect in the case of high speed water entry by Cointe (1991).

The generation of waves by ships involves considerable mathematical complexity and until now formal asymptotic methods, although applied, have failed to result in an innovative useful theory. Meanwhile useful ad-hoc theories abound: Guilloton, Neuman-Kelvin, Dawson (Slow Ship), fully non-linear Computational. All of these essentially capture the mechanics of the generation and propagation of the transverse waves in the normal range of ship operation. They fail, however, to capture adequately divergent wave phenomena.

As we have noted, the ad-hoc $2D + t$ theory does seem to capture the mechanics of the divergent waves, including splash, and not only at high speeds.

Very helpful asymptotic analysis of the situation, Fontaine (1996), Fontaine & Cointe (1997), Fontaine, Faltinsen & Cointe (not yet published), have recently been carried out. They justify the $2D + t$ approximation using matched asymptotic expansions. Using the slenderness of the body as the perturbation parameter, these analyses lead to

the determination of three different zones in which these asymptotic expansions are performed and matched, see figure 1. Their analysis is based on the heuristic condition that the length Froude number, U/\sqrt{gL} , is $O(L/h)^{1/2}$. This is a high speed region defined and studied in an early asymptotic analysis by Ogilvie (1967).

3.2 The Near-field Flow

The near-field flow is based on the longitudinal length scale L and the transverse length scale h . The slender body assumption justifies the neglect of longitudinal variations of the flow in comparison to the transverse. Close to the body Laplace's equation reduces, to first order in (h/L) , to its two dimensional expression in the cross-plane (y, z) .

To first order, the initial three-dimensional unsteady nonlinear problem reduces in the near-field to a set of two-dimensional unsteady nonlinear boundary value problems. The simplified problem, which takes into account an incoming wave, and, heave and pitch motion of the ship is presented in fig. 2. Most of the terms of the initial equations are retained in the simplified equations. In particular, the boundary conditions are expressed on the actual positions of the boundaries, and quadratic terms describing variations in the cross-plane are retained in the free-surface conditions. The three-dimensionality of the near-field flow is accounted for through a memory effect in the free-surface conditions, which leads to a downstream interaction between the strips.

In order to give a physical interpretation of the simplified problem, consider a cross-plane, perpendicular to the velocity of the ship and fixed with respect to the fluid (see fig. 3). For an observer in that cross-plane, the flow appears to be generated by a two-dimensional deformable wavemaker whose section corresponds to the track of the ship in the cross-plane (see fig. 2). The time variation of the hull cross-section area leads to the generation of nonlinear diverging waves that eventually interact with the incident incoming wave.

The near-field solution can be obtained numerically by solving for the time evolution of the flow in each cross-section along the body. It is however necessary to impose initial conditions in the first strip, and conditions at infinity in each strip. These are provided by matching the near-field solution to, respectively, the upstream and far-field solutions.

3.3 The Far-field Flow

The far-field domain is defined on the single length scale L , so that the three-dimensional Laplace equation has to be solved. However, from the far-field point of view, the details of the hull shape can not be distinguished, so that the hull appears as a straight line segment along the x axis. The body boundary condition is thus replaced by a matching condition between the near-field and far-field solutions. This

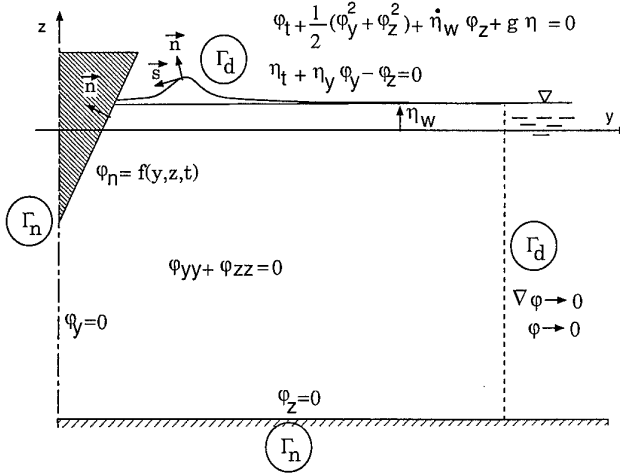


Figure 2: Simplified equations governing the flow in each cross-section (Maruo, 1994).

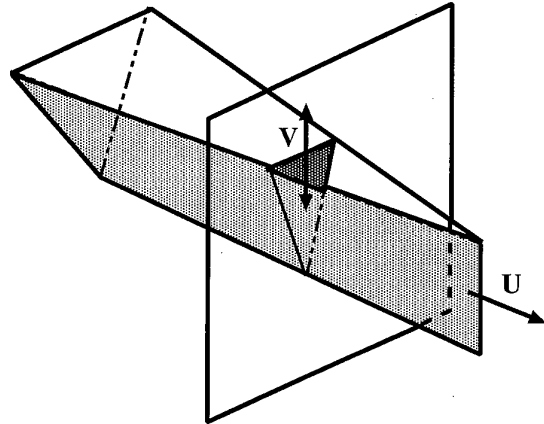


Figure 3: Schematic of the simplified problem.

condition also provides a description of the behavior of the near-field solution far from the body.

The asymptotic analysis leads to the conclusion that free-surface conditions reduce for the potential to an homogeneous Dirichlet condition on the unperturbed free-surface. Gravity effects which give the necessary balance between kinetic and potential energy for waves to propagate are negligible in the far-field aside the hull. The diverging waves which have been generated in the vicinity of the hull propagate with a speed of order $O(\epsilon U)$ and reach the far-field far behind the ship, typically at a distance of order $O(L/\epsilon)$.

Matching the near-field and far-field solutions leads to the conclusion that, far aside from the body, the near-field flow appears to be generated by a two dimensional vertical dipole placed at the origin. Since this is the natural behavior of the near-field solution, the far-field solution is completely deduced from the near-field and does not influence the latter.

3.4 The Upstream Flow

The initial conditions in the first strip are found by matching the near-field solution to a local solution describing the flow in front of the hull. The near-bow domain is based on the single length scale h so that the three-dimensional Laplace equation and the exact body boundary condition have to be taken into account.

However, the free-surface condition for the potential reduces to a simple homogeneous Dirichlet condition, since the asymptotic analysis leads to the conclusion that gravity is negligible in this region. Dimensional analysis then leads to the conclusion that the free surface disturbance in front of the ship does not depend on the ship speed.

An analytical near-bow flow solution that matches both the near-field and the far-field solutions can be obtained for a thin ship, i.e. where the beam is much smaller than the draft. The matching between the near-field and near-bow flow solutions leads to the justification of the classical assumptions used to compute the two-dimensional near-field solution: the near-field solution starts from rest in the first strip.

A composite solution which is by definition uniformly valid over the different domains can be derived by adding the near-bow and near-field solutions, and subtracting the common part of the two developments. Since the near-field solution vanishes in front of the bow, the composite solution is equal to the near-bow solution in front of the ship. However, along the ship, a three-dimensional correction must be added to the near-field solution.

4. EXAMPLES OF COMPUTATIONS

The near-field problem shown in fig.2 is solved numerically using a Mixed Eulerian Lagrangian method. Details of the numerical schemes can be found in Maruo & Song (1994), Fontaine (1996). The aim of this section is to demonstrate the capability of the method to perform high resolution simulations of nonlinear flows where phenomena such as jet formation and wave breaking occur.

4.1 Steady Flows

4.1.1 Wave pattern

Figure 4 shows a typical picture of the wave pattern obtained by $2D + t$ computation, corresponding to the flow around a Wigley hull. The main features are the presence of diverging dispersive waves that originate both in the bow and the stern regions. In the latter case, they seem to be generated by the relaxation of the "rooster tail".

A general discussion of the generation mechanism and characteristics of these diverging waves is given by Tulin & Wu (1996). Although the transverse waves are not present in these simulations, comparison with the three-dimensional fully nonlinear

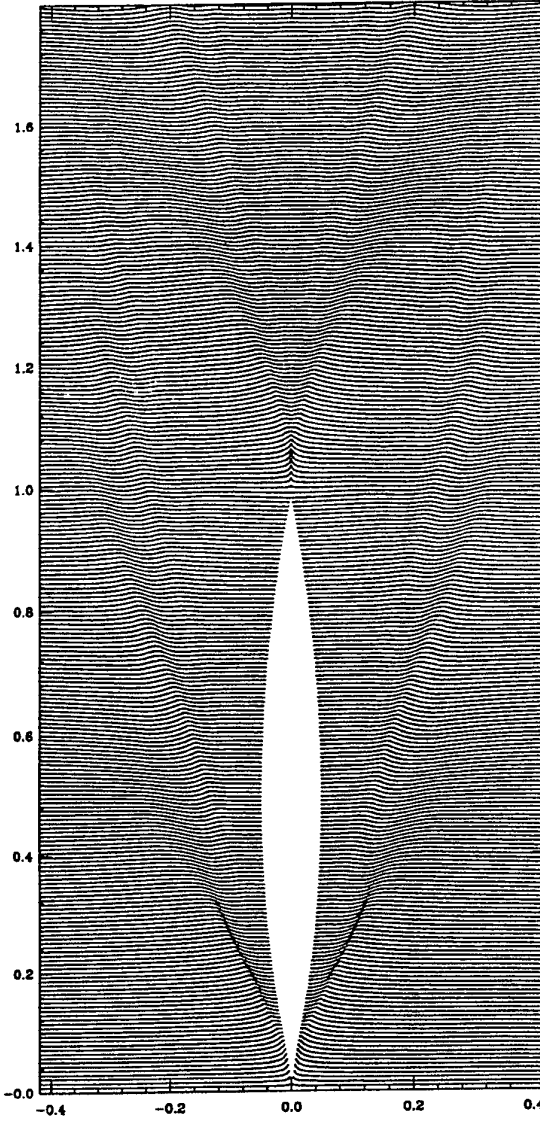


Figure 4: Free-surface elevation around a Wigley hull, $b/L=0.05$, $h/L=0.1$, $F_L=0.30$, from Tulin & Wu (1996).

results of Raven (1996) for the wave pattern gives confidence in the general pattern obtained by the $2D + t$ theory.

Compared to a fully three-dimensional approach, a big advantage of the $2D + t$ approach is that the mesh size can be refined so that really high-resolution simulations are achieved. As can be seen from fig.4 through 8, diverging waves may be very steep and may eventually break as confirmed by observations. Their evolution is therefore influenced by nonlinear effects, which require high resolution simulation to be properly taken into account. Another advantage of the $2D + t$ approach is that highly nonlinear phenomena such as jet formation and wave breaking can be simulated.

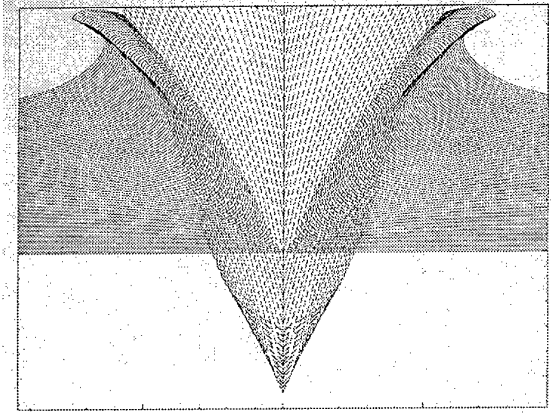


Figure 5: $2D + t$ simulated bow wave by frigate hull, $F_L = 0.5$, from Tulin & Wu (1996).

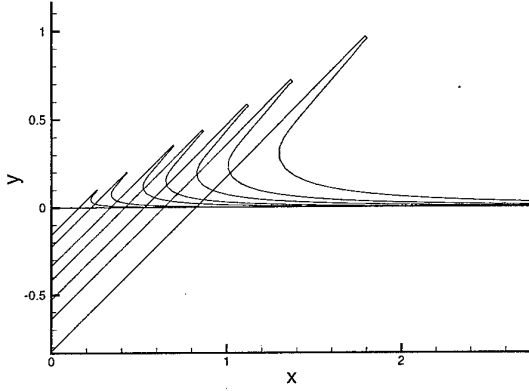


Figure 6: $2D + t$ simulated flow around V shaped bow, $F_L \rightarrow \infty$, from Fontaine & Cointe (1997).

4.1.2 Bow splash

The $2D + t$ approach has been extensively used to compute bow flows. Again, good agreement has been reported for the wave profile along the hull by Calisal & Chang (1989), Tulin & Wu (1996), Fontaine & Cointe (1997). It is however necessary to account for three-dimensional effects that arise in front of the bow. Examples of strongly overturning bow wave and jets are presented, fig.5 and 6, corresponding respectively to the flow around a frigate bow and a prismatic hull. In the latter case, the jet that develops along the hull has been cut. A special numerical algorithm has been developed so that the numerical solution is matched to an asymptotic solution describing the flow within the jet. The numerical solution is self-similar and agrees with the asymptotic solution by Cointe (1991); no gravity.

4.1.3 High-speed flows

As the speed of the ship increases, the diverging wave system becomes more and more important compared to the transverse. At high-speeds, the $2D + t$ theory alone gives an accurate description of the flow. Good agreement between $2D + t$ simulations and experimental results for the wave profile along the hull and for the loads has been reported by Faltinsen & Zhao (1991) and Fontaine & Cordier (1997).

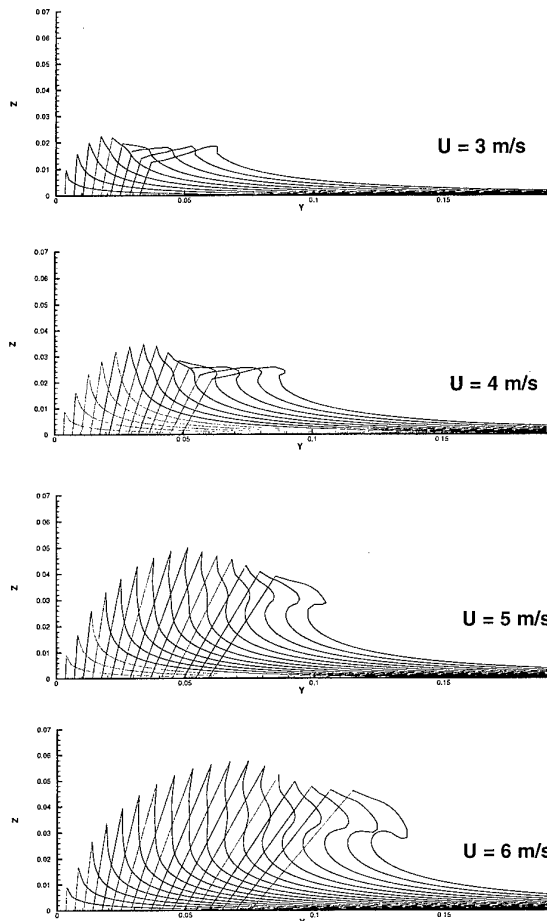


Figure 7: Evolution of the free-surface elevation in different cross section along the hull shown in fig.3. The characteristics of the model test are $L=1m$, $h=0.1m$ and final angle 45° .

Figure 7 shows the evolution of the free-surface elevation with speed for a paraboloid hyperbolic hull presented in fig.3. The Froude number of the model test varies from 1 to 2. As expected at these high Froude numbers, simulations show violent deformations of the free surface, leading to the formation of a jet which develops in the fore part of the hull, and then breaks under the influence of gravity.

Figure 8 shows the free-surface elevation around a Wigley hull at Froude number $F_L=0.5$. A thin jet develops at the bow and the two diverging waves that are generated after breaking. The simulation has been continued after breaking by cutting the plunging jets that develop at the top of the breaker just before they re-enter the free-surface. Note the breaking process is strong since it takes place over the length of the ship.

4.2 Unsteady Flows

Simulation of unsteady flows can also be carried out using $2D + t$ approach either in the frequency domain, Chapman (1975), Faltinsen & Zhao (1991),

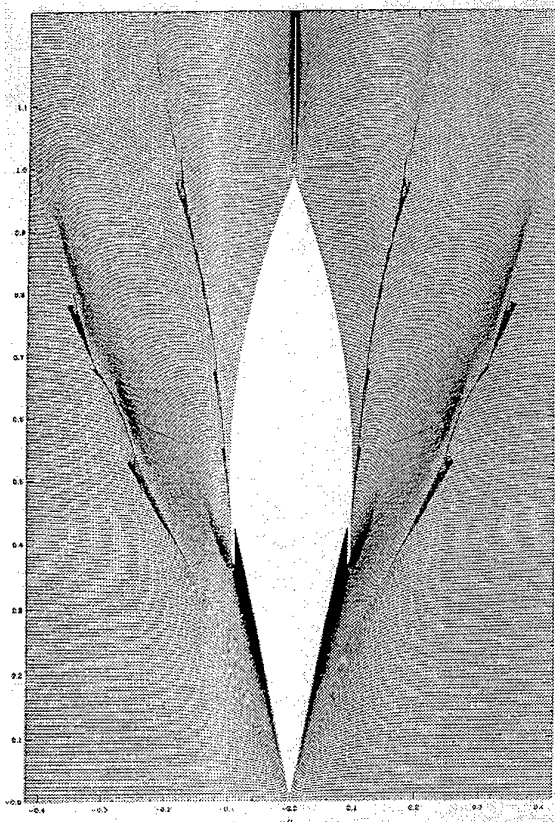


Figure 8: Free surface elevation around a Wigley hull, including jets and breaking waves $L/b=5, L/h=10, F_L = 0.45$, from Wu (1997).

Fontaine (1996), or in the time domain, Maruo & Song (1994), Wu (1997).

Figure 9 shows the effects of a forced heave motion of the paraboloid hyperbolic at Froude number $F_L = 1.93$. The time evolution of the free-surface in the control strip is plotted for different amplitudes of the heave motion. The position of the center of gravity of the ship is given by $z_G = A \sin(\pi Ut/2L)$ so that the maximum draft is obtained at the stern at time $t = L/U$. In the asymptotic analysis, heave motion leads to an additional contribution in the body boundary condition to take into account the vertical velocity of the ship. The position of the ship is also updated. Heave motion leads to a reinforcement of the jet development and a decrease of gravity effects so that the jet is higher and tends to break later.

In the latter case, the evolution in time of the flow at a given position has been computed. In order to get a three-dimensional picture of the flow, it is necessary to compute the time evolution of the flow at different positions, and then to reassemble the results to obtain the three-dimensional picture of the flow at a given time.

Following the work of Maruo (1994) on deck wetness prediction, a systematic study of the flow as the

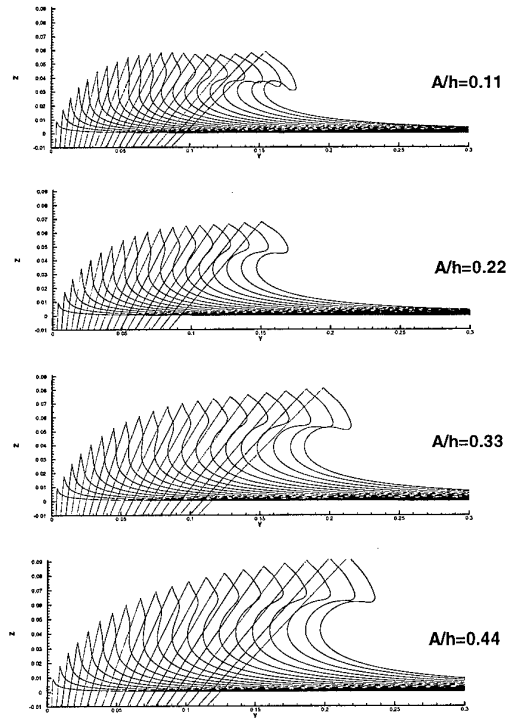


Figure 9: Time evolution of the free surface in a fixed cross-section.

bow of a frigate enters an incoming wave has been performed by Wu (1997). The influence of the phase and amplitude of the incoming wave on deck wetness and slamming has been studied. An example of computation that shows a three-dimensional picture of the bow flow is presented, fig.10. The water rises above the deck line so that deck wetness is likely to begin in these navigation conditions. This result is confirmed by experimental observations, which tends to prove that the interaction between the steady flow and the periodic one, due to the ship motions and the incoming wave, is properly taken into account within the $2D + t$ computation. Indeed, for the prediction of deck wetness it is necessary to account for the dynamic rise of the water due to nonlinearities of the flow in the vicinity of the hull.

5. CONCLUSIONS

The basis and evolution of the $2D + t$ theory has been described through a review of the literature. This approach can be derived formally using the method of matched asymptotic expansions. $2D + t$ theory accounts for the main nonlinearities of the flow, as well as forward speed, gravitational and three-dimensional effects. It therefore represents an efficient tool for prediction of diverging waves. These effects are important in simulations of bow flows and high-speed flows. Since two-dimensional computation can be done with high resolution, jets that develop along the hull and breaking diverging waves can be realistically simulated.

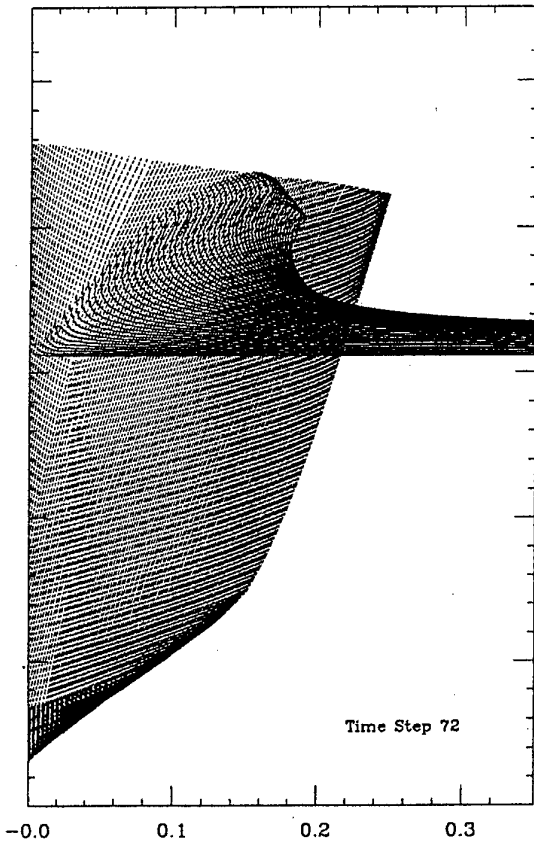


Figure 10: Picture of the flow as the bow enter the wave, from Wu (1997).

AKNOWLEDGEMENT

The authors are grateful for support from the ONR Ocean Technology Program, Dr. Tom Swean, Jr, Program Manager. E.F. also acknowledges the support of the French Navy, DRET and Bassin d'Essais des Carennes.

REFERENCES

- Adams, M.C., Sears, W.R. 1953. Slender-body theory-review and extensions. *J. Aeron. Sci.* 20, No. 2, 85-98.
- Ashley, H., Landahl, M., 1965. *Aerodynamics of Wings and Bodies*, Addison-Wesley Publishing Co.
- Calisal, S.M., Chan, J.L.K., 1989. A Numerical Modeling of Ship Bow Waves, *Journal of Ship Research*, Vol 33, pp. 21-28.
- Chapman, R.B., 1975. Numerical solution for hydrodynamics forces on a surface piercing plate oscillating in yaw and sway, *Proc. 1st Int. Conf. Numerical Ship Hydrodynamics*, pp.333-350.
- Chapman, R.B., 1976. Free surface effects for yawed surface-piercing plate, *Journal of Ship Research*, vol. 20, pp. 125-136.
- Cointe, R., 1991. Free-surface flows close to a surface-piercing body, *Mathematical Approaches in Hydrodynamics*, SIAM T. Miloh, Ed..
- Cole, J.D., 1968. *Perturbation Methods in Applied Mathematics*, Blaisedell Publishers. Waltham, Mass.
- Faltinsen, O.M. & Zhao, R., 1991. Numerical prediction of ship motion at high forward speed. *Phil. Trans. Royal Society (Ser. A)*, vol. 334, pp. 241-252.
- Faltinsen, O.M. & Zhao, R., 1991. Flow prediction around high-speed ships in waves, *Mathematical Approaches in Hydrodynamics*, T. Miloh, Ed., Society for Industrial and Applied Mathematics (SIAM).
- Faltinsen, O.M., 1993. On seakeeping of Conventional and High-Speed Vessels, *Journal of Ship Research*, Vol. 37, No. 2 (June), pp. 87-101.
- Fontaine, E., 1996. Simulation de l'écoulement potentiel engendré par un corps élancé percant la surface libre à forts nombres de Froude, *Thèse de Doctorat de l'Ecole Nationale des Ponts et Chaussées, Paris* (in french).
- Fontaine, E. & Cointe, R., 1997. A Slender Body Approach to Nonlinear Bow Waves, *Philosophical Transaction of the Royal Society, London (A)*, Vol. 355, pp. 565-574.
- Fontaine, E. & Cointe, R., 1997. Etude de l'écoulement autour d'un navire planant, *6^{ème} Journées de l'Hydrodynamique*, pp. 3-16, Nantes.
- Fontaine E. & Cordier S., 1997. Recent Experience using high-speed slender body theory, *Fourth International Conference on Fast Sea Transportation, Sydney, Australia*.
- Fontaine E. & Faltinsen O.M., 1997. Steady flow near a wedge shaped bow, *12th International Workshop on Water Waves and Floating Bodies, Marseille*.
- Fontaine E., Faltinsen, O.M. & Cointe, R. Some new insight into the generation of ship bow waves, submitted to *J. Fluid Mech.*
- Fritts, M.J., Meinholt, M.J. and Von Kerczek, C.H., 1988. The calculation of nonlinear bow waves, *Proc. 17th ONR symposium on Naval Hydrodynamics*.
- Jones, R.T., 1946. Properties of low aspect ratio pointed wings at speeds below and above the speed of sound. *NACA Rept. 835*.
- Korvin-Kroukovsky, B.V., 1956. *SNAME* vol. 64.
- Lewis, E.V., 1955. *SNAME* vol. 63, pp 134-202.
- Magee, A.R., Fontaine, E., 1998. A coupled approach for the evaluation of slamming loads. *Proc. 3rd International Conference for Practical Design of Ships, Amsterdam*.
- Maruo, H., 1990. Prediction of deck wetness: A theoretical development. *Technical Report 90-53, OEL, University of California, Santa Barbara*.

- Maruo H. & Song W., 1994. Nonlinear Analysis of Bow Wave Breaking and Deck Wetness of a High-Speed Ship by the Parabolic Approximation, 20th Symposium on Naval Hydrodynamics, University of California, Santa Barbara.
- Michell, 1898. The wave-resistance of a ship. *Philosophical Magazine, Serie 5, Vol. 45, 1968.*
- Munk, M.M. 1924. The aerodynamic forces on airship hulls. *NACA Rept. 184.*
- Ogilvie, T.F., 1967. Non-linear High-Froude-Number Free-Surface Problems, *Journal of Engineering Mathematics, volume 1, p.215-235.*
- Ogilvie, T.F., 1972. The wave generated by a fine ship bow, *Ninth Symposium Naval Hydrodynamics, Vol. 2, pp. 1483-1525.*
- Raven, H.C., 1996. A solution method for the non-linear ship wave resistance problem. PhD dissertation, *Delft Technical University.*
- Song, W and Maruo, H., 1993. Bow impact and deck wetness: simulations based on nonlinear slender body theory. *Proc. ISOPE conf., Singapore.*
- Takagi, K., Niimi, A., 1990. A Theoretical Approach to Bow Deck Wetness of a High-Speed Ship, *Journal of Ship Research, No. 3, Sept., pp.163-171.*
- Tulin, M.P., 1957. The theory of slender surfaces planing at high speeds, *Schiffstechnik Bd. 4, Heft 21, pp 125-133.*
- Tulin, M.P., 1959. Supercavitating flow past slender delta wings, *Journal of Ship Res., vol. 3, no. 3, pp. 17-22.*
- Tulin, M.P., 1964. Supercavitating flows, small perturbation theory, *Journal of Ship Research, vol. 3, no. 3.*
- Tulin, M.P., 1976. Ship Wave Resistance, A Survey, *In Proceedings of the 8th U.S. National Congress of Applied Mechanics, pp. 217-246.*
- Tulin, M.P., Hsu C.C., 1986. "Theory of high speed displacement ships with transom sterns, *J. Ship Res., 30(3):186-193.*
- Tulin, M.P. Wu, M., 1996. Diverging Bow Waves, 21th Symposium on Naval Hydrodynamics, Trondheim, Norway.
- Van Dyke, M., 1975. *Perturbation Methods in Fluid Mechanics*, The Parabolic Press, Stanford, CA.
- Von Karman, T., 1929. The impact on seaplane floats during landing, *NACA Tech. Note No. 321.*
- Vorus, W.S., 1996. A flat cylinder theory for vessel impact and steady planing resistance. *Journal of Ship Research, no. 2, pp. 89-106.*
- Ward, G.N., 1949. Supersonic flow past slender pointed bodies. *Quart. J. Mech. Appl. Math. 2, Part 1, 75-97.*
- Wu, M., 1997. Prediction of deck wetness, divergent bow waves on fine ships-nonlinear numerical studies. *Ph.D. thesis, University of California, Santa Barbara.*
- Wagner, H., 1932. Über Stoß und Gleitvorgänge an der Oberfläche von Flüssigkeiten.", *ZAMM, Vol. 12 ,pp. 193-215.*
- Zhao, R., Faltinsen, O.M. & Haslum, H. A., 1997. A simplified nonlinear analysis of a high-speed planing craft in calm water. *Fourth International Conference on Fast Sea Transportation, Sydney, Australia.*

The Complex Boundary Integral Equation Method for a Problem of Entry of a 2D Solid Body in an Incompressible Liquid

Dmytro I. Cherniy

Department of Cybernetics, Taras Shevchenko National University
64, Vladimirska st., 252601 Kiev, Ukraine.

Summary

The aim of this paper is extension of complex boundary integral equations method for non-linear non-stationary problems, in which appearance of separation and accumulative effects is taken into account.

The problem of heavy liquid movement in a domain with moving boundary is considered as two-dimensional and non-stationary. Properties of some boundary elements can be altered, under change of boundary conditions. The boundary contour is not already the current line and can be deformed: it does not always consist of the same liquid particles but is filled by new ones. Non-linear initial boundary value problem is confined to finding the changing with respect to time, complex potential of velocities under given initial conditions in the deforming domain D .

Introduction

The problem of entry of a 2D solid body in an incompressible liquid is reduced to a mathematical problem with moving boundary.

On examination of fluid mechanics problems an analytical functions theory techniques is often used [1-10], but its application is limited, as a rule, to stationary problems. A solving of non-stationary problems presents a considerable difficulty [4-10], whose resolving is possible only using numerical methods. Using appropriate approximations [11,20] an approximate solution can be built, but because of essential deformation of boundaries it is necessary to take into account the accuracy of representation of the solution on every step with respect to time.

The solution for a complex potential problem is looked for as analytical in a coherent domain D function expressed by a sum of integrals of Cauchy type.

The use of Sokhotsky-Plemel formulas and dynamic and kinematic conditions on boundary elements of different types permits to obtain singular integral and integral-differential equations for complex defined by independent variables: complex z and real t . Conditions on region boundary smoothness are satisfied by spline-interpolation of the contours. A boundary problem is solved on every time layer. A combined Euler-Lagrange approach is used. A numerical integration of motion equation of liquid

particles defining the moving boundary is performed with explicit second-order method.

1. On a model of a domain with moving boundary

In the Lagrange terms, a law of continuum motion is determined by the trajectory of individual particles, whose total makes up a certain volume. It is assumed that for any particle from D^+ , individualized by its initial position $z(t_0) = z_0$, a motion law in the form of an analytical function of time t may be posed. Then the domain \bar{D}^+ is a certain deformable volume filled up with liquid, every point $z \in \bar{D}^+$ considered as a particle of liquid moving with complex velocity of $V = u + iv$. Complex velocity of liquid particles forming a boundary

$L = \partial D$ will be determined in the limit points of

D^+ and denominated as $W(\omega, t) = \frac{d\omega}{dt}$, where $\omega \in L$.

If a complex potential of a flow

$$\Phi(z, t) = \varphi + i\psi$$

is represented as:

$$\Phi(z, t) = \frac{1}{2\pi i} \int_{L(t)} f(\omega(t), t) \ln(z - \omega(t)) d\omega(t) \quad (1.1)$$

then for a derivative with respect to time t it is true that:

$$\begin{aligned} \frac{\partial}{\partial t} \Phi(z, t) &= -\frac{1}{2\pi i} \int_{L(t)} \frac{W(\omega(t), t) f(\omega(t), t)}{z - \omega(t)} d\omega(t) + \\ &+ \frac{1}{2\pi i} \int_{L(t)} \ln(z - \omega(t)) \frac{d}{dt} (f(\omega(t), t) d\omega(t)) + \quad (1.2) \\ &+ \frac{1}{2\pi i} W_0(\omega_0, t) \ln(z - \omega_0) f(\omega_0, t) \end{aligned}$$

where $W_0 = W(\omega_0, t)$ is a velocity of filling of the moving boundary with new liquid particles in a boundary point ω_0 .

For the determination of the pressure function in any point z of D^+ a presentation of a Cauchy-Lagrange's integral may look like:

$$\frac{P(z, t)}{\rho} = -\operatorname{Re} \left\{ \hat{\partial} \Phi(z, t) + \frac{V(z, t)\bar{V}(z, t)}{2} - G(z) \right\} \quad (1.3)$$

where for a complex conjugate and complex velocity in a point $z \in D^+$ a following presentation is justified:

$$\bar{V}(z, t) = \frac{\partial \Phi(z, t)}{\partial z} = \frac{1}{2\pi i} \int_{L(t)} \frac{f(\omega(t), t) d\omega(t)}{z - \omega(t)}. \quad (1.4)$$

$$V(z, t) = \overline{\bar{V}(z, t)}. \quad (1.5)$$

Let a boundary L of a closed domain D^+ is a set of sectionally Lapunov's curves and in every point $z = \omega$ of the responding curve tangent

$$\tau(\omega) = e^{i\alpha(\omega)}$$

and normal $n(\omega) = ie^{i\alpha(\omega)}$ basis vectors are defined, where $\alpha(\omega)$ is an inclination of a tangent to the OX-axis in a point ω of the boundary L .

In this case an impenetrability of solid boundaries in a point ω_0 may be presented as:

$$\operatorname{Re} \left\{ \bar{V}(\omega_0, t) - \bar{V}_e(\omega_0, t) \right\} n(\omega_0) = 0 \quad (1.6)$$

Since in D^+ a field of complex (correspondingly, complex conjugate) velocity and a complex potential of a flow are defined, a Cauchy problem on deformation of the \bar{D}^+ domain may be stated:

$$\frac{dz}{dt} = V(z, t), \quad \left(\frac{d\bar{z}}{dt} = \bar{V}(z, t) \right). \quad (1.7)$$

$$\frac{d\Phi}{dt} = \frac{V(z, t)\bar{V}(z, t)}{2} - G(z) + \frac{P(z, t)}{\rho}. \quad (1.8)$$

$$\bar{z}(t_0) = \bar{z}_0. \quad (1.9)$$

$$\Phi(z, t_0) = \Phi_0(z) \quad (1.10)$$

taking place before the time $t = t_0 + T$, when any marked particle $z(t)$ will coincide with any other particle of \bar{D}^+ (i.e. before violating the condition of uniqueness of solution).

At the boundary points $z = \omega$ of the domain \bar{D}^+

$$G^+(z) = G(\omega), P(z, t) = P(\omega, t), \quad (1.11)$$

$$\Phi(z, t) = \Phi(\omega, t), \quad \bar{V}(z, t) = \bar{V}^+(\omega, t),$$

where the singular integrals are regarded in terms of principal value of Cauchy.

In view of analyticity of the $z(t), \bar{V}(z, t)$ functions, for an operator of an individual derivative it is true that:

$$\frac{d^k}{dt^k} z(t) = \frac{D^{k-1}}{D} \frac{V(z, t)}{t^{k-1}}, \quad k \geq 1, \quad (1.12)$$

where

$$\frac{D}{Dt} = \left(\frac{\partial}{\partial t} + \bar{V}(z, t) \frac{\partial}{\partial \bar{z}} + V(\bar{z}, t) \frac{\partial}{\partial z} \right). \quad (1.13)$$

Since all the kinematic and dynamic characteristics of the flow inside the domain are determined through the boundary integrals, the problem (1.6)-(1.11) is stated on the boundary $L = \partial D^+$, at that the pressure $P(\omega, t)$ is regarded as specified in all its points and determines external effect on the boundary. A potential of mass forces is an analytical function given in \bar{D}^+ .

For the particle trajectory in the vicinity of its initial position a Taylor series expansion is valid:

$$z(t) = \sum_{k=0}^{\infty} \frac{z^{(k)}(t_0)}{k!} (t - t_0)^k. \quad (1.14)$$

For the determination of a potential Φ value in a moving particle $z(t)$, in similar manner as before, it is true, that:

$$\Phi(z(t), t) = \sum_{k=0}^{\infty} \frac{\Phi^{(k)}}{k!} (t - t_0)^k. \quad (1.15)$$

where

$$z^{(k)} = \frac{d^k z}{dt^k}, \quad \Phi^{(k)} = \frac{d^k}{dt^k} \Phi(z(t), t), \quad (1.16)$$

$t \in [t_0, t_0 + T]$ where T is a radius of convergence of the series (1.15) and (1.16).

The expansion is complex conjugate and according to (1.7), (1.12) and (1.13) may be presented as:

$$\bar{z}(t) = \bar{z}(t_0) + \sum_{k=0}^{\infty} \frac{D^k}{D} \frac{V(z, t_0)}{t^k} \frac{(t - t_0)^{k+1}}{(k+1)!} \quad (1.17)$$

Leaving in the expansion a necessary number of terms, we can determine with required accuracy a trajectory, kinematic and dynamic characteristics of an elementary liquid particle of \bar{D}^+ changing its position at the time $t_0 + \Delta t$.

2.Digitization problems

Let a boundary $\partial D^+ \equiv L$ be a sectionally smooth curve and let analytical functions be specified in D^+ (by way of specifying $f(\omega)$ on L), and the following presentation is true:

$$\Phi_0(z) = \frac{1}{2\pi i} \int_L f(\omega) \ln(z - \omega) d\omega = \\ = \sum_{k=1}^m \frac{1}{2\pi i} \int_{\omega_{k-1}}^{\omega_k} f(\omega) \ln(z - \omega) d\omega \quad (2.1)$$

$$\Phi_1(z) = \frac{1}{2\pi i} \int_L \frac{f(\omega)}{z - \omega} d\omega = \\ = \sum_{k=1}^m \frac{1}{2\pi i} \int_{\omega_{k-1}}^{\omega_k} \frac{f(\omega)}{z - \omega} d\omega \quad (2.2)$$

where a set of real numbers defines bundles of partitioning along the length of the curve L :

$$\{\omega\}_m = \{\omega_k = \omega(l_k), k = 0, \dots, m\}. \quad (2.3)$$

L^k - an arc between the points ω_{k-1}, ω_k ,

$$L = \bigcup_{k=1}^m L^k \quad (2.4)$$

A norm of partitioning $\{\omega\}_m$ of the curve L is defined by the correlation:

$$\sigma_m = \max_k |L^k| = l_k - l_{k-1}, k = 1, \dots, m \quad (2.5)$$

Theorem [19]: If an analytical has in D^+ one of representations (2.1), (2.2), where density f is a sectionally continuous bounded function on a smooth L , then $\exists m$ and $\exists \{\omega\}_m$ and $\{\omega_0\}_m$ (coherent partitioning of the curve L) that for

$\forall z \in D^+ \setminus \Omega^m$ the following estimations are valid:

$$\left\| \frac{1}{2\pi i} \int_L f(\omega) \ln(z - \omega) d\omega - \sum_{k=1}^m \frac{1}{2\pi i} \int_{\omega_{k-1}}^{\omega_k} f(\omega) \ln(z - \omega) d\omega \right\|_C \leq \\ \leq A_0 \hat{f}_0 m \sigma_m \lambda^2 \quad (2.6)$$

$$\left\| \frac{1}{2\pi i} \int_L \frac{f(\omega)}{z - \omega} d\omega - \sum_{k=1}^m \frac{1}{2\pi i} \int_{\omega_{k-1}}^{\omega_k} \frac{f(\omega)}{z - \omega} d\omega \right\|_C \leq \\ \leq A_1 \hat{f}_0 m \lambda^3 \quad (2.7)$$

where $\Omega^m = \bigcup_{k=1}^m \Omega_k$, (2.8)

$$\Omega_k = \{z : |z - z_{0k}| \leq \delta'_{0k} = \max_{\omega \in L^k} |\omega - z_{0k}| \} \quad (2.9)$$

$$\Delta_k = |z - z_{0k}|, \quad (2.10)$$

$$\Delta_0 = \min_k |z - z_{0k}|, \quad (2.11)$$

$$\lambda'_{0k} = \frac{\delta'_{0k}}{\Delta_k} < 1, \quad (2.12)$$

$$\lambda = \max_k \lambda'_{0k} < 1, \quad (2.13)$$

$$\hat{f}_0 = \max_{\omega \in L} |f(\omega)|. \quad (2.14)$$

A_j - a certain constant, $j = 0, 1$.

In order to determine the values of the function f on boundary elements L^k it is necessary to consider the corresponding integrals in the sense of principal value of Cauchy.

The motion of boundary elements L^k is determined by motion of their end points $\omega_k, \omega_{k+1}, k = 0, \dots, m$, the velocities value of which is determined by way of spline-interpolation between the values in medium point ω_{0k} of boundary elements L^k .

Unimprovable estimations (2.6), (2.7) for internal points of the domain $z \in D^+ \setminus \Omega^m$ will be conserved in every time layer under the following condition:

$$|\omega_{0k} - \omega_k| = |\omega_{0k} - \omega_{k+1}|, k = 0, 1, \dots$$

i.e. the corresponding item of the sums (2.1), (2.2) must have a peculiarity in the middle ω_{0k} of its boundary element L^k . (See Fig.1).

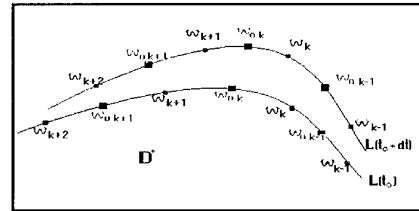


Fig. 1

3. Consideration of kinematic effects

Since the maximal over module values of velocity take place at boundary points of the domain D^+ , a relative (tangent to the boundary) motion of liquid particles adjacent to the boundary $L = \partial D^+$ are considered.

In a case of coincidence of positions of the particles at time $t + T$ ($l_1(t + T) = l_2(t + T)$) a violation of uniqueness of solution of the problem (1.6)-(1.11) occurs.

$$T(l) = - \left(\frac{dW}{dl} \right)^{-1} \quad (3.1)$$

local time in which a „collapse” of element dl of the boundary L with coordinate l occurs.

Since $T_0(l) \geq 0$, we receive that the necessary condition of the „collapse“ occurring is:

$$\frac{dW}{dl} < 0, \quad (3.2)$$

where $W(l)$ is the tangent to L velocity.

From (3.1) one may introduce local „kinematic“ restriction at the partitioning of L during to boundary elements L^k :

$$|L^k| \leq \min \left\{ \frac{1}{2} \max_{l \in L^k} |W| / \max_{\omega \in L^k} \frac{dW}{dl}, 1 / \max_{\omega \in L^k} |\kappa(\omega)| \right\} \quad (3.3)$$

$k = 1, \dots, m$.

where $\kappa(\omega)$ is the local curvature of L .

Local time (3.1) restricts as a first approximation a radius of convergence of the series (1.14)-(1.17) and limits the choice of integration step with respect to time at the numerical solution of the problem (1.6)-(1.11).

From (3.3) we get a condition for the partitioning norm $\{\omega\}_m$ of the boundary L :

$$\sigma_m \ll \max_k \min \left\{ \Delta, \min_{l \in L} \left| \frac{1}{|\kappa(l)|} \right|, \frac{1}{2} \max_{l \in L} |W| / \max_{l \in L} \left| \frac{dW}{dl} \right| \right\} \quad (3.4)$$

is satisfied then the estimations (2.6), (2.7) are valid exactly for a canonical partitioning and finite covering Ω_0^m of curve L consists of a chain of circles

Ω_{0k} , $k = 1, \dots, m$ and measure

$\mu(\Omega_0^m) \rightarrow 0$ when the canonical partitioning is thickened (at $m \rightarrow \infty$).

and restriction on the time of existence of unique solution:

$$t < T_1 = \min_l T_0(l) \quad (3.5)$$

4. Results

External influence on a flow domain D^+ is determined by way of distribution of pressures $P(\omega)$ along the boundary of the domain $L = \partial D$.

To determine the influence an integral equation (1.6) is solved by way of reduction to a system of linear algebraic equations. On every time layer $t + \Delta t$ a problem of determination of a new position of $\omega(t + \Delta t)$ and a value of potential in these points is solved.

A numerical integration of a Cauchy problem (1.7)-(1.11) is performed according to a scheme:

$$\omega_{n+1} = \omega_n + \frac{\Delta t_{n+1}}{2} \left(V_n \left(2 + \frac{\Delta t_{n+1}}{\Delta t_n} \right) - \frac{\Delta t_{n+1}}{\Delta t_n} V_{n-1} \right) \quad (4.1)$$

which in the case of constant step is reduced to the second-order Adams scheme.

Fig. 1 shows a scheme of moving of boundary elements.

As a test example (see Fig.2) a simulation of breakdown of a wave of 4π period at decreasing of the liquid depth to 1.

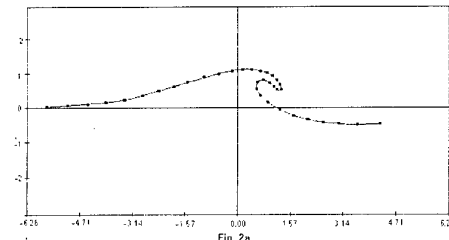


Fig. 2a

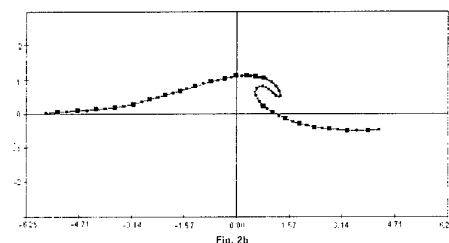


Fig. 2b

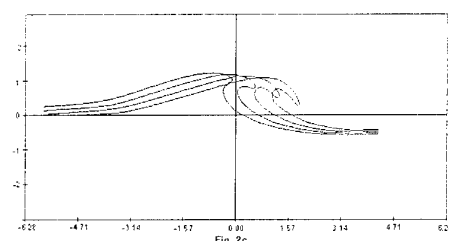


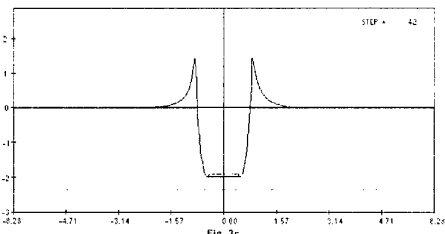
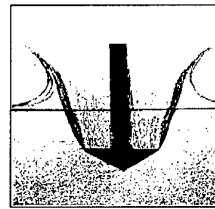
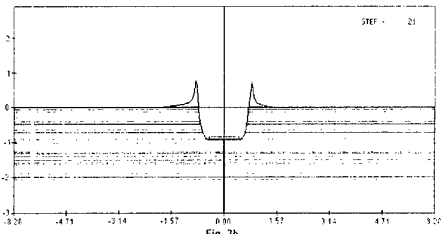
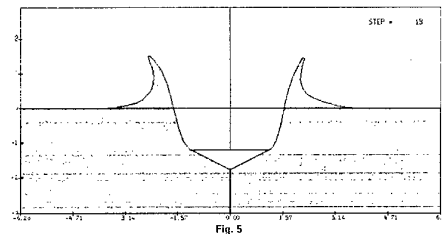
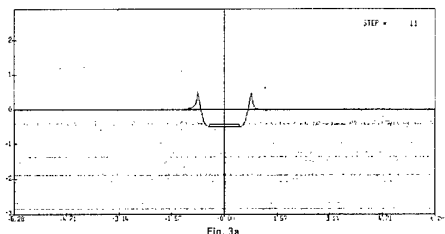
Fig. 2c

It should be remarked that for the calculation 34 boundary elements were used while usually more than a hundred is used. It is visible that boundary elements of minimal size concentrate on a spray jet.

The same effect is observed also during spray jets formation when a plane or a wedge are immersed.

At the top of spray jets a forcible instability was observed. Applying different procedures of smoothing at the top of spray jets one may build a stable solution which corresponds sufficiently well to experimental data [20].

Fig. 3.4 are a comparison of the numerical solution to experimental data for entry of a flat plate.



The most stable solution is observed when the condition (3.5) and the demand of ω_{0k} :

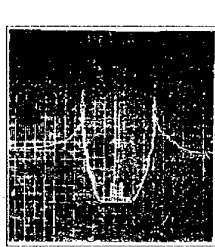
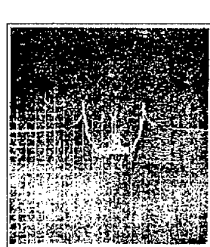
$$|\omega_{0k} - \omega_k| = |\omega_{0k} - \omega_{k+1}|, k = 1, \dots \quad (4.2)$$

are observed.

References

1. М.А. Лаврентьев, Б.И. Шабат
Методы теории функций комплексного переменного. М.: "Наука", 1987, 688 с.
2. Н.И. Мусхелишвили
Сингулярные интегральные уравнения. М.: ГИФМЛ, 1962, 600 с.
3. Ф.Д. Гахов
Краевые задачи. М.: "Наука", 1977, 639 с.
4. А. И. Некрасов
Собрание сочинений, Т. 2, М.: Издательство АН СССР, 1962, 708 с.
5. Н. Е. Кочин
Собрание сочинений, Т. 2, М.: Издательство АН СССР, 1962, 584 с.
6. Л. И. Седов
Плоские задачи гидродинамики и аэродинамики. М., «Наука», 1980, 448 с.
7. Г.В. Логвинович
Гидродинамика течений со свободными границами. Киев, Наукова думка, 1969, 216 с.
8. G. Birkhoff, E. H. Zarantonello
Jets, Wakes and Cavities. Academic Press Inc. Publishers, New York, 1957.
9. В.Н. Монахов
Краевые задачи со свободными границами для эллиптических систем уравнений. Новосибирск: "Наука", 1977, 424 с.
10. L. M. Milne-Thomson
Theoretical Hydromechanics. London Macmillan and Co. LTD, New York, St. Martin's Press, 1960.
11. J.L. Walsh
Interpolation and Approximation by Rational Functions in the Complex Domain. AMS Colloquium Publications. Second Edition. 1960.

Fig. 5-6 is the same comparison for a wedge (angle 30°).



12. И.К. Лифанов
Метод сингулярных интегральных уравнений и
численный эксперимент. М.: ТОО "Янус", 1995.
520 с.
13. С.М. Белоцерковский, В.Н. Котовский, М.И.
Ништ, Р.М. Федоров
Математическое моделирование плос-
когаралльного отрывного обтекания тел. М.:
"Наука", 1988. 232 с.
14. В.В. Мелешко, М.Ю. Константинов
Динамика вихревых структур. Киев: «Наукова
думка», 1993. 280 с.
15. М. А. Лаврентьев
О построении потока, обтекающего дугу
заданной формы. Труды ЦАГИ, выпуск 118. М.:
ГААИ. 1932. 53 с.
16. T. Sarpkaya
Computational Methods With Vortices - The 1998
Freeman Scholar Lecture, Journal of Fluids En-
gineering, 1989, No. 1, p. 5.
17. T. Hromadka II, C. Lai
The Complex Variable Boundary Element Method in
Engineering Analysis. Springer Verlag. New York
Inc., 1987.
18. Черній Д.І.
Про інтегральні характеристики рухомих гра-
ниць. Вісник Київського університету. Серія
"Фізико-математичні науки". випуск 3. 1997. с.
217-221.
19. Черній Д.И.
Аппроксимация решения начально-краевой за-
дачи с подвижными границами. Обчислювальна
та прикладна математика. Випуск 82. Київ 1998.
с.110-125.
20. Д.А.Теселкин, Л. Ю. Тормахов
Численное и экспериментальное исследование
входа в воду плоской пластины. Ученые записки
ЦАГИ 1987 г., т. XVIII, № 4, с. 33-42.

EVOLUTION DE LA BULLE DE CULOT ET JETS RENTRANTS DERRIERE UN PROJECTILE LANCE EN IMMERSION

PAQUET J.B., FLODROPS J.P.

ONERA-Lille Département d'Aérodynamique Appliquée
5 Bd. Painlevé 59000 Lille, France

DYMENT A.,

Université des Sciences et Technologies de Lille
59655 Villeneuve d'Ascq cedex France

Résumé

La prévision du comportement de la bulle de culot lors du lancement sous-marin d'un projectile est un problème complexe : il s'agit d'un écoulement à surface libre, instationnaire, couplé avec des effets thermodynamiques liés aux gaz de chasse chauds et condensables. Dans une première partie, un modèle hydrodynamique de la striction de la bulle, déjà publié [1 à 3], est rappelé et commenté en fonction des résultats récents. L'assimilation de la bulle à un corps élancé fournit les paramètres de similitude essentiels et permet une première estimation numérique jusqu'à la fermeture de la bulle. Dans une seconde partie une décomposition des phénomènes thermodynamiques basée sur une modélisation et des calculs numériques [4 à 6] montre que la condensation en masse induit une variation quasi-polytropique de la pression du gaz tandis que la faible influence de la condensation à la paroi doit être respectée à petite échelle. Dans une troisième partie les derniers perfectionnements de l'installation développée à l'IMFL [3,7,8] sont présentés. Ils permettent, dans des conditions représentatives du réel, de voir les jets rentrants et de mesurer les pressions et les efforts induits par leur impact sur le projectile. Ces résultats ne sont pas encore accessibles par le calcul.

1- INTRODUCTION

Lors de son lancement par une chasse à gaz un projectile immergé entraîne derrière lui une bulle de gaz. Après la sortie du tube de lancement, la détente du gaz de chasse qui accompagne l'avance du projectile produit la striction de la bulle jusqu'au moment de sa rupture, instant où la convergence radiale de l'eau peut engendrer des jets rentrants susceptibles de percuter l'arrière du projectile. L'objectif est de prédire les conditions d'apparition des jets rentrants pour choisir, si possible, des conditions de tir telles que ces jets n'atteignent pas le projectile ou pour caractériser les effets de leur impact sur le culot. Le problème est compliqué car l'écoulement est instationnaire, avec une surface libre ; de plus la compressibilité du fluide intervient au moment de la rupture de la bulle, moment auquel naissent les jets rentrants.

La phase d'expulsion du projectile est assimilée au remplissage de la fosse de lancement, supposée contenir un gaz homogène. Cette phase s'achève lors du passage au plancher du

culot du projectile. Une fois le projectile libéré, la phase de striction de la bulle gazeuse est supposée d'abord de nature purement hydrodynamique. Le phénomène de striction est formulé dans le cadre des écoulements axisymétriques autour de corps élancés, et en supposant que le gaz de chasse est parfait, en évolution adiabatique. Une normalisation, résultant d'une approche asymptotique, permet de réduire au minimum le nombre de paramètres de similitude. L'influence de ces paramètres est caractérisée par une résolution numérique qui indique aussi certaines limites de validité du modèle.

Des effets thermodynamiques interviennent si les gaz de chasse sont condensables. C'est ce qui arrive lorsque ces gaz résultent d'une combustion et qu'ils sont refroidis par une aspersion d'eau avant leur injection dans la fosse. L'effet thermodynamique essentiel est la variation de pression due à la condensation en masse et aux frontières : parois de la fosse durant la phase d'expulsion, surface libre et culot pendant la striction. Ces deux phénomènes sont formulés de façon élémentaire et évalués numériquement. Bien qu'une simulation de la condensation ne soit pas réalisable à petite échelle, il est montré que son influence sur la pression dans la bulle peut être approximée.

La conception de l'installation expérimentale s'est tout d'abord appuyée sur la modélisation hydrodynamique de la striction. Les résultats expérimentaux dans des conditions schématiques étaient initialement prévus pour valider le code de calcul Flow3D mis en œuvre à l'Aérospatiale [3]; leur interprétation est nécessaire pour éliminer les risques liés aux jets rentrants. Différentes techniques de visualisation rapide ont été mises en œuvre pour suivre l'évolution de la bulle et les jets rentrants. Des capteurs de pression et un capteur de force sont montés au culot de la maquette pour estimer les effets d'impacts de jets en simulant l'ensemble des conditions de tir envisageables au réel.

2 - MODELE HYDRODYNAMIQUE

2.1 - Analyse

Le lancement sous-marin d'un projectile à l'aide d'une chasse à gaz comprend deux phases. Au cours de la première phase le projectile est expulsé de la fosse de lancement par injection d'un gaz provenant d'un réservoir annexe. Dans la seconde phase, dès que le culot passe au plancher, le projectile poursuit son mouvement librement dans l'eau suivi par les gaz contenus dans la fosse qui viennent former une bulle attachée au culot. Cette bulle s'allonge et finit par se scinder avec, dans certains cas, apparition de jets rentrants (figure1).

En supposant que la striction de la bulle et l'apparition de jets rentrants sont d'origine essentiellement hydrodynamique, la seconde phase peut être modélisée indépendamment de la

première ; les seuls paramètres résultant de la première phase qui conditionnent la seconde phase sont la pression du gaz p_o et la vitesse du projectile U_o au débouchage. Différentes hypothèses sont faites pour établir un modèle simple : les effets de la viscosité et de la capillarité sont négligés ; les perturbations produites par l'ogive du projectile sont ignorées ; le projectile, cylindrique et élancé, est assimilé à un cylindre semi-infini. La longueur de la bulle est supposée petite par rapport à l'immersion de tir de sorte que l'effet de la surface libre de la mer peut être négligé. La pression p_o du gaz au débouchage est supposée voisine de la pression hydrostatique au plancher P_∞ de sorte que la bulle soit élancée, conformément aux observations faites lors de tirs réels. Il a été démontré de façon théorique [1,2] et numérique [9] que les hypothèses de bulles élancées et d'homogénéité du gaz nécessitent que $F \gg 1$, $F^{4/3} \delta \ll 1$ avec $F = U_o(gR_o)^{-1/2}$, g , R_o , F et δ étant respectivement l'accélération de la pesanteur, le rayon de la partie cylindrique du projectile, le nombre de Froude et la densité du gaz par rapport à l'eau.

2.2 - Formulation

La modélisation hydrodynamique de la striction de la bulle de culot ayant déjà fait l'objet de publications [1 à 3], on présente surtout ici les éléments nécessaires à la compréhension des développements expérimentaux et à la schématisation élémentaire des effets thermodynamiques. Le modèle s'apparente à celui développé pour les corps supercavants [10].

Les effets dissipatifs étant négligés, l'écoulement de l'eau est irrotationnel, car partant du repos. Le potentiel des vitesses vérifie l'équation de Laplace $r\Phi_{xx} + (r\Phi_r)_r = 0$ où x est l'abscisse le long de l'axe ascendant, avec l'origine au plancher, et où r est la distance à l'axe. La solution est fournie par une répartition de sources sur une portion de l'axe dont l'intensité est fixée par la condition cinématique linéarisée à l'interface. Cette intensité est proportionnelle à S_i , où t est le temps et $S=R^2$, $R(x,t)$ étant le rayon de la bulle. La condition d'imperméabilité au plancher est assurée par la méthode des images. Par ailleurs, l'examen de l'équation régissant le mouvement du projectile montre que sa vitesse U diffère peu de U_o pendant la durée de la striction [2]. Cela étant on a :

$$\phi = \frac{1}{4\pi} \int_0^{U_o t} \left([(x-\xi)^2 + r^2]^{-1/2} + [(x+\xi)^2 + r^2]^{-1/2} \right) S_i(\xi, t) d\xi \quad (1)$$

$$-\frac{1}{4\pi} \int_0^{U_o t} \left([(x-\xi)^2 + r^2]^{-1/2} + [(x+\xi)^2 + r^2]^{-1/2} \right) S_i(\xi, t) d\xi \quad (1)$$

La formulation est complétée par l'équation de Bernoulli écrite à l'interface :

$$\frac{p - P_\infty}{\rho_e} = -\phi_t(x, R, t) - \frac{R_t^2}{2} - gx \quad (2)$$

où ρ_e est la masse volumique de l'eau, p la pression du gaz dans la bulle et où, conformément à la théorie des corps élancés, on a négligé la vitesse axiale devant la vitesse radiale. Les conditions aux limites sont celles de vitesses nulles à l'infini, et de section constante $S=S_o$ avec $S_x=S_i=0$ au culot. La détente adiabatique du gaz supposé parfait et homogène s'écrit :

$$p(V_o + \int_0^{U_o t} S d\xi)^\gamma = p_o V_o^\gamma \quad (3)$$

V_o étant le volume du tube de lancement et γ le rapport des chaleurs spécifiques c_p/c_v .

2.3 - Normalisation

L'ordre de grandeur L de la longueur de la bulle est tel que $R_o < L$. Dans le cadre de la théorie des corps élancés on sait

que l'ordre de grandeur de Φ est $\frac{R_o^2}{L} U_o$, de sorte que ϕ_t et R_t^2

sont de l'ordre de grandeur de $(R_o U_o / L)^2$. Dans le cas général les effets de pression imposée, de pesanteur et de pénétration, figurant explicitement dans l'équation de Bernoulli (2), doivent être du même ordre de grandeur :

$$\rho_e g L \approx \rho_e U_o^2 R_o^2 / L^2 \approx |P_\infty - p_o| \quad (4)$$

Il s'en déduit que L est de l'ordre de grandeur de $R_o F^{2/3}$. La longueur de référence permettant de normaliser les équations étant précisément L , on pose :

$$\begin{aligned} x^* &= \frac{x}{R_o F^{2/3}} & \xi^* &= \frac{\xi}{R_o F^{2/3}} & t^* &= \frac{U_o t}{R_o F^{2/3}} \\ S^* &= \frac{S}{S_o} & p^* &= \frac{P_\infty - p}{\rho_e g R_o F^{2/3}} \end{aligned} \quad (5)$$

Les équations (2), (3) et (4) deviennent, compte tenu de (1) :

$$\frac{1}{4} \int_0^{t^*} \left[(x^* - \xi^*)^2 + F^{-4/3} S^* \right]^{-1/2} S_i^* d\xi^* + \quad (6)$$

$$\frac{1}{4} \int_0^{t^*} \left[(x^* + \xi^*)^2 + F^{-4/3} S^* \right]^{-1/2} S_i^* d\xi^* = x^* - p^* + \frac{S_{i^*}^{*2}}{8S^*} \quad (6)$$

$$p^* - p_o = \frac{p_o}{\rho_e g L} \left\langle 1 - \left[1 + \frac{S_o L}{V_o} \int_0^{t^*} S^* d\xi^* \right]^{-\gamma} \right\rangle \quad (7)$$

Si le volume de la bulle est petit par rapport à celui du tube V_o le second membre de (7) peut être linéarisé ce qui donne en première approximation :

$$p^* - D = E \int_0^{t^*} S^* d\xi^* \quad (8)$$

avec

$$D = \frac{P_\infty - p_o}{\rho_e g R_o F^{2/3}} \quad E = \frac{\gamma p_o S_o}{\rho_e g V_o} \quad (9)$$

2.4 - Similitude

Le paramètre de similitude principal D représente un écart de pression qui doit être petit. La linéarisation de la détente du gaz peut être insuffisante pour calculer cet écart avec précision. Une approximation au second ordre s'écrit :

$$p^* - D = \frac{E}{1 + (\gamma + 1)V_o / 2V_o} \int_0^{t^*} S^* d\xi^* \quad (10)$$

V étant le volume de la bulle. Le terme $(\gamma + 1)V_o / 2V_o$ fait apparaître un paramètre de similitude supplémentaire de la forme $S_o R_o F^{2/3} / V_o$. Pour une similitude stricte de la détente du gaz, il faudrait d'après (7) respecter les nombres D , $p_o / \rho_e g R_o F^{2/3}$, $S_o R_o F^{2/3} / V_o$ et γ . Le nombre de Froude apparaît dans (6) comme un paramètre de similitude secondaire, car comme on le verra, il n'intervient dans le développement asymptotique que par son logarithme.

Le modèle obtenu en linéarisant la détente du gaz met en évidence les deux paramètres de similitude D et E qui correspondent à la pression relative au débouchage et à sa dérivée à l'origine. E ne change pas si V_o et p_o sont augmentés simultanément si bien que la pression ambiante peut être choisie voisine de la pression atmosphérique en choisissant un volume V_o supérieur à celui qu'aurait une fosse de lancement en similitude géométrique. Ce degré de liberté sur V_o facilite la mise en œuvre expérimentale et il permet d'éviter des conditions d'essais à petite échelle qui feraient apparaître des effets parasites non représentatifs du réel. En particulier pour une similitude stricte le paramètre $p_o / \rho_e g R_o F^{2/3}$ impose des essais à une pression ambiante très faible; dans certains cas il arrive même que la pression au-dessus de la surface libre, qui est égale à $p_o - \rho_e g H$, avec H la profondeur d'eau dans l'installation, devrait être inférieure à la pression de vapeur saturante. Les conditions de similitude stricte n'étant pas toujours matériellement réalisables, l'approximation de la

détente permet d'obtenir une similitude partielle. Lorsque la similitude stricte est réalisable, la pression p_o est faible, car inversement proportionnelle à l'échelle géométrique ; il apparaît alors des phénomènes tels que la cavitation et le dégazage de l'eau qui ne sont pas représentatifs du réel. De plus la pression partielle de la vapeur d'eau dans la bulle devient importante à p_o faible ce qui influe sur la quantité d'eau condensée avant la fermeture de la bulle (voir §3).

Pour simuler au mieux les phénomènes réels, on serait tenté, lorsque c'est possible, de respecter la similitude stricte avec cinq paramètres adimensionnés ; mais il est plus judicieux de commencer par des essais en similitude partielle, ne faisant intervenir que D et E dans des conditions d'essais de référence pour la validation numérique du modèle et pour l'interprétation d'expériences ultérieures en similitude stricte.

Pour préciser l'effet de la linéarisation de la détente du gaz supposé parfait et incondensable, les évolutions de $(p^* - D)/E$, en supposant $S^* \equiv 1$, sont représentées sur la figure 2, pour la relation exacte (7), l'approximation linéaire (8) et quadratique (10). L'approximation linéaire n'est justifiée que pour x^* petit, c'est à dire des bulles courtes, soit globalement pour $D > 0$.

La rupture de la bulle présente un point singulier où la compressibilité peut intervenir du fait essentiellement du choc des masses d'eau qui viennent se heurter sur l'axe. Il est évident que la naissance des jets rentrants consécutifs à la fermeture de la bulle n'était pas prévisible dans le cadre de la théorie des corps élancés. Le cadre de cette théorie peut être dépassé pour améliorer la prédiction des bulles courtes et surtout pour tenter de prédire les conditions d'apparition des jets. En supposant uniquement que l'écoulement est potentiel, la relation (1) peut être remplacée par la condition cinématique complète, non linéaire à l'interface et par une équation de Green pour ϕ . Le terme R_x n'étant plus négligeable par rapport à R_t , il doit être introduit dans la relation (2). La résolution numérique est plus difficile que précédemment : des singularités doivent être distribuées sur toute l'interface de la bulle, du tube et du projectile. Cette approche purement numérique permettrait de prédire la striction de n'importe quelle bulle, y compris les jets rentrants. Le fait que R_x n'est plus négligeable par rapport à R_t comme pour une bulle allongée oblige à considérer le nombre de Froude comme un paramètre de similitude essentiel vis à vis en particulier des jets rentrants.

2.5 - Solution asymptotique

L'élimination de p^* entre les relations (6) et (7) fournit une équation intégrale-différentielle dont l'inconnue est la section de la bulle, fonction de l'abscisse et du temps. La résolution numérique est délicate : il s'agit d'une méthode de singularités axisymétriques placées à l'intérieur de la bulle, alors que généralement pour améliorer le conditionnement numérique les singularités sont placées sur l'interface. La convergence numérique est obtenue pour un nombre limité de singularités par une technique du type Gauss-Seidel avec un coefficient de sous-relaxation petit. Les difficultés de la résolution numérique peuvent être évitées en extrayant de l'intégrale figurant dans (6) sa valeur principale au voisinage de $\xi^* = x^*$. Le premier terme de l'intégrale s'écrit :

$$\int_0^{x^*} \frac{S_{t^*, t^*}^* d\xi^*}{\sqrt{(x^* - \xi^*) + F^{-4/3} S^*}} = \int_0^{x^*} \frac{S_{t^*, t^*}^*(\xi^*, t^*) - S_{t^*, t^*}^*(x^*, t^*) d\xi^*}{\sqrt{(x^* - \xi^*) + F^{-4/3} S^*}} + S_{t^*, t^*}^*(x^*, t^*) \int_0^{x^*} \frac{d\xi^*}{\sqrt{(x^* - \xi^*) + F^{-4/3} S^*}} \quad (11)$$

La relation (6) est approximée par :

$$p^* - x^* = \frac{S_{t^*, t^*}^{*2}}{8S^*} + \frac{S_{t^*, t^*}^*(x^*, t^*)}{4} \log(F^{-4/3} S^*) \quad (12)$$

La résolution numérique de (12) montre que le principal paramètre de similitude est la variation de la pression réduite au débouchage D , et que le nombre de Froude a une influence secondaire car logarithmique. Le modèle asymptotique permettant seulement de prévoir la striction jusqu'au voisinage de la rupture de la bulle, on a représenté sur la figure 3 les valeurs calculées des temps réduits de rupture de la bulle t_r^* en fonction de D pour trois valeurs de E , ainsi que des valeurs expérimentales. Lorsque la bulle est en dépression au moment du débouchage ($D > 0$), son allongement à la rupture est faible ($L \sim 0.5 R_o F^{2/3}$) et dépend peu de la détente du gaz. L'hypothèse de bulle élancée ($R_x \ll 1$) n'est donc pas justifiée au voisinage de la fermeture. Pour $D \approx 0$, le temps de rupture varie rapidement. Pour $D \ll -1$, t_r^* tend vers une limite : la résorption de la bulle à une abscisse intermédiaire entre le plancher et le culot dépend peu de D , le gaz initialement en forte surpression s'échappant latéralement le long du plancher.

La résolution numérique permet aussi de confirmer le résultat obtenu en 2.4 : la linéarisation de la détente du gaz est insuffisante pour prévoir t_r^* quand $D < 0$. Quand la bulle est longue, la pression calculée par linéarisation est trop faible ce qui induit une rupture un peu trop rapide de la bulle.

Différentes méthodes numériques ont été adaptées pour calculer la striction de la bulle [11,12]. Les résultats les plus probants sont ceux obtenus à l'Aérospatiale [4] en adaptant le code Flow3D basé sur une technique VOF : les temps de fermeture de la bulle calculés sont égaux, à la précision de mesure près, à ceux mesurés (§4). Par contre, la fiabilité des jets rentrants axisymétriques calculés est insuffisante et les effets calculés de l'impact des jets ne semblent pas réalistes

3 - MODELE THERMODYNAMIQUE

3.1 - Analyse

Les gaz de chasse proviennent de la combustion d'une poudre dans un réservoir annexe. Les gaz très chauds sont refroidis par l'aspersion de gouttelettes d'eau. Le mélange de gaz condensable et incondensable ainsi obtenu, qui contient aussi des gaz solubles dans l'eau, est injecté par plusieurs tubulures en bas du tube de lancement jusqu'à pratiquement le moment du débouchage du projectile.

Le mélange gazeux dont la température est de l'ordre de 150°C, est refroidi par la paroi métallique du tube puis, dans la phase de striction, par l'interface liquide de la bulle, ce qui provoque la condensation. La détente du gaz, en particulier dans la phase de striction, induit, en plus de la condensation sur les parois froides, de la condensation sous forme de brouillard. L'évolution du gaz pendant une durée de l'ordre de la seconde est complexe : sa masse dépend de l'injection et de la condensation, la condensation représente une source de chaleur et l'absorption de chaleur par la paroi dépend de l'écoulement du gaz.

Une analyse dimensionnelle montre qu'une simulation de la mise en vitesse du projectile, de la striction de la bulle, de la chasse à gaz avec condensation aux parois et en masse et de l'échange de chaleur aux parois n'est réalisable qu'à l'échelle 1. Il convient donc de faire des hypothèses drastiques pour prévoir les effets thermodynamiques principaux vis à vis de la striction de la bulle et pour définir des conditions d'essais à petite échelle représentatives du réel.

Les évolutions de très petites bulles de dimension de l'ordre du millimètre dans un liquide peuvent être considérées comme isothermes car la constante de temps des échanges thermiques avec l'eau est petite. La quantité de chaleur nécessaire pour changer de ΔT la température d'une bulle de volume V et de

chaleur spécifique c_v est $\rho V c_v \Delta T$ tandis que la quantité de chaleur diffusée dans le liquide est de l'ordre de $\lambda A \Delta t \Delta T / (\Delta t \chi)^{0.5}$ avec χ coefficient de diffusivité thermique de l'eau et A surface de l'interface. La constante de temps des échanges thermiques est donc de l'ordre de $\rho c_v \chi^{0.5} V / \lambda A$ soit $\sim 0.02 \mu\text{s}$ pour une bulle d'air de 1 mm de diamètre à la pression atmosphérique dans de l'eau dégazée. Pour un temps d'observation plus long l'évolution d'une petite bulle est par conséquent isotherme. La taille des cavités gazeuses qui nous concernent étant de l'ordre de 1m, les échanges par conduction thermique dans la couche limite le long des parois ne peuvent pas être négligés.

Dans le modèle hydrodynamique la loi d'évolution du gaz est supposée polytropique. D'après l'observation des phénomènes thermodynamiques, l'évolution n'est bien sûr ni adiabatique ni isotherme ; la condensation se traduit par une loi d'évolution qui n'est pas a priori polytropique et il n'existe pas de relation directe entre la pression p et le volume V du gaz à un instant t : p dépend de l'évolution thermodynamique depuis le début de l'injection.

La durée des phases de lancement étant de l'ordre de la seconde, la variation de la masse du gaz par dissolution dans l'eau est négligée. Par exemple la constante de diffusion de l'air dans l'eau est de $2 \cdot 10^{-9}$ et la dissolution d'un petit volume d'air nécessite plusieurs minutes en statique [13]. L'écoulement de l'air et du gaz accélère fortement la dissolution, mais la constante de temps reste probablement beaucoup plus grande que la seconde. Ce résultat est corroboré par des tests de dégazage d'eau réalisés dans la cuve dépressurisée décrite en 4. La constante de temps pour le dégazage y est de plusieurs minutes en présence d'écoulement et avec une interface air-eau de grande surface.

L'hypothèse principale du modèle élémentaire développé ci-dessous repose sur la constatation que la chaleur latente de vaporisation L est grande par rapport à la quantité de chaleur nécessaire à un échauffement de quelques degrés : $L=2,3 \cdot 10^6 \text{ J/Kg}$ et $C_v=1,5 \cdot 10^3 \text{ J/Kg}$ pour la vapeur d'eau. La détente du gaz devrait être principalement régie par la condensation en masse lorsque la vapeur est saturée et les échanges thermiques devraient être régis par le transfert de la chaleur latente de condensation à la paroi. Les études sur les transferts de masse et de chaleur avec condensation dans une couche limite [14] montrent que le problème est difficile ; il semble que pour une forte proportion de condensable, la vapeur reste sursaturée dans la couche limite et que la condensation s'effectue uniquement sur la paroi. Les conductivités thermiques du tube, de l'eau et de la vapeur étant respectivement d'environ 40, 0.5 et $0.01 \text{ W/m}^\circ\text{C}$, la vapeur peut être considérée en première approximation comme parfaitement isolante et le tube comme parfaitement conducteur. Le film d'eau condensée constitue un écran thermique qui régule la condensation à la paroi.

Le modèle thermodynamique est validé en comparant les prévisions numériques et des mesures à grande échelle pendant l'expulsion du projectile. Ces résultats qui portent sur des évolutions de la vitesse du projectile et de pressions dans le tube et au culot du projectile ne sont pas reproduits ici. Ce modèle de la phase d'expulsion est mis en œuvre en supposant d'abord le gaz incondensable, puis en prenant en compte les effets de la condensation. Le modèle thermodynamique élaboré est ensuite couplé avec le modèle hydrodynamique présenté en 2 pour estimer les effets de la condensation sur la striction de la bulle. Les effets thermodynamiques principaux ayant été mis en équation, il suffit ensuite de normaliser ces équations pour mettre en évidence les paramètres de similitude et déterminer des conditions d'essais à petite échelle.

3.2 - Chasse avec un gaz incondensable

On considère la phase d'expulsion du projectile de la fosse. Le gaz est supposé homogène, de sorte que la seule variable est t . Soit q_1 le débit du gaz injecté dans la fosse, ρ la masse volumique du gaz et x_c l'abscisse du culot comptée à partir du fond de la fosse. La conservation de la masse s'exprime par :

$$S_o x_c \frac{dp}{dt} + \rho U S_o = q_1 \quad (13)$$

En négligeant l'énergie cinétique du gaz dans la fosse par rapport à son énergie interne, la conservation de l'énergie s'écrit, en l'absence d'échange de chaleur avec l'extérieur :

$$x_c \frac{dp}{dt} + \gamma p \frac{dx_c}{dt} = (\gamma - 1) C_p T_l (1 + \frac{\gamma - 1}{2} M_l^2) \frac{q_1}{S_o} \quad (14)$$

L'indice 1 correspond à l'injection : M_l est le nombre de Mach et T_l la température. L'équation du mouvement du projectile s'écrit en négligeant la traînée de forme devant la poussée au culot :

$$\frac{M}{S_o} \left(\frac{dU}{dt} - g \right) - \rho g (x_c - x_{co}) = p - P_\infty \quad (15)$$

avec M masse du projectile et x_{co} abscisse initiale. La résolution des équations (13) à (15) donne les valeurs de $U(t)$, x_c , p et ρ pour différents gaz injectés [4].

3.2 - Chasse avec un gaz condensable

La condensation a pour effet de diminuer la masse du gaz. Avec q_{cp} et q_{cm} les débits de condensation à la paroi et en masse, la relation (13) devient :

$$x_c S_o \frac{dp}{dt} + \rho U S_o = q_1 - q_{cp} - q_{cm} \quad (16)$$

La quantité de chaleur dégagée par la condensation étant supposée entièrement transmise à la paroi, l'énergie du gaz est diminuée de l'énergie interne $c_v T q_{cp}$ et du travail des forces extérieures comblant le vide laissé par le gaz condensé, soit $(\gamma - 1) c_v T q_{cp}$ [4]. A l'équilibre la température du gaz T est T_{sat} , température de la vapeur saturante. L'équation de l'énergie (14) devient :

$$x_c \frac{dp}{dt} + \gamma p \frac{dx_c}{dt} = (\gamma - 1) C_p T_l (1 + \frac{\gamma - 1}{2} M_l^2) \frac{q_1}{S_o} - \gamma c_v T_{sat} q_{cp} \frac{\gamma - 1}{S_o} \quad (17)$$

Le tube étant supposé parfaitement conducteur et à température constante T_p , l'écran thermique qui limite la condensation est le film d'eau condensée sur les parois. L'eau condense sous la forme d'un film d'épaisseur $e(x, t)$ qui dépend de l'abscisse et du temps. L'écoulement du gaz et la pesanteur provoquent un mouvement vertical dans ce film. Une étude des ordres de grandeur [4] et des estimations numériques [6] montrent que l'écoulement du condensat influe peu sur les échanges thermiques ; les effets de gravité compensent en partie l'entrainement dû au gaz. Le film de condensat étant mince, ($\sim 0.3 \text{ mm}$), la variation de température suivant l'épaisseur est presque linéaire. La chaleur latente de condensation est égale au flux de chaleur transmis par le film, soit :

$$\lambda \frac{T_{sat} - T_p}{e} = \rho_e L \frac{\partial e}{\partial t} \quad (18)$$

λ étant la conductivité du condensat. Si la variation de T_{sat} est négligeable, on en déduit :

$$e^2 = \frac{2\lambda}{\rho_e L} (T_{sat} - T_p)(t - \tau) \quad (19)$$

où t est compté à partir du démarrage du projectile et τ est l'instant de mise en contact avec le gaz. τ est nul sauf sur la surface latérale de la fosse de lancement.

3.3-Chasse avec un mélange de gaz condensable et incondensable

Le gaz condensable diffuse à travers le gaz incondensable pour atteindre la paroi et y condenser : donc, la pression partielle p_c de gaz condensable diminue en s'approchant de la paroi froide ce qui induit, à l'équilibre, une diminution de la température de vapeur saturante. Soit J le flux global du mélange gazeux vers la paroi froide, J_c le flux de vapeur et J_i le flux de gaz incondensable. D'après la loi de Fick on a :

$$J_c = J_{c_i} + K \frac{dc_c}{dy} \quad (20)$$

$$J_i = J_{c_i} + K \frac{dc_i}{dy} \quad (21)$$

avec c concentration en gaz incondensable pour l'indice i et condensable pour l'indice c , K est un coefficient de diffusion. Le gaz incondensable ayant une vitesse moyenne nulle ($J_i=0$), on a :

$$J_c = -K \left(\frac{c_c}{c_i} + 1 \right) \frac{dc_i}{dy} \quad (22)$$

Par intégration suivant l'épaisseur y de la couche de diffusion des gaz, on en déduit le flux de vapeur par interdiffusion des gaz :

$$J_c = k_1 \text{Log} \left(\frac{p - p_{vi}}{p - p_{v\infty}} \right) \quad (23)$$

avec p_{vi} et $p_{v\infty}$ pressions partielles de vapeur à l'interface et à l'infini. La chaleur latente dégagée à l'interface du film d'eau condensée y est absorbée par conduction. L'écoulement du gaz induit à l'interface un apport de chaleur schématisé par $k_2(T_\infty - T_i)$ avec T_i température de vapeur saturante à l'interface, T_∞ température du gaz au loin et k_2 un coefficient de conduction thermique. L'équation de conduction à la paroi s'écrit sous forme implicite :

$$\frac{\lambda}{e} (T_i - T_p) = k_1 \text{Log} \left(\frac{p - p_{vi}}{p - p_{v\infty}} \right) + k_2 (T_i - T_\infty) \quad (24)$$

Dans la relation (18) la température T_{sat} doit être remplacée par la température de l'interface T_i . Lorsque la température du gaz devient inférieure à T_{sat} , le gaz condense. Il faut ajouter dans l'équation de l'énergie la chaleur latente et l'énergie nécessaire pour réchauffer les gouttelettes formées antérieurement. Pour la résolution numérique, il faut adjoindre aux équations (16),(17),(18),(24), les équations d'état des gaz condensables et incondensables, la relation intégrale reliant l'épaisseur de vapeur condensée e au débit q_{cp} , et l'équation de Clapeyron à l'équilibre de la vapeur saturante :

$$\frac{dp_v}{p_v} = \frac{LdT}{R_c T^2} \quad (25)$$

avec R_c la constante d'un gaz supposé parfait.

Dans la phase d'expulsion du projectile les tests numériques indiquent que la température du mélange gazeux reste inférieure à celle de saturation. Les constantes k_1 et k_2 nécessaires pour résoudre (24) sont extraites de résultats expérimentaux [15,16] dans des conditions qui ne sont pas parfaitement transposables. En effet, les seuls résultats connus concernent un mélange de gaz avec une faible proportion de condensable ce qui ne correspond pas au mélange que l'on étudie. Les calculs présentés en [4] donnent une épaisseur du condensat toujours inférieure à 0.3mm et un débit maximal de condensat de l'ordre de 20 litres par seconde, qui peut atteindre 30% de la vapeur injectée. La condensation modifie peu la pression au débouchage p_o , mais, elle augmente de l'ordre de un le paramètre principal vis à vis de la striction de la bulle, qui est l'écart adimensionné de pression au débouchage D .

3.4 - Striction de la bulle

La prise en compte de la condensation dans le modèle hydrodynamique de striction de la bulle revient à remplacer la relation (7) par un calcul de la pression dans la bulle p en fonction de la position du culot. Pour simplifier le problème de conduction thermique dans l'eau, à partir de l'interface, et ne pas avoir à calculer le champ de température, le schéma de la condensation sur le tube est transposé à l'interface de la bulle qui est supposée parfaitement conductrice : ceci donne un majorant pour la quantité d'eau condensée à l'interface. La géométrie de la bulle intervient uniquement par sa surface d'échange thermique.

L'injection du gaz étant achevée avant le débouchage du projectile, l'équation de l'énergie (17) s'écrit pendant la striction :

$$Ldm_c + pdV + (m_c c_{vc} + m_i c_{vi})dT + (m_{co} - m_c)CdT - R_c T dm_c = 0 \quad (26)$$

l'indice c correspondant comme précédemment au gaz condensable et i au gaz incondensable, m étant la masse de gaz, c_v la chaleur spécifique à volume constant et C la chaleur spécifique de l'eau. Elle traduit que la somme de l'énergie latente de condensation, du travail des forces extérieures, de la variation de l'énergie interne, de la quantité de chaleur pour réchauffer les gouttelettes et du travail d'expansion pour combler le vide laissé par le condensat est nulle. Les autres équations du problème sont les mêmes qu'en 2.5 et en 3.3.

En tenant compte de la condensation, les deux phases du lancement ne sont pas, a priori, dissociables, mais on montrera par l'approximation présentée en 3.5 et, a posteriori, d'après les résultats numériques, qu'il est tout de même possible de décomposer ces deux phases. Pour estimer l'effet de la condensation sur la striction de la bulle, les comparaisons numériques portent sur des conditions d'essais identiques à l'instant du débouchage (D,E,F invariants). Le volume du tube et la composition des gaz de chasse sont inchangés. Dans le calcul de référence, on impose artificiellement une condensation nulle bien que le gaz soit sursaturé. La durée d'injection du mélange gazeux est ajustée pour parvenir à la même pression p_o au débouchage avec et sans condensation. Pour simplifier l'interprétation, le résultat présenté sur la figure 4 correspond à un calcul avec un gaz entièrement condensable qui est de la vapeur d'eau. La forme de l'interface avec et sans condensation y est présentée pour trois positions du culot de la maquette. L'accélération de la striction due à une plus grande dépression de la bulle en présence de condensation y apparaît comme un phénomène secondaire. La présence d'un gaz incondensable ayant tendance à diminuer l'effet de la condensation, on en conclut que l'influence de la condensation sur la striction de la bulle est faible quelle que soit la composition du gaz. La prise en compte de la conduction du tube tend aussi à diminuer la condensation [4]. Ce résultat tend à confirmer l'hypothèse de départ suivant laquelle la striction de la bulle et l'apparition de jets rentrants sont essentiellement d'origine hydrodynamique.

Cette conclusion sur le faible effet de la condensation est liée à l'hypothèse suivant laquelle le film d'eau déposé sur les parois fait écran thermique. Si la condensation s'effectue en gouttelettes sur les parois au lieu d'un film, elle serait beaucoup plus intense à cause de la forte conductivité thermique du tube. Une estimation faite en [6] de la condensation en gouttelettes montre qu'elle peut être approximée, de même que la condensation en masse, par une loi d'évolution polytropique du gaz.

3.5- Approximation par une loi d'évolution polytropique

Pour mieux comprendre l'effet de la condensation en masse, on propose un schéma simplifié qui ne se limite pas à la présentation de résultats numériques. Si tout le gaz est condensable, l'équation de l'énergie (26) peut être réduite à une relation linéaire entre dT et dV ou dp et dV . En effet la dérivation de l'équation d'état du gaz donne une relation linéaire entre dm_v , dp , dV et dT ; l'équation de Clapeyron (25) relie dp à dT . Par élimination de dp et dm_v entre ces trois équations, on a :

$$L \frac{dV}{V} + dT \left[c_{cv} + \left(\frac{m_{co}}{m_c} - 1 \right) C + R_c \left(\frac{L}{R_c T} - 1 \right)^2 \right] \quad (27)$$

Comme $L \gg R_c T$, si T et m_v varient peu, cette relation peut être approximée par une évolution polytropique ;

$$\frac{dV}{nV} \approx \frac{dT}{T} \frac{L}{R_c T} \approx \frac{dp}{p} \quad (28)$$

Dans les tirs à l'échelle 1, l'indice polytropique obtenu est d'environ 1,1. En présence d'un mélange gazeux contenant des gaz incondensables, les déductions précédentes peuvent être généralisées : il est montré en [6] que l'évolution du gaz peut encore être approximée par une loi polytropique tant que la masse de gaz incondensable n'est pas supérieure à environ 20 fois celle de gaz condensable. Malgré la complexité des phénomènes thermodynamiques il semble qu'ils peuvent être schématisés par une loi $pV^n = Cste$ avec un indice n déterminé lors d'essais à l'échelle réelle. Il convient lors des simulations à une petite échelle de vérifier que la valeur de ce paramètre n est bien reproduite. Pour s'en assurer il suffit de calculer n par régression sur les mesures pendant la phase d'expulsion du projectile.

3.6 - Similitude

Exprimons les effets de la condensation sous forme normalisée (5). L'épaisseur d'eau condensée (19) devient :

$$e^{*2} = 2(t^* - \tau^*) \quad (29)$$

avec $e^{*2} = e^2 \frac{\rho_e L}{\lambda \Delta T} R_o^{1/2} g^{1/2} F^{1/3}$

τ^* est nul, sauf sur les parois de la fosse et de la bulle où il est égal à $x^* - x_{co}^*$. ΔT est la différence de température entre les deux cotés du film. On en déduit le débit réduit

$$q_{cp}^* = \int_{parois+bulle} \frac{de^*}{dt} dS^* \text{ par :}$$

$$q_{cp}^* = q_{cp} \left(\frac{\rho_e L}{\lambda \Delta T} \right)^{1/2} R_o^{-7/4} g^{-1/4} F^{-1/6} \quad (30)$$

qui est fonction de e^* . L'équation de l'énergie (26) peut s'écrire pour un gaz entièrement condensable en éliminant les termes de chaleur latente et de réchauffement des gouttelettes :

$$dp = -\gamma \frac{p U \pi R_o^2 dt}{V} - \gamma \frac{R_v T_i q_{cp} dt}{V} \quad (31)$$

Si ΔT et T_i varient peu pendant la striction, on en déduit, compte tenu de (5), (30) et (31), l'équation de la pression réduite :

$$(1 + N_v \int_0^{t^*} R_o^{*2} dx^*) dp^* = dt^* (E + H q_{cp}^*) \quad (32)$$

avec

$$N_v = \frac{\pi R_o^3 F^{2/3}}{V_o}, \quad H = \frac{g R_v T_i}{V_o} \frac{R_o^{5/4}}{F^{5/16} g^{5/4}} \sqrt{\frac{\lambda \Delta T}{\rho L}}$$

En l'absence de conduction ($q_{cp}=0$) on retrouve la relation (8) sous forme différentielle. Dans les conditions de tir réel, un calcul numérique montre que $H q_{cp}^*$ est de l'ordre de 10% de E ; c'est à dire que la condensation à la paroi a un effet modéré.

Pour simuler à petite échelle la condensation en film il faudrait respecter l'invariance du paramètre de similitude H qui varie comme l'échelle géométrique à la puissance 7/4. Cette similitude ne semble pas réalisable : si dans une petite installation on utilisait un gaz condensable à une température élevée et dans des proportions importantes, la condensation aurait un effet prépondérant par rapport à la détente du gaz $H q_{cp}^* \gg E$. Le film de condensat à petite échelle est trop mince pour représenter un écran thermique comme à l'échelle un. Pour une simulation à petite échelle, il faudrait une valeur de ΔT très petite pour respecter la valeur de H . Il est préférable d'utiliser un gaz incondensable à la température ambiante avec $\Delta T=0$ de façon à ce que $q_{cp}=0$ plutôt que de chauffer le mélange gazeux en contact avec de l'eau. L'évolution du gaz pourrait d'après (32) être approximée par une loi polytropique. Il suffit pour la similitude de s'assurer que l'indice n moyen est bien respecté.

La même démarche de normalisation des équations est réalisable pour les équations de la condensation en masse ; ceci permet de mettre en évidence des paramètres de similitude tels que (32). La chaleur latente étant grande par rapport à la quantité de chaleur nécessaire pour échauffer le mélange de gaz $L \gg R_c T$, la condensation en masse induit d'après le contenu de la section 3.5 une évolution presque polytropique, quelles que soient les conditions d'essais. En première approximation la similitude thermodynamique nécessite donc que l'indice n soit voisin de la valeur 1,1 mesurée à l'échelle un. Une similitude plus complète de la condensation en masse nécessiterait de tenir compte de la composition du mélange gazeux ce qui est incompatible avec la similitude de la condensation sur les parois.

4 - EXPERIENCES

4.1 - Moyen d'essais

Un moyen d'essais a été développé à l'IMF-Lille pour simuler des lancements à petite échelle. Tous les résultats présentés ici ont été obtenus dans cette installation. L'objectif initial étant d'obtenir une base de données pour valider des codes de calcul, des conditions d'essais schématiques et de référence ont été recherchées. En particulier la vitesse d'avance du projectile n'est pas simulée et le plancher est horizontal, ce qui correspond à des écoulements axisymétriques. Etant donné que les conditions de tirs les plus défavorables vis à vis des risques de jets rentrants sont celles sans vitesse d'avance, la configuration axisymétrique choisie permet d'évaluer le risque maximum.

Au lieu de simuler directement les conditions de tirs réels, on a cherché à dissocier les effets des différents paramètres pour tenter de comprendre les phénomènes et d'en modéliser les caractéristiques principales. L'objectif final est de prédire les jets rentrants dans la bulle de culot à partir d'essais à petite échelle et aussi d'optimiser des conditions de lancement. L'installation a aussi été prévue pour d'autres applications telles que la pénétration de projectiles dans l'eau [1,2,9].

La partie centrale de l'installation est constituée par une cuve verticale cylindrique de diamètre intérieur 0,75 m et de hauteur 2,7 m, composée de trois parties démontables (figure 5). Le système de chasse est situé sous la cuve. Le lancement s'effectue à partir d'une fosse étanche où la pression initiale p_i est ajustable. Un calcul de la détente du gaz de chasse permet de choisir p_i de manière à obtenir la valeur voulue de p_o . La pression du gaz qui surmonte l'eau contenue dans la cuve est également ajustable entre la pression de vapeur saturante et 6 bars absolu. La mise en vitesse de la maquette est réalisée avec un vérin hydraulique de façon à fixer la vitesse U_o indépendamment de la pression du gaz. L'asservissement en

position du système permet de simuler une loi de mise en vitesse pré-programmée.

Un élément important de l'analyse expérimentale étant la visualisation de la striction de la bulle et des jets rentrants, la cuve est munie de quatre hublots en verre de dimension de $1,2 \times 0,2 \text{ m}^2$. Pour éviter que la cuve ne se déforme trop aux pressions élevées, ce qui pourrait induire des contraintes dangereuses vis à vis de la résistance des hublots, l'enveloppe métallique de la cuve a été prévue très rigide.

La course du vérin est de 1,5 m avec une vitesse maximale de 5 m/s et une accélération maximale de 125 m/s². Il est susceptible d'entraîner une maquette de 10 kg. Il est équipé d'un capteur de position linéaire qui a été étalonné en statique par rapport à un cathétomètre. L'entrée du vérin en bout de course dans la fosse de lancement est rendue possible grâce à un jeu de 1 mm entre les rayons de la fosse et de la maquette. Après la mise en place de la maquette la fosse est rendue étanche en gonflant un joint placé près du plancher.

La fosse est prévue démontable pour tester différentes volumes V_o conformément à l'analyse de similitude. Elle est composée d'une partie haute cylindrique de 150 mm de long au diamètre de la maquette augmenté des jeux mécaniques, et d'une partie basse interchangeable de 190 mm de diamètre. Les caractéristiques de l'installation sont prévues pour couvrir largement le domaine des conditions de lancement envisageable en D , E et F . Des essais ont été réalisés pour deux valeurs du volume V_o , dont l'une est environ six fois plus grande que l'autre, en gardant constant D , E et F . En général, le gaz de chasse utilisé est de l'air, mais, pour certains essais avec le petit volume, on a aussi utilisé un gaz lourd dont la valeur de γ est voisine de 1.09. L'indice n moyen de l'évolution approximativement polytropique est calculé à chaque essai par régression pendant la phase de mise en vitesse de la maquette, pour vérifier qu'il est proche de la valeur réelle. Deux maquettes, géométriquement semblables, de rayons R'_o et R''_o ($R''_o = 1,6 R'_o$) ont été utilisées. La hauteur d'eau au dessus du plancher ne peut pas toujours correspondre à la profondeur d'immersion en similitude géométrique, soit que la pression ambiante devienne trop faible soit que la cuve ne soit pas assez haute.

Le circuit étanche d'alimentation de la fosse peut être connecté à un réseau d'air comprimé, à une pompe à vide ou une bouteille de gaz.

4.2 - Équipement de mesure

Le culot de la maquette est équipé de capteurs de pression Druck pdcr42, dont la bande passante estimée à partir de mesures faites au tube à choc est de l'ordre de 32 kHz, ainsi que d'une rondelle de force piézo-électrique Kistler 9104; la fonction de transfert du capteur de force mesurée dans l'air et dans l'eau indique une fréquence de coupure d'environ 1 kHz. La contre-pression dans la maquette est celle de la surface libre, ce qui permet de choisir des capteurs d'une étendue de mesure de 0,35 bar qui peuvent cependant subir une surpression de 3 bars sans endommagement. Les capteurs de pression ne pouvant détecter les jets rentrants que s'ils percutent leur partie sensible, la configuration du culot avec un capteur de force est, parmi celles testées, la mieux adaptée à la détection des jets rentrants. Un capteur de pression est placé au centre du culot, tandis qu'un second capteur est placé derrière le plateau de mesure des efforts pour fournir la pression dans la bulle même pendant l'impact d'un jet. L'équipement du culot de la maquette est représenté sur la figure 6.

En plus des efforts transitoires d'impact des jets, le capteur de force est sensible à l'accélération de la maquette et à la différence de pression entre la cavité gazeuse et l'intérieur de

la maquette. L'effort transitoire du jet est obtenu en soustrayant de ce signal global des termes provenant des mesures de l'accélération par un accélémètre installé dans la maquette. Les termes de pression et d'accélération, assimilés à une surface apparente et à une masse sont calculés à chaque tir, pendant la phase d'expulsion du projectile, par corrélation double entre les signaux d'effort, d'accélération et de pression. Des contrôles sont faits dans l'air pour s'assurer qu'en l'absence de jet le traitement du signal fournit effectivement un effort nul.

La pression initiale dans la fosse p_i est mesurée par un capteur statique eau-eau. Pour parvenir à une précision d'environ 0.5 mbar (soit environ 0.05 sur D), on mesure la différence de pression $p - P_\infty$ entre la fosse et le plancher. La pression de l'air dans la cuve est aussi mesurée, mais la précision nécessaire pour l'interprétation de cette mesure est moindre. Toutes les mesures sont acquises pendant environ une demie seconde sur un système d'enregistreurs de transitoire Lecroy 6810 à une fréquence d'échantillonnage choisie à 10 kHz. L'acquisition est déclenchée par une barrière optique détectant le passage de la maquette.

Une tentative de mesure de la température dans la bulle a été infructueuse car l'inertie thermique des petits thermocouples utilisés est encore trop grande pour parvenir à une constante de temps de l'ordre de 1 ms.

4.3- Visualisations

La durée de la striction étant de l'ordre de 50 ms, la visualisation doit être rapide. Une technique d'ombroscopie a tout d'abord été utilisée. Deux stroboscopes placés l'un au dessus de l'autre fournissent une énergie de l'ordre de 0,25 Joules chacun en environ 18 µs jusqu'à une cadence de 1000 images par seconde. Une rafale d'un nombre réglable d'éclairs est déclenchée à la cadence souhaitée par un signal émis par la station de travail pilote. Un écran diffusant est placé devant un hublot pour obtenir un éclairage uniforme. La striction de la bulle est enregistrée soit sur un film de 35mm avec une caméra à tambour tournant soit en mémoire avec une caméra vidéo rapide. Bien que les flashes soient très courts, le mouvement de la caméra à tambour tournant induit un flou de bouger. La vidéo rapide ne présente pas cet inconvénient, mais sa résolution est limitée par le nombre de pixels.

La technique ombroscopique ne permettant pas de bien voir les jets rentrants (figure 7a), des essais de visualisations ont été effectués en éclairage stroboscopiques indirect. Les résultats sont un peu meilleurs que précédemment mais insuffisants pour caractériser les jets (figure 7b). Ensuite une technique de visualisation par fluorescence induite par laser a été développée. Un plan lumineux perpendiculaire à la direction d'observation est obtenu avec un laser continu de puissance 30W. De la rhodamine dissoute dans l'eau émet par fluorescence une lumière de faible intensité dont la fréquence est différente de celle de l'éclairage. Des filtres optiques permettent de dissocier la lumière se réfléchissant sur l'interface perturbée de la bulle de la lumière émise par fluorescence, ce qui fait apparaître l'eau des jets rentrants sans être ébloui par la lumière réfléchie. L'intensité lumineuse étant très faible, l'utilisation d'une caméra vidéo rapide intensifiée est nécessaire (figure 8).

Le comportement de la striction de la bulle change en fonction de sa longueur, c'est à dire principalement en fonction de la valeur de D [3]. Pour $D > 0$ la bulle se ferme rapidement au plancher. Lorsque D décroît, il apparaît une fermeture non ponctuelle le long de l'axe qui laisse une émulsion dans son sillage. Pour D fortement négatif le gaz s'échappe latéralement le long du plancher tandis que la bulle se scinde à une abscisse

intermédiaire entre le plancher et le culot. Si de plus E est petit (<3), la pression du gaz reste longtemps supérieure à P_∞ , les bulles sont très longues et leur rupture s'effectue parfois après la sortie de l'eau du projectile.

4.4 - Temps de rupture

Des temps de rupture adimensionnés t_r^* calculés et mesurés sont présentés sur la figure 3. Bien que l'approximation de la théorie asymptotique ne soit pas bien respectée pour des bulles courtes avec $D>0$, les valeurs calculées sont proches de celles mesurées quel que soit E . Pour $D>0$ l'augmentation prévue de t_r^* avec E décroissant est bien confirmée par l'expérience, mais on constate que les valeurs calculées sont généralement inférieures à celles mesurées. Les valeurs de t_r^* , relativement peu précises pour la maquette de rayon R_0 , ne semblent pas dépendre du diamètre.

Suivant les prévisions du modèle thermodynamique, il est nécessaire que l'évolution de la pression soit en moyenne polytropique d'indice n voisin de 1,1. Lors des essais réalisés avec de l'air et une fosse de grand volume, l'indice de la détente du gaz est voisin de 1,4. Lors d'essais réalisés avec de l'air mais avec un faible volume de fosse, la vapeur d'eau condense subitement juste avant le débouchage du projectile (figure 9) ; la pression présente un palier au voisinage du débouchage qui est caractéristique d'un flash de condensation. Il en résulte une augmentation du temps de fermeture de la bulle t_r^* (figure 10). ; lorsque $D<-1$ les valeurs de t_r^* obtenues avec la fosse de petit volume V_0 sont relativement plus élevées que celles avec un grand volume. Pour une détente d'un gaz incondensable avec $\gamma=1,4$, par suite du rapport des volumes, la température au moment du débouchage devrait être de -38°C pour la petite fosse et 9°C pour la grande fosse. En présence d'une faible proportion de gaz condensable, le gaz devient sursaturé avant le débouchage dans le premier cas, ce qui déclenche une variation de pression non représentative du réel. Ce phénomène parasite a été éliminé en utilisant un gaz lourd, dont le rapport des chaleurs spécifiques plus proche de 1 induit des variations de température plus faibles.

4.5 - Jets rentrants

Lorsque $D>0$, les bulles sont courtes et quelques millisecondes après la rupture, un jet fin et rapide est projeté sur le culot. Il est suivi d'un jet de forme conique dont le diamètre atteint de l'ordre de 25% du diamètre du projectile. L'eau provenant du jet qui s'écoule le long du culot rejoint l'interface de la bulle et la rend opaque. Dans certains cas cette perturbation de l'interface met en oscillation la bulle à sa fréquence propre, ce qui se traduit, dans le cas où un jet percute le culot, par des oscillations importantes de l'effort mesuré (figure 11). Cette oscillation disparaît lorsque l'eau s'écoulant le long du culot est déviée avant d'atteindre l'interface. Lorsque $D<0$ les caractéristiques des jets ne semblent pas parfaitement reproductibles : ils sont parfois dissymétriques et précédés d'une émulsion d'air et d'eau. Au moment de la rupture les perturbations de l'interface la rendent parfois trop opaque pour voir distinctement le jet. On a représenté sur la figure 12 la valeur maximale de l'effort d'impact mesuré en fonction de D pour différentes valeurs des nombres E et F : les essais ont été réalisés à P_∞ constant, et non à p_0 constant comme l'aurait exigé le respect de la condition $E=Cste$. Le capteur de force détecte presque toujours un impact dont l'intensité est minimale au voisinage de $D=0,5$. Pour D fortement négatif la bulle se scinde presque simultanément à deux abscisses produisant deux jets rentrants ; les efforts maximaux mesurés présentent alors une grande dispersion, dépassant largement les valeurs obtenues dans les autres

conditions de lancement. Lorsque la bulle est très longue les caractéristiques des jets présentent une dispersion importante dont il est difficile de cerner l'origine. Sur le plan structural, l'effort maximal dû à l'impact d'un jet n'est pas significatif, la grandeur intéressante est l'impulsion.

Les recouplements entre les visualisations et les mesures au culot de la maquette permettent de caractériser les conditions d'apparition de jets rentrants, d'estimer les évolutions de leur vitesse et de leur section en fonction du temps. Pour de raisons de confidentialité il n'est pas possible de donner ici l'ensemble des résultats obtenus. La figure 13 présente un exemple d'enregistrement de pression et d'effort avec des clichés au moment de l'apparition de jets rentrants. En repérant sur les clichés l'instant de rupture de la bulle et sur les enregistrements de pression et d'effort l'instant de l'impact d'un jet, on en déduit le temps mis par le jet pour atteindre le culot et donc une estimation de sa vitesse moyenne. Des essais dans des conditions bien maîtrisées d'impact de jets dans l'axe du capteur ont montré que le signal enregistré par le capteur de pression est de l'ordre de grandeur de la pression d'arrêt stationnaire $pU_0^2/2$, car la constante de temps des phénomènes transitoires n'est que de l'ordre de 0,2 msec. Les mesures de pression d'impact sont ainsi transposables à l'échelle réelle et elles fournissent une estimation de la vitesse des jets à l'impact. Ces vitesses des jets déduites des clichés, de l'intensité de la pression d'impact et du temps écoulé entre la fermeture de la bulle et l'impact sont toutes de l'ordre de $2U_0$ en valeur absolue. Cette vitesse augmente avec D pour D fortement négatif, car le jet principal est précédé par une projection de gouttelettes à grande vitesse. La comparaison entre la pression et la force d'impact permet, en supposant l'écoulement quasi-stationnaire, d'estimer la section du jet et de la comparer à celle visualisée.

La durée d'existence des jets ne se déduit des visualisations car l'interface de la bulle se perturbe trop rapidement pour voir le jet jusqu'au moment de la sortie de l'eau ; les estimations de la durée du jet à partir des enregistrements d'effort et de pression indiquent de fortes variations en fonction des paramètres de similitude.

A l'aide d'un traitement d'images on peut extraire des visualisations le contour extérieur des bulles et en déduire leur volume apparent. Si la pression dans la bulle évolue de façon polytropique, le volume de gaz V après la rupture s'obtient à l'aide de la mesure de p ; la différence entre le volume apparent et V correspond au volume occupé par le jet rentrant. On peut ainsi estimer le débit moyen du jet. La figure 14 présente ce résultat, comparé aux estimations obtenues directement de l'observation du jet (supposé de révolution).

5 - CONCLUSION

Le modèle hydrodynamique asymptotique de la striction de la bulle a mis en évidence les deux paramètres de similitude D et E qui correspondent à la différence de pression entre le gaz et l'eau au moment du débouchage et à la dérivée normalisée de cette grandeur. La résolution numérique montre que le paramètre influant le plus sur le temps de rupture de la bulle, par exemple, est D , que l'influence du nombre de Froude est faible comme prévu et que la linéarisation de la détente du gaz n'est pas une approximation suffisante pour $D<0$. Le modèle ne permet pas de dépasser le point singulier de la rupture de la bulle.

La thèse soutenue est que l'effet thermodynamique principal vis à vis de la striction et l'apparition des jets rentrants est la condensation de la vapeur en masse. La condensation sur les parois du tube et sur l'interface accélère un peu la striction ; pour que la condensation ne devienne pas prépondérante à

petite échelle, il ne faut pas chauffer le gaz et il faut que la pression partielle de vapeur soit faible. La loi d'évolution $p(V)$ doit être en similitude à petite échelle ; il suffit, en première approximation, qu'elle soit de la forme $pV^n = Cste$ avec le même indice n qu'à l'échelle un.

La théorie et les calculs ne permettent pas de prévoir les jets rentrants et leurs effets lors d'impacts ; l'installation de l'IMF-Lille a été adaptée pour simuler des jets axisymétriques dans des conditions représentatives du réel. Les visualisations et les mesures simultanées de pression et d'effort au culot montrent qu'il existe toujours des jets rentrants, mais que dans certains cas, ils n'atteignent pas le culot, tout au moins avant que le projectile ne sorte de l'eau. L'extrapolation des mesures d'efforts et de pression permet de dimensionner les structures pour éviter tout risque de détérioration par des jets rentrants. La prévision théorique ou numérique de ces jets rentrants reste un problème ouvert.

6 - REMERCIEMENTS

Les travaux présentés dans ce document ont été réalisés avec le support financier de la Direction des Systèmes de Force et de la Prospective du Ministère de la Défense français.

REFERENCES

- 1 - Dymant A., "Modèle asymptotique de l'écoulement produit par l'impact d'un projectile dans un liquide", Comptes rendus de l'Académie des Sciences t.310 Série II, p.1589-1594, 1990
- 2 - Dymant A., "Transient behavior of a gaseous cavity attached to a projectile in a two phase flow", Symposium in honour of Pr. Guiraud, Paris, Lecture notes in physics n°442 p205-220, Springer 1994
- 3 - Dymant A., Flodrops J.P., Paquet J.B., Dupuis D., Marchand D., "Gaseous cavity at the base of an underwater projectile", Aerospace Science and Technology. Gauthier-Villars à paraître en 1998
- 4 - Danis-Gobert A., "Etude du lancement en immersion d'un projectile par une chasse à gaz incondensable et condensable", Thèse. Université de Lille 1994
- 5 - Gobert A., Flodrops J.P., Paquet J.B., "Résorption de la cavité gazeuse derrière un projectile lancé en immersion", Association Technique Maritime et Aéronautique 1994
- 6 - Paquet J.B., Gobert A., "Modèle élémentaire de la bulle de culot d'un missile hydrobalistique", Rapport IMFL n°95/21 1995
- 7 - Paquet J.B., Flodrops J.P., Dymant A., Gobert A., "Simulation sur modèle réduit et éléments de modélisation de la bulle de culot au lancement d'un missile hydrobalistique", Rapport IMFL n°93/46 1993
- 8 - Paquet J.B., Flodrops J.P., "Bulle de culot d'un missile hydrobalistique : moyens pour caractériser des jets rentrants à une petite échelle", Rapport IMFL n°97/16 1997
- 9 - Paquet J.B., "Cavité formée par un cylindre semi-infini pénétrant dans une nappe d'eau", Rapport IMFL n°90/22 1990
- 10 - Semenenko V.N., "Computer simulation of unsteady supercavitating flows", AGARD R-827 High speed body motion in water 1998
- 11 - Mahjoub F., "Modélisation diphasique des évolutions transitoires d'interfaces liquide-gaz ; application aux bulles attachées à des corps en mouvement", Thèse. Institut national polytechnique de Grenoble 1995
- 12 - Molin B., Diéval L., Marcer R., Arnaud M., "Modélisation instationnaire de poches de cavitation par la méthode potentiel et par la méthode VOF", 6^{èmes} Journées de l'hydrodynamique Nantes 1997
- 13 - Lefranc J.P. & al, "La cavitation", Presses Universitaires de Grenoble 1995
- 14 - Legay-Desesquelles F., Prunet-Foch B., "Heat and mass transfer with condensation in laminar and turbulent boundary layer along a flat plane", I.J.H.M.T,29, 95-105, 1986
- 15 - Collier J.G., "Convective boiling and condensation", Mc Graw Hill 1981
- 16 - Huetz J., Petit J.P., "Techniques de l'ingénieur. Notions de transfert de chaleur", A1541, A1550
- 17 - May A., "Water entry and the cavity running behavior of missiles". NAVSEA AD-A020.429 report 75-2 1975
- 18 - Waugh J.G. & all, "Hydroballistics modeling", NUC report TP447, AD-A007.529, 1975
- 19 - Paquet J.B., "Water jet impact on a rigid wall", Conference on offshore Mechanics and arctic engineering. Lisbon 1998

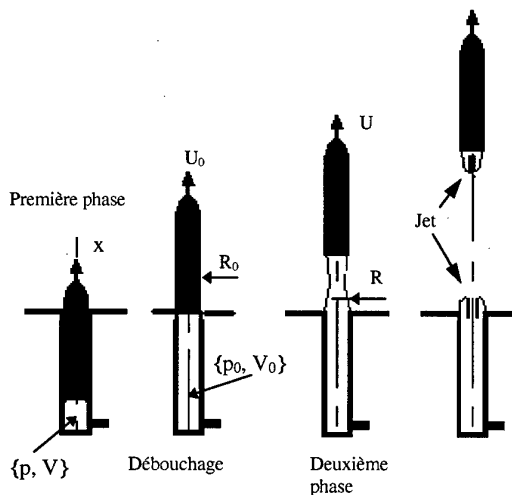


Figure 1 Lancement du projectile

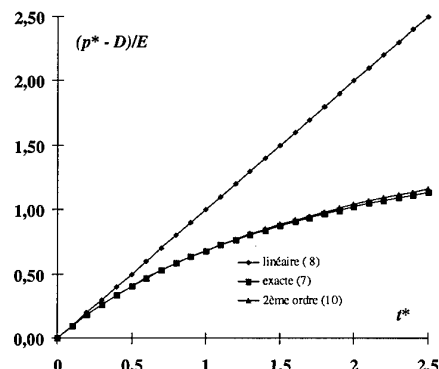
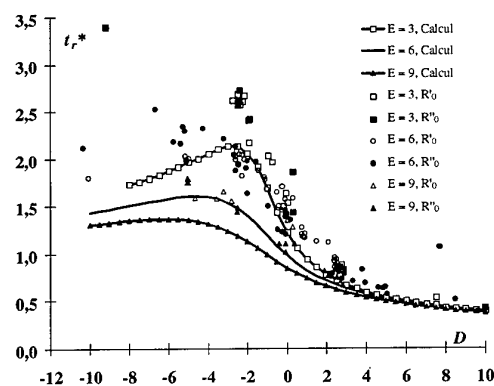


Figure 2 Approximation de la détente du gaz
fosse de petit volume, $F = 8$, $\gamma = 1,4$



**Figure 3 Temps de rupture de la bulle
Comparaison entre modèle et Expérience**

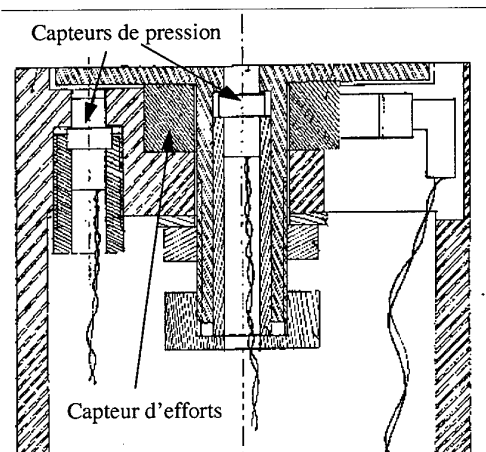
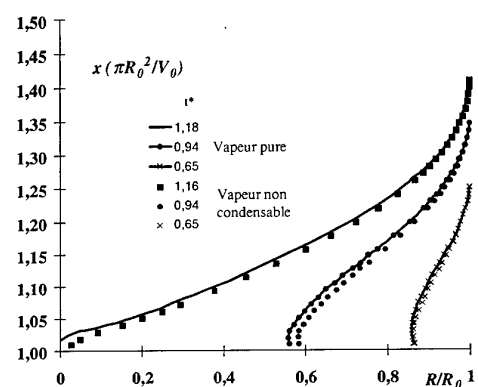


Figure 6 Schéma du culot de la maquette



**Figure 4 Effets de la condensation sur la striction de la bulle
 $D = -0,6, E = 5, F = 8$**

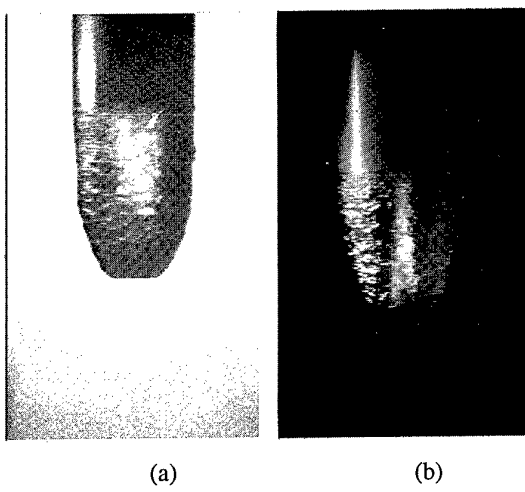


Figure 7 Photographies de la bulle ($D = 1, E = 6, F = 6$)
a) *Ombroscopie*

b) *Eclairage stroboscopique indirect*

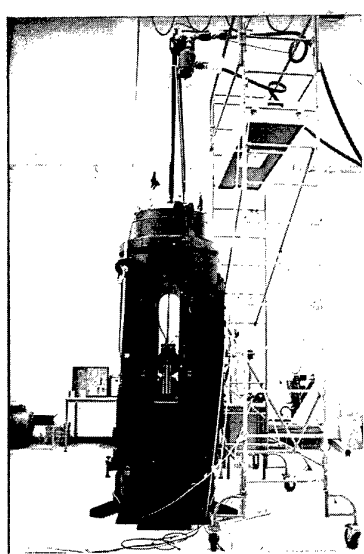


Figure 5 Vue générale de l'installation expérimentale

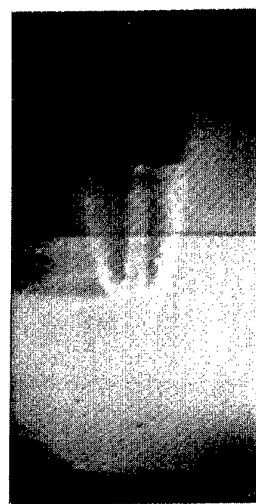


Figure 8 Cliché tomoscopique de la bulle et du jet
 $D = 1, E = 6, F = 5$

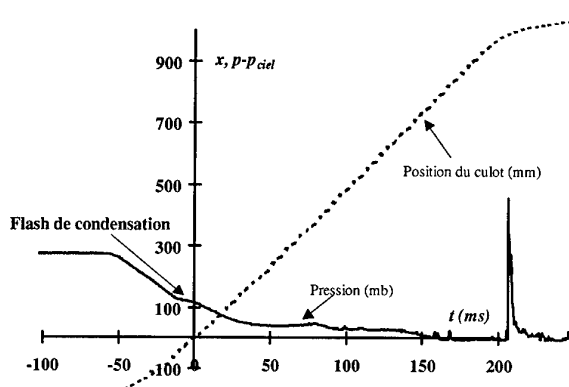


Figure 9 Evolution de la pression
 $D = -2,2, F = 7,7, E = 6,4$

Essai à volume V0 petit

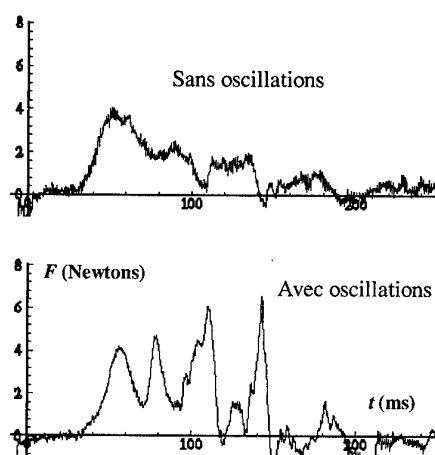


Figure 11 Enregistrements d'efforts
 $D = 3,25, E = 2,58, F = 4,5$

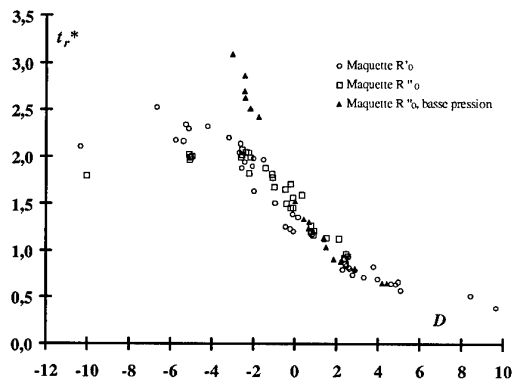


Figure 10 Temps de rupture de la bulle ($E = 6$)
Influence de la pression p_0

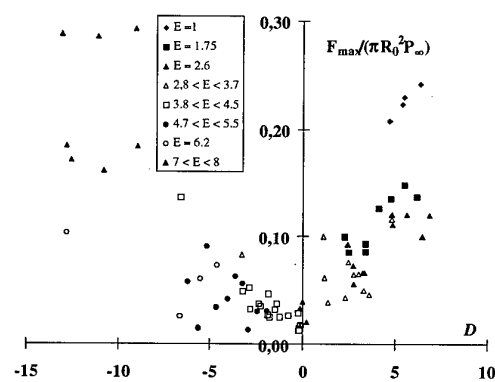


Figure 12 Valeur maximale de l'effort du au jet
E et F variables

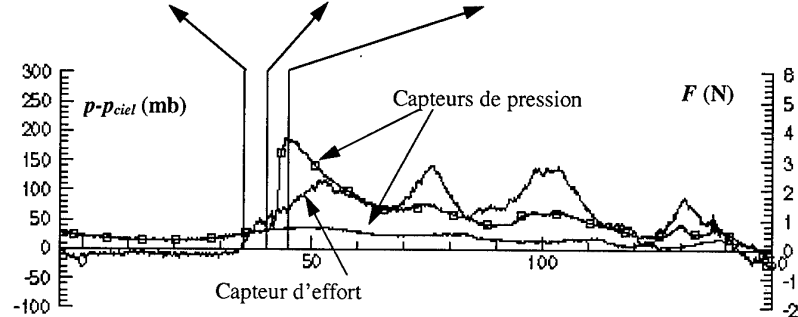
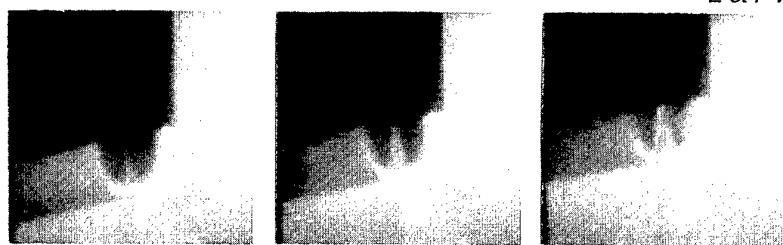


Figure 13 Exemple d'enregistrement ; Synchronisation des prises de vue
 $D = 3,3, E = 3,1, F = 4,6$

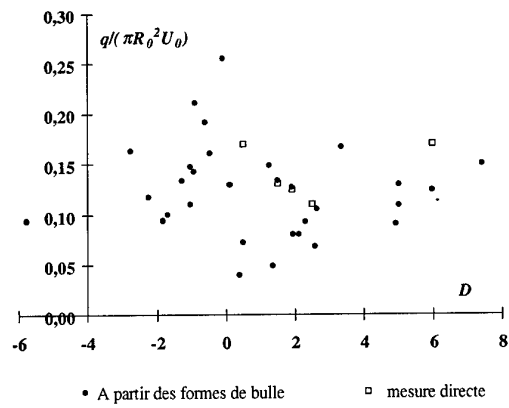


Figure 14 Débit estimé du jet rentrant
 $E = 6, F = 6$

Undisturbed Motion of Vehicles in the Fluid

Yu.N.Savchenko

National Academy of Sciences - Institute of Hydromechanics

8 / 4 Zhelyabov str., Kiev, 252057

Ukraine

Fax: (044) 446 42 29, e-mail: sav@ihm.kiev.ua

1. SUMMARY

The purpose of this work consists in searching such body shapes and such ways of the motion creation under which the disturbances of the velocity and pressure fields will absent or, at least, will be reduced to some minimum outside some control volume enclosing the moving body. The basic possibility of such motion in frameworks of the ideal fluid model is shown in works of V.I. Merculov and Yu.N. Savchenko [1 - 3].

According to [1] the undisturbed motion will be named such a motion, when in each point of some closed finite control surface the disturbances induced by the body motion are equal to zero. According to the principle of maximum the disturbance outside this control surface will be equal to zero too.

Two main schemes of undisturbed motion "Body in channel" and "Body with channel" were considered theoretically and experimentally. It was shown that system of surface waves disappeared and wave drag was absent when models moved near the free surface of water.

2. INTRODUCTION

The displacement body motion in fluid always results in change of physical fields describing its state. The velocities, pressure and temperature change. The changes of acoustic and electromagnet fields are possible. Hereinafter these changes will be named disturbances.

The nature of disturbances arising at motion of bodies in fluid depends on the fluid properties, on body shape, on motion nature and on way of creation and maintenance of this motion.

The traditional direction of researches are the minimization of wave drag of ship. In some cases the result is reached by excluding the arising unnecessary component of disturbances [7-10]. In this case the minimization is reached by means of interference of wave systems created by ship [5, 6, 12, 13].

In the elementary case the ship creates two wave systems: nose and stern ones including cross and expending waves.

The screws of expending waves are located on lines forming certain angle with ship motion direction. The cross waves place in the boundaries of this angle. An area outside this angle is practically undisturbed. The proper choosing of ship length is possible to be created the favorable interaction of nose and stern systems of cross waves.

To create similar interference for expending waves on single-hull ship is impossible, as far as the expending wave and adjoining to them the parts of cross waves of nose system are outside "zone of reach" of stern system of waves.

In the case of multihull ship [6] we can create such shape of ship hull and arrange them in such way that wave disturbances outside a catamaran contour will be absent.

The propeller interaction with ship hull is in detail considered in papers [14, 15, 16]. The feature of these works is consideration of the hull and propeller not as the independent systems as was done earlier, and as the unified complex.

According to analysis conducted in [14] the total force acting to body-propeller complex represents the difference between propulsion of ideal water-jet propeller and "foil drag of ship along wake outside jet of working water-jet propeller".

The propeller propulsion represents the difference between the jet reaction and drag induced by fluid sucking in the propeller. Analyzing the energy relations, we mark that if whole boundary layer drawn in propeller, the its power should be equal to the energy lost in the boundary layer. Hence, it is approximated to minimum, and disturbances of the velocity field on infinity behind the body may be reduced to zero. However, the thermal disturbances remain, since in the boundary layer the mechanical energy goes into the thermal energy by irreversible

way.

To obtain accurate measurements of physical parameters in the ocean, the housings of the moving sensor or probe must not perturb the water. Until recently it was believed that it is impossible for water-displacing body to travel in the water without perturbing it. This point of view was supported by a number of fundamental arguments. In analyzing this problem, we shall define a undisturbed motion as that in which no disturbances exist beyond some control envelope surrounding the moving body. Several variants of this envelope may exist, whereby the envelope may lie outside of the body, or be fully or partial coincident with its surface. To achieve the first case in practice we must solve the complex problem of producing an electric or magnetic field that has the requisite properties. In the other cases it is obvious that the body must have a permeable surface with specific distribution of sources and sinks. Practical attainment of such an undisturbed flow is complicated by viscous effects familiar from attempts at producing a flow about a dipole or a source in an ideal fluid. The only case in which such flow can readily produced with a viscous fluid is that of a jet discharging from a channel into a flow of the same velocity as that jet.

The purpose of present work consists in search of such body shapes and such ways of their motion creation that outside some control volume enclosing the moving body the disturbances of fields of the velocity and pressure will absent or, at least, will be hold to some minimum.

Theoretical part of the paper uses the model of incompressible low-viscous fluid. It is assumed that the viscosity influence is considerably within the limits of thin boundary layer and wake only. In another part of space the flow is described by equations of motion of ideal incompressible fluid.

The basic opportunity of such motion creation in frameworks of ideal fluid model is shown in papers of V.I. Merculov and Yu.N. Savchenko [1–3].

3. PRINCIPLES OF UNDISTURBED MOTION

The general case of undisturbed motion may be demonstrated in scheme (Fig. 3). The object occupying area N moves with velocity V into anisotropic two-dimensional area Q of ideal medium. Each element n_{ij} has the self location $N(x, y)$ in space.

The main idea of undisturbed motion consists in that the object should be moved not moving the medium apart but moving it inside self. Thus, the object saves the former order of elements in wake

behind it.

It is assumed that the moving object takes the area N and has the useful volume N_{us} , and dimensions l_N and h_N in longitudinal and cross directions.

The analysis shows that the realization of uniform rectilinear motion of the object without medium disturbances should include the six sufficient and necessary operations.

1. Capture of K elements of medium from the front contact surface of object - AD

$$K = V l_n^{-1} h_N h_n^{-1} \left[\frac{1}{sec} \right],$$

where l_n , h_n are longitudinal and cross dimensions of medium element from area Q .

2. Compression of medium elements to value

$$K_c = (N - N_{us})/N,$$

where N and N_{us} are the total and useful volumes of the object.

3. Transferring the elements inside the object N to characteristic length $l_{NC} \leq l_N$.
4. Delay of medium elements inside the area N for time $\Delta T = l_{Ni}/V$.
5. Reconstruction of characteristics of medium elements.
6. Ejection of medium elements from the back contact surface of object to the former locations in area Q .

At undisturbed motion in an isentropic incompressible medium, where the medium elements in area Q are identical, the number of necessary operations is reduced in two times. The following operations remain:

1. Capture of medium elements from the front contact surface;
2. Transferring the elements inside the object area;
3. Ejection of medium elements from the back contact surface.

In this way, the operations of compression, reconstruction, time delay and arrangement of elements on the locations become unnecessary. In incompressible medium the necessity of medium motion velocity V_N increase inside the object appears

$$\frac{V_N}{V} > 1.$$

The possible scheme of realization of undisturbed motion of object in two-dimensional area is presented in Fig. 2.

The useful volume on scheme is shown by dotted line. This scheme is possible to be named by scheme "Body with channel" in the case of axisymmetric execution. It is interesting that if we reflect

the half of this scheme relative to the solid wall, we can obtain another scheme (Fig. 3) named "Body in channel".

In Fig. 3, the updating of scheme "Body in channel" is shown in the case of viscous fluid flow with formation of boundary layer with displacement thickness δ^* . Then, to reduce potential disturbances the corresponding restriction of channel to value of boundary layer calculation thickness δ^* is necessary.

The water-jet propeller is a special case of the propeller in closed channel. The theory of such propeller is worked out in detail [14, 15, 18].

The initial moment of research is the theory of impulses enabling to connect the force P_0 acting on the complex body – propeller with velocities far behind a body. In difference from the case of the isolated propeller, the total force P_e is considered not as external on attitude to the moving body and as the sum of all forces arising at motion of body with propeller in fluid. At uniform rectilinear motion it should be equal to zero [16].

The theorem of impulses permits to obtain the expression for P_e due to the velocity on infinity. Using the continuity equation, it is possible to pass from velocities on infinity to velocities and pressures on the propeller exit. Now it is possible to allocate two components of hydrodynamic force: one is determined by characteristics of flow part passing through the propeller, the second is determined by characteristics of flow part not passed through the propeller.

The first force represents the propeller propulsion P_{ei} . The second force is the resistance induced by boundary layer on the external surface of body R_{ps} :

$$P_e = P_{ei} - R_{ps},$$

where

$$P_{ei} = \rho \int_{F_2} V'_2 \left(\sqrt{V'^2_2 + 2 \frac{P_2 - P_0}{\rho}} - V_0 \right) dF$$

$$R_{ps} = - \int_{F_2} V'_2 \left(\sqrt{V'^2_2 + 2 \frac{P_2 - P_0}{\rho}} - V_0 \right) dF.$$

Here, F_2 and F_e are the jet section areas and another part of the wake:

V'_2 is the velocity in jet or wake past a body;

P_2 is the pressure in this place.

If in the propeller jet the velocity V_2 and pressure P_2 are constant then presented relations can be represented in the form

$$P_{ei} = \rho Q V_2 \sqrt{1 + \kappa_{2q}} - \rho Q V_0,$$

$$\text{where } \kappa = \frac{2(P_2 - P_0)}{\rho V_2^2},$$

Q is the flow rate through the propeller.

The first component is the reaction of the propeller jet, the second is the sink resistance i.e. the reaction of fluid drawn in the propeller. We note that outside the boundary layer

$$V_2 \sqrt{1 + \kappa_{2q}} = V_0. \quad (1)$$

Comparing the flow energy in front of the body with energy behind one, we can calculate the power transmitted to flow by the propeller:

$$N = \frac{\rho}{2} \int_{F_2} [V_q^2(1 + \kappa_{2q}) - V_0^2] V_2 dF + \quad (2)$$

$$+ N_{R1} + N_{R2} - N_{ps},$$

where N_{R1} is the power lost in the boundary layer on the external body surface;

N_{R2} is the power lost inside the propeller (hydraulic losses);

$$N_{os} = - \frac{\rho}{2} \int_{F_{ca}} [V'_q{}^2(1 + \kappa_{2q}) - V_0^2] V'_q dF \quad (3)$$

is the increment of the power carried-over by flow not passed through the propeller.

If whole boundary layer passes through the propeller then $R_{ps} = 0$ and $N_{ps} = 0$. Hence, $P_{ei} = 0$.

If within the limits of area F_2 the velocity V_2 and pressure P_2 is constant then equality (1) is executed for points of this area F_2 and the first summand in (2) is equal to zero. Hence,

$$N = N_{R1} + N_{R2},$$

i.e. power is equal to a sum of energy losses in the boundary layer and in the water-jet channel and also $V_2 = V_0$.

If the boundary layer thickness in the stern part of the body is equal to δ , and the displacement thickness is equal to δ^* , then the minimum quantity of fluid necessary to be taken away in the propeller is equal to

$$Q_{min} = V_0 \cdot L_p (\delta - \delta^*),$$

where L_p is the perimeter of this body part.

For numerical analysis of described schemes the uniform mathematical model was developed. It permits to calculate axially symmetric configuration including the central body, displacement walls of the channel, thin shielding surfaces and two propellers: nose and stern (Fig. 4). The dimensions of elements of this system and their mutual location can be arbitrary. Action of the central body and thick channel walls on flow is taken into account by using ring sources located on the body surface and the channel walls. The action of shielding surfaces

— by action of system of ring vortices located on this surface. The velocity field created by propeller is treated as a disk of sinks and a jet located behind it. The velocity in jet is defined according to the propeller load [4]. This velocity value, radius and propeller location were given.

Some results of computations are shown in Figs. 5, 6. The figures represent axial and radial velocity distributions along the body axes at two distances from it for conditions with shielding surface (curves V_x and V_r) and without it (curves V_{x0} and V_{r0}), the former is being multiplied 10 times.

The problem of flow according to the hydrodynamic scheme "Body with channel" (Fig. 2) was analyzed by Merculov V.I. [1–2]. He showed that the disturbances of the external flow introduced by the motion of such a body can be made small by selecting the length of the bounding planes so that $x = \pm x_0$. The velocity and pressure disturbances on the inner wall in the plane $y = \pm 1$ are equal to [2]

$$\Delta u_x = \frac{\pi \sigma_{dr}}{2Sh^2 \frac{\pi x}{2}}, \quad \Delta p = \frac{\pi \sigma_{dr} \rho}{2Sh^2 \frac{\pi x}{2}}.$$

It follows from these equations that the required length x of the bounding planes at a given water displacement σ_{dr} can be computed if one assumes the permissible velocity and pressure disturbances. The practicality of this flow pattern with constraints on disturbances of the surrounding fluid was demonstrated experimentally.

4. EXPERIMENTAL INVESTIGATION

In the experiment the two models made according to two main schemes considered above are used:

- 1) body with channel (Fig. 2)
- 2) body in channel (Fig. 3)

In the experiments the flow around models was investigated in inverted scheme of flow: the flow moves, the model is stationary.

To visualize the velocity disturbances the particles of aluminum powder were added to the flow. At photoregistration from long exposition they showed the streamlines.

To visualize the wave disturbances the model are located near the free surface or in half-submerged condition. At flow the system of surface waves was result of disturbed fields of velocities and pressures around the model, and absence of surface waves definitely points to absence of velocity and pressure disturbances in fluid around the body.

The experiment was carried out in range of Reynolds numbers $Re = 2 \cdot 10^5$ and Froude numbers $Fr = \frac{V}{\sqrt{gH}} = 0,2 \div \infty$.

The model parameters are:

The length L is equal 1000 mm;
The diameter D is equal 212 mm;
The diameter of internal channel d is equal 80 mm;
The electric motor power is 60 Wt (27 V);
The mass is 14.25 kg;
The buoyancy P_b is 1.75 kg;

The screw with four blades D_s is 75 mm.

The experiment with described model was conducted in the hydraulic laboratory of the Institute. The horizontal hydraulic channel with length 17 m was used. Water to the channel is carried by pump station from underground basin of the laboratory by closed cycle. The scheme of execution of experiment is shown in Fig. 7. The hydraulic channel 1 with width 0.6 m with glass walls with height 1.0 m is equipped by devices for water rate regulation, flow damper in entrance part of the channel and backwater board in the channel end for regulation of flow depth. The water rate value was determined by triangular weir gauge.

The model 2 was installed in flow by described way with help flexible wires - tension members 4 hooked up to plugs 3. The supplying wires 5 were stacked on channel bottom in the water flow direction and removed through the free surface to the removal distance about 3 m from model. In this way the influence of disturbances created by them was eliminated. The power supply of model was executed from control block 6. The electric motor revolutions were regulated and the parameters of consumed currents were measured due to it.

The accepted scheme of model suspension in flow provided the possibility of small motion of it in axial direction for account of deviation of the flexible tension members 4 from the vertical. In the given experiment the sign and value of such motion were determined by ratio of two forces applied along the model axis: the hydrodynamic drag F induced by mainstream effect and opposite directed force of effective propulsion Pe created by model propeller. Hereinafter we shall name balanced the model location in flow corresponding to its zero longitudinal moving, i.e. the vertical location of tension members 4. Since it is realized at mutual balance of axial forces, i.e. at $|F| = |Pe|$. The similar location takes the model with inoperative propeller in water at rest.

The visualization of streamlines in flow around the body was made with help of aluminum powder spraying on the free surface. In this case the model was in semisubmerged location in the flow.

In next experiments the water level in the channel was increased so that the model was located in flow on depth 15 mm under the free surface.

The most convincing demonstration of wave drag

destruction is given by photos of experiments for three regimes (Fig. 8 a) b) c)):

- a) the self-propelled regime of internal displacement object (body) ($Pe = F$);
- b) the tugging regime ($Pe = 0$) (internal object inside a body, scheme "Body in channel");
- c) the self-propelled regime ($Pe = F$) for scheme "Body in channel".

5. CONCLUSIONS

In present work we define the undisturbed motion of body as such motion, when the information about this motion will absent outside some limited area of space containing the moving body.

To create such motion it is necessary to move through the internal cavity of body to its stern part the fluid particles located in front of the body and to restore their initial characteristics.

The work confirms the basic opportunity of similar motion creation for the case of uniform rectilinear motion of the special shaped body in low-viscous fluid. The feature of this shape is the internal channel availability inside the body. The analytical expressions for computations of the body shape and necessary differences of the velocity and pressure on surfaces bounded the control volume are presented.

The experiments with models executed according to the two main theoretical schemes "Body with channel" and "Body in channel" have shown that in regime of uniform motion $Pe = F$ in fluid around the body the disturbed fields of the velocity and pressure did not arise (excepting the turbulent wake area).

The presented results of experiments have the demonstration nature and show that the similar method of the disturbance reduction is possible to be realized both on real underwater vehicles and on elements of their constructions.

REFERENCES

1. Merculov, V.I., "About opportunity of undisturbed motion of body in fluid" Izv. SO AN SSSR. Ser. tehn. nauk, No 2, 1981, pp 37–44.
2. Merculov, V.I., "The fluid motion control", Nauka, Novosibirsk 1983, 174 p.
3. Savchenko, Y.N., "Some Special Cases of flows over Bodies", Fluid Mechanics - Soviet Research, vol. 21, No.1, Jan. 1992.
4. "The propeller screws. The modern methods of calculation", Sudostroenie, Leningrad, 1983, 296 p.
5. Kostyukov, A.A., "The interaction of bodies moving in fluids", Sudostroenie, Leningrad, 1972, 309 p.

6. Dubrovsky, V.A., "The research of wave drag of catamaran", Sudostroenie, Leningrad, 1968, No 7.
7. Dubrovsky, V.A. "The main features of hydrodynamics and technical-operational qualities of ships with small areas of waterline", Sudostroenie, 1993, No 8–9, pp 3–6.
8. Numata, E., "Predicting Hydrodynamic Behavior of Small-Waterline-Area Twin-Hull Ships", Marine Technology, 1981, 1, vol. 18, N 1.
9. Solomentzev, O.I., "The comparison analysis of one-hull ships and catamarans", Sudostroenie, Leningrad, 1990, No 5, pp 6–8.
10. Dubrovsky, V.A., "The expansion of operational opportunities of high-speed SWATH ships", Sudostroenie, Leningrad, 1990, No 1, pp 5–6.
11. Nilsen, J., "Aerodynamics of controlled shells", Oborongiz, Moscow, 1962, 474 p.
12. Busemann, A., "Aerodynamischer Auftrieb bei Überschallgeschwindigkeit", Luftfahrt-Forsch, 1935, 12, pp. 210–220.
13. Leibenberg, L., Bunt, E.A., "Wave drag coefficient of a model 'Busemann biplane catamaran'", Experiments in fluids, 9, 1990, pp. 352–354.
14. Kulikov, S.V., Hramkin, M.F., "Water-jet propellers", Sudostroenie, Leningrad, 1970, 352 p.
15. Basin, A.M., "Some problems of theory of water-jet propellers", Trudy Academii rechnogo transporta, No II, 1953.
16. Ivchenko, V.M., "About most profitable propeller complex" Trudy NTO Sudproma, 1963, No 45, pp 73–76.
17. Miln - Tompson, L.M., "The theoretical hydrodynamics". Mir, Moscow, 1964, 655 p.
18. Basin, A.M., Miniovich, I.Ya., "The theory and design of propeller screws", Sudpromgiz, Leningrad, 1963, 760 p.

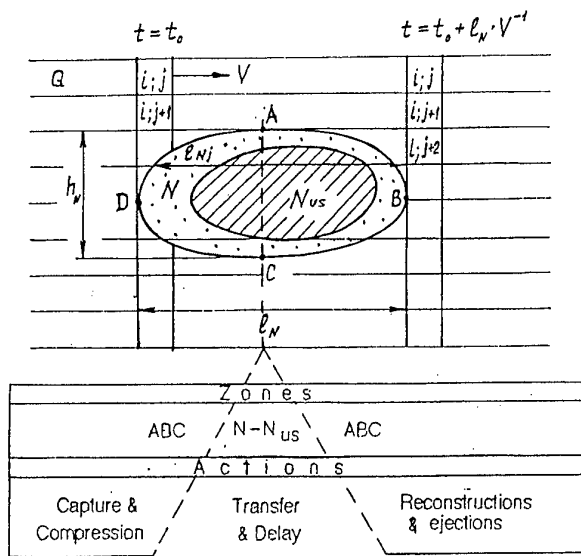


Fig. 1

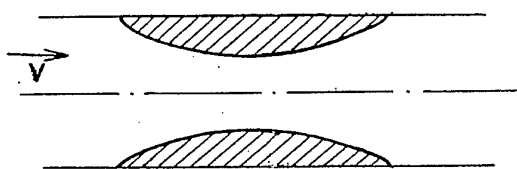
SCHEME "BODY WITH CHANNEL"

Fig. 2

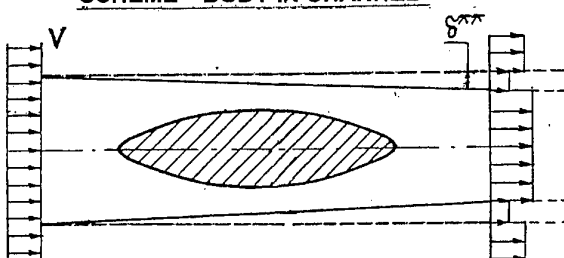
SCHEME "BODY IN CHANNEL"

Fig. 3

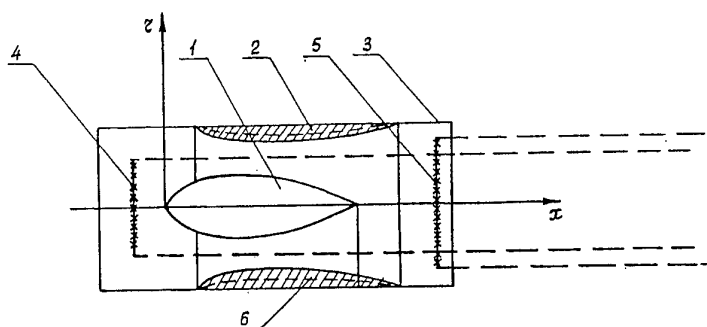


Fig. 4

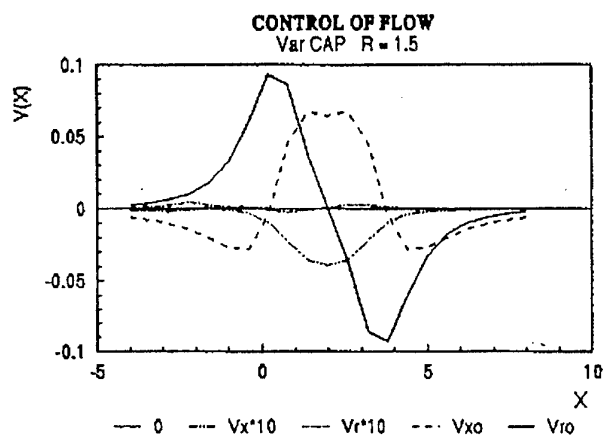


Fig. 5

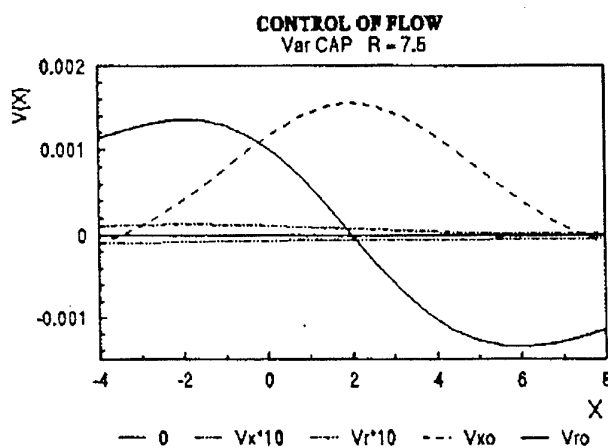
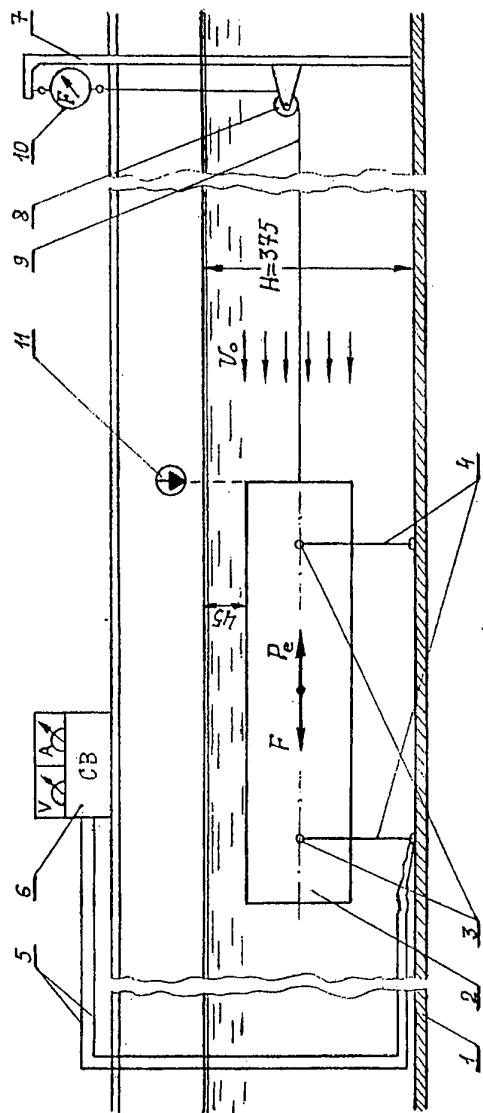


Fig. 6



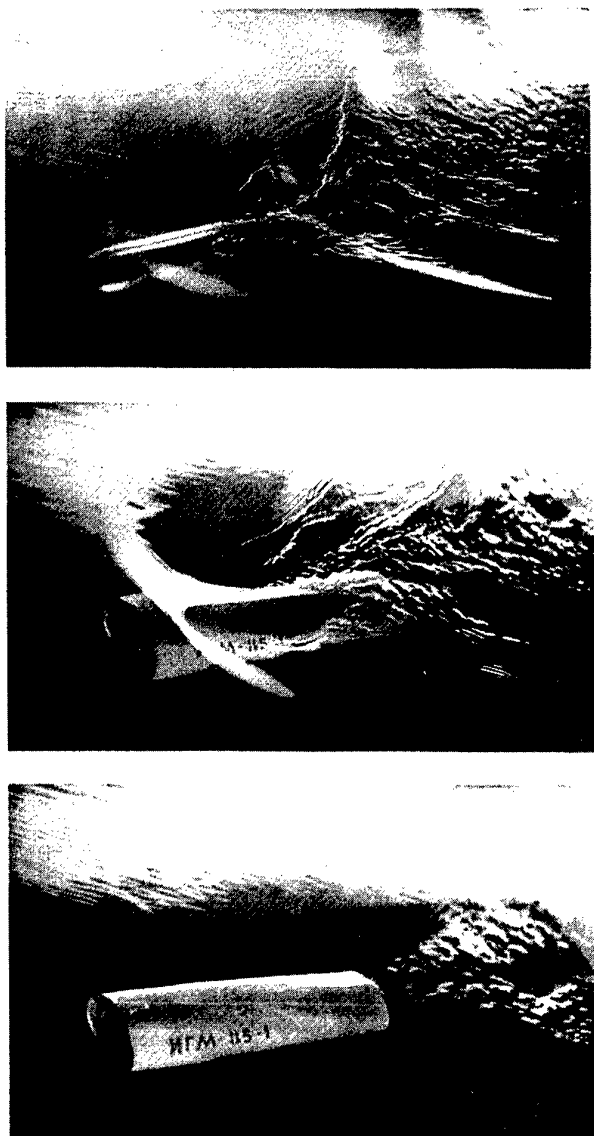


Fig. 8 a) b) c)

The Hoverwing Technology-Bridge between WIG and ACV

Hanno Fischer and Klaus Matjasic
 Fischer - Flugmechanik
 Kickenstraße 88
 47877 Willich / Germany

Summary

Wingships (WIG, Wing In Ground) utilise water as runways to reach their lift-off speed, which is determined by the wing loading. High Wing loadings are desirable for high cruising speeds with inherent height and longitudinal stability. To build up the necessary dynamic air pressure under the wings, they need roughly 3 times more power to overcome the hydrodynamic hump-drag compared to the drag during ground effect flight. So it is necessary to develop suitable devices as lift-off-aids in order to reduce the recommended power. With support of the German Ministry for R&D (BMB+F) Fischer-Flugmechanik (FF) has developed the „Hoverwing - Technology“ in order to further reduce the necessary lift-off power. The principle of this technology, for which FF has patent rights, is the building up of static air pressure between the catamaran float. After lift-off the dynamic pressure will replace the static pressure and the craft operates as a WIG with high lift to drag ratios.

FF is developing the „Hoverwing 80“, with the target to transport 80 passengers at 100 kts. Some test results with a scaled down two Seater will be demonstrated by video extracts.

1. Introduction

The transport velocity of passengers and goods is well above 100 km/h

during surface transport. Changing from surface to water transport, the speed is reduced by as much as 20% because of the low speed of waterbound vessels, thus increasing the tendency to switch over to fast but expansive airtransport. Utilising the so called ground effect, the gap between slow and inexpensive ships and fast but expensive aircraft can be filled. Fig.1 As WIGs lift off from the water during cruise, they avoid the high drag from the high density of the water. In order to achieve the necessary aerodynamic lifting forces for taking off, it is also necessary to overcome the hydrodynamic drag, which can be extremely high on a conventional WIG and determines the engine power to be installed. Contrary to aircraft, this excessive installed power cannot be used to increase the cruise speed. The economic efficiency of WIGs, therefore, relies on the drag being overcome during take-off.

The Hoverwing technology uses a small portion of the propeller slip stream to create a static air cushion between the floats, which are designed, as catamarans. Thus the displacement of the vessel's floats is reduced by 80%. This results in a reduction of the wetted surfaces, that enables a drastic reduction of installed engine power.

2. Take-off aids reduce the engine power to be installed.

The attempts to reduce the hydrodynamic drag in order to achieve higher speeds led to numerous different designs. Figure 2 Morphologic Triangle shows the different systems known today, which are supported by static air cushions at increasing speed but which cannot avoid water contact completely. By using a static air cushion during take-off, which at take-off speed is replaced by a dynamic air cushion, the Hoverwing can lift off from the water completely, and reaches glide ratios which are significantly higher than those of today's vessels. Figure 3 Weight to Thrust Ratio gives an impression of the different thrust requirements of different vehicles. A seaplane or flying boat has a very high thrust, as it is able to use this excessive power for cruise. WIGs, having the disadvantage compared with waterplanes in that they cannot change the angle of attack during a take-off run in order to maintain the best lift to drag ratios. They must have an improved float design, allowing them to take-off with a constant angle of attack. Tested WIGs show a thrust-to-weight ratio of about 1:4. The optimized float design of the Airfisch-3 increased that number to 1:5,2 and with the manned Hoverwing Testbed we reached already 6,5 and we expect to come to 1:8 with our current optimisation programm.

3. Hoverwing Technology

Figure 4 (Technology) shows the relationship of the different transport systems to each other. On the left hand side, those systems are shown which do not need any forward speed to carry their weight. On the right hand side, those systems are shown which require speed to create their operational lift, hydrofoils and aircraft. Correspondingly, the Hovercraft is the link between the

displacement vessel and helicopter, while on the right hand side the WIG is the link between hydrofoils and aircraft. The Hoverwing Technology is the bridge between ACV and WIG.

FF has developed the Hoverwing - Technology in which the catamaran float design is comparable with the SES, but in which the supply of the air cushion is achieved by using a small part of the propeller stipstream. Fig. 5 Hoverwing principle explains the working principle of the Hoverwing Technology.

Between displacement and approximately 90% of take-off speed, the air cushion is able to lift up to 80% of the vessel's take-off weight. When reaching take-off speed, sealing of the air cushion by the catamarans and skirts cannot be maintained, and the dynamic pressure from the free air replaces the static air cushion. The sealing finger skirts are moved by the dynamic airpressure automatically until they lay flat on the underside of the hull, where the additional drag is minimised in order to maintain the high glide ratio of WIGs.

In the Hoverwing design, the cabin actually is a fall-out. The cordlength of the airfoil section between the catamarans allows already a cabin-height that 30 passengers can stay upright. The benefit of not having a separated fuselage to accommodate passengers or freight, results in a significant reduction of structure, weight, drag and construction expenses.

To maintain the unconditional, inhe-rent longitudinal stability of WIGs during transition when taking-off, the aerodynamic centers of static and dynamic air cushions and aerodynamic outer wings may not shift. By adjusting the rear sealing of the static air cushion, which is a bag type skirt, and the forward sweep of the outer wings, the aerodynamic centers are kept at one longitudinal position. So even during

take-off transition, the vessel maintains stability, and no manual control is necessary.

As soon as the so-called „flare“ mode is taken after take-off, the inlet port behind the propeller is closed, and full thrust is available for cruise. Closing the inlet port also deflates the bag-type skirt sealing at the end of the air cushion, and is then also folded.

Before landing, the inlet port is opened again, the rear sealing inflates immediately after throttling up when touching the water surface. The build up of the air cushion makes the front finger skirt sealing swing down automatically, so that the air cushion is fully working again during touch down. This makes the landing extremely soft and reduces structural loads.

One problem of this basically new configuration was the catamaran float design. The best position for the step, the design of the sealing skirts and the best trim for take-off, were optimized in cooperation with the Ver-suchsanstalt für Binnenschifflbau e.V (VBD) at Duisburg, Germany. Using scale models with extensive measurement equipment which transmitted the test data, the complete speed range from displacement to flare mode was analysed in order to achieve reliable information about the dynamic characteristics and performance of the new configuration. The achievable reduction of drag, and the resulting possible reduction of power to be installed, is shown in Figure 6 Performance potential.

3. Proof of the concept with Hoverwing 2 VT

In order to achieve operational experience under realistic conditions, the manned test craft HW 2 VT was designed and build. This representative vessel is scaled down in the ratio of

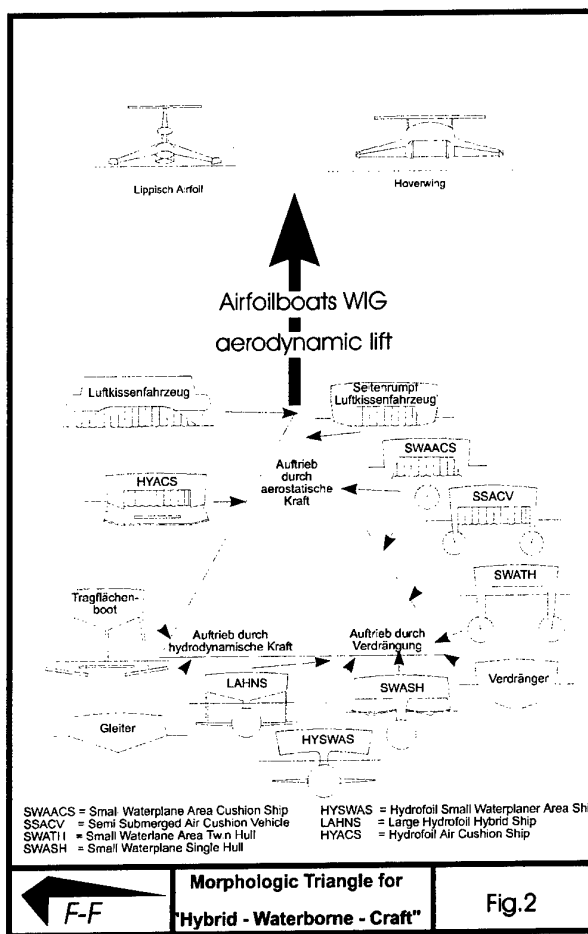
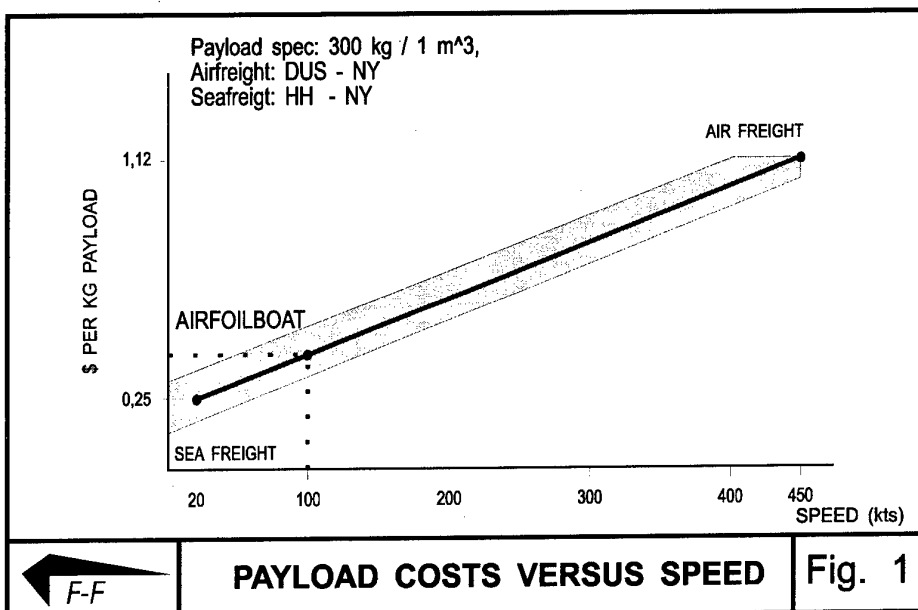
1:3.35 from the 80 Seater HW 80 and were tested 1997. Hoverwing 2-VT completely fulfilled the performance and characteristics in accordance with the given requirements in regard to take-off, cruise, manoeuvrability and landing, during tests on the Baltic Sea and on the IJsselmeer in the Netherlands. Fig.7 shows HW 2 VT in Operation

6. Conclusion.

Creating a static air cushion by using parts of the propeller slip stream du-ring take-off, a reduction of hydrodynamic drag comparable to that of an SES is achieved. During cruise the dynamic pressure of the airspeed replaces the static air cushion and automatically folds the sealing skirts to the lower side of the catamaran body, which then creates aerodynamic lift and makes the vessel become a ground effect craft.

The catamaran body functioning as the main wing, offers, due to its size and airfoil shape, a thickness which allows the comfortable accommodation of passengers inside without the need building a separate fuselage.

FF holds patent rights for the Hoverwing Technology and could confirm the required performance and characteristics as predicted by calculation and experiment with the manned test craft, the Hoverwing 2 VT.



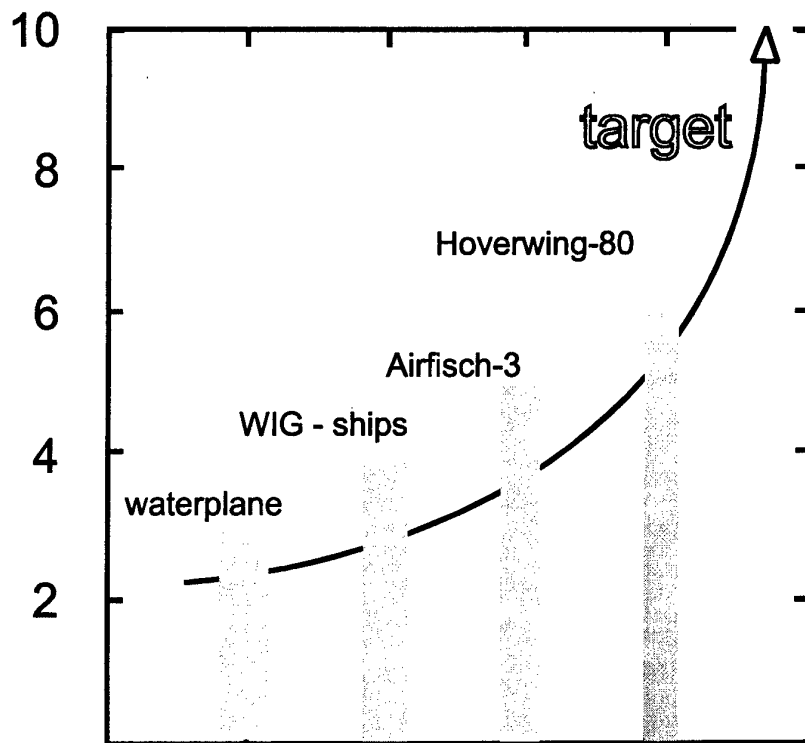
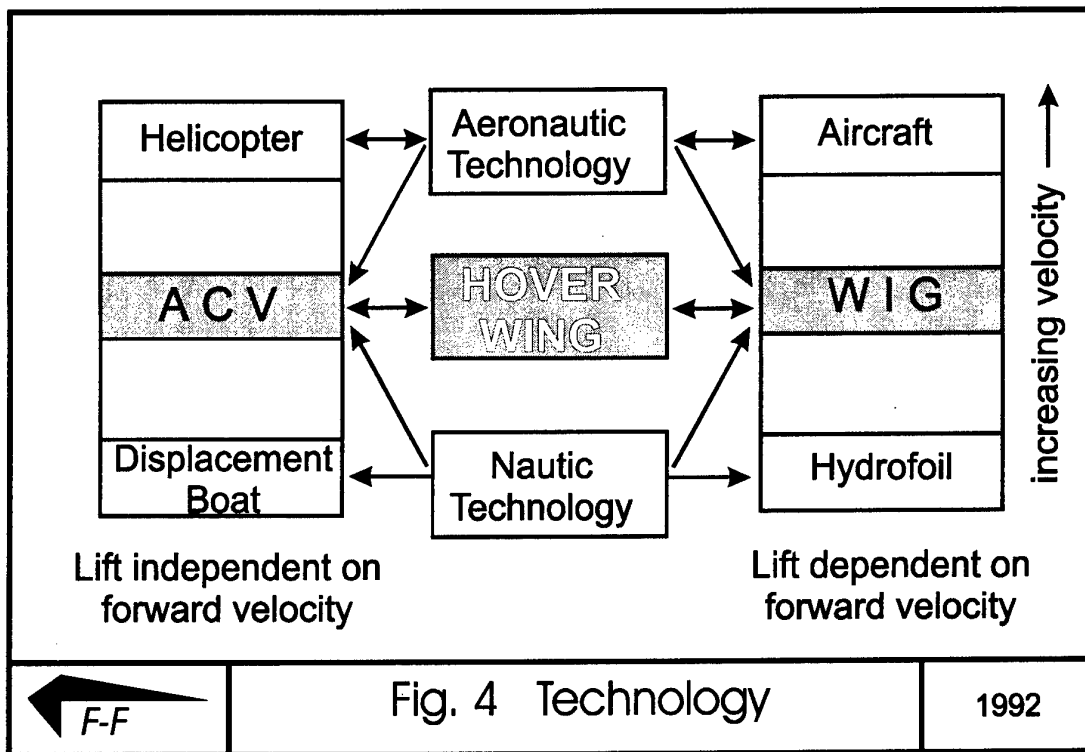
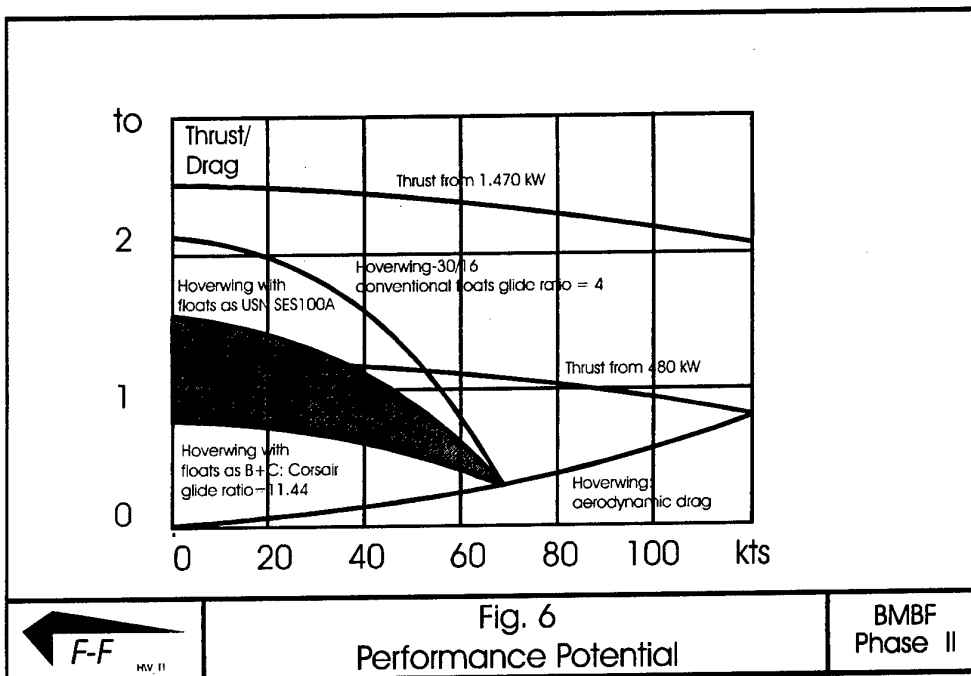
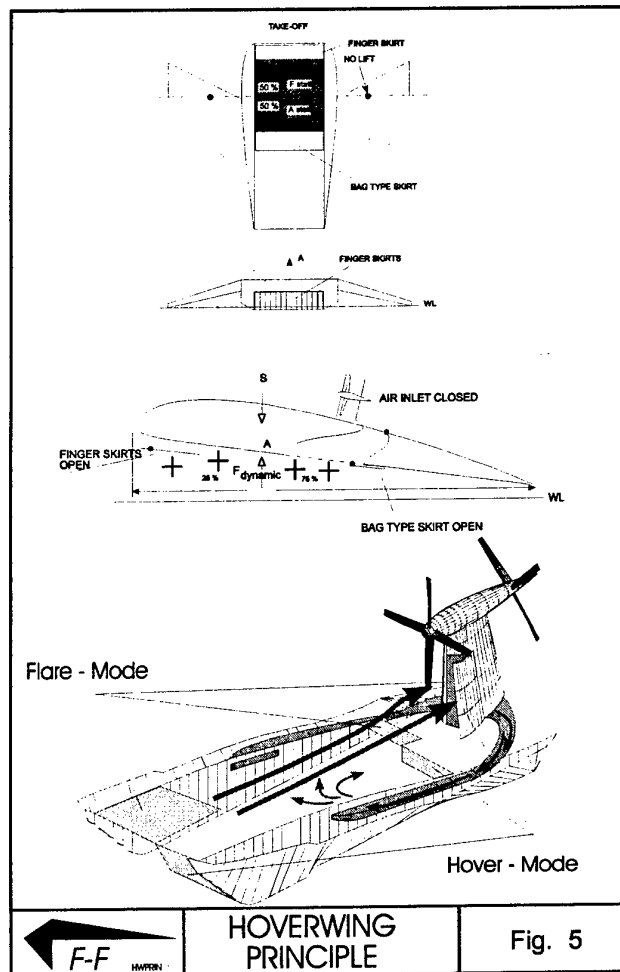


Fig. 3





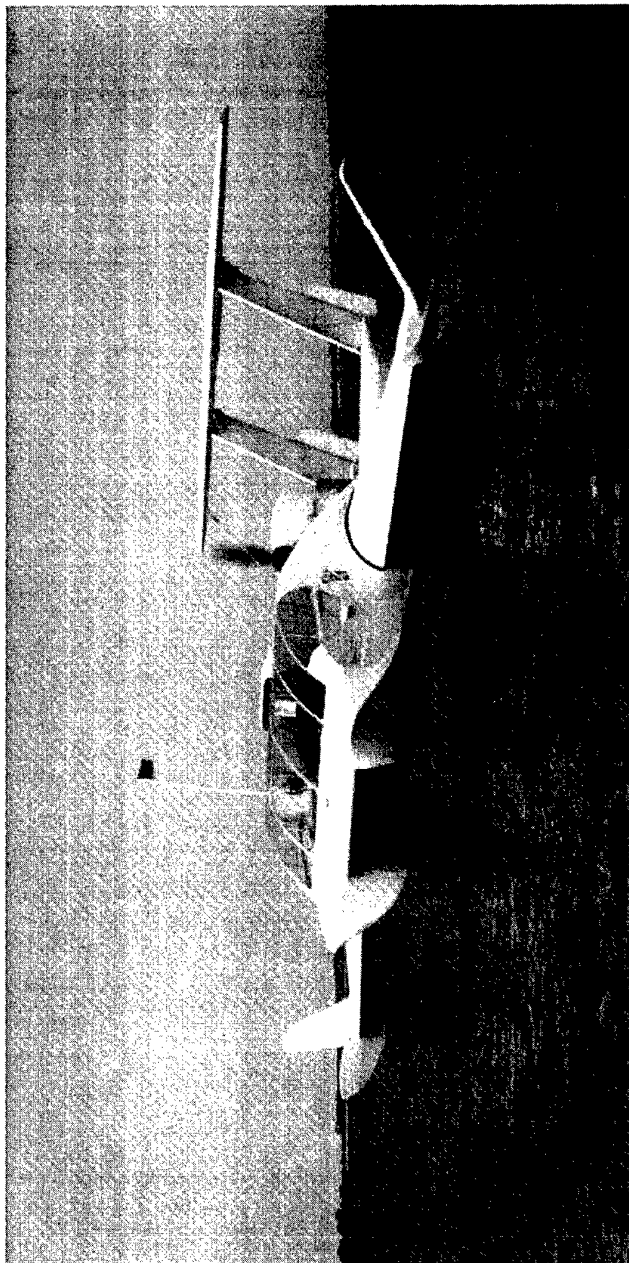


Fig. 7 HOVERWING 80 VT
on the Baltic Sea

F-F
Vf_OSTI

1997

Fischer - Flugmechanik, Kickenstr. 88, 47877 Wuppertal, Tel. 49 - 2156 - 5129, FAX. 49 - 2156 - 60977 (all Rights reserved)

GENERAL DISCUSSION

Fluid Dynamics Problems of Vehicles
Operating Near or in the Air-Sea Interface
Amsterdam, The Netherlands
5-8 October 1998

I.G.A. B. Masure, Université d'Orléans, France

Ladies and Gentlemen, let us start with our General Discussion and before this we have the Technical Evaluator's remarks. As Technical Evaluator, we have Professor Tulin from the Ocean Engineering Laboratory. I introduced him before; he gave a paper this morning. Professor Tulin, you have the floor.

Prof. M.P. Tulin, Ocean Engineering Laboratory, UCSB, USA

This has been a most interesting and unusual meeting, and several kinds of fusions have taken place here, as intended by the Organizers. One of these was to bring together aerodynamicists and naval hydrodynamicists to talk about some problems around the interface. I think Bernard Masure had that consciously in mind during the organizing phase. Workers like ourselves in these two fields work in parallel in general, we run on parallel tracks, and we don't very often meet together as we did here. Although there are, of course, people in this room who came from one field and went into the other, - I did myself. Connections between these two fields were very great in the beginning of Aeronautics, where naval architects played a very important role. Today our fields have reached equivalent states of sophistication. That wasn't always the case, or at least aerodynamicists often didn't think so. Now there is a much greater respect for what has happened in hydrodynamics, especially in the post war period where naval hydrodynamics had a great boom with the challenges of the Navy.

The other fusion that took place here is between the scientists and engineers from Western Europe, North America, Australia, Russia and Ukraine. I think that this was a very important aspect of this meeting, and I will have a little more to say about that later. Of course, it takes money to do these things, and I think I would like to say thank you from all of us for the funding. I hope that our East-West cooperation will be long and fruitful and continue in the future. It is very stimulating.

The meeting has, if you look at the title, had two aspects. I think that is the way it worked out. One concerned the fluid dynamics connected with these vehicles, and there are people here who are more interested in fluid dynamics and the aerodynamics or hydrodynamics of the vehicles, than the vehicle engineering and performance itself, and then there are the vehicles. That makes the meeting a little hard to discuss from a technical viewpoint, but I am going to try. My remarks must of necessity be very informal since time hasn't permitted a proper digestion of everything heard here - that will come later in a written report.

There was a continuum of vehicles represented here. Dr. Fischer in his last very fascinating talk extended that continuum by suggesting a marriage here at the interface between hydrofoils and Ekranoplanes. In the overall picture, there is a larger continuum starting at one end with stationary platforms in ocean engineering, where there are huge developments

and very wonderful engineering and science. Then ships, including the problem of helicopter mating. I hadn't been aware of that problem, but it seems most serious. Beyond ships and at higher speeds we have hydrofoils and SES vehicles and then at the high speed end, the Ekranoplane. There were some members of this continuum which were not specifically discussed here in the regime of fast ships, which are getting very accelerated development now: planing boats, catamarans, and swath ships. Finally, at the low speed end I mention the MOB, which means Mobile Offshore Base, and the US Navy is now conducting a research program connected with studying the feasibility of building a floating base which would be at least 5,000 feet long and at the present time is conceived to be 400 feet in breadth, which would be able to land our largest aircraft, the C-130, and which has enormous storage capacity inside these structures, which would detach into maybe 1,000 foot modules for self-propulsion to sites around the world. This is, of course, motivated by the desire to have independent bases offshore to conduct whatever operations are necessary, as in the Persian Gulf, for instance. That leads to fascinating problems of various kinds. Finally, beyond the Ekranoplane in the high speed end of the continuum we have seaplanes, which detach from the surface. I think that Bernard Masure had hoped that seaplanes would get a greater discussion than took place here; there was a paper on the subject which was canceled. Just before I came up to speak, Mr. Swick from Lockheed Martin put in my hands an amazing picture of a proposed C-130 float plane. I asked him if there is a requirement for that, and he said we are working on it. So, there may be a future in seaplanes. Of course, we have seaplanes for fire fighting, I see those often in Santa Barbara. That is a part of the continuum not to be neglected, especially by all of you. So that is the continuum, and it would be nice to settle the question whether Ekranoplanes have a future in it and what it might be, and the same for seaplanes, too. I don't think in a meeting of this duration or representation it is really possible to do that, but we had some indications for the future and some hopes expressed by various people.

As far as fluids are concerned, there was not a continuum of fluids here. Particular problems and areas were spotlighted which arose in connection with specific interface technologies; for example, in connection with deck aerodynamics, which was the subject of the first set of lectures here. I would say there are two fluid subjects which arose from that. One was organized vortical flows. Here I am thinking particularly of the flows around carriers where you have these large vortex structures. We heard about some very nice experiments from TsAGI presented by Dr. Maslov, and we also saw some numerical calculations which we shall refer to shortly. On the frigates, where you have the backward facing step that the deck represents, the flow underway and due to wind is very complicated. It is a bluff body flow, a 3-D unsteady flow with separation, and it was very apparent that our means of calculating these flows is developing but limited. This is an area which everybody in fluid dynamics recognizes as a frontier, i.e. to develop the ability to go on and calculate 3-D complex flows with separation. There are a number of fields in which these flows are important in ocean engineering and building aerodynamics. It would be interesting to compare what they do in those fields in comparison with what we heard here in connection with the frigate deck problems, especially from the building field, where they have exactly those same flows and where they are very important in practice.

I can identify some issues in connection with these flows and one is the issue of Euler equations versus turbulence modeling. It was fascinating to see that people use Euler equations without viscous or turbulent stresses, and nevertheless, they can get separated

flows, vortical instabilities and so forth. As I learned from a British aerodynamicist here, more is known about this in terms of the fundamentals than was evident in the lectures. Apparently, flow separation can occur as an artifice of the numerical process. I understand that it is a function of the corner radius of the body and of the grid size. Of course, if you get a shear zone started, i.e. if you introduce some vorticity into the flow, even artificially through numerical means, then that interface can be unstable in the Kelvin-Helmholtz sense and a kind of turbulence ensues. So, you can see how you can get complicated unsteady flows from Euler equations alone. However, whether you can accurately predict something like the size of the separation region behind the deck, which is important, in connection with the helicopter problem, without introducing real stresses, is very doubtful, I should think. But these simulation phenomena are most interesting, and I think that the question of the validity of Euler simulation is an important issue for people to deal with in future.

The other great issue is the balance between experiments and numerical modeling. I think a lot of wisdom has to be exercised in connection with deciding how to go about some of these things. When we don't have analytical means or means which are still in doubt, where there are big questions, experiments then become extremely important. We saw here a number of interesting experiments and experimental results. These things have to go hand in hand, but it is obviously very important, especially in connection with questions about Euler equations, that numerical modellers do systematic comparisons and careful comparisons with experiments. In my experience in life, it doesn't pay to assume a theory is correct in fluid dynamics; if you don't check it with experiments, you will usually pay seriously. So, there are very important things to do. I think there are many research opportunities in these fluid dynamic areas involving unstable and separated flows and their simulation. The right balance between experiments and theory plus simulations will be required.

The second general area, where we can group things together, is ground effect aerodynamics. Here we have the Ekranoplanes which use the Russian terminology. We have several aerodynamic regimes here, the image regime, in accord with Kiril Rozhdestvensky's span regime; the ram regime; and the chord regime. It is obvious from what we heard in Rozhdestvensky's talk and others that a vast amount of useful aerodynamics has been done that is directly useful for the analysis of stability near the ground. There are emerging numerical methods which will also be useful. Remarkable applications have been made in Russia to the actual design of vehicles. I am thinking particularly here of Alexeev of Nizhny-Novgorod, and I will say more about him later; we have heard here about really remarkable developments, that I hadn't known about in detail before. Although much has been done, there obviously is still good aerodynamics to do and systematic validation. It wasn't clear to me for example how much of the theory we heard about has actually been compared with detailed experiments. Of course, it is more than force coefficients, if you are talking about details of the flow. Eventually, if these vehicles evolve, improvements, even marginal improvements, will be sought, and that means more aerodynamic testing. The very successful and innovative developments of Fischer in Germany, which we heard about only this morning should also be mentioned, including his technique for tethered testing indoors.

Regarding applications of Ekranoplanes, we heard Aframeev's suggestion about a grand air/sea rescue system; that somehow resonated with me. I thought that it was a bold suggestion which should be thought about and perhaps considered seriously. He is conceiving a global marine disaster response system based on large Ekranoplanes which

would carry very heavy equipment, including a tug. Following this suggestion, it occurred to me that a subject for future meetings might be "marine vehicles in rapid disaster response." If you think about such marine vehicles, you go from lifeboats to cutters to air/sea rescue, and Ekranoplanes; it seems an interesting and important subject involving the interface; I would include the SES and ground effect aerodynamics.

Regarding SES, we had a talk by Faltinsen on Cushion Acoustics, concerning the serious problems of wave induced loads due to oscillations in the pressure under the vehicle. This phenomenon must also involve structural response of the flexible seals, etc. We didn't hear much about structural response here, as this is a meeting about fluid dynamics. However, we should not forget that in the marine field, the loadings are very large and, in view of the increase in speed, hydroelastic problems are getting increasing attention. It is obvious that this will be the case here with vehicles operating in the interface. The design of compliant structures might be in order, as Fischer suggested; i.e. compliant to water, but not to air. SES cushion problems are hard to model, because there is a Mach number involved, the speed of the craft over the speed of sound arising from the compressibility of the cushion. As a result, these problems are notoriously hard to deal with experimentally, because we normally can't test at full-scale speeds.

A third general area at this Symposium was stability and control. When we are operating in the interface, load control and vertical control are very difficult, and extraordinarily important. Much more important than when flying in the atmosphere in an airplane, as is obvious. The problems of vertical control had earlier been crucial for submarines which often have very little vertical room to maneuver under the sea surface, considering their length. Here we heard here a number of talks dealing with the stability and control of Ekranoplanes which are now designed to be inherently stable, which was very fascinating to understand, and a wonderful achievement, i.e. to achieve that stability through purely passive aerodynamic means. We heard a talk by Nebylov from Saint Petersburg on automatic control, especially alleviation of wave motion, and I did see some figures put up by Kiril Rozhdestvensky on accelerations. I remember from my own experience with hydrofoils many decades ago that the tolerance of humans to vertical accelerations is very small. As I recall, it is necessary to get the mean accelerations under 1/10th of a G. Otherwise, you are not going to carry anybody very long, and quarter of a G is probably too much. I saw numbers like that quoted here, so that this is a very serious problem for hydrofoils and for the SES, where we heard about the cobblestone effect, and for all interface vehicles in fact.

We heard some papers by Mr. Kummer from France on ship control with a new implementation of the moving weight idea, automated, and including sophisticated fins. It is always welcome to hear of advances like that. Finally, we heard of the problem of autopilot landing of helicopters on decks, in the case of the unmanned helicopter by M. Reboulet. Finally, we had lectures on foils and impact and bow splash hydrodynamics. We heard a little bit about hydrofoil ventilation which is a very dangerous and destabilizing phenomenon at the interface. At these high speeds the foils are going to cavitate and generally our solution is to go into the supercavitating mode. This field has had an earlier very active life and reached a peak; a great deal of research was done in that time. Some applications were made, too. However, I think there are still new application opportunities and more research and testing to do. In impact, more and more work is being done, as slamming of ships is an important problem area, and more so at increased speeds. The 2D&T methods I showed you

this morning can also be used here. When we consider ship moving in waves, the forefoot emerges and slams down and these methods can be used to calculate the loads on the bottom. There is quite a bit of interest in that subject now, combined with hydroelastic effects, because of fast ship developments in the last 10 years. In these areas, as in many others mentioned here, we have to keep doing research on these things, to put fundamental information and applied information into the designer's reservoir of assets. If we don't maintain this reservoir, design and innovation will suffer.

In my closing remarks, I would like to draw special attention to the Russian work, particularly the Russian innovations. It is very remarkable to me that very bold engineering innovations were made by Russians even in the Soviet regime, when I imagine the cost for failure was not so pleasant. Nevertheless, remarkably bold things were done. I myself started to work on supercavitating foils in 1952 and then someone put in my hands information about supercavitating propeller developments in Russia, where a man named Pozdunine had started developing supercavitating propellers by himself during WWII. He, in fact, used the word superkavitatsia which I translated as supercavitation, that is how the word came about. We have the phenomena of Alexeev, who, as somebody here said, made two engineering revolutions. He was the man whose design bureau was responsible for the wonderful Russian hydrofoil boats. I don't know if any of you have traveled on a Russian hydrofoil boat; I had the pleasure in 1963 to travel on a big boat that was and still is running on the Neva in Saint Petersburg. They are beautiful boats, beautiful interiors. They have very shallow draft, they have a passive automatic system for altitude control. He also built fast boats and sea keeping boats. Then he conceived the Ekranoplane. I understand that there were people earlier in different countries talking about wings in ground effect and I know there was a Finn who did pioneering work all by himself on ram effect wings when hovercrafts first came out. However, to build the Caspian Sea Monster and all these other Ekranoplanes is a remarkable thing. Alexeev and colleagues grappled with the fundamentals and made stable boats. We also have Russian innovation with high speed supercavitating missiles, Logvinovich and Professor Savchenko who you heard from this morning, in Kiev, and these are really remarkable innovative developments. We owe a lot also for fundamental fluid dynamics to Russian workers. To mention only a few: in turbulence, Kolmogoroff; and Yaglov and Monin who wrote famous texts in the 60's; in waves, Kochin and Stretensky; and in cavitation, Gurevich and Epstein. Professor Maslov told me that his Professor was Epstein, who was a wonderful worker on problems of ventilation and cavitation and who wrote a most interesting book which I don't think has been translated. I hope we can all continue to work together and to profit from the knowledge of our Eastern colleagues and especially from their innovative spirit.

Regarding the future of Ekranoplanes, we had a good forecast by Aframeev and further heard some hope about the future in the last talk by Dr. Fischer. I don't know the reality myself, but several speakers here obviously believe in the possibility of transporting in the speed range of Ekranoplanes, say 200 kts, and it is true, there is a transportation gap there. Many of us in the same field have thought about that; we studied, in my own company, 100 kt SES's when they were under naval development, it did appear difficult though to beat a 747 for overseas transport at high speed with the SES. You have to make realistic economic studies, including sea state operability. So the future isn't clear yet. Perhaps disaster response, as proposed by Aframeev is worth pursuing.

The other thing I want finally to comment on the fluid dynamics side is the breadth of fluid dynamics at the interface. In the United States, one gets the impression sometimes that all that we don't know in fluid dynamics is turbulence. This is of course a joke, actually. If you look at fluid dynamics in this meeting, you will see we started off with some problems involving separated flows and turbulence, even though the Euler equations can apparently make wakes and everything else without any Reynolds stresses. Overall, we see the enormous range of problems which are not turbulent but have to do with working at the interface, things we don't yet understand despite our advances, like cavitation, re-entrant jets and so forth. I myself work on waves and wind waves and I have a big facility where I blow wind over waves just to understand the ocean. That is complicated and interesting enough, but here we are putting vehicles into that complex situation. In addition, to the problems which were hinted at here, propulsion at the interface is also very difficult. We heard very clearly in Fischer's talk about the problem of takeoff propulsion because of the big hump drag there. This is also the case with hydrofoil boats where the water propeller has to work very hard, and is going to cavitate even at low speeds because of the high thrust loadings, and become very inefficient. I am sure that the audience could obviously add more items to this list for the future. This completes my technical remarks.

I do think it is a nice idea to do this again some time. After some years Professor Masure's questions may come closer to being answered, and we will see future developments, and it might be productive to review progress and add some new subjects. In the interface, I don't think anybody else is dealing specifically with these vehicles with this breadth.

We all owe a great debt to the organizers and the funders for this meeting. Thank you.

Mr. B. Masure, Université d'Orléans, France

Thank you Professor Tulin for your very interesting remarks. Now, we have the General Discussion as Professor Tulin mentioned. The theme of this Symposium was decided by AGARD. When I was named Chairman, I had the idea to try to respond to questions about the future. To repeat two of these questions that Professor Tulin noted which are very important; firstly, will there be a renewal of interest for hydroplanes? Considering the problems for classical airplanes, problems at airports, problems for the environment, noise problems, overcrowding problems; perhaps thanks to hydroplanes, we can find new solutions to the present problems.

I will now very rapidly show you a few hydroplane photos. Here is an old hydroplane constructed by Dornier. In the past, there was strong interest and activity in these hydroplanes. Mr. Stilton, an English specialist in seaplanes, could eventually discuss this. Here is the celebrated Russian seaplane, the Albatros which weighed 90 tons, the largest jet powered hydroplane in the world. It is quite recent, and the question is whether there is a future for this type of seaplane. Now, I will show you the BE 200 from Beriev design bureau. You see it, I think, in the New York sky, but this photo is an artist view. This is a civilian hydroplane which made its first flight 10 days ago, with great success. It was built by a consortium including Russia, Switzerland, Singapore, and the US - a real international project.

In the U.S., as Mr. Tulin told us, the Lockheed Company, represented here by Michael Swick, is working on a floatplane version of the C130 Hercules. You see here this navalized

version of this plane. That is to say, concerning the military aspects, it could be of interest to develop hydroplanes. In Canada, everyone knows the seaplanes developed by Canadair-Bombardier which are used to control fires. The latest of these seaplanes from Canadair, is the CL 415. The Russian design bureau Beriev proposes, with a lot of imagination, the development of giant hydroplanes of about 1000 to 5000 tons.

I wrote to all of these organizations to request information and papers on all the seaplanes, which, of course, have problems dealing with the sea/air interface, and I had no response! No one replied. Knowing the special interest of this Symposium and this subject, I find it regrettable that no one replied. The second question I would like to discuss concerns Ekranoplanes. I will try to provoke some comments here. Personally, I doubt that in the future Ekranoplanes will become the general means of transport replacing airplanes. I doubt this and I open the discussion for your responses.

Mr. H. Fischer, Fischer-Flugmechanik, Germany

I would like to comment on your first photo, which showed the giant aircraft Do X. This waterborne aircraft could fly the first 3 hours only in ground effect, since it was too heavy to climb out of ground effect when it was fully loaded to make a nonstop flight from Europe to the USA. After that, it was light enough to climb to free flight.

Mr E.A. Aframeev, Krylov Shipbuilding Research Inst. St. Petersburg, Russia

I will speak Russian for the sake of clarity. I will say a few words about hydroplanes to introduce the theme, then, it would be interesting to speak about the future of Ekranoplanes and hydroplanes. Unfortunately, Mr Sokoliansky who prepared this lecture was not able to attend the seminar. He has made quite an interesting economic study on the operation of aircraft and Ekranoplanes. It showed that where heavy loads are to be transported over long distances, and since aircraft can climb to high altitudes and cruise for long periods, one should use aircraft, because Ekranoplanes are not cost effective for these kind of missions. If an aircraft is required to take off and land frequently, and if the distances involved are small and the landings numerous, it is not economical to use hydroplanes and this is precisely the kind of situation where Ekranoplanes should be used, because under such circumstances they are more cost-efficient than hydroplanes. So much for the economic issues. As regards the future of Ekranoplanes, I am thinking about their use at sea. Today, there are no specific technical facilities to assist humanity in its conquest of the oceans. An urgent mid-ocean destination can only be reached by air, and then the team has to remain at work on the surface of the sea for long periods of time. A variety of tasks need to be carried out and for such missions there is no other solution than the use of Ekranoplanes, as it must be possible to remain at sea for long periods, and this function cannot be fulfilled by hydroplanes : I can see nothing else but Ekranoplanes for this type of situation.

The prospects. Today, we are already able to build Ekranoplanes of up to 800 or perhaps 1000 tons, because the only critical factor in such projects is the power system.. The necessary propulsion systems are already available, and the turbines currently developed, in fact, enable the construction of such machines, today. We already have the materials needed for the hulls, as well as the avionics, and there is therefore, no practical reason for not building these machines. In my opinion, further development is technologically feasible up to 2000-3000 tons, 4000 at the most. These Ekranoplanes will be able to provide transoceanic transport throughout the Pacific and Atlantic oceans. There is no need to look

any further. These machines will have the range and capacity to carry loads which are impossible to transport by aircraft : steel structures of huge dimensions, heavy bulk goods, which can be handled only by Ekranoplanes. Thank you.

Mr A.I. Maskalik, Technologies & Transport JSC, Nizhny-Novgorod, Russia

Ekranoplanes have been developed since the fifties under the direction of Alekseev, yet here are our colleagues, advocates of hydroplanes, among them Sokolansky et al., presenting the option of a hydroplane development, when since the twenties, hydroplanes have achieved only 1 m floating capacity, and there is no way to improve on this performance, for reasons known to all of us. As I have already mentioned, as early as the sixties, Ekranoplanes, in their 600 ton version, had attained a floating capacity of 3.5m. In the Russian Navy, we had a complete squadron of warships comprising amphibious vehicles, each carrying more than 100 marines, and we have acquired extensive experience in the operation of these machines at wave heights in excess of 1.5 m. Unfortunately, due to the fall of the Soviet Union, studies on the Ekranoplanes in this area were interrupted, but it would be a pity if this development option were to be abandoned, due to erroneous information supplied by hydroplane designers. This opinion has already been expressed by Mr. Masure. I would like to reiterate this point. Thank you.

Prof. C. Ciray, Middle East Technical University, Turkey

The question that you have raised, Mr. Chairman, about the future of Ekranoplanes has been in my mind during this symposium. Ekranoplanes are novel for me. I think I understood how they are operating, and what they can do. In the western world, Ekranoplanes are not very widely known or used, at least to my knowledge. If they are going to have a future, I think one of the questions that has to be answered is their economy. I have seen here in one of the presentations, an Ekranoplane of 750 tons carrying only 70 tons as a payload. So, this is 10 to 1. I think this is not a very enviable ratio. If a thrust in the direction of Ekranoplanes will take place, it should either come from military needs or from the civilian side for transportation. If it will come from the civilian side, its economy must clearly be understood and known, and must be enviable too. In these presentations, the only one related to the economy and whether it can be called an Ekranoplane or not, was something given by Dr. Fischer. Apart from this, I didn't see anything in this direction. Also I didn't see anything about the engines. The answer to this comment can be very easy, i.e., no problems for engines. However, if the idea of Ekranoplanes is coming, since they are operating near the sea – the type of engines they are using is important to be known. Are they conventional that are known, or are they different? What is the economy, the specific fuel consumption of the engines, and so forth? There are lots of questions. I wonder if taking this opportunity, some light can be thrown by our Russian and Ukrainian colleagues on this matter. Thank you very much.

Mr. H. Fischer, Fischer-Flugmechanik, Willich, Germany

This is not my answer. The acceptance of any transport system will be decided finally by the market. Without regarding the comfort-seasickness, noise level, vibration, safety and so on, the driving factor is economy. To judge the importance of the factors and to be able to compare the different systems, the so-called "Merit factor" determining the cost effectiveness. This is: "payload, X useful volume, X speed, X range, divided by purchase price, X operation cost". This factor makes the decision for selecting the best transport system depending on the given mission. If this factor is higher than with aircraft, than the

WIG craft can fill the gap between the fast but expensive air, and slow but cheap sea transport. I think this is the answer in the end, and since WIG craft with their best lift-drag ratio and the biggest useful room, they have a good chance for selected missions.

Dr. D. Stinton, Darrol Stinton Ltd, U.K.

I am an aeromarine consultant – cross-fertilizing between aircraft and marine craft design and operation. This has involved working on a number of projects for clients, one of which is a jet-propelled ram-wing designed to break the world water-speed record at a speed in excess of Mach 0.5. It makes no sense to attempt to break the record with a hull in direct contact with the water, but it might be achieved by flying in ground-effect while trailing a skeg – a fin – which remains in contact with the water. Another is a seven-seat ram-wing with the potential to be a coastguard or ambulance vehicle. Others are a 150-seater, and a fourth to carry a payload of 200 tons from the UK, transiting over the North Polar sea-ice to the South Pacific. The record-breaker project and the last are published in outline in the recent *second edition* of a textbook of mine, *The Anatomy of the Aeroplane*.

When such craft have sidewalls, or floats which act as sidewalls, they satisfy Hoerner's definition of a ram-wing – which is why I prefer that term to WIG. Low altitude flight at high speed for prolonged periods is exhausting. For many years I was a professional test pilot. While at the then Royal Aircraft Establishment at Farnborough in the early 1960s, I was involved in experimental testing at very low altitude and high speed, in connection with the TSR 2, designed to operate at Mach 1.0 at 200 ft altitude (60 m). While that is faster than an Ekranoplane, they, nevertheless, must be capable of 300 or 400 knots at even lower altitudes, to be economically useful. To cruise more slowly involves carrying around an excess of 'wetted area' (airframe surface in contact with air in relative motion). The point about flying at 400 knots and low altitude is that in rain special windscreens clearance systems are needed. I found that during tests at 565 knots and 200 ft (60 m) in heavy rain off Singapore, the water repeatedly cut the glass of a navigation light. All-weather operation is essential if Ekranoplane-type aircraft are to be cost-beneficial.

Later, during twenty years certification test flying with the Civil Aviation Authority, I also tested floatplanes and flying boats. They are useful aircraft, but they have their limitations, forced by operation from water. Yet, during the 1939 war the small single-engine Supermarine Walrus biplane flying boat, which had a crew of three, weighed about 3.5 tons and was designed to be catapulted from warships, once squeezed 9 on board. It could operate in Sea State 3, and rescued more than 1000 aircrew, both allied and enemy. The flying boat was much used along the air routes of the former British Empire during the 1930s. Had there been no World War it is possible that they would have continued in a more advanced state of development today. Even so, two four-engine Short Sunderlands (developed out of the Short Empire boats before that war) rescued the crew of the Kensington Court, torpedoed by a U-boat off southwest Ireland. One, loaded to the edge of the door, leaving no further freeboard, is said to have taken 15 miles to become airborne. What killed off the flying boat was the same war and the heavy bombers which needed hard-surface runways. Imagine attempting to load even a 2 ton bomb into a high-performance seaplane on water, to leave via a bomb-door in the keel, let alone a 10 ton bomb, designed to penetrate the reinforced concrete of a U-boat pen. The same bombers were modified to become the first airliners after the war, while airfields grew to become major terminals, like Gatwick, Heathrow and Manchester, in the UK.

A second ‘killer’ of the flying boat was the jet engine. These could be used more conveniently on long-range land planes, like the De Havilland Comet (the world’s first jet airliner) and the Boeing 707, than in seaplanes which threw up vast quantities of blister and ribbon spray, depending upon weight, altitude and sea state. Then, no seaplane designer had tried installing the engines above and behind the wings, near the tail, being developed now by Beriev, for example, in Russia.

The Wright Brothers flew their aircraft of 1903 in ground-effect, needing a catapult by means of a falling weight to accelerate it to flying speed. If someone had told those two bicycle-makers that they had started something big, they might not have believed it. Yet, within less than 100 years we have massive aeroplanes in operation, especially in Russia and in the USA. To make Ekranoplane and surface-effect machines equally successful, they must be fast, with high-order (computerised) controls. One dare not trust hand-flying by a human pilot at high speed and low altitudes for long periods. There is the ever-present danger of pilot-induced oscillations to contend with, leading to contact with the sea in a split second. It happens. For such low altitude and high-speed operations, more advanced materials are needed. Composites currently available will be dented, and shredded. I lost the wooden leading-edge of the fin of an experimental aeroplane in rain and hail at high speed. It wore away. Special metal leading-edges or other forms of reinforcement are needed. A hole in the gel coat of a composite material lets water get inside the structure of the material, with unpleasant consequences. Personally, I do not think that the IMO is adequately equipped and experienced enough yet to cope with certification of large, heavy, fast Ekranoplane/ram-wing/surface-effect aircraft for public transport operation. A mixture of airworthiness thinking is needed when carrying passengers – ten of which, in the West, weigh around 1 ton with baggage. I believe that a joint organization must be created out of ICAO (International Civil Aviation Organization) and IMO (International Maritime Organization), both of which are organs of the United Nations, if their regulation is to be practical and commercially useful.

I.G.A. B. Masure, Université d'Orléans, France

Therefore, you are saying that if the hydroplane has disappeared, it is because of WWII?

Dr. D. Stinton, Darrol Stinton Ltd, U.K.

Sadly, seaplanes did not develop because of the very large heavy land plane bomber that came with WWII. There were ideas for advanced flying boats throughout that war, appearing afterwards in response to requirements of the Brabazon Committee. First there was the ten-engine turboprop Saunders Roe Princess flying boat, which flew in the UK, but had technical problems. The same company devised the beautiful Duchess, jet-engine flying boat, but that never flew. Money, in short supply after a crippling war, went into the passenger-carrying land plane, aerodromes (which kept their feet dry!), and not specialized seaplanes.

I.G.A. B. Masure, Université d'Orléans, France

Actually, there is no longer any war, fortunately, and since there is no more war, the hydroplanes might therefore reappear.

Prof. K.V. Rozhdestvensky, State Marine Technical University, Russia

I would like to comment on a remark by Dr. Ciray related to economic efficiency of Ekranoplanes.

First of all, it has been explained by Dr. Sinitsyn that his estimates for his marine passenger Ekranoplane show that the fuel consumption can be reached of the order of 30 grams per seat per kilometer. That is the first thing. Secondly, if you say that this is a future projection, we may refer even to the history. You know that Lippisch X113 craft had a fuel consumption comparable to an automobile, which is about 20 grams per seat per kilometer. This is quite a remarkable fuel consumption. So, it is a concrete example that fuel consumption matters can be resolved when you go for efficient aerodynamic configuration. Of course, although we all have a lot of respect and give credit to naval Ekranoplane developments in Russia, nonetheless, these naval Ekranoplanes were intended to fulfill another task. This was a task of destroying rather than getting commercial viability. Economically viable aerodynamic configurations come with commercialization of Ekranoplanes and can be developed within aerodynamic concepts of the second generation.

Secondly, speaking about feasibility studies, I should say that if one estimates direct operating costs and takes into account the necessity to return invested (loaned) money, one finds that the building cost is the most important. Therefore, even if the fuel consumption is halved, this would be economy within fraction of the fuel costs, which is only a small part of total direct operating costs. So, what is really important concerns reduction of building costs, and that has been explained by Mr. Fischer, and it is also prompted by our own estimates. In particular, there was an article by Dr. Kirillovkh from the Central Hydrofoil Bureau, where the building costs for Ekranoplane were estimated to be of the order of 70% of a similar aeroplane. So 30% better as far as economic feasibility is concerned.

Among other economic factors related to feasibility, one can single out transport productivity, defined as a product of payload by speed. This is where, evidently, the Ekranoplane can even get comparable with aeroplanes. Although the speeds are lower, the capacity to carry large weights and large volumes is very important. And this has been indicated again by Mr. Fischer. Just in time and large cargo – I think this is an obvious advantage of the future applications of Ekranoplanes.

We should also take into account that you don't need runways. When thinking about costs, the price should be considered of not just a craft but that of the whole system and infrastructure.

Lastly, but not less important, - and it brings us to a comment by Mr. Stinton - is the safety issue. Note, that we are very exigent towards the Ekranoplane as far as safety is concerned, whereas all of us are flying aeroplanes, and we know once something happens, then the casualty percentage nears 100. We do not question that because we all are prepared to die once there is something. Here, where the casualty percentage will be very low (maybe of the order of several percent), there have not been casualties during the flights of the large Ekranoplanes. Of course, there were some cases where people suffered, there was some damage to health, but your runway, your airport is always beneath. To add, in the case of emergency, you do not drop with severe impact, there is a cushion underneath which one sustains, either by dynamic or static air cushion. So, I think issues of safety of the

Ekranoplanes are largely exaggerated by people who are probably not quite acquainted with the possibilities of this emerging novel means of very fast sea transportation.

Mr. D.N. Sinitzin, Technologies & Transport JSC, Nizhny-Novgorod, Russia

This is an interesting discussion, comparing hydroplanes to Ekranoplanes. Unfortunately, Russia has had a sad experience in this area. You have certainly heard of the « Komsomolets » submarine catastrophe. In this accident, more than 300 men were left floating at sea with no chance of being rescued. In fact, I can be very precise about this because I participated in the proceedings of the inquiry commission studying this case. What happened was that a storm suddenly blew up at the scene of the catastrophe and the hydroplanes flying over the men were not able to land in this area and rescue them. They threw rafts which fell 300 m away, and the men were unable to swim to reach those rafts. Under these atmospheric conditions, they perished. This is the second example of how a well developed fleet air arm in Russia, part of a military force, proved unable to save lives. I can say that if the Ekranoplane which was to the South, on the Caspian Sea, had been with the Northern Fleet at that time, all the men who were there in the water would have been saved. But it was 700 km away ! I must emphasize that there is no difference between the behavior of a LUN Ekranoplane landing on calm water and landing on the sea during a storm, as was the case. There is no difference in comfort or maneuverability resulting from the loads imposed by landing under such conditions. This is why I think that this is a good example of the real capacities of contemporary Ekranoplanes.

With respect to economic indicators, I am supposed to address questions concerning engines, which Mr. Nebylov asked me to answer. Today, the engines used in Ekranoplanes or being developed for this purpose are ordinary turbofan aircraft engines, i.e. engines used in a different class of aircraft. They are exactly the same, they require only one thing, they must be modified or slightly adapted for extended operation in the presence of sea water splash. Our experience proves that aircraft engines must be equipped with a fresh water rinsing system, in order to remove salt deposits after flight, and undergo some relatively small design improvements. So much for the engines. Now, let's talk about the economic aspects. I have already said a little bit on this subject, when I compared the technical parameters such as : carrying capacity and fuel consumption and related them to general economic issues. In my presentation, I gave tables showing the actual reality today. But if we speak about critical operating costs, it is neither fuel consumption savings, nor design weight, nor even weight-to-payload ratio which is at stake, and here I must add, that I am amazed by the figures quoted, showing that a machine weighing 700 tons carries only a 70 ton payload. As far as I remember, in fact, there is a 50% payload-to-weight index i.e. 350 tons is the weight of the craft with its fuel and the remainder is the payload. Thus, the previously given figures should be corrected.

In my opinion, the most important impact on economics does not come from the technical parameters, even if this seems strange, but from the infrastructure which accompanies the operation of Ekranoplanes. If we consider the dispatching services, air traffic control, airport maintenance, we see that these constitute the lion's share of operating expenses incurred for transporting these difficult loads. That is why I wish to particularly stress this aspect. Thank you.

I.G.A. B. Masure, Université d'Orléans, France

Before the closing remarks, I would like to thank all of you for coming, the authors and the participants and especially those of you who have presented papers.

Dr. H. Koerner, Institute of Design Aerodynamics, Germany

Everything comes to an end, and I think we had an excellent 3 1/2 days meeting, and AVT will consider to have something like this in the future. I think that it is really a fascinating topic, and we will come back to this again.

Now that we come to the closing, I would like to thank a number of people. First, I want to thank Prof. Masure, the Chairman of the Program Committee for this Symposium. He has done a tremendous amount of work, and I thank him very much for this. I would also like to thank the National Coordinator from the Netherlands, Leo Sombroek who has organized this for us in these nice surroundings of the Academy of Sciences in the Netherlands. Also, thank you very much for the social events that you have planned for us. Very many thanks to his assistant Mayke Langelaar. I would like to thank all of you who have presented papers and who have taken part in the discussion. Very cheerful thanks to our Technical Evaluator, Prof. Tulin from Santa Barbara. A very special thanks to our interpreters who have done a terrific job here, changing from one language to the other. These are Mrs. Goffinet, Mrs. Celie, Mrs. De Susbielle, Mrs. Pasco, Mr. Bartchenkov and Mr. Kinley. Furthermore, I would like to thank the technicians who brought all the videos here in time, and organized the audiovisual system. These are Mr. Yundsen, Mr. Parker and Mr. Allen. Last, but not least, I would like to thank the staff from the RTA, Research and Technology Agency in Paris. Our secretary Danielle Pelat, and a very special thanks to Jack Molloy, who has served the Fluid Dynamic Panel for 5 years and is now serving the Applied Vehicles Technology Panel. He is leaving us by the end of the year. Jack, thanks very much for the tremendous work you did for the Fluid Dynamics Panel and for the Applied Vehicles Technology Panel. With this I would like to close this meeting. At 14:00 hours, we have our Technical Advancement Exchange Forum, and everybody here is invited to attend this meeting. In this meeting, we will discuss the future activities of the AVT Panel.

REPORT DOCUMENTATION PAGE			
1. Recipient's Reference	2. Originator's References	3. Further Reference	4. Security Classification of Document
	RTO-MP-15 AC/323(AVT)TP/9	ISBN 92-837-0004-X	UNCLASSIFIED/ UNLIMITED
5. Originator	Research and Technology Organization North Atlantic Treaty Organization BP 25, 7 rue Ancelle, F-92201 Neuilly-sur-Seine Cedex, France		
6. Title	Fluid Dynamics Problems of Vehicles Operating Near or in the Air-Sea Interface		
7. Presented at/sponsored by	The RTO Applied Vehicle Technology Panel (AVT) Symposium (organised by the former AGARD Fluid Dynamics Panel), held in Amsterdam, The Netherlands, 5-8 October 1998.		
8. Author(s)/Editor(s)	Multiple		9. Date February 1999
10. Author's/Editor's Address	Multiple		11. Pages 380
12. Distribution Statement	There are no restrictions on the distribution of this document. Information about the availability of this and other RTO unclassified publications is given on the back cover.		
13. Keywords/Descriptors	Fluid dynamics Air water interactions Aerodynamics Surface ships Three dimensional flow Boundary layer separation Ground effect Drag Reduction Shipboard landing Computational fluid dynamics Wakes Surface effect ships Hydrofoils Hydrofoil craft Ground effect machines Hydrodynamics		
14. Abstract	<p>The papers prepared for the RTO Applied Vehicle Technology (AVT) Symposium on "Fluid Dynamics Problems of Vehicles Operating Near or in the Air-Sea Interface" which was held 5-8 October 1998 in Amsterdam, The Netherlands, are contained in this report. In addition, a Technical Evaluator's Report aimed at assessing the success of the Symposium in meeting its objectives, and an edited transcript of the General Discussion held at the end of the Symposium are also included.</p> <p>In addition to presentations from the NATO Countries, this Symposium included several presentations by Russian and Ukrainian authors. In total, 30 papers were presented during sessions on the following subjects:</p> <ul style="list-style-type: none"> • Aerodynamics and Flight Dynamics around Ships • Stabilization and Control Techniques for Ships • Non-Classical Aircraft Flying Near the Air-Sea Interface 		

NORTH ATLANTIC TREATY ORGANIZATION

RESEARCH AND TECHNOLOGY ORGANIZATION
 BP 25 • 7 RUE ANCELLE
 F-92201 NEUILLY-SUR-SEINE CEDEX • FRANCE
 Télécopie 0(1)55.61.22.99 • Télex 610 176

DIFFUSION DES PUBLICATIONS
RTO NON CLASSIFIEES

L'Organisation pour la recherche et la technologie de l'OTAN (RTO), détient un stock limité de certaines de ses publications récentes, ainsi que de celles de l'ancien AGARD (Groupe consultatif pour la recherche et les réalisations aérospatiales de l'OTAN). Celles-ci pourront éventuellement être obtenues sous forme de copie papier. Pour de plus amples renseignements concernant l'achat de ces ouvrages, adressez-vous par lettre ou par télécopie à l'adresse indiquée ci-dessus. Veuillez ne pas téléphoner.

Des exemplaires supplémentaires peuvent parfois être obtenus auprès des centres nationaux de distribution indiqués ci-dessous. Si vous souhaitez recevoir toutes les publications de la RTO, ou simplement celles qui concernent certains Panels, vous pouvez demander d'être inclus sur la liste d'envoi de l'un de ces centres.

Les publications de la RTO et de l'AGARD sont en vente auprès des agences de vente indiquées ci-dessous, sous forme de photocopie ou de microfiche. Certains originaux peuvent également être obtenus auprès de CASI.

CENTRES DE DIFFUSION NATIONAUX**ALLEMAGNE**

Fachinformationszentrum Karlsruhe
 D-76344 Eggenstein-Leopoldshafen 2

BELGIQUE

Coordinateur RTO - VSL/RTO
 Etat-Major de la Force Aérienne
 Quartier Reine Elisabeth
 Rue d'Evere, B-1140 Bruxelles

CANADA

Directeur - Gestion de l'information
 (Recherche et développement) - DRDGI 3
 Ministère de la Défense nationale
 Ottawa, Ontario K1A 0K2

DANEMARK

Danish Defence Research Establishment
 Ryvangs Allé 1
 P.O. Box 2715
 DK-2100 Copenhagen Ø

ESPAGNE

INTA (RTO/AGARD Publications)
 Carretera de Torrejón a Ajalvir, Pk.4
 28850 Torrejón de Ardoz - Madrid

ETATS-UNIS

NASA Center for AeroSpace Information (CASI)
 Parkway Center, 7121 Standard Drive
 Hanover, MD 21076-1320

FRANCE

O.N.E.R.A. (Direction)
 29, Avenue de la Division Leclerc
 92322 Châtillon Cedex

GRECE

Hellenic Air Force
 Air War College
 Scientific and Technical Library
 Dekelia Air Force Base
 Dekelia, Athens TGA 1010

NASA Center for AeroSpace Information (CASI)
 Parkway Center
 7121 Standard Drive
 Hanover, MD 21076-1320
 Etats-Unis

ISLANDE

Director of Aviation
 c/o Flugrad
 Reykjavik

ITALIE

Aeronautica Militare
 Ufficio Stralcio RTO/AGARD
 Aeroporto Pratica di Mare
 00040 Pomezia (Roma)

LUXEMBOURG

Voir Belgique

NORVEGE

Norwegian Defence Research Establishment
 Attn: Biblioteket
 P.O. Box 25
 N-2007 Kjeller

PAYS-BAS

NDRCC
 DGM/DWOO
 P.O. Box 20701
 2500 ES Den Haag
 The Netherlands

PORTUGAL

Estado Maior da Força Aérea
 SDFA - Centro de Documentação
 Alfragide
 P-2720 Amadora

ROYAUME-UNI

Defence Research Information Centre
 Kentigern House
 65 Brown Street
 Glasgow G2 8EX

TURQUIE

Millî Savunma Başkanlığı (MSB)
 ARGE Dairesi Başkanlığı (MSB)
 06650 Bakanlıklar - Ankara

AGENCES DE VENTE

The British Library Document Supply Centre
 Boston Spa, Wetherby
 West Yorkshire LS23 7BQ
 Royaume-Uni

Canada Institute for Scientific and Technical Information (CISTI)
 National Research Council
 Document Delivery,
 Montreal Road, Building M-55
 Ottawa K1A 0S2
 Canada

Les demandes de documents RTO ou AGARD doivent comporter la dénomination "RTO" ou "AGARD" selon le cas, suivie du numéro de série (par exemple AGARD-AG-315). Des informations analogues, telles que le titre et la date de publication sont souhaitables. Des références bibliographiques complètes ainsi que des résumés des publications RTO et AGARD figurent dans les journaux suivants:

Scientific and Technical Aerospace Reports (STAR)

STAR peut être consulté en ligne au localisateur de ressources uniformes (URL) suivant:

<http://www.sti.nasa.gov/Pubs/star/Star.html>

STAR est édité par CASI dans le cadre du programme NASA d'information scientifique et technique (STI)

STI Program Office, MS 157A

NASA Langley Research Center

Hampton, Virginia 23681-0001

Etats-Unis

Government Reports Announcements & Index (GRA&I)

publié par le National Technical Information Service
 Springfield

Virginia 2216

Etats-Unis

(accessible également en mode interactif dans la base de données bibliographiques en ligne du NTIS, et sur CD-ROM)



Imprimé par le Groupe Communication Canada Inc.

(membre de la Corporation St-Joseph)

45, boul. Sacré-Cœur, Hull (Québec), Canada K1A 0S7



RESEARCH AND TECHNOLOGY ORGANIZATION
BP 25 • 7 RUE ANCELLE
F-92201 NEUILLY-SUR-SEINE CEDEX • FRANCE
Telex 0(1)55.61.22.99 • Telex 610 176

**DISTRIBUTION OF UNCLASSIFIED
RTO PUBLICATIONS**

NATO's Research and Technology Organization (RTO) holds limited quantities of some of its recent publications and those of the former AGARD (Advisory Group for Aerospace Research & Development of NATO), and these may be available for purchase in hard copy form. For more information, write or send a telefax to the address given above. Please do not telephone.

Further copies are sometimes available from the National Distribution Centres listed below. If you wish to receive all RTO publications, or just those relating to one or more specific RTO Panels, they may be willing to include you (or your organisation) in their distribution.

RTO and AGARD publications may be purchased from the Sales Agencies listed below, in photocopy or microfiche form. Original copies of some publications may be available from CASI.

NATIONAL DISTRIBUTION CENTRES

BELGIUM

Coordonateur RTO - VSL/RTO
Etat-Major de la Force Aérienne
Quartier Reine Elisabeth
Rue d'Evere, B-1140 Bruxelles

CANADA

Director Research & Development
Information Management - DRDIM 3
Dept of National Defence
Ottawa, Ontario K1A 0K2

DENMARK

Danish Defence Research Establishment
Ryvangs Allé 1
P.O. Box 2715
DK-2100 Copenhagen Ø

FRANCE

O.N.E.R.A. (Direction)
29 Avenue de la Division Leclerc
92322 Châtillon Cedex

GERMANY

Fachinformationszentrum Karlsruhe
D-76344 Eggenstein-Leopoldshafen 2

GREECE

Hellenic Air Force
Air War College
Scientific and Technical Library
Dekelia Air Force Base
Dekelia, Athens TGA 1010

ICELAND

Director of Aviation
c/o Flugrad
Reykjavik

ITALY

Aeronautica Militare
Ufficio Stralcio RTO/AGARD
Aeroporto Pratica di Mare
00040 Pomezia (Roma)

LUXEMBOURG

See Belgium

NETHERLANDS

NDRCC
DGM/DWOO
P.O. Box 20701
2500 ES Den Haag
The Netherlands

NORWAY

Norwegian Defence Research Establishment
Attn: Biblioteket
P.O. Box 25
N-2007 Kjeller

PORTUGAL

Estado Maior da Força Aérea
SDFA - Centro de Documentação
Alfragide
P-2720 Amadora

SPAIN

INTA (RTO/AGARD Publications)
Carretera de Torrejón a Ajalvir, Pk.4
28850 Torrejón de Ardoz - Madrid

TURKEY

Milli Savunma Başkanlığı (MSB)
ARGE Dairesi Başkanlığı (MSB)
06650 Bakanlıklar - Ankara

UNITED KINGDOM

Defence Research Information Centre
Kentigern House
65 Brown Street
Glasgow G2 8EX

UNITED STATES

NASA Center for AeroSpace Information (CASI)
Parkway Center, 7121 Standard Drive
Hanover, MD 21076-1320

**NASA Center for AeroSpace
Information (CASI)**

Parkway Center
7121 Standard Drive
Hanover, MD 21076-1320
United States

SALES AGENCIES

The British Library Document

Supply Centre
Boston Spa, Wetherby
West Yorkshire LS23 7BQ
United Kingdom

**Canada Institute for Scientific and
Technical Information (CISTI)**

National Research Council
Document Delivery,
Montreal Road, Building M-55
Ottawa K1A 0S2
Canada

Requests for RTO or AGARD documents should include the word 'RTO' or 'AGARD', as appropriate, followed by the serial number (for example AGARD-AG-315). Collateral information such as title and publication date is desirable. Full bibliographical references and abstracts of RTO and AGARD publications are given in the following journals:

Scientific and Technical Aerospace Reports (STAR)

STAR is available on-line at the following uniform
resource locator:
<http://www.sti.nasa.gov/Pubs/star/Star.html>
STAR is published by CASI for the NASA Scientific
and Technical Information (STI) Program
STI Program Office, MS 157A
NASA Langley Research Center
Hampton, Virginia 23681-0001
United States

Government Reports Announcements & Index (GRA&I)

published by the National Technical Information Service
Springfield
Virginia 22161
United States
(also available online in the NTIS Bibliographic
Database or on CD-ROM)



Printed by Canada Communication Group Inc.
(A St. Joseph Corporation Company)
45 Sacré-Cœur Blvd., Hull (Québec), Canada K1A 0S7